DESIGN OPTIMIZATION OF HEAVY MOTOR VEHICLE CHASSIS

by

ABHISHEK AGARWAL

submitted in accordance with the requirements for
the degree of

DOCTOR OF PHILOSOPHY

in the subject

ENGINEERING

at the

UNIVERSITY OF SOUTH AFRICA

SUPERVISOR: DR. L. MTHEMBU

March 2022

DECLARATION

Name: Abhishek Agarwal

Student number: 68983832

Degree: Doctor of Philosophy in Engineering (90040 SET)

Exact wording of the title of the thesis as appearing on the electronic copy submitted for examination:

DESIGN OPTIMIZATION OF HEAVY MOTOR VEHICLE CHASSIS

I declare that the above thesis is my own work and that all the sources that I have used or quoted have been indicated and acknowledged by means of complete references.

I further declare that I submitted the thesis to originality checking software and that it falls within the accepted requirements for originality.

I further declare that I have not previously submitted this work, or part of it, for examination at Unisa for another qualification or at any other higher education institution.

(The thesis will not be examined unless this statement has been submitted.)

27/03 2022

_____   _____

SIGNATURE   DATE

ACKNOWLEDGEMENT

(Abhishek Agarwal)

LIST OF TABLES

LIST OF FIGURES

TABLE OF CONTENTS

ABSTRACT

A vehicle chassis is one of the most vital components of an automobile. It supports various components like the vehicle body, engine, and suspension and transmission system. The purpose of heavy-duty motor vehicles (HMV) is to carry large loads, and this is often in harsh conditions. Therefore, the chassis design should withstand undesired static and dynamic loads experienced by the vehicle when in operation. Identifying and improving the properties of the chassis that affect the field performance of these vehicles is the key challenge faced by HMV designers.

In this work, the chassis considered for improvement is the steel (St52E) TATA 1612 truck. The main measures identified for a compliant chassis are; satisfactory equivalent stresses, deformation, strain energy, safety factor and weight reduction. The chassis properties identified for improvement are the geometry (dimensions and cross-sections) and chassis material. In terms of geometry, different chassis member cross-sections (square, C, I and T) were studied under static loading. The above geometry studies are then adopted on a number of proposed metal matrix composite (MMC) materials. These are Graphite Al GA 7-230, P100/6061 and Al 6092/SiC/17.5P. In order to systematically improve these chassis variable properties, finite element model (FEM), modal analysis and Taguchi response surface methods (RSM) are used. Utilizing Taguchi design of experiments (DOE), the optimization design points are generated. The methods used are the central composite design (CCD), optimal space fill (OSF), Behnken-Box (B-B), Sparse Grid Initialization (SGI) and the Latin Hypercube (LH) design schemes.

The I and T cross sections are found not to be compliant with acceptable industry requirements for application on HMV chassis. The Graphite Al GA 7-230 material, using the square profile, shows the lowest deformation of 78.33 mm and Al 6092/SiC/17.5p shows a maximum deformation of 694.83 mm under static loading. The optimization results show that the percentage of weight reduction obtained is 5.37% for the St52E material using the CCD scheme. By using P100/6061 Al and Al 6092/SiC/17.5P materials, the chassis weight reduction is 68.15% and 64.3% lower respectively over the standard St52E.

Keywords: Heavy Motor Vehicle; Chassis; Modelling; Optimization; Structural Steel; Metal Matrix Composites; Stress; Deformation; Solid Mass; Modal Analysis.

JOURNAL PUBLICATIONS/ CONFERENCE PROCEEDINGS/BOOK CHAPTERS (SEE APPENDIX B FOR SHORT SUMMARY)

1. A. Agarwal, L. Mthembu (2021). **Numerical Modelling and Multi-Objective Optimization Analysis of Heavy Vehicle Chassis**. Processes, 9(11), 2028. DOI: http://dx.doi.org/10.3390/pr9112028. **SCOPUS, SCIE (IF 3.352)**

2. A. Agarwal, L. Mthembu (2021). **Weight Optimization of Heavy-Duty Truck Chassis by Optimal Space Fill Design Using Light Weight Graphite Al GA 7-230 MMC**. Materials Today: Proceedings. DOI:10.1016/j.matpr.2021.11.053. **SCOPUS, CPCI**

3. A. Agarwal, L. Mthembu (2021). **Modelling And FE Simulation of HVC Using Multi-Objective Response-Surface Optimization Techniques**. Revue des Composites et des Matériaux Avancés-Journal of Composite and Advanced Materials, Vol. 31, No. 6, pp. 307-315. DOI: https://doi.org/10.18280/rcma.310601. **SCOPUS, ESCI**

4. A. Agarwal, L. Mthembu (2022). **Design & Response surface Optimization of Heavy Motor Vehicle Chassis Using P100/6061 Al MMC**. Lecture Notes in Mechanical Engineering, Springer Singapore. DOI: https://doi.org/10.1007/978-981-19-0244-4_1. **SCOPUS, CPCI**

5. A. Agarwal, L. Mthembu (2022). **FE Design Analysis and Optimization of Heavy-Duty Truck Chassis Using Sparse Grid Initialization Technique**. Materials Today: Proceedings, ISSN 2214-7853. DOI: https://doi.org/10.1016/j.matpr.2022.01.471. **SCOPUS, CPCI**

6. A. Agarwal, L. Mthembu (2022), **Structural Analysis and Optimization of Heavy Vehicle Chassis Using Aluminium P100/6061 Al and Al GA 7-230 MMC**. Processes, 10, 320. DOI: https://doi.org/10.3390/pr10020320. **SCOPUS, SCIE (IF 3.352)**

7. A. Agarwal, L. Mthembu (2022). **Structural Analysis and Weight Optimization of Automotive Chassis by Latin Hypercube Sampling Using Metal Matrix Composites.** Materials Today: Proceedings, ISSN 2214-7853. DOI: https://doi.org/10.1016/j.matpr.2022.02.059. **SCOPUS, CPCI**

8. A. Agarwal, L. Mthembu (2022**). Investigation of dynamic factors in different Sections of HVC by Static and Free Vibration Modal Analysis**; Annales de Chimie - Science des Matériaux, Vol. 46, No. 2, pp. 75-84. DOI: https://doi.org/10.18280/acsm.460203 **SCOPUS, ESCI**

9. A. Agarwal, L. Mthembu (2022). **FE Structural Analysis and Experimental Investigation of HMV Chassis**. Emerging Trends in Mechanical and Industrial Engineering. Lecture Notes in Mechanical Engineering, Springer Singapore DOI: 10.1007/978-981-19-6945-4_70. **SCOPUS, ESCI**

This chapter presents the introduction of the work and the background importance of the topic. It also includes the problem statement, objectives of the research along with an outline of the thesis chapter layout.

1.1 The Chassis and Global Market

The chassis is the internal frame that continues to support all body parts and integrates the functions of all vehicles in various systems. Therefore, it is one of the most important & one of the highly valued components of the global automotive industry, whether it is used for defence, transportation, mining, domestic, or any other purpose. According to a report [1], the global market for automotive chassis, which was previously anticipated to be worth US$49.2 billion in 2020, is expected to increase to US$74.6 billion by 2027, expanding at a CAGR of 6.1 percent from 2020 to 2027 [1]. The primary raw materials used to build the vehicle chassis system include carbon steel, aluminum alloys, etc. The demand for fuel-efficient, lightweight chassis structures is growing as a result of fluctuating fuel prices and supply, as well as unpredictability in the world economy [2]. Figure 1 shows the top impacting factors in the global automotive chassis industry considering the period 2017-2025.
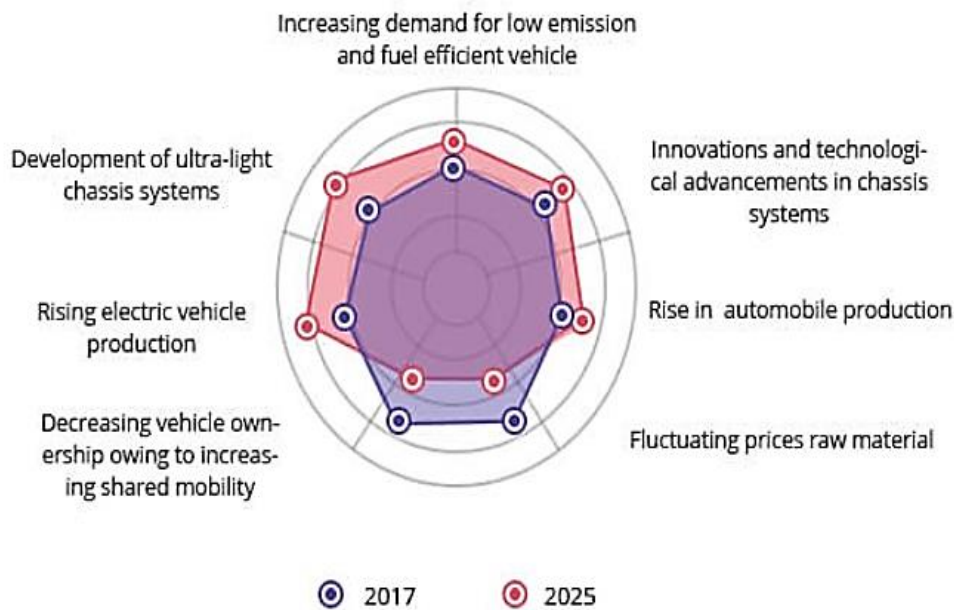
Figure 1.1: Top impacting factors in the global automotive chassis industry [2]

1.2 Demand for fuel-efficient, light weight vehicle chassis

Governments in many nations have implemented strict pollution control regulations, increasing the demand for low-emission and fuel-efficient automobiles [3]. A vehicle's weight affects the amount of fuel it burns and the number of hazardous gases it emits from its exhaust. As a result, manufacturing vehicles with lightweight chassis systems will lower the vehicle's weight and increase fuel efficiency.

1.2.1 Heavy motor vehicle Industry

A heavy motor vehicle, such as a truck, is primarily designed to carry a heavy load, which includes the axles, suspension, power train, cab, trailer, payload, passenger, and so on. The primary goal of the truck manufacturing industry is to create vehicles with greater payload capacity. This automotive market sector is very interested in designing lightweight chassis using various materials discovered that are light in weight and can also provide better strength than the conventionally used steel without affecting the safety and overall performance of the vehicle.

1.2.2 Design and testing requirements

The design of a vehicle structure is of fundamental importance to vehicle performance, and the structure plays an essential role in the vehicle's reliability. Several designs and testing methods exist to ensure that chassis structures are appropriately designed and developed to the required standard. Historically, chassis structure testing has been done experimentally, with the structure being rigorously tested until it is destroyed. Most chassis structural integrity testing can now be performed through simulation due to the rapid advancement of computer and simulation technology. Computational design and analysis produce faster results at a lower cost than experimental analysis.

The current work focuses on modeling and optimizing a heavy motor vehicle chassis with various constraints using finite element techniques while taking into account various materials and methods, followed by a sensitivity analysis for weight reduction.

1.3 Problem Statement

The requirement for high strength-to-weight ratio designs of heavy-duty motor vehicles (HMV) is a continuous enterprise in the HMV industry. This requirement is critical because it influences the structural dynamics, handling and fuel consumption (all summarized by a word: performance) of the vehicle. For vehicle designers to improve the strength, weight, and performance of the vehicle, there is a need to study the properties/variables that affect these desired outputs.

In a heavy motor vehicle (HMV), the main component that affects the strength-to-weight ratio is its chassis. The chassis considered here, consists mainly of longitudinal and lateral members. The geometry (dimensions, cross-sectional shape) and locations of these members can have significant effects on the stresses and deformation experienced by the vehicle.

Another important factor is the choice of chassis material. This can have a very significant influence on the overall weight of the vehicle (affecting handling dynamics) and subsequently on its fuel consumption and carbon emissions [4]. This is not only a concern for the vehicle operator (in terms of running costs) but pollutant emissions have become an increasingly important environmental consideration. Thus, reducing the mass of the vehicle by changing the material from steel to newer composites will be an important research development.

The broad research objectives are presented in the next section.

1.4 Broad objective of the Study

The primary goal of this study is to develop a computational approach to assisting engineers in designing an optimal heavy vehicle chassis (HVC). The optimality of the design is, in this research, defined as achieving satisfactory equivalent stresses, deformation, strain energy, safety factor and weight reduction. As this work is a computational study, this goal is to be achieved by using a software together with a number of optimization techniques (which will be discussed in chapter 3). These techniques will take as inputs - the geometry, dimensions, and material specifications.

The following specific objective are to be achieved in order to meet our project goal.

1.4.1 Specific objectives

a) To computationally model the chassis in CAD for all considered settings.
b) To identify the optimization variables.
c) To identify the geometry to be optimized
d) To identify the optimal chassis material
e) To study the resultant free vibration modal analysis of the optimized chassis
f) To calculate the output variables and present them (RSM).
g) To calculate the stress experienced by the chassis
h) To calculate the chassis deformation
i) To calculate the mass of the chassis
j) To run the different optimization methods on the chassis.
k) Finally, compare the results of the different optimization methods.

1.5 Research Hypothesis

The performance of heavy vehicle chassis can be significantly improved by varying the main chassis member geometry (both shape and dimension) and adopting metal-matrix composites as the chassis material.

The main research questions are then:

- How does one optimally vary the geometry of an HMV chassis and
- What is the best way of performing this optimization and
- What weight reduction material choices are available and practical for HMV chassis?

1.6 Research Justification

Improved heavy vehicle (HMV) chassis performance is an ongoing challenge in that industry. Competition for transporting goods by the airline, rail and smaller trucking industry is a constant threat to the heavy trucking industry [5]. Thus, there is a need for constant design improvements of these vehicles.

Passenger vehicles (and to some extent the light trucking industry) and airlines have changed and adopted new materials available [6]. HMV chassis designs using steel is a well-understood problem [7], but incorporating metal composites in these designs is not [8]. Although there are many studies on metal matrix composites (MMC) in the material science field [9], there is very limited research on its applicability to HMV chassis design. The mechanical behaviour that MMCs bring to the chassis design industry needs to be better understood. Engineering wise it is prudent to start research with a fundamental computational study of the proposed ideas. In mechanics, these would be static structural simulations. Once the geometric and material behaviours have been understood in this setting the next step would then be to invest in research laboratories for more advanced work, e, g, real world dynamic simulations and tests of these.

Besides chassis material enhancements, the identification of the other actors that affect the dynamics and performance of truck chassis need to be distilled. Chassis layouts vary depending on the use of the vehicle (See chapter 2); thus, this project seeks to develop a systematic study of how a given chassis (TATA 1612) will behave under a variety of modifications. To this end, this research has identified that the geometry and certain locations on the chassis are very crucial factors to be studied and improved. Having multiple variables that affect performance can lead to a combinatorial type of problem. This is negated by using a number of different optimization techniques to try and find the best variables to improve. This exercise can be a very long and iterative process; thus, some limitations need to be defined in order to bound areas where one can make novel contributions.

The next sub-section presents the scope and limitations of the study.

1.7 Limitations & Scope:

- The work is limited to ladder-type chassis (TATA 1612).
- Static structural analysis is conducted on chassis which is limited to static loading conditions based on smooth road conditions.
- Free vibration analysis is conducted on chassis, the effect of significant external road irregularities on vibration characteristics are not considered.

- Experimental testing conducted on St52E chassis is limited to 4 points (Appendix A) bending conditions. The effect of dynamic loading conditions is neglected.
- Six Sigma analysis is conducted on chassis considering two variables as the solver was unable to compute results with the higher number of variables due to failed convergence.
- Finite Element Method techniques are used to optimize and structurally analyse MMC material chassis.
- The fatigue life analysis requires data on alternating stress versus the number of cycles for metal matrix composites that are not currently available from the industry.
- The work does not compare modelling results from multiple software platforms but proposes a particular approach to optimizing an HMV chassis. The proposed approach is not platform-dependent.

1.8 Novelty / Significance of the Research

The principle of chassis optimization and the use of a few materials has previously been reported in the literature, however, the research presented in this thesis is novel in the aspects presented below:

1.   Optimization Techniques: In the automotive industry, no work (to the author's knowledge) has been done in improving the design of an existing chassis using advanced optimization techniques as considered in this work.

2.   Material consideration: There is no report/ literature (to the author's knowledge) on the optimization of heavy motor vehicle (HMV) chassis that includes the analysis by using the different metal matrix composites (as considered here).

3.   Comprehensive static stress and pre-stressed modal analysis of the HMV chassis model is provided by considering the individual effect of dimensions of lateral members and different cross-section profiles. Laboratory tests on these are provided.

4.   Successful application of the response-surface optimization techniques in the improvement of the weight of the HMV chassis.

5.   The significance of the work is appreciated by the industry as can be seen from the feedback reports and is supported in line with the required R & D approach in the automotive field as considered in this study.

The publications emanating from this thesis have been listed under the Journal publications/Conference Proceedings/Book Chapters on page xxiv.

In the next sub-section, the thesis outline is presented.

1.9 Thesis Layout

Chapter 1

Introduces the research area and background context for the current study. This chapter includes the problem statement, the research objectives, the research hypothesis, limitations and the novel contributions.

Chapter 2

Summarizes many benchmarks literature review that is relevant to this research study especially bringing out where the gaps in the research are and helps to fill in one or more of these gaps.

Chapter 3

Outlines the methodology part, especially the material consideration, data collection, and technical approach which are most suitable to address the research objectives discussed earlier.

Chapter 4

Investigates the findings and clearly outlines the results and validation of the data analyses using necessary figures, tables, and charts to support the presentation of results involving 9 sub-chapters.

Chapter 5

Concludes the summary of key findings, a discussion, and references in the context of potential research direction for the engineering issues.

Appendix A

Presents detailed information on material testing, manufacturing, and experimental testing of heavy motor vehicle chassis to determine equivalent-stress, and deformation.

Appendix B

Presents the publication outputs and a short discussion of the results published.

Appendix C

Presents the external feedback reports from the industry.

1.10 Chapter Summary

The chapter has presented the introduction and necessary background of the global automotive chassis market. The thesis problem statement and the main objectives of the work have been described. The research hypothesis and research justification have been formulated. Next, the scope that is not covered by the research is presented. Lastly, the novel aspects of the research are presented.

The next chapter presents the enhanced literature review in line with the objectives of the work.

CHAPTER 2

LITERATURE REVIEW

This chapter summarizes details of chassis structure, functions, types, and the literature that is relevant to the objectives of this research study. The main areas of research in terms of chassis and especially bring out where the gaps in the research are highlighted.

2.1 Chassis Structures

The chassis is an important part of a vehicle as it supports many components like the suspension system, wheels, and engine. Both static and dynamic loads should be supported by the chassis material and design. In addition to these loads, the chassis is subjected to torsional and shock loads, which vary depending on the driving circumstances. After forces are released, the chassis' stiffness should be sufficient to allow it to restore its previous shape.

2.2 Commercial Vehicle Chassis

Ladder chassis are commonly found in heavy commercial vehicles such as trucks, trailers, and semi-trailers. They typically consist of two parallel beams parallel to the longitudinal axis of the frame and a number of transverse beams positioned laterally between the beams. Therefore, the axles, as well as the power plant, the driver's cab, and the platform or other structures are easy to repair. The side parts of the lead frames in ladder chassis are usually open channels or an I section. Although an I-section is very effective at providing bending stiffness, manufacturers prefer the channel section's side elements.

Because of the cost and the simple construction. Crossbars often consist of rectangular hollow profiles, channels, cylinders, or I-shaped profiles. Rectangular hollow profiles offer effective bending and torsional rigidity but can lead to an overall high torsional rigidity of the frame. The most flexible frame construction would have cross-sectional elements with an open section attached to the dies of the side elements by end plates.

Chassis have molded elements that serve as engine mounts, cabin mounts, also elements whose depth is reduced in the central area so as not to have the gear arrangements. There are a wide variety of connection designs between the cross members and the side members, both in terms of the connection configuration and the method of attaching. Joints can strongly influence the frame's torsional rigidity and lead to the development of high-stress concentrations. The desired torsional stiffness of a frame mustn't put very heavy loads on the joints, which can lead to it breaking. Welded connections are more difficult and therefore more expensive to manufacture. Although screws and rivets in the joints are the simplest methods of fastening, they can cause stress concentration in the area of the holes through which they run.

2.3 Types of Chassis

2.3.1 Ladder Frames

It is made up of two symmetrical beams that cross each other along the length of the vehicle [10]as shown in figure 2.1. The torsional stiffness of the chassis is very low. This type of chassis is used in land rovers, light commercial vehicles, and vans due to its adaptability for different types of vehicle bodies [11]. The ladder chassis contains a few basic pieces that can be used in the building process.

Figure 2.1: A ladder chassis frame [10]

• Channel Segment — This is a C-shaped section with excellent bending resistance.

• Tubular Segment - This is a circular tube section that has good torsion resistance.

• Box Segment – This is a rectangular-shaped section that offers good bending and torsion resistance.

The ladder frame is cost-effective and possesses low torsional stiffness with good adaptability to accommodate different body shapes. The only limitation is ladder frame has low torsional rigidity as compared to other chassis frames when dealing with vertical loads or bumps.

2.3.2 Backbone tube Chassis:

This chassis has rectangular cross-sections and connects to the front and rear suspension attachments of the vehicle. This design was first developed in 1923 by Hans Edwina who was the chief designer at Tatra heavy trucks. He further enhanced this design with the 6*4 model Tatra 26, which had great off-road abilities. Some of the vehicles which are using this chassis design are Europa, Lotus E spirit and Skoda, etc" [12]. The Backbone tube chassis frame is shown in figure 2.2.
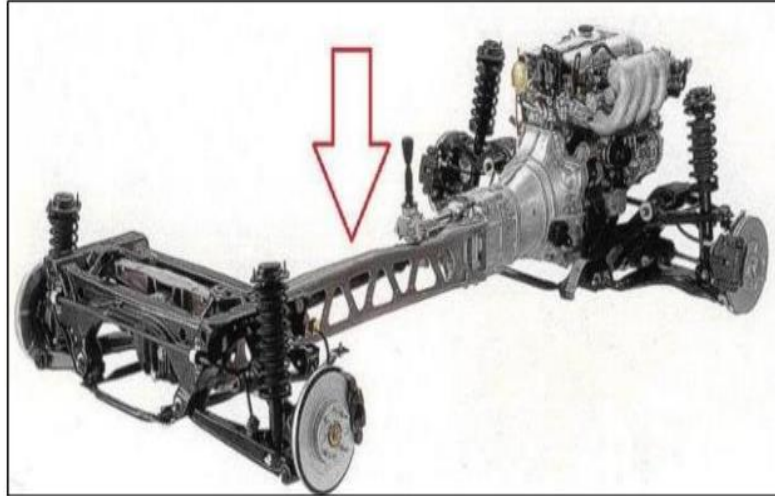
Figure 2.2: Backbone tube chassis frame [12]

2.3.3 X- Frame or Cruciform Frame

These types of chassis frames were used in the late '50s by General Motors. The bodywork and chassis were integrated to reduce the overall vehicle weight as shown in figure 2.3. This type of frame lacked side rails which compromised protection from bumps and collisions. Due to this reason the X-frame chassis failed and led to the development of a perimeter frame [11].

Figure 2.3: X frame chassis frame [12]

2.3.4. Perimeter Frame

The perimeter frame tries to overcome the disadvantages of the X-frame design. It is mainly used in motorcycles of different shapes and sizes. The design ensures high stability and rigidity between high-stress components of the motorcycle. The perimeter frame is visible for use on the Bajaj Pulsar 200 Ns motorcycle in which the engine is mounted in the center with a metal frame around it as shown in figure 2.4 [13]. The load exerted by the shaft increases the stiffness

of the chassis which causes centralization and thus improves the driving characteristics of the vehicle [14].
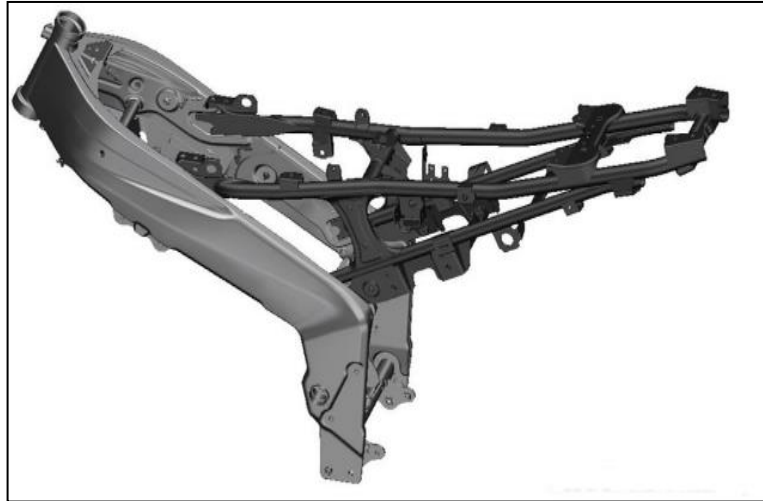
Figure 2.4: Perimeter Frame [13]

2.3.5 Space Frame:

A three-dimensional frame is another name for a space frame. Its name comes from the fact that, unlike other chassis types, which are essentially two-dimensional and only have length and width in this construction, the third dimension has been considered. The 3D frame was able to boost the entire design's flexural strength and stiffness due to the depth of the frame [11]. The 3D space frame is shown in figure 2.5.
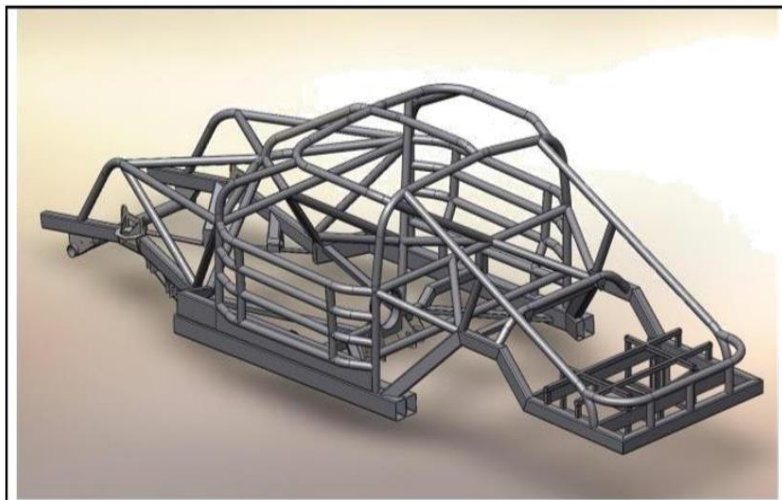
Figure 2.5: Space Frame [11]

These chassis were mostly utilized for high-performance vehicles, such as sports racing cars. Audi R8, Ferrari 360, Lamborghini Gallardo, Mercedes-Benz SLS AMT, and Pontiac Fiero are all instances of space chassis.

2.3.6 Uni-body Frame

The chassis and body are combined into a single solid construction in this style of frame, as seen in figure 2.6. This results in the entire vehicle behaving as a single load-bearing unit that handles all load acting on it.

.

Figure 2.6: Uni-body Frame [15]

Integrated bodywork for wheeled vehicles is made by molding or joining entire parts in one piece, welding metal plates and other components together, or by combining all of these techniques.

The outer skin and cladding of the car are designed as rib supports, bull heads, and box profiles to strengthen the entire body. The regulations for vehicle safety became more stringent in the '90s and thus compelled automobile manufacturers to develop more rigid frames.

In the next sub-section, the typical loads experienced by a chassis will be discussed.

2.4 Load Types: Loads acting on the Chassis

The different types of loads acting on chassis frame are:

1. Vertical bending of side components due to vehicle and passenger weight
2. Induced longitudinal twisting when vehicles hit a bump.
3. The loads operate, creating lateral bending of the side components when the vehicle turns.
4. Vertical bending of side members caused by braking torque and engine torque.
5. Sudden impact load that causes the structure to collapse due to collision.

Figure 2.7 shows torsion and moment acting on ladder chassis due to reaction load from the ground i.e., R_f for the front and R_r for the rear.
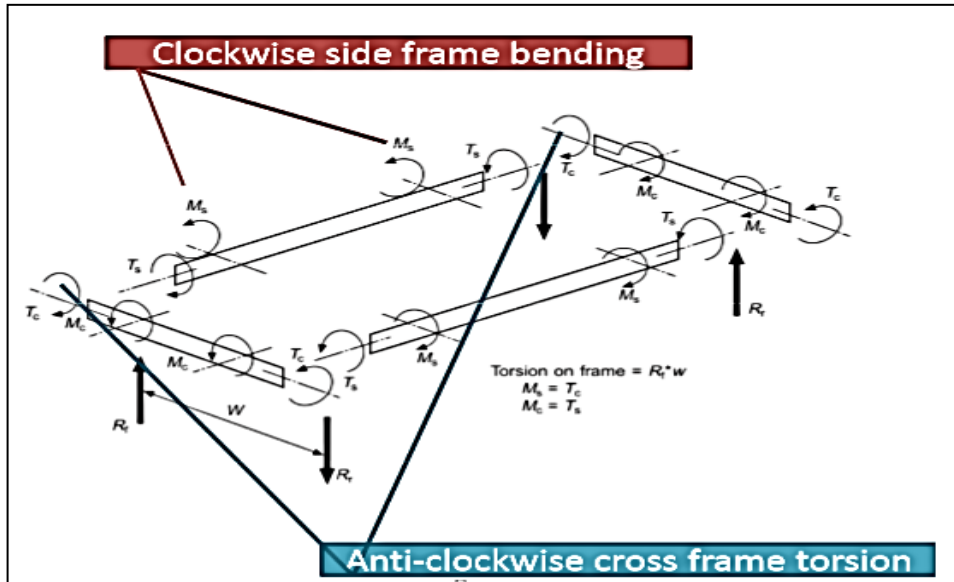
Figure 2.7 Torsion and moment acting on the ladder frame [16]

For the given frame, the torsion in cross members is reacted by bending the in-side frame and bending in cross members is reacted by torsion in-side frames.

In the next sub-section, the material choices typically used for vehicle chassis are discussed.

2.5 Chassis Material

The choice of chassis material is influenced by a number of factors, including weight, cost, safety, recyclability, and life cycle. Some of the following factors are client requirements, while others are the outcome of laws and regulations. The following are the most commonly used chassis materials:

2.5.1 Steel

Steel is the first choice for frame construction. Steel's performance characteristics, such as strength and rigidity, have improved in recent decades. The steel is economical, light, and possesses good crash absorbing characteristics which makes it suitable for application in chassis structures [17], [18]

2.5.2 Aluminium

Aluminum possesses high energy absorption characteristics, is light in weight, and has good corrosion resistance. Aluminum's use in the vehicle industry has expanded dramatically as a result of these considerations, particularly in chassis. Aluminum material has been found to reduce

weight by approximately 50%, according to recent results [8]. However, the increased cost of production prevents it from being used in high-end vehicles such as the Audi A8 and BMW 7 Series. [17], [18].

2.5.3 Magnesium:

Magnesium exhibits lower fatigue and tensile properties than aluminum with a higher coefficient of thermal expansion. The manufacturability and faster solidification make it the preferred choice for automobile manufacturers [17], [18].

There are advanced materials that are being experimented on, as will be discussed in the literature review. For now, a brief discussion for a few is presented.

2.6 Advanced materials

2.6.1. Plastic composites: The high strength-to-weight ratio and good crash absorption characteristics make it the best choice for racing cars and therefore find its application in formula 1 racing cars. The other advantage of this material is its weight savings and easy transport options, which offer consumers better fuel consumption [17], [18]

2.6.2. Fiber Reinforced Compounds - They are popular for their advantages that offer the potential for low-density weight reduction. Since weight reduction could result in lower fuel consumption, this would have a greater economic and environmental impact. They have excellent resistance to corrosion and other chemical environments, which could help the manufacturer extend the life of individual vehicle components. Fiber-reinforced composites consist of high-strength modulus fiber that are embedded in or connected to a matrix with separate interfaces [17], [18].

2.6.3. Carbon fiber epoxy composites: Recently, racing car manufacturers have used compounds in the form of plastic compounds such as Kevlar and especially carbon fiber epoxy compounds. Composite structures have high strength or light weight, which is particularly advantageous for racing car structures. The basic chassis of the Formula 1 racing car is a 3-layer monocoque construction [17], [18].

2.6.4. Glass Fiber Composites:

This material is lighter than aluminium, easily fabricated, and corrosion-resistant which makes it the best choice for Formula one racing cars than the plastic one. Furthermore, it is inexpensive when produced in smaller quantities. Currently, Lotus, TVR, Camaro, Venturi, etc., have used glass fiber in the non-stressed upper body [17], [18].

In the next sub-section, the software that will be used (to model the chassis) throughout this thesis is discussed.

2.7 Software Package

There are several commercial finite element analysis (FEA) software packages that are available to analyse structure both statically and dynamically. In all these FEA software the underlying mechanical engineering principles of node interaction are fundamentally the same. The major differences are often the user interface, the allowable user-defined parameters, and the "openness" of the software. ANSYS is the software of choice because the author is most familiar with it.

The ANSYS is an FEA-based analysis software encompassing various analysis systems like static structural, vibration, CFD, acoustics, and buckling. The software is used for various engineering disciplines like aerospace, automobile, and marine to test the feasibility of design and material for any given application. Apart from these analysis systems the software also possesses magnetostatics, kinetic-dynamics, and piezoelectric. The overall ANSYS capabilities are given in figure 2.8.

Figure: 2.8: ANSYS Multiphysics Software Solution/Workbench capabilities [19], [20]

Analyzing the issue in the ANSYS software program must go via three stages. That is discussed.
1) Pre-processor
2) Solution
3) Postprocessor

The values for examination would be ready through the pre-processor. The main general idea of the pre-processor includes powerful solid modeling as well as mesh generation abilities. Mesh generation is an important step in FEA as poor meshing can lead to simulations not converging or pre-mature convergence. Validating a model's results is thus crucial at this stage of the analysis. This is required to state all other examines information with advantages of database system

statements and handling of examining information. The inputs of parameters, user documents, macros documentation as well as graphics ability are also available with the ANSYS program involving isoperimetric, parts, edge line shows of 3D designs. The solution stage involves the Matrix formulation, multiplication, and inversions

The post-processor is used for outcomes in used form after completion of modeling as well as examination. The general post-processor is required to display results that do not alter with time or frequency, and it can display results in natural frequencies. The past theory of post-processor provides outcomes, which vary with time or frequency, and shows the results in graphical form which is easier to examine the system. Figure 1.9 shows the ANSYS Simulation workflow.

Figure 2.9: ANSYS Simulation workflow [21]

2.8 Design and optimization considerations

The primary purpose of the vehicle chassis is to support the vehicle under various loads that are applied to it and provide the necessary strength. The structure often accounts for a substantial percentage of the new vehicle program's development and manufacturing expenditures, and the designer has a variety of structural options to choose from. It's critical to pick the best design to provide an acceptable structural implementation under other design restrictions like cost, volume and mode of manufacturing, product applications, and so on.

Besides design constraints and considerations, there are a number of different directions in which vehicle chassis optimization is concentrated. Some of the more relevant directions in optimization are reported in the following sections.

2.8.1 Topology

In topology optimization, one is often interested in reducing the amount of material used to make the part. This is to be done without compromising the structural integrity. Chiandussi et al. [22] considered improving the McPherson suspension arm, which is one of the most important pieces of a car. They were able to reduce the component elements such that less than 60 % of the original element remain after the optimization process. This was accomplished while adhering to the upper limit Von Mises stresses and the smallest first natural frequency.

Reddy et al. [23]applied topology optimization to conceptual structures. They presented three crashworthiness examples of how this optimization technique can be used to model structures based on varying criteria. Duddeck [22] reported on research done by BMW on the need for multi-disciplinary optimization research that is done on vehicle designs. This included a full vehicle noise, vibration and harness (NVH) optimization combined with vehicle shape optimization.

The HMV industry is constantly changing, and new performance requirements are sort, hence what was optimal a decade ago is no longer so. The immediate next trend is electric and self-driving heavy vehicles, prototypes are already in existence [24]. These vehicles might have different performance requirements, such as to carry heavier loads due to higher power available from electric motors. These new vehicle designs will now have to deal with batteries, electronics and electric motors and appropriate drive systems. These loads might have to be distributed differently on HMV chassis. This will not only introduce new chassis designs and topology, but newer materials will have to be adopted.

Although the area of topology optimization is an important avenue for research it often deals with optimizing the volume of the currently used materials. This does not necessarily reduce the weight of the structure in question. If weight reduction is the optimization criterion in topology optimization then often the resultant structure has a larger volume than perhaps desired. This leads to a multi-objective optimization problem which is not within the scope of this thesis. Furthermore, the resultant topology is more nature-like and does not fit standard manufacturing processes and jigs. The proposed study is not rebutting this approach in totality but is proposing the adoption of newer materials for weight reduction for chassis designs. This is proposed to be viable with currently available manufacturing processes. Once the behavious of these materials on chassis structures is understood, their topological optimization will have to be carried out.

The next section discusses chassis member cross-sections.

2.8.2 Chassis beam cross-section & mode analysis

In this area, one is interested in selecting the best cross-section for the chassis members. The most common choices are the C, I, Box and tubular beams. These cross-sections are often selected after finite element analysis and for having satisfied specified main chassis stresses, deflections, and stiffness requirements. The method of assembling (i.e., bolting, welding, etc.) these beams is also an active area of research that is not considered in our work. The authors in [23] used the FEM to develop and analyze a container frame with stiffeners to improve load-carrying capacity and reduction of frame failure when folding. They concluded that rectangular stiffeners should be installed between the crossbeams and screwed to the chassis. With the introduction of stiffeners, the FEA study anticipated a 37.11 percent reduction in stress and a 36.23 percent reduction in stress intensity.

Bhat et al. [25] analyzed a tractor chassis by modifying the cross-section from "C" to "I" made from mild steel. The findings showed that nearly 31.79 kg of weight is reduced by changing the cross-section type while keeping the other dimensions the same as before. Swami et al. [26] investigated the structural integrity of an Eicher 20 chassis frame with a C-shaped cross-section. The data reveal that the equivalent-stress generated is influenced by the thickness of cross members. With an increase in in-side member thickness, the equivalent stress rises to a certain point and then falls. To evaluate maximal deformation and stress, M. Azizi et al. [27] performed a static structural analysis on a 35-ton trailer. The FEA results obtained were in close agreement with analytical results concerning the position of maximum deformation and maximum tension. However, the magnitude of maximum deformation obtained from FEA analysis differed from theoretical results.

One of the research questions in this area is how to choose the chassis members to optimize as the most critical aspect of vehicle design is dynamic behavior. One way is by reviewing the FEM stress and deformation results. The dynamic properties of a structure can be studied using modal or harmonic analysis, which can be performed using experiments or simulations [28]. The overall dynamic characteristic of a car chassis were studied by Mrrzuki et al. [28]using mode shape analysis and frequencies, and it was determined to be safe for human use and adequate for use in racing car applications.

According to Bedri et al. [29] the effect of pre-stressed load on the structure can cause a noticeable variation in the extracted mode shape frequencies, particularly on the first mode compared to the higher methods. Y. Ren et al. [30] worked on a Dump truck frame's dynamic mode analysis. The largest deformation was detected in the central region of the chassis frame, according to the static structural study. T. Fui et. al. [31] conducted a dynamic analysis of heavy motor vehicle chassis of 4.5 tons and dynamic responses are captured under static loading conditions. The findings have shown that the top cross-member generates maximum local bending vibrations. The FEA analysis showed regions of maximum stresses which are at the mounting brackets of the suspension system.

With the ever-increasing developments in material processing, material formulation and capabilities, an area that is open to exploitation is material selection for vehicle chassis. The next section presents some work that has been done in this space.

2.8.3 Chassis material selection & analysis

Nalawade et al. [32] investigated the structural integrity of the TATA 407 truck chassis. E-glass was chosen as the novel material for comparison with structural steel. The data reveal that using E-glass to reduce weight by 60-68 percent is achievable; deformation is also within acceptable limits, but the stress created is higher than that of steel. Static structural analysis of the TATA LPS 2515 EX chassis was performed by Sharma et al [33]. The materials employed in the analysis were AISI 4130 alloy steel and ASTM A710 steel grade A (class III), with B, C, and I type cross-sections being examined for chassis. The findings revealed that AISI 4130 steel, which is lighter than other materials, is the ideal choice for this purpose.

Because the box channel shape cross-section has higher durability and reduced deformation, it's ideal for heavy truck chassis construction. TATA LP 912 chassis were subjected to an FEA study done by Singh et al. [34]. Alloy steel was employed for the analysis, and the cross-sections used were C type, I type, rectangular box (solid), and rectangular box (open) (hollow). The rectangular (solid) section is more robust than other forms of cross-sections, according to the data. The TATA axle frame was also subjected to a static structural examination by S. Godse et. al. [35]. Increased thickness and reinforcements were added to the current design to improve it even more. According to the findings, the conventional design generated stress of 37.04 N/mm2, whereas the optimized design generated stress of 22.97 N/mm^2, indicating that increasing thickness and adding reinforcements result in a significant stress reduction.

Bajwa et al. [36] performed an FEA analysis on a TATA ACE chassis with a C-type cross-section. The FEA findings from the Ansys program were quite close to the analytical results. The stress distribution on a genuine bus construction was examined by A. Gauchia et al [37]. The structural behavior of the bus was studied using the finite element approach when it was subjected to weight and torsion. A Genetic algorithm was used to achieve geometrical optimization without compromising vehicle safety. The researchers discovered that "choosing an appropriate fitness function has a significant impact on the solution obtained." Only four of the 55 beams' cross-sections were changed, resulting in a 4 percent reduction in bus weight structure and a 0.23 percent improvement in torsion stiffness."

A truck chassis was designed by Singh et al. [38]. They used static analysis to look at the various stresses acting on it, such as the maximum main stress, shear stress, and corresponding Von Mises stress, as well as the resulting deformation, and chose HLSA steel for the chassis. The design was proven to be safe with a maximum deformation of 0.0084 mm. H.K. Asker et al [39] conducted static and vibrational analysis on standard truck chassis. The analysis was conducted to determine stress intensity and vibration mode shapes during ramping of a block. The

numerical results showed that FEA can be used to determine bending and torsional stresses on vehicle frame with reasonable accuracy.

The research on which the present work is based on the basic study initiated by Monika S. [40]. A numerical analysis of a Tata 1612 chassis frame was performed in this study. For structural and dynamic loading conditions, ANSYS FEA software was employed. Natural frequencies and deformation mode shapes were determined using modal analysis. For self-weight reduction under impact loading situations, Ingole et al. [41] performed an FEA study on an eight-ton four-wheeler trailer chassis. The FEA analysis was conducted with "variation in cross-sectional areas of cross members and changing position of cross members". The FEA results showed an increase in safety factors with the usage of plates and significant weight reduction was achieved.

On the Eicher E2 chassis, Tidke [42] performed an FEA analysis. ASTM A710 steel, ASTM A302 steel, and the metal alloy 6063-T6 were employed in the analysis. C type and rectangular box cross-sections were used in the analysis. According to the structural study, the rectangular box section has more strength than the C cross-section. Furthermore, rectangular box sections have less deflection, stress, and deformation than square box sections. Using finite element methods, C. Karao, S. Kuralay [43] examined the effect of lateral member thickness on truck chassis. The results showed that increasing the thickness of the in-side member reduced joint stress but raising the thickness of the side member also increased weight and the usage of local plates at joint locations could be a solution. Using finite analysis, Kutay et al. [44] focused on chassis optimization. Their main goal was to lower the chassis' weight, thus using "three thicknesses of 4 mm, 5 mm, and 6 mm. After the analysis, the authors concluded that the 4 mm thickness is better as it resulted in better chassis stress and displacement as compared to the other two dimensions [44].

Rahman et al. [31][45] worked on the fatigue life characteristics of heavy vehicle chassis and concluded that the durable loading of the chassis frame is a significant factor that ensures good fatigue life. The critical points (which are prone to fatigue failure) were determined using techniques of the Finite Element Method subjected to static loading conditions.

Veloso et al. [46] conducted experimental testing to determine fatigue failure of automobile chassis on the longitudinal member. The stresses on the critical regions are determined using Hyper-mesh software. Certain models are suggested for improving the fatigue life of the component. These models are basically of reinforcement type. S. Krishna et al. [47] conducted an FEA simulation on a Baja roll cage chassis made of different materials i.e., AISI 10 l8, AISI 1020, and AISI 4130. The study shows that the AISI 4130 material has a high yield strength and strength-to-weight ratio hence it was selected for the chassis. Denny et al. [48] conducted an FEA simulation of solar-powered vehicle monocoque chassis made of woven carbon fiber composite material. The design and simulation of the chassis were performed, and the critical regions of high stresses and deformation are obtained.

K.J Sandeep [49] conducted an FEA simulation on an ATV with AISIS 4130 and AISI 1018 materials with varying cross-sections. The strength of AISI 4130 material has shown better results as compared to AISI 1018. N. Sinha et al. [50] studied the various types of chassis and suggested that the ladder frame chassis are suitable for heavy vehicles. They prefer the use of carbon-reinforced epoxy-based polymeric (CSE-p) composites rather than steel amalgams.

M. Hanif et al. [51] conducted a FEM structural analysis of ECO car chassis. The space frame type chassis was modeled using mild steel and further analyzed to bear high loads and the structure possessed sufficient strength. S. Kapadne et. al. [52] reviewed the structure analysis and FE simulation on all-terrain vehicle chassis. The CAD modeling of the chassis was done to consider the weight reduction. Kesarinath et al. [53] conducted the design and analysis of an ATV. Numerical analysis shows that the vehicle can take frontal impacts of up to 160 MPa and indicated the ability to withstand extreme conditions. Murthy et al. [54] conducted a design and structural analysis on the ATV RC frame. The stress, deformation and factor of safety were considered as the output parameters. Crash and torsion analyses were carried out to check the safety of the design. S. Mane [55] conducted an FEA analysis on the BAJA ATV chassis frame. The chassis was modelled using AISI 4130 material with adequate ground clearance and a lightweight structure as the design parameters of the chassis. Study shows that the design of the chassis should not compromise strength and ergonomics.

N. Sharma [56] has worked on minimizing the unsprung mass of the chassis of ATVs. Using AISI 1018 material. The FOS and stresses are determined from ANSYS simulation. The results obtained for ATV simulation results were in close agreement with analytical results. H. Raj [57] discussed the possible ways for designing ATVs and what are the difficulties that are incorporated with the designing and analysis of the ATV. The author tried to increase the FOS of the vehicle and has tried to make the RC with better ergonomics and aesthetic looks.

V. Lopez et al. [58] discussed the need for Global Chassis Control (GCC) for the control of vehicle dynamics. The author discussed different control system topologies, e.g.: centralized, decentralized & multi-layer control structures and integrated chassis control (ICC) approaches. V. Saplinova et al. [59] worked on the design and structural analysis of tubular space frame chassis for a race car. The analysis of the chassis is conducted for frontal impact and rear impact. And results show that the chassis is structurally sound and capable of shielding during any crashing situation.

The following subsection will discuss the research gap based on the literature review presented in the previous sub-section.

2.9 Research Gap

Technological advancement aims to meet the market's ever-increasing standards for faster, more comfortable, and hassle-free & economic transportation. As per the literature review, it is observed that the previous investigations were based on the design and material optimization of

chassis using an experimental method or FEA simulation techniques [23]- [38]. The chassis analysed are of trucks, SUVs, and other LMVs as well as a two-wheeler. The materials investigated are grey cast iron, AISI 4130 alloy steel, and ASTM A710 category A (CLASS III) steel. For the 2-wheeler chassis, the materials investigated are alloy steel, magnesium, A360 aluminium alloy, and carbon-reinforced fibers.

Optimizing the frame design is largely limited to the use of different cross-sections [25][33][34][36], such as the I shape, the L shape, the C shape, and the box shape in the frame manufacturing. Some researchers analysed the dimensional parameters of these transverse beams and concluded their results with the experimental method or the FEA method [43]. The ladder chassis comprises lateral members of a hollow rectangular section and sidebars are made of a C section.

Although there have been numerous studies on chassis structure vibration analysis, the majority of them do not fully address the modal analysis of the HCV chassis, as in our case. The mode shape analysis should be performed using the ANSYS software package to check the vibrational characteristics of the initial chassis structure design and to ensure that the natural frequencies are not uncomfortable. By thorough literature study, it was found that comparatively less emphasis was given to the prestressed analysis while assessing the dynamic performance. On roads, as seen, trucks and many heavy-duty vehicles tend to operate much higher than their allowable payload limit. Therefore, static stress analysis and pre-stressed modal analysis should be performed on TATA 1612 chassis model to see if significant changes occur to the natural frequencies.

The dimensions of lateral members (hollow rectangular sections) have a significant effect on the magnitude of stress generated, deformation, and weight of the chassis frame. Therefore, it is necessary to investigate the individual effect of dimensions of lateral members on the - discussed output parameters.

Although steel is the primary choice of the manufacturers because of its low cost, considerable relative strength, and ductility, several composite materials [60] offer higher strength and modulus better than any conventional metals. Material properties are constantly being improved to meet safety and operational standards while keeping up with technological advancements. Some research [32] [33][38][38] are conducted on the investigation of composite materials and other alloys for chassis application but none of the research is conducted on the application of MMC (Metal Matrix Composite) materials for the improvement of chassis strength.

A lot of new materials have been developed which have the same load-carrying capacity as those of the existing materials yet weigh significantly less than their current opponents [61]. Composite materials [60], with their distinctive combination of high stiffness and low coefficient of thermal expansion (CTE), offer the essential physical attributes of lightweight and durable structures [60]. Generous advancement in the improvement of light metal matrix

composites has been accomplished in the last few years, with the goal that they could be brought into the main applications. The technical viability of MMCs in various applications has been well demonstrated. MMCs with various types of reinforcements produced by solid-state and liquid-state processing have been used in a variety of engineering applications [28], [62]. Particularly in the automotive business, MMCs have been utilized in fiber-reinforced pistons and Al crankcases with fortified chamber surfaces [63]. These materials have a good number of properties, including a high young's modulus, high compression, and tensile strength, mechanical compatibility, high compression, tensile strength, economic efficiency, etc. [63]. Such a combination of properties of composite materials can be valuable in the automotive quality and manufacturing sector where vibration, toughness, and increasing fuel prices are serious concerns, along with other technical requirements [64].

In the automotive industry, presently, no work has been done in improving the design of existing chassis using the advanced optimization techniques as indicated in the specific objectives in chapter 1. As MMCs have shown encouraging results in space applications, there is a reasonable probability that MMC will be a feasible material for chassis application.

In the next sub-section, the basics and importance of the Response-Surface Methodology for Design Optimization used in the study will be discussed.

2.10 Design-Optimization Using the RSM (Response-Surface Methodology)

The Response-Surface method (RSM) is a "set of mathematical and statistical techniques that are useful for analyzing problems in which several independent variables affect a dependent variable or response" [65]. The goal is to improve on this response. "We denote the independent variables $x_1, x_2, x_3, x_3 \ldots \ldots x_n$ and assume that these variables are continuous and that the experimenter can control them with negligible error" [66]. The dependent variable's relationship to the independent variable can be represented as-

$$y = f(x_1, x_2, x_3, x_3 \ldots \ldots x_n) + \epsilon$$

where ϵ represents the noise or error observed in the " y " response.

If denoting the expected answer with

$$E(y) = f(x_1, x_2, x_3, x_3 \ldots \ldots x_n) = \eta$$

The surface is represented by $(x_1, x_2, x_3, x_3 \ldots \ldots x_n)$ is referred to as the Response-Surface [69].

In the next sub-sections, the design of the experiment is discussed. Plotting and goodness of fit curves as an essential part of the simulation study.

2.11 DOE: Design of Experiments

The experimental design (DOE) is a "systematic method to determine the relationship between the factors that affect a process and the results of that process. In other words, it is used to search for cause-and-effect relationships. This information is necessary to manage the process inputs and optimize the output. The selected ANSYS optimization is the core composite design scheme" [70].

Some terminology for a design problem needs to be defined first:
- Parameters: are the "nobs" or available "settings" for the project, for example, the geometry (sizes, shapes), materials and profit control.
- Variables: A subset of the design parameters that you want to optimize (the other parameters are resolved during design). The design space is the set of all possible variable parameters [71].
- Objectives: A design's quality is defined by its objectives. In general, it is the project's performance that piques your interest (vehicle safety, driver stability, etc.). In many cases, the objective is to create more than one goal. To keep things simple, the discussion will be limited to one topic. how to manage multiple goals will be presented [71].
- Constraints are design variables that define the variable space that can be reached. For example, the maximum stress in the construction of a bridge must be less than the critical one (sometimes a safety factor) [72].

2.12 Plotting Response Surface, Goodness of Fit curves

Once the design points have been created using the empirical design, the output responses are determined by the central composite design scheme. These initial parameters are shear stress and strain energy [73]

The response area diagram illustrates the variation of the output variables (shear stress and strain energy) in relation to the input variable. The fit quality curve illustrates the difference between the observed and predicted values in the model under consideration [74] The sensitivity analysis diagram shows the percentage influence of the input parameter on the desired reaction, i.e., the equivalent voltage and voltage.

In the next sub-sections, the types of optimization techniques will be briefly discussed as a sub-part of the Response-Surface optimization method presented in section 1.4.

2.13 Optimization Types used for research

2.13.1 CCD: Central Composite Design

These designs are frequently used in tandem with second-order response models. The design is made up of three types of points: [75]

a. Axial Points: Axial points are generated as a result of a screening analysis.

b. Cube Points: A full faculty level yields 2n cube points.

c. Center: Using a nominal design, a single center is created.

The control parameter ranges (minimum and maximum values) are changed to [-1, + 1] for a more detailed description of the drawings. Figure 2.10 illustrates a Central Composite (CC) diagram of a circumscribed three-dimensional design.

The axial points in this case are in a hypercube with radius b1. The cube formed by the cube points has a lateral length of two [74]
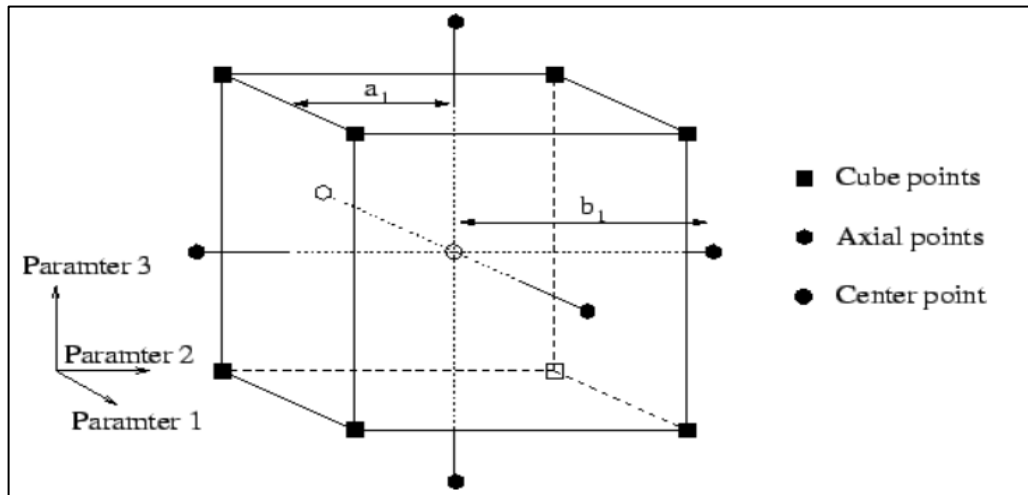
Figure 2.10: Central Composite design with 3-Input parameters [74].

2.13.2 OSF: Optimal space-filling design

Space fill designs are recommended for testing with deterministic models because the design points are evenly distributed in the design area. To use these design options, an important assumption is necessary: Computer simulation must reflect the actual physical system [75]Due to diffusion points, space fill projects can capture different reaction behavior in different areas of the design area. Due to the complexity of these simulations, the response behavior in the design space can change significantly. Space fill projects generally try not to have replicas in k dimensions (where k is the number of factors).

If the size of the design space is reduced when looking for factors that do not have a statistical impact on the response, an ideal space fill design does not have replication points in the smallest design space. For example, if you find that a factor is not significant and the plan is projected onto the smallest dimension of the remaining factors, there is no response. In this way, more information about the system can be obtained because the replicated test points do not provide additional information and the answer is deterministic [19]

• Due to the noise associated with physical testing, traditional DOEs (e.g., CCD) would focus on adjusting parameters close to the scope of the design area.

• The computer simulation is not subject to this restriction (or at least not so much).

• A room-filling system distributes the design parameters evenly in the design room.

• The aim is to achieve maximum understanding with the fewest points.

• When you only have a limited amount of time to calculate, this is extremely useful (the user can specify the number of points).

• The cover of the design room is not uniform. Angles and/or centers are not necessarily included.

• Certain dangers are included in the selection of the starting point. Figure 2.11 illustrates the best space-filling design.
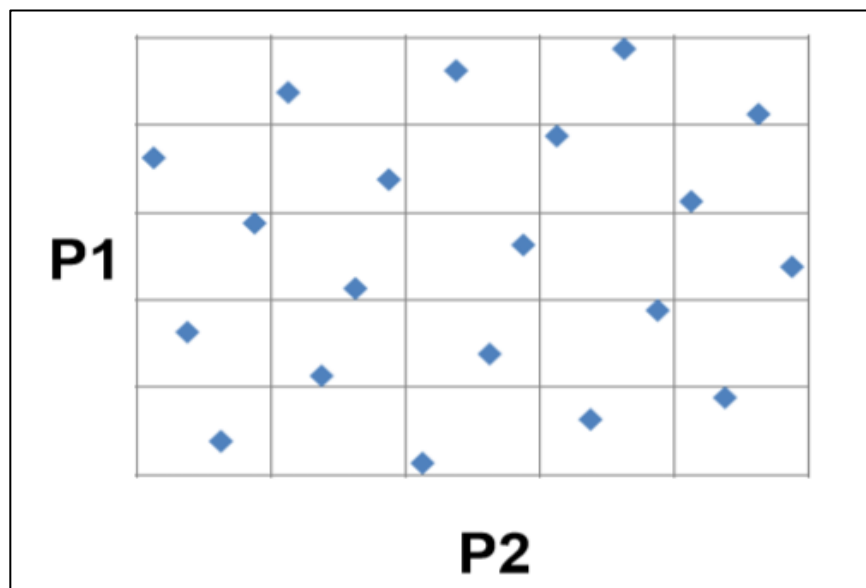
Figure 2.11: Optimal space-filling design [19]

Advantage: The user can specify the number of design points. - Improved functions to fill the space, making it more suitable for use with more complex metamodeling techniques such as kriging, non-parametric regression, or neural networks.

Disadvantage: The ends are not always covered. - Choosing an excessive number of design points may result in poor response prediction quality.

2.13.3 B-B: Box Behnken design

The box-Behnken design is an independent square design because it does not contain an integrated factorial or fractional design. "In this design, treatment combinations are in the middle of the edges of the treatment room and the middle. These designs are rotatable (or

nearly rotatable) and require 3 levels for each factor. The structures have a limited locking capacity orthogonal to the central composite structures"[19]. Box-Behnken projects have "processing combinations that lie in the middle of the edges of the test room and require at least three continuous factors as shown in figure 2.12.
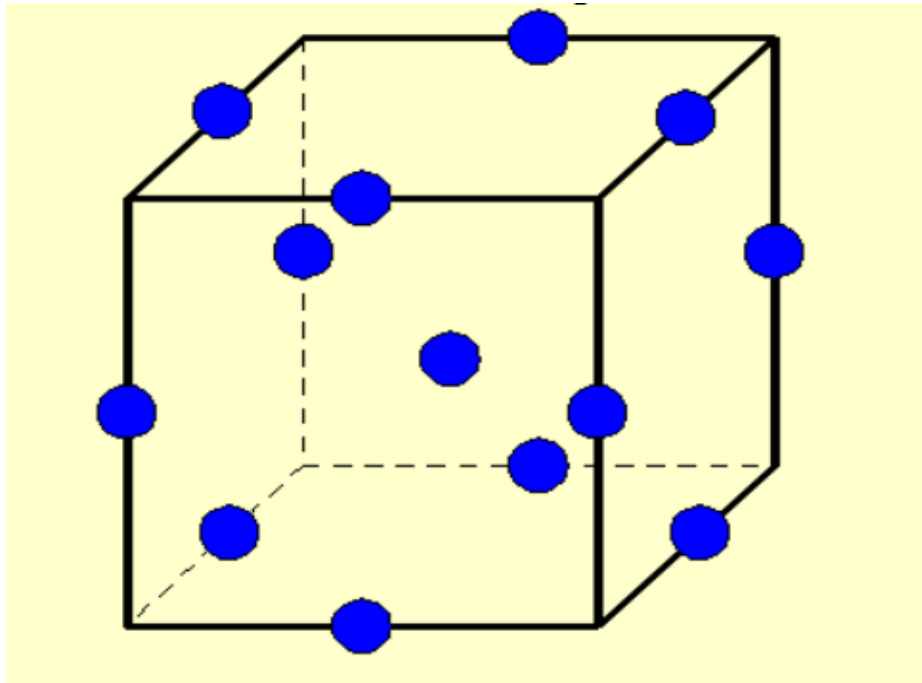
Figure 2.12: Box-Behnken Design for Three Factor[19]

The following illustration shows a three-factor box barrier design. These plans allow efficient estimation of the first and second-order coefficients. Since Box-Behnken designs often have fewer design points, they can be less expensive to manufacture than central composite designs with the same number of factors. However, since they do not have an integrated factorial design, they are not suitable for sequential experiments.

Box Behnken projects can also be helpful if the safe area of operation for your process is known. Central composite structures generally have axial points outside the cube. These points may not be of interest to the region or may not be accessible because they exceed safe operating limits. Box-Behnken projects have no axial points, so you can be sure that all design points are in the safe operating area. Box-Behnken designs also ensure that not all factors are set to their high level at the same time" [50].

2.13.4 SGI: Sparse grid initialization

The sparse grid method is a "special discretization technique, which allows coping with the curse of dimensionality of grid-based approaches to some extent"[19] It is based on a hierarchical basis [76][77][78], "a representation of a discrete function space which is

equivalent to the conventional nodal basis, and a sparse tensor product construction. The sparse grid method was originally developed for the solution of partial differential equations" [79][80][81]. Sparse grids originated by [82], who used them for numerical integration. The idea is also linked to hyperbolic crosses[83]; Boolean methods, discrete blending methods, and splitting extrapolation methods." The sparse grid approach uses O (hn-1.log(hn-1) d-1 grid points in the discretization process to represent a function f defined over a d-dimensional domain, where hn: = 2n denotes the mesh size and n is the discretization level. For accuracy of $O(h_n^2)$., the order of approximation to describe a function f under certain smoothness conditions is O $(h_n^2.\log(h_n^{-1})$ $^{d-1}$. As a result, sparse grids require far fewer points in higher dimensions to achieve comparable approximation quality than regular full grids, as shown in figure 2.13.
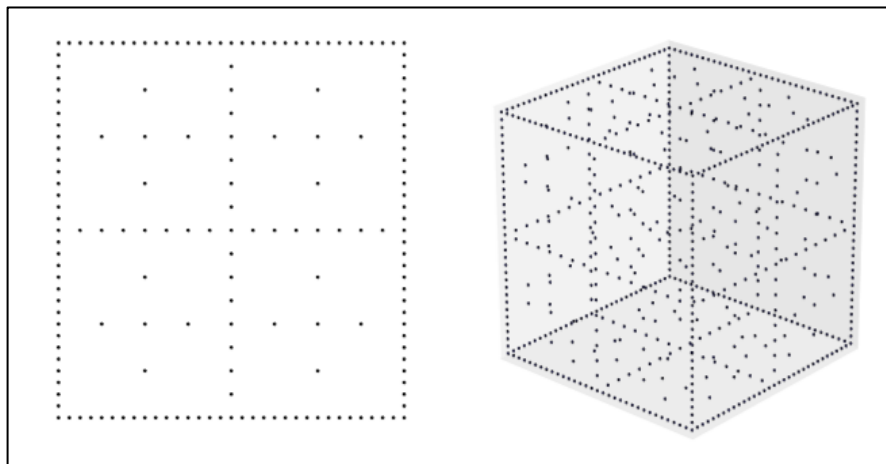
Figure 2.13: 2D sparse grid and 3D sparse grid[19]

2.13.5 LHS: Latin Hypercube Sampling

The Latin-hypercube sampling conducted significantly fewer iterations and is based on the stratification of the input probability distributions [19] "Stratification divides the cumulative curve into equal intervals on the cumulative probability scale (0 to 1.0). A sample is then randomly taken from each interval or stratification of the input distribution. Sampling is forced to represent values in each interval, and thus, is forced to recreate the input probability distribution" [19]. The cumulative curve shown in figure 2.14 is subdivided into five intervals and using Latin hypercube the value distribution is more accurately reflected without replacement.
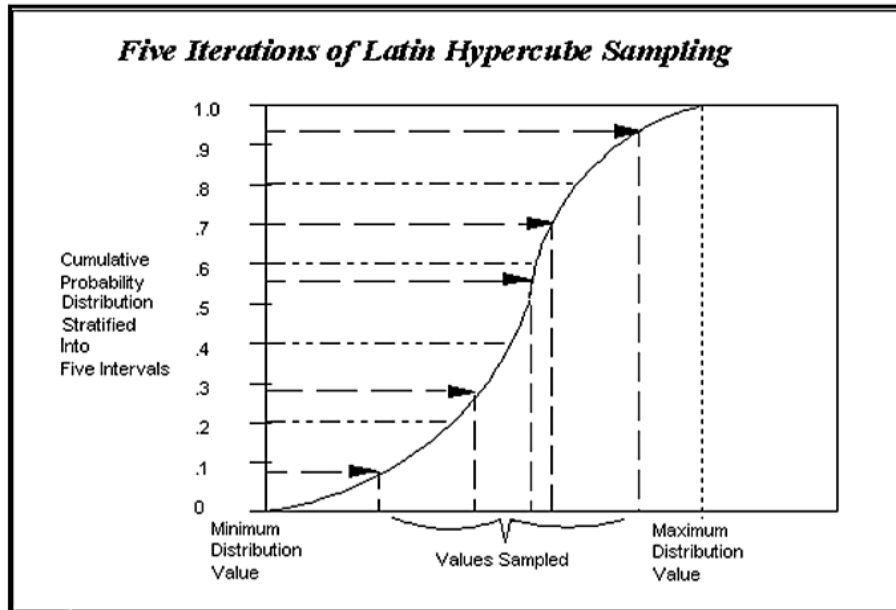
Figure 2.14: Latin hypercube sampling [19]

The iteration numbers depend upon stratification. "Latin Hypercube offers great benefits in terms of increased sampling efficiency and faster runtimes. Latin Hypercube also aids the analysis of situations where low probability outcomes are represented in input probability distributions. By forcing the sampling of the simulation to include the outlying events, Latin Hypercube sampling assures they are accurately represented in simulation outputs" [19]

The next sub-section presents the 6-sigma robust design scheme.

2.14 Design for Robustness

The robust optimization design is an "effective method for reducing the effects of various uncertain factors on the target response value". It fulfills the primary objective of a "lower sensitivity value for the target response under the randomness of the uncertainty factors" [84]. The method involves the combination of 6 sigma quality management theory along with robust optimization technique which helps to minimize objective "response value and thereby meeting reliability design requirement" [85]. 6 sigma robust design scheme is displayed in figure 2.15.
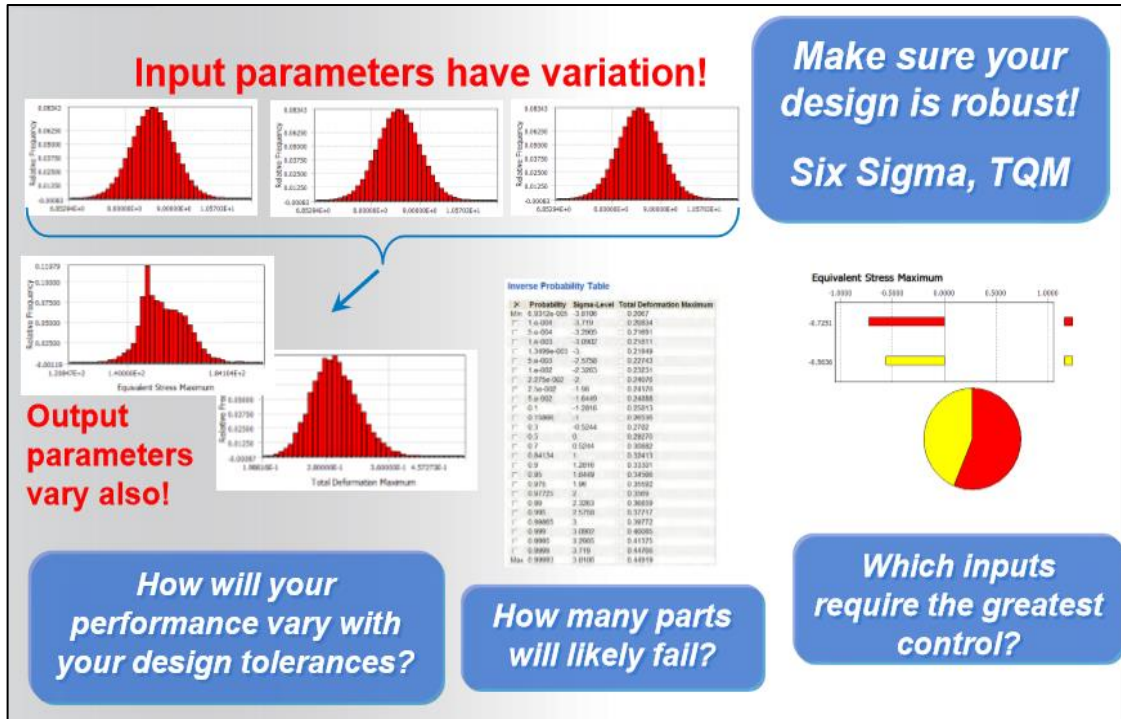
Figure 2.15: 6 sigma robust design scheme [86]

The 6-sigma analysis would determine the following:

a> Change in performance compared to project tolerance

b> Number of parts that could break

2.15 Chapter Summary

Various papers have summed up existing benchmark issues or have proposed new topics that could fill in as reasonable benchmarks. In this chapter, several works on the tractor, truck, bus and other vehicle systems, material optimization, Finite element analysis and many other models have discussed, which gives a transparent background of the research gap in this area are considered. Therefore, it is essential to investigate the effect of new materials on chassis strength, including the application of various optimization techniques to be used are provided in detail along with their advantages. The layout of chassis cross members also affects the chassis strength and requires investigation.

Based on the literature review; the methodology, material selection, and methods are discussed in the next chapter.

RESEARCH METHODOLOGY

The current chapter presents the detailed methodology carried out in structural analysis and design optimization of heavy motor vehicle chassis. The steps of FEA analysis and optimization of chassis are presented in detail. The optimization techniques presented are central composite design scheme, optimal space-filling design, sparse grid initialization, Box-Behnken, and Latin hypercube sampling along with six sigma.

3.1 Materials and Sources

The material used for the FEA analysis is structural steel and the source of availability is the ANSYS library file. The properties are shown in the table 3.1.

Table 3.1: Material properties [40][87]

Material Name	Youngs Modulus (GPa)	Poisson's ratio	Density (kg/m^3)
St 52 E	210	.33	7830

The main element when selecting material, especially for the body/chassis is that the body has to perform in a wide variety of conditions. These could be thermal, chemical, etc. Steel stands as the first choice for manufacturers with all the required characteristics. The best reason for using steel as a body structure is its natural capability to absorb the impact energy produced in a crash" [88]. Finding an acceptable balance of strength, stiffness, toughness, and density is difficult with standard chassis materials. These problems can be solved by using composite materials, which are lighter and stronger than pure metals.

"Metal matrix composites (MMCs) possess significantly improved properties including high specific strength; specific modulus, damping capacity, and good wear resistance compared to unreinforced alloys. MMCs expand the possibilities for broader material applications by manipulating their processing to suit the required properties in different working environments. Furthermore, finite element modeling techniques can be used to create composite materials with specific properties. Using these techniques, it is possible to predict the properties of a particular material of a given composition.

There has been an increasing interest in composites containing low density and low-cost reinforcements" [89]. P100/6061 Al, Graphite Al GA 7-230, and Al6092/SiC/17.5p are the MMC materials chosen for investigation; Table 3.2 lists their properties.

Table 3.2: Reinforced Al-Matrix Composite Material Properties [89]

Material	Unidirectional MMC	Discontinuously Reinforced Aluminium Matrix Composites	
Properties	P100/6061 Al	Graphite Al GA 7-230	Al6092/SiC/17.5p
Density, ρ (gm/cm^3)	2.5	2.45	2.8
Young's Modulus (GPa)	342.5	88.7	100
Compressive Yield Strength (MPa)	-	109.6	406.5
Tensile Ultimate Strength (MPa)	905 (Y)	76.8	461.6

The best feasible methods and strategies for carrying out the study following the study's goal will be analyzed, which is covered in section 1.4 of chapter 1.

3.2 Methods

A CAD model of the chassis is developed as per the dimensional data from the literature [40]. There are two main tracks followed in the research methodology, these are the chassis being modeled using i) St52E and ii) MMCs. In each case, there is the static-structural analysis and the modal analysis.

Consider the left-hand side of figure 3.1. The structural analysis studies the different cross-sections (Square and C section) of the chassis members and evaluates their responses using four output parameters. These are the equivalent stress, strain energy, deformation and safety factor. The cross-section with the best outputs is then optimized using the design of experiments. The techniques considered are the central composite design (CCD), optimal space-filling design (OSF), sparse grid initialization (SGI), Latin hypercube sampling (LHS), and Box-Behnken design (B-B). The D.O.E methods were evaluated using equivalent stress, deformation and mass. The best results are then from the sensitivity analysis.

The same process was followed for all three metal matrix composites (MMCs): P100/6061 Al, Graphite Al GA 7-230 MMC, and Al 6092/SiC/17.5p.

In order to fully explore the possible geometries of a chassis (and to satisfy some specific research objectives), two other cross sections are modeled, these are the I and T cross-sections (See the middle of figure 3.1). Their equivalent stresses and deformation characteristics are analysed using FEA in order to compare with the other earlier cross-sections. Commercial tests are also carried out to validate these models.

Furthermore, the modal analysis for both original steel and MMCs was carried out as shown on the right-hand side of figure 3.1. Six sigma evaluation is also presented.
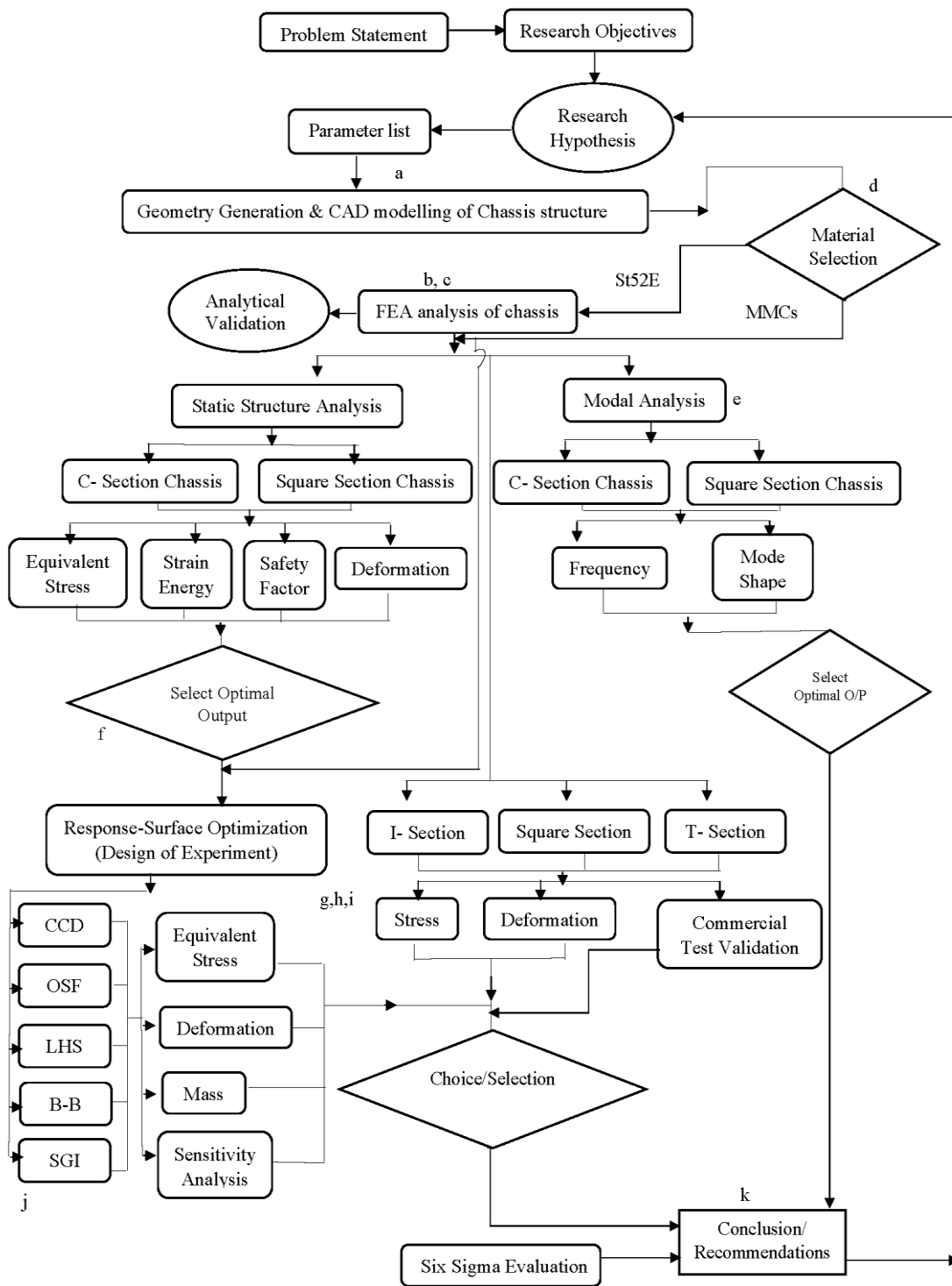
Figure 3.1 Project methodology adopted (the alphabets represent the specific objectives)

In the next sub-sections, the necessary steps for finite element analysis and formulation followed by the simulation environment and modeling of the chassis are discussed.

3.3 Finite Element Analysis Steps

FEA analysis is performed according to the following steps [90]

1>   Preprocessing: This phase involves CAD modeling, meshing, applying loads, and boundary conditions. The structure of the designed frame has the shape of a ladder and a C section.

"TATA 1612 is the vehicle's name."

The C-type of frame section (116mm x25mm x5 mm)

Front Overhang (a) = 740 mm, Rear Overhang (c) = 1400 mm, Frame width-884mm

6670 mm (b) wheelbase

The chassis' side bars are made of "C" material. 116mm x 25mm x 5 mm channels

Total load operating on the chassis = Chassis Capacity + Body and Engine Weight = (25000+600+400+200) * 9.81 = 257022N

The chassis is held (clamped) together by the shock absorber and the leaf spring. As demonstrated in Figure 3.2, the Chassis is a Simply Supported Beam with an evenly distributed load. 128511N [40] is the load acting throughout the entire span of the beam. The Beam is 8810 millimeters long. 128511/8810 =14.58 N/mm is the uniformly distributed load.
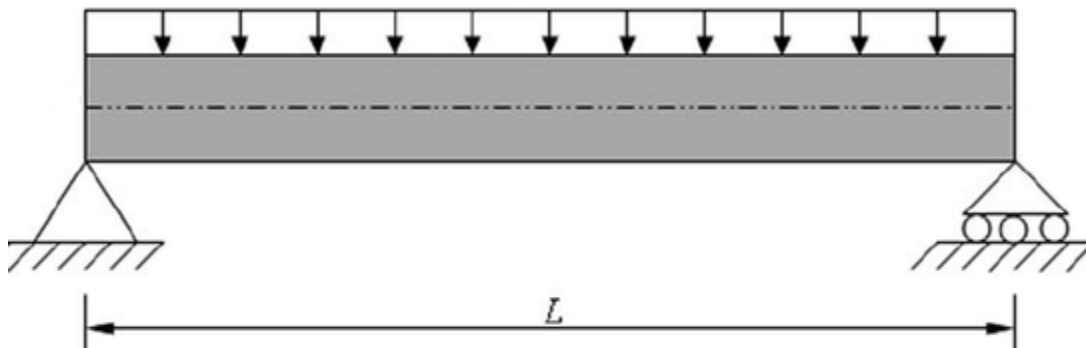
Figure 3.2: As a simply supported beam with overhang (the chassis)

M_{max} = 72022530.91 N-mm, while the moment of inertia around the x-y axis is 1266840 mm^4. The modulus section about the X-X axis is 21842.06897 mm^3, and the stress produced on the beam is calculated as 3297.422 N/mm^2.

2>   Solution: Matrix formulation, multiplication, and inversions are all performed by the software. The results are computed at the nodes and interpolated along the length of the element boundary.

3>   **Post-processing:** This phase consists of showing the results and proposing the necessary changes in the design and the material" [65]

3.4   FE: Finite Element Formulation

Following the sub-section 3.2.1, design optimization is carried out utilizing the planned design scheme, as stated in the objectives. The simulation's pre-processing stage includes CAD modelling, meshing, and applying the required loads and boundary conditions. The solution stage includes element matrix formulations, global stiffness element assembly, inversions, and multiplications as indicated earlier. The final post-processing involves analyzing and modifying the findings using chassis characteristics obtained from the previous stage [40].

3.4.1   Modelling and Simulation Environment

The static structural kind of simulation is being used in the study. ANSYS V18.1 is the version of the 120-simulation package. A graphical user interface was used to communicate with the software (GUI). The software's built-in language, on the other hand, is C++. ANSYS design modeler was used to create the chassis' CAD model. Figure 3.3 illustrates the CAD model that was created.
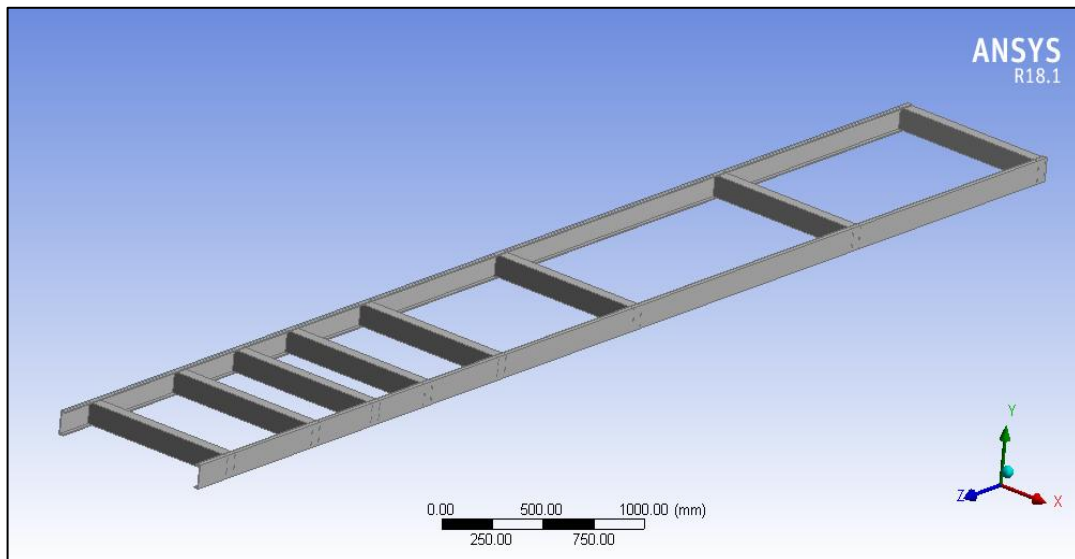
Figure 3.3: CAD modelling of the chassis.

As illustrated in figure 3.4, the next step is to define the optimization variables, which are cross-member (CM) 1, cross-member (CM) 2, and cross-member (CM) 3.
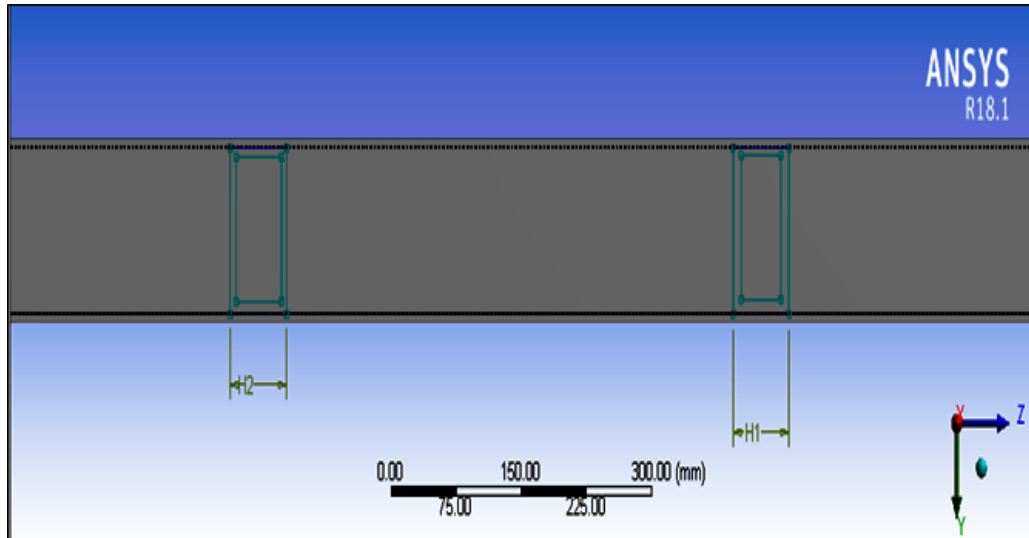
Figure 3.4: Variable assignment.

As indicated in Table 3.3, all three dimensions chosen for optimization are linear in nature and have a length of 65 mm each.

Table 3.3. Defining and naming variables [91].

Name	Value
CM 1	65 mm
CM 2	65 mm
CM 3	65 mm

The composite material is defined in the material property cell of the static structural module in the ANSYS workbench. The structural properties defined are modulus of elasticity, Poisson's ratio, and density.

The chassis design features sharp edges and curvatures, and the tetrahedral element is well suited to such complex geometries. Figure 3.5 shows the mesh model for the HMV chassis.

The chassis design was discretized using tetrahedral components with a growth rate of 1.2, inflation set to normal, and the number of layers set to 5. There was a total of 20,080 elements and 42,840 nodes produced in all. Applying loads and boundary conditions is the next stage.
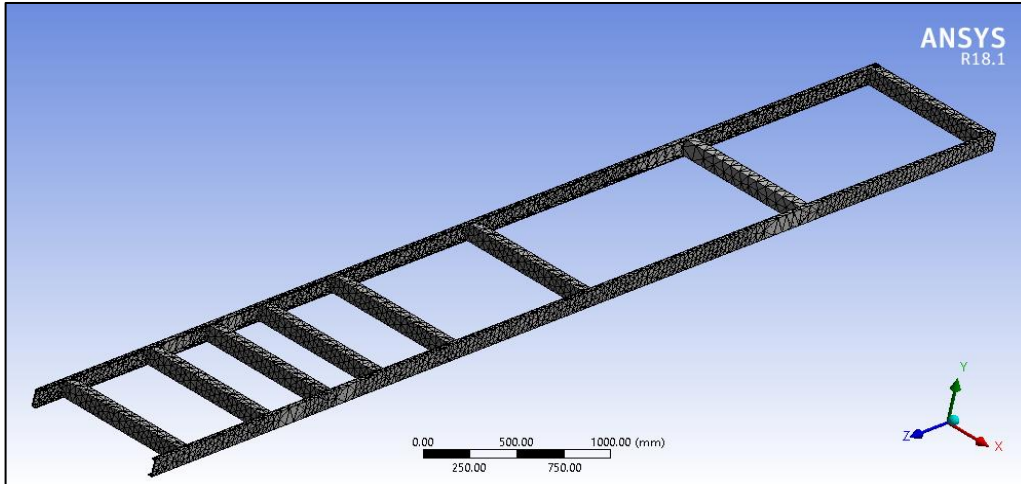
Figure 3.5: Meshed model of the chassis.

The boundary conditions were established using publicly available literature and quantitative computations that simulated real-world physical conditions on the HMV chassis. The experimental testing conditions are identical to those used in the FEA simulation. The downward force was applied to both longitudinal members, and fixed support was applied to the first and last transverse members, as shown in Figure 3.6.
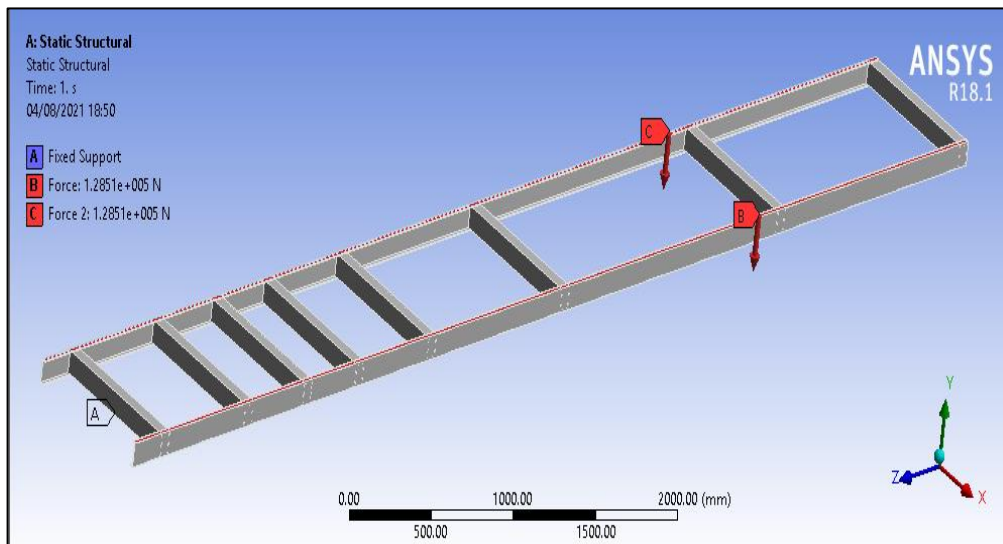
Figure 3.6: Assigned loads and boundary conditions.

After applying the loads and boundary conditions, the solver was run using the sparse matrix solver. The solution process involves the generation of stiffness matrices associated with each element, assemblage of a global stiffness matrix followed by matrix inversions, and multiplication.

Table 3.4 shows the input parameters that were chosen for optimization and are illustrated in figure 3.7.

Table 3.4: Input variables for optimization

X_1	CM 1 width
X_2	CM 2 width
X_3	CM 3 width
X_4	CM 4 width
X_5	CM 5 width
X_6	CM 6 width
X_7	CM 7 width
X_8	CM 8 width
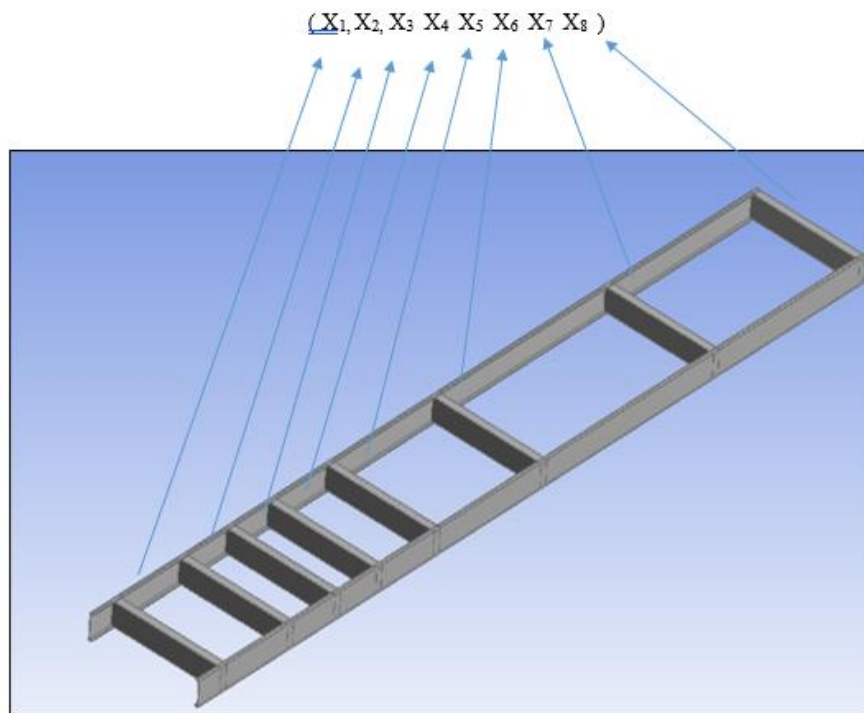
Figure 3.7: 8 parameters for optimization using RSO

3.5 Chapter Summary

This chapter introduced the methodology to be followed to carry out the research. The information on the design of the chassis, dimensions, and selected variables is presented. The steps of FEA analysis and optimization of chassis are presented which is an essential part of the design analysis.

This chapter explains the research findings and clearly outlines the results of the data analyses, employing figures, tables, and charts as needed to support the presentation of results in line with research objectives and hypotheses. The chapter is divided into nine sub-chapters in-line with the objectives specified in chapter 1.

4.1 Static Structural Analysis

The static structural analysis of the chassis structure is performed to determine equivalent stress, shear stress, and deformation. The chapter compares structural analysis results based on various sections and materials and the findings are validated in sub-chapter 4.9 using the St52E chassis test.

4.1.1 Cross-section results comparison using steel material (St52E)

From the static structural analysis, equivalent-stress plots and total defamation plots are generated for the square section and C section profile of the chassis. From the equivalent-stress plot, as displayed in figure 4.1 and figure 4.2 respectively, it is evident that the square section chassis profile has lower equivalent stress as compared to the C section chassis profile.
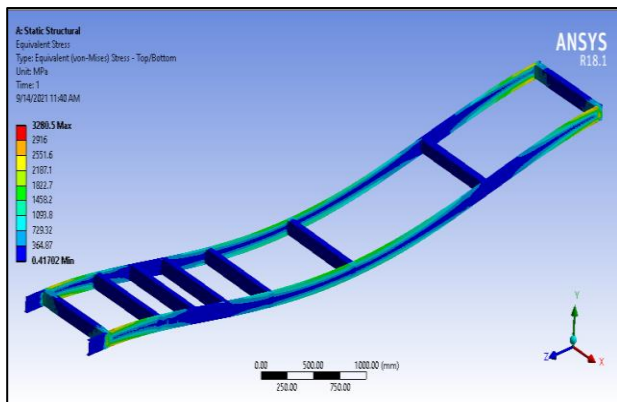
Figure 4.1: Equivalent stress for square section using St52E	Figure 4.2: Equivalent stress for C section using St52E
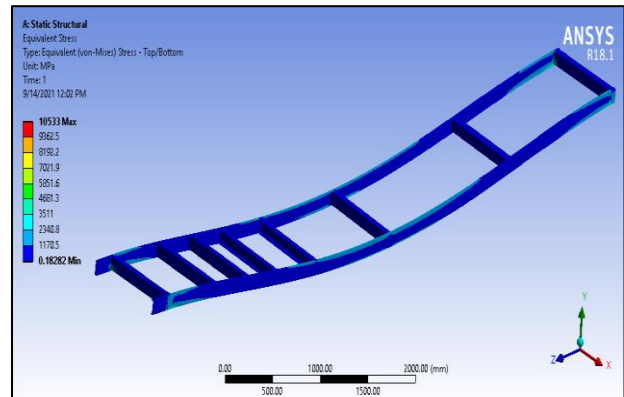
The equivalent-stress for a square square-section chassis is 3280 MPa, while the equivalent-stress for a C section profile is 10533 MPa.
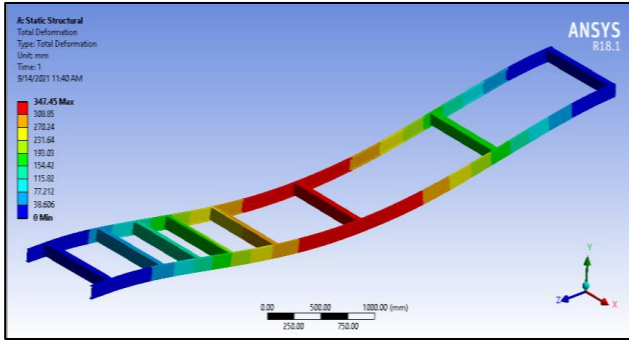
Figure 4.3: Total deformation for square section using St52E
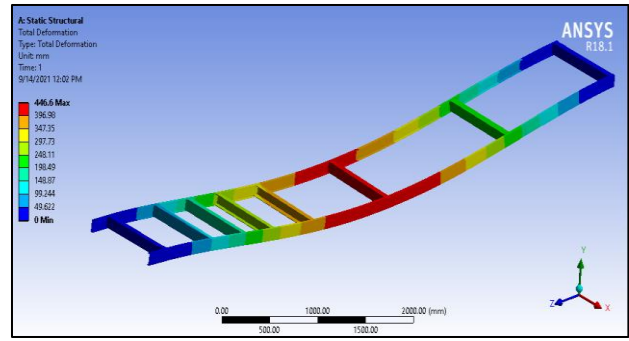
Figure 4.4: Total deformation for C section using St52E

The maximum deformation plots are also obtained for both the square section profile and the C section profile of the chassis as shown in figures 4.3 and 4.4. The C-profile chassis has higher deformation of 446.6 mm and the square profile chassis has lower deformation of 347.45 mm due to high stiffness which increases the resistance of the lateral load.
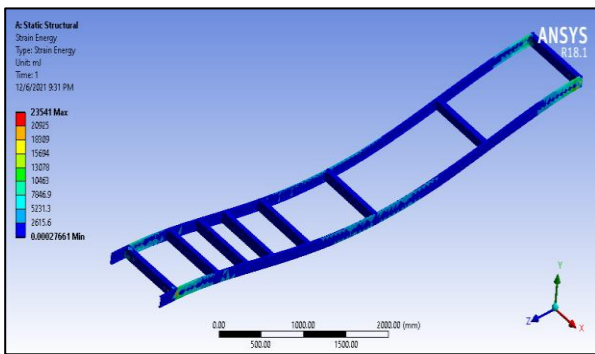
Figure 4.5: Strain energy for square section using St52E
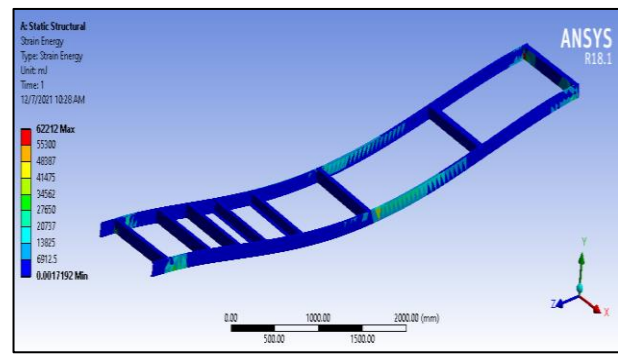
Figure 4.6: Strain energy for C section using St52E
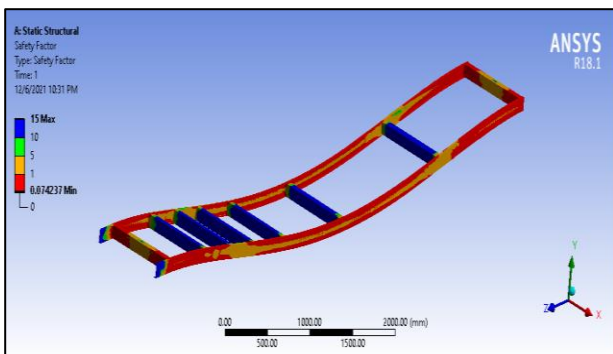
Figure 4.7: Safety factor using square section using St52E
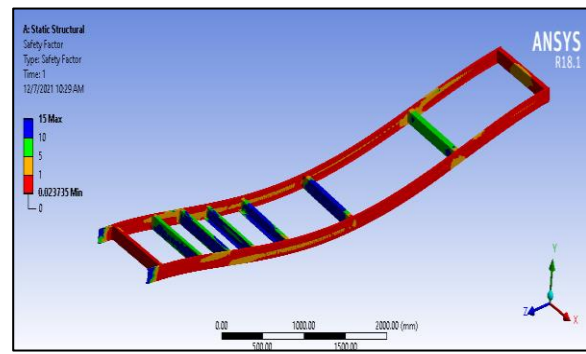
Figure 4.8: Safety factor for C section using St52E

The strain energy and safety factor are evaluated for both square and C section chassis as shown in figures 4.5 to 4.8. For the square section, the maximum strain energy is observed at the frontal and last transverse member of the chassis. For the C section, the maximum strain energy is observed at the mid-region transverse member. For both square and C sections, the maximum safety factor is observed for the transverse section and the minimum safety factor is observed for the longitudinal member as shown by the blue and red zone respectively.

4.1.2 Cross-section results comparison using P100/6061 Al material

From the equivalent-stress plot of P100/6061 Al MMC material, it is evident that the square section chassis profile has lower equivalent-stress as compared to the C section chassis profile. The equivalent-stress observed for square-section chassis is 3277.6 MPa and the equivalent-stress observed for the C-section profile is 10530 MPa as shown in Figures 4.9 and 4.10 respectively.
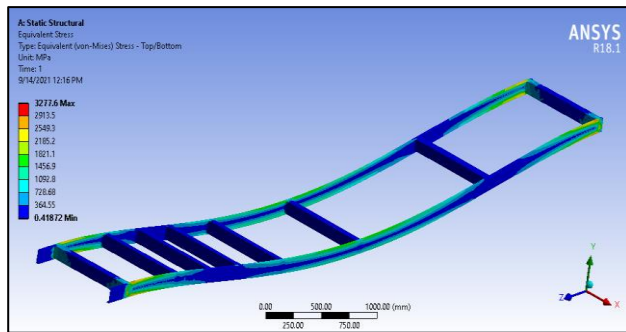
Figure 4.9: Equivalent stress for square section using P100/6061 Al
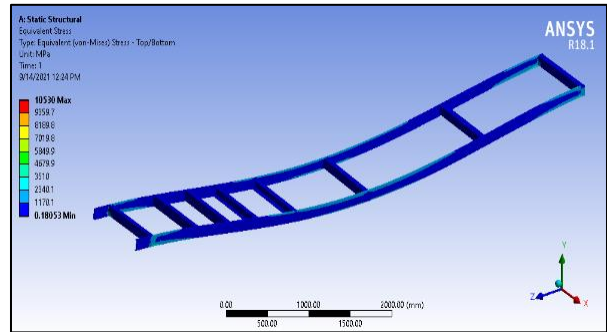
Figure 4.10: Equivalent stress using C section using P100/6061 Al
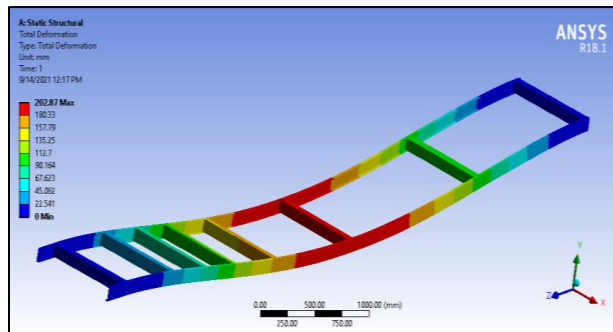
Figure 4.11: Deformation for square section using P100/6061 Al
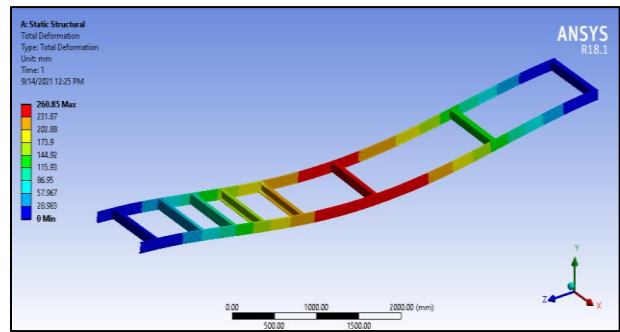
Figure 4.12: Deformation for C section using P100/6061 Al

Maximum deformation plots are also obtained for the chassis' square section profile and C section profile, as shown in figures 4.11 and 4.12. Because of its high stiffness, the C-profile chassis has a higher deformation of 260.85mm and the square profile chassis has a lower deformation of 202.87mm.
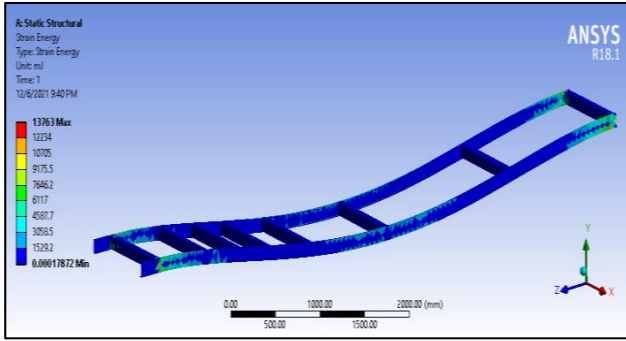
Figure 4.13: Strain energy for square section
using P100/6061 Al
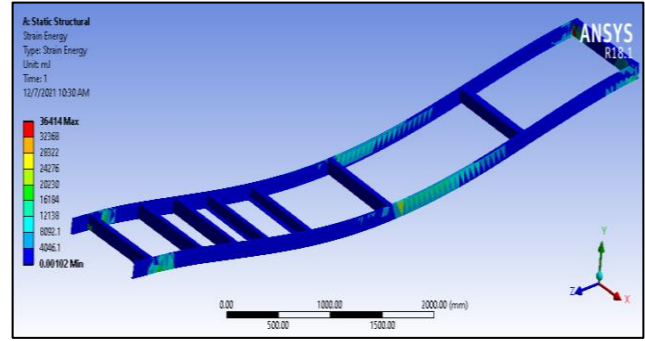
Figure 4.14: Strain energy for C section
using P100/6061 Al
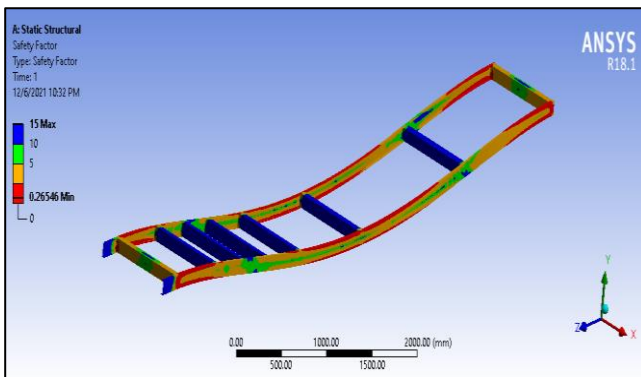
Figure 4.15: Safety factor for square section
using P100/6061 Al
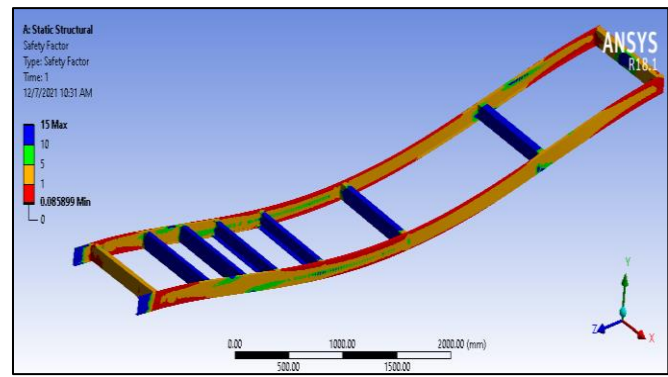
Figure 4.16: Safety factor for C section
using P100/6061 Al

The strain energy and safety factor are evaluated for both square and C section chassis as shown in figures 4.13 to 4.16. For the square section, the maximum strain energy is observed at the frontal and last transverse member of the chassis. For the C section, the maximum strain energy is observed at the mid-region transverse member. For both square and C sections, the maximum safety factor is observed for the transverse section and the minimum safety factor is observed for the longitudinal member.

4.1.3 Cross-section results comparison using Graphite Al GA 7-230 MMC material

From the equivalent-stress plot of Graphite Al GA 7-230 MMC material, it is evident that the square section chassis profile has lower equivalent-stress as compared to the C section chassis profile. The equivalent-stress observed for square-section chassis is 3277.6 MPa and the equivalent-stress observed for the C-section profile is 10541 MPa as shown in Figures 4.17 and 4.18 respectively.
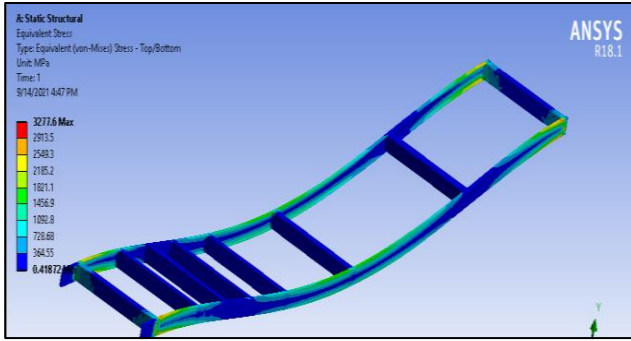
Figure 4.17: Equivalent stress for square section using Graphite Al GA 7-230 MMC
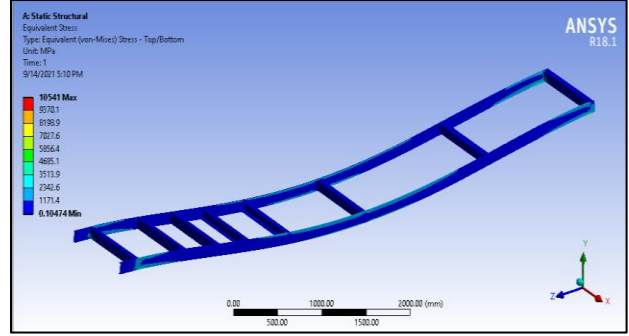
Figure 4.18 Equivalent stress for C section using Graphite Al GA 7-230 MMC
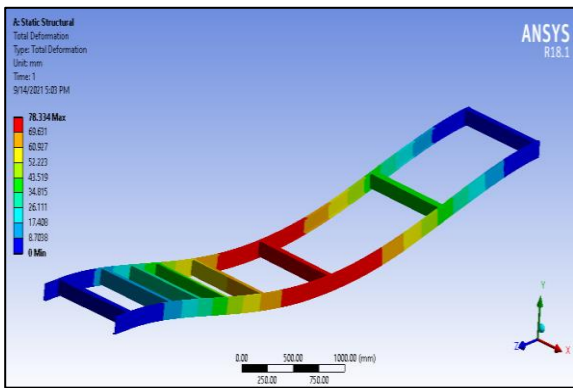
Figure 4.19: Deformation for square section using Graphite Al GA 7-230 MMC
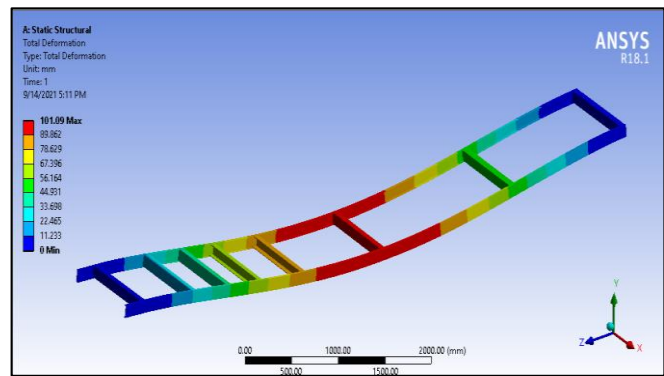
Figure 4.20: Deformation for C section using Graphite Al GA 7-230 MMC

Maximum deformation plots are also obtained for the cassis's square section profile and C section profile, as shown in figures 4.19 and 4.20. Because of its high stiffness, the C-profile chassis has a higher deformation of 101.09mm and the square profile chassis has a lower deformation of 78.334mm.
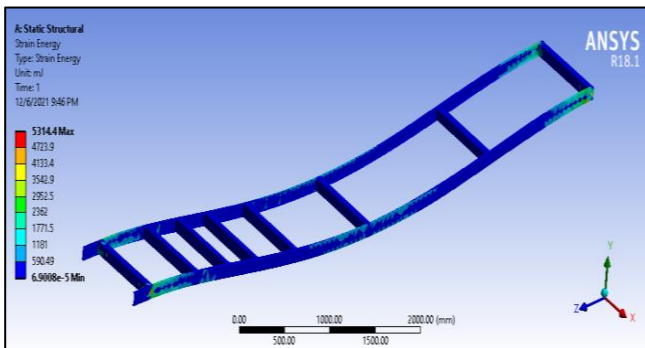
Figure 4.21: Strain energy for square section using Graphite Al GA 7-230 MMC
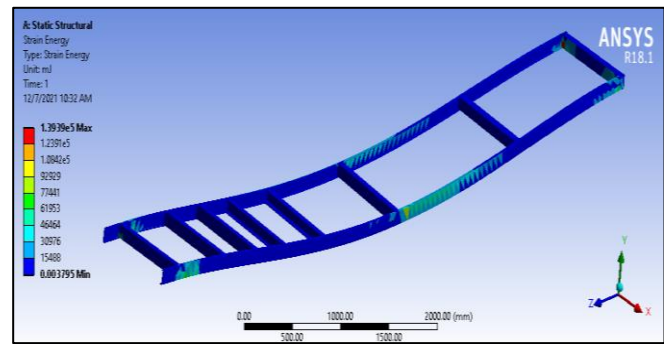
Figure 4.22: Strain energy for C section using Graphite Al GA 7-230 MMC
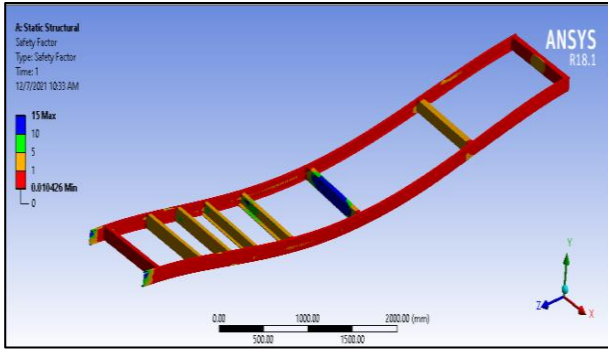
Figure 4.23: Safety factor for square section
using Graphite Al GA 7-230 MMC
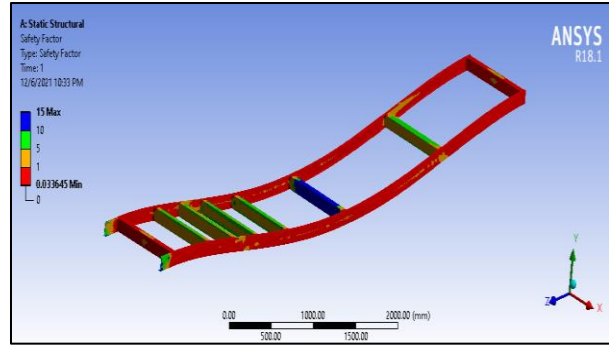
Figure 4.24: Safety factor for C section
using Graphite Al GA 7-230 MMC

The strain energy and safety factor are evaluated for both square and C section chassis as shown in figures 4.21 to 4.24. For the square section, the maximum strain energy is observed at the frontal and last transverse member of the chassis. For the C section, the maximum strain energy is observed at the mid-region transverse member. For both square and C sections, the maximum safety factor is observed for the transverse section and the minimum safety factor is observed for the longitudinal member.

4.1.4 Cross-section results comparison using Al 6092/SIC/17.5P material

From the equivalent-stress plot of Al 6092/SIC/17.5P material, it is evident that the square section chassis profile has lower equivalent-stress as compared to the C section chassis profile. The equivalent-stress observed for square-section chassis is 3277.6 MPa and the equivalent-stress observed for the C-section profile is 10497 MPa as shown in Figures 4.25 and 4.26 respectively.
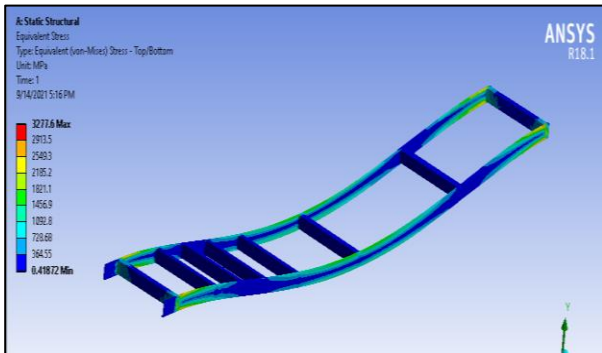
Figure 4.25: Equivalent stress for square section
using Al 6092/SIC/17.5P MMC
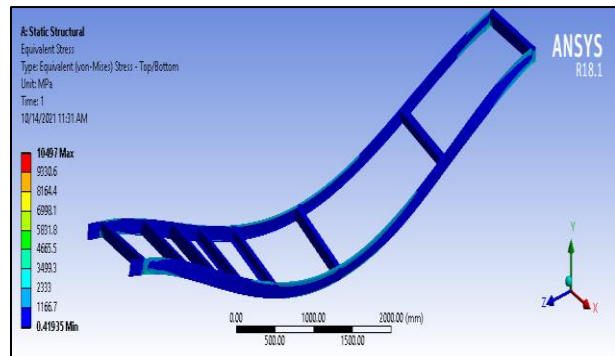
Figure 4.26: Equivalent stress for C section
using Al 6092/SIC/17.5P MMC
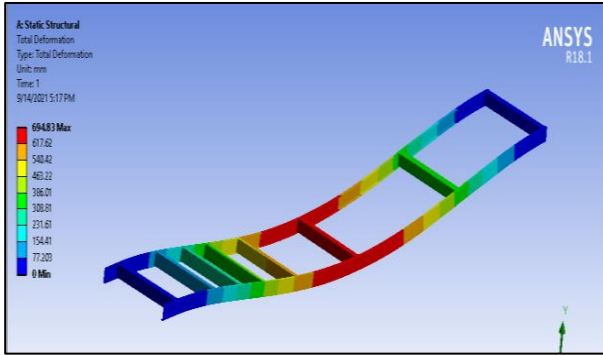
Figure 4.27: Deformation for square section using Al 6092/SIC/17.5P MMC
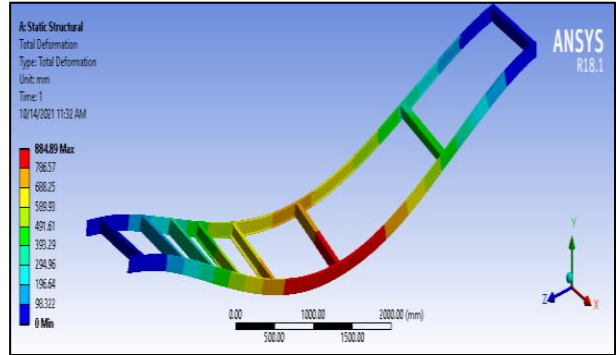
Figure 4.28: Deformation for C section using Al 6092/SIC/17.5P MMC

Maximum deformation plots are also obtained for the chassis' square section profile and C section profile, as shown in figures 4.27 and 4.28. Because of its high stiffness, the C-profile chassis has a higher deformation of 884.89mm and the square profile chassis has a lower deformation of 694.83mm.
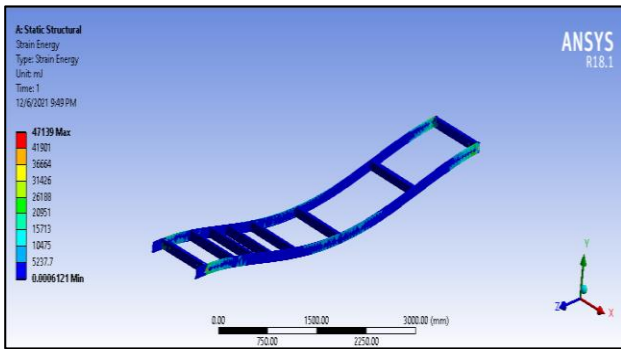
Figure 4.29: Strain energy for square section using Al 6092/SIC/17.5P MMC
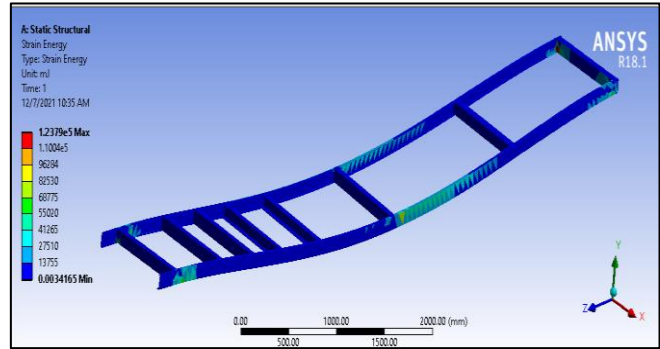
Figure 4.30 Strain energy for C section using Al 6092/SIC/17.5P MMC
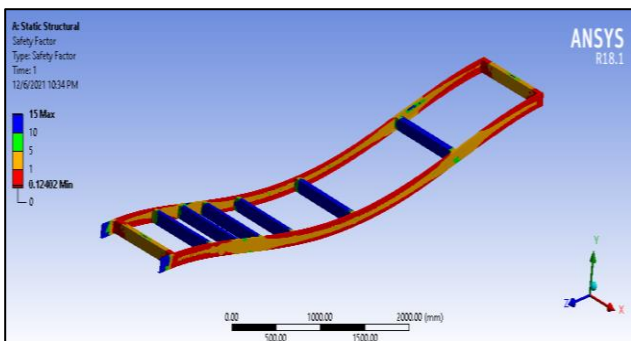
Figure 4.31: Safety factor for square section using Al 6092/SIC/17.5P MMC
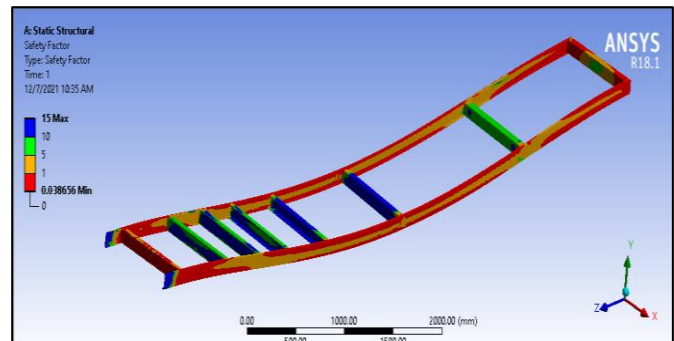
Figure 4.32: Safety factor for C section using Al 6092/SIC/17.5P MMC

The strain energy and safety factor are evaluated for both square and C section chassis as shown in figures 4.29 to 4.32. For the square section, the maximum strain energy is observed at the frontal and last transverse member of the chassis. For the C section, the maximum strain energy is observed at the mid-region transverse member. For both square and C sections, the maximum safety factor is observed for the transverse section and the minimum safety factor is observed for the longitudinal member. Table 4.1 shows the output parameters for square section results.

Table 4.1: Output parameters for square section results

Material Type	Equivalent-stress (MPa)	Deformation (mm)	Strain Energy (MJ)	Safety Factor
St52E	3280.5	347.45	23541	.074
P100/6061 Al	3277.6	202.87	13763	.265
Graphite Al GA 7-230	3277.6	78.33	5314.4	.033
Al 6092/SiC/17.5p	3277.6	694.83	47139	.124

Figure 4.33 shows the equivalent-stress comparison between materials for the square section while Figure 4.34 indicates the deformation comparison between materials for the square section.
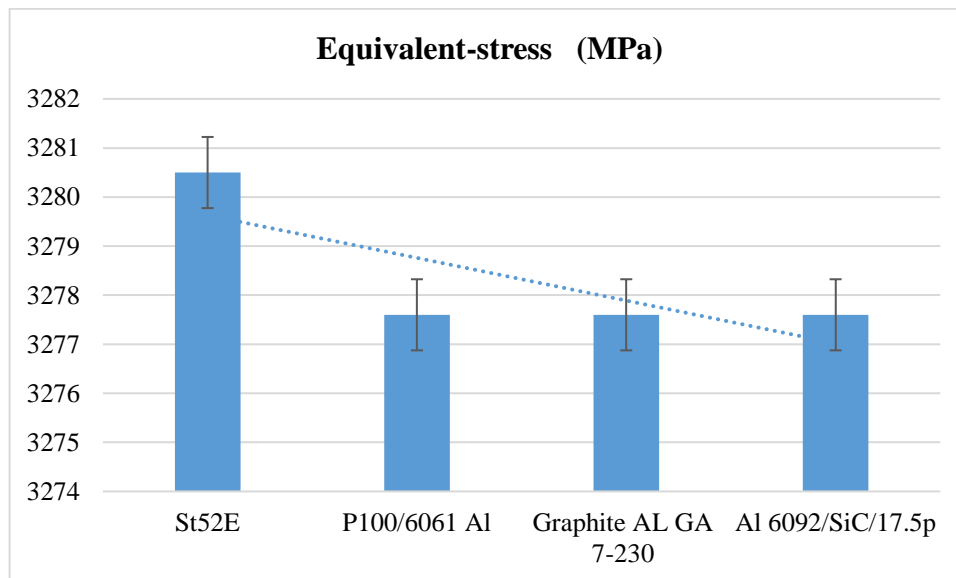
Figure 4.33: Equivalent-stress comparison between materials for square section
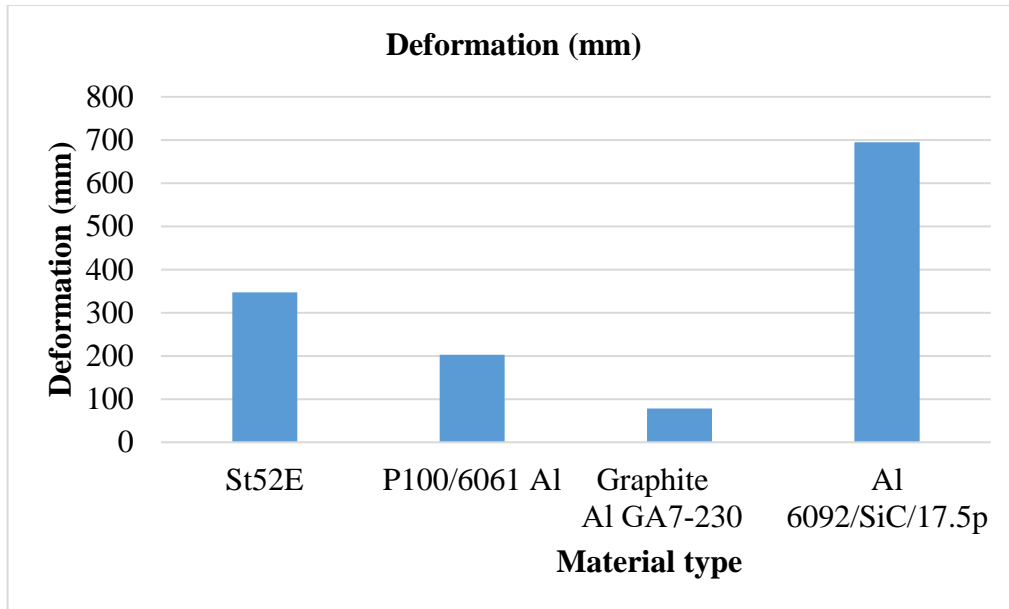
Figure 4.34: Deformation comparison between materials for square section

The equivalent-stress is maximum for St52E material with the magnitude of 3280.5 MPa and is lower for material matrix composite chassis. The P100/6061 Al has a lower equivalent-stress of 3277.6 MPa. Figure 4.35 shows the strain energy comparison between materials for the square section while Figure 4.36 indicates the Safety factor comparison between materials for the square section.
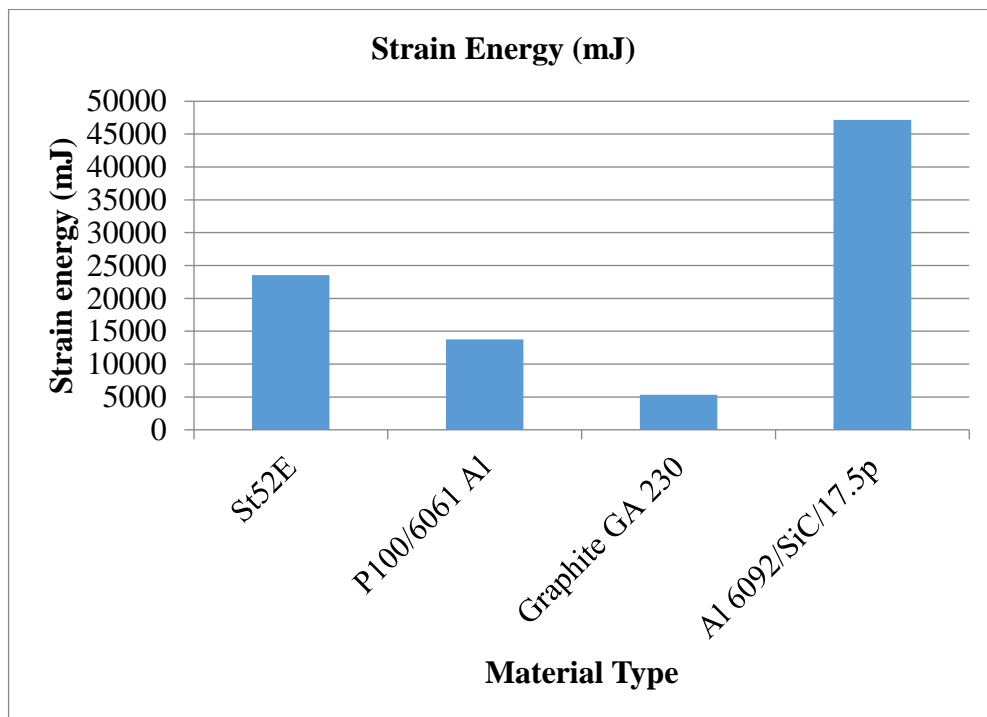
Figure 4.35: Strain energy comparison between materials for square section
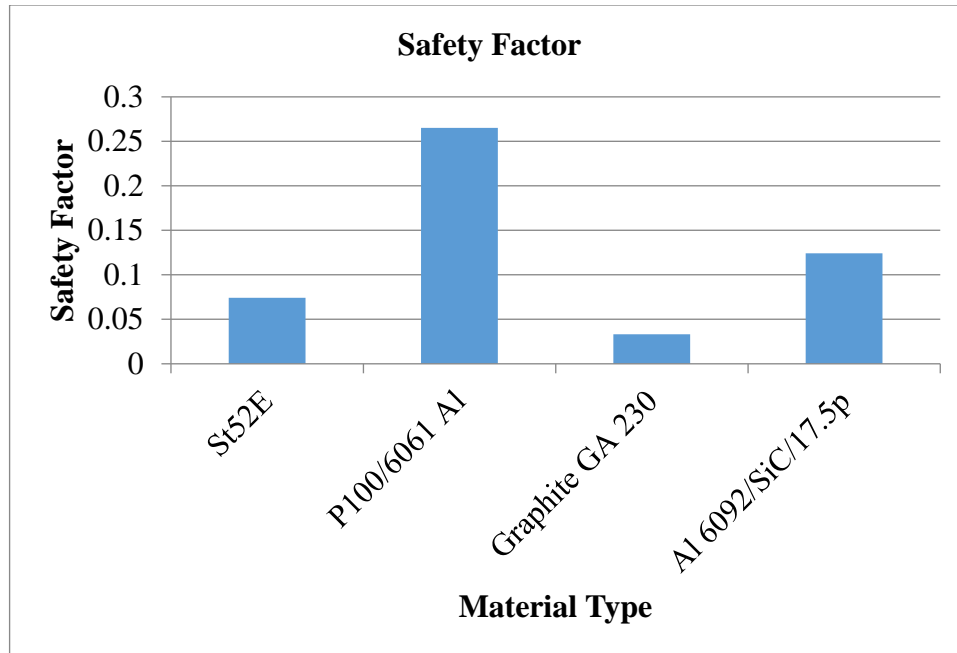
Figure 4.36: Safety factor comparison between materials for square section

The material with the highest energy absorption characteristics is al 6092/SiC/17.5p, while the material with the lowest energy absorption characteristics is Graphite Al GA 7-230 MMC. For each material, a safety factor comparison chart is generated. P100/6061 Al has the highest safety factor, while Graphite Al GA 7-230 MMC has the lowest. Table 4.2 shows the output parameters for the C section results.

Table 4.2: Output parameters for C section results

Material Type	Equivalent-stress (MPa)	Deformation (mm)	Strain Energy (MJ)	Safety Factor
St52E	10533	446.6	62212	.0237
P100/6061 Al	10530	260.85	36414	.0858
Graphite Al GA 7-230	10541	101.09	139390	.0104
Al 6092/SiC/17.5p	10497	884.89	123790	.0386

Figure 4.37 shows the equivalent-stress comparison between materials for the C section while Figure 4.38 shows the deformation comparison between materials for the C section.
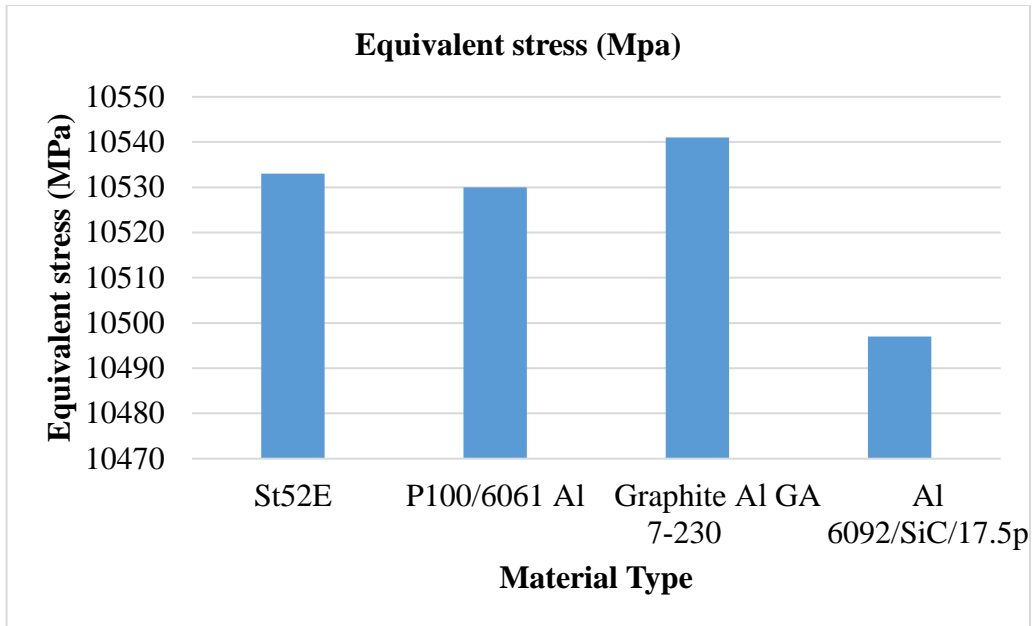
Figure 4.37: Equivalent-stress comparison between materials for C section

The equivalent-stress comparison plot shows that Graphite Al GA 7-230 MMC has the highest equivalent-stress value with a magnitude of 10541 MPa and Al 6092/SiC/17.5p has the lowest equivalent-stress value with a magnitude of 10497 MPa. The deformation of all four materials is compared and the maximum deformation is observed for Al 6092/SiC/17.5p with a magnitude of 884.89mm, and the minimum deformation is observed for Graphite Al GA 7-230 MMC with a magnitude of 101.09mm.
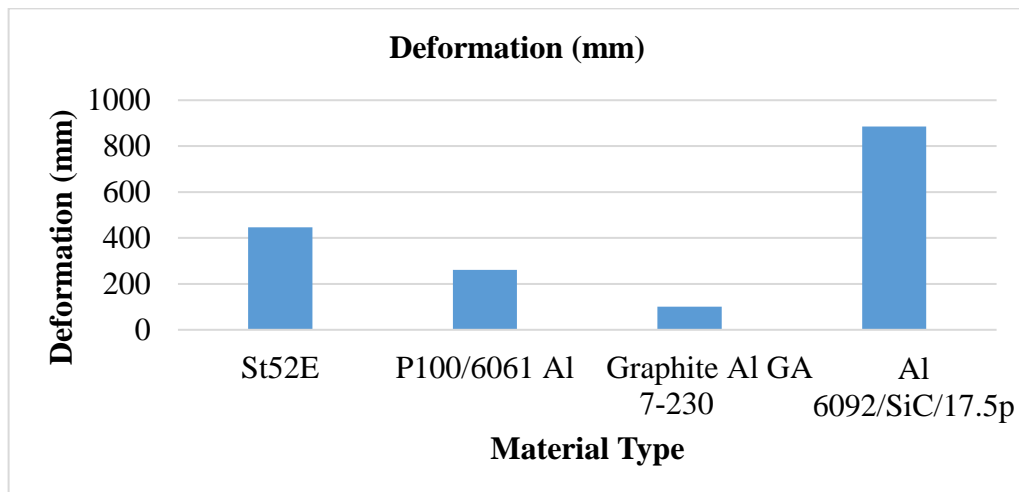
Figure 4.38: Deformation comparison between materials for C section

The strain energy of materials for the C section is compared in Figure 4.39, and the Safety Factor of materials for the C section is compared in Figure 4.40.
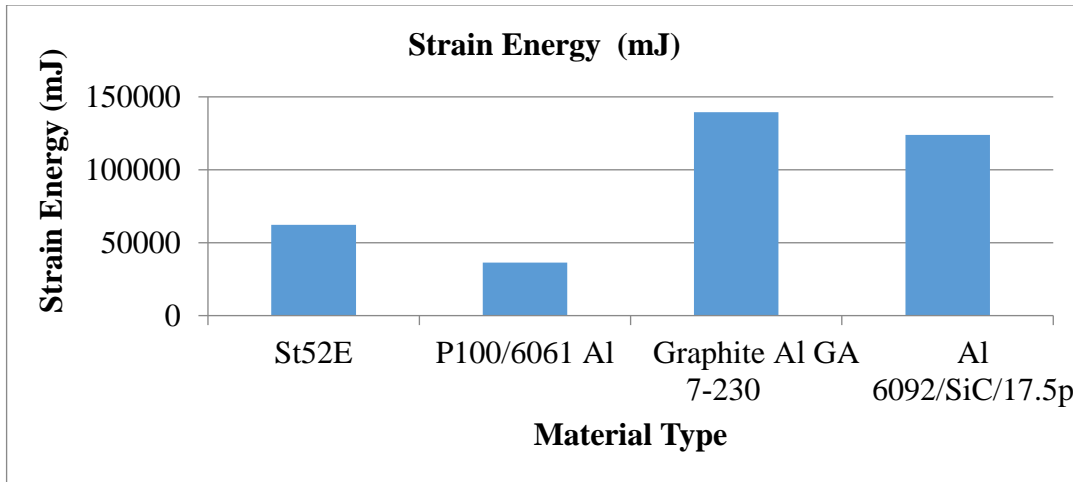
Figure 4.39: Strain energy comparison between materials for C section
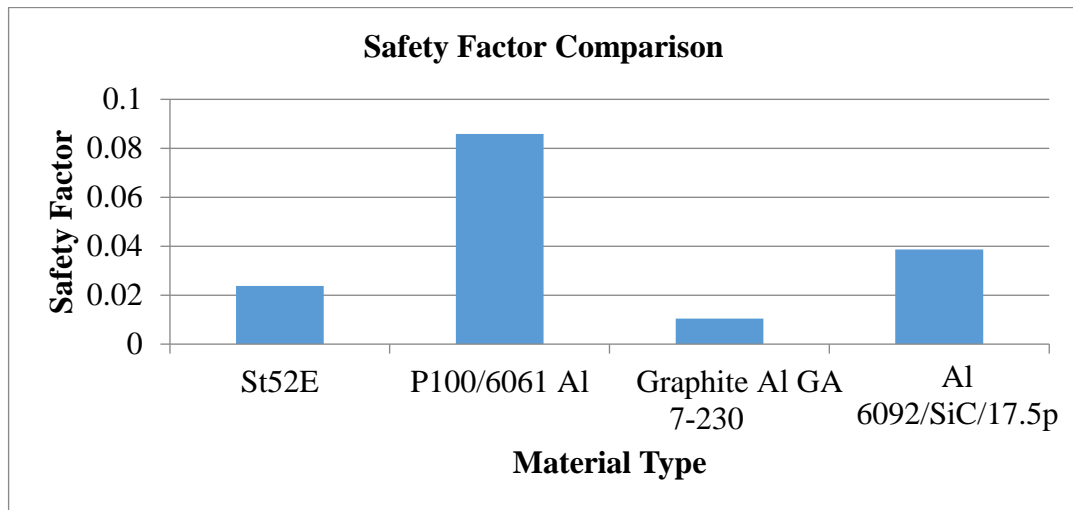
Figure 4.40: Safety Factor comparison between materials for C section

4.1.5 Sub-Chapter Summary

The strain energy and safety factor comparison plot are generated for different materials within the square and the C-sections. The maximum energy absorption characteristics are exhibited by Graphite Al GA 7-230 MMC material and minimum energy absorption characteristics are exhibited by P100/6061 Al MMC. The safety factor comparison chart is generated for different materials and cross-sections. The maximum safety factor is obtained for P100/6061 Al and is minimum Graphite Al GA 7-230 MMC. Sub-Chapter 4.1 has shown that a chassis made of square profile lateral cross members has higher strength and lower deformation as compared to C-type lateral cross-sections. This fulfills some specific objectives given in § 1.4.

The next sub-chapter presents the free vibration analysis on the chassis in the case of the square section and C-section using St52E and three MMCs respectively as mentioned in section 3.1 earlier.

4.2 Vibration Analysis of the chassis

The chassis is subjected to a free vibration analysis to determine natural frequencies and mode shapes considering square and C sections and using St52E, P100/6061 Al MMC, Graphite Al GA 7-230 MMC and Al 6092/SiC/17.5p respectively. This analysis would be useful in determining the resonant frequency and mass participation factor in each direction.

4.2.1 Modal analysis of Square Section using St52E

The mode shapes and natural frequencies are determined by keeping similar loading conditions as in structural analysis. The mode shapes are shown in Figure 4.41.
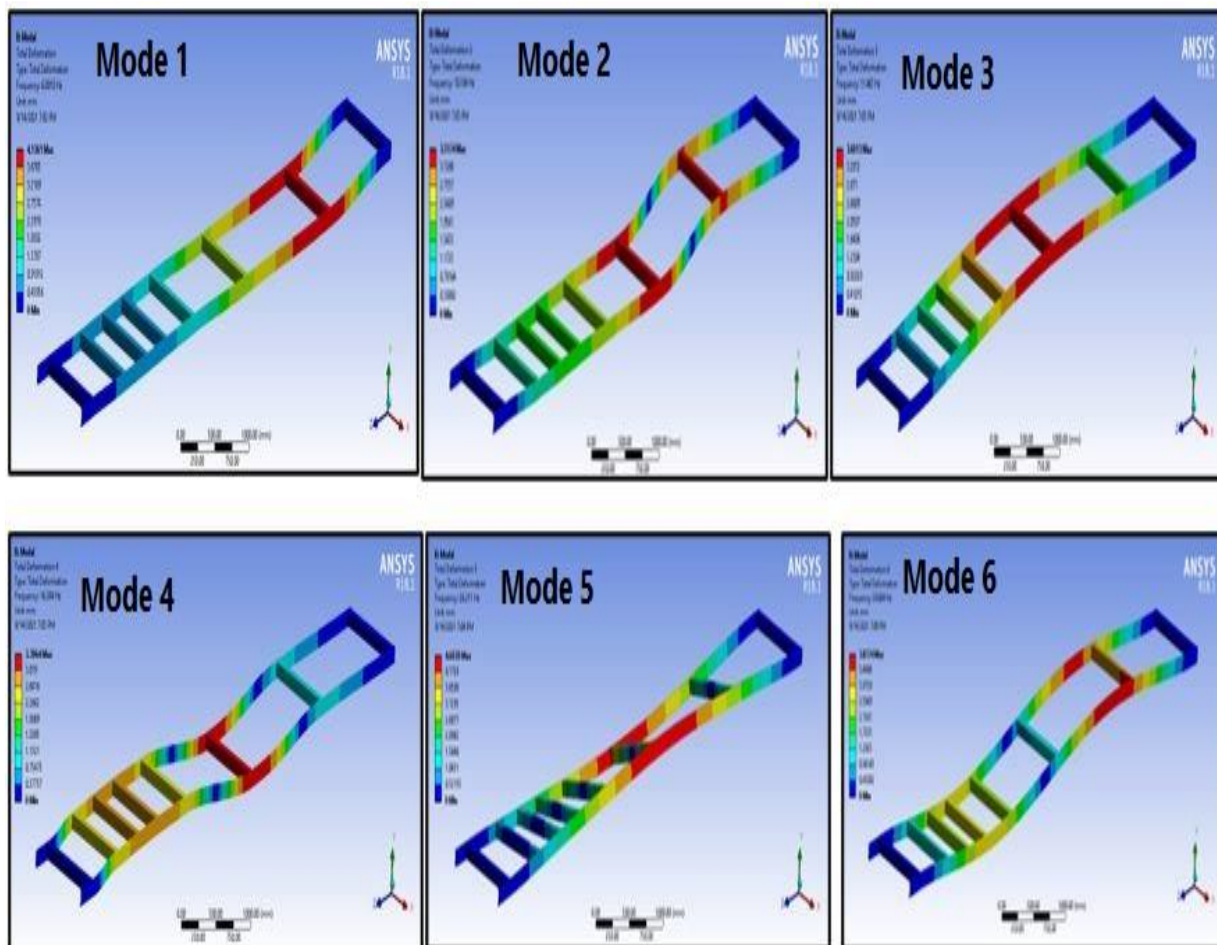
Figure 4.41: Mode shapes of Square Section using St52E (Combined)
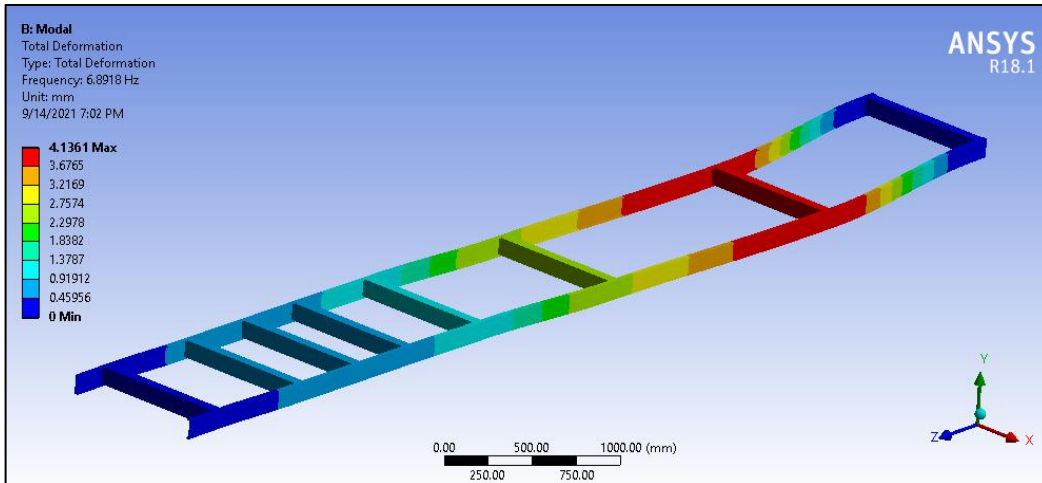
Figure 4.42: Mode shape of 1st natural frequency of Square Section using St52E

The 1st frequency mode shape is shown in figure 4.42. The mode shape shows a lateral mode shape with a magnitude of 4.13mm and a natural frequency of 6.89Hz. The 2nd frequency mode shape is shown in figure 4.43 which shows a transverse type of mode shape with maximum deformation of 3.517mm and a frequency of 10.184Hz.

Figure 4.43: Mode shape of 2nd natural frequency of Square Section using St52E

The 3rd frequency mode shape is shown in figure 4.44. The mode shape shows a lateral mode shape with a magnitude of 3.69mm and a natural frequency of 11.463Hz.

Figure 4.44: Mode shape of 3rd natural frequency of Square Section using St52E

The 4th frequency mode shape is shown in figure 4.45 which shows a transverse type of mode shape with maximum deformation of 3.39mm and a frequency of 16.284Hz.

Figure 4.45: Mode shape of 4th natural frequency of Square Section using St52E

The 5th frequency mode shape is shown in figure 4.46 which shows a torsional type of mode shape with maximum deformation of 4.69mm and a frequency of 26.211Hz.

Figure 4.46: Mode shape of 5th natural frequency of Square Section using St52E

The 6th frequency mode shape is shown in figure 4.47 which shows a transverse type of mode shape with maximum deformation of 3.87mm and a frequency of 29.684Hz.

Figure 4.47: Mode shape of 6th natural frequency of Square Section using St52E

The mass participation factor is evaluated for all the directions and the maximum mass participation factor is observed for translational x-direction i.e., 0.779. The high mass participation factor along the x-direction signifies that any external excitation along this direction would likely cause resonance and amplitude build-up. The mass participation factor along other directions is low and therefore any excitation along other directions would not cause resonance. Frequency and mass participation factors are shown in Table 4.3.

Table 4.3: Frequency and mass participation factor for Square Section using St52E

***** PARTICIPATION FACTOR CALCULATION ***** X DIRECTION					CUMULATIVE	RATIO EFF.MASS
MODE	FREQUENCY	PERIOD	PARTIC.FACTOR	RATIO	EFFECTIVE MASS	MASS FRACTION	TO TOTAL MASS
1	6.89178	0.14510	0.34725	1.000000	0.120581	0.700927	0.546320
2	10.1844	0.98190E-01	0.15998	0.460713	0.255942E-01	0.849704	0.115960
3	11.4632	0.87235E-01	-0.25697E-03	0.000740	0.660345E-07	0.849704	0.299184E-06
4	16.2836	0.61412E-01	-0.16079	0.463038	0.258530E-01	0.999985	0.117133
5	26.2109	0.38152E-01	-0.15789E-02	0.004547	0.249296E-05	1.00000	0.112949E-04
6	29.6836	0.33689E-01	0.58257E-04	0.000168	0.339392E-08	1.00000	0.153769E-07
----							
sum					0.172031		0.779425

4.2.2 Modal analysis of C Section using St52E

The mode shapes and natural frequencies are determined by keeping similar loading conditions as in structural analysis. The mode shapes are shown in figure 4.48.
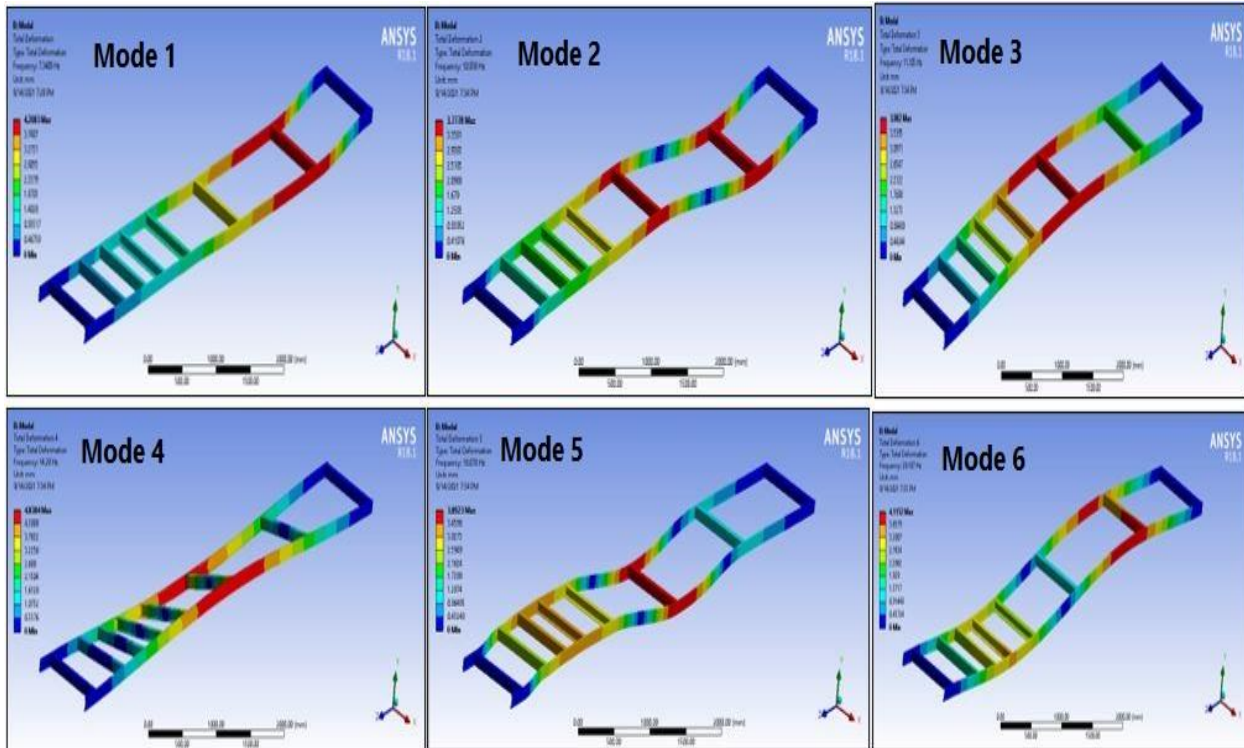
Figure 4.48: Mode shapes (Combined) of C-Section using St52E
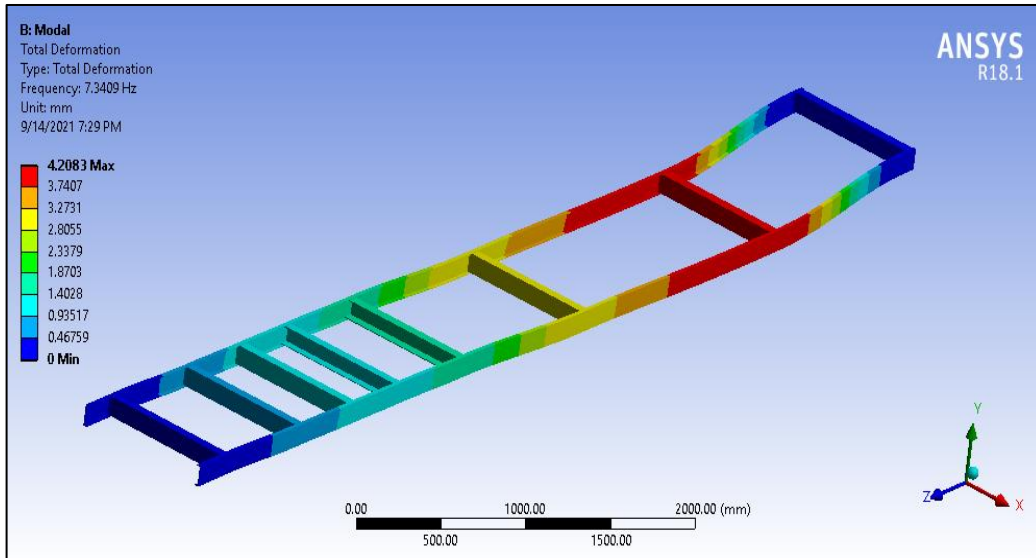
Figure 4.49: Mode shape of 1st natural frequency of C-Section using St52E

The 1st frequency mode shape is shown in figure 4.49. The mode shape shows a lateral mode shape with a magnitude of 4.208mm and a natural frequency of 7.34Hz. The 2nd frequency mode shape is shown in figure 4.50 which shows a transverse type mode shape with maximum deformation of 3.777mm and a frequency of 10.938Hz.

Figure 4.50: Mode shape of 2nd natural frequency of C-Section using St52E

The 3rd frequency mode shape is shown in figure 4.51. The mode shape shows a lateral mode shape with a magnitude of 3.982mm and a natural frequency of 11.105Hz.
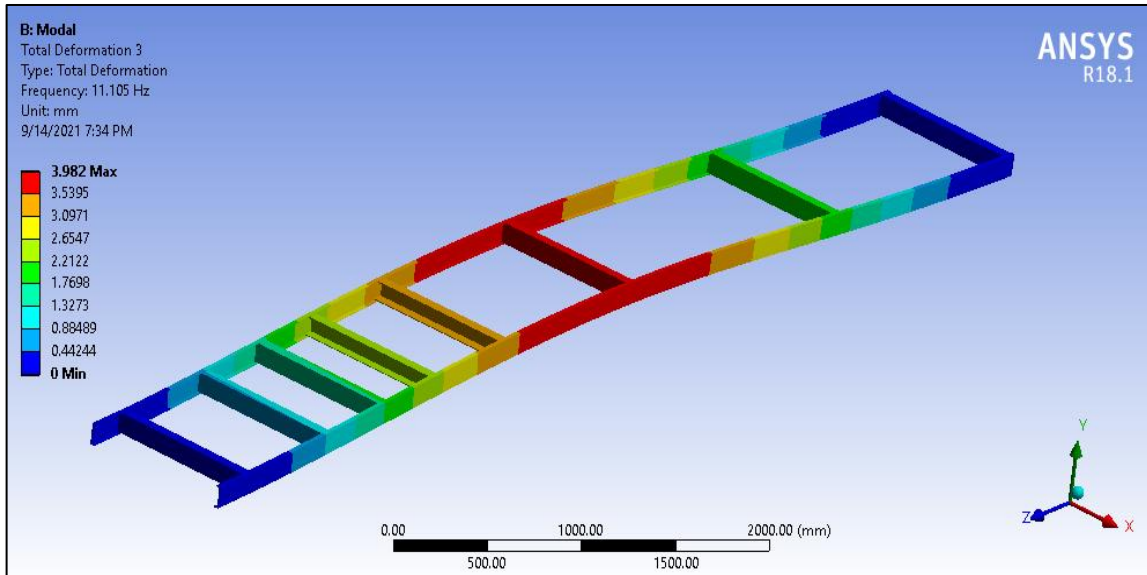
Figure 4.51: Mode shape of 3rd natural frequency of C-Section using St52E

The 4th frequency mode shape is shown in figure 4.52 which shows a transverse type mode shape with maximum deformation of 4.83mm and a frequency of 14.29Hz.
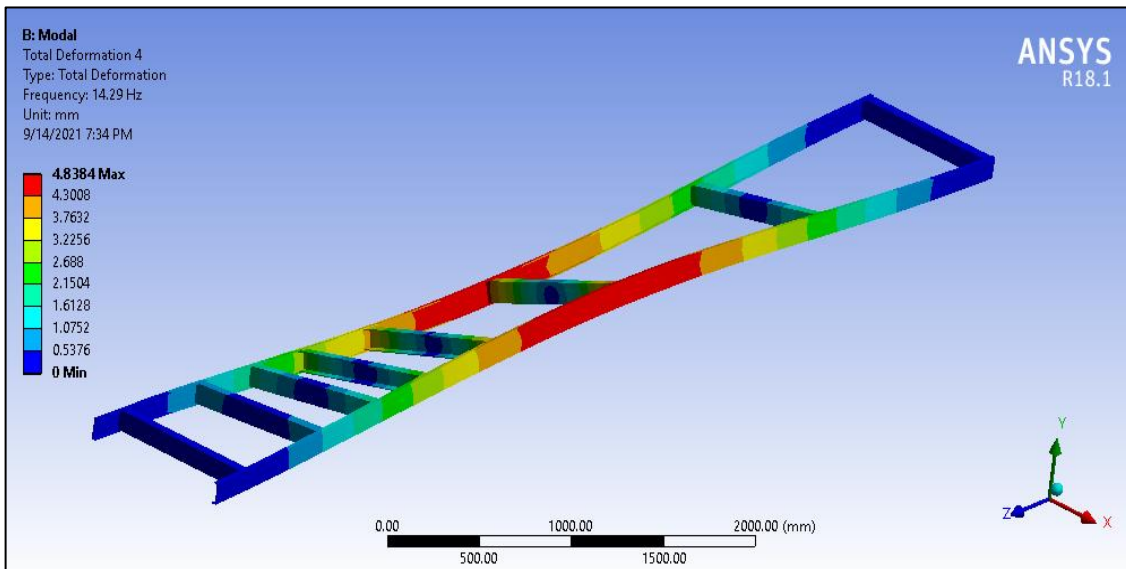
Figure 4.52: Mode shape of 4th natural frequency of C-Section using St52E

The 5th frequency mode shape is shown in figure 4.53 which shows a torsional type of mode shape with maximum deformation of 3.89mm and a frequency of 18.078Hz.
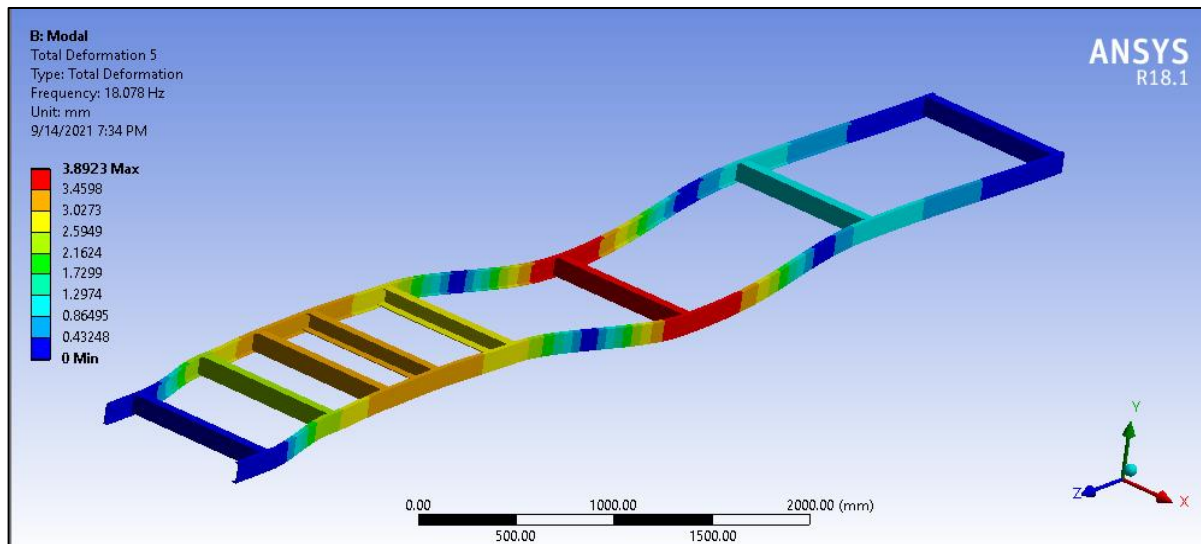
Figure 4.53: Mode shape of 5th natural frequency of C-Section using St52E

The 6th frequency mode shape is shown in figure 4.54 which shows a transverse type mode shape with maximum deformation of 4.11mm and a frequency of 29.187Hz.
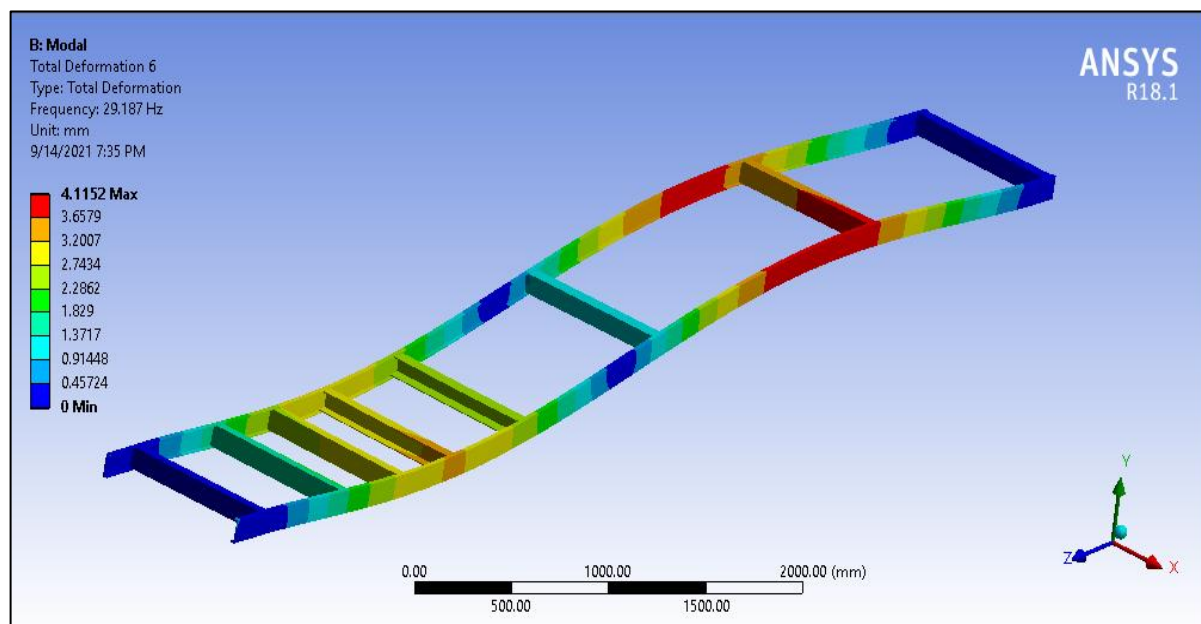
Figure 4.54: Mode shape of 6th natural frequency of C-Section using St52E

The mass participation factor is evaluated for all the directions and the maximum mass participation factor is observed for translational x-direction i.e., 0.764. The high mass participation factor along the x-direction signifies that any external excitation along this direction would likely cause resonance and amplitude build-up. The mass participation factor along other directions is low and therefore any excitation along other directions would not cause resonance as indicated in table 4.4.

Table 4.4: Frequency and mass participation factor for C- Section using St52E

						CUMULATIVE	RATIO EFF.MASS	
MODE	FREQUENCY	PERIOD	PARTIC.FACTOR	RATIO	EFFECTIVE MASS	MASS FRACTION	TO TOTAL MASS	
1	7.34092	0.13622	0.33119	1.000000	0.109684	0.781239	0.597589	
2	10.9382	0.91422E-01	-0.11553	0.348825	0.133462E-01	0.876300	0.727139E-01	
3	11.1048	0.90051E-01	-0.66910E-02	0.020203	0.447696E-04	0.876619	0.243917E-03	
4	14.2901	0.69978E-01	-0.78883E-02	0.023818	0.622245E-04	0.877062	0.339016E-03	
5	18.0784	0.55315E-01	-0.13138	0.396689	0.172602E-01	1.00000	0.940380E-01	
6	29.1869	0.34262E-01	0.26419E-03	0.000798	0.697987E-07	1.00000	0.380282E-06	
--								
sum					0.140398		0.764924	
--								

***** PARTICIPATION FACTOR CALCULATION ***** X DIRECTION

4.2.3 Modal analysis of Square Section using P100/6061 Al MMC

The mode shapes and natural frequencies are determined by keeping similar loading conditions as in structural analysis. The mode shapes are shown in figure 4.55.

Figure 4.55: Mode shapes (Combined) of Square Section using P100/6061 Al MMC
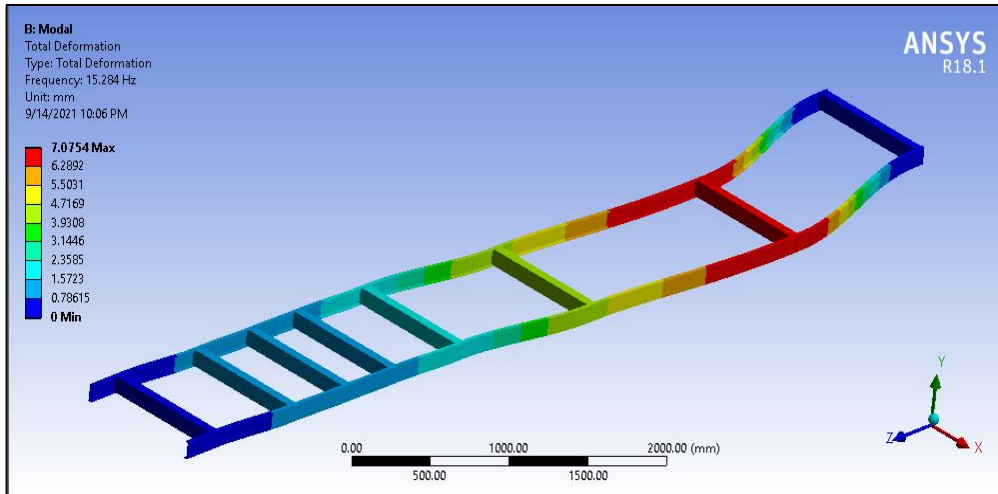
Figure 4.56: Mode shape of 1st natural frequency of Square Section using P100/6061 Al MMC

The 1st frequency mode shape is shown in figure 4.56. The mode shape shows a lateral mode shape with a magnitude of 7.075mm and a natural frequency of 15.284Hz. The 2nd frequency mode shape is shown in figure 4.57 which shows a transverse type of mode shape with maximum deformation of 6.076mm and a frequency of 22.732Hz.
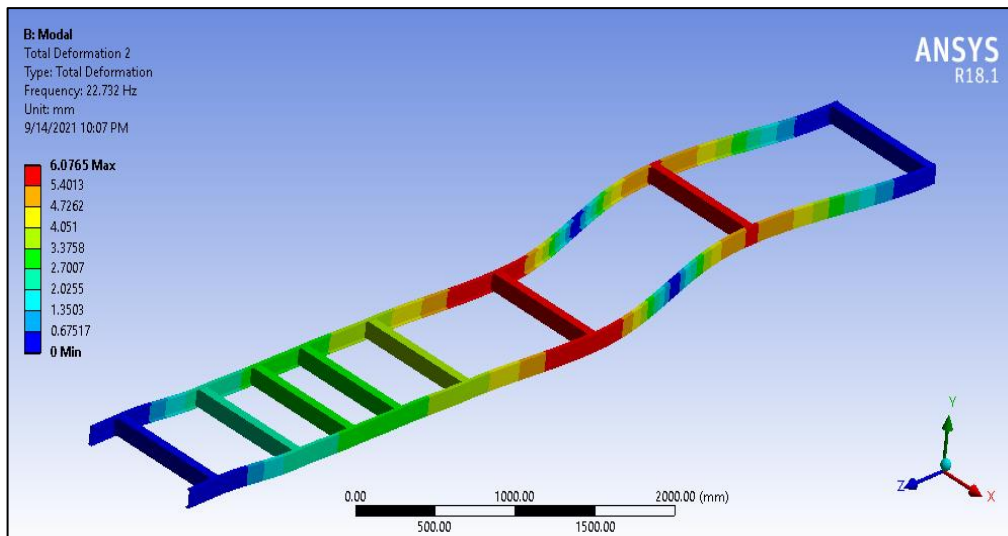
Figure 4.57: Mode shape of 2nd natural frequency of Square Section using P100/6061 Al MMC

The 3rd frequency mode shape is shown in figure 4.58. The mode shape shows a lateral mode shape with a magnitude of 6.412mm and a natural frequency of 25.454Hz.
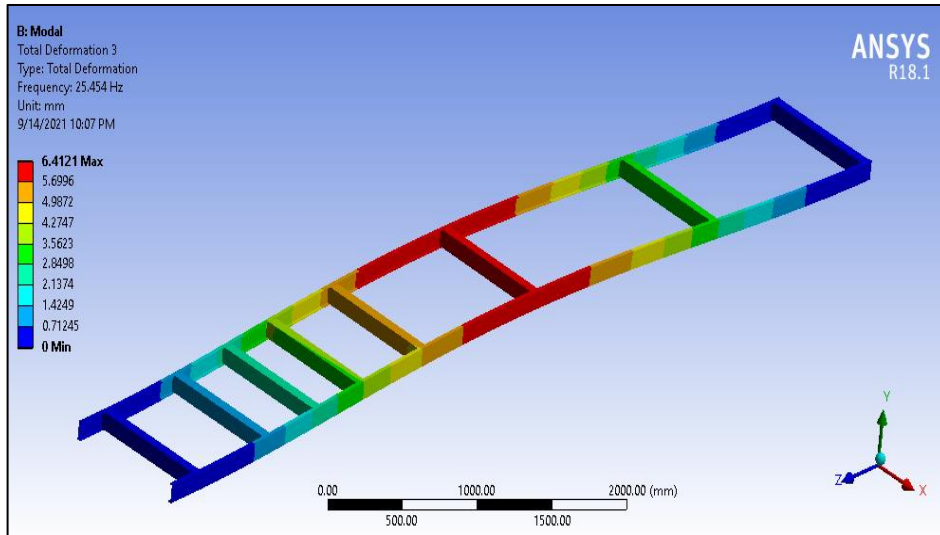
Figure 4.58: Mode shape of 3rd natural frequency of Square Section using P100/6061 Al MMC

The 4th frequency mode shape is shown in figure 4.59 which shows a transverse type of mode shape with maximum deformation of 5.781mm and a frequency of 36.505Hz.
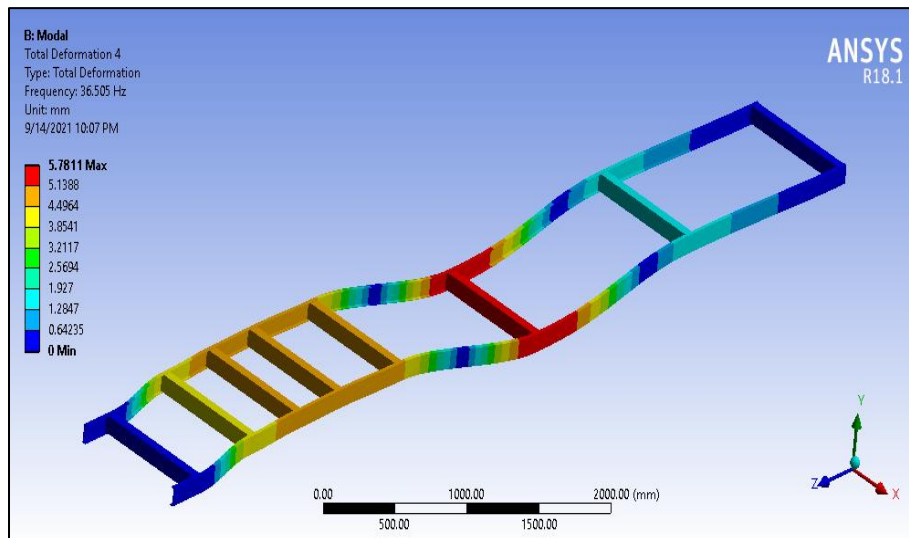
Figure 4.59: Mode shape of 4th natural frequency of Square Section using P100/6061 Al MMC

The 5th frequency mode shape is shown in figure 4.60 which shows a torsional type of mode shape with maximum deformation of 8.35mm and a frequency of 57.796Hz.
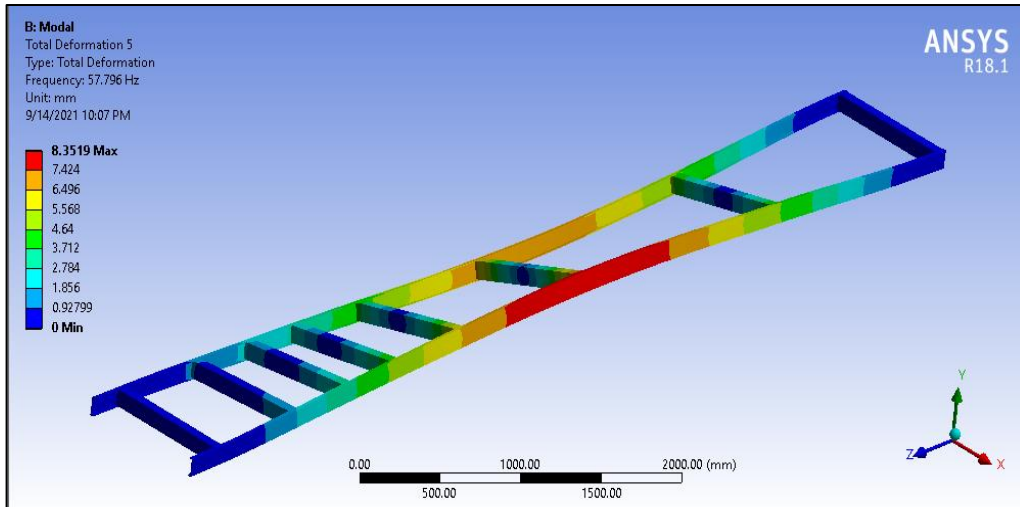
Figure 4.60: Mode shape of 5th natural frequency of Square Section using P100/6061 Al MMC

The 6th frequency mode shape is shown in figure 4.61 which shows a transverse type of mode shape with maximum deformation of 6.87mm and a frequency of 66.2Hz.
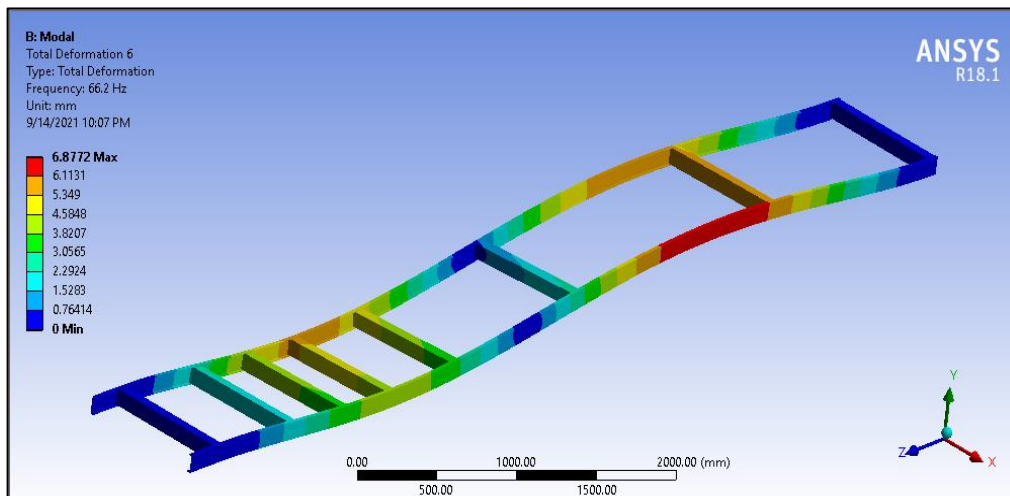
Figure 4.61: Mode shape of 6th natural frequency of Square Section using P100/6061 Al MMC

The mass participation factor is evaluated for all the directions and the maximum mass participation factor is observed for translational x-direction i.e., 0.7821. The high mass participation factor along the x-direction signifies that any external excitation along this direction would likely cause resonance and amplitude build-up.

The mass participation factor along other directions is low and therefore any excitation along other directions would not cause resonance as shown in table 4.5.

Table 4.5: Frequency and Mass participation factor for *Square Section* using P100/6061 Al MMC

***** PARTICIPATION FACTOR CALCULATION ***** X DIRECTION							
					CUMULATIVE	RATIO EFF.MASS	
MODE	FREQUENCY	PERIOD	PARTIC.FACTOR	RATIO	EFFECTIVE MASS	MASS FRACTION	TO TOTAL MASS
1	15.2840	0.65428E-01	0.20252	1.000000	0.410163E-01	0.704541	0.551066	
2	22.7317	0.43991E-01	0.91758E-01	0.453070	0.841952E-02	0.849163	0.113119	
3	25.4542	0.39286E-01	0.60460E-05	0.000030	0.365542E-10	0.849163	0.491116E-09	
4	36.5053	0.27393E-01	-0.93704E-01	0.462678	0.878042E-02	0.999985	0.117968	
5	57.7959	0.17302E-01	-0.90971E-03	0.004492	0.827575E-06	1.00000	0.111187E-04	
6	66.1998	0.15106E-01	-0.14074E-03	0.000695	0.198079E-07	1.00000	0.266125E-06	
--							
sum					0.582171E-01		0.782164	
--							

4.2.4 Modal analysis of C Section using P100/6061 Al MMC

The mode shapes and natural frequencies are determined by keeping similar loading conditions as in structural analysis. The mode shapes are shown in figure 4.62.
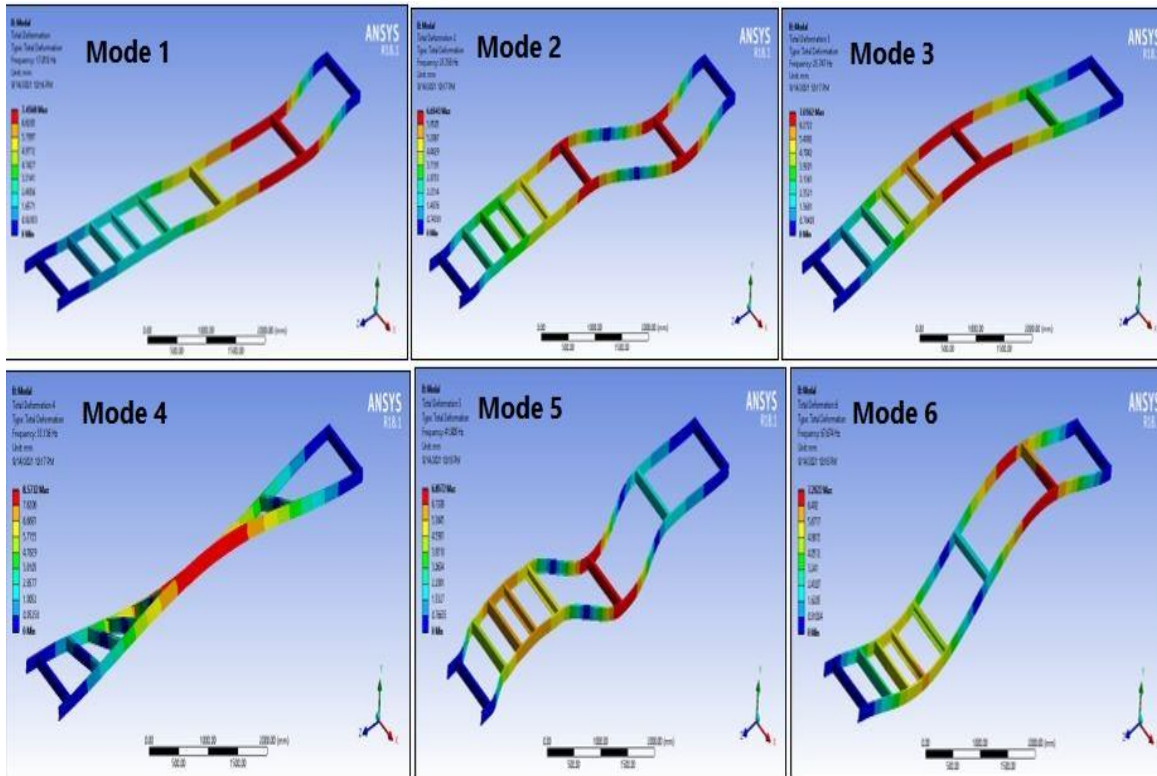
Figure 4.62: Mode shapes (Combined) of C-Section using P100/6061 Al MMC
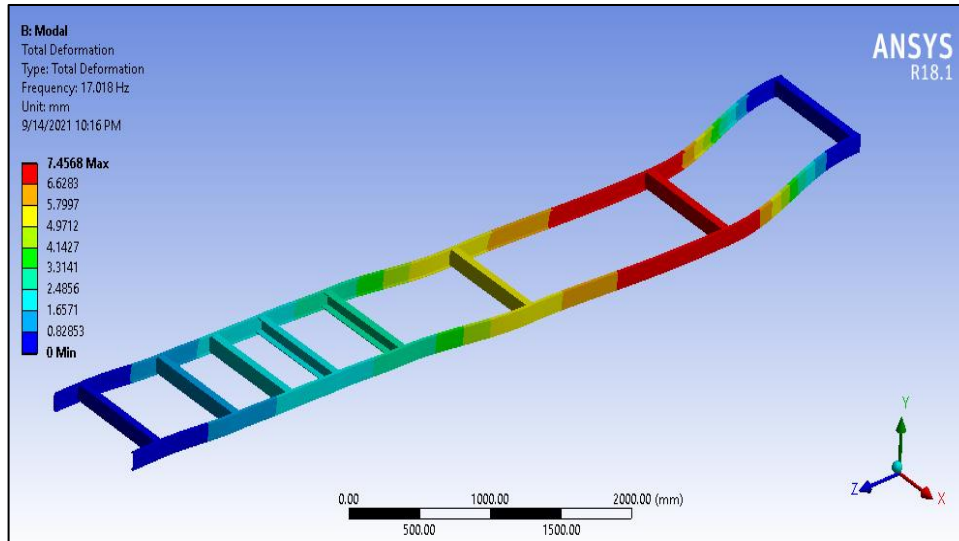
Figure 4.63: Mode shape of 1st natural frequency of C-Section using P100/6061 Al MMC

The 1st frequency mode shape is shown in figure 4.63. The mode shape shows a lateral mode shape with a magnitude of 7.456mm and a natural frequency of 17.018Hz. The 2nd frequency mode shape is shown in figure 4.64 which shows a transverse type of mode shape with maximum deformation of 6.694mm and a frequency of 25.358Hz.
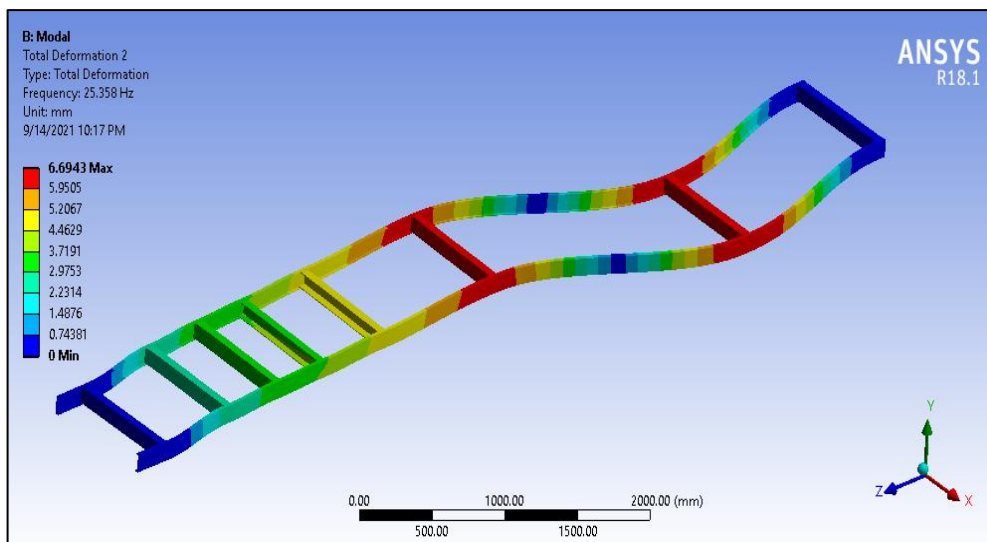
Figure 4.64: Mode shape of 2nd natural frequency of C-Section using P100/6061 Al MMC

The 3rd frequency mode shape is shown in figure 4.65. The mode shape shows a lateral mode shape with a magnitude of 7.056mm and a natural frequency of 25.747Hz.
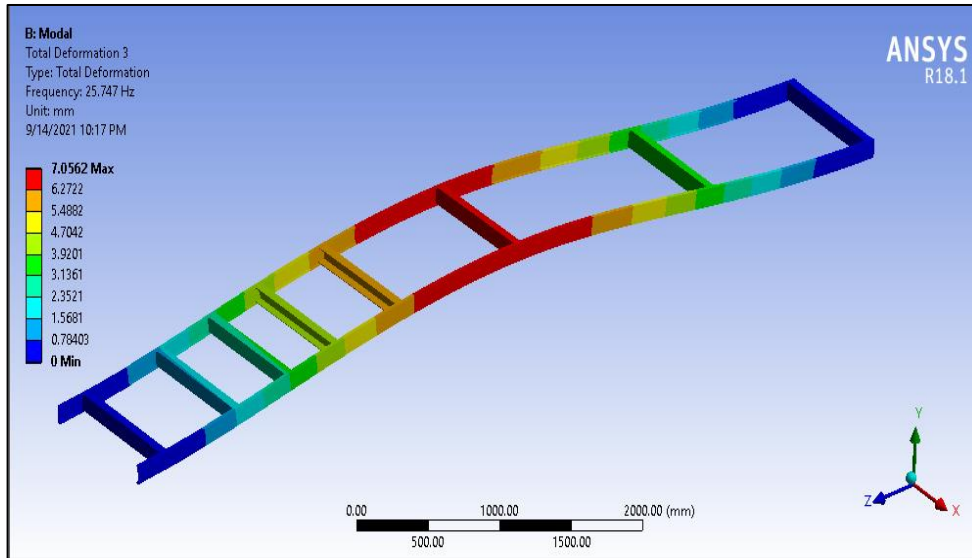
Figure 4.65: Mode shape of 3rd natural frequency of C-Section using P100/6061 Al MMC

The 4th frequency mode shape is shown in figure 4.66 which shows a torsional type of mode shape with maximum deformation of 8.573mm and a frequency of 33.136Hz.
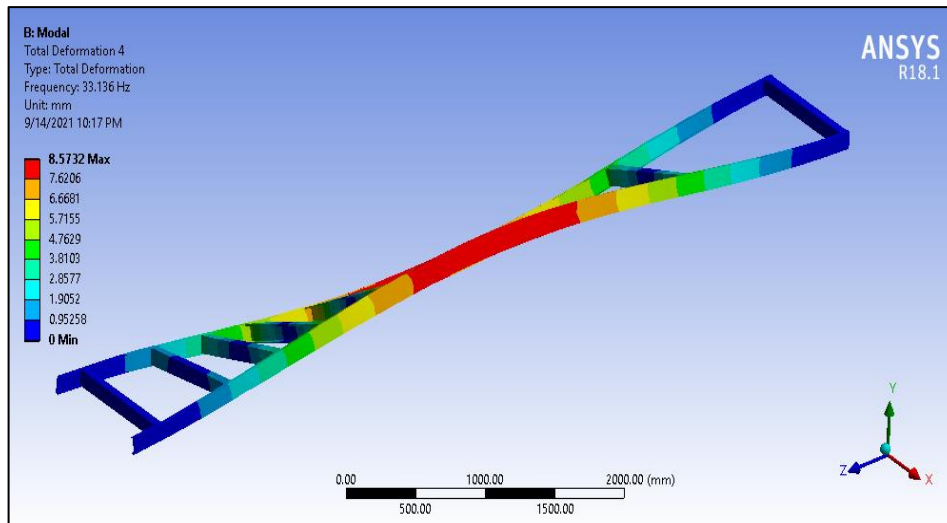
Figure 4.66: Mode shape of 4th natural frequency of C-Section using P100/6061 Al MMC

The 5th frequency mode shape is shown in figure 4.67 which shows a torsional type of mode shape with maximum deformation of 6.89mm and a frequency of 41.909Hz.
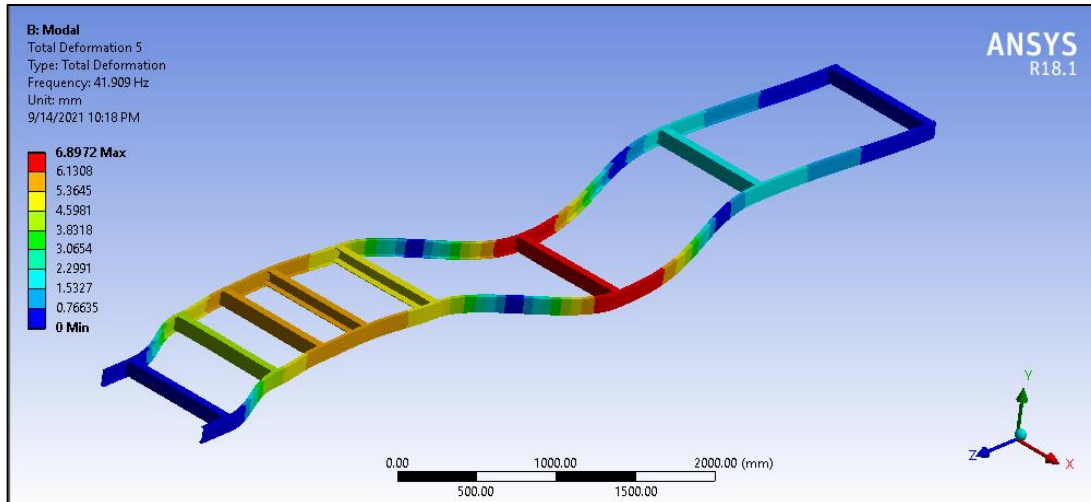
Figure 4.67: Mode shape of 5th natural frequency of C-Section using P100/6061 Al MMC

The 6th frequency mode shape is shown in figure 4.68 which shows a transverse type mode shape with maximum deformation of 7.292mm and a frequency of 67.674Hz.
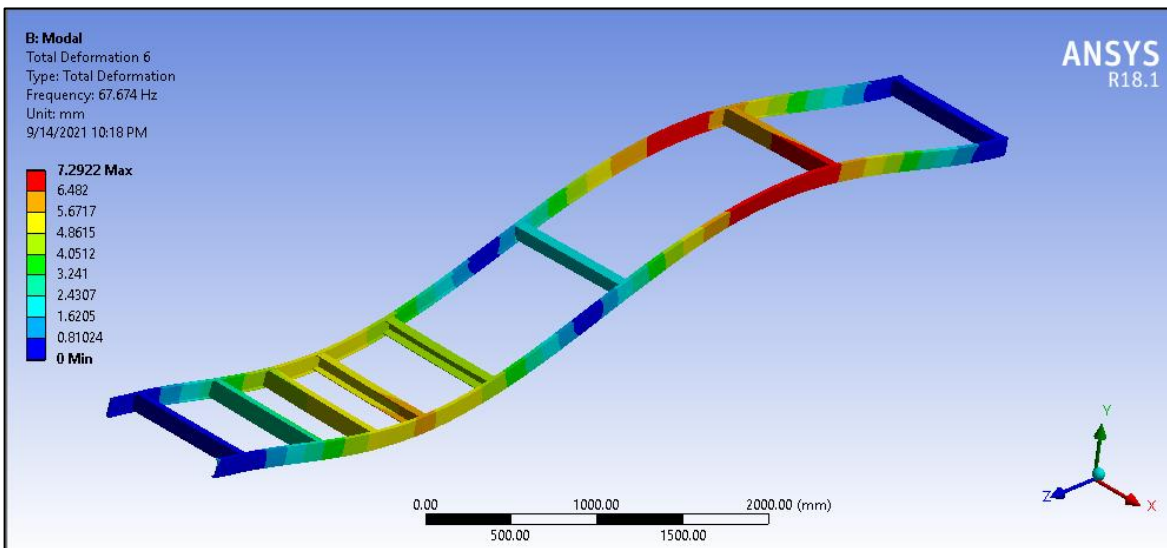
Figure 4.68: Mode shape of 6th natural frequency of C-Section using P100/6061 Al MMC

The mass participation factor is evaluated for all the directions and the maximum mass participation factor is observed for translational x-direction i.e., 0.7821. The high mass participation factor along the x-direction signifies that any external excitation along this direction would likely cause resonance and amplitude build-up. The mass participation factor along other directions is low and therefore any excitation along other directions would not cause resonance as shown in table 4.6.

Table 4.6: Frequency and Mass participation factor for C- Section using P100/6061 Al MMC

***** PARTICIPATION FACTOR CALCULATION ***** X DIRECTION						
					CUMULATIVE	RATIO EFF.MASS
MODE	FREQUENCY	PERIOD	PARTIC.FACTOR	RATIO	EFFECTIVE MASS	MASS FRACTION	TO TOTAL MASS
1	15.2840	0.65428E-01	0.20252	1.000000	0.410163E-01	0.704541	0.551066
2	22.7317	0.43991E-01	0.91758E-01	0.453070	0.841952E-02	0.849163	0.113119
3	25.4542	0.39286E-01	0.60460E-05	0.000030	0.365542E-10	0.849163	0.491116E-09
4	36.5053	0.27393E-01	-0.93704E-01	0.462678	0.878042E-02	0.999985	0.117968
5	57.7959	0.17302E-01	-0.90971E-03	0.004492	0.827575E-06	1.00000	0.111187E-04
6	66.1998	0.15106E-01	-0.14074E-03	0.000695	0.198079E-07	1.00000	0.266125E-06
--						
sum					0.582171E-01		0.782164
--						

4.2.5 Modal analysis of Square Section using Graphite Al GA 7-230 MMC

The mode shapes and natural frequencies are determined by keeping similar loading conditions as in structural analysis. The mode shapes are shown in the figure 4.69.
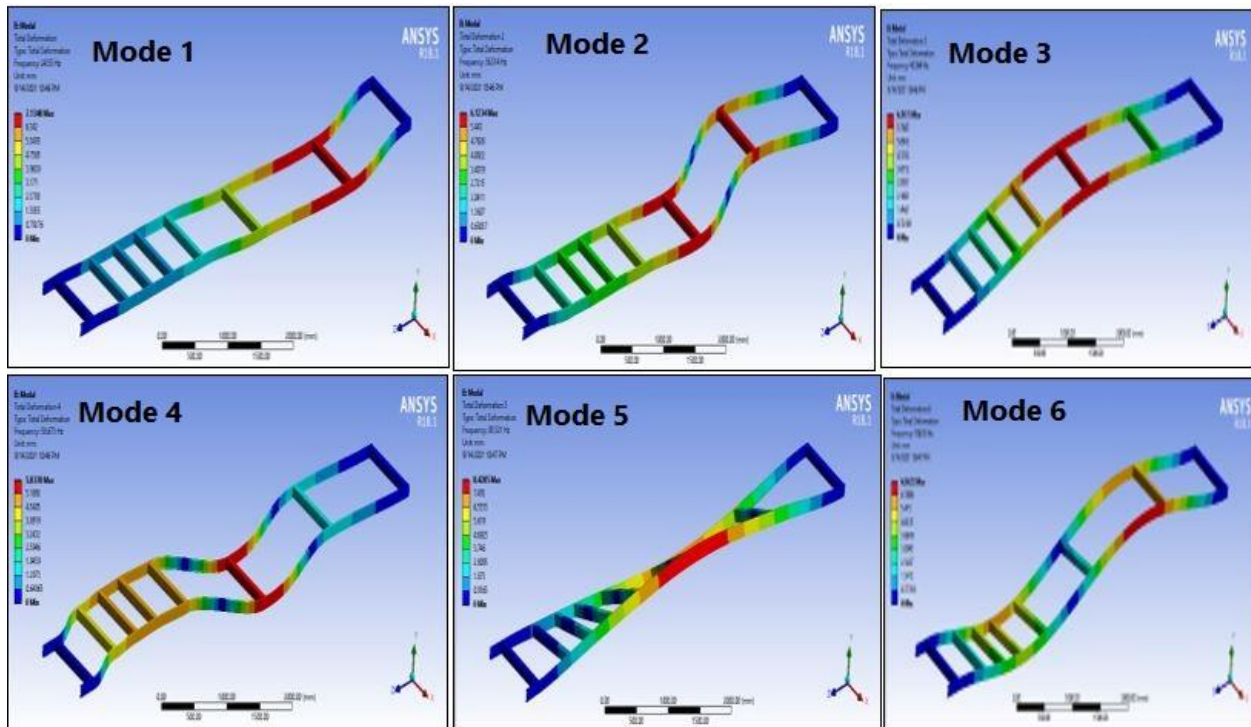
Figure 4.69: Mode shapes (Combined) of Square Section using Graphite Al GA 7-230 MMC
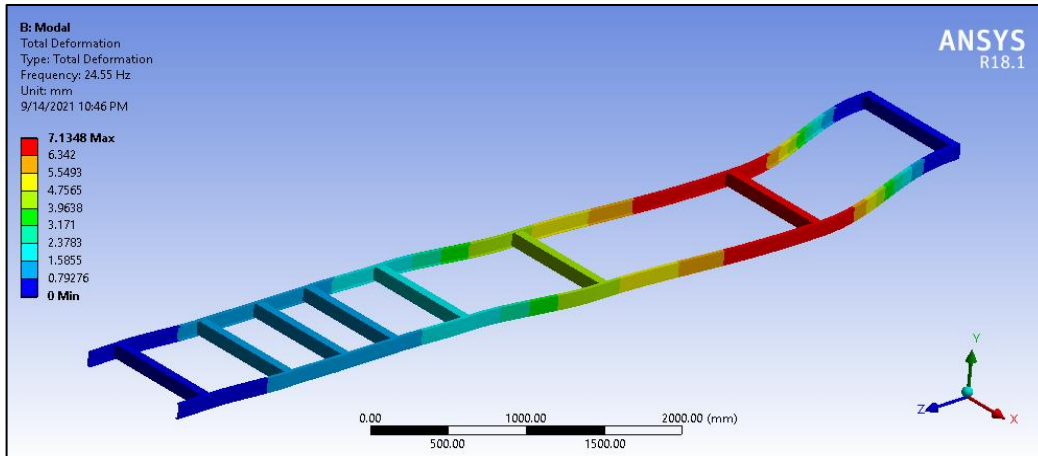
Figure 4.70: Mode shape of 1st natural frequency of Square Section using Graphite Al GA 7-230

The 1st frequency mode shape is shown in figure 4.70. The mode shape shows a lateral mode shape with a magnitude of 7.134mm and a natural frequency of 24.55Hz. The 2nd frequency mode shape is shown in figure 4.71 which shows a transverse type of mode shape with maximum deformation of 6.123mm and a frequency of 36.514Hz.
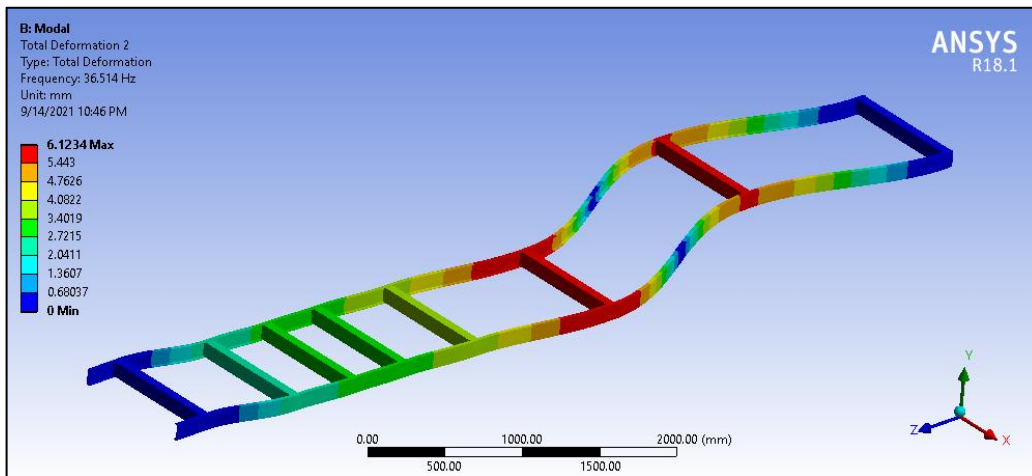
Figure 4.71: Mode shape of 2nd natural frequency of Square Section using Graphite Al GA 7-230

The 3rd frequency mode shape is shown in figure 4.72. The mode shape shows a lateral mode shape with a magnitude of 6.5073mm and a natural frequency of 40.964Hz.
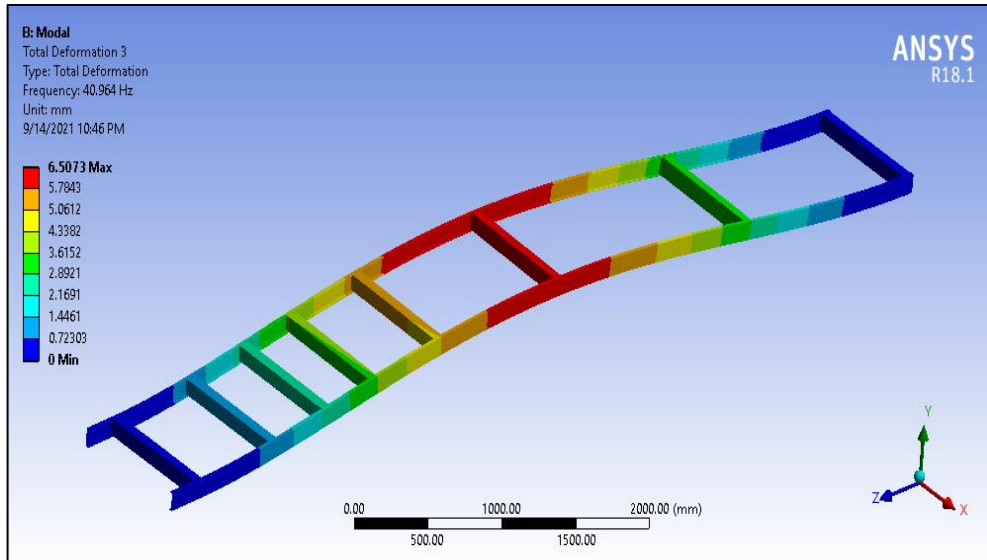
Figure 4.72: Mode shape of 3rd natural frequency of Square Section using Graphite Al GA 7-230

The 4th frequency mode shape is shown in figure 4.73 which shows a transverse type of mode shape with maximum deformation of 5.8378mm and a frequency of 58.673Hz.

Figure 4.73: Mode shape of 4th natural frequency of Square Section using Graphite Al GA 7-230

The 5th frequency mode shape is shown in figure 4.74 which shows a torsional type of mode shape with maximum deformation of 8.428mm and a frequency of 93.521Hz.

Figure 4.72: Mode shape of 3rd natural frequency of Square Section using Graphite Al GA 7-230

The 4th frequency mode shape is shown in figure 4.73 which shows a transverse type of mode shape with maximum deformation of 5.8378mm and a frequency of 58.673Hz.
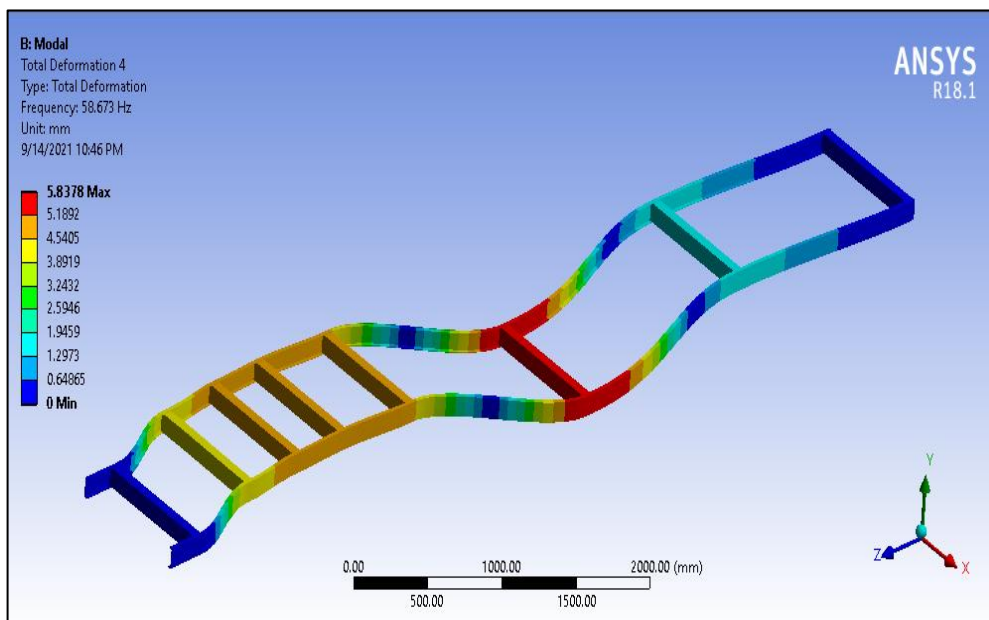
Figure 4.73: Mode shape of 4th natural frequency of Square Section using Graphite Al GA 7-230

The 5th frequency mode shape is shown in figure 4.74 which shows a torsional type of mode shape with maximum deformation of 8.428mm and a frequency of 93.521Hz.
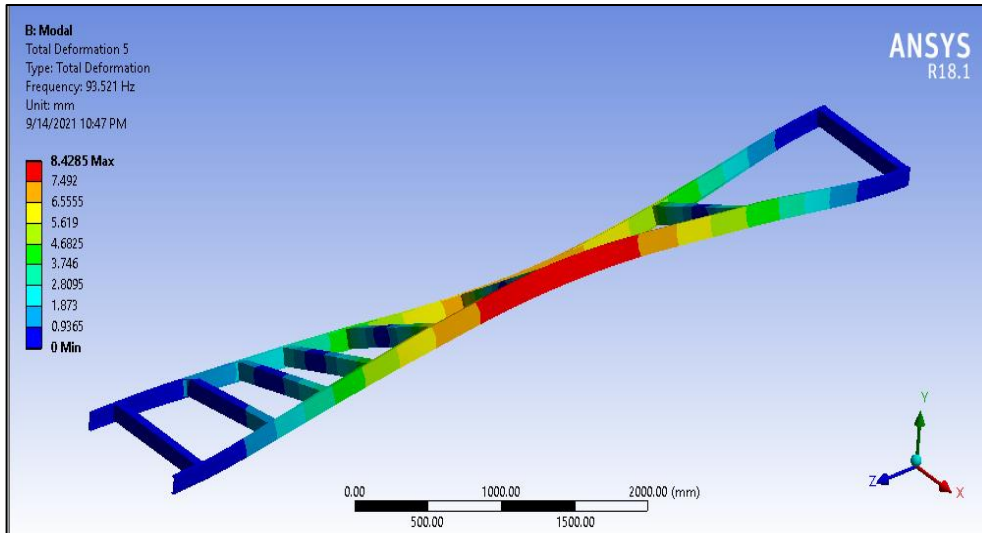
Figure 4.74: Mode shape of 5th natural frequency of Square Section using Graphite Al GA 7-230

The 6th frequency mode shape is shown in figure 4.75 which shows a transverse type mode shape with maximum deformation of 6.96mm and a frequency of 106.55Hz.
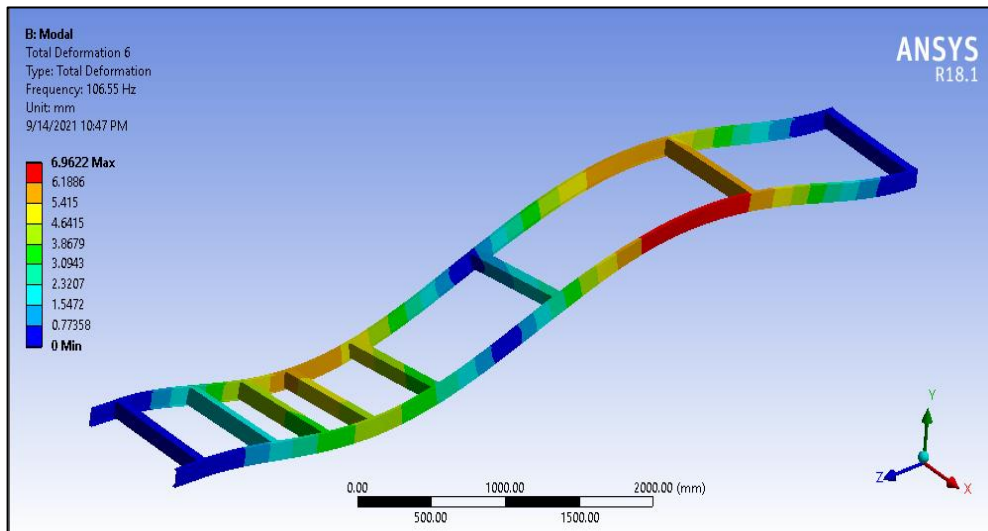
Figure 4.75: Mode shape of 6th natural frequency of Square Section using Graphite Al GA 7-230

The mass participation factor is evaluated for all the directions and the maximum mass participation factor is observed for translational x-direction i.e., 0.7821. The high mass participation factor along the x-direction signifies that any external excitation along this direction would likely cause resonance and amplitude build-up.

The mass participation factor along other directions is low and therefore any excitation along other directions would not cause resonance as shown in table 4.7.

Table 4.7: Frequency and mass participation factor for Square Section using Graphite Al GA 7-230

***** PARTICIPATION FACTOR CALCULATION ***** X DIRECTION								
						CUMULATIVE	RATIO EFF.MASS	
MODE	FREQUENCY	PERIOD	PARTIC.FACTOR	RATIO	EFFECTIVE MASS	MASS FRACTION	TO TOTAL MASS	
1	15.2840	0.65428E-01	0.20252	1.000000	0.410163E-01	0.704541	0.551066	
2	22.7317	0.43991E-01	0.91758E-01	0.453070	0.841952E-02	0.849163	0.113119	
3	25.4542	0.39286E-01	0.60460E-05	0.000030	0.365542E-10	0.849163	0.491116E-09	
4	36.5053	0.27393E-01	-0.93704E-01	0.462678	0.878042E-02	0.999985	0.117968	
5	57.7959	0.17302E-01	-0.90971E-03	0.004492	0.827575E-06	1.00000	0.111187E-04	
6	66.1998	0.15106E-01	-0.14074E-03	0.000695	0.198079E-07	1.00000	0.266125E-06	
--								
sum					0.582171E-01		0.782164	
--								

4.2.6 Modal analysis of C Section using Graphite Al GA 7-230 MMC

The mode shapes and natural frequencies are determined by keeping similar loading conditions as in structural analysis. The mode shapes are shown in figure 4.76.
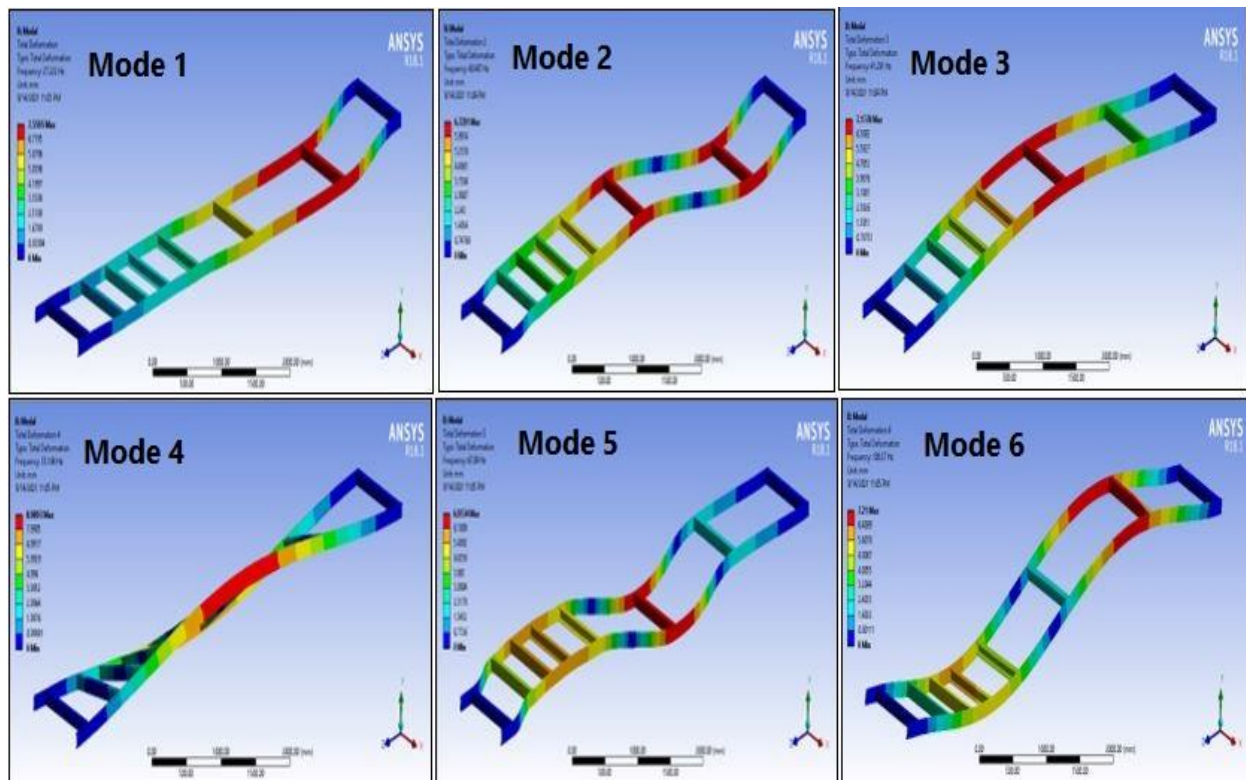
Figure 4.76: Mode shapes (Combined) of C-Section using Graphite Al GA 7-230 MMC
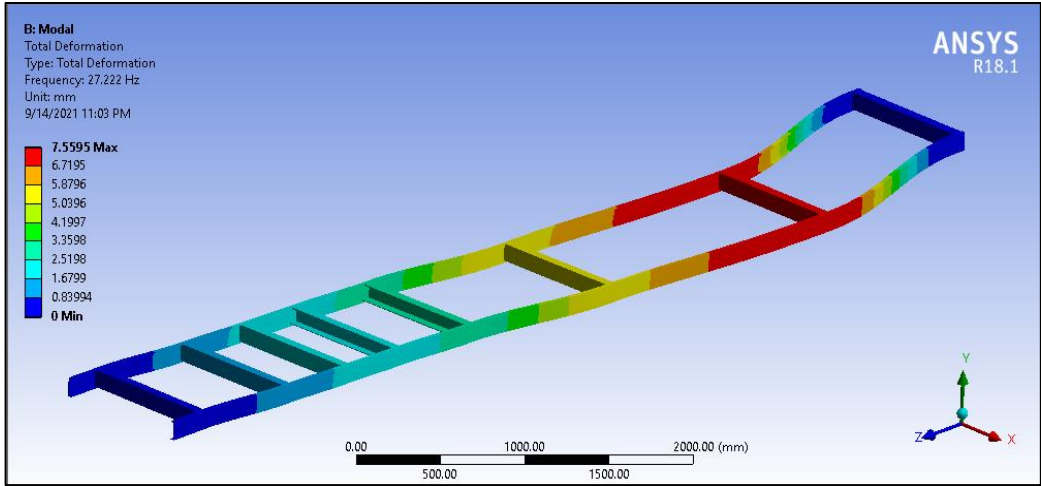
Figure 4.77: Mode shape of 1st natural frequency of C-Section using Graphite Al GA 7-230 MMC

The 1st frequency mode shape is shown in figure 4.77. The mode shape shows a lateral mode shape with a magnitude of 7.55mm and a natural frequency of 27.222Hz. The 2nd frequency mode shape is shown in figure 4.78 which shows a transverse type of mode shape with maximum deformation of 6.729mm and a frequency of 40.497Hz.
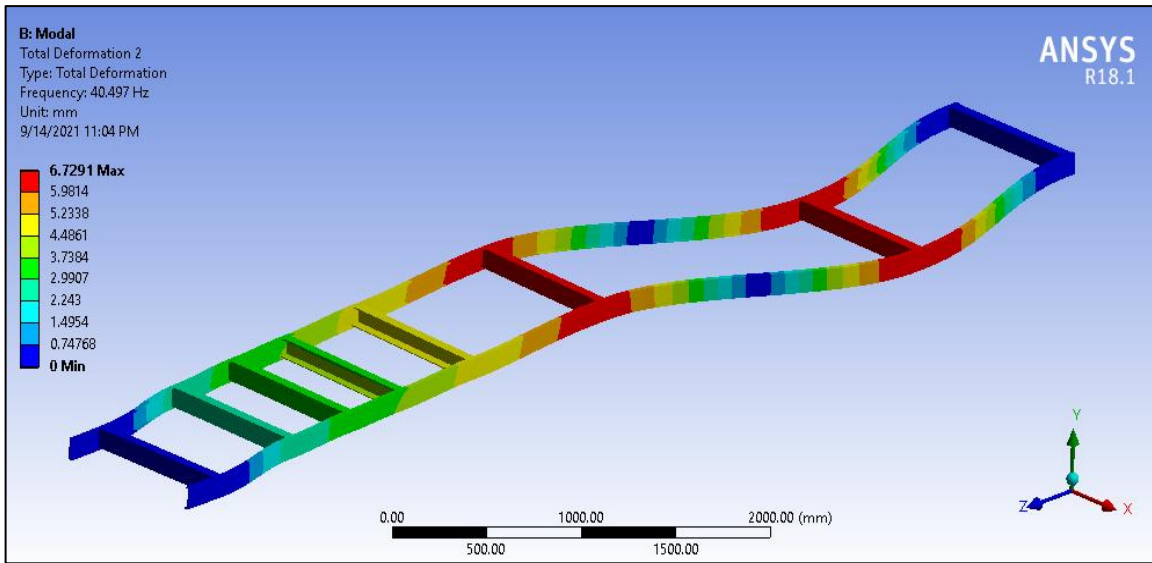
Figure 4.78: Mode shape of 2nd natural frequency of C-Section using Graphite Al GA 7-230 MMC

The 3rd frequency mode shape is shown in figure 4.79. The mode shape shows a lateral mode shape with a magnitude of 7.1778mm and a natural frequency of 41.291Hz.
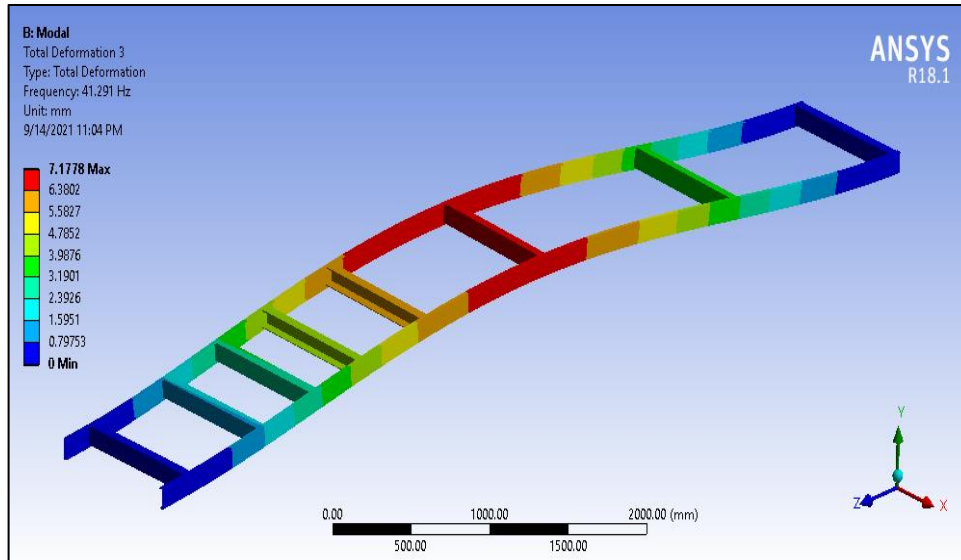
Figure 4.79: Mode shape of 3rd natural frequency of C-Section using Graphite Al GA 7-230 MMC

The 4th frequency mode shape is shown in figure 4.80 which shows a transverse type mode shape with maximum deformation of 8.989mm and a frequency of 53.194Hz.
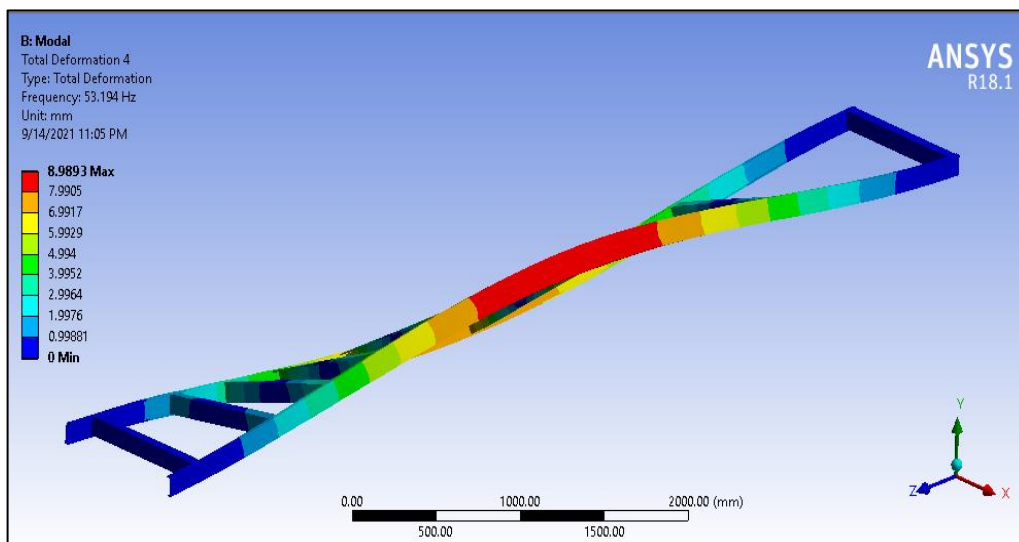
Figure 4.80: Mode shape of 4th natural frequency of C-Section using Graphite Al GA 7-230 MMC

The 5th frequency mode shape is shown in figure 4.81 which shows a torsional type of mode shape with maximum deformation of 6.953mm and a frequency of 67.04Hz.
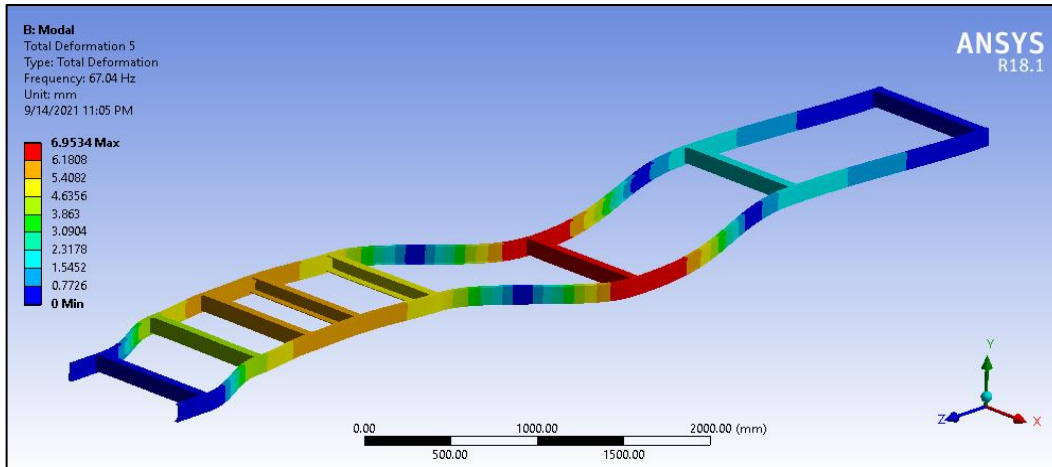
Figure 4.81: Mode shape of 5th natural frequency of C-Section using Graphite Al GA 7-230 MMC

The 6th frequency mode shape is shown in figure 4.82 which shows a transverse type of mode shape with maximum deformation of 7.21mm and a frequency of 108.57Hz.
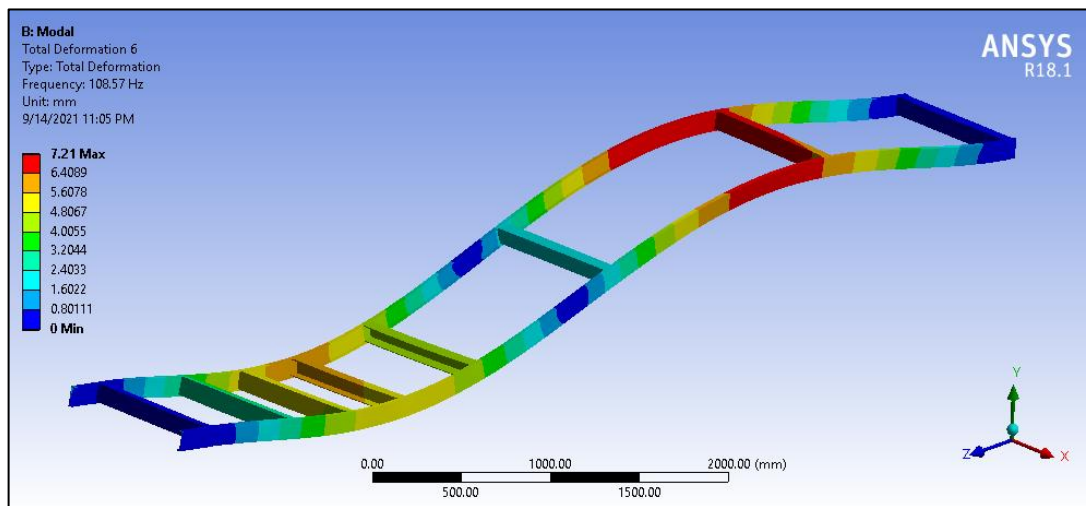
Figure 4.82: Mode shape of 6th natural frequency of C-Section using Graphite Al GA 7-230 MMC

The mass participation factor is evaluated for all the directions and the maximum mass participation factor is observed for translational x-direction i.e., 0.765. The high mass participation factor along the x-direction signifies that any external excitation along this direction would likely cause resonance and amplitude build-up. The mass participation factor along other directions is low and therefore any excitation along other directions would not cause resonance as indicated in table 4.8.

Table 4.8: Frequency and Mass participation factor for C section using Graphite Al GA 7-230 MMC

***** PARTICIPATION FACTOR CALCULATION ***** X DIRECTION						
					CUMULATIVE	RATIO EFF.MASS
MODE	FREQUENCY	PERIOD	PARTIC.FACTOR	RATIO	EFFECTIVE MASS	MASS FRACTION	TO TOTAL MASS
1	27.2223	0.36735E-01	0.18472	1.000000	0.341209E-01	0.777959	0.595237
2	40.4974	0.24693E-01	-0.65539E-01	0.354804	0.429534E-02	0.875894	0.749319E-01
3	41.2910	0.24218E-01	-0.84768E-03	0.004589	0.718556E-06	0.875910	0.125352E-04
4	53.1944	0.18799E-01	-0.43393E-02	0.023492	0.188298E-04	0.876339	0.328485E-03
5	67.0404	0.14916E-01	-0.73646E-01	0.398692	0.542370E-02	1.00000	0.946160E-01
6	108.568	0.92108E-02	-0.14013E-04	0.000076	0.196353E-09	1.00000	0.342536E-08
-----					-----		-----
sum					0.438595E-01		0.765126
-----							-----

4.2.7 Modal analysis of Square Section using Al 6092/SIC/17.5P MMC

The mode shapes and natural frequencies are determined by keeping similar loading conditions as in structural analysis. The mode shapes are shown in figure 4.83.
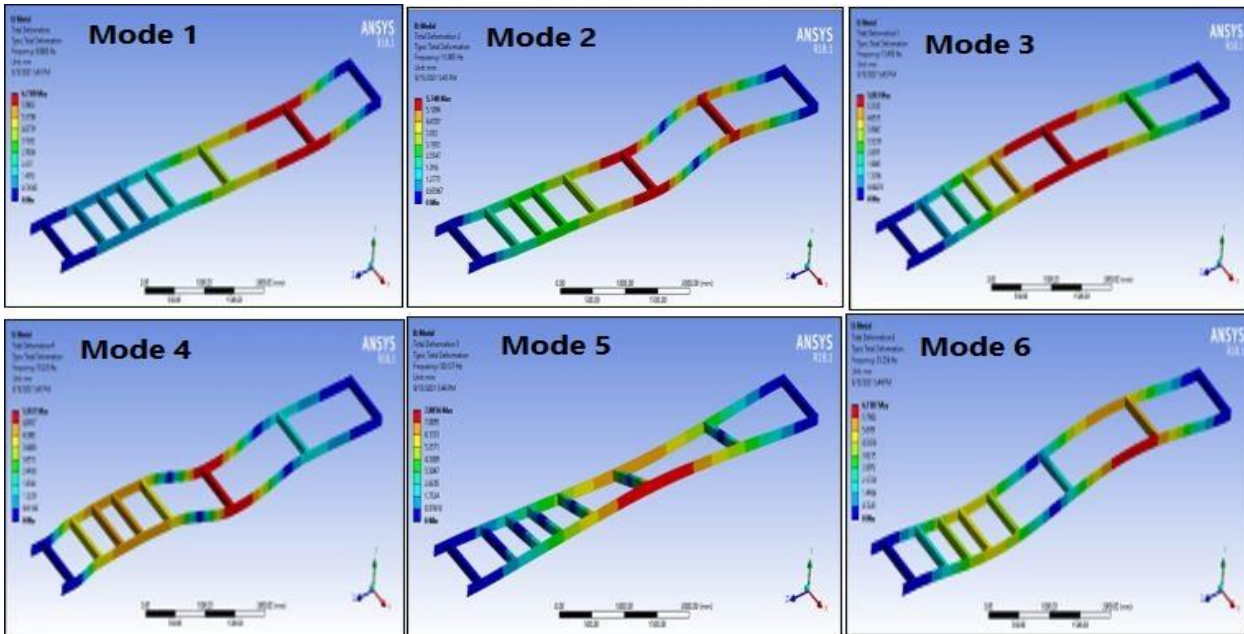
Figure 4.83: Mode shapes (Combined) of Square Section using Al 6092/SIC/17.5P MMC
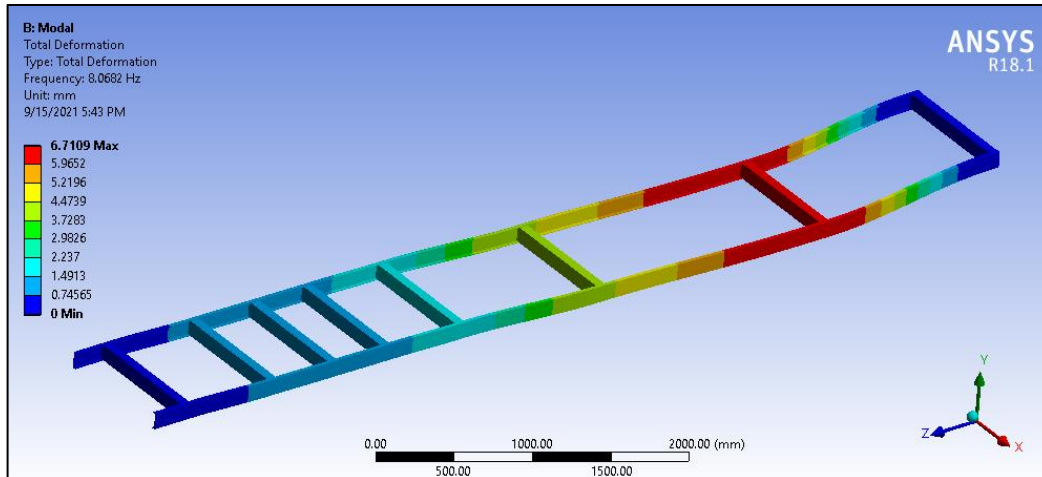
Figure 4.84: Mode shape of 1ˢᵗ natural frequency of Square Section using Al 6092/SIC/17.5P MMC

The 1ˢᵗ frequency mode shape is shown in figure 4.84. The mode shape shows a lateral mode shape with a magnitude of 4.71mm and a natural frequency of 8.0682Hz. The 2ⁿᵈ frequency mode shape is shown in figure 4.85 which shows a transverse type of mode shape with maximum deformation of 5.748mm and a frequency of 11.985Hz.
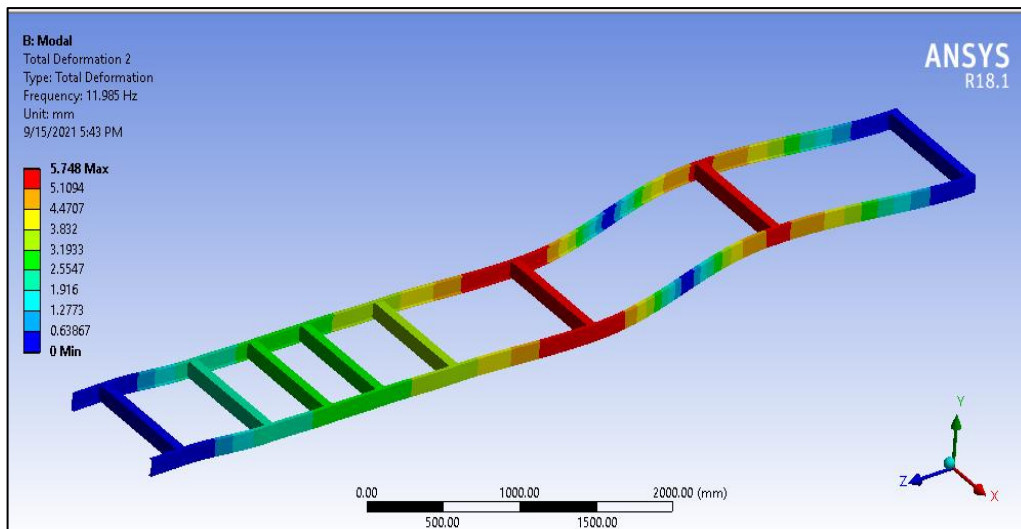
Figure 4.85: Mode shape of 2ⁿᵈ natural frequency of Square Section using Al 6092/SIC/17.5P MMC

The 3ʳᵈ frequency mode shape is shown in figure 4.86. The mode shape shows a lateral mode shape with a magnitude of 5.983mm and a natural frequency of 13.492Hz.
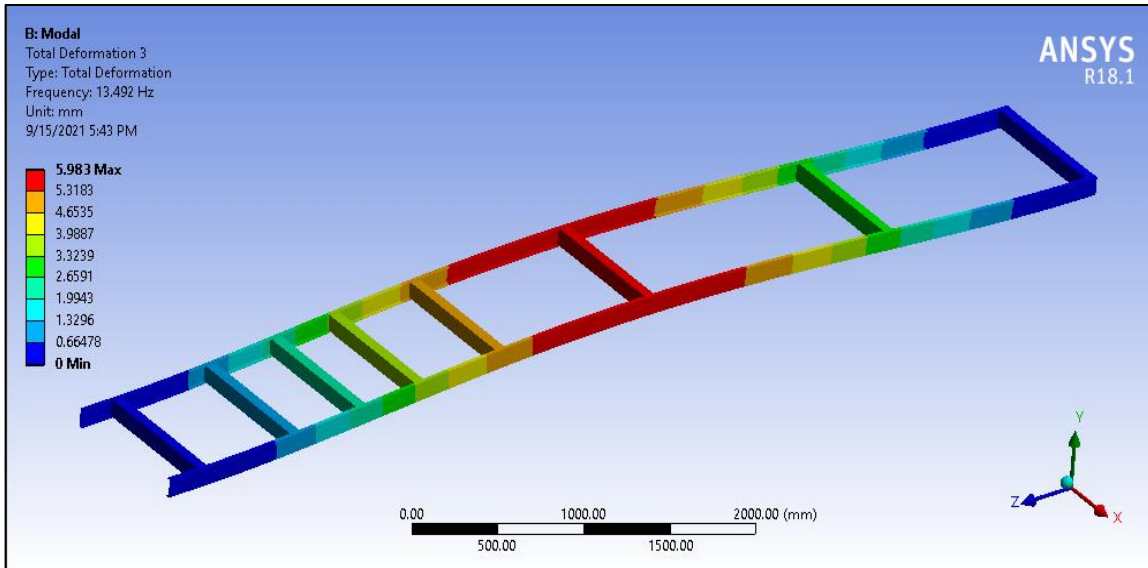
Figure 4.86: Mode shape of 3rd natural frequency of Square Section using Al 6092/SIC/17.5P MMC

The 4th frequency mode shape is shown in figure 4.87 which shows a transverse type mode shape with maximum deformation of 5.5031mm and a frequency of 19.228Hz.

Figure 4.87: Mode shape of 4th natural frequency of Square Section using Al 6092/SIC/17.5P MMC

The 5th frequency mode shape is shown in figure 4.88 which shows a torsional type mode shape with maximum deformation of 7.8856mm and a frequency of 30.127Hz.

Figure 4.86: Mode shape of 3rd natural frequency of Square Section using Al 6092/SIC/17.5P MMC

The 4th frequency mode shape is shown in figure 4.87 which shows a transverse type mode shape with maximum deformation of 5.5031mm and a frequency of 19.228Hz.
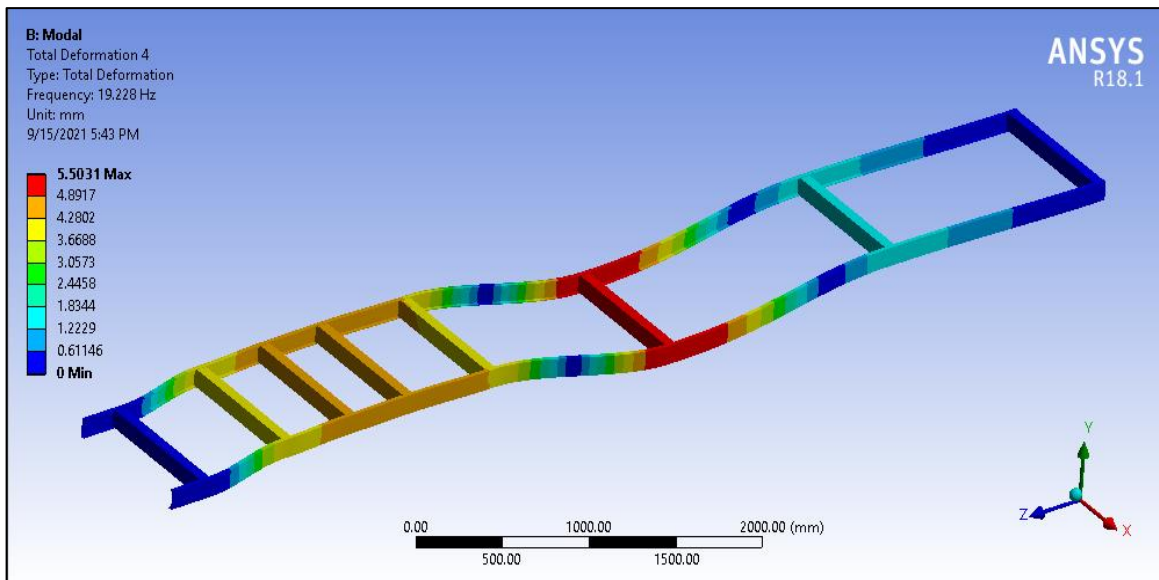
Figure 4.87: Mode shape of 4th natural frequency of Square Section using Al 6092/SIC/17.5P MMC

The 5th frequency mode shape is shown in figure 4.88 which shows a torsional type mode shape with maximum deformation of 7.8856mm and a frequency of 30.127Hz.
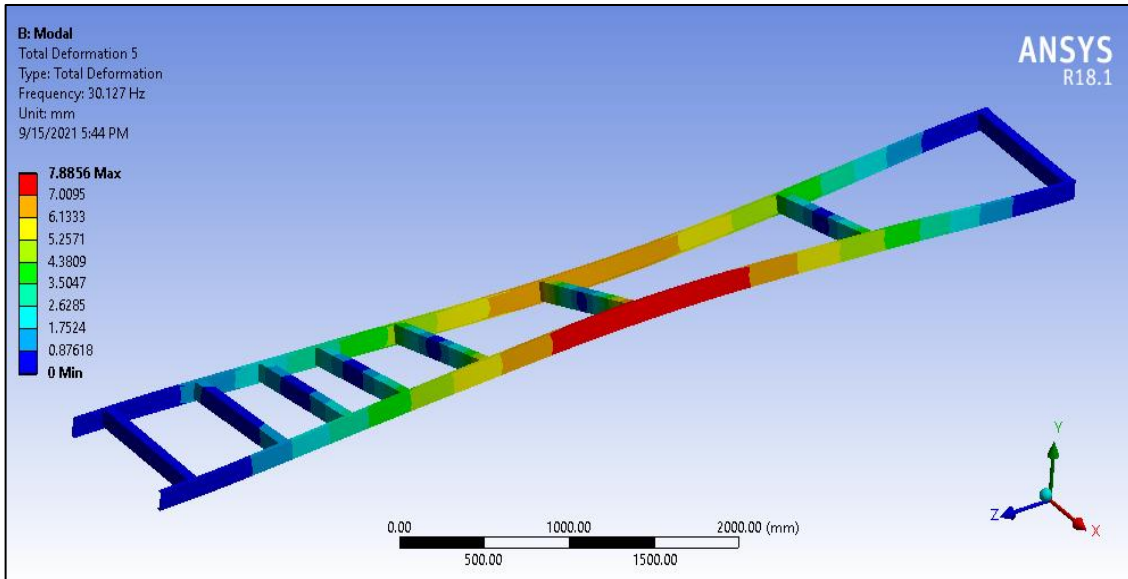
Figure 4.88: Mode shape of 5th natural frequency of Square Section using Al 6092/SIC/17.5P MMC

The 6th frequency mode shape is shown in figure 4.89 which shows a transverse type mode shape with maximum deformation of 6.518mm and a frequency of 35.036Hz.
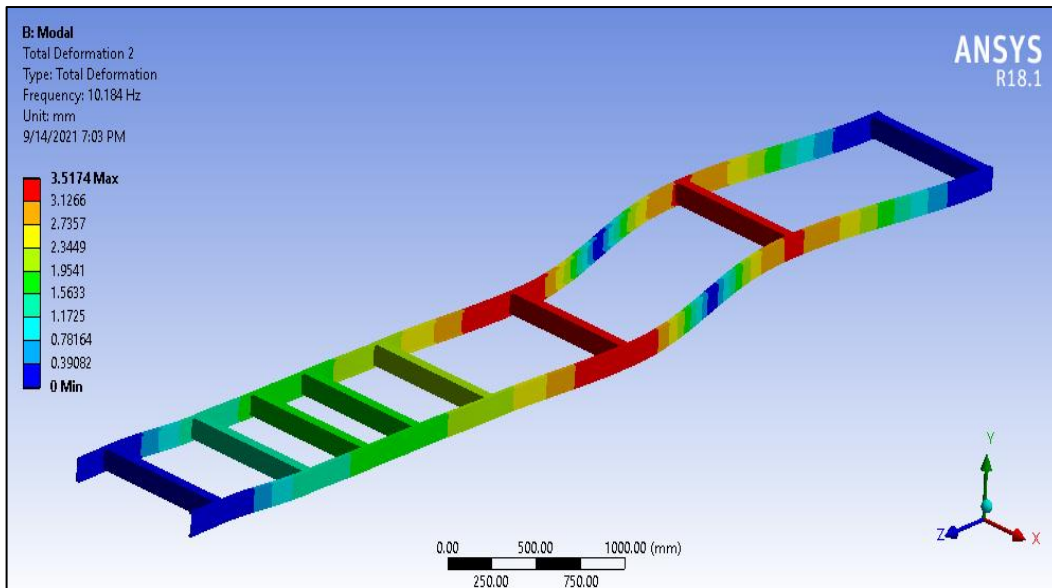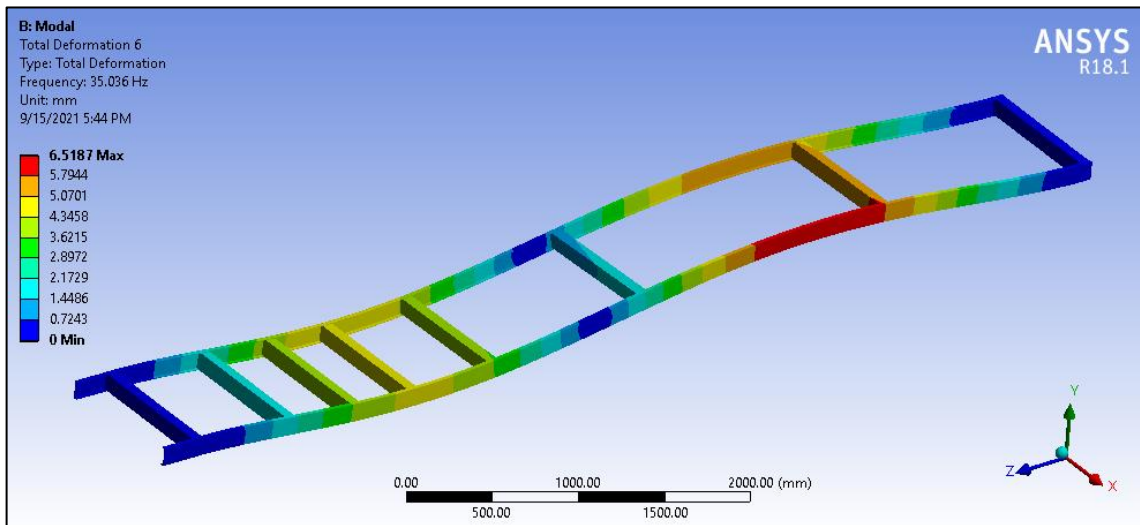

Figure 4.89: Mode shape of 6th natural frequency of Square Section using Al 6092/SIC/17.5P MMC

The mass participation factor is evaluated for all the directions and the maximum mass participation factor is observed for translational x-direction i.e., 0.781. The high mass participation factor along x-direction signifies that any external excitation along this direction would likely cause resonance and amplitude build-up. The mass participation factor along other directions is low and therefore any excitation along other directions would not cause resonance as shown in table 4.9.

Table 4.9: Frequency and Mass participation factor for *Square Section* using Al 6092/SIC/17.5P MMC

***** PARTICIPATION FACTOR CALCULATION ***** X DIRECTION							
					CUMULATIVE	RATIO EFF.MASS	
MODE	FREQUENCY	PERIOD	PARTIC.FACTOR	RATIO	EFFECTIVE MASS	MASS FRACTION	TO TOTAL MASS
1	8.06819	0.12394	0.21346	1.000000	0.455659E-01	0.705407	0.551421
2	11.9855	0.83434E-01	0.96482E-01	0.451988	0.930880E-02	0.849516	0.112651
3	13.4925	0.74115E-01	-0.11793E-03	0.000552	0.139063E-07	0.849516	0.168289E-06
4	19.2281	0.52007E-01	-0.98588E-01	0.461852	0.971957E-02	0.999985	0.117622
5	30.1271	0.33193E-01	-0.97990E-03	0.004591	0.960210E-06	1.00000	0.116201E-04
6	35.0357	0.28542E-01	-0.17720E-04	0.000083	0.314002E-09	1.00000	0.379992E-08
--							
sum					0.645953E-01		0.781707
--							

4.2.8 Modal analysis of C Section using Al 6092/SIC/17.5P MMC material

The mode shapes and natural frequencies are determined by keeping similar loading conditions as in structural analysis. The mode shapes are shown in figure 4.90.
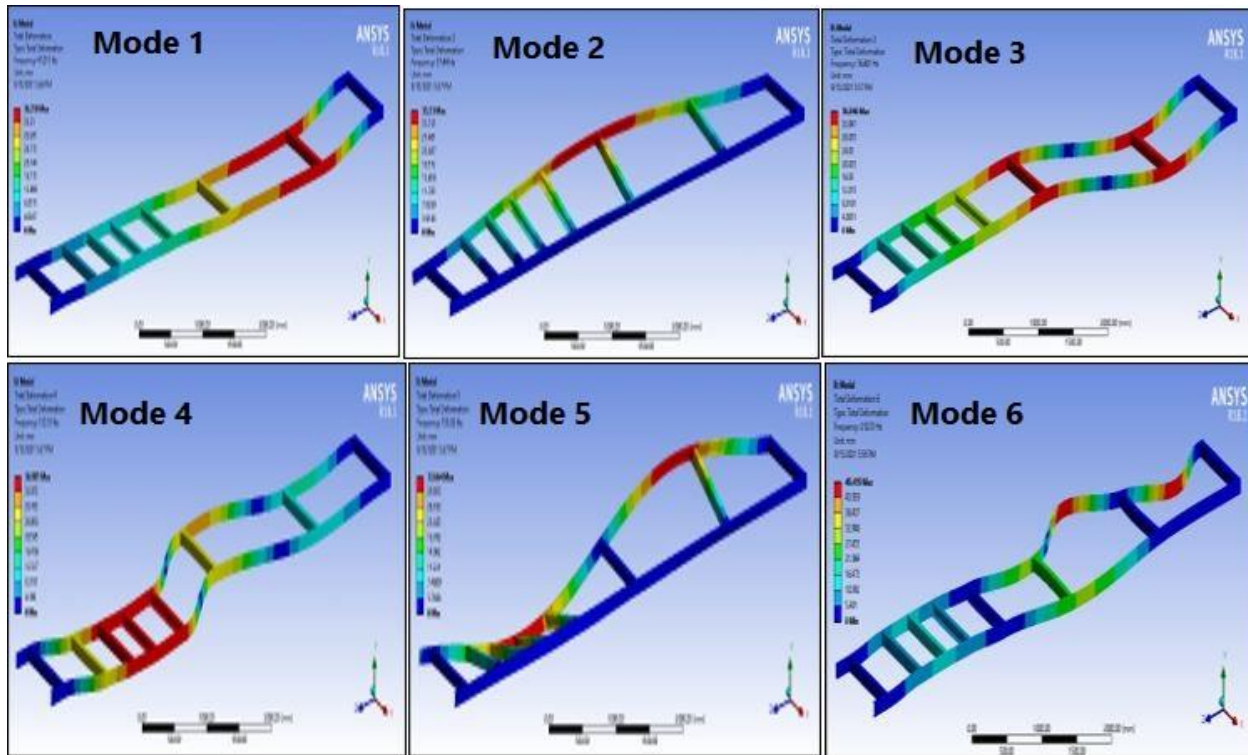
Figure 4.90: Mode shapes (Combined) of C-Section using Al 6092/SIC/17.5P MMC
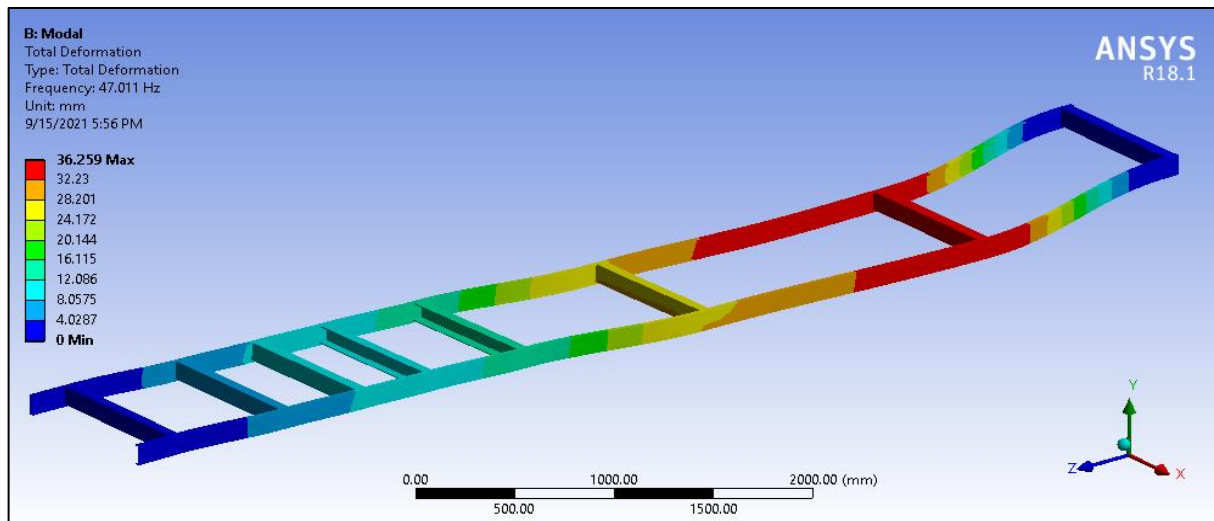
Figure 4.91 Mode shape of 1st natural frequency of C-Section using Al 6092/SIC/17.5P MMC

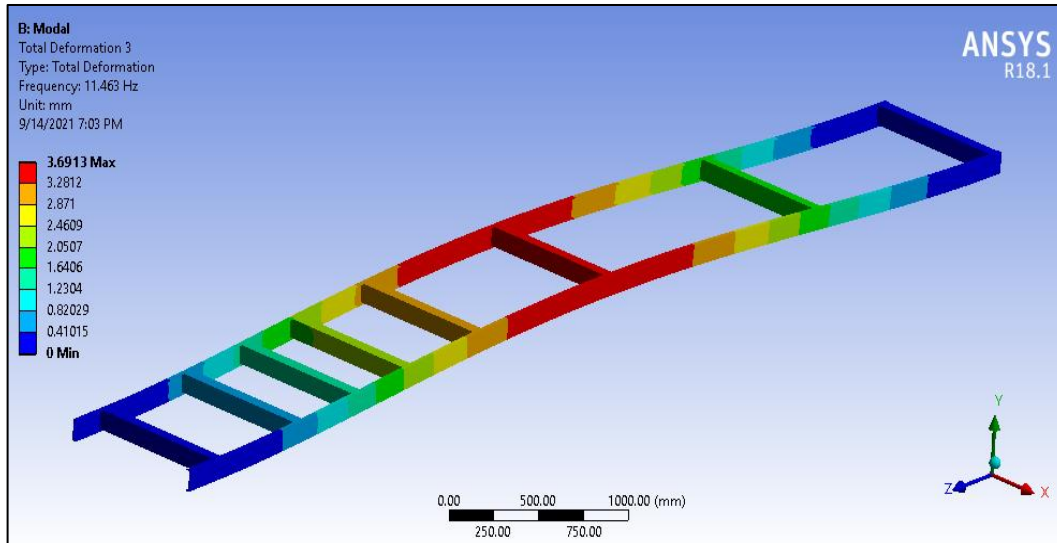The 1st frequency mode shape is shown in figure 4.91. The mode shape shows a lateral mode shape with a magnitude of 36.259mm and a natural frequency of 47.011Hz. The 2nd frequency mode shape is shown in figure 4.92 which shows a transverse type mode shape with maximum deformation of 35.23mm and frequency of 57.44Hz.
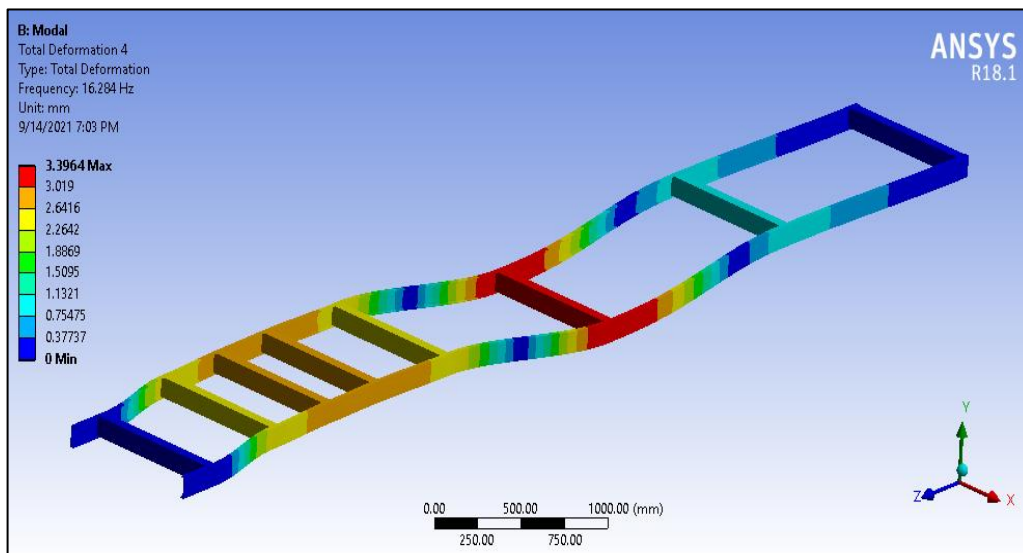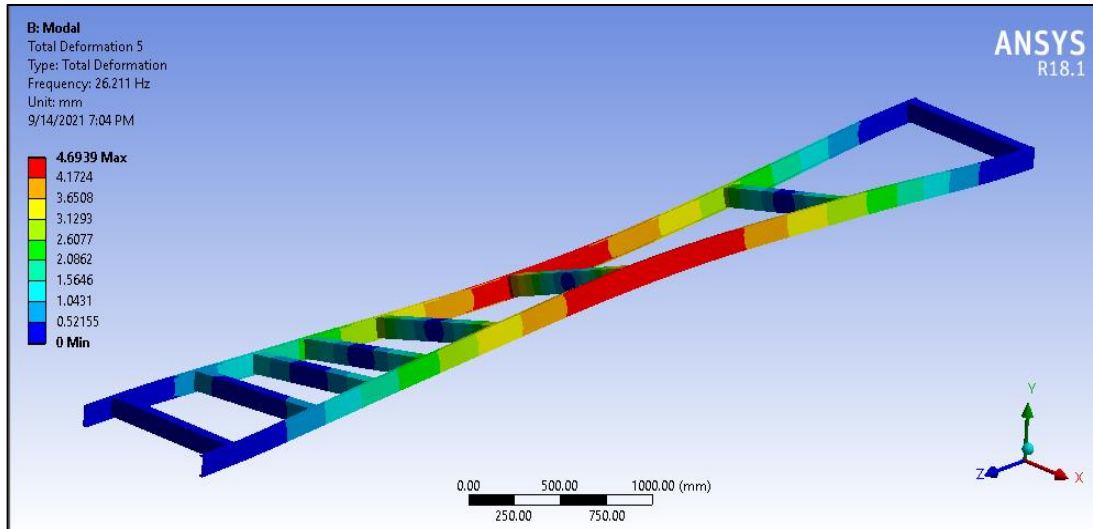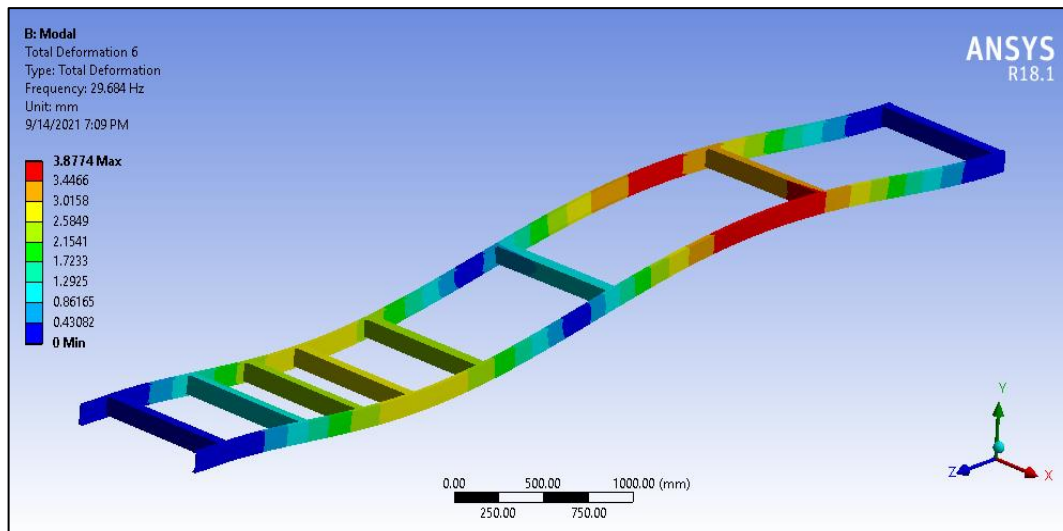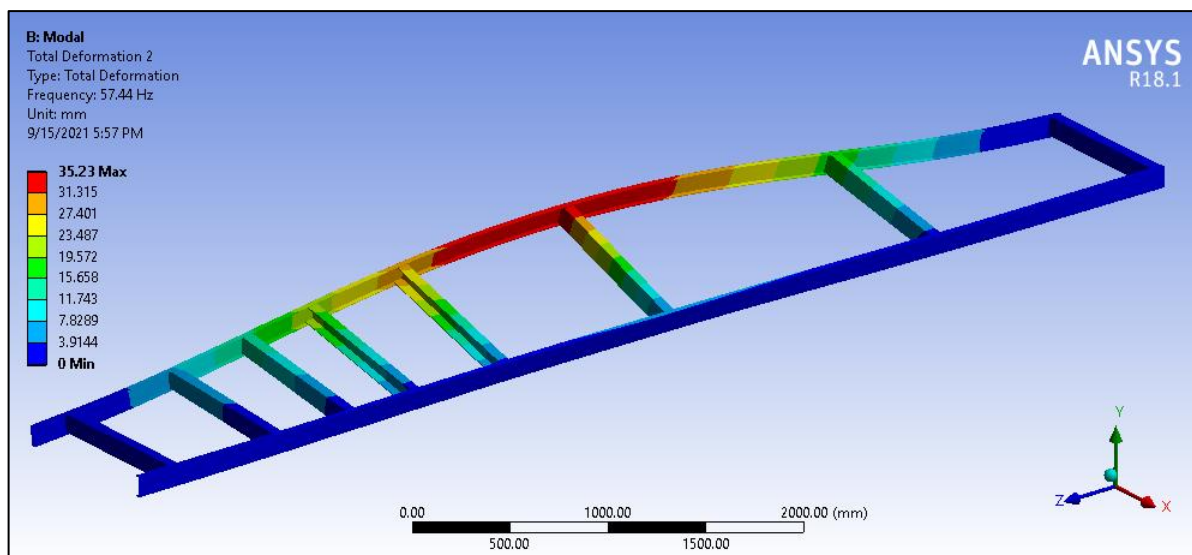

Figure 4.92: Mode shape of 2nd natural frequency of C-Section using Al 6092/SIC/17.5P MMC

The 3rd frequency mode shape is shown in figure 4.93. The mode shape shows a lateral mode shape with a magnitude of 36.046mm and a natural frequency of 76.601Hz.
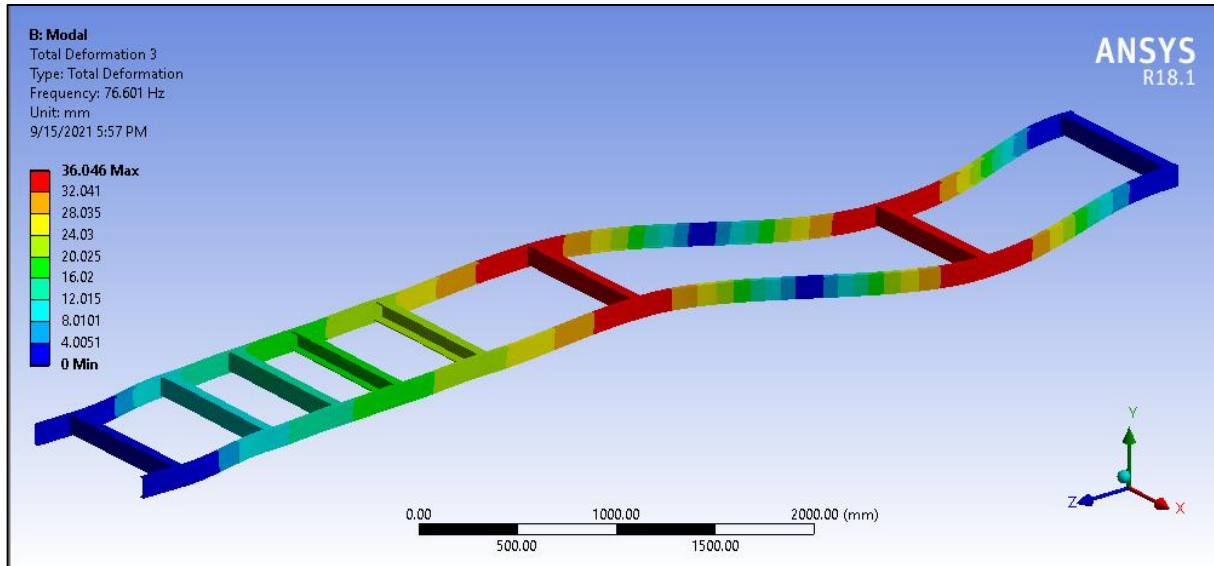
Figure 4.93: Mode shape of 3rd natural frequency of C-Section using Al 6092/SIC/17.5P MMC

The 4th frequency mode shape is shown in figure 4.94 which shows a transverse type mode shape with maximum deformation of 36.981mm and a frequency of 133.57Hz.
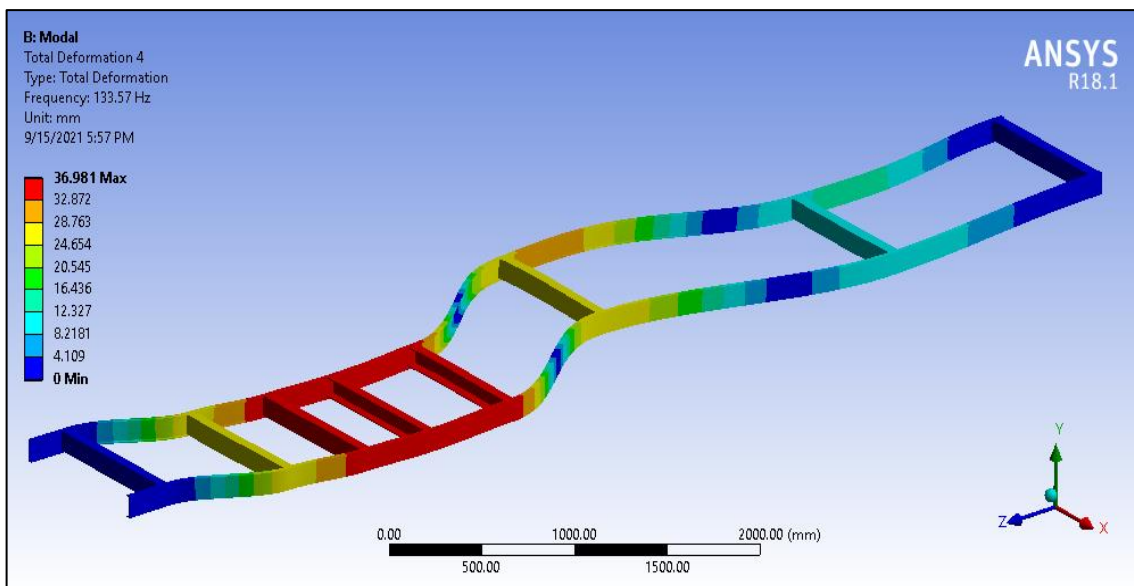
Figure 4.94: Mode shape of 4th natural frequency of C-Section using Al 6092/SIC/17.5P MMC

The 5th frequency mode shape is shown in figure 4.95 which shows a torsional type of mode shape with maximum deformation of 33.664mm and a frequency of 155.82Hz.
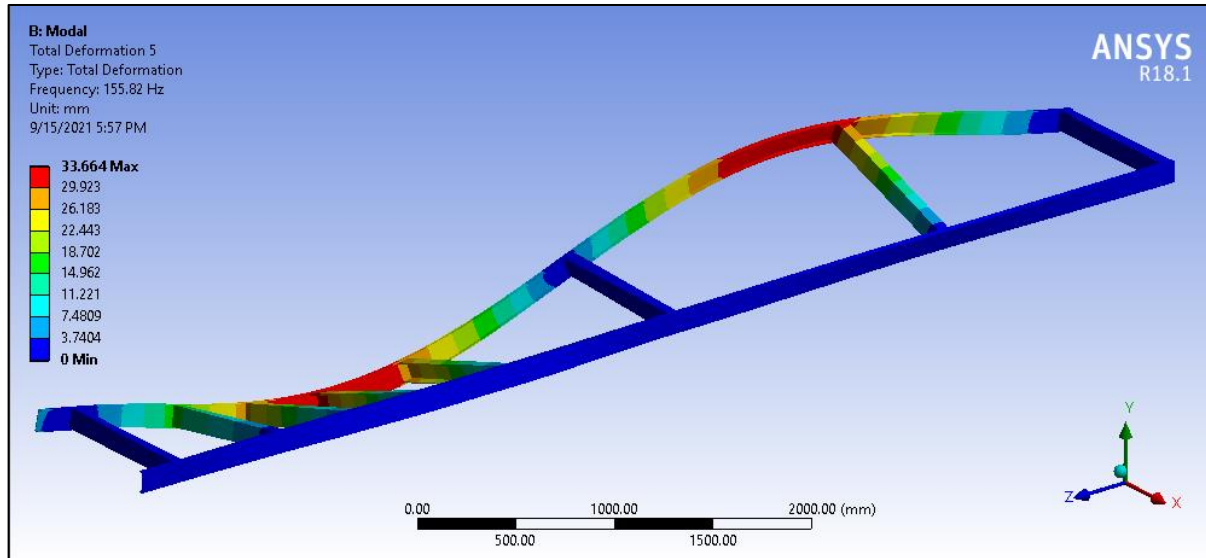
Figure 4.95: Mode shape of 5th natural frequency of C-Section using Al 6092/SIC/17.5P MMC

The 6th frequency mode shape is shown in figure 4.96 which shows a transverse type mode shape with maximum deformation of 49.419mm and a frequency of 210.33Hz.
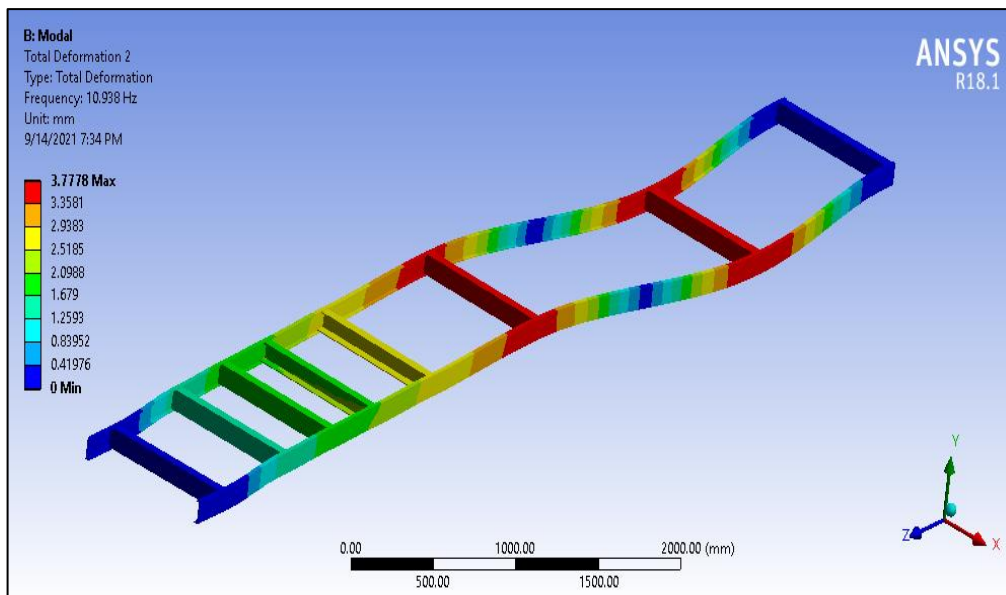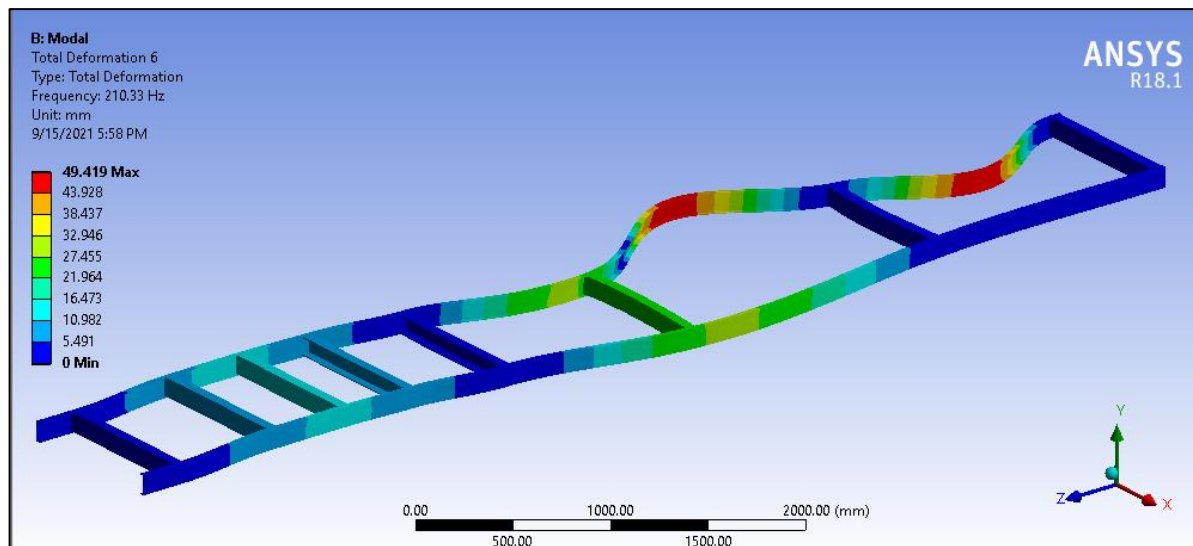

Figure 4.96: Mode shape of 6th natural frequency of C-Section using Al 6092/SIC/17.5P MMC

The mass participation factor is evaluated for all the directions and the maximum mass participation factor is observed for translational x-direction i.e., 0.831. The high mass participation factor along the x-direction signifies that any external excitation along this direction would likely cause resonance and amplitude build-up. The mass participation factor along other directions is low and therefore any excitation along other directions would not cause resonance as indicated in table 4.10.

Table 4.10: Frequency and Mass participation factor for *C Section* using Al 6092/SIC/17.5P MMC

MODE	FREQUENCY	PERIOD	PARTIC.FACTOR	RATIO	EFFECTIVE MASS	CUMULATIVE MASS FRACTION	RATIO EFF.MASS TO TOTAL MASS	
***** PARTICIPATION FACTOR CALCULATION ***** X DIRECTION								
1	47.0112	0.21272E-01	0.36805E-01	1.000000	0.135457E-02	0.815504	0.678100	
2	57.4401	0.17409E-01	0.12440E-02	0.033800	0.154755E-05	0.816435	0.774706E-03	
3	76.6011	0.13055E-01	-0.89696E-02	0.243708	0.804532E-04	0.864871	0.402749E-01	
4	133.573	0.74865E-02	0.14693E-01	0.399206	0.215873E-03	0.994834	0.108066	
5	155.816	0.64178E-02	-0.38655E-03	0.010503	0.149422E-06	0.994924	0.748007E-04	
6	210.329	0.47545E-02	0.29036E-02	0.078892	0.843083E-05	1.00000	0.422047E-02	
--								
sum					0.166103E-02		0.831511	
--								

The next sub-section summarizes the comparison based on the results studied in previous sub-sections.

4.2.9 Vibration Analysis Comparison

The frequency comparison is made for different materials as shown in table 4.11. Together, 6 different modes of vibration are generated, and corresponding frequency values are tabulated in Table 4.11.

Table 4.11: Frequency comparison for different materials for the square cross-section

Frequency	St 52 E	P100/6061 Al	Graphite Al GA 7-230 MMC	Al 6092/SIC/17.5P
1st mode	6.8918	15.284	24.55	8.0682
2nd mode	10.184	22.732	36.514	11.985
3rd mode	11.463	25.454	40.964	13.492
4th mode	16.284	36.505	58.673	19.228
5th mode	26.211	57.796	93.521	30.127
6th mode	29.684	66.2	106.55	35.036
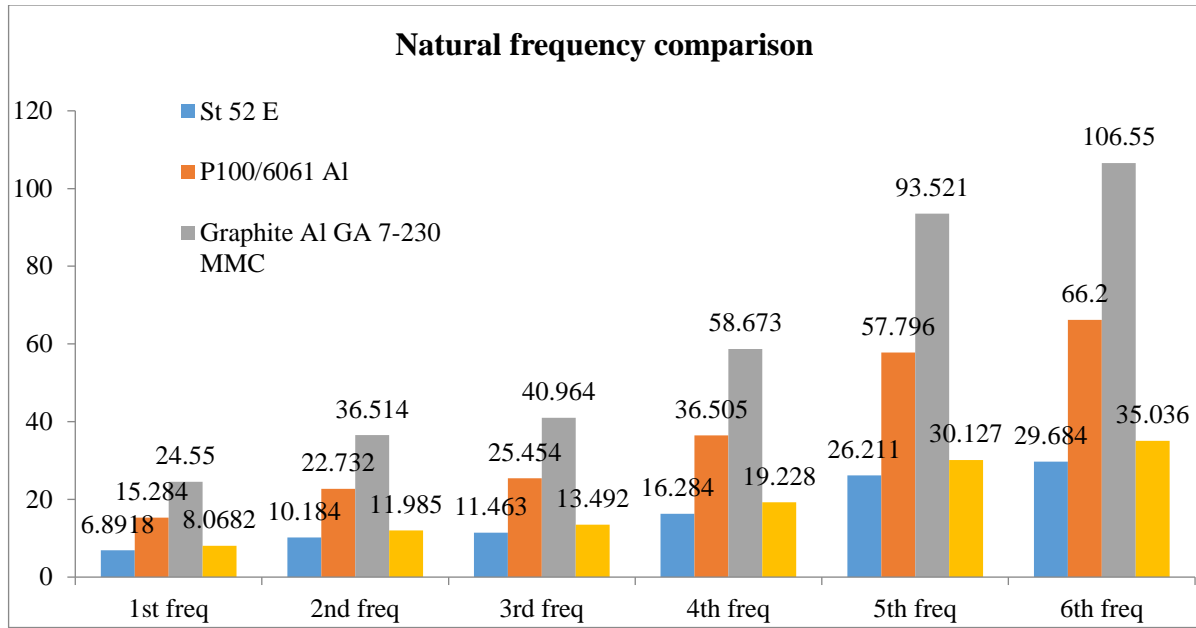
Figure 4.97: Natural frequency comparison chart for different modes and materials

The natural frequency comparison in figure 4.97 shows a higher frequency for Graphite Al GA 7-230 MMC material for all the modes i.e., 1st, 2nd, 3rd, 4th and 5th mode whereas the St52E material shows the lowest frequency value. The 6th natural frequency is observed to be maximum for all the materials. Table 4.12 shows the deformation comparison for different materials.

Table 4.12: Deformation comparison for different materials for the square cross-section

Deformation	St 52 E	P100/6061 AL	Graphite Al GA 7-230	Al 6092/SIC/17.5P
1st mode	4.1361	7.0754	7.134	6.7109
2nd mode	3.5174	6.0765	6.1234	5.748
3rd mode	3.6913	6.4121	6.5073	5.983
4th mode	3.3964	5.7811	5.8378	5.5031
5th mode	4.6939	8.3519	8.4285	7.8856
6th mode	3.8774	6.8772	6.9622	6.5187

The deformation comparison chart is shown in figure 4.98. The deformation of the chassis increases with an increase in natural frequency. The Graphite Al GA 7-230 MMC material is observed to be maximum for all mode shapes. The maximum deformation is obtained for the 6th mode shape with a magnitude of 6.96 mm. This has been observed in [92] that the density of Al-Gr alloy decreases as the graphite concentration increases and damping lowers as the natural frequency increases as in figure 4.97. Al/SiC composites' damping capabilities are known to improve with particle size and vibration frequency (figure 4.98[92], [93].
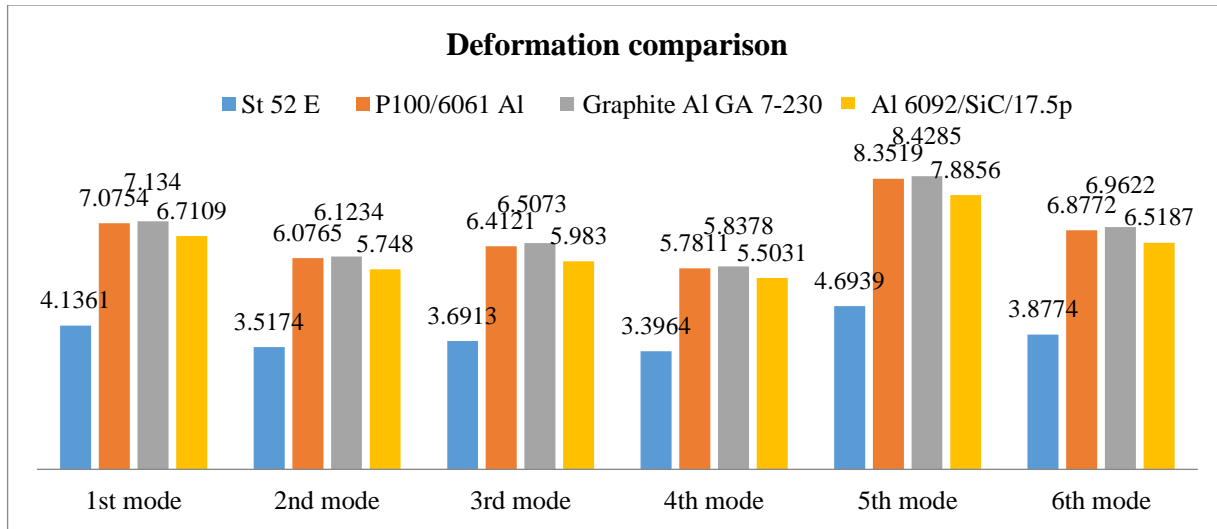
Figure 4.98: Deformation comparison chart for different modes and materials

4.2.10 Sub-Chapter Summary

This section has shown that the leading mass participation factor is obtained along the lateral direction from modal vibration analysis, and any external excitation along this direction would likely cause resonance and amplitude build-up. For all the materials, the mass participation factor is evaluated for all the directions and the maximum mass participation factor is observed for translational x-direction. The high mass participation factor along the x-direction signifies that any external excitation along this direction would likely cause resonance and amplitude build-up. The mass participation factor along other directions is low and therefore any excitation along other directions would not cause resonance.

The energy absorption and safety factor are evaluated for both square and C profiles. The maximum safety factor is obtained for P100/6061 Al MMC and is minimum Graphite Al GA 7-230 MMC. From the modal analysis, the maximum natural frequency and deformation are observed for Graphite Al GA 7-230 MMC because the distribution of reinforcing particles in the matrix and interfacial connections strength among reinforcing particles and the matrix affect the mechanical properties of composite products [94]. Due to the interaction between the reinforcement and matrix, MMCs offer damping capacity and stiffness but it depends on the selection criteria for constituents, reinforcement's geometry, processing methods, and heat treatment [95].

The next Sub-chapter presents the optimization of conventional structural steel (St52E) chassis using Response-Surface optimization methods as discussed in sub-section 2.10.

4.3 Response-Surface Optimization using St52E material with square section chassis

The current sub-chapter demonstrates the use of various optimization techniques, such as central composite design, optimal space-filling design, sparse grid initialization, Latin hypercube sampling, and Box-Behnken design, on heavy motor vehicles chassis made of St52E material. Using 3D Response-Surface plots and sensitivity plots, the effect of different design variables on equivalent-stress, deformation, and mass is evaluated.

4.3.1 Selection of Optimization Variables

The optimization variables, which are cross-member dimensions, are defined in the ANSYS design modeler. These variables are the widths of cross members 1, 2, and 3, as depicted in figures 4.99, 4.100, and 4.101, respectively. Table 4.13 provides the dimensions corresponding to these variables, namely H12, H14, and H6. The three cross-sections chosen are from the cassis's rightmost transverse member. Figure 4.99 illustrates the values of these dimensions.
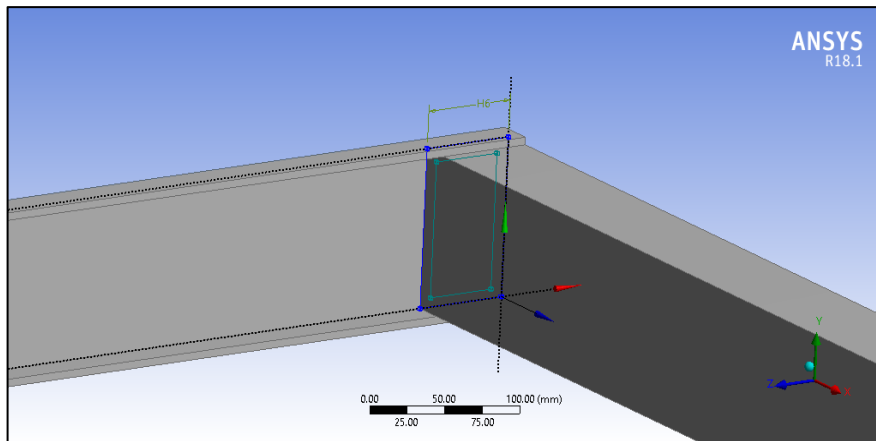
Figure 4.99: H6 dimension (cross-member width)
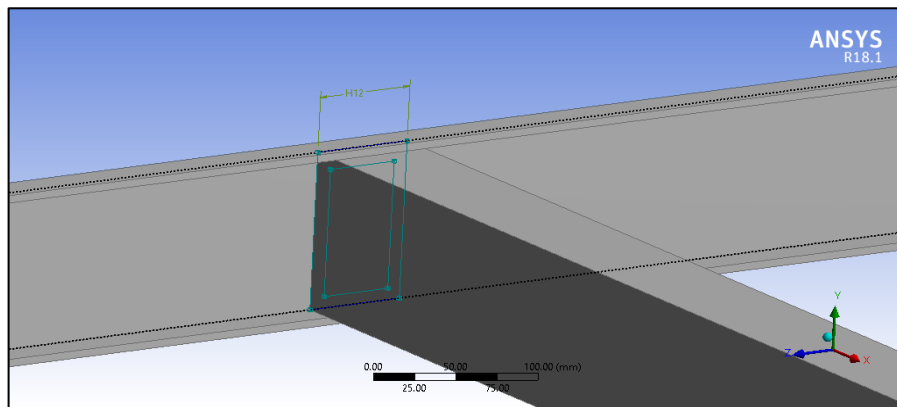
Figure 4.100: H12 dimension (cross-member width) selected for optimization
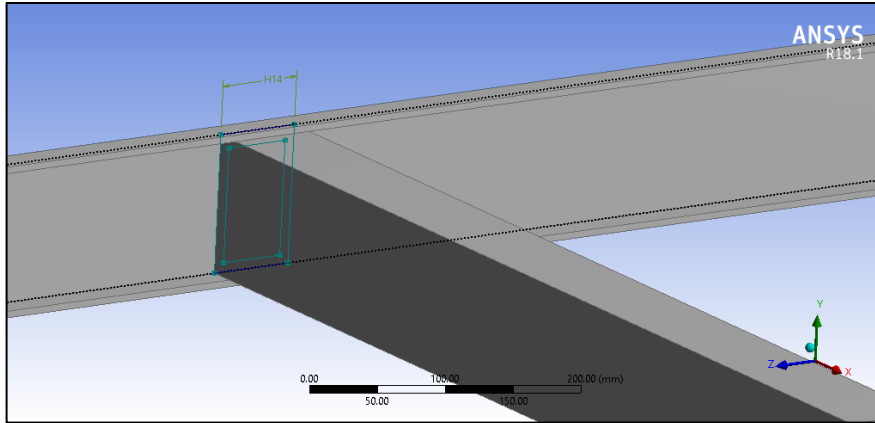
Figure 4.101: H14 dimension (cross-member width) selected for optimization

Table 4.13: Dimensions of cross-member variables

Variable Name (Cross member)	Value
CM 1	65mm
CM 2	65mm
CM 3	65mm

The lower bound and upper bound values are defined for each optimization variable i.e., "cross members one, two and three as shown in table 4.14.

Table 4.14: Values of distinct variables' lower and upper bounds

Variable Name	Lower Bound	Upper Bound
CM 1	58.5	71.5
CM 2	58.5	71.5
CM 3	58.5	71.5

4.3.2 CCD Scheme using St52E material with square section chassis

4.3.2.1 Generation of DOE table for CCD using St52E material

The software used Finite Element Analysis to evaluate the output parameters at these design points. As shown in Table 4.15 in columns E and F, the output parameters are equivalent-stress and total deformation.

Table 4.15: DOE Table for CCD scheme using St52E material

A	B	C	D	E	F	G
Name DP	P5 - cross-member 1 (mm)	P6 - cross-member 2 (mm)	P7 - cross-member 3 (mm)	P3 - Equivalent-stress Max (MPa)	P4 - Total Deformation Maximum (mm)	P8 - Solid Mass (kg)
1	65	65	65	3280.49	347.45	214.64
2	58.5	65	65	3264.45	347.89	209.91
3	71.5	65	65	3520.14	347.13	219.37
4	65	58.5	65	3273.63	347.76	209.91
5	65	71.5	65	3527.46	347	219.37
6	65	65	58.5	3259.3	343.93	209.91
7	65	65	71.5	3220.32	340.78	219.37
8	59.72	59.72	59.72	3345.58	341.99	203.11
9	70.28	59.72	59.72	3433.41	341.76	210.8
10	59.72	70.28	59.72	3439.45	341.55	210.8
11	70.28	70.28	59.72	3313.5	341.14	218.48
12	59.72	59.72	70.28	3466.48	342.2	210.8
13	70.28	59.72	70.28	3231.43	341.76	218.48
14	59.72	70.28	70.28	3293.05	341.71	218.48
15	70.28	70.28	70.28	3464.08	341.27	226.17

Design point number two (2) exhibits the greatest deformation, while design point number seven exhibits the least deformation (7). The dimensions for design point number two (2) are as follows:

• 58.5 mm for cross-member number one, 65 mm for cross-member number two, and 65 mm for cross-member number three.

The magnitude of maximum deformation obtained from the analysis is 347.89 mm and the magnitude of minimum deformation obtained from the analysis is 340.78 mm.

4.3.2.2 Solid Mass

The initial solid mass is 214.64 kg using St52E material. At design point 15, the highest solid mass acquired by optimization is 226.1 kg, while the minimum solid mass obtained through analysis is 203.1 kg. The dimension matching to design point number 15 is 70.285 for all cross members.

4.3.2.3 Response-Surface Plots for CCD using St52E material with square section chassis

The Response-Surface plot assists in determining the range of optimization variable values for which equivalent-stress is maximum or minimum. Figure 4.102 illustrates the Response-Surface (RS) plot of equivalent-stress vs cross-member one and two.
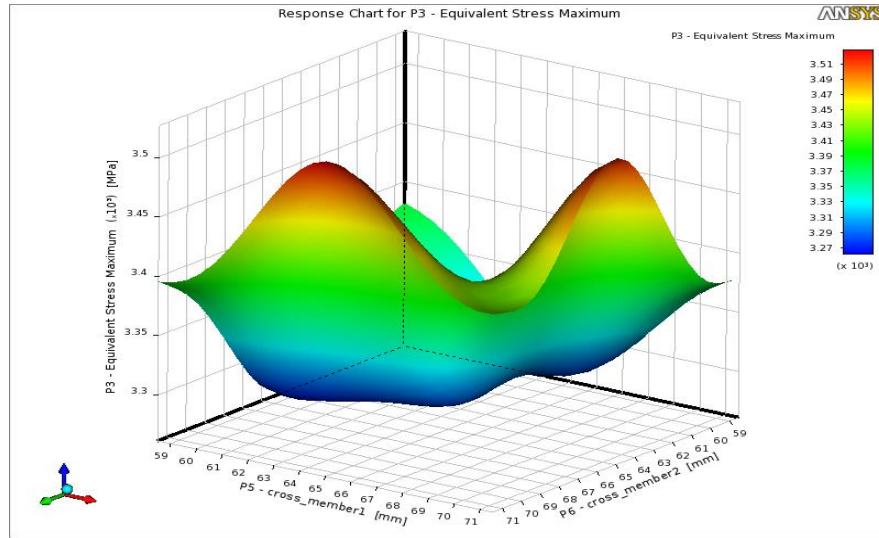
Figure 4.102: Response-surface of equivalent-stress vs. cross members 1 and 2 for CCD scheme using St52E material with square section chassis

Two peaks of equivalent-stress are observed as shown in the red-coloured region. As per the first peak that appeared along the cross-member 1 dimension, the equivalent-stress is maximum for cross-member 1 dimension varying from 62mm to 67mm and cross-member 2 dimensions varying from 69mm to 71mm. As per the second peak that appeared along the cross-member 2 dimension, the equivalent-stress is maximum for cross-member 1 dimension varying from 69mm to 71mm and cross-member 2 dimensions varying from 61mm to 67mm. The equivalent-stress is minimum for other dimensions of cross-member 1 and cross-member 2 as shown in the dark blue coloured region.

Figure 4.103: Response-Surface plot of equivalent-stress vs cross-member 2 and 3 for CCD scheme

Figure 4.103 illustrates the Response-Surface plot of equivalent-stress vs cross-member 2 and cross-member 3 dimensions. As shown in the red region, a single peak of equivalent-stress is observed.

The interpolation method is used to obtain the dimensions corresponding to the maximum equivalent-stress. Cross-member 3 dimension values varying from 61mm to 67mm and cross-member 2 values varying from 69mm to 71mm exhibit the highest equivalent-stress. For other values of cross-member 2 and cross member, the equivalent-stress is minimal, as represented by the dark blue coloured region.
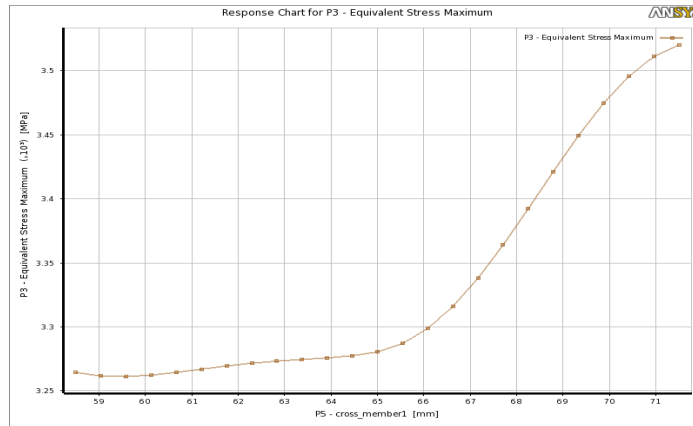
Figure 4.104: Equivalent-stress vs cross-member 1 for CCD scheme using St52E material

Figure 4.104 illustrates the variation of equivalent-stress in relation to cross-member 1 dimensions. The graph illustrates a progressive increase in equivalent-stress up to cross-member 1 dimension value of 65mm. The equivalent-stress then grows exponentially to a maximum of 3570 MPa at a cross-member 1 dimension of 71mm.
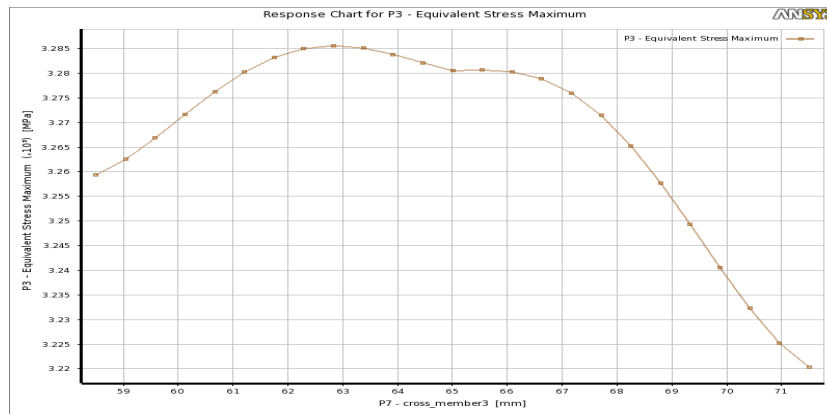
Figure 4.105: Equivalent-stress vs cross-member 3 for CCD scheme using St52E material

Figure 4.105 illustrates the variation of equivalent-stress with respect to cross-member 3 dimensions. The graph shows a gradual increase in equivalent-stress up to 63mm cross-member 3 dimensions, after which it decreases linearly as cross-member 3 dimensions increase. With a cross-member 3 dimension of 71.5mm, the minimum equivalent-stress is observed.
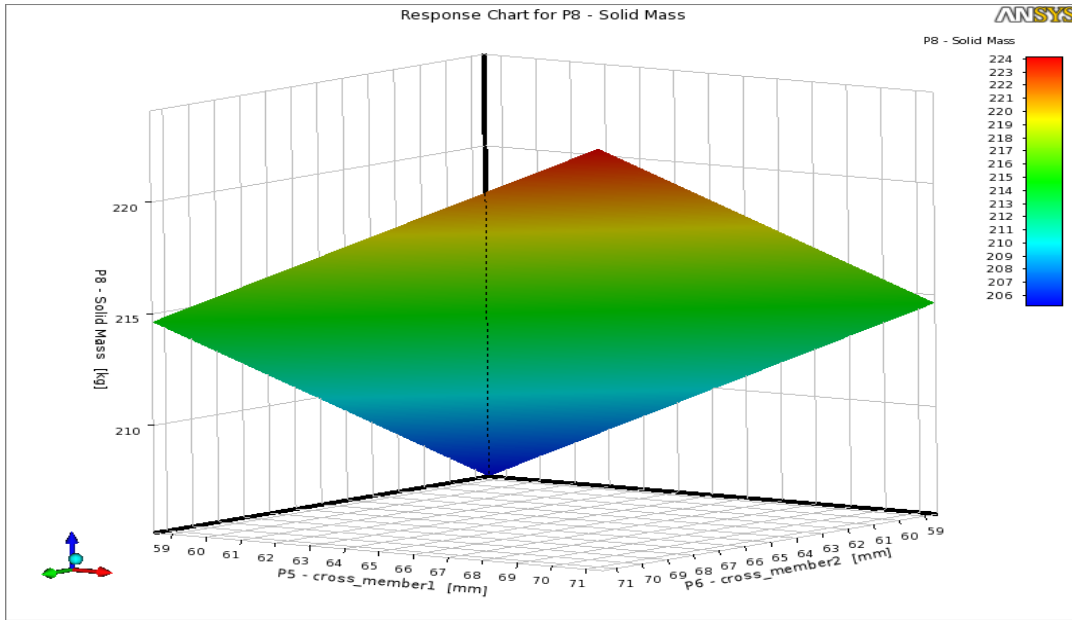
Figure 4.106: 3D Response-Surface plot of solid mass for CCD scheme using St52E material

The response-surface plot in figure 4.106 illustrates the variation of mass with respect to cross members 1 and 2 dimensions. The maximum mass is shown in the red region, while the minimum mass is shown in the blue region. The highest mass is found in cross-member 1 dimensions varying from 68mm to 71mm and cross-member 2 dimensions varying from 68mm to 71mm. Cross members 1 and 3 have the lowest mass, with dimensions varying from 58.5mm to 61mm.
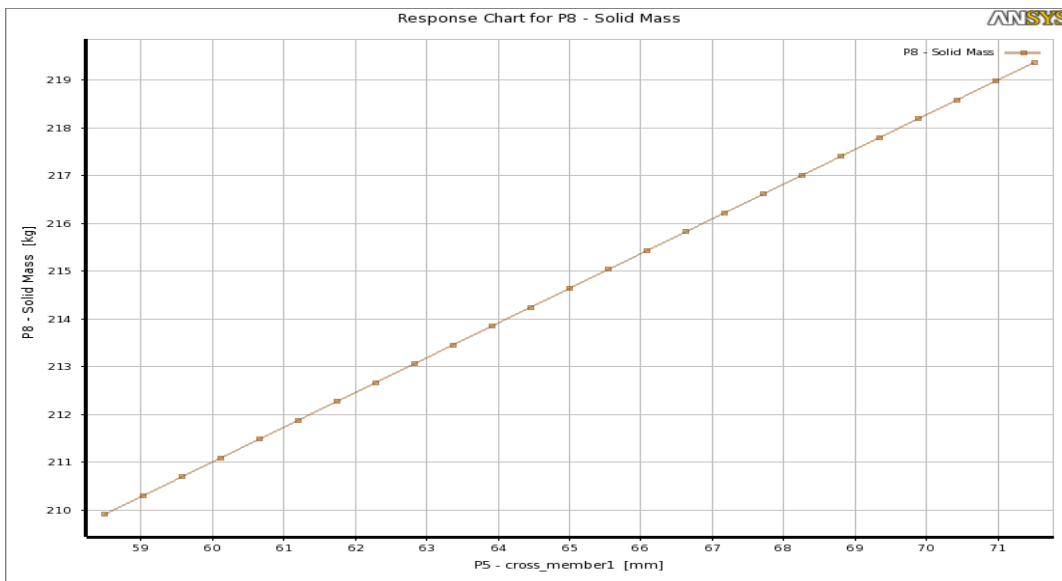
Figure 4.107: Solid mass vs cross-member 1 for CCD scheme using St52E material

Figures 4.107 and 4.108 show the variation in chassis mass as a function of cross-member 1 and cross-member 3 dimensions. The solid mass is observed to increase linearly as the cross-member 1 and

cross-member 3 dimensions increase. The cross-member 1 dimension of 58.5mm results in the lowest chassis mass. The 58.5mm cross-member 3 and cross-member 1 dimensions result in the lowest chassis mass.
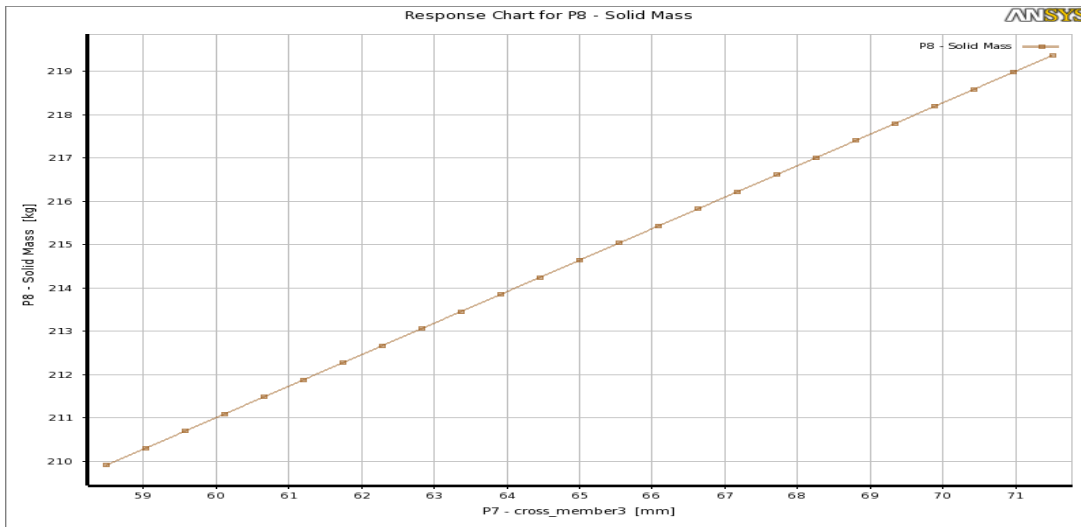
Figure 4.108: Solid mass vs cross-member 3 for CCD scheme using St52E material
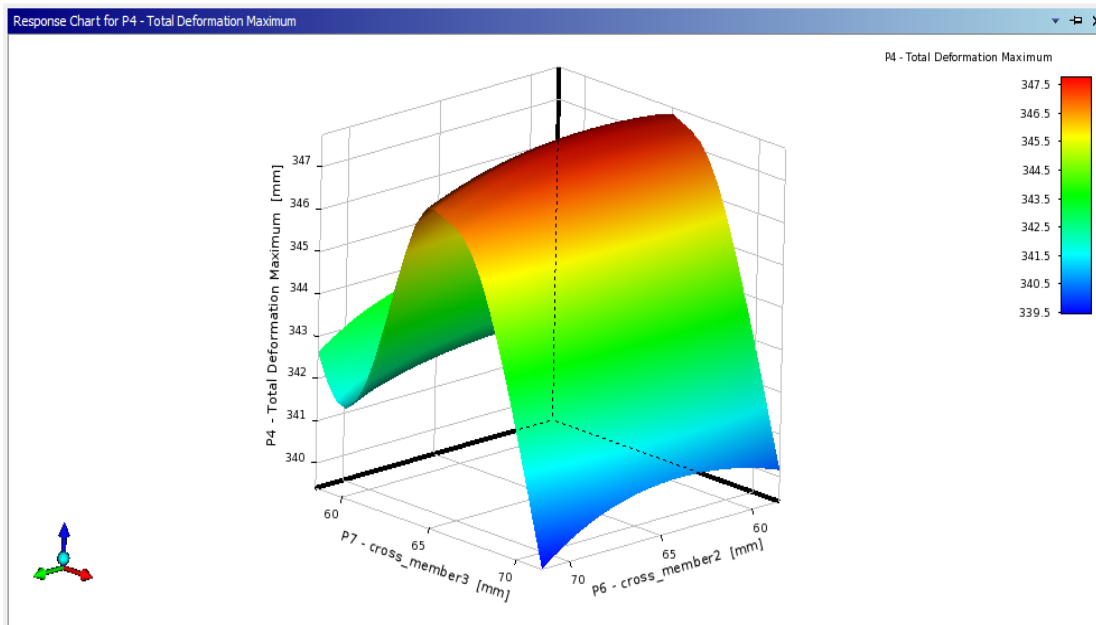
Figure 4.109: Response-Surface plot of total deformation for CCD scheme using St52E material

The Response-Surface plot (figure 4.109) of total deformation is generated. The maximum deformation is obtained for cross-member 3 dimensions varying from 64mm to 67mm and cross-member 2 dimensions varying from 59mm to 71mm.

	Equivalent Stress Maximum	Total Deformation Maximum	Solid Mass
■ P5 - cross_member1 (mm)	84.01933967	-7.265287109	33.33333333
■ P6 - cross_member2 (mm)	82.58221875	-8.266325519	33.33333333
■ P7 - cross_member3 (mm)	-21.23103645	-70.48870257	33.33333333

Figure 4.110: Sensitivity plot for CCD scheme using St52E material

Cross-member 1 has the highest sensitivity percentage for equivalent-stress (84.019 percent), and cross-member 3 has the lowest sensitivity percentage (21.231 percent), indicating that equivalent-stress has the greatest effect on cross-member 1 and has the least effect on cross-member 3 as illustrated in figure 4.110. Cross member-3 represents the maximum sensitivity percentage for deformation, while cross member-1 represents the minimum sensitivity percentage. This means that total deformation has the greatest effect on cross member-3 dimensions. For solid mass, all three variables have the same sensitivity percentage, indicating that all three optimization variables have the same effect on chassis mass.

4.3.3 Optimal Space-filling (OSF) design scheme using St52E material

Because the design points are evenly distributed in the design area, space fill designs are recommended for testing with deterministic models. An important assumption must be made in order to use these design options: computer simulation must accurately represent the actual physical system. While ANSYS has a number of DOE methods available, we recommend Latin-Hypercube Sampling (LHS) and Optimal-space-filling design (OSF) scheme with user-defined sample points. The primary benefit of these methods is that the number of samples is independent of the number of parameters [96]. Figure 4.111 illustrates a design Exploration window.
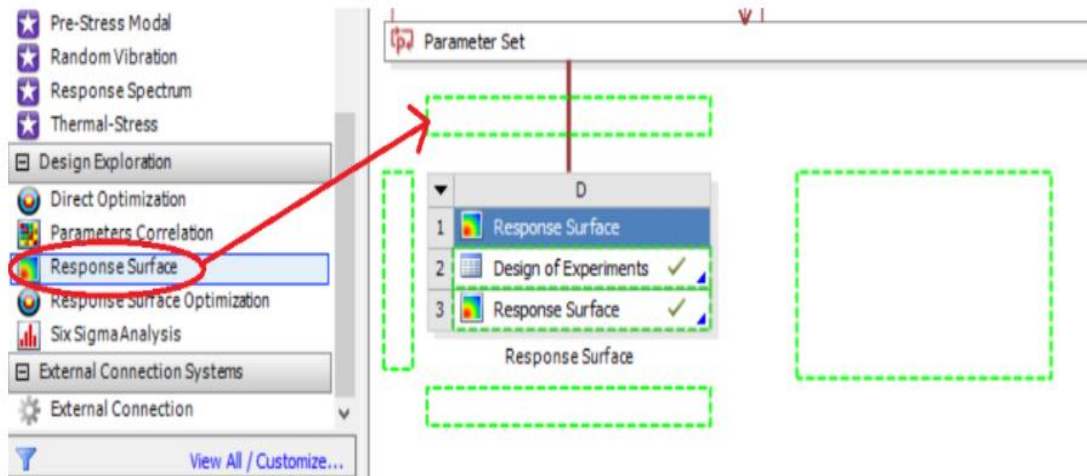
Figure 4.111: Design Exploration window [96]

An optimal space-filling design scheme is used to generate the design points. These design points are derived from a linear regression model, as shown in columns B, C, and D of Table 4.16. Finite Element Analysis was used by the software to evaluate output parameters at these design points. As shown in columns E and F, the output parameters are equivalent-stress and total-deformation.

Table 4.16: DOE Table for OSF scheme using St52E material

A	B	C	D	E	F	G
Name	P5 - cross-member 1 (mm)	P6 - cross-member 2 (mm)	P7 - cross-member 3 (mm)	P3 - Equivalent-stress Max (MPa)	P4 - Total Deformation Maximum (mm)	P8 - Solid Mass (kg)
1	69.33	68.47	60.67	3494.4	345.09	217.16
2	63.27	69.33	59.8	3237.66	341.53	212.75
3	59.8	66.73	68.47	3352.96	344.48	214.64
4	68.47	59.8	67.6	3498.67	345.34	215.27
5	58.93	60.67	65.87	3507.02	347.05	207.71
6	71.07	63.27	63.27	3348.54	348.9	216.53
7	66.73	62.4	58.93	3249.31	342.53	209.6
8	70.2	65.87	69.33	3320.9	343.09	222.2
9	65.87	64.13	64.13	3286.35	348.26	214.01
10	65	67.6	71.07	3469.52	341.16	220.94
11	61.53	71.07	65	3478.07	347.15	216.53
12	60.67	65	61.53	3506.21	351.44	208.97
13	64.13	58.93	62.4	3305.28	350.45	207.71
14	67.6	70.2	66.73	3475.77	345.39	221.57
15	62.4	61.53	70.2	3236.13	342.58	214.01

Design point number 5 has the highest equivalent-stress, while design point number 15 has the lowest equivalent-stress. Cross-member 1 has a dimension of 58.933mm, cross-member 2 has a dimension of 60.667mm, and cross member-3 has a dimension of 65.867mm. The maximum equivalent-stress determined by the analysis is 3507 MPa, and the minimum equivalent-stress determined by the analysis is 3236.1mm.

Cross-member 1 has a dimension of 62.4mm, cross-member 2 has a dimension of 61.533mm, and cross-member 3 has a dimension of 70.2mm. The maximum solid mass obtained from optimization is 222.2 kg at design point number 8 and the minimum solid mass obtained from the analysis is 207.71 kg at design point number 5. The dimensions corresponding to design point number 8 are 70.2mm for cross-member 1, 65.867mm for cross-member 2, and 69.333mm for cross-member 3.

Design point number 12 exhibits the greatest deformation, while design point number 10 exhibits the least deformation. Cross-member 1 has a dimension of 60.667mm, cross-member 2 has a dimension of 65mm, and cross-member 3 has a dimension of 61.533mm. The maximum deformation measured by the analysis is 347.15mm, and the minimum deformation measured by the analysis is 341.16mm.
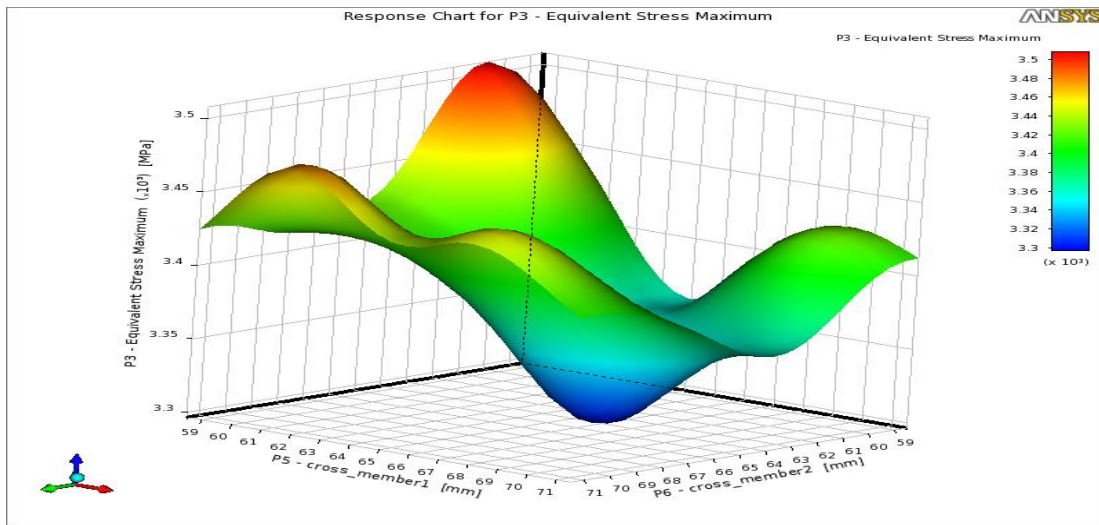
Figure 4.112: Response-surface plot of equivalent-stress vs cross-member 1 and 2 for OSF scheme using St52E material

Figure 4.112 illustrates the Response-Surface plot of equivalent-stress vs cross-member 1 and cross-member 2 dimensions. Two equivalent-stress peaks can be seen in the red-coloured region. The equivalent-stress is greatest for cross-member 1 dimensions varying from 59mm to 62mm and cross-member 2 dimensions varying from 59mm to 62mm, according to the first peak that appeared along the cross-member 2 dimensions.

The equivalent-stress is greatest for cross-member 1 dimensions varying from 61mm to 63mm and cross-member 2 dimensions varying from 69mm to 71mm, according to the second peak that appeared

along the cross-member 1 dimension. The equivalent-stress is lowest for the other dimensions of cross members 1 and 2, as shown in the dark blue region.
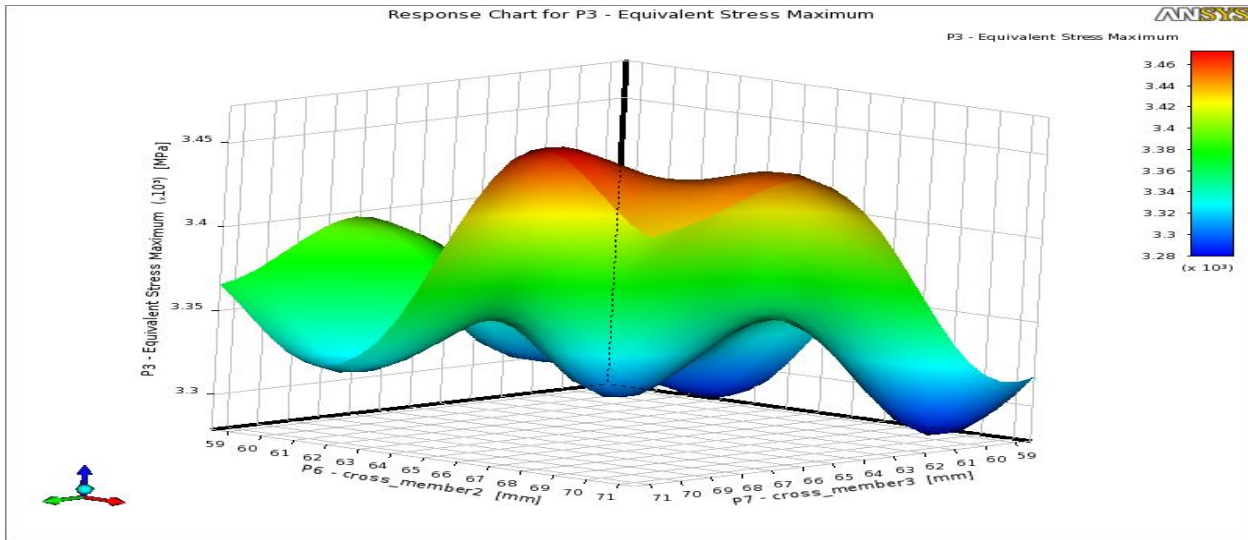
Figure 4.113: Response-Surface plot of equivalent-stress vs cross-member 2 and cross-member 3 for OSF scheme using St52E material

Figure 4.113 illustrates the Response-Surface plot of equivalent-stress vs cross-member 2 and cross-member 3. As shown in the red region, a single peak of equivalent-stress is observed. The interpolation method is used to obtain the dimensions corresponding to the maximum equivalent-stress. Cross-member 3 values varying from 64mm to 71mm and cross-member 2 values varying from 66mm to 71mm exhibit the highest equivalent-stress. For other values of cross-member 2 and cross member, the equivalent-stress is minimal, as represented by the dark blue coloured region.
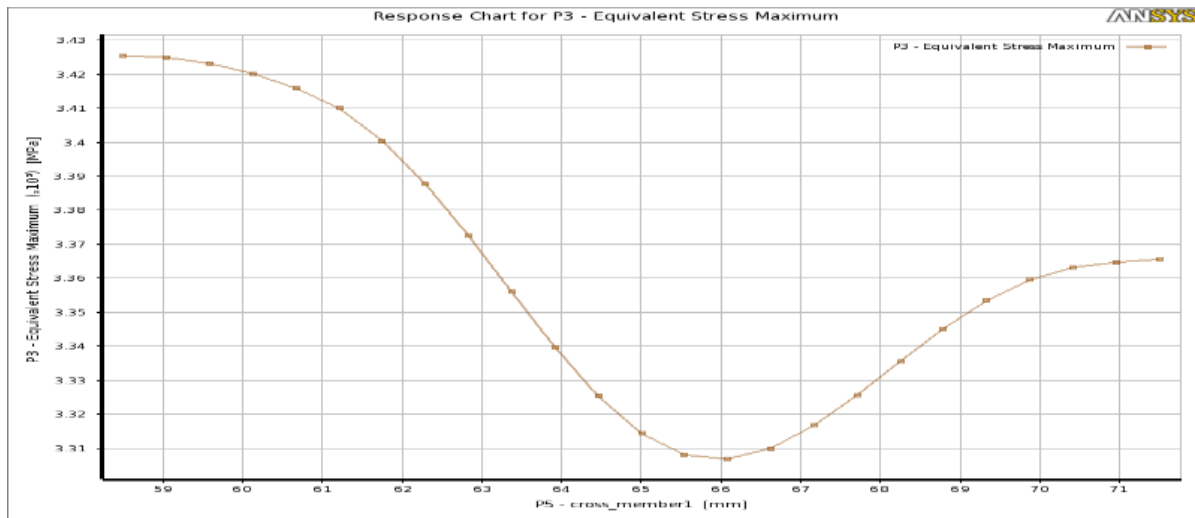
Figure 4.114: Equivalent-stress vs cross-member 1 for OSF scheme using St52E material

The equivalent-stress initially decreases and reaches a minimum value of 66mm at cross-member 1 dimension. The equivalent-stress then increases linearly until it reaches its maximum value at the 71mm cross-member 1 dimension as illustrated in figure 4.114. For a cross-member 1 dimension of 58.5mm, the initial maximum equivalent-stress is obtained.
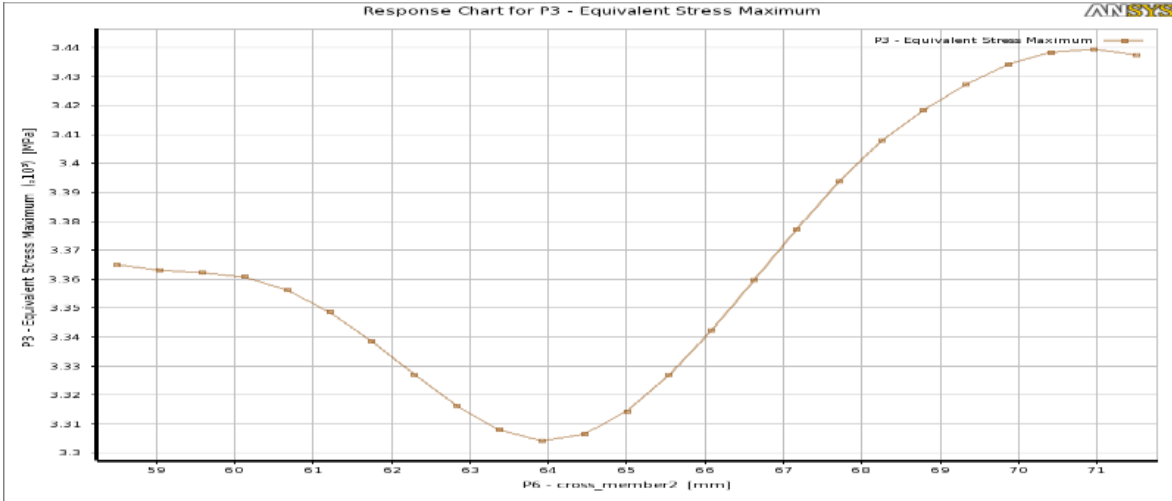
Figure 4.115: Equivalent-stress cross-member 2 for OSF scheme using St52E material

The equivalent-stress decreases as cross-member 2 dimensions increase and reaches a minimum at cross-member 2 dimensions of 64mm as illustrated in figure 4.115. Following that, a linear increase in equivalent-stress is observed, reaching a maximum at cross-member 2 dimensions of 71mm.
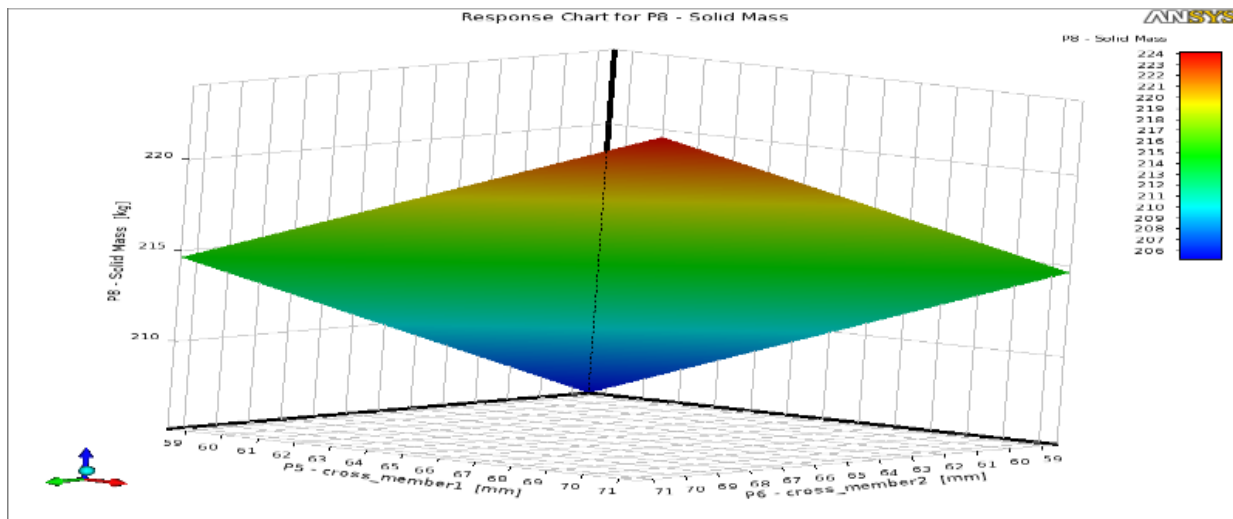
Figure 4.116: 3D Response-Surface plot of solid mass for OSF scheme using St52E material

The variation of mass with respect to cross members 1 and 2 dimensions is depicted in the Response-Surface plot depicted in figure 4.116. The maximum mass is depicted in the red region, while the minimum mass is depicted in the blue region. Cross-member 1 dimensions vary from 68mm to 71mm

and cross-member 2 dimensions varying from 65mm to 71mm have the highest mass. Cross-member 1 and cross-member 3 dimensions varying from 58.5mm to 61mm have the lowest mass.
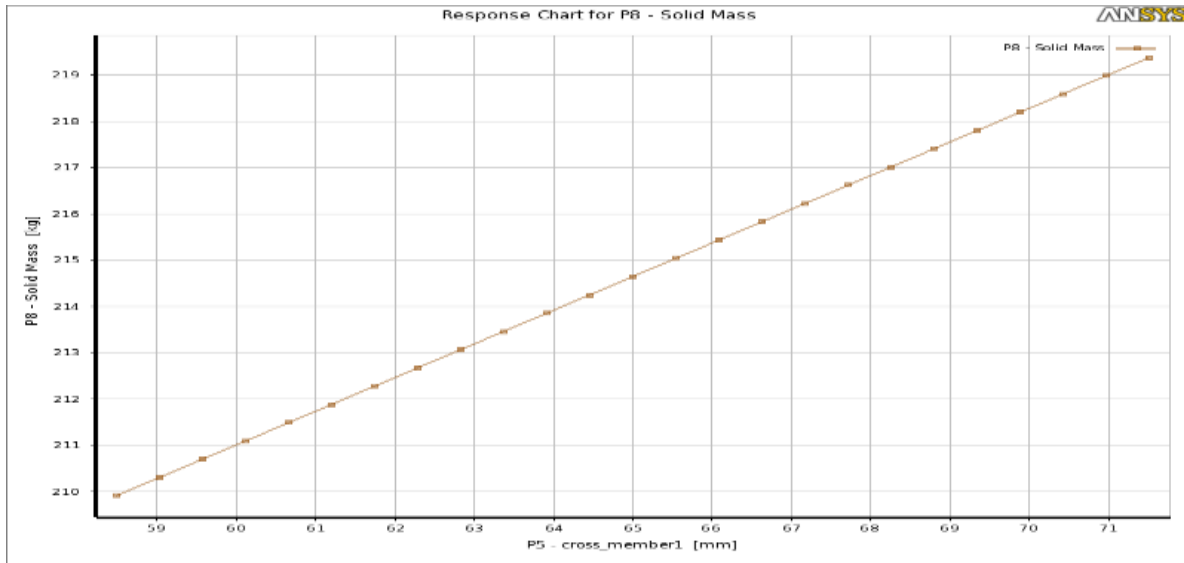
Figure 4.117: Solid mass vs cross-member 1 for OSF scheme using St52E material
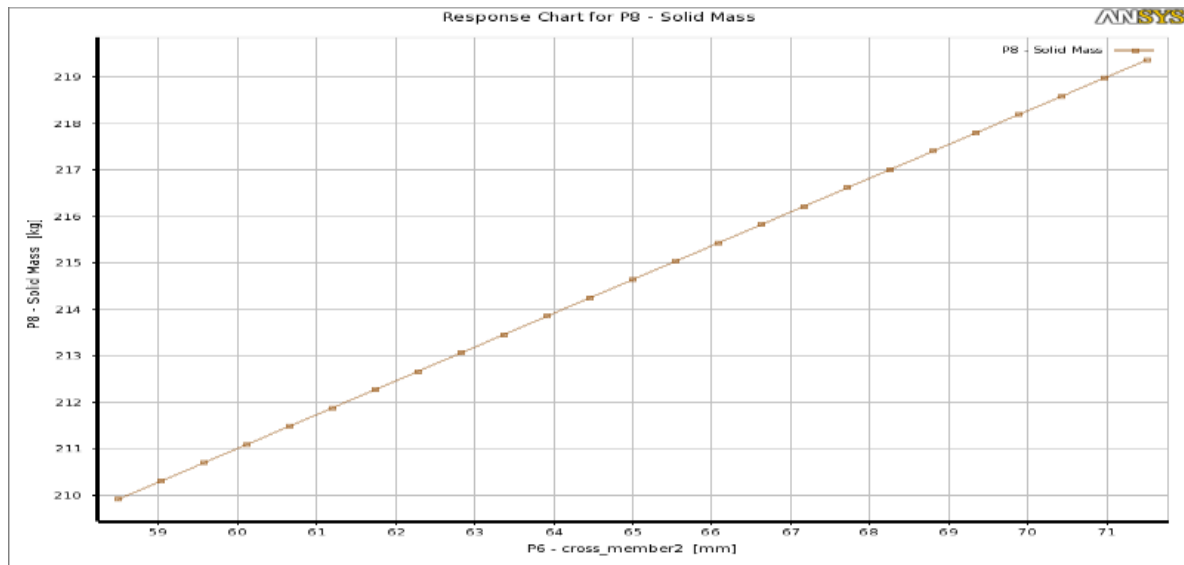
Figure 4.118: Solid mass vs cross-member 2 for OSF scheme using St52E material

Figures 4.117 and 4.118 show the variation of chassis mass with respect to cross-member 1 and cross-member 3 dimensions. The solid mass increases linearly as the dimensions of cross-member 1 and cross-member 3 increase. The minimum mass of the chassis is observed for dimensions of 58.5mm

cross-member 3 and cross-member 1, and the maximum mass is observed for dimensions of 71.5mm cross-member 3 and cross-member 1.
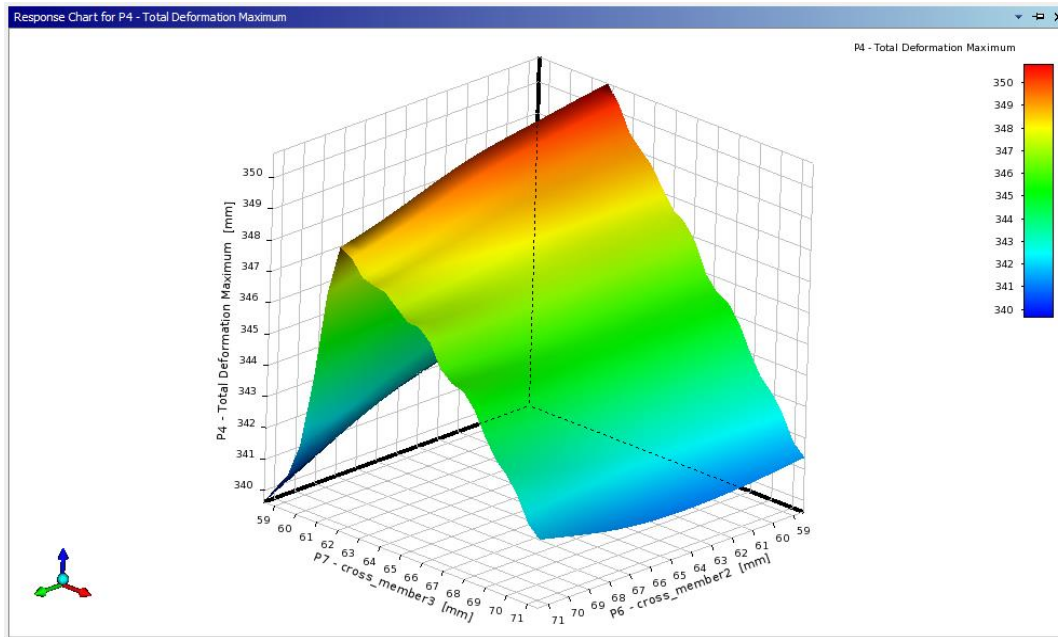
Figure 4.119: 3D Response-Surface plot of total deformation for OSF scheme using St52E material

The analysis yields the Response-Surface plot of total deformation, as shown in the figure 4.119. Maximum deformation is obtained for cross member3 dimensions of 62mm to 64mm and cross member2 dimensions of 59mm to 67mm. Other regions, as shown in dark and light blue, have the least amount of deformation.

	Equivalent Stress Maximum	Total Deformation Maximum	Solid Mass
cross_member1 (mm)	-43.04865881	-2.210484538	33.33333333
cross_member2 (mm)	48.18682995	-4.226894698	33.33333333
cross_member3 (mm)	31.68112627	-69.28850744	33.33333333
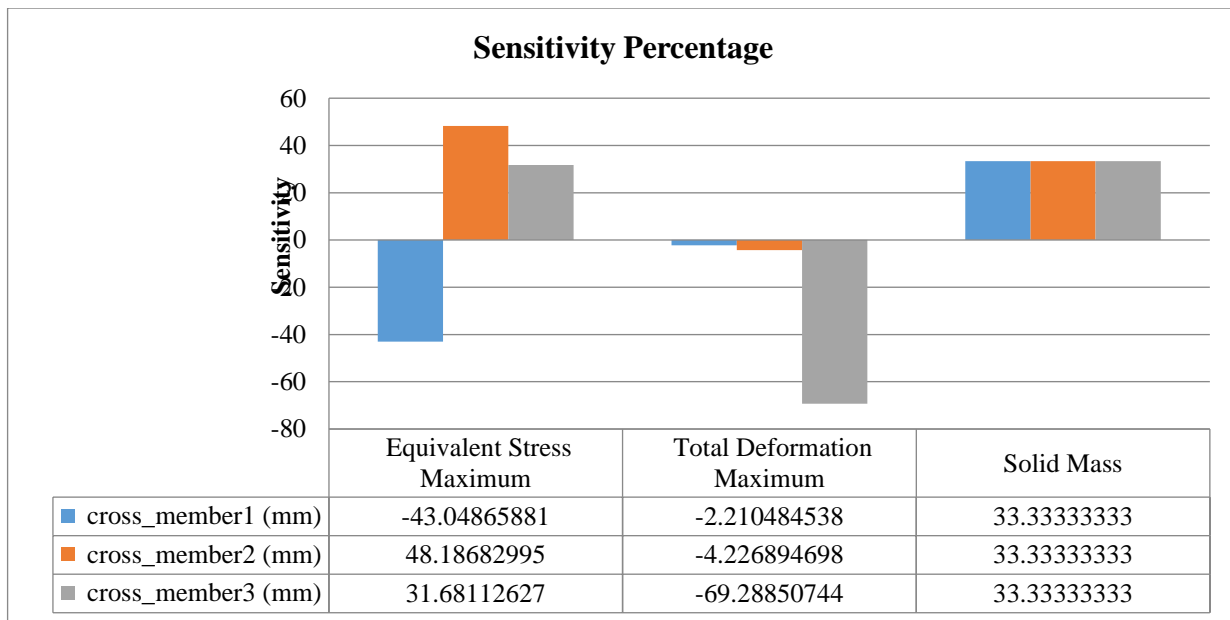
Figure 4.120: Sensitivity plot for OSF scheme using St52E material

Cross-member 2 has the highest sensitivity percentage for equivalent-stress, while cross-member 3 has the lowest, indicating that equivalent-stress has the greatest effect on cross-member 2 as illustrated in figure 4.120. Cross-member 3 has the highest sensitivity percentage for deformation, while cross-member 1 has the lowest, indicating that total deformation has the greatest effect on cross-member 3. For solid mass, all three variables have the same sensitivity percentage, indicating that all three optimization variables have the same effect on chassis mass.

4.3.4 Box-Behnken (B-B) design scheme using St52E material

The design points are generated using the Box-Behnken (B-B) design scheme. These design points are generated based on a linear regression model as shown in column B, column C, and column D in table 4.17. The software evaluated output parameters at these design points using Finite Element Analysis. These output parameters are equivalent-stress and total deformation as shown in columns E and column F.

Table 4.17: DOE Table for B-B scheme using St52E material

A	B	C	D	E	F	G
Name	P5 - cross-member 1 (mm)	P6 - cross-member 2 (mm)	P7 - cross-member 3 (mm)	P3 - Equivalent -stress Max (MPa)	P4 - Total Deformatio n Maximum (mm)	P8 - Solid Mass (kg)
1	65	70	70	3418.83	342.13	221.91
2	62	62	70	3225.5	342.76	213.91
3	68	62	70	3447.9	342.54	218.28
4	62	78	70	3489.33	341.84	225.55
5	68	78	70	3495.78	341.49	229.91
6	62	70	62	3504.15	350.19	213.91
7	68	70	62	3523.64	349.97	218.28
8	62	70	78	3464.99	337.3	225.55
9	68	70	78	3490.21	337.02	229.91
10	65	62	62	3325.16	350.8	210.28
11	65	78	62	3548.44	349.52	221.91
12	65	62	78	3455.83	337.66	221.91
13	65	78	78	3458.25	336.72	233.55

The maximum equivalent-stress is observed for design point number 11 and minimum equivalent-stress is observed for design point number 2. The dimensions corresponding to design point number 11 are 65mm for cross-member 1, 78mm for cross-member 2, and 62mm for cross-member 3. The

maximum solid mass obtained from optimization is 233.5 kg at design point 13 and the minimum is 210.28 kg at design point 10. The maximum deformation is observed for design point number 10 and minimum deformation is observed for design point number 13.
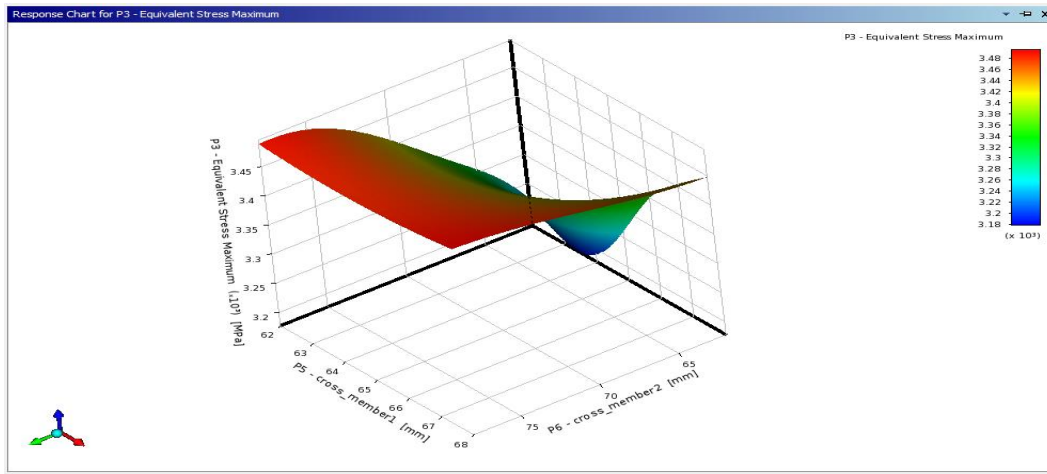
Figure 4.121: Response-Surface plot of equivalent-stress vs cross-member 1 and cross-member 2 for B-B scheme using St52E material

Figure 4.121 illustrates the Response-Surface plot of equivalent-stress vs cross-member 1 and cross-member 2. Two equivalent-stress peaks can be seen in the red-coloured region. Maximum equivalent-stress is observed for cross member1 with dimensions varying from 62mm to 68mm and cross member2 with dimensions varying from 62mm to 78mm. The equivalent-stress is lowest for regions depicted in dark blue and cross member1 values varying from 62mm to 65mm, as well as cross member1 dimensions varying from 62mm to 65mm.
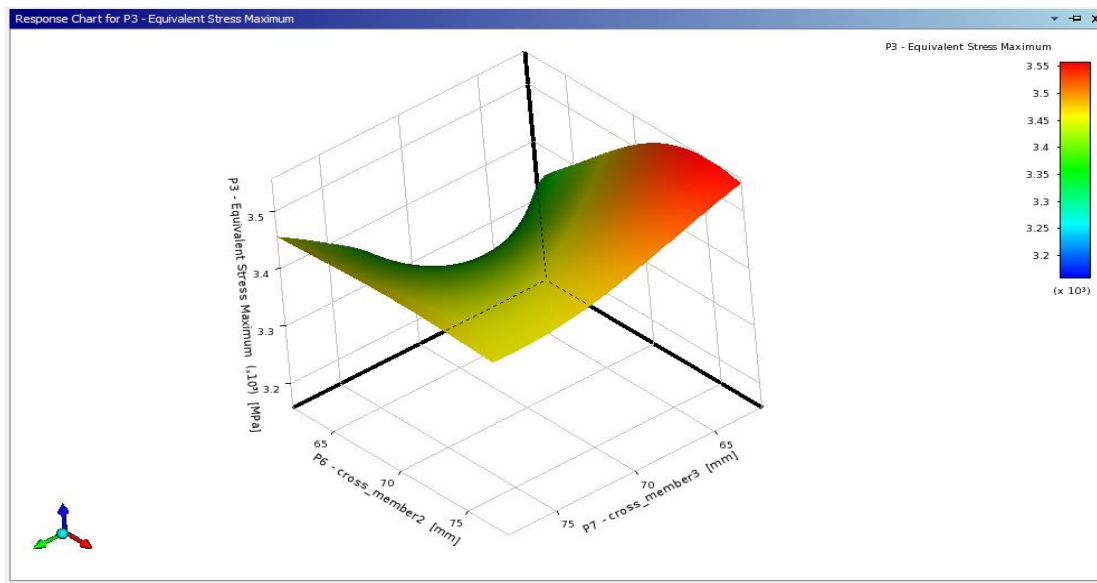
Figure 4.122: Response-Surface plot of equivalent-stress vs cross-member 2 and cross-member 3 for B-B scheme using St52E material

Figure 4.122 illustrates the Response-Surface plot of equivalent-stress vs cross-member 2 and cross-member 3. Cross member2 dimensions vary from 67mm to 78mm and cross member3 dimensions varying from 62mm to 72mm exhibit the highest equivalent-stress. The equivalent-stress is found to be lowest in regions represented by dark blue color. This corresponds to cross member3 dimensions varying from 64mm to 72mm and cross member2 dimensions varying from 62mm to 64mm.
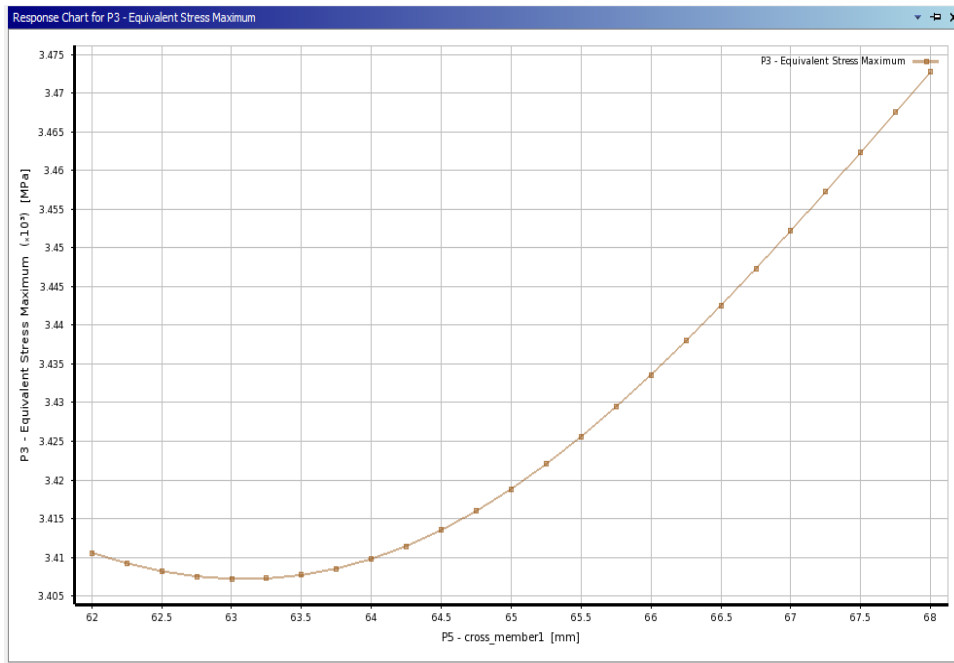
Figure 4.123: Equivalent-stress vs cross-member 1 for B-B scheme using St52E material

The equivalent-stress initially decreases and reaches a minimum value at cross-member 1 dimension of 63mm as shown in figure 4.123. The equivalent-stress then increases linearly and reaches the maximum value at cross-member 1 dimension of 38mm.
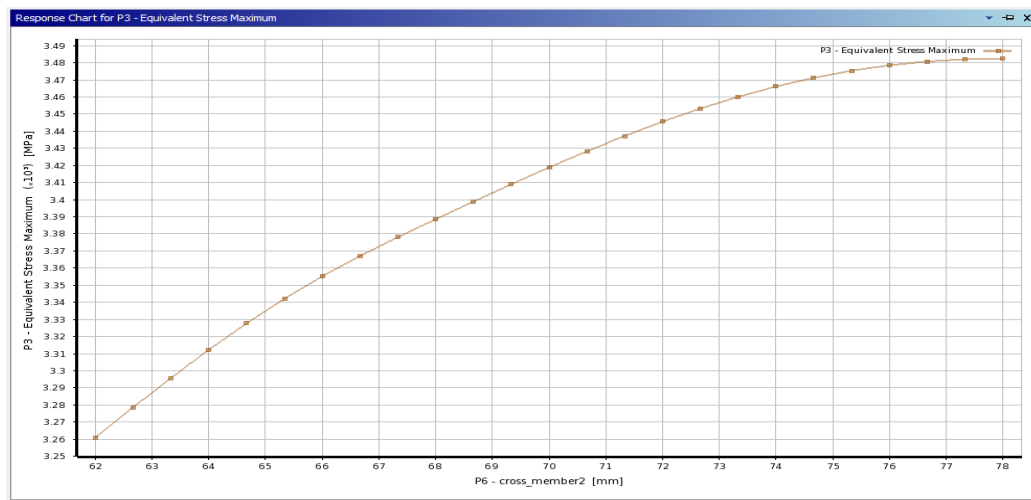
Figure 4.124: Equivalent-stress vs cross-member 2 for B-B scheme using St52E material

The equivalent-stress is minimum for cross-member 2 dimensions of 62mm and then increases linearly and reaches the maximum value at cross-member 2 dimensions of 77mm as shown in figure 4.124.
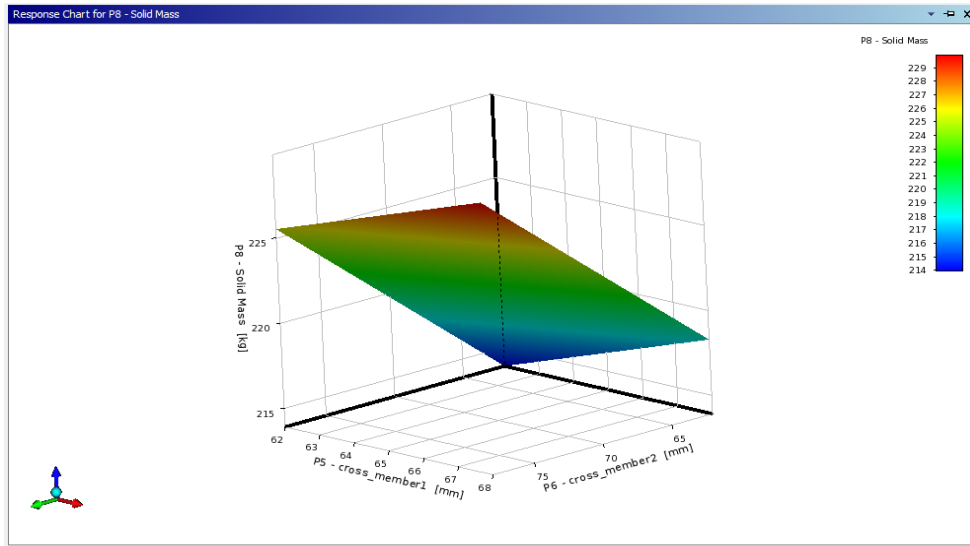
Figure 4.125: 3D Response-Surface plot of solid mass for B-B scheme using St52E material

The Response-Surface plot in figure 4.125 illustrates the variation of mass with respect to cross members 1 and 2. The maximum mass is depicted in the red region, while the minimum mass is depicted in the blue region. Cross-member 1 dimensions vary from 66mm to 68mm and cross-member 2 dimensions varying from 75mm to 78mm have the highest mass. Figure 4.126 illustrates a 2D linear graph of solid mass vs cross-member 1. The solid mass increases linearly as the cross member1 dimensions increase. The cross member1 dimension of 62mm has the lowest mass and the cross member1 dimension of 68mm has the highest solid mass.
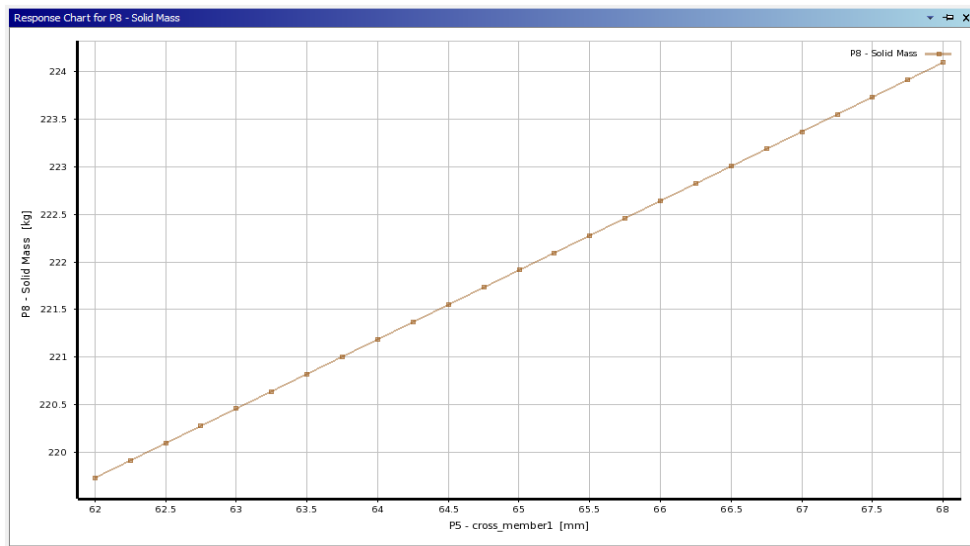
Figure 4.126: Solid mass vs cross-member 1 for B-B scheme using St52E material
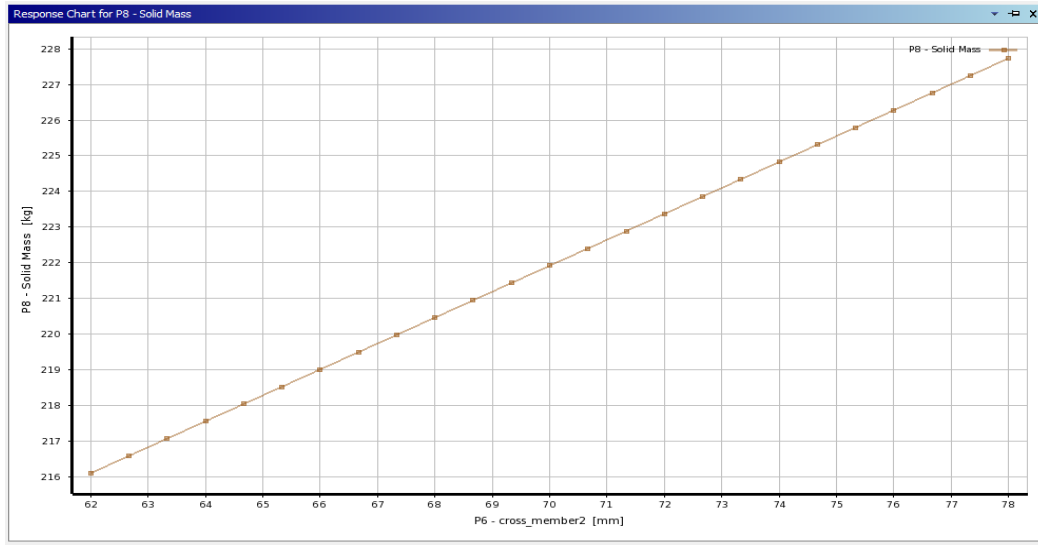
Figure 4.127: Solid mass vs cross-member 2 for B-B scheme using St52E material

The variation of chassis mass with respect to cross-member 2 dimensions is shown in figure 4.127. The mass is minimum for the cross-member 2 dimensions of 62mm and increases linearly to reach the maximum value at the cross-member 2 dimensions of 78mm.
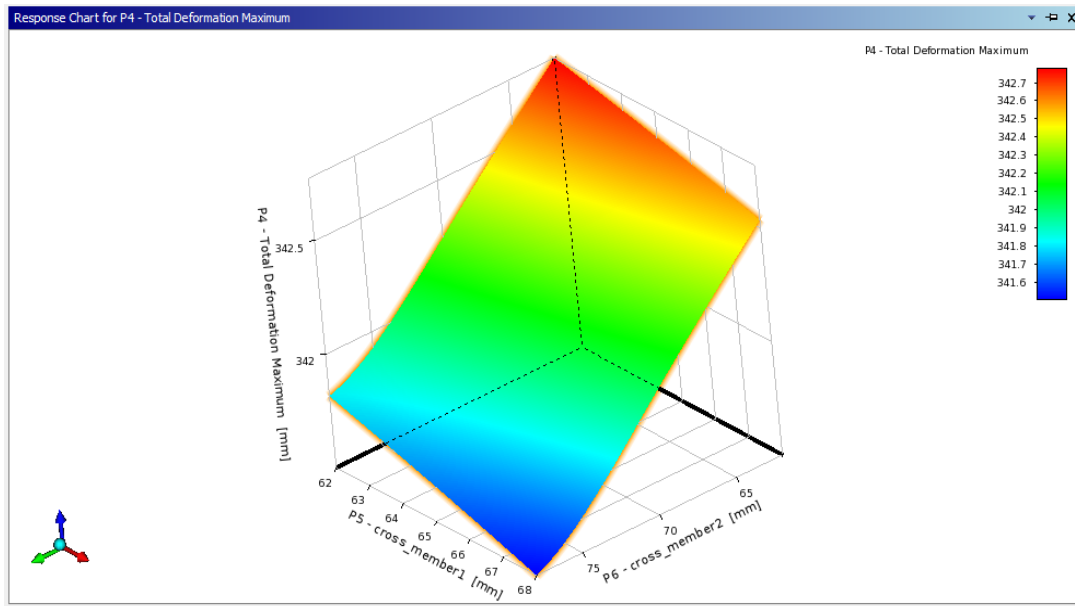
Figure 4.128: Response-Surface plot of total deformation for B-B scheme using St52E material

The Response-Surface plot of deformation is obtained using the box Behnken scheme as illustrated in figure 4.128. The maximum deformation is obtained for cross-member 2 dimensions varying from 62mm to 65mm and cross-member 1 dimensions varying from 62mm to 66mm.

	Equivalent Stress Maximum	Total Deformation Maximum	Solid Mass
■ cross_member1 (mm)	12.77745259	-1.830906328	15.78947368
■ cross_member2 (mm)	43.27693419	-6.946441412	42.10526316
■ cross_member3 (mm)	-17.17473163	-90.14478608	42.10526316
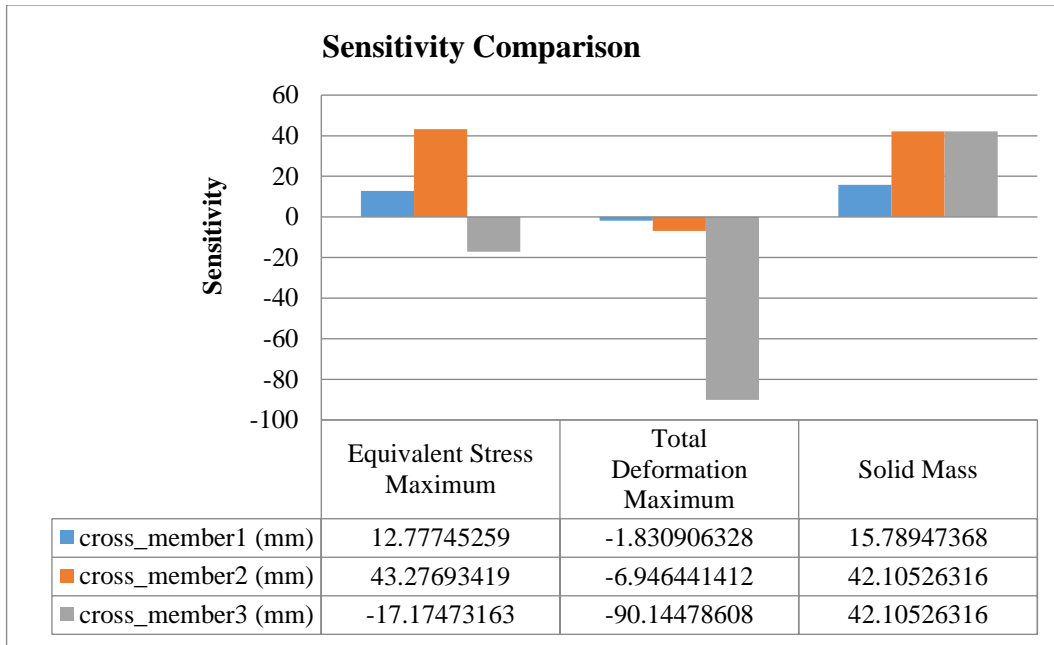
Figure 4.129: Sensitivity plot using optimal for B-B scheme using St52E material

Cross-member 2 has the highest sensitivity percentage for equivalent-stress, while cross-member 1 has the lowest, indicating that equivalent-stress has the greatest effect on cross-member 2 as illustrated in figure 4.129. Cross-member 3 has the highest sensitivity percentage for deformation, while cross-member 1 has the lowest, indicating that total deformation has the greatest effect on cross-member 3. For solid mass, cross member1 has the lowest sensitivity percentage of 42.105, while cross member2 and cross member3 have similar sensitivity percentages of 42.105.

4.3.5 Latin Hypercube Sampling using St52E material

The design points are generated using a Latin Hypercube sampling (LHS) scheme. These design points are generated based on a linear regression model as shown in column B, column C, and column D in table 4.18. The software evaluated output parameters at these design points using Finite Element Analysis. These output parameters are equivalent-stress and total deformation as shown in columns E and column F.

Table 4.18: DOE Table for LHS using St52E material

A	B	C	D	E	F	G
Name	P5 - cross-member 1 (mm)	P6 - cross-member 2 (mm)	P7 - cross-member 3 (mm)	P3 - Equivalent-stress Max (MPa)	P4 - Total Deformation Maximum (mm)	P8 - Solid Mass (kg)
1	65.87	68.47	65.87	3463.66	346.31	218.42
2	68.47	65	66.73	3499.24	345.66	218.42
3	58.93	65.87	60.67	3516.17	352.83	207.71
4	67.6	58.93	70.2	3470.86	342.28	215.9
5	59.8	60.67	61.53	3387.61	351.78	205.19
6	71.07	59.8	59.8	3443.17	342.24	211.49
7	66.73	70.2	69.33	3445.78	342.89	222.84
8	70.2	67.6	68.47	3249.31	343.98	222.84
9	62.4	61.53	65	3269.96	347.8	210.23
10	61.53	66.73	71.07	3341.73	341.32	217.79
11	64.13	63.27	63.27	3279.95	349.31	211.49
12	60.67	69.33	62.4	3487.81	349.95	212.75
13	65	64.13	64.13	3490.37	348.32	213.38
14	69.33	71.07	58.93	3457.46	343.88	217.79
15	63.27	62.4	67.6	3333.05	345.56	213.38

The maximum equivalent-stress is observed for design point number 3 and minimum equivalent-stress is observed for design point number 8. The dimensions corresponding to design point number 3 are 58.933mm for cross-member 1, 70.2mm for cross-member 2, and 60.667mm for cross-member 3. The maximum solid mass obtained from optimization is 222.84 kg at design point 7, and the minimum solid mass obtained from the analysis is 205.19 kg at design point 5. The maximum deformation is observed for design point number 3 and minimum deformation is observed for design point number 10.
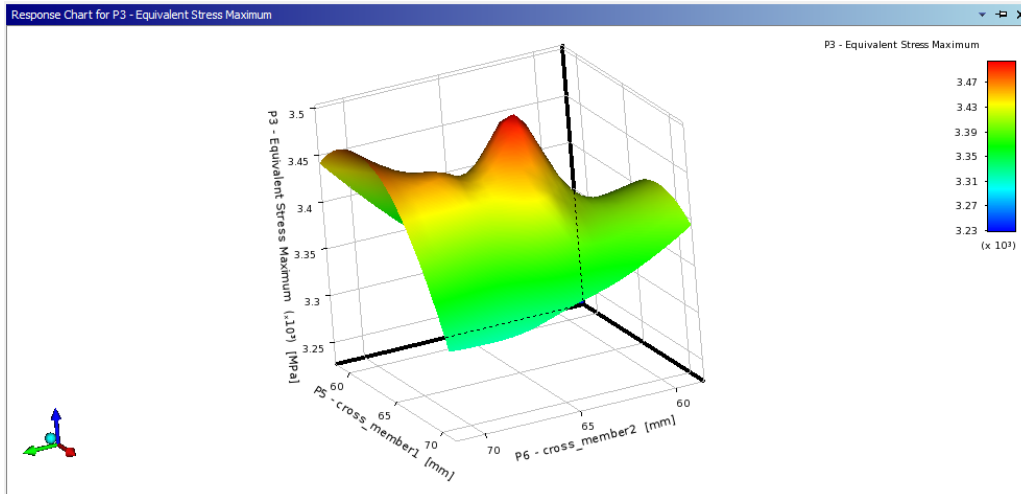
Figure 4.130: Response-Surface plot of equivalent-stress vs cross-member 1 and for LHS using St52E

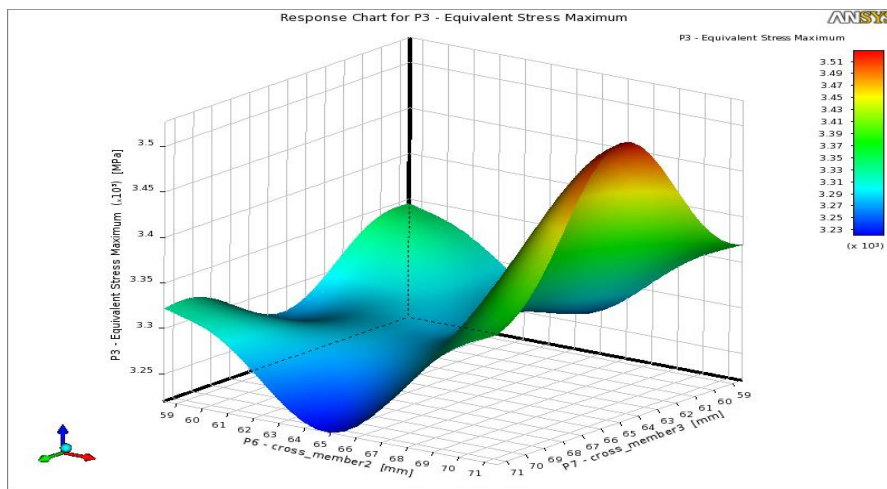Figure 4.130 illustrates the Response-Surface plot of equivalent-stress vs cross-member 1 and cross-member 2 dimensions. Two equivalent-stress peaks can be seen in the red-coloured region. Maximum equivalent-stress is observed for cross member1 with dimensions varying from 62mm to 66mm and cross member2 with dimensions varying from 63mm to 67mm. The equivalent-stress is lowest in the regions depicted in dark blue.
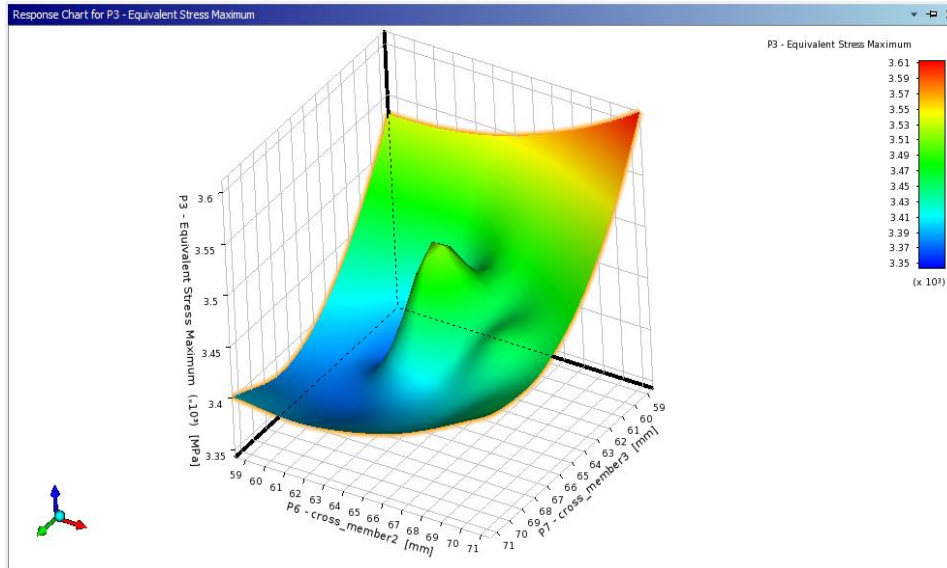
Figure 4.131: Response-Surface plot of equivalent-stress vs cross-member 2 and cross-member 3 for LHS using St52E material

The Response-Surface plot of equivalent-stress vs cross-member 2 and cross-member 3 is shown in figure 4.131. The maximum equivalent-stress is observed for cross-member 2 dimension varying from

67mm to 71mm and cross-member 3 dimensions varying from 59mm to 61mm. The equivalent-stress is observed to be minimum for regions represented in dark blue color.
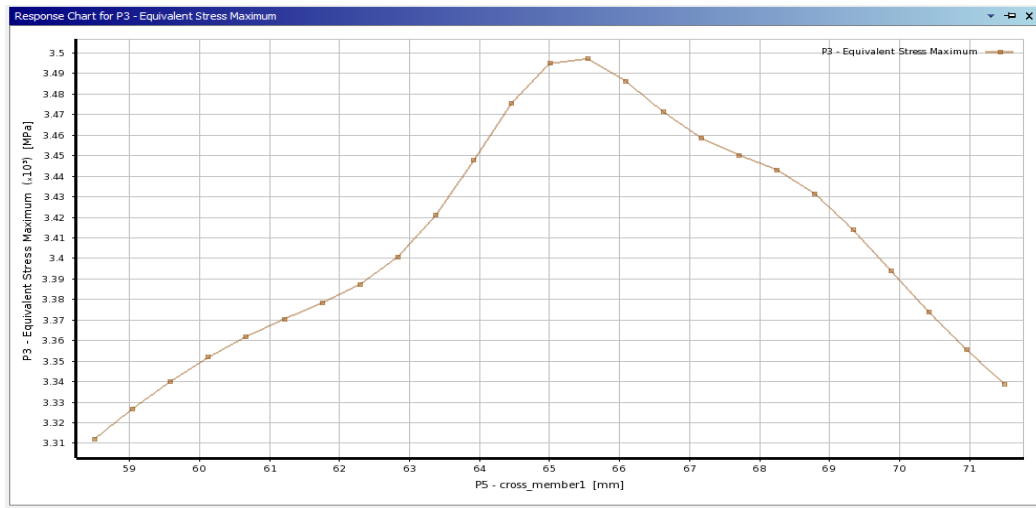
Figure 4.132: Equivalent-stress vs cross-member 1 for LHS using St52E material

The equivalent-stress is initially minimal at 58.5mm cross member1 and then increases linearly to a maximum at 65.5mm cross member1. As shown in Figure 4.132, the equivalent-stress decreases after that.
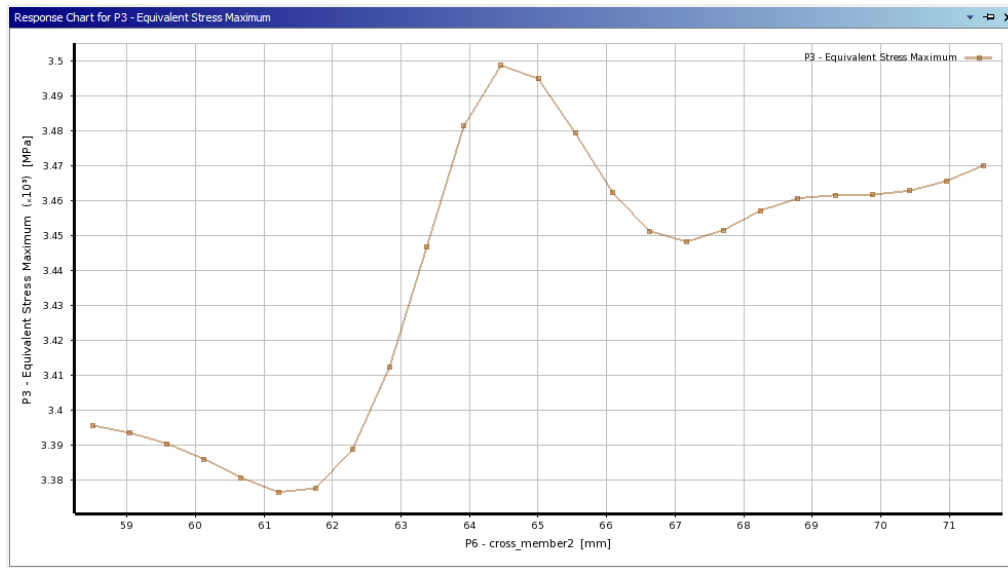
Figure 4.133: Equivalent-stress vs cross-member 2 for LHS using St52E material

The equivalent-stress is minimum for the cross-member 2 dimension of 61.2mm and then increases linearly and reaches the maximum value at the cross-member 2 dimension of 64.5mm as shown in figure 4.133.
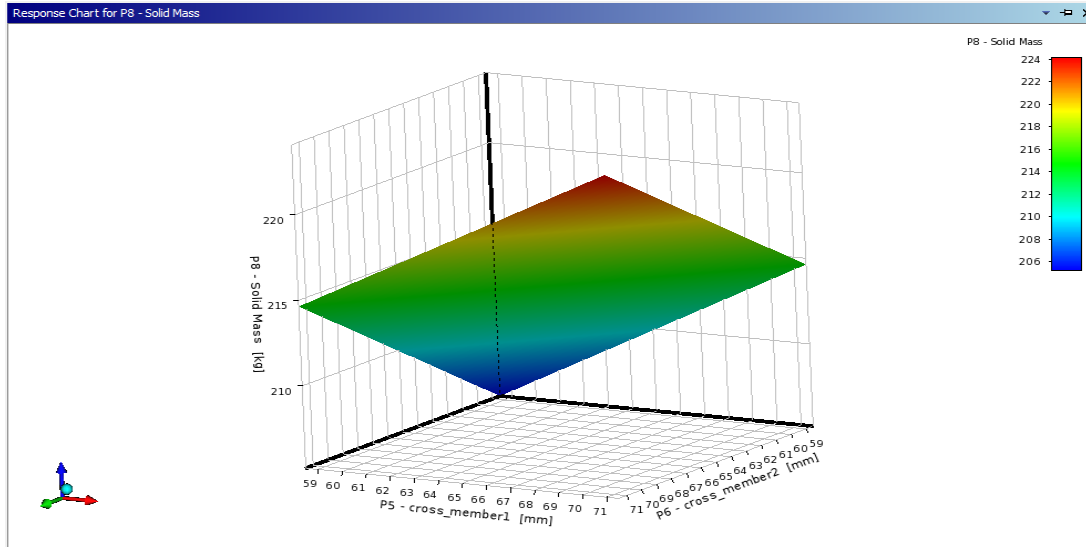
Figure 4.134: 3D Response-Surface plot of solid mass for LHS using St52E material

The variation of mass with respect to cross members 1 and 2 is depicted in the Response-Surface plot depicted in figure 4.134. The maximum mass is depicted in the red region, while the minimum mass is depicted in the blue region. Cross-member 1 dimensions vary from 67mm to 71mm and cross-member 2 dimensions varying from 67mm to 71mm have the highest mass. Figure 4.135 illustrates a 2D linear graph of solid mass vs cross-member 1. The solid mass increases linearly as the cross member1 dimensions increase. The cross member1 dimension of 58.5mm has the lowest mass and the cross member1 dimension of 71.5mm has the highest solid mass.
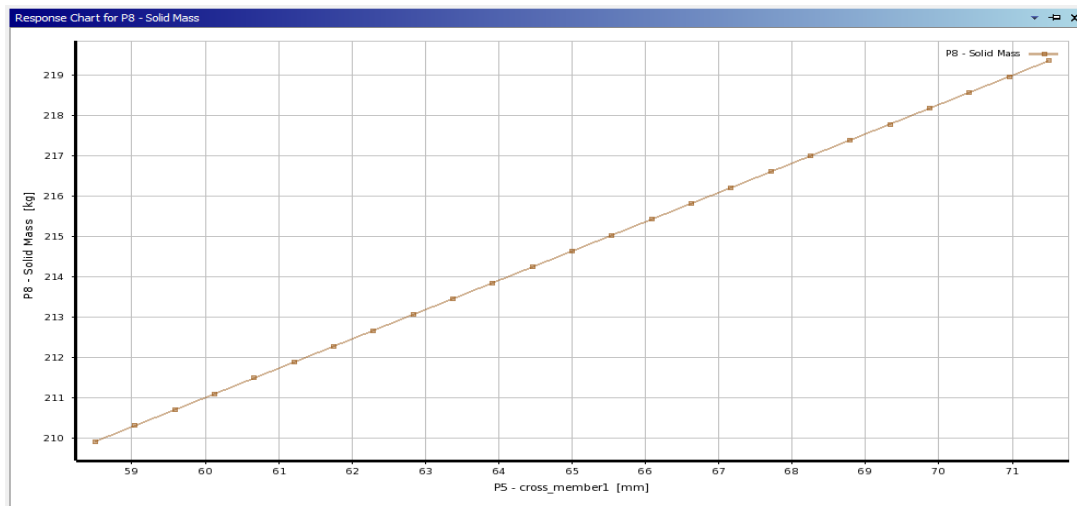
Figure 4.135: Solid mass vs cross-member 1 for LHS using St52E material
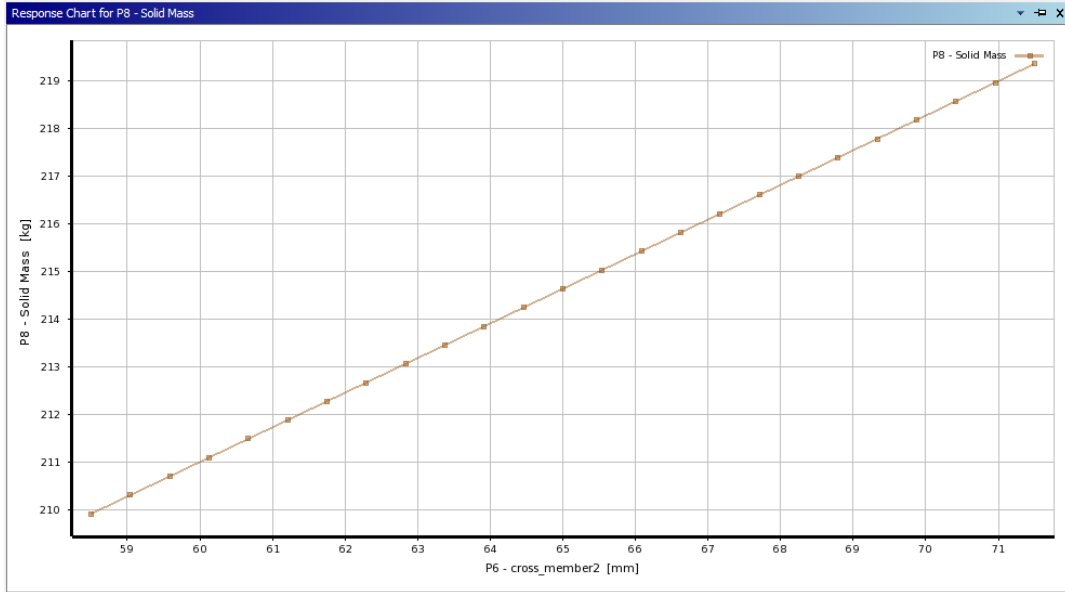
Figure 4.136: Solid mass vs cross-member 2 for LHS using St52E material

The variation of chassis mass with respect to cross-member 2 is shown in figure 4.136. The mass is minimum for the cross-member 2 dimension of 58.5mm and increases linearly to reach the maximum value at the cross-member 2 dimension of 71.5mm.
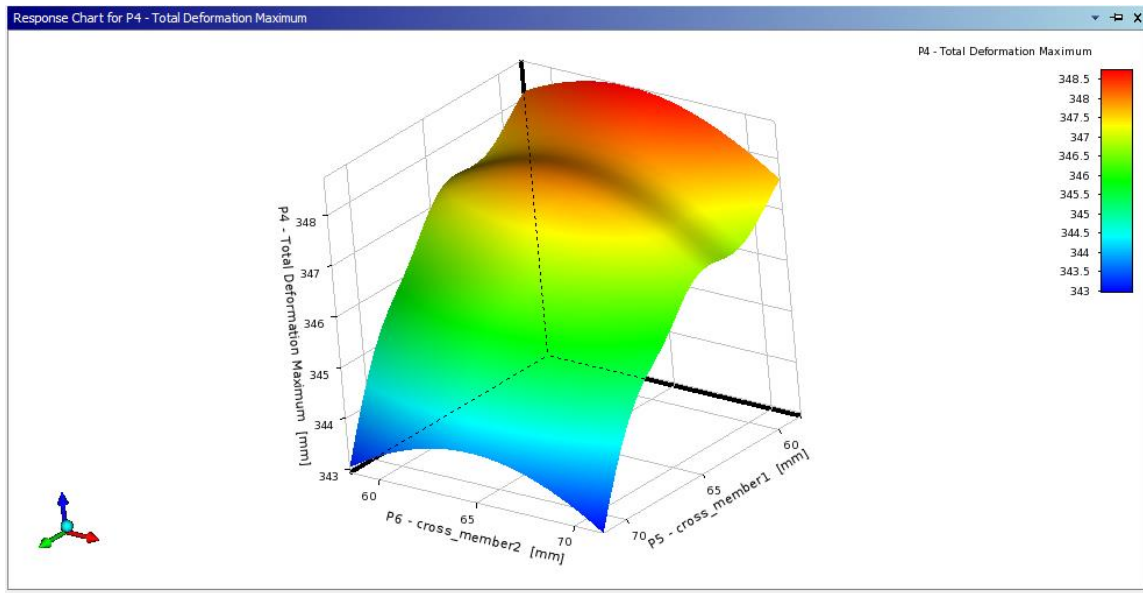
Figure 4.137: Response-Surface plot of total deformation for LHS using St52E material

The Response-Surface plot of total deformation is generated to determine maximum and minimum deformation values and corresponding dimensions of cross-member 2 and cross-member 1. The maximum deformation is obtained for cross-member 1 dimension varying from 559mm to 61mm and cross-member 2 dimensions varying from 59mm to 69mm as shown in figure 4.137.
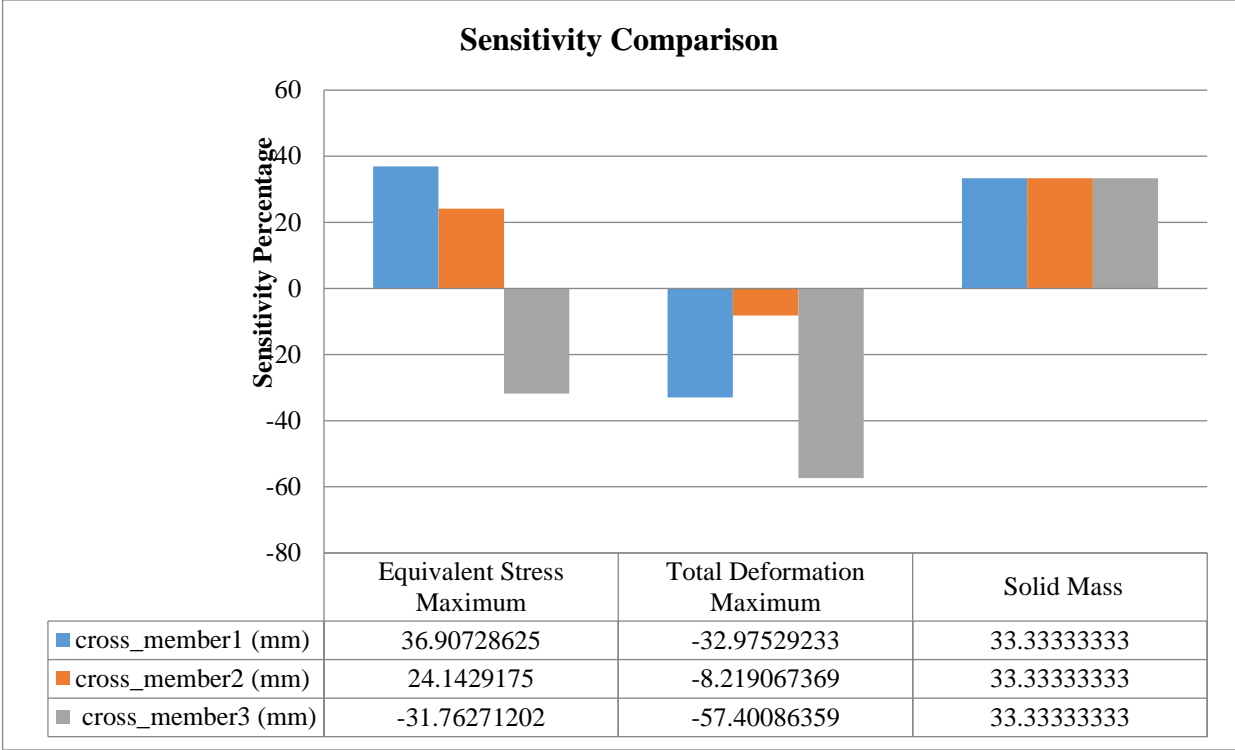
Figure 4.138: Sensitivity plot for LHS using St52E material

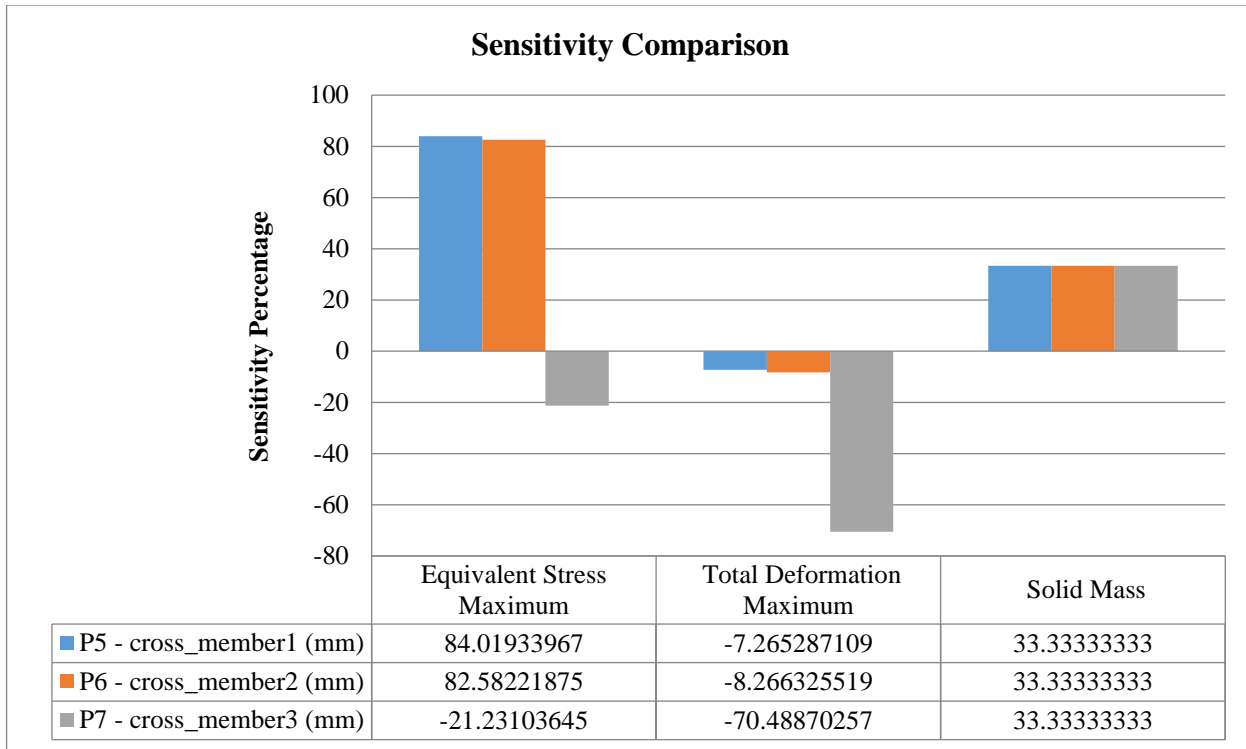Cross-member 1 has the highest sensitivity percentage for equivalent-stress, while cross-member 2 has the lowest, indicating that equivalent-stress has the greatest effect on cross-member 1, as shown in figure 4.138. Cross-member 3 has the highest sensitivity percentage for deformation, while cross-member 2 has the lowest, indicating that total deformation has the greatest effect on cross-member 3. Cross member2 and cross member3 dimensions, as well as cross member1 dimensions, have a similar sensitivity percentage of 33.33 for solid mass.

4.3.6 Sparse Grid Initialization (SGI) using St52E material

The design points are generated using a sparse grid initialization scheme (SGI). These design points are generated based on a linear regression model as shown in column B, column C, and column D in table 4.19. The software evaluated output parameters at these design points using Finite Element Analysis. These output parameters are equivalent-stress and total deformation as shown in column E and column F.

Table 4.19: DOE Table for sparse grid initialization using St52E material

A	B	C	D	E	F	G
Name	P5 - cross-member 1 (mm)	P6 - cross-member 2 (mm)	P7 - cross-member 3 (mm)	P3 - Equivalent-stress Max (MPa)	P4 - Total Deformation Maximum (mm)	P8 - Solid Mass (kg)
1	65	65	65	3280.49	347.45	214.64
2	58.5	65	65	3264.45	347.89	209.91
3	71.5	65	65	3520.14	347.13	219.37
4	65	58.5	65	3273.63	347.76	209.91
5	65	71.5	65	3527.46	347	219.37
6	65	65	58.5	3259.3	343.93	209.91
7	65	65	71.5	3220.32	340.78	219.37

Design point number 5 has the highest equivalent-stress, while design point number 7 has the lowest equivalent-stress. Cross-member 1 has a dimension of 65mm, cross-member 2 has a dimension of 71.5mm, and cross-member 3 has a dimension of 65mm.The maximum solid mass obtained through optimization is 219.37 kg at design point number 5, while the minimum solid mass obtained through analysis is 209.91 kg at design point number 2.The maximum deformation is observed for design point number 2 and minimum deformation is observed for design point number 7.
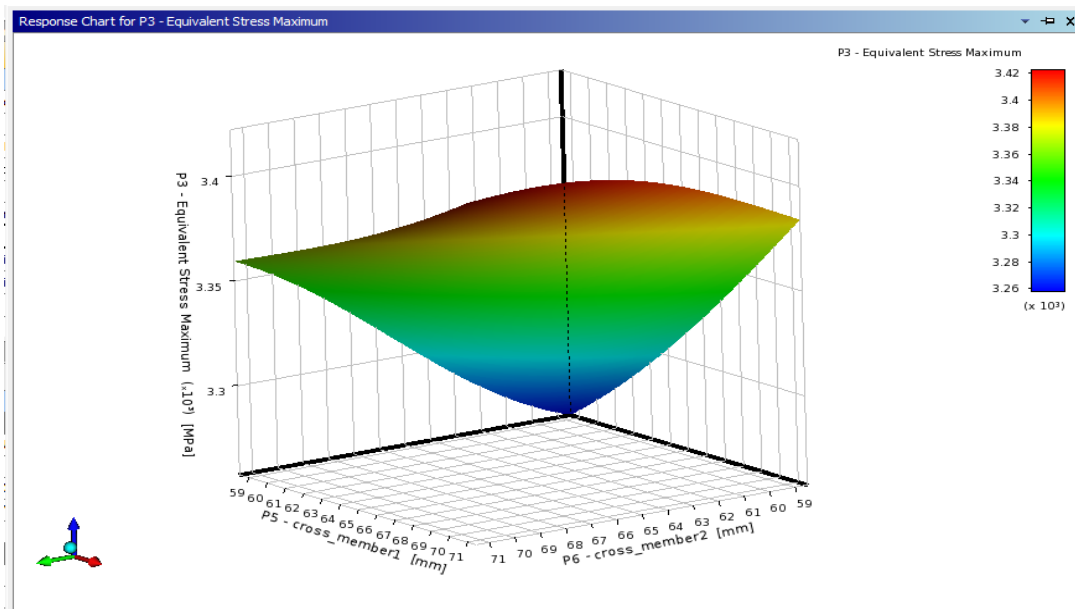
Figure 4.139: Response-Surface plot of equivalent-stress vs cross-member 1 and cross-member 2 for SGI using St52E material

Figure 4.1394 illustrates the Response-Surface plot of equivalent-stress vs cross-member 1 and cross-member 2. As shown in the red region, a single peak of equivalent-stress is observed.

Maximum equivalent-stress is observed for cross member1 with a length varying from 61mm to 71mm and cross member2 with a length varying from 59mm to 71mm. The equivalent-stress is lowest in the regions depicted in dark blue.
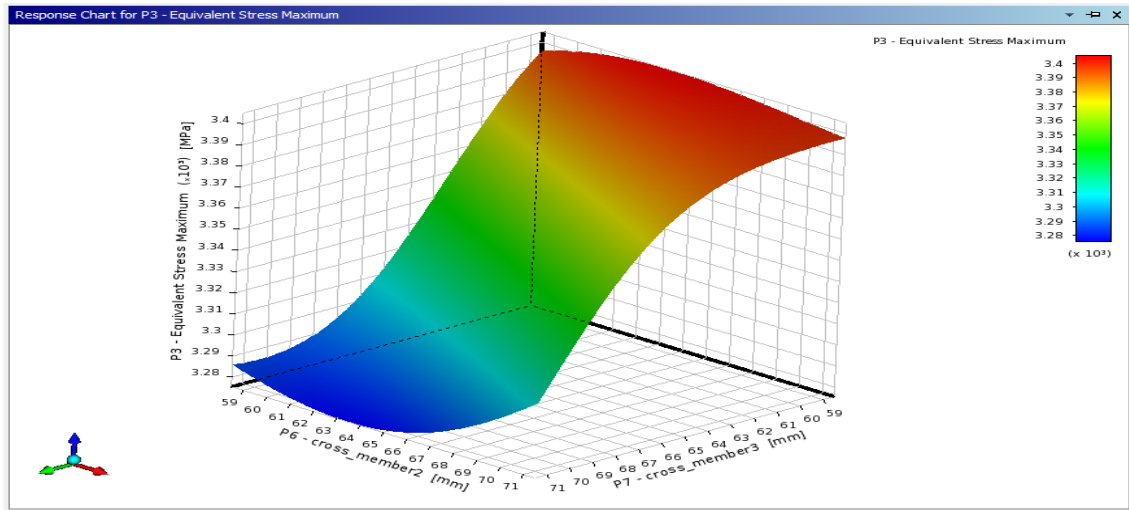
Figure 4.140: Response-Surface plot of equivalent-stress vs cross-member 2 and 3 for SGI using St52E material

The Response-Surface plot of equivalent-stress vs cross-member 2 and cross-member 3 dimensions is shown in figure 4.140. The maximum equivalent-stress is observed for cross-member 2 dimension varying from 59mm to 71mm and cross-member 3 dimension varying from 59mm to 66mm. The equivalent-stress is observed to be minimum for regions represented in dark blue color.
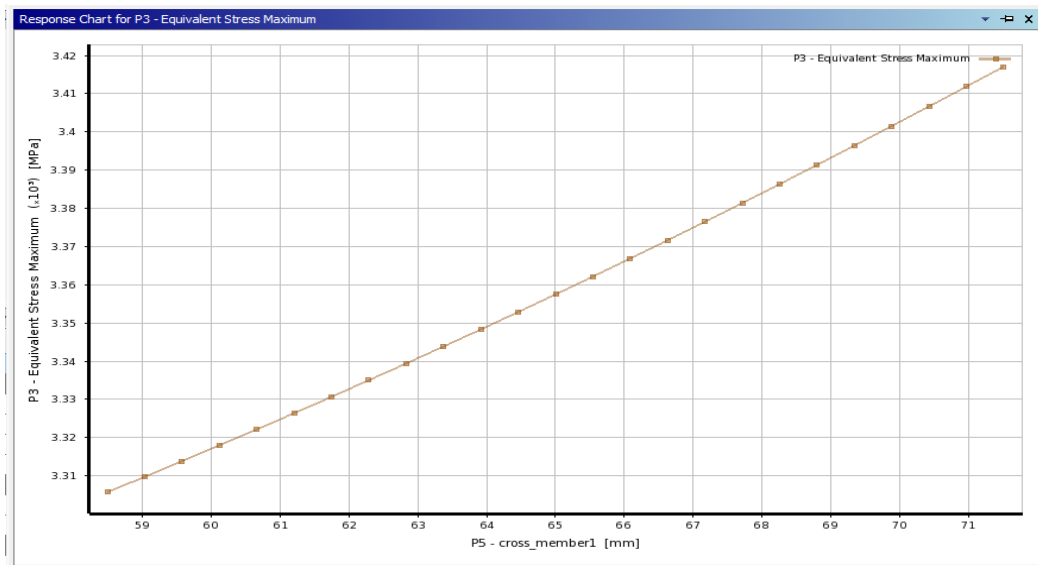
Figure 4.141: Equivalent-stress vs cross-member 1 for SGI using St52E material

The equivalent-stress increases linearly with an increase in cross-member 1 dimensions. The equivalent-stress initially minimum at cross-member 1 value of 58.5mm and then increases linearly to reach a maximum value at cross-member 1 value of 71.5mm as shown in figure 4.141.
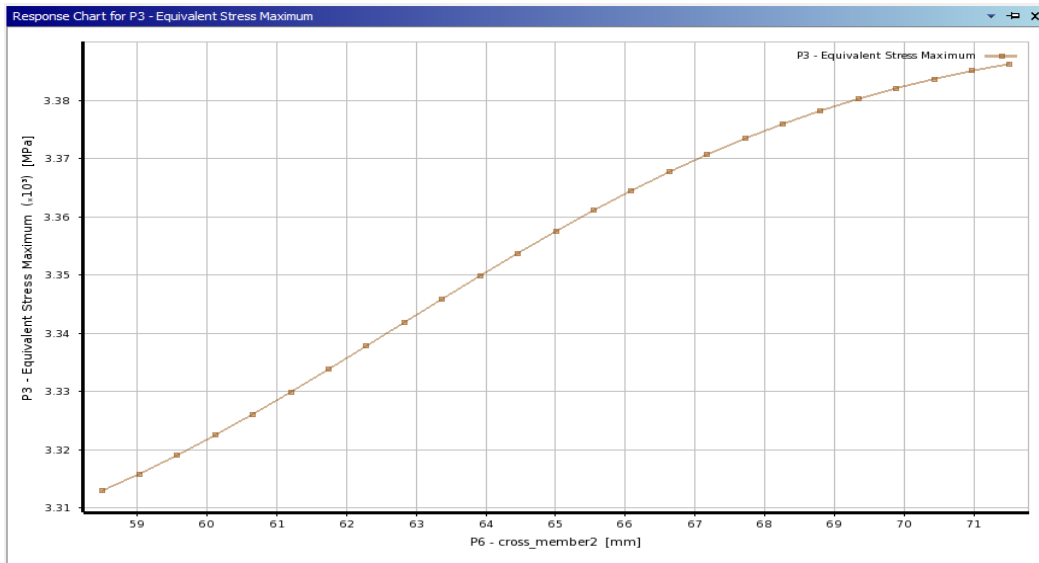
Figure 4.142: Equivalent-stress vs cross-member 2 for SGI using St52E material

The equivalent-stress increases with the increase on cross-member 2 dimension as shown in figure 4.142. The equivalent-stress is minimum for the cross-member 2 dimension of 58.5mm and then increases linearly and reaches the maximum value at the cross-member 2 dimension of 71.5mm.
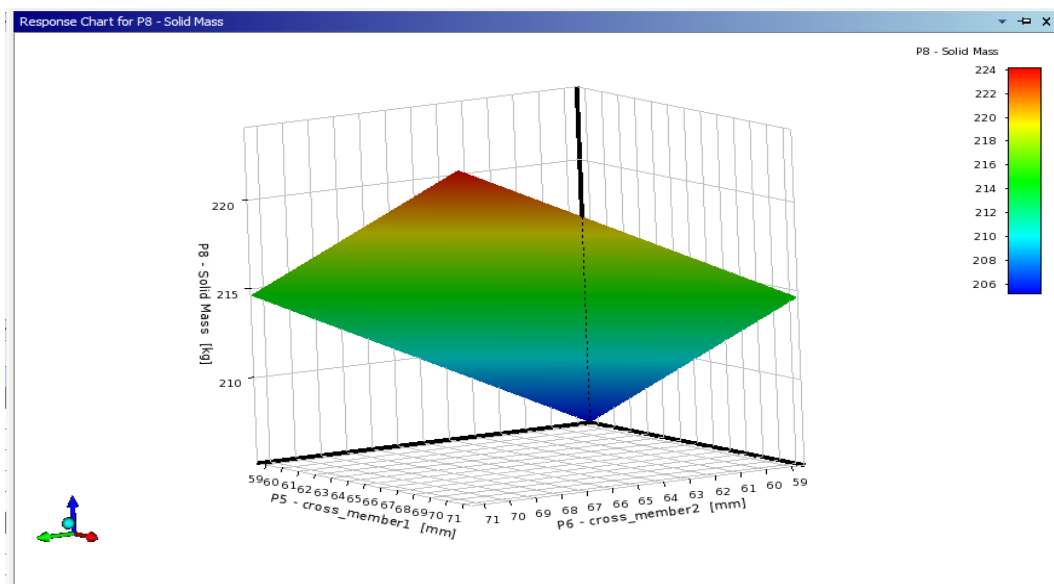
Figure 4.143: 3D Response-Surface plot of solid mass for SGI using St52E material

The variation of mass with respect to cross members 1 and 2dimensions is depicted in the Response-Surface plot depicted in figure 4.143. The maximum mass is depicted in the red region, while the

minimum mass is depicted in the blue region. Cross-member 1 dimensions vary from 67mm to 71mm and cross-member 2 dimensions varying from 67mm to 71mm have the highest mass.
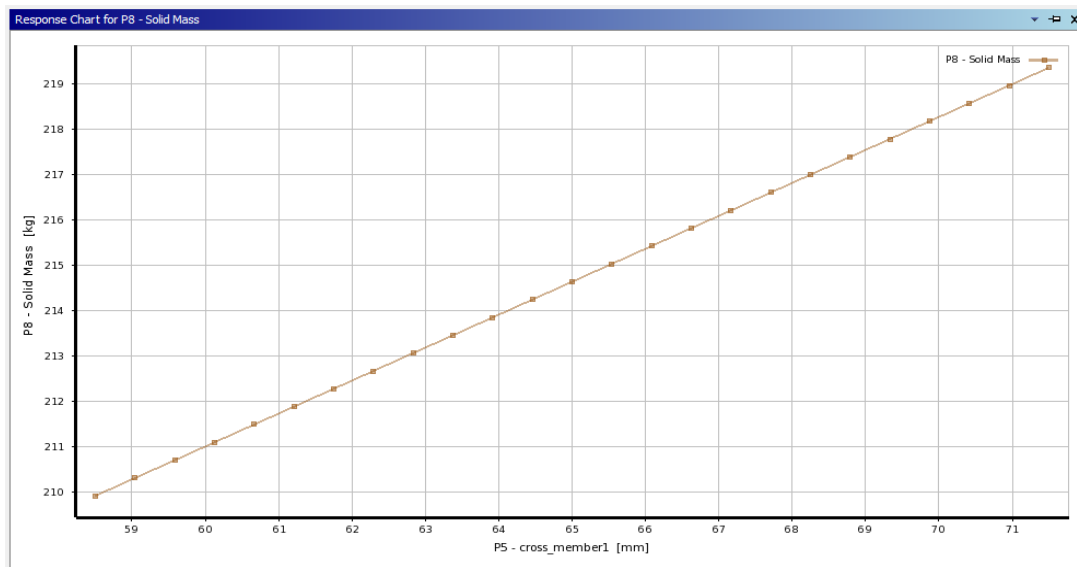
Figure 4.144: Solid mass vs cross-member 1 for SGI using St52E material

The 2D linear graph of solid mass vs cross-member 1 dimensions is shown in figure 4.144. The solid mass increases linearly with an increase in cross-member 1 dimensions. The minimum mass is observed for the cross-member 1 dimension of 58.5mm and reaches the maximum solid mass for the cross-member 1 dimension of 71.5mm.
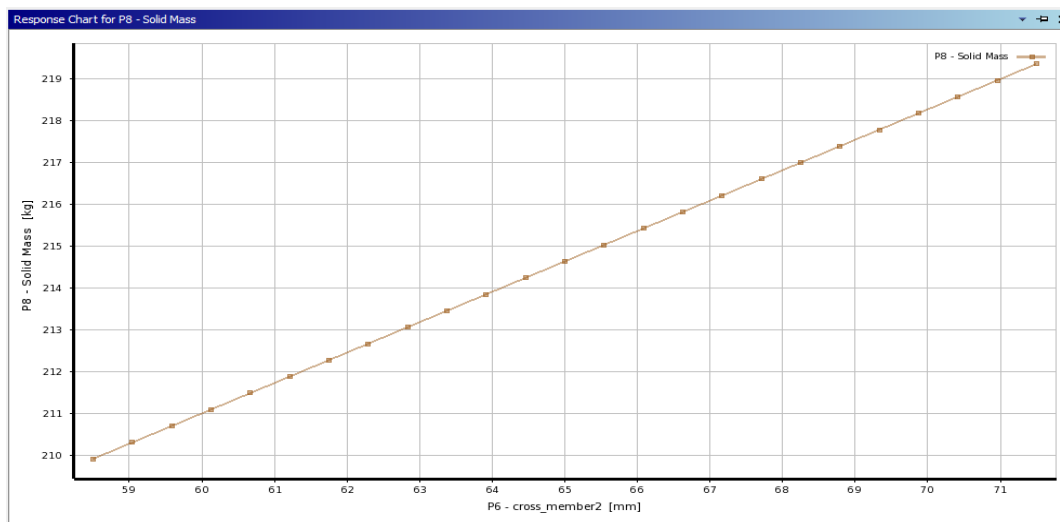
Figure 4.145: Solid mass vs cross-member 2 for SGI using St52E material

The variation of chassis mass with respect to cross-member 2 dimensions is shown in figure 4.145. The mass is minimum for the cross-member 2 dimension of 58.5mm and increases linearly to reach the maximum value at the cross-member 2 dimension of 71.5mm.
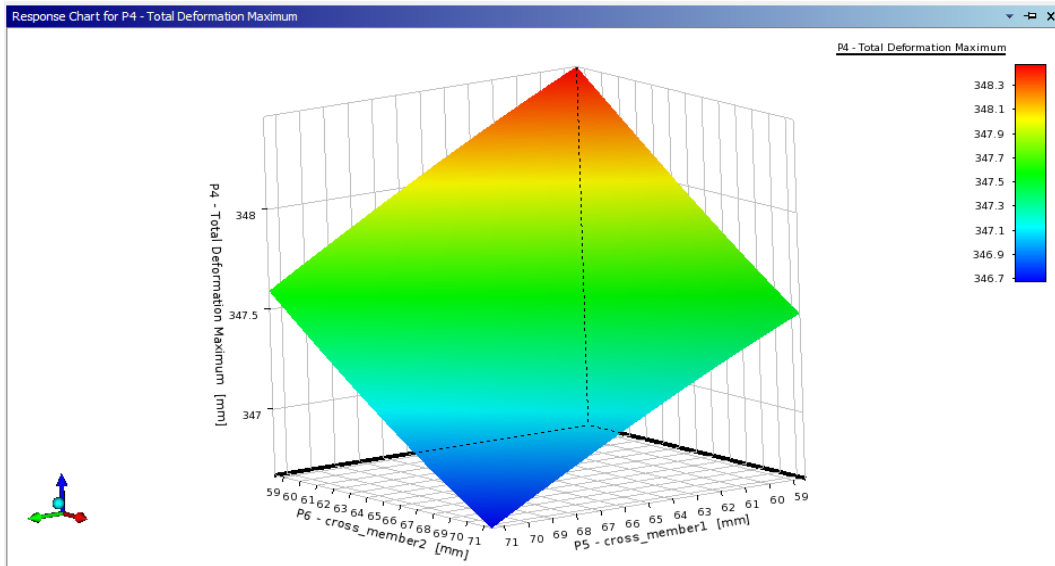
Figure 4.146: Response-Surface plot of total deformation for SGI using St52E material

The Response-Surface plot of total deformation in figure 4.146 is generated for the sparse grid initialization scheme. The maximum deformation is obtained for cross-member 1 dimension varying from 59mm to 64mm and cross-member 2 dimension varying from 59mm to 64mm.

	Equivalent Stress Maximum	Total Deformation Maximum	Solid Mass
cross_member1 (mm)	32.96573308	-7.797461233	33.41731252
cross_member2 (mm)	21.70518483	-8.492497294	33.41719473
cross_member3 (mm)	-37.96104035	-80.67555762	33.41749684
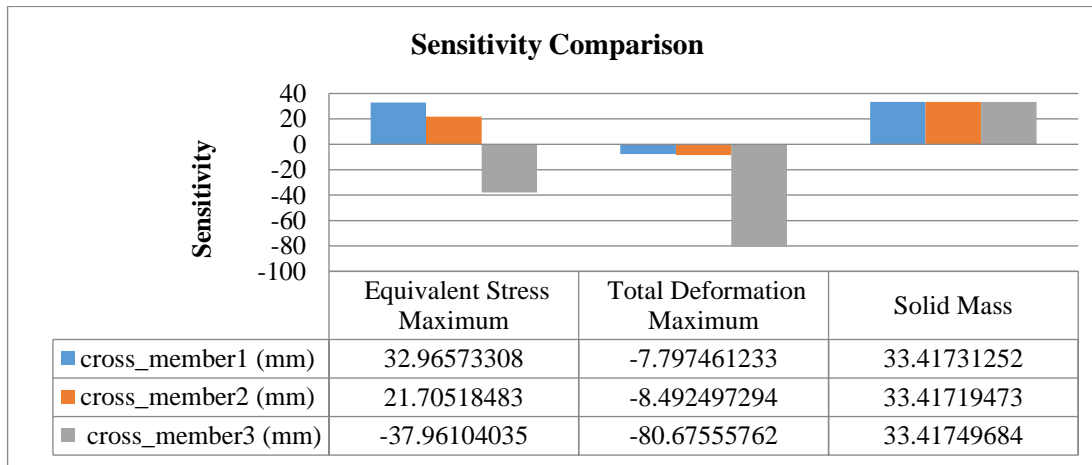
Figure 4.147: Sensitivity plot for SGI using St52E material

Cross-member 1 has the highest sensitivity percentage for equivalent-stress, whereas cross-member 2 has the lowest sensitivity percentage, showing that equivalent-stress has the biggest effect on cross-member 1, as seen in figure 4.147. Cross-member 3 has the highest deformation sensitivity %, whereas cross-member 1 has the lowest, implying that cross-member 3 has the most impact on overall deformation. The sensitivity percentage of the cross member2 and cross member3 dimensions, as well as the cross member1 dimension, is 33.33 for solid mass.

	A	B	C	D
1		P3 - Equivalent Stress Maximum	P4 - Total Deformation Maximum	P8 - Solid Mass
2	⊟ Coefficient of Determination (Best Value = 1)			
3	Learning Points	⭐ 1	⭐ 0.99814	⭐ 1
4	Cross-Validation on Learning Points	✗✗ 0	⭐⭐ 0.9734	⭐ 1
5	⊟ Root Mean Square Error (Best Value = 0)			
6	Learning Points	4.4692E-06	0.11849	2.4272E-13
7	Cross-Validation on Learning Points	127.01	0.44783	4.3927E-13
8	⊟ Relative Maximum Absolute Error (Best Value = 0%)			
9	Learning Points	⭐ 0	— 9.0951	⭐ 0
10	Cross-Validation on Learning Points	✗✗ 187.86	✗✗ 48.615	⭐ 2.0207E-11
11	⊟ Relative Average Absolute Error (Best Value = 0%)			
12	Learning Points	⭐ 0	⭐ 3.5391	⭐ 0
13	Cross-Validation on Learning Points	✗✗ 108.39	✗ 10.275	⭐ 5.4846E-12

Figure 4.148: Errors in optimization results

The maximum and minimum values obtained from optimization can be evaluated based on actual values (without errors) and observed values (with errors) as illustrated in figure 4.148. The statistical methods have error estimation techniques which include root mean square error, relative maximum absolute error, and relative average absolute error. Relative Absolute Error (RAE) is a way to measure the performance of a predictive model. It is expressed as a ratio, comparing a mean error (residual) to errors produced by a trivial or naive model.

Mathematically, the relative absolute error, E_i of an individual model i is evaluated by the equation:

$$E_i = \frac{\sum_{j=1}^{n} \left| P_{(ij)} - T_j \right|}{\sum_{j=1}^{n} \left| T_j - \overline{T} \right|}$$

where $P_{(ij)}$ is the value predicted by the individual model i for record j (out of n records); T_j is the target value for record j, and T bar is given by the formula:

$$\overline{T} = \frac{1}{n} \sum_{j=1}^{n} T_j$$

For a perfect fit, the numerator is equal to 0 and $Ei = 0$. So, the Ei index ranges from 0 to infinity, with 0 corresponding to the ideal. For the current research, the results are evaluated based on actual values.

4.3.7 Sub-Chapter Summary

The sub-Chapter has shown the application of optimization techniques in improving the design of chassis made of St52E material. The effect of optimization variables on equivalent-stress, deformation, and solid mass is discerned from 3D Response-Surface plots, 2D linearized plots, and sensitivity plots. The maximum solid mass obtained from optimization is 226.1 kg, and the minimum solid mass obtained from the analysis is 203.1 kg. The optimization results have shown that cross-member 3 has a maximum effect on chassis deformation compared to other variables which are the part of our key specific objectives as presented in section 1.4.

The next sub-chapter presents the investigation of the application of different optimization techniques using P100/6061 Al MMC material in line with the objectives & research hypothesis.

4.4 Response-Surface Optimization using P100/6061 Al MMC with Square section chassis

The current sub-chapter presents the application of different optimization techniques i.e., central composite design, optimal space-filling design, sparse grid initialization, Latin hypercube sampling, Box-Behnken design on heavy motor vehicle chassis made of P100/6061 Al MMC material. The effect of different design variables on equivalent-stress, deformation, and mass is evaluated using 3D Response-Surface plots and sensitivity plots.

4.4.1 Central Composite Design Scheme using P100/6061 Al MMC

Using Finite Element Analysis, the software analyzed the output parameters at these design points. As illustrated in columns E and F of Table 4.20, these output parameters are equivalent-stress and total deformation.

Table 4.20: DOE Table for CCD scheme using P100/6061 Al MMC

A	B	C	D	E	F	G
Name	P5 - cross-member 1 (mm)	P6 - cross-member 2 (mm)	P7 - cross-member 3 (mm)	P3 - Equivalent-stress Max (MPa)	P4 - Total Deformation Maximum (mm)	P8 - Solid Mass (kg)
1.00	65.00	65.00	65.00	3277.61	202.87	68.36
2.00	58.50	65.00	65.00	3261.58	203.12	66.85
3.00	71.50	65.00	65.00	3514.87	202.68	69.86
4.00	65.00	58.50	65.00	3270.74	203.05	66.85
5.00	65.00	71.50	65.00	3522.25	202.60	69.86
6.00	65.00	65.00	58.50	3256.64	200.83	66.85
7.00	65.00	65.00	71.50	3217.43	198.97	69.86
8.00	59.72	59.72	59.72	3344.10	199.70	64.69
9.00	70.28	59.72	59.72	3429.54	199.56	67.13
10.00	59.72	70.28	59.72	3435.59	199.44	67.13
11.00	70.28	70.28	59.72	3312.01	199.20	69.58
12.00	59.72	59.72	70.28	3461.23	199.80	67.13
13.00	70.28	59.72	70.28	3228.51	199.54	69.58
14.00	59.72	70.28	70.28	3291.50	199.51	69.58
15.00	70.28	70.28	70.28	3458.88	199.26	72.03

The maximum deformation is observed for design point number two (2) and minimum deformation is observed for design point number seven (7). The dimensions corresponding to design point number two (2) are as follows:

- 58.5 mm for cross-member 1, 65 mm for cross-member 2, and 65 mm for cross-member 3. The magnitude of maximum deformation obtained from the analysis is 203.12 mm and the magnitude of minimum deformation obtained from the analysis is 198.97 mm.

At design point number 15, the maximum solid mass acquired by optimization is 72.029 kg, while the minimum solid mass obtained through analysis is 64.685 kg at design point number 8. For all cross members, the dimensions corresponding to design point number 15 are 70.285.The Response-Surface plot can be used to determine the range of values for which equivalent-stress is maximum or least for optimization variables. Figure 4.149 shows a Response-Surface plot of equivalent-stress against cross-member 1 and cross-member 2.
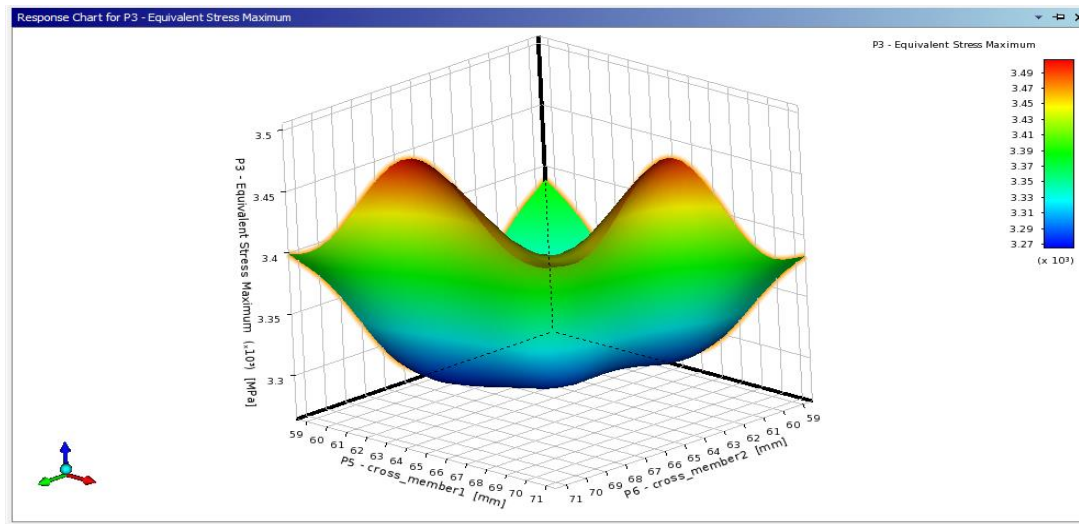
Fig 4.149: Response-Surface plot of equivalent-stress vs cross-member 1 and cross-member 2 for the CCD scheme using P100/6061 Al MMC

As illustrated in the red-coloured zone, there are two peaks of equivalent-stress. The equivalent-stress is highest for cross-member 1 dimensions varying from 62mm to 67mm and cross-member 2 dimensions varying from 69mm to 71mm, according to the first peak that formed along the cross-member 1 dimension. The equivalent-stress is highest for cross-member 1 dimensions varying from 69mm to 71mm and cross-member 2 dimensions varying from 61mm to 67mm, according to the second peak that formed along the cross-member 2 dimension. Other dimensions of cross-member 1 and cross-member 2 have the lowest equivalent-stress, as seen in the dark blue coloured region.
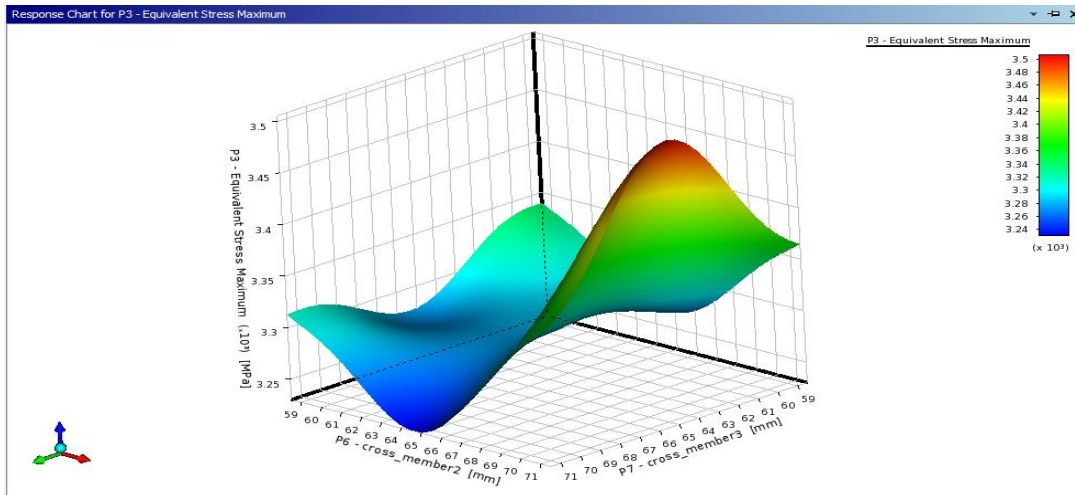
Fig 4.150: Response-Surface plot of equivalent-stress vs cross-member 2 and cross-member 3 for CCD using P100/6061 Al MMC

Figure 4.150 shows a Response-Surface plot of equivalent-stress versus cross-member 2 and cross-member 3 dimensions. As demonstrated in the red-coloured zone, there is a single peak of equivalent-stress. The interpolation approach is used to find the dimensions corresponding to maximal equivalent-stress. Cross-member 3 values varying from 61mm to 67mm and cross-member 2 values varying from 69mm to 71mm have the highest equivalent-stress. Other values of cross-member 2 and cross-member 3 which are represented by a dark blue coloured region have the lowest equivalent-stress.
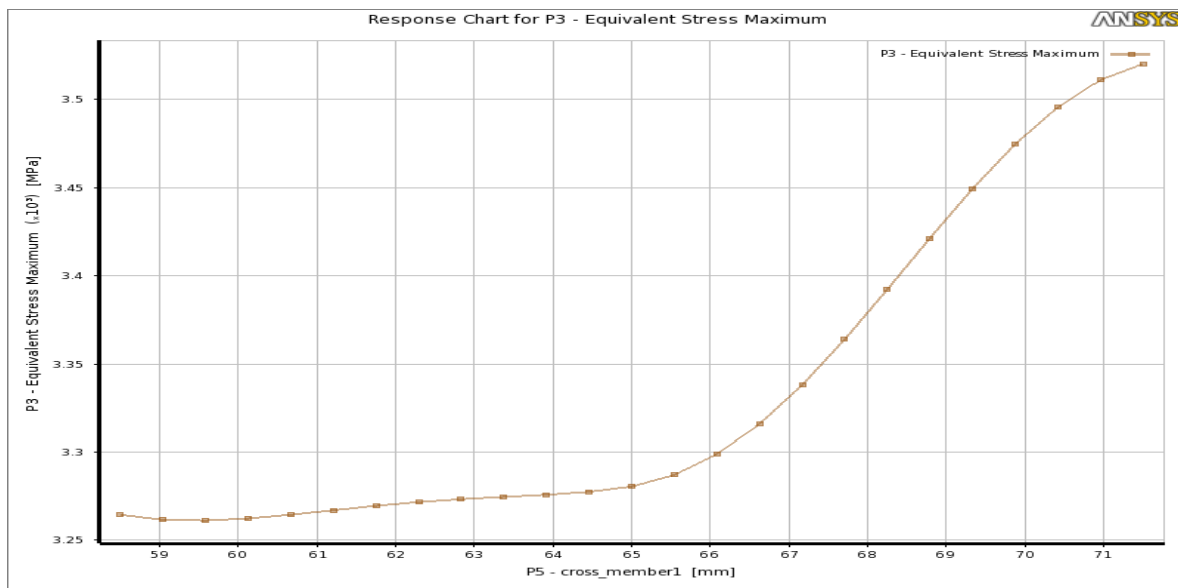
Fig 4.151: Equivalent-stress vs cross-member 1 for CCD using P100/6061 Al MMC

Figure 4.151 illustrates the variation of equivalent-stress with respect to cross-member 1 dimensions. The graph represents a progressive increase in equivalent-stress until it reaches the 65 mm value of

cross member 1. At a cross-member dimension of 71mm, the equivalent-stress increases exponentially to a maximum value of 3570 MPa.
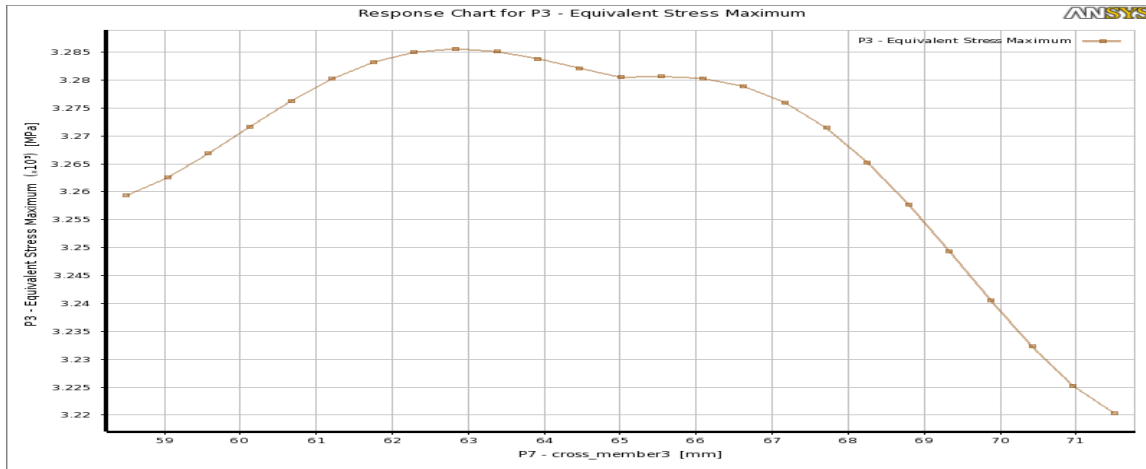
Fig 4.152: Equivalent-stress vs cross-member 3 for CCD using P100/6061 Al MMC

Figure 4.152 illustrates the variation of equivalent-stress with respect to cross-member 3. Up to 63mm cross-member 3 dimensions, the graph indicates a progressive increase in equivalent-stress, which then reduces linearly as cross-member 3 dimensions increase. With a cross-member 3 dimension of 71.5mm, the least equivalent-stress is recorded.
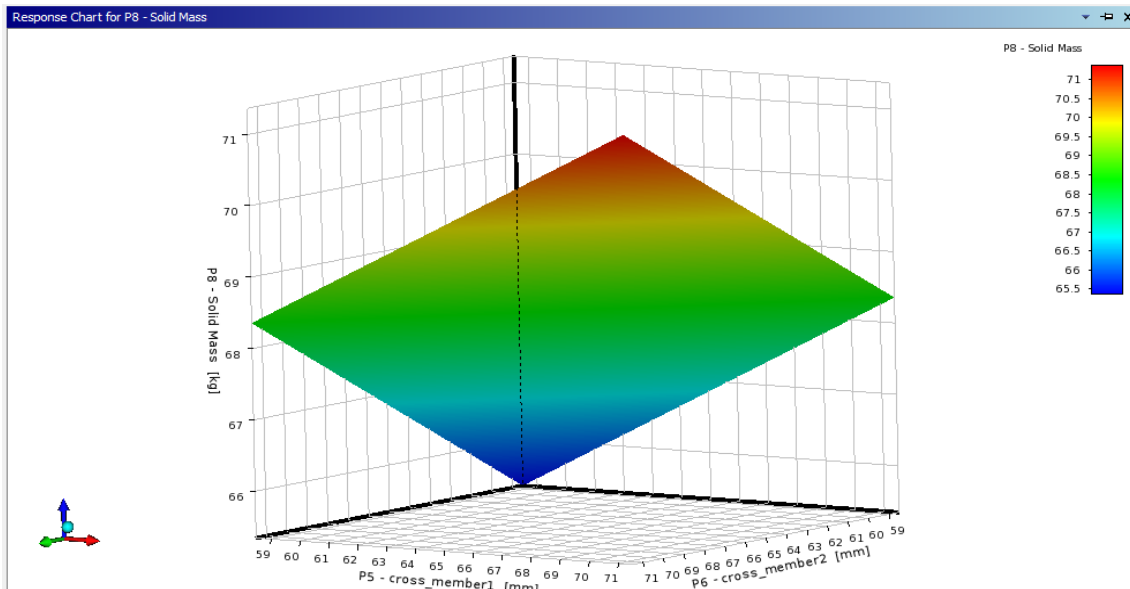
Fig 4.153: 3D Response-Surface plot of solid mass for CCD using P100/6061 Al MMC

The Response-Surface plot of figure 4.153 illustrates the fluctuation of mass with regard to cross-member 1 and cross-member 2. The red-coloured region represents the largest mass, while the blue-coloured region represents the least mass. Cross-member 1 dimensions vary from 68mm to 71mm

and cross-member 2 dimensions varying from 68mm to 71mm have the highest mass. Cross-member 1 and cross-member 3 dimensions varying from 58.5mm to 61mm have the lowest mass.
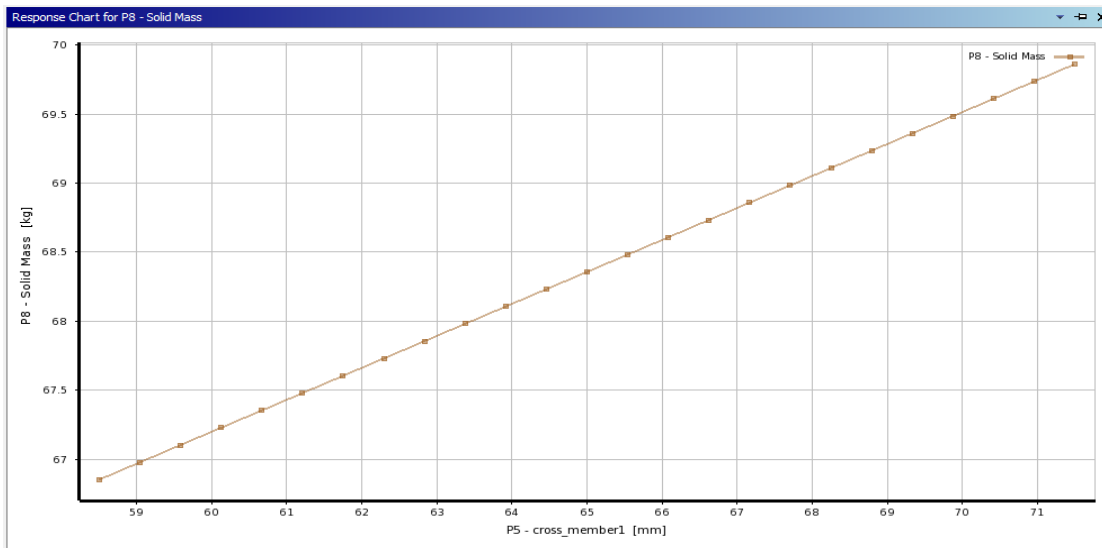
Fig 4.154: Solid mass vs cross-member 1 for CCD using P100/6061 Al MMC

Figures 4.154 and 4.155 depict the variation in chassis mass as a function of cross-member 1 and cross-member 3 dimensions. With increasing cross-member 1 and cross-member 3 dimensions, the solid mass appears to increase linearly. The cross-member 1 dimension of 58.5mm has the smallest mass of the chassis. The 58.5mm cross-member 3 and cross-member 1 dimensions have the lowest chassis mass.
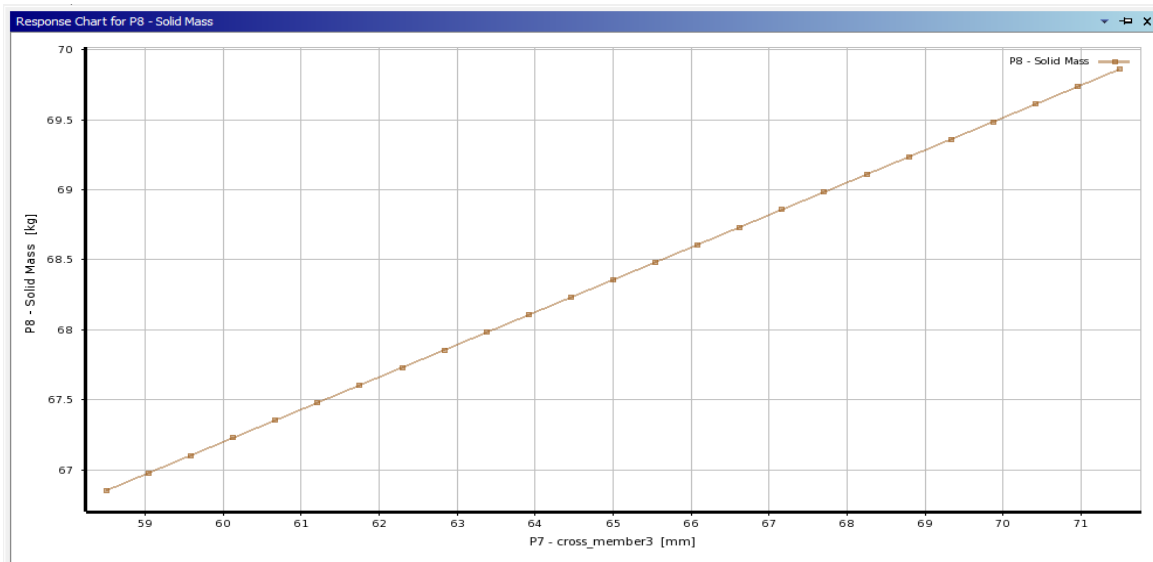
Fig 4.155: Solid mass vs cross-member 3 for CCD using P100/6061 Al MMC

Sensitivity Comparison

	P3 - Equivalent Stress Maximum	P4 - Total Deformation Maximum	P8 - Solid Mass
■ P5 - cross_member1 (mm)	76.9416042	-7.24402515	33.33333333
■ P6 - cross_member2 (mm)	75.85788054	-8.255243579	33.33333333
■ P7 - cross_member3 (mm)	-19.03350961	-70.49200478	33.33333333
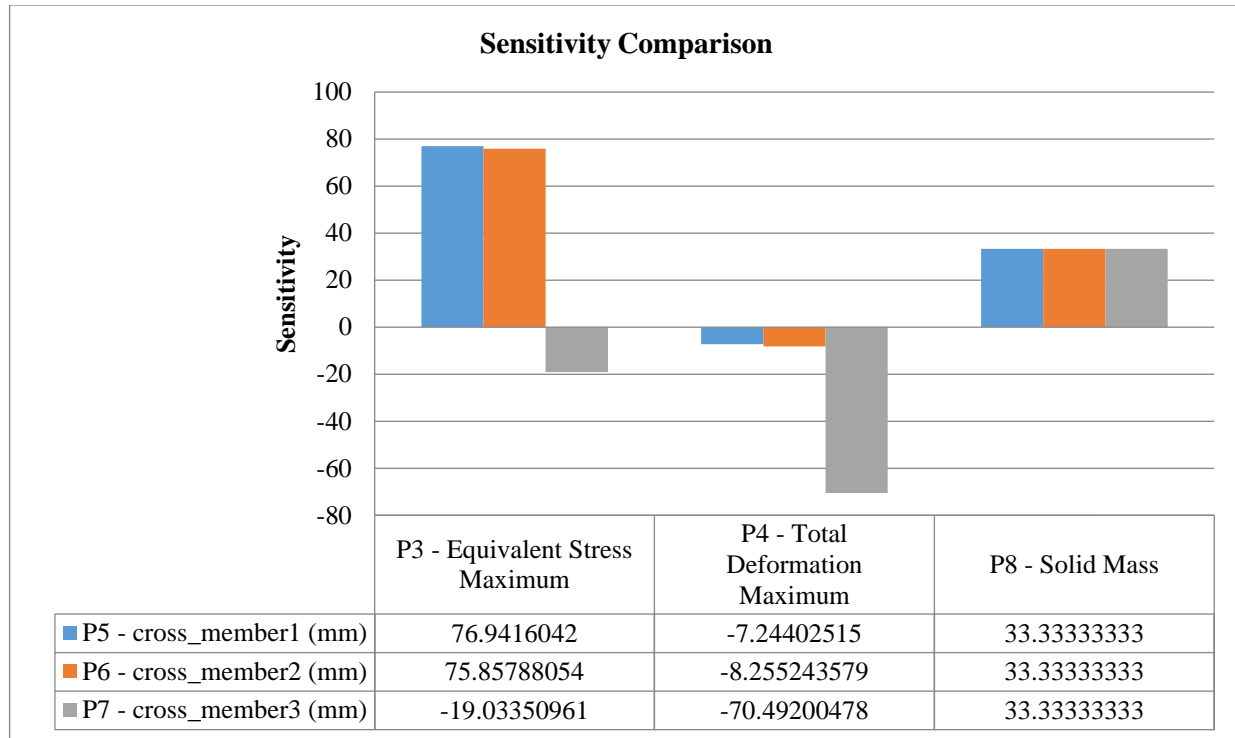
Fig 4.156: Sensitivity plot using CCD using P100/6061 Al MMC

Cross-member 1 has the highest sensitivity percentage for equivalent-stress (76.94%), and cross-member 3 has the lowest sensitivity percentage (19.034%), indicating that equivalent-stress has the greatest effect on cross-member 1 and the least effect on cross-member 3 as illustrated in figure 4.156. Cross-member 3 shows the maximum sensitivity percentage for deformation, while cross-member 1 shows the minimum sensitivity percentage. This means that cross-member 3 has the greatest influence on total deformation. For solid mass, all three variables have the same sensitivity percentage, indicating that all three optimization variables have the same effect on chassis mass.

4.4.2 Optimal Space Filling Design using P100/6061 Al MMC

The design points are generated using optimal space-filling (OSF) design as shown in table 4.21. Different combinations of cross-member 1, cross-member 2, and cross-member 3 dimensions are generated based on an optimal space-filling design scheme. The equivalent-stress, deformation, and solid mass are generated for each design point. The maximum and minimum values of these output parameters are shown in table 4.22.

Table 4.21: DOE Table for OSF design using P100/6061 Al MMC

A	B	C	D	E	F	G
Name	P5 - cross-member 1 (mm)	P6 - cross-member 2 (mm)	P7 - cross-member 3 (mm)	P3 - Equivalent-stress Max (MPa)	P4 - Total Deformation Maximum (mm)	P8 - Solid Mass (kg)
1.00	65.67	65.53	64.33	3265.16	203.20	68.48
2.00	64.73	65.67	64.20	3335.86	203.29	68.26
3.00	64.20	65.27	65.53	3332.14	202.54	68.36
4.00	65.53	64.20	65.40	3247.26	202.63	68.39
5.00	64.07	64.33	65.13	3467.14	202.79	68.02
6.00	65.93	64.73	64.73	3482.95	202.91	68.45
7.00	65.27	64.60	64.07	3463.09	203.36	68.11
8.00	65.80	65.13	65.67	3497.54	202.41	68.73
9.00	65.13	64.87	64.87	3344.83	202.87	68.33
10.00	65.00	65.40	65.93	3364.45	202.24	68.67
11.00	64.47	65.93	65.00	3222.14	202.84	68.45
12.00	64.33	65.00	64.47	3381.37	203.13	68.08
13.00	64.87	64.07	64.60	3346.09	203.15	68.02
14.00	65.40	65.80	65.27	3524.58	202.71	68.70
15.00	64.60	64.47	65.80	3460.50	202.30	68.33

Table 4.22: Maximum and minimum values for OSF design using P100/6061 Al MMC

1	A	B	C
	Name	Calculated Min	Calculated Max
2	P3 - Equivalent-stress Max (MPa)	3217.6	3524.6
3	P4 - Total Deformation Max (mm)	202.19	203.51
4	P8 - Solid Mass (kg)	67.662	69.052

The maximum equivalent-stress obtained through optimization is 3524.6 MPa, while the minimum equivalent-stress obtained through optimization is 3217.6 MPa. The maximum and minimum values of deformation and solid mass output vary less. The solid mass with structural steel is 214.64 kg, while the solid mass of steel with P100/6061 Al is 69.052 kg.

Figure 4.157 illustrates the Response-Surface plot of equivalent-stress, which shows two peaks in the red-coloured region.
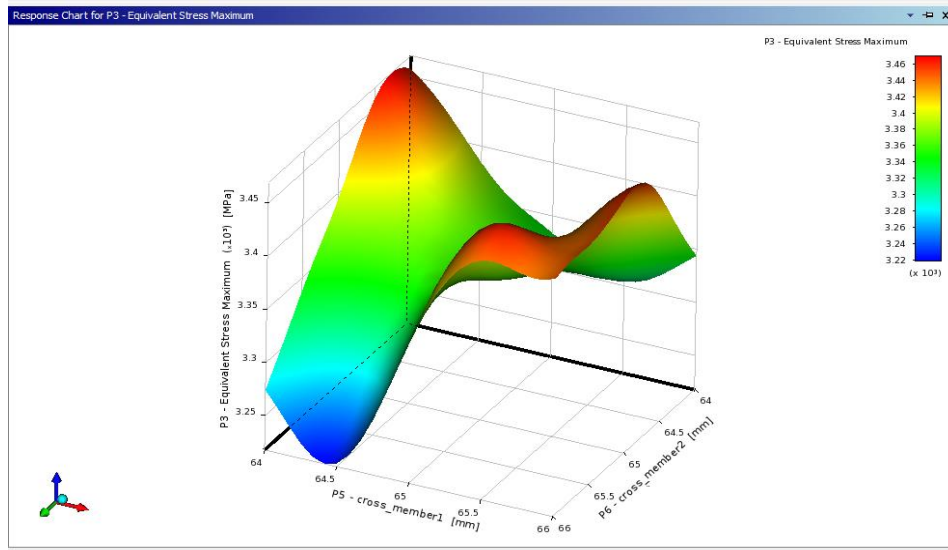
Figure 4.157: Response-Surface plot of equivalent-stress vs cross-member 1 and cross-member 2 for OSF design using P100/6061 Al MMC

The maximum equivalent-stress is obtained for cross-member 2 with a length varying from 64.5mm to 66mm and cross-member 1 with a length varying from 65mm to 66mm. The equivalent-stress is found to be lowest in regions represented by dark blue color.
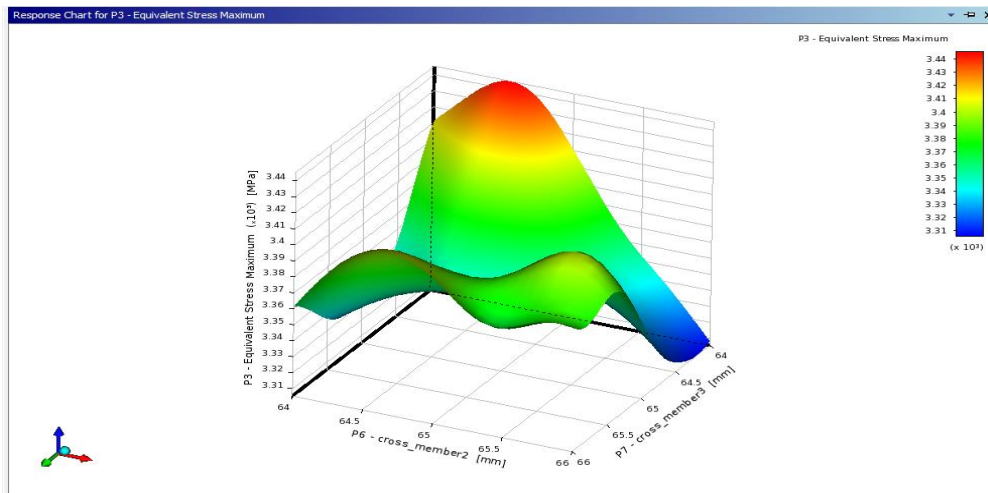
Figure 4.158: Response-Surface plot of equivalent-stress vs cross-member 2 and cross-member 3 for OSF design using P100/6061 Al MMC

Figure 4.158 illustrates the Response-Surface plot of equivalent-stress vs cross-member 2 and cross-member 3 dimensions. The plot illustrates the maximum equivalent-stress in the red region, where

the cross-member 2-dimension ranges from 64mm to 65mm and cross-member 1 ranges from 64.25mm to 64.5mm. The equivalent-stress is lowest in the region depicted in dark blue.
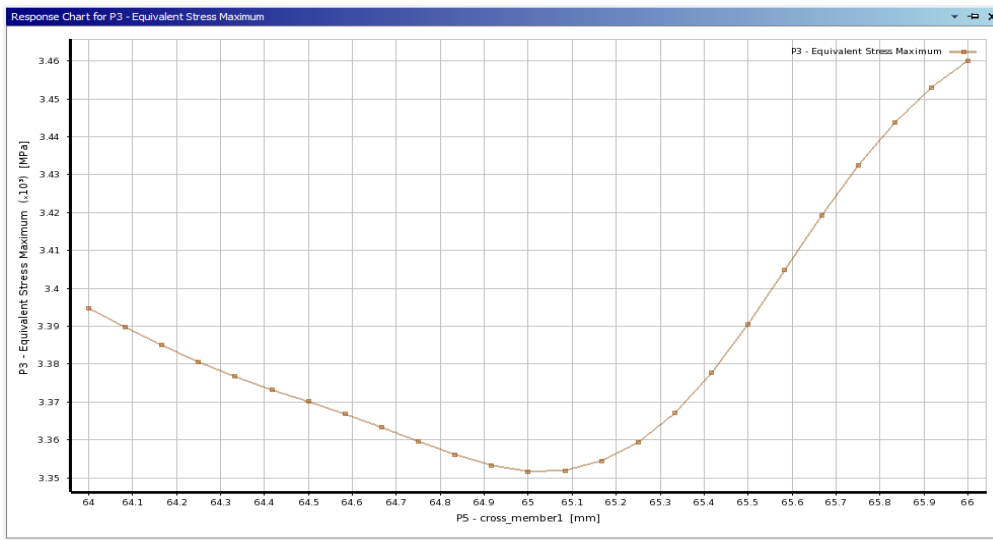
Figure 4.159: Equivalent-stress vs cross-member 1 for OSF design using P100/6061 Al MMC

The variation of equivalent-stress versus cross-member 1 dimensions is seen in Figure 4.159. The equivalent-stress initially drops, reaching a minimum value of 65mm at the cross member1 dimension, before growing linearly to a maximum value of 66mm at the cross member1 dimension.
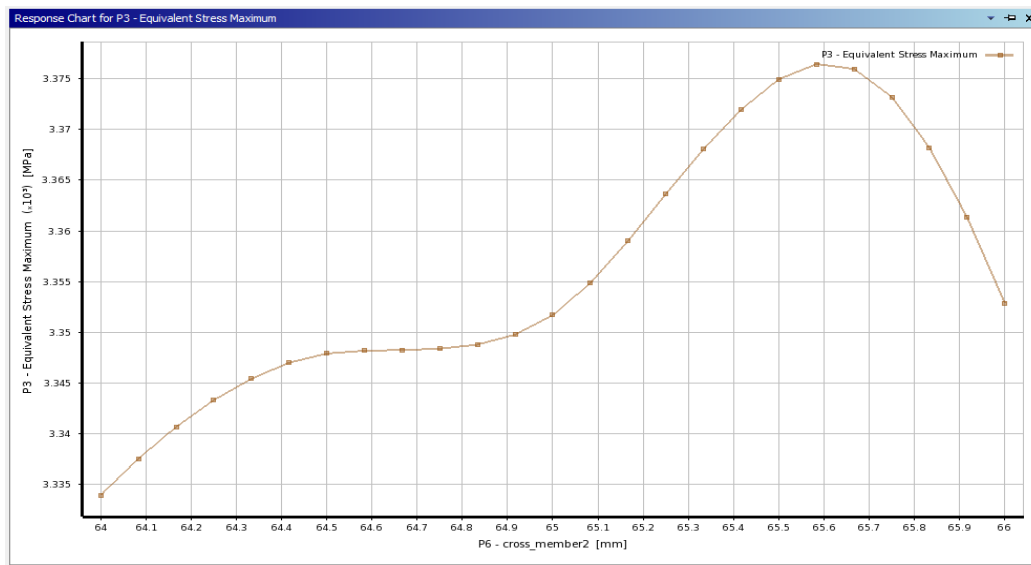
Figure 4.160: Equivalent-stress vs cross-member 2 for OSF design using P100/6061 Al MMC

Figure 4.160 illustrates the variance of equivalent-stress versus cross member 2 dimensions. The equivalent-stress grows until it reaches dimension value of 64.5mm, then plateaus until it reaches 65mm dimension value of cross member 2. The stress then gradually increases until it reaches a maximum dimension value of 65.6mm, after which it declines.
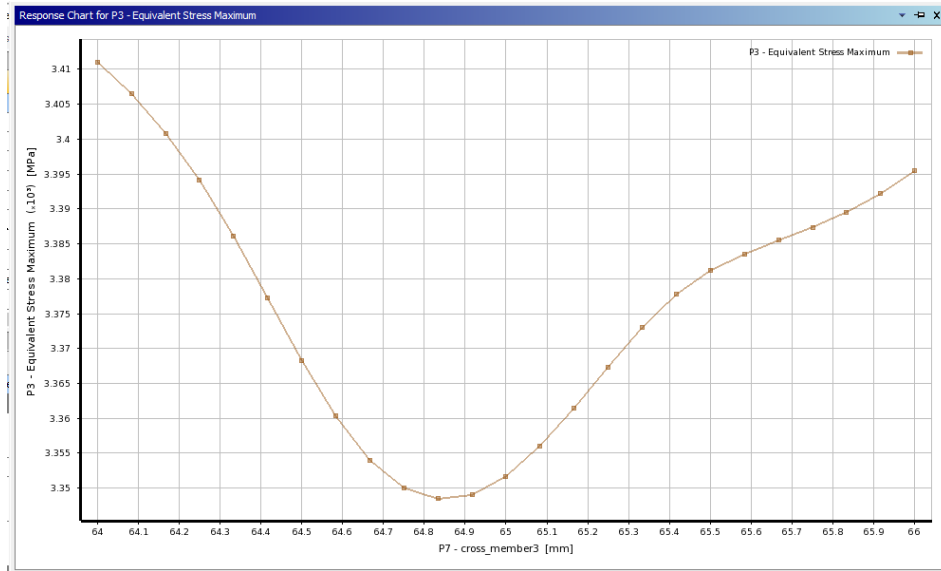
Figure 4.161: Equivalent-stress vs cross-member 3 for OSF design using P100/6061 Al MMC

Figure 4.161 illustrates the fluctuation of equivalent-stress vs cross member 3 dimensions. The equivalent-stress initially lowers and achieves a minimum value, at 64.8 mm dimension value of cross member 3. After that, the equivalent stress grows linearly until it reaches the value of 65 mm of cross member 3 dimensions.
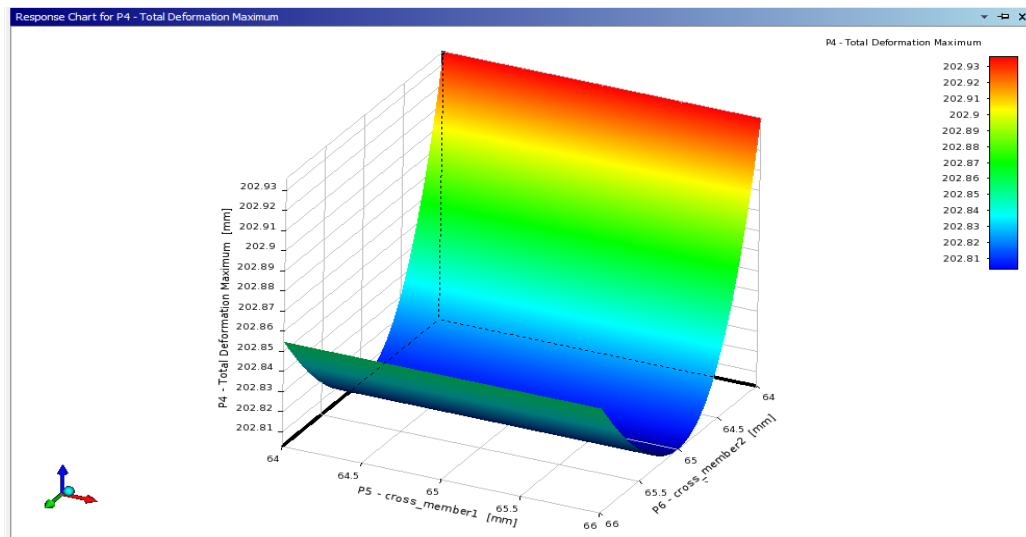
Figure 4.162: Response-Surface plot of total deformation vs cross-member 1 and cross-member 2 for OSF design using P100/6061 Al MMC

Figure 4.162 shows the Response-Surface plot of deformation cross-member 1 and cross-member 2 dimensions. Higher deformation is observed for cross member 2 dimension varies from 64.2 mm to 64.6 mm, while cross member 1 dimension varies from 64.3 mm to 65.2 mm, as shown in the graph. The deformation in other dimensions indicates a minimum value, which is represented by the blue-coloured zone.
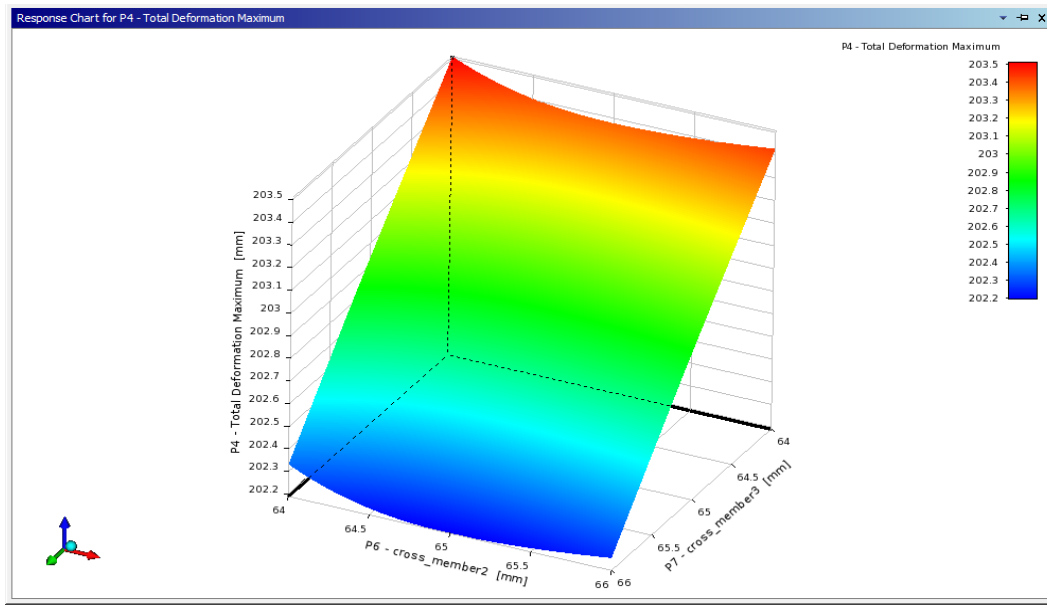
Figure 4.163: Response-Surface plot of total deformation vs cross-member 2 and cross-member 3 for OSF design using P100/6061 Al MMC

The variation of deformation vs cross-member 2 and cross-member 3 dimensions is presented in figure 4.163. The higher deformation is observed for cross-member 3 dimensions varying from 64 mm to 64.5mm and cross-member 2 dimensions varying from 64mm to 66mm.
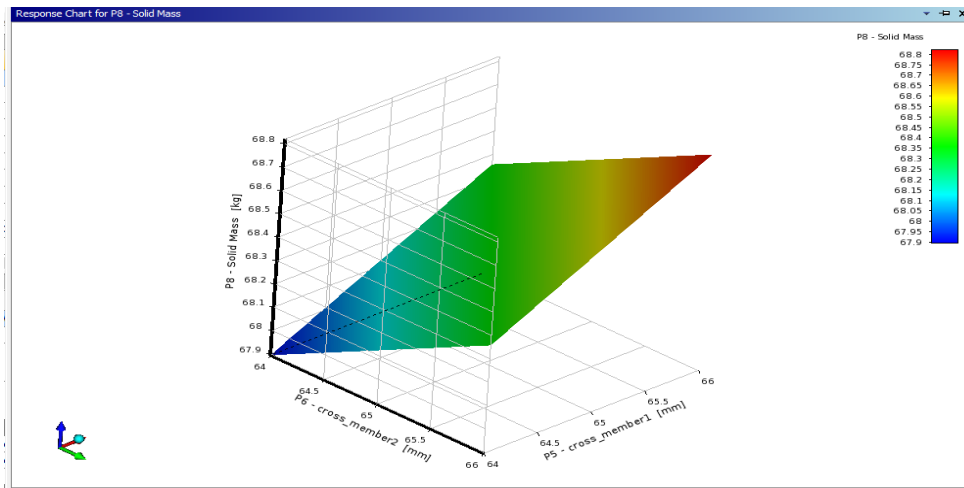
Figure 4.164: Response-Surface plot of mass vs cross-member 1 and cross-member 2 for OSF design using P100/6061 Al MMC

Figure 4.164 illustrates the variation in mass as a function of cross-member 1 and cross-member 2 dimensions. Maximum solid mass for cross-member 1 dimensions varying from 65mm to 66mm and cross-member 2 dimensions varying from 65mm to 66mm is shown in the graph. Cross-member 1 and cross-member 2 dimensions varying from 64mm to 65mm have the lowest mass.
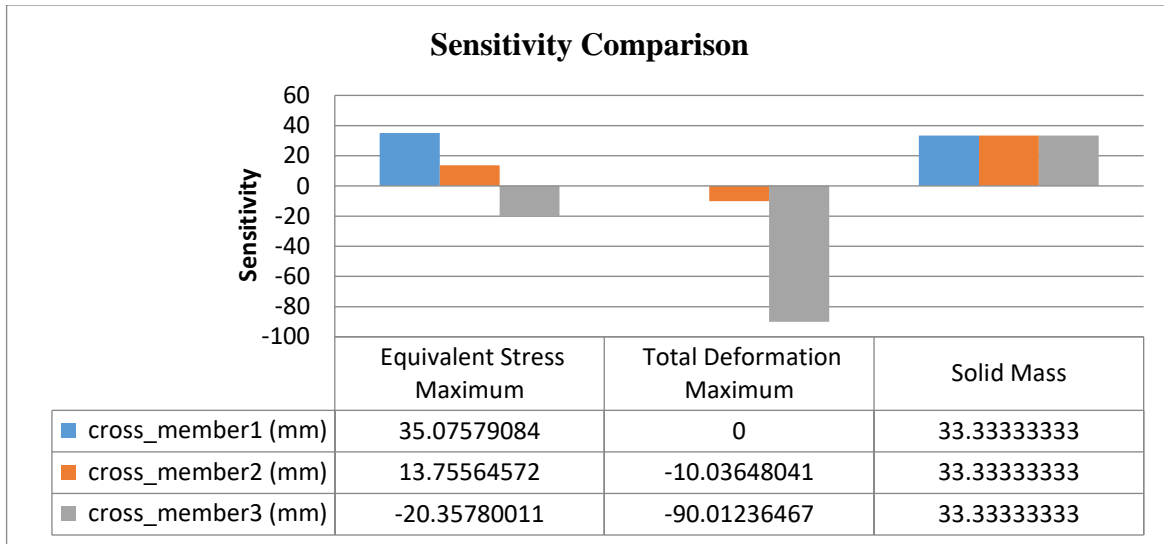
Figure 4.165: Sensitivity plot for OSF design using P100/6061 Al MMC

As illustrated in figure 4.165, the sensitivity map is constructed for all three output parameters: equivalent-stress, deformation, and solid mass. For equivalent-stress, cross-member 1 has the highest sensitivity %, indicating that equivalent-stress has the most effect on cross-member1 while the least effect on cross-member 2. The biggest sensitivity percentage for total deformation is shown by cross-member 3, indicating that total deformation has the greatest effect on cross-member 3. All three optimization variables have the same influence on the mass of the chassis when it comes to a solid mass.

4.4.3 Box Behnken (B-B) Scheme using P100/6061 Al MMC

The FE simulation is conducted on the chassis to determine stresses and deformation. The equivalent-stress plot is shown in figure 4.166. The stresses near the support are higher and are minimum in other zones. The maximum stress is generated on longitudinal members and is observed to be minimum for lateral members.
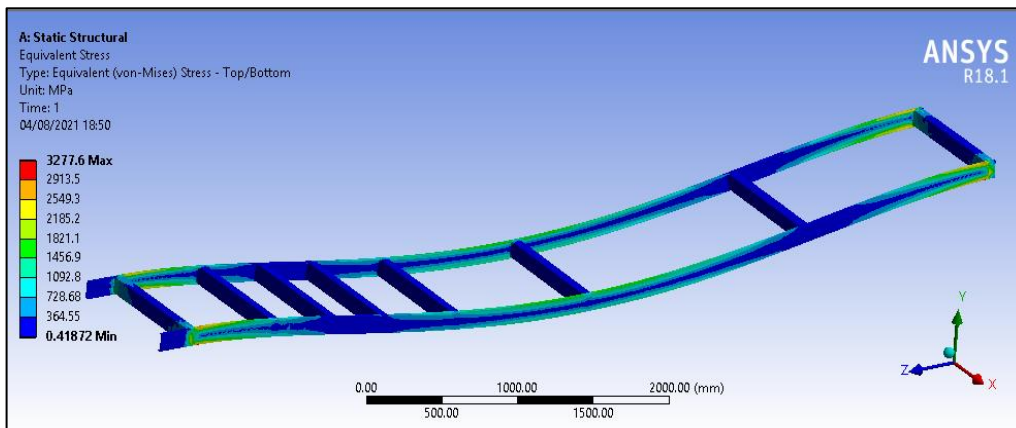
Figure 4.166: Equivalent-stress generated

Figure 4.167 illustrates the deformation resulting from the analysis. The most distortion is seen in the center of the chassis, and it decreases as you move closer to the fixed support of the chassis ends.
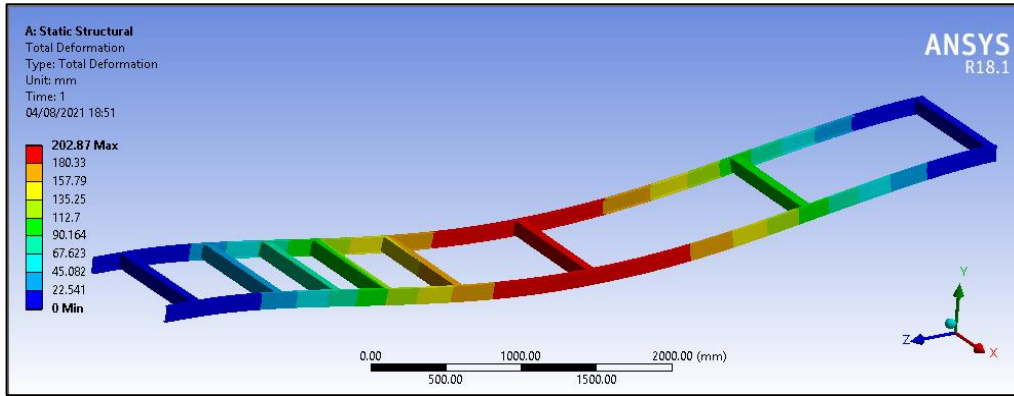
Figure 4.167: Total deformation plot

The maximum deformation measured at the cassis's center is 202.8mm. After that, a space-filling design technique is used to optimize the chassis design. As indicated in Table 4.23, the design points are developed utilizing the Box Behnken design approach. The Box Behnken technique is used to construct various combinations of cross-member 1, cross-member 2, and cross-member 3 dimensions. As shown in the diagram, equivalent-stress, deformation, and solid mass are calculated for each design point. Table 4.24 shows the maximum and minimum values of various output parameters.

Table 4.23: DOE Table for Box Behnken Scheme using P100/6061 Al MMC

A	B	C	D	E	F	G
Name	P5 - cross-member 1 (mm)	P6 - cross-member 2 (mm)	P7 - cross-member 3 (mm)	P3 - Equivalent-stress Max (MPa)	P4 - Total Deformation Maximum (mm)	P8 - Solid Mass (kg)
1.00	65.50	65.50	65.50	3270.48	202.47	68.70
2.00	63.00	63.00	65.50	3499.41	202.68	67.55
3.00	68.00	63.00	65.50	3472.20	202.53	68.70
4.00	63.00	68.00	65.50	3464.30	202.44	68.70
5.00	68.00	68.00	65.50	3473.26	202.31	69.86
6.00	63.00	65.50	63.00	3275.90	204.14	67.55
7.00	68.00	65.50	63.00	3490.20	203.89	68.70
8.00	63.00	65.50	68.00	3451.13	201.36	68.70
9.00	68.00	65.50	68.00	3512.72	201.28	69.86
10.00	65.50	63.00	63.00	3517.04	204.11	67.55
11.00	65.50	68.00	63.00	3359.96	203.97	68.70
12.00	65.50	63.00	68.00	3502.71	201.40	68.70
13.00	65.50	68.00	68.00	3353.10	201.23	69.86

Table 4.24: Maximum and minimum values for Box Behnken Scheme using P100/6061 Al MMC

1	A	B	C
	Name	**Calculated Min**	**Calculated Max**
2	P3 - Equivalent-stress Max (MPa)	3270.5	3517
3	P4 - Total Deformation Max (mm)	201.22	204.21
4	P8 - Solid Mass (kg)	66.967	70.442

The highest equivalent-stress attained by optimization is 3517 MPa, with the lowest equivalent-stress of 3270.5 MPa. Between maximum and minimum values, deformation and solid mass output show minimal variance. The mass of a chassis made of structural steel is 214.64 kilograms (Sub-section 4.3.2.2), while the mass of a chassis made of P100/6061 aluminium is 66.967 kilograms.
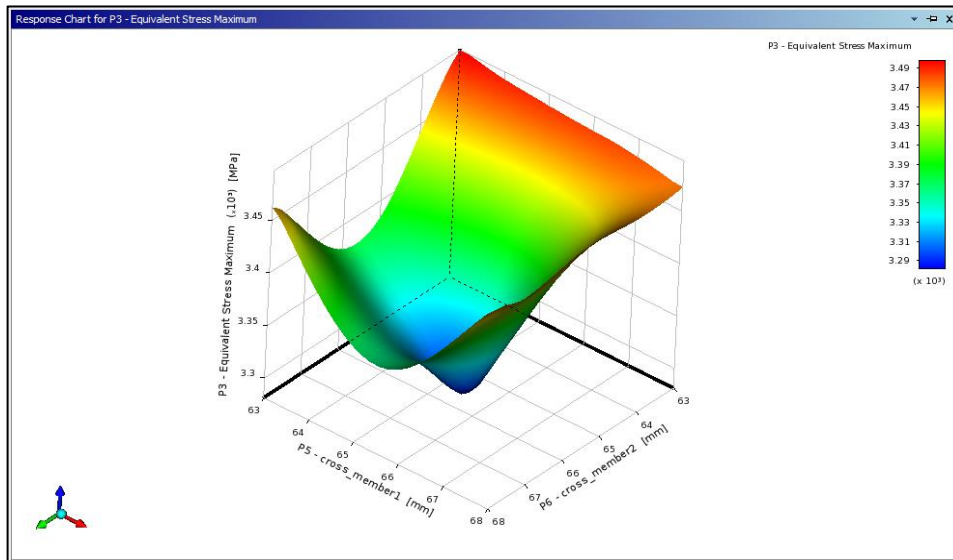
Figure 4.168: Response-Surface plot of equivalent-stress vs cross-member 1 and cross-member 2 for B-B Scheme using P100/6061 Al MMC

Figure 4.168 illustrates the Response-Surface plot of equivalent-stress, which reveals two peaks in the red-coloured region. Higher equivalent-stress is observed with cross-member 2-dimensions varies from 63mm to 64mm, and cross-member 1 dimensions vary from 63mm to 68mm. For places indicated in dark blue color, the equivalent-stress is found to be the lowest.
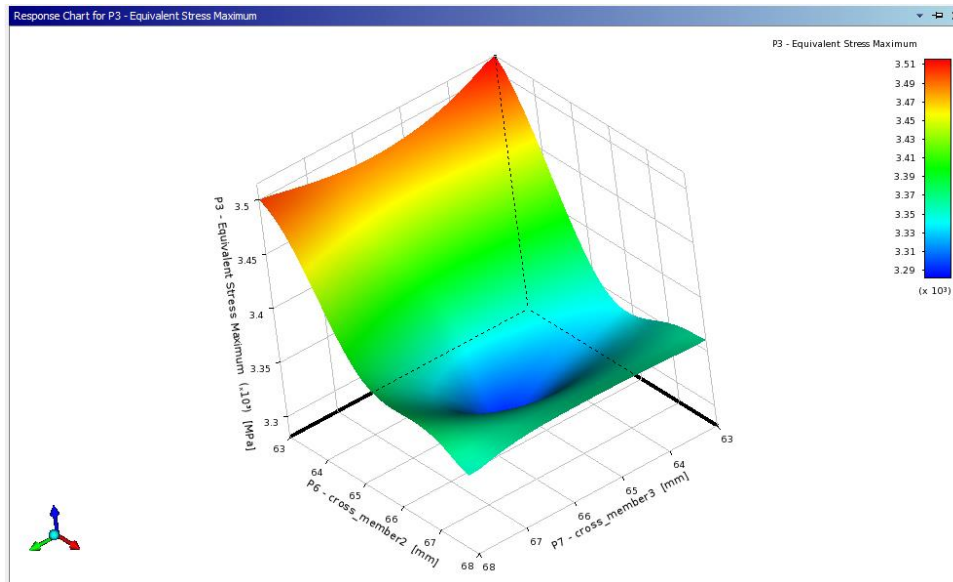
Figure 4.169: Response-Surface plot of equivalent-stress vs cross-member 2 and cross-member 3 for B-B Scheme using P100/6061 Al MMC

Figure 4.169 shows a Response-Surface plot of equivalent-stress vs cross-member 2 and cross-member 3 dimensions. The graph illustrates higher equivalent-stress in the red-coloured zone, with cross-member 2-dimensions varying from 63mm to 63.5mm and cross-member 3-dimensions varying from 63mm to 68mm. For the region depicted in dark blue, the equivalent-stress is at its lowest.
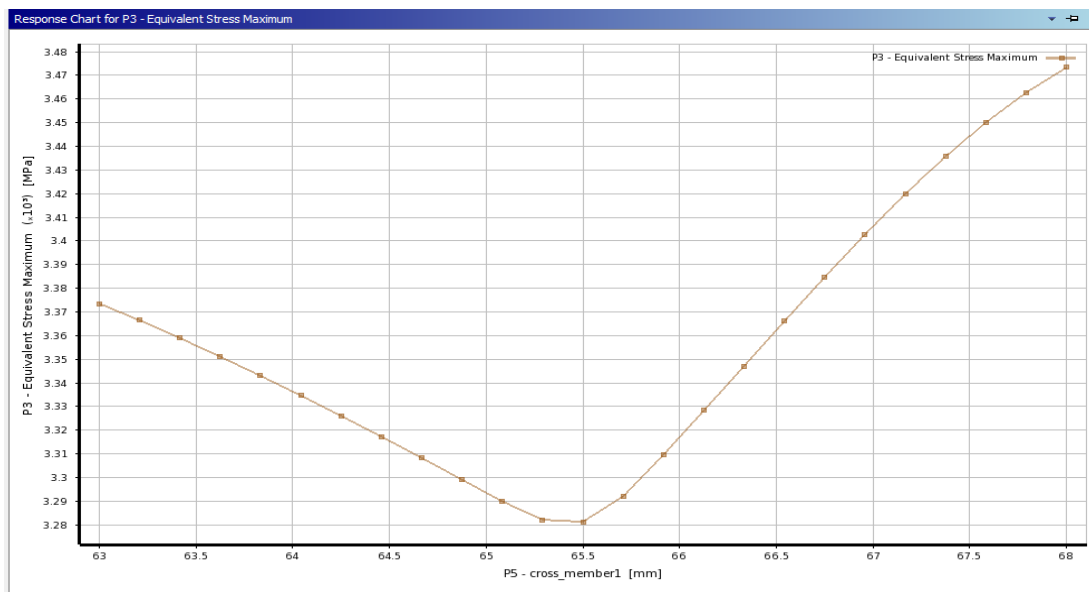
Figure 4.170: Equivalent-stress vs cross-member 1 for B-B Scheme using P100/6061 Al MMC

Figure 4.170 illustrates the variation of equivalent-stress vs cross member 1 dimensions. The equivalent-stress decreases initially and reaches a minimum value at the cross-member 1 dimension

of 65.5mm before increasing linearly and reaching a maximum value at the cross-member 1 dimension of 68mm.
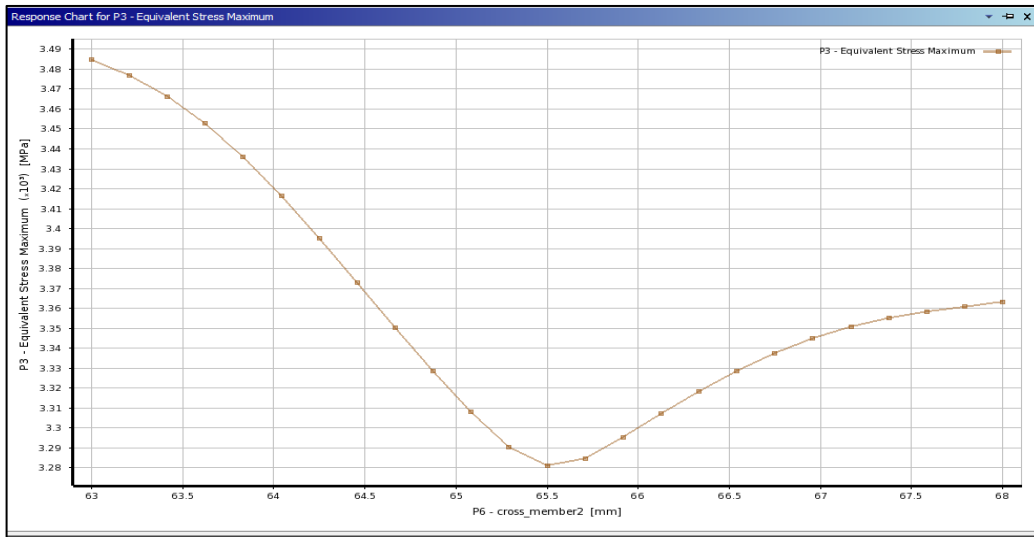
Figure 4.171: Equivalent-stress vs cross-member 2 for B-B Scheme using P100/6061 Al MMC

Figure 4.171 represents the variation of equivalent-stress vs cross member 2 dimensions. The equivalent-stress initially decreases up to cross member 2 dimensions value of 65.5mm before increasing parabolically to a maximum of 68mm.
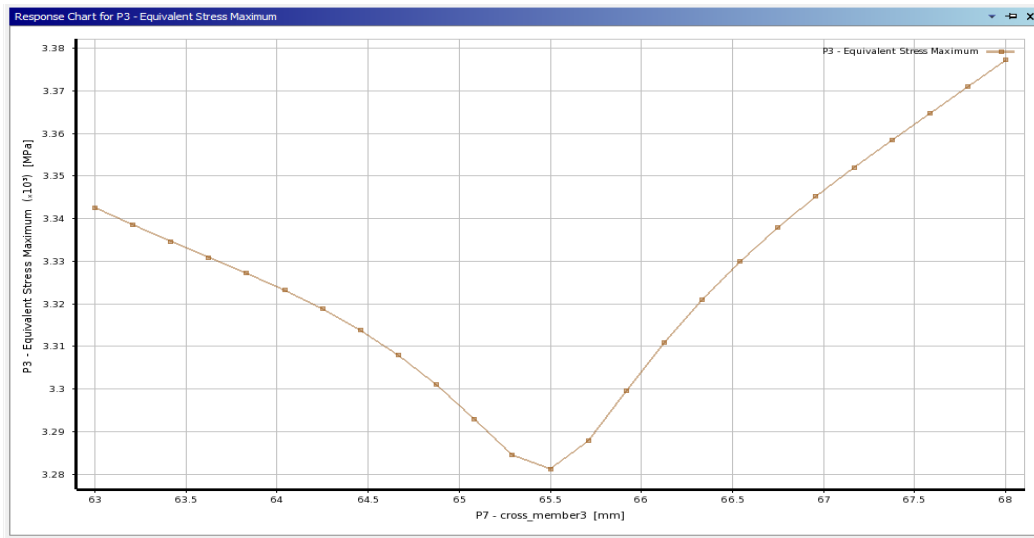
Figure 4.172: Equivalent-stress vs cross-member 3 for B-B Scheme using P100/6061 Al MMC

Figure 4.172 illustrates the fluctuation of equivalent-stress vs cross-member 3. The high equivalent-stress initially declines and achieves a minimum value of cross-member 3 dimensions i.e., 65.5mm. After then, the equivalent-stress rises linearly to a maximum value of cross-member 3 dimensions i.e., 68mm.
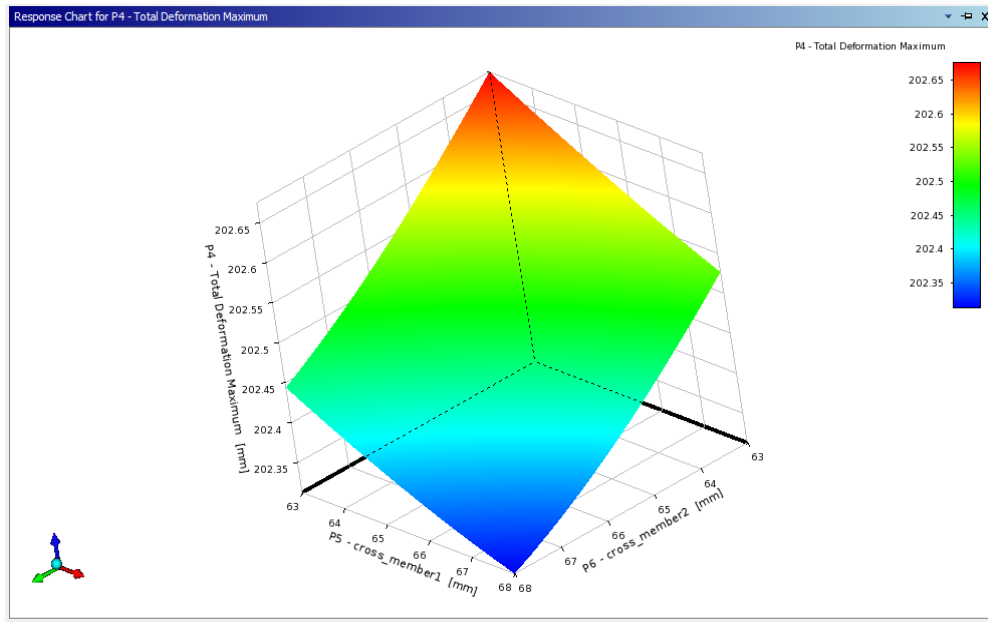
Figure 4.173: Response-Surface plot of total deformation vs cross-member 1 and cross-member 2
for B-B Scheme using P100/6061 Al MMC

Figure 4.173 shows the Response-Surface plot of deformation cross-member 1 and cross-member 2
dimensions. Maximum deformation is shown for cross-member 2 dimensions varying from 63mm to
63.5mm, as well as cross-member 1 dimensions varying from 63mm to 63.5mm. The deformation in
other dimensions indicates a minimum value, which is represented by the blue-coloured zone.
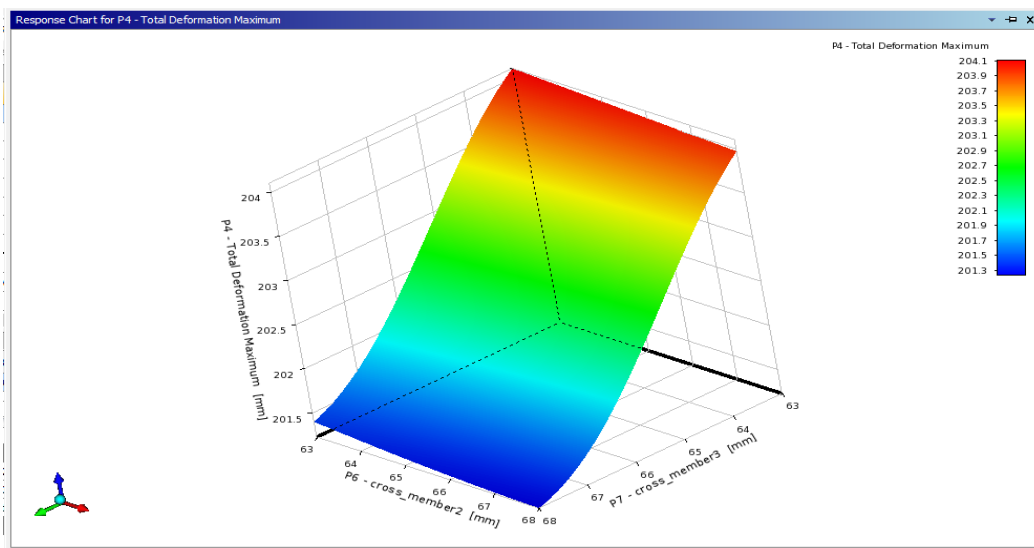
Figure 4.174: Response-Surface plot of total deformation vs cross-member 2 and cross-member 3
for B-B Scheme using P100/6061 Al MMC

Figure 4.174 illustrates the variation of deformation vs. cross-member 2 and cross-member 3 dimensions. Cross-member 3 dimensions varying from 63mm to 64mm and cross-member 2 dimensions varying from 63mm to 68mm exhibit the greatest deformation.
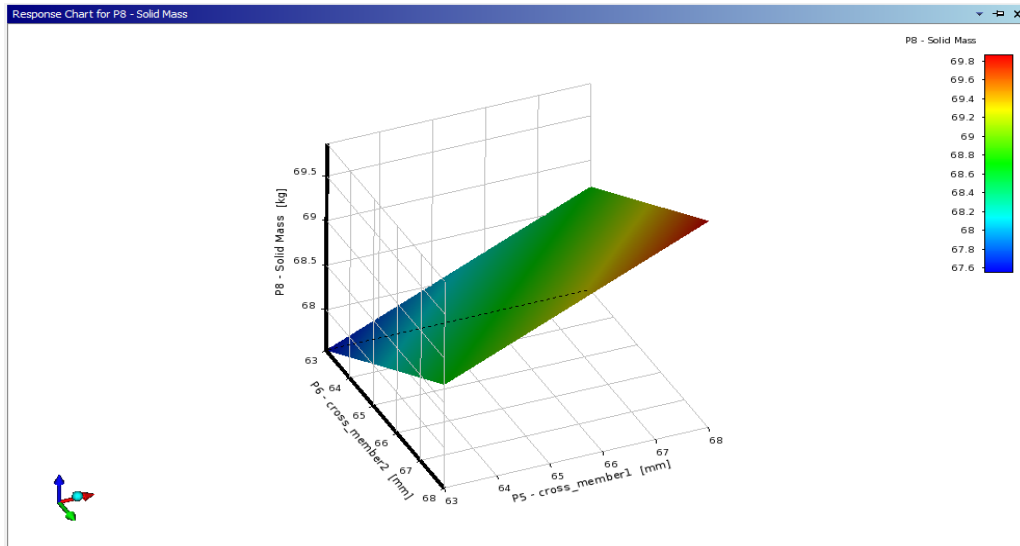
Figure 4.175: Response-Surface plot of mass vs cross-member 1 and cross-member 2 for B-B Scheme using P100/6061 Al MMC

Figure 4.175 illustrates the variation in mass as a function of cross-member 1 and cross-member 2 dimensions. The high solid mass is observed for cross-member 1 dimensions varying from 67mm to 68mm and cross-member 2 dimensions varying from 67mm to 68mm. Cross-member 1 and cross-member 2 dimensions varying from 63mm to 64mm have the lowest mass.

	Equivalent Stress Maximum	Total Deformation Maximum	Solid Mass
P5 - cross_member1	76.68219967	-4.76617673	33.33333333
P6 - cross_member2	-79.7814346	-7.558471445	33.33333333
P7 - cross_member3	36.56220787	-92.04640198	33.33333333
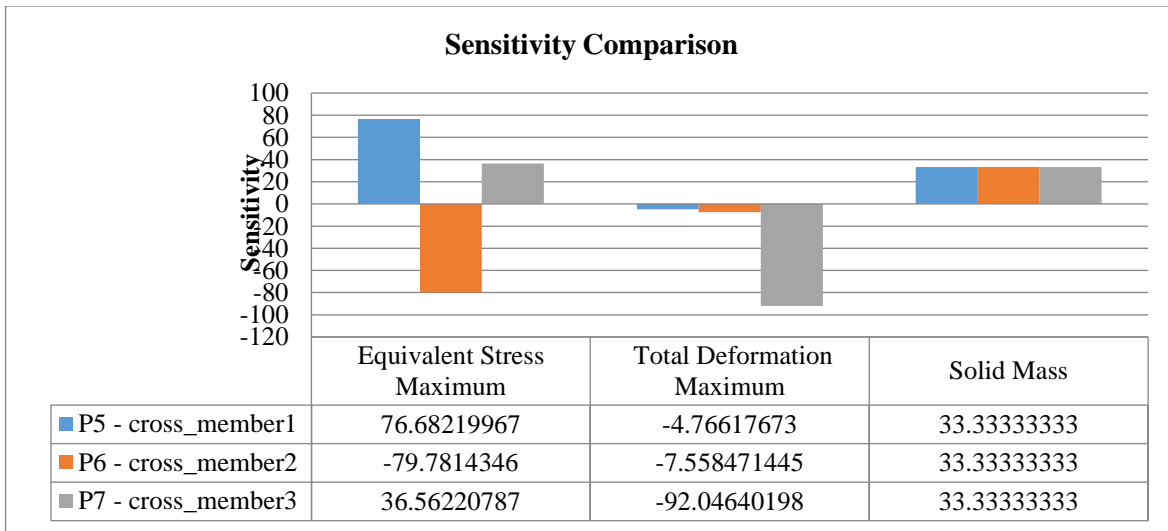
Figure 4.176: Sensitivity plot for B-B Scheme using P100/6061 Al MMC

As shown in figure 4.176, the sensitivity plot is produced for all three output parameters, equivalent-stress, deformation, and solid mass. Cross-member 2 has the highest sensitivity percentage for equivalent-stress, indicating that equivalent-stress has the greatest effect on cross-member 2 and the least effect on cross-member 3. Cross-member 3 has the highest sensitivity percentage for total deformation. All three optimization variables have the same effect on the mass of the chassis for solid mass.

4.4.4 Latin Hypercube Sampling using P100/6061 Al MMC

The design points are generated using the Latin-hypercube sampling technique. The different design points generated are shown in table 4.25. The design points are shown in column B, column C, and column D. The output parameters evaluated are shown in column E, column F and column G. Table 4.26 shows the maximum and minimum values.

Table 4.25: DOE Table for Latin hypercube sampling using P100/6061 Al MMC

A	B	C	D	E	F	G
Name	P5 - cross-member 1 (mm)	P6 - cross-member 2 (mm)	P7 - cross-member 3 (mm)	P3 - Equivalent-stress Max (MPa)	P4 - Total Deformation Maximum (mm)	P8 - Solid Mass (kg)
1.00	65.87	68.47	65.87	3459.62	202.20	69.56
2.00	68.47	65.00	66.73	3493.97	201.82	69.56
3.00	58.93	65.87	60.67	3512.16	206.02	66.15
4.00	67.60	58.93	70.20	3465.76	199.85	68.76
5.00	59.80	60.67	61.53	3391.49	205.40	65.35
6.00	71.07	59.80	59.80	3439.20	199.84	67.35
7.00	66.73	70.20	69.33	3441.64	200.20	70.97
8.00	70.20	67.60	68.47	3246.41	200.84	70.97
9.00	62.40	61.53	65.00	3267.07	203.07	66.95
10.00	61.53	66.73	71.07	3340.14	199.28	69.36
11.00	64.13	63.27	63.27	3277.09	203.95	67.35
12.00	60.67	69.33	62.40	3483.71	204.33	67.75
13.00	65.00	64.13	64.13	3486.33	203.38	67.96
14.00	69.33	71.07	58.93	3453.63	200.80	69.36
15.00	63.27	62.40	67.60	3331.45	201.76	67.96

Table 4.26: Maximum and minimum values for LHS using P100/6061 Al MMC

1	A	B	C
	Name	**Calculated Min**	**Calculated Max**
2	P3 - Equivalent-stress Max (MPa)	3246.4	3512.2
3	P4 - Total Deformation Max (mm)	199.28	206.02
4	P8 - Solid Mass (kg)	65.346	70.967

The maximum equivalent-stress obtained through optimization is 3512.2 MPa, while the minimum equivalent-stress obtained through optimization is 3246.4 MPa. The maximum and minimum values of deformation and solid mass output vary less. The mass of the chassis made of structural steel is 214.64 kg, while the mass of the chassis made of P100/6061 Al is 65.346 kg.
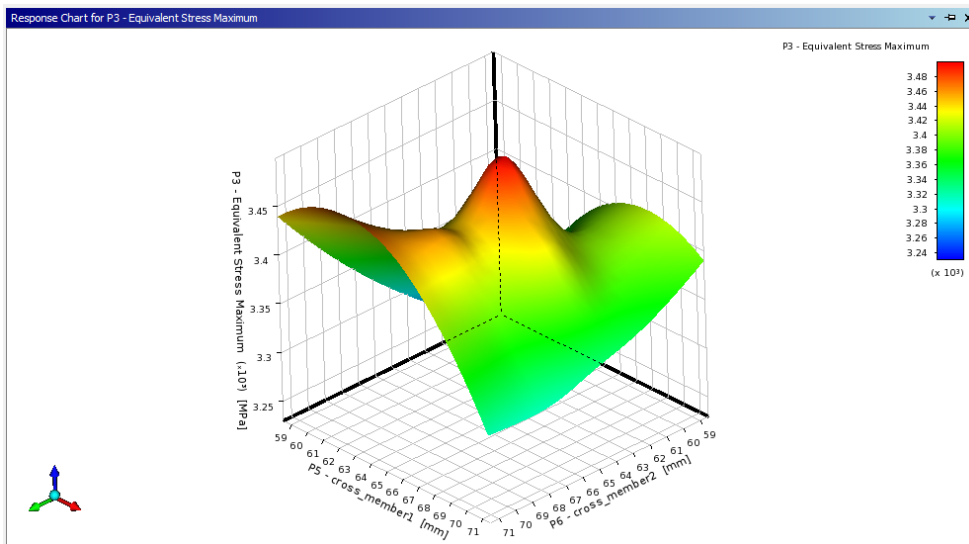
Figure 4.177: Response-Surface plot of equivalent-stress vs cross-member 1 and cross-member 2 for LHS using P100/6061 Al MMC

The equivalent-stress Response-Surface plot shows two peaks, which are illustrated in the red region. The maximum equivalent-stress is obtained for cross-member 2 with a length varying from 60mm to 64mm and cross-member 1 with a length varying from 61mm to 66mm. The equivalent-stress is found to be lowest in regions represented by dark blue color as illustrated in figure 4.177.
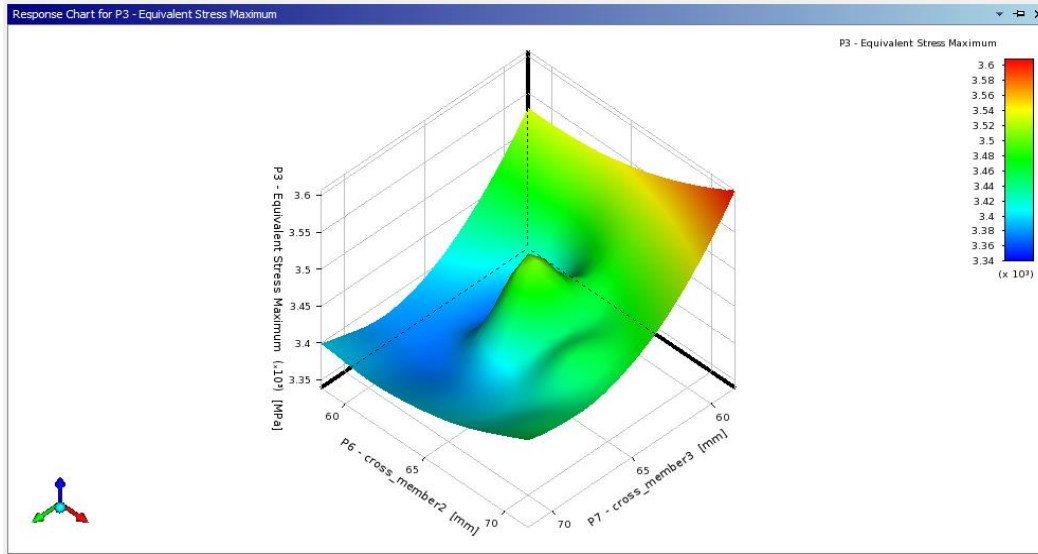
Figure 4.178: Response-Surface plot of equivalent-stress vs cross-member 2 and 3 for LHS using P100/6061 Al MMC

Figure 4.178 shows a Response-Surface plot of equivalent-stress versus cross-member 2 and cross-member 3 dimensions. The plot illustrates maximum equivalent-stress in the red-coloured region, where cross-member 2-dimensions range from 66mm to 71mm, and cross-member 3-dimensions range from 59mm to 61mm. For the region depicted in dark blue, the equivalent-stress is at its lowest.
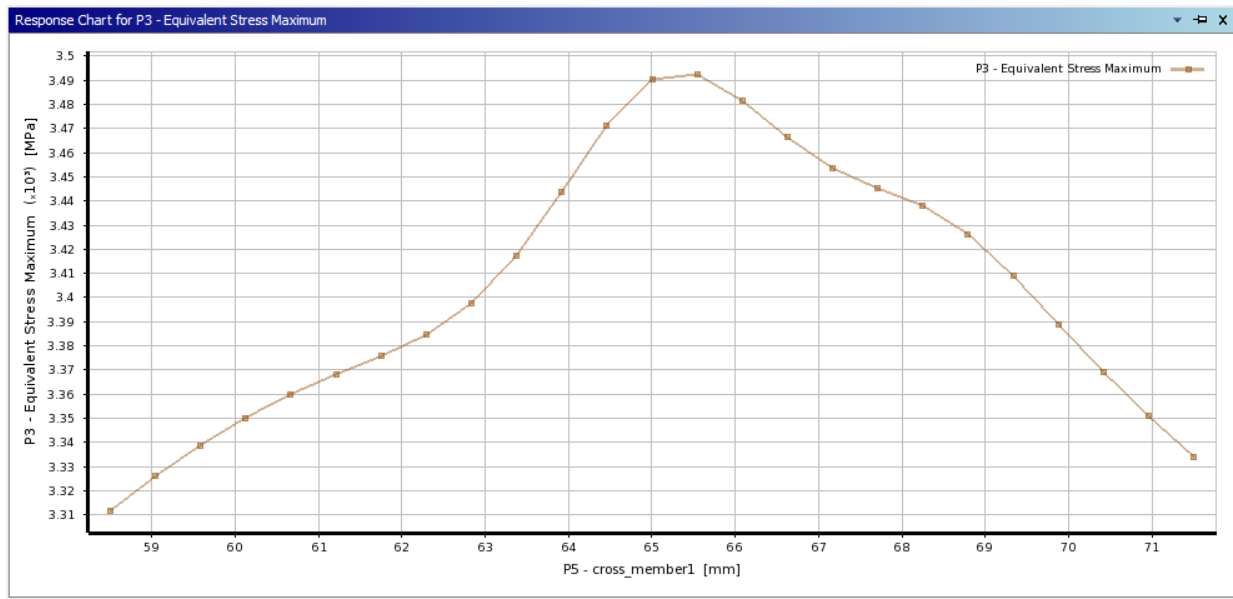
Figure 4.179: Equivalent-stress vs cross-member 1 for LHS using P100/6061 Al MMC

Figure 4.179 illustrates the fluctuation of equivalent-stress versus cross member 1. The equivalent-stress increases at first, reaching a maximum to cross-member 1 dimension value of 65.5mm, and then drops linearly to a minimum cross-member 1 dimension value of 71.5mm.
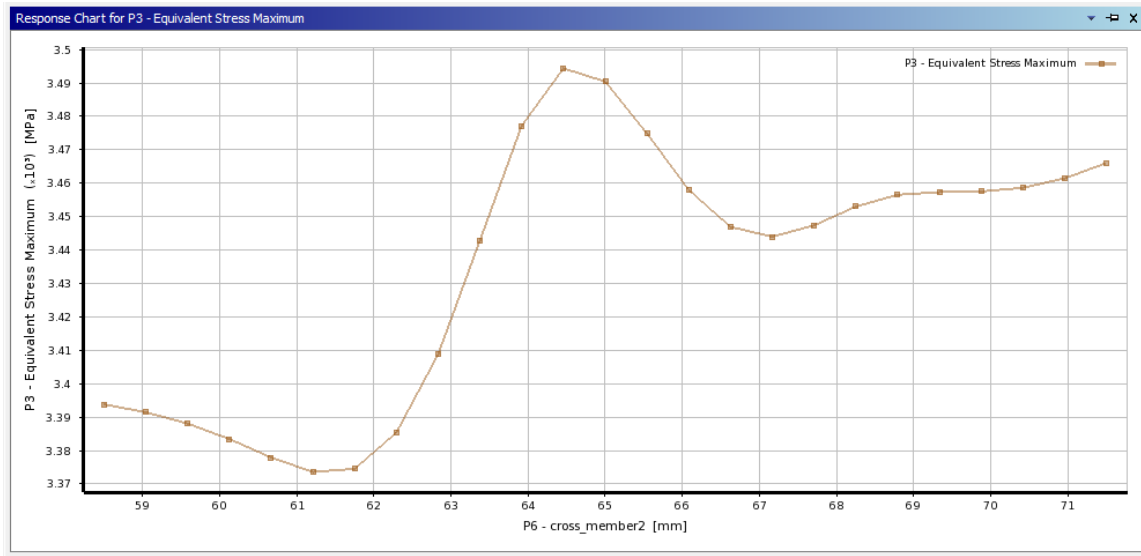
Figure 4.180: Equivalent-stress vs cross-member 2 for LHS using P100/6061 Al MMC

Figure 4.180 illustrates the fluctuation of equivalent-stress versus cross member 2. The equivalent-stress drops up to cross member 2-dimension value of 61.5mm before increasing linearly to the maximum dimension. value of 64.5mm. After that, the equivalent-stress reduces linearly.
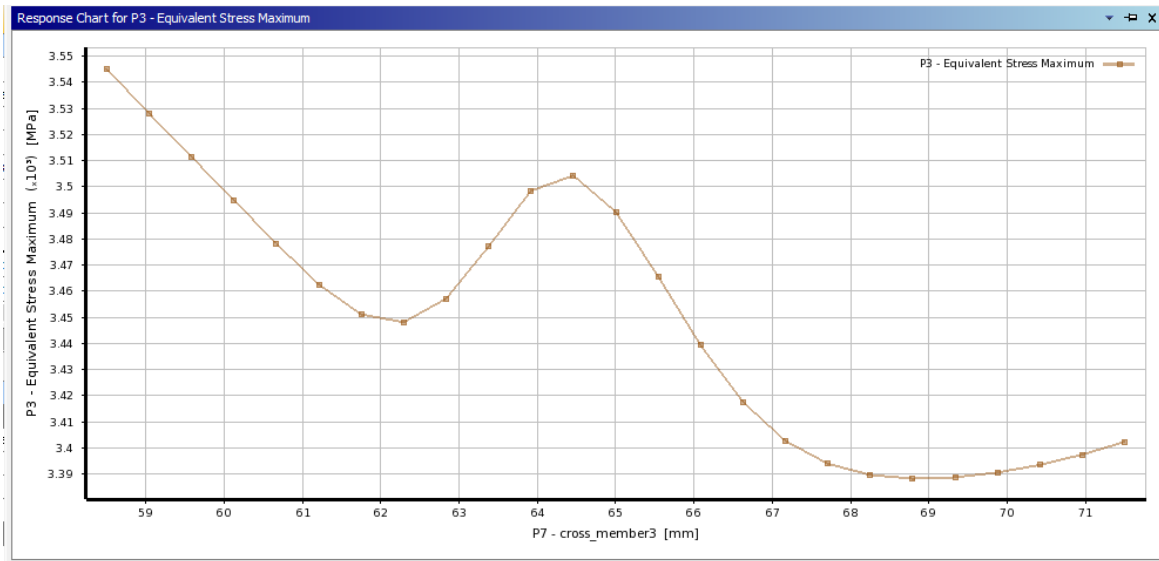
Figure 4.181: Equivalent-stress vs cross-member 3 for LHS using P100/6061 Al MMC

Figure 4.181 illustrates the variations of equivalent-stress vs cross-member 3 dimensions. The equivalent-stress, which was originally high, reduces linearly to a minimum at cross-member 3-dimension value of 62.5mm. After that, the equivalent-stress rises to a higher value at 64.5mm dimension and then falls in a parabolic pattern.
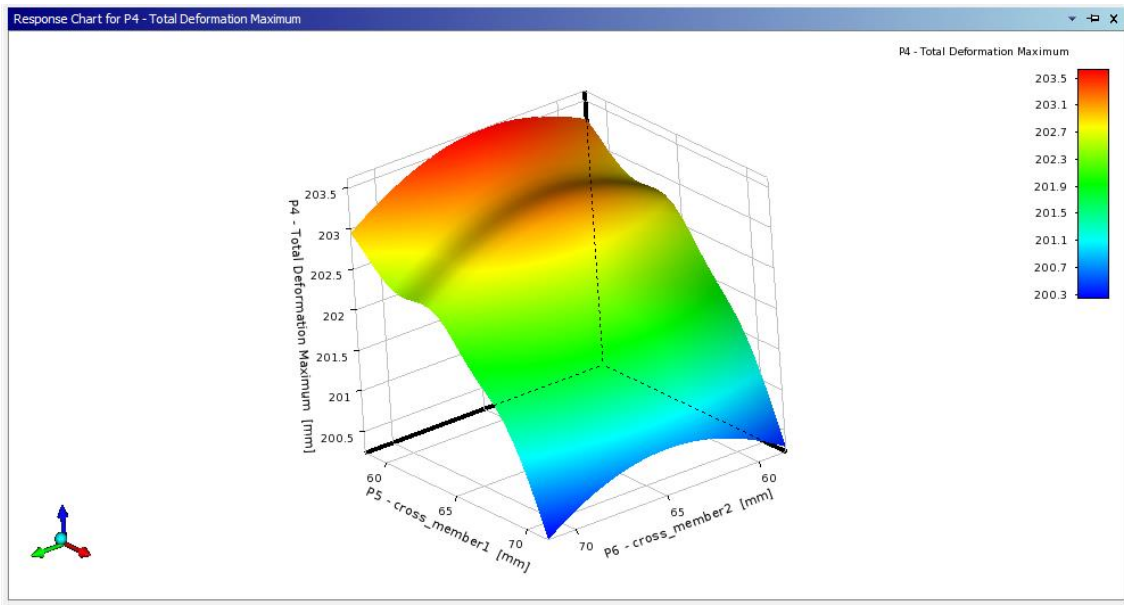
Figure 4.182: Response-Surface plot of total deformation vs cross-member 1 and cross-member 2 for LHS using P100/6061 Al MMC

The Response-Surface plot of deformation cross-member 1 and cross-member 2 is shown in figure 4.182. The plot shows higher deformation for cross-member 2 dimensions varying from 59mm to 71mm and cross-member 1 dimensions varying from 59mm to 64mm. For other dimensions, the deformation shows a lower value as represented by the blue-colored zone.
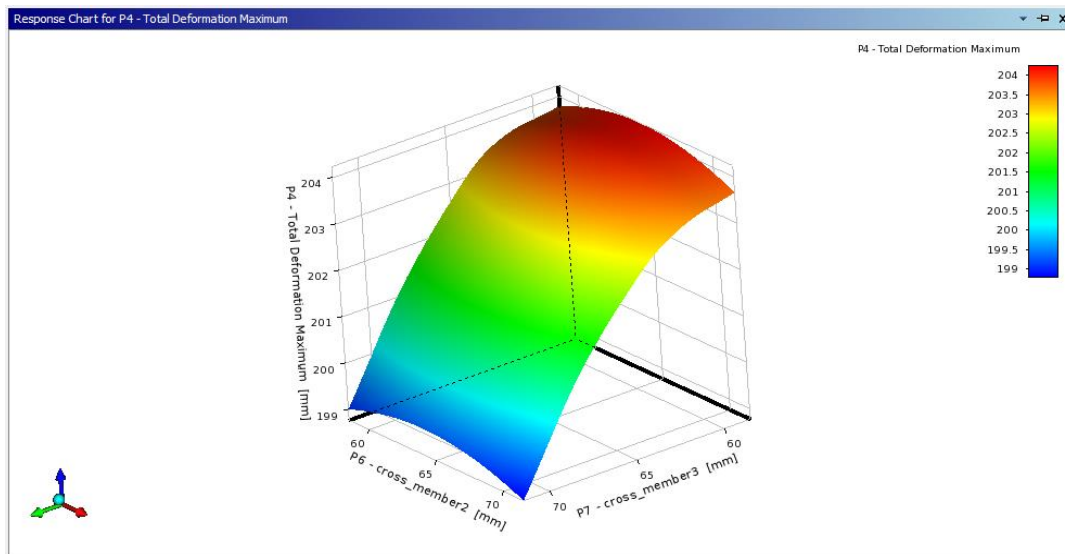
Figure 4.183: Response-Surface plot of total-deformation vs cross-member 2 and 3 for LHS using P100/6061 Al MMC

The variation of deformation vs cross-member 2 and cross-member 3 dimensions is shown in figure 4.183. The higher deformation is observed for cross-member 3 dimensions varying from 59mm to 63mm and cross-member 2 dimensions varying from 59mm to 71mm.
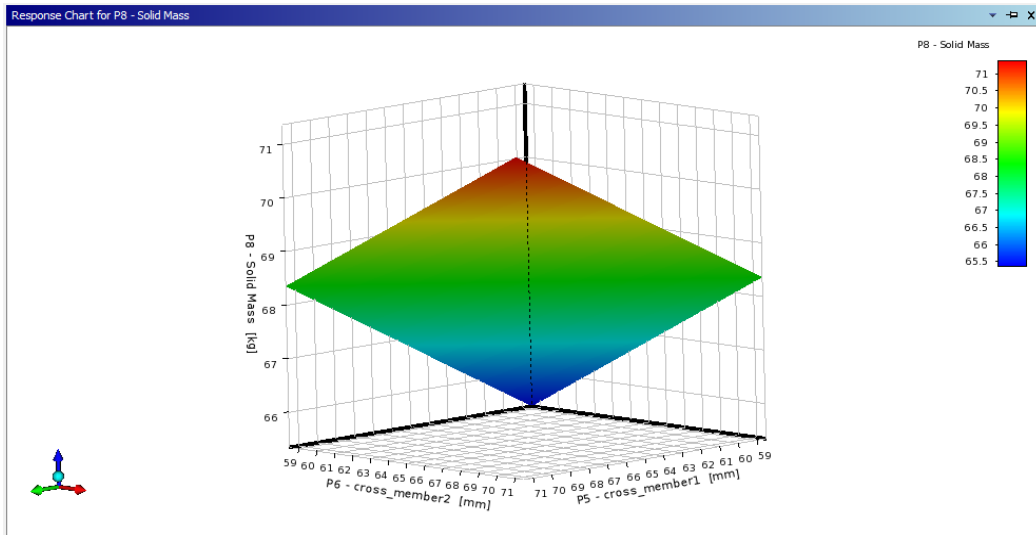
Figure 4.184: Response-surface plot of mass vs cross-member 2 and cross-member 1 for LHS using P100/6061 Al MMC

Figure 4.184 illustrates the variation in mass as a function of cross-member 1 and cross-member 2 dimensions. The higher solid mass is observed for cross-member 1 dimensions varying from 67mm to 71mm and cross-member 2 dimensions varying from 67mm to 71mm. Cross-member 1 and cross-member 2 dimensions varying from 59mm to 62mm have the lowest mass.

	Equivalent Stress Maximum	Total Deformation Maximum	Solid Mass
P5 - cross_member1 (mm)	36.58321462	-33.23631318	33.33333333
P6 - cross_member2 (mm)	24.25317507	-8.299082811	33.33333333
P7 - cross_member3 (mm)	-32.163198	-58.14438091	33.33333333
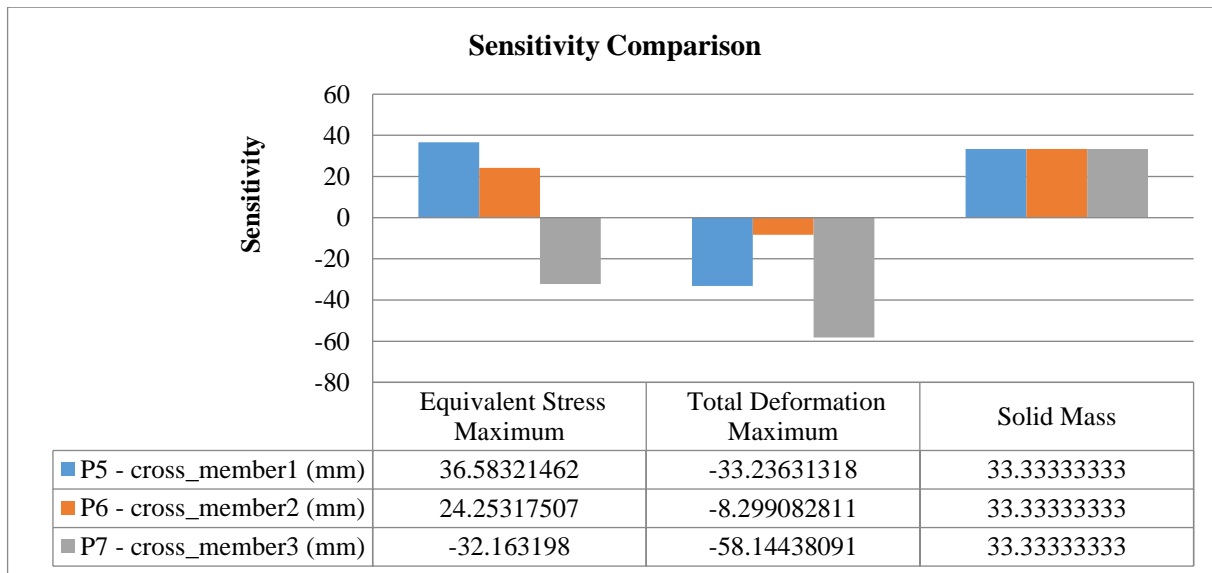
Figure 4.185: Sensitivity plot for LHS using P100/6061 Al MMC

As illustrated in figure 4.185, the sensitivity plot is constructed for all three output parameters: equivalent-stress, deformation, and solid mass. Cross-member 1 has the highest sensitivity percentage for equivalent-stress, indicating that equivalent-stress has the most effect on cross-member 1 and the least effect on cross-member 2. Cross-member 3 has the highest sensitivity % for total deformation, indicating that total deformation has the greatest impact on cross-member 3. All three optimization variables have the same influence on the mass of the chassis.

4.4.5 Sparse grid initialization using P100/6061 Al MMC

The design points are generated using the sparse grid initialization technique. The different design points generated are shown in table 4.27. The design points are shown in column B, column C, and column D. The output parameters evaluated are shown in column E, column F, and column G of Table 4.28.

Table 4.27: DOE Table for sparse grid initialization using P100/6061 Al MMC

A	B	C	D	E	F	G
Name	P5 - cross-member 1 (mm)	P6 - cross-member 2 (mm)	P7 - cross-member 3 (mm)	P3 - Equivalent-stress Max (MPa)	P4 - Total Deformation Maximum (mm)	P8 - Solid Mass (kg)
1	65	65	65	3277.61	202.86	68.35
2	64	65	65	3466.61	202.84	68.12
3	66	65	65	3494.89	202.79	68.58
4	65	64	65	3344.65	202.93	68.12
5	65	66	65	3347.44	202.80	68.58
6	65	65	64	3280.18	203.45	68.12
7	65	65	66	3324.30	202.27	68.58

Table 4.28: Maximum and minimum values for sparse grid initialization using P100/6061 Al MMC

# Output Parameter Minimums						
Name	P5 - cross-member 1 (mm)	P6 - cross-member 2 (mm)	P7 - cross-member 3 (mm)	P3 - Equivalent-stress Max (MPa)	P4 - Total Deformation Maxim (mm)	P8 - Solid Mass (kg)
P3 - Equivalent-stress Max	65.49039	64	64	3260.348	202.6646	68.10671
P4 - Total Deformation Max	66	66	64	3486.346	202.5215	68.65434
P8 - Solid Mass	64	64	64	3447.862	202.757	67.92213
# Output Parameter Maximums						
Name	P5 - cross-member 1 (mm)	P6 - cross-member 2 (mm)	P7 - cross-member 3 (mm)	P3 - Equivalent-stress Max (MPa)	P4 - Total Deformation Maximum (mm)	P8 - Solid Mass (kg)
P3 - Equivalent-stress Max	66	66	66	3553.507	202.8626	68.78759
P4 - Total Deformation Max	65.43383	64	66	3325.518	203.1807	68.36863
P8 - Solid Mass	66	66	66	3553.507	202.8626	68.78759

The maximum equivalent-stress attained by optimization is 3553.5 MPa, with a minimum equivalent-stress of 3260.3 MPa. Between maximum and minimum values, deformation and solid mass output show minimal variance. The mass of a chassis made of structural steel is 214.64 kilograms, while the mass of a chassis made of P100/6061 aluminium is 67.922 kilograms.
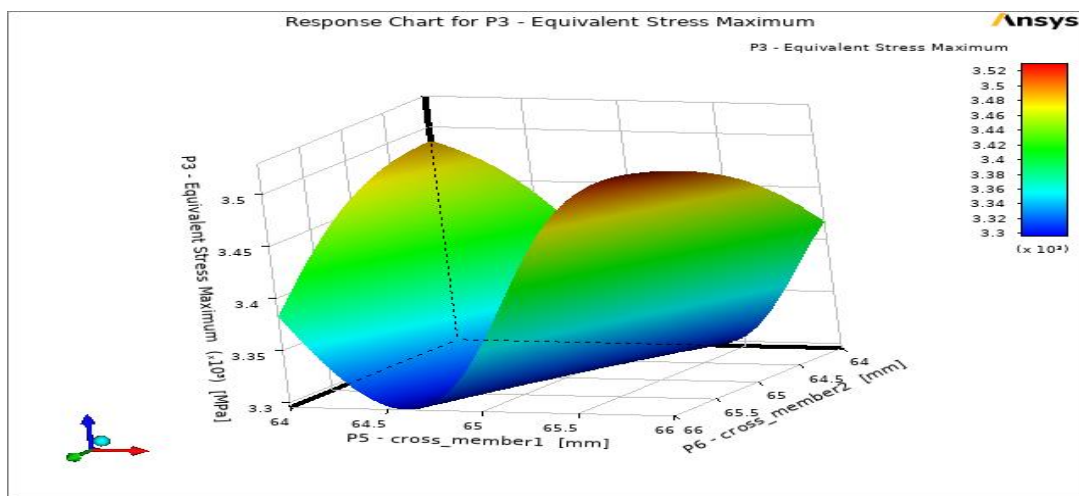
Figure 4.186: Response-Surface plot of equivalent-stress vs cross-member 1 and cross-member 2 for sparse grid initialization using P100/6061 Al MMC

The equivalent-stress Response-Surface plot displays one peak, which is represented by the red-coloured region as illustrated in figure 4.186. The higher equivalent-stress is observed for the cross-member 2 dimension varies from 64.5mm to 66mm and cross-member 1 dimension varies from 65.7mm to 66mm. For places indicated in dark blue color, the equivalent-stress is found to be the lowest.
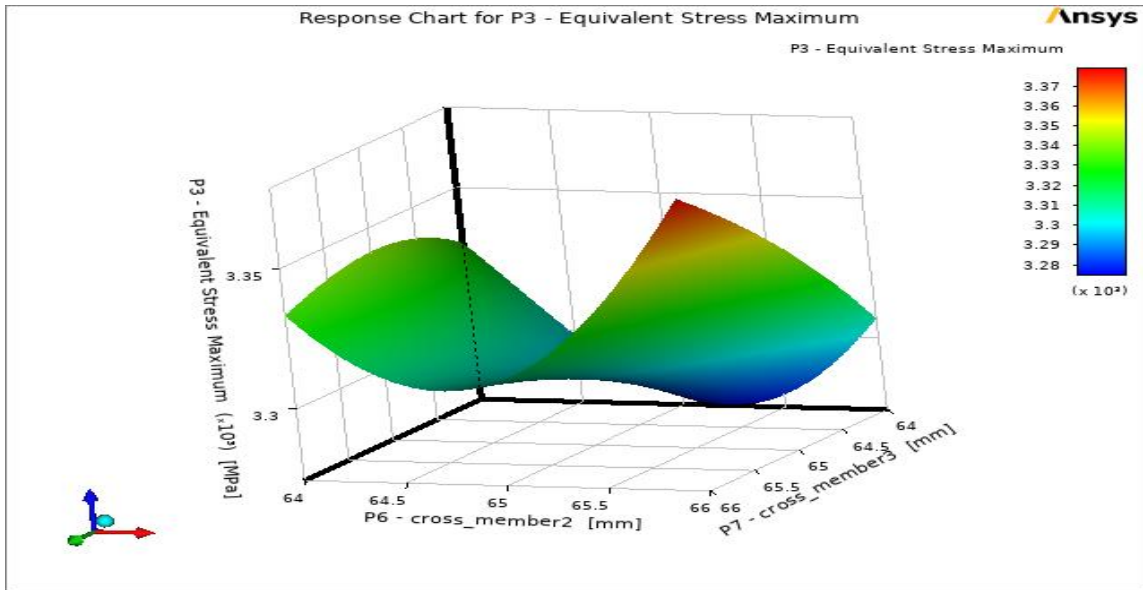
Figure 4.187: Response-Surface plot of equivalent-stress vs cross-member 2 and cross-member 3 for sparse grid initialization using P100/6061 Al MMC

Figure 4.187 shows a Response-Surface plot of equivalent-stress versus cross-member 2 and cross-member 3. The graph illustrates maximum equivalent-stress in the red-coloured region, with cross-member 2-dimensions varying from 65.8mm to 66mm and cross-member 3-dimensions varying from 65.7mm to 66mm. For the region depicted in dark blue, the equivalent-stress is at its lowest.
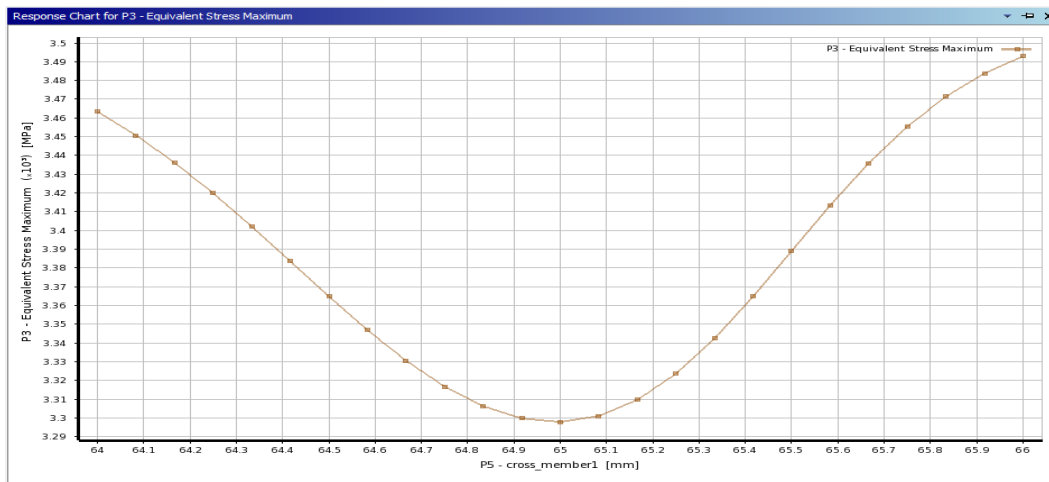
Figure 4.188: Equivalent-stress vs cross-member 1 for SGI using P100/6061 Al MMC

Figure 4.188 illustrates the variations of equivalent-stress versus cross member 1 dimensions. The equivalent-stress declines at first, reaching a minimum at the cross-member 1 dimension value of 65mm, and then grows linearly, reaching a higher value at the cross-member 1 dimension of 66mm.
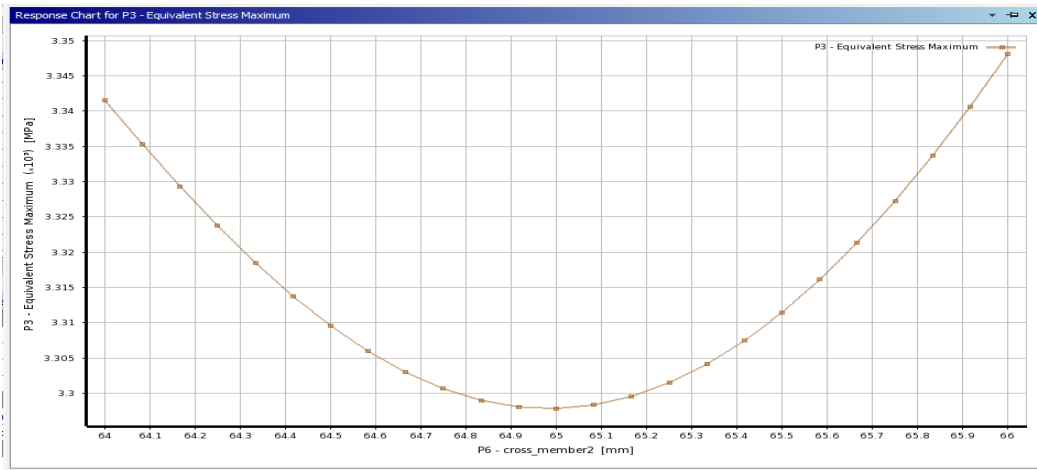
Figure 4.189: Equivalent-stress vs cross-member 2 for sparse grid initialization using P100/6061 Al

Figure 4.189 illustrates the variations of equivalent-stress versus cross member 2 dimensions. The equivalent-stress reduces up to 65mm before increasing linearly to its maximum value of 66mm at the cross member 2 dimensions.
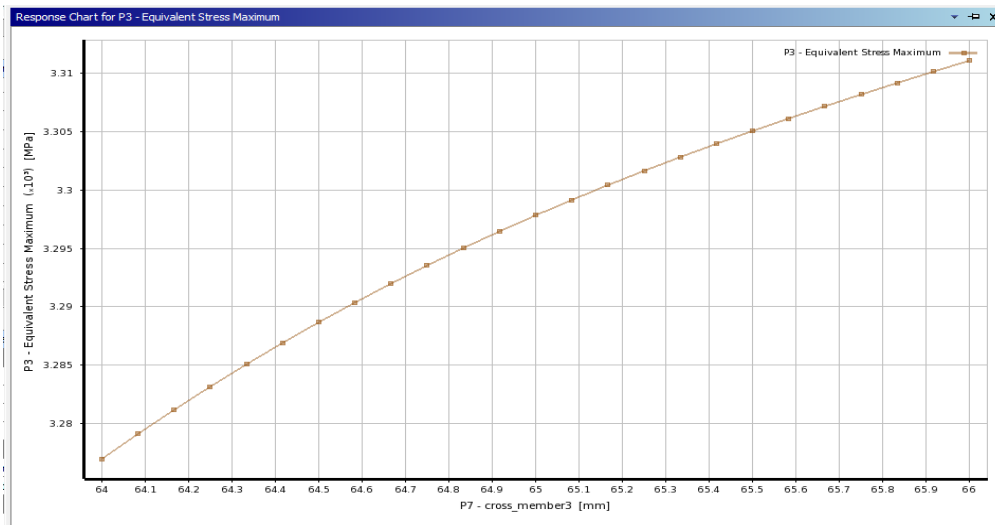
Figure 4.190: Equivalent-stress vs cross-member 3 for sparse grid initialization using P100/6061 Al

Figure 4.190 illustrates the fluctuation of equivalent-stress vs. cross-member 3 dimensions. The equivalent-stress is initially lowest at a cross-member 3-dimension value of 64mm, then grows linearly to a maximum dimension value of 66mm.
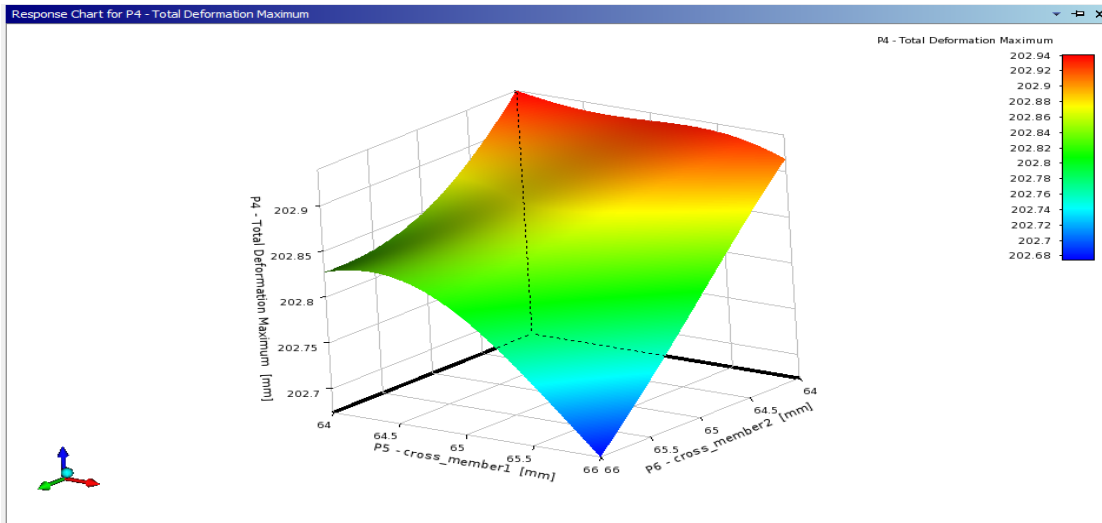
Figure 4.191: Response-Surface plot of total deformation vs cross-member 1 and cross-member 2 for sparse grid initialization using P100/6061 Al MMC

Figure 4.191 illustrates the Response-Surface plot of deformation cross-member 1 and cross-member 2 dimensions. Higher deformation is observed for cross-member 1 dimensions varying from 64mm to 66mm and cross-member 2 dimensions varying from 64mm to 64.75mm. The deformation in other dimensions indicates a lower value, which is represented by the blue-coloured zone.
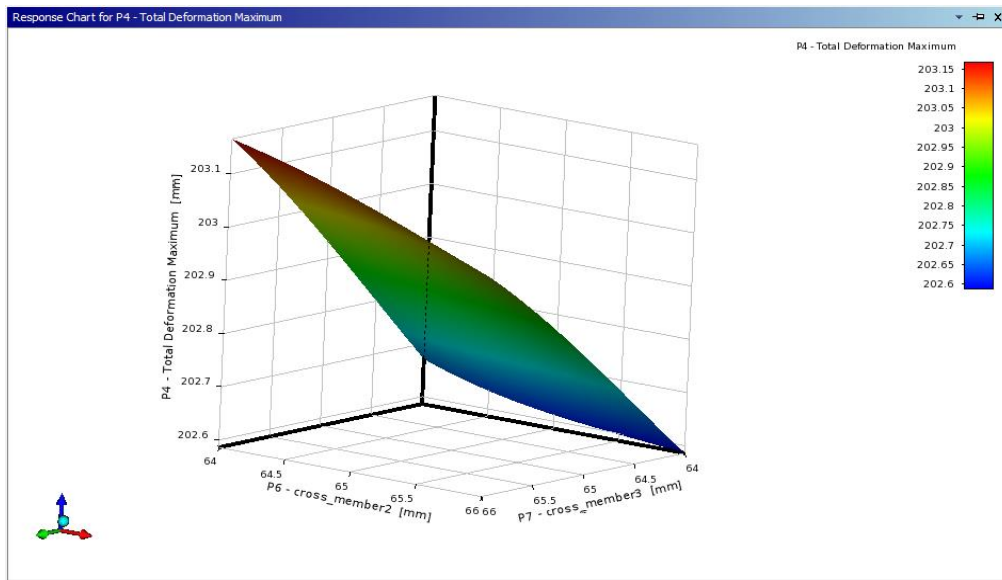
Figure 4.192: Response-Surface plot of total deformation vs cross-member 2 and cross-member 3 for sparse grid initialization using P100/6061 Al MMC

Figure 4.192 illustrates the variations of deformation vs. cross-member 2 and cross-member 3 dimensions. Cross-member 2 dimensions varying from 64mm to 65.5mm and cross-member 3 dimensions varying from 65.5mm to 66mm show the most distortion.
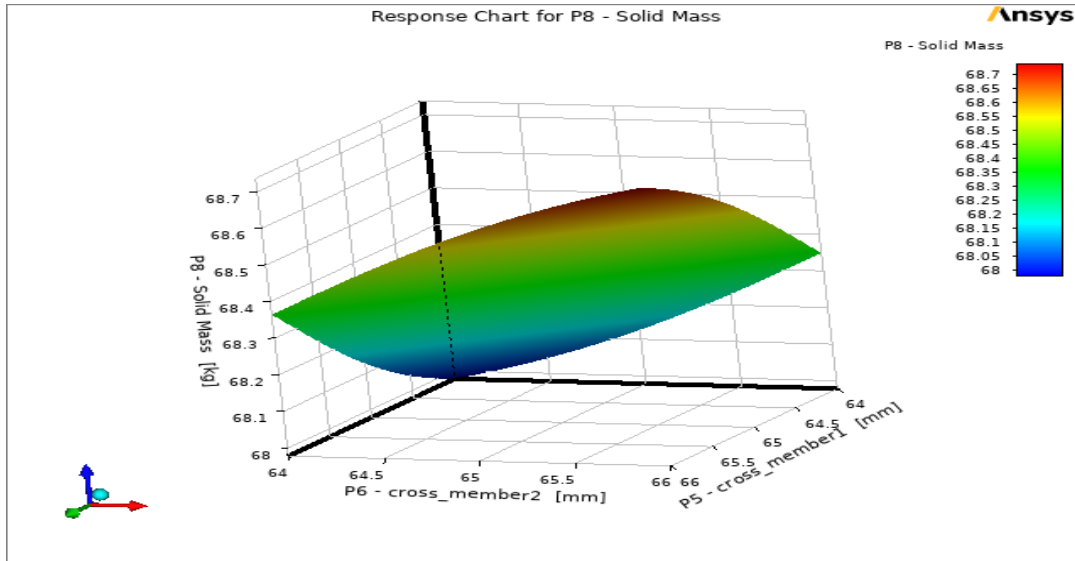
Figure 4.193: Response-Surface plot of mass vs cross-member 2 and cross-member 1 for sparse grid initialization using P100/6061 Al MMC

Figure 4.193 illustrates the variation in mass as a function of cross-member 1 and cross-member 2 dimensions. Maximum solid mass for cross-member 1 dimensions varying from 65mm to 66mm and cross-member 2 dimensions varying from 65mm to 66mm is shown in the graph. Cross-member 1 and cross-member 2 dimensions varying from 64mm to 64.5mm have the lowest mass.

	Equivalent Stress Maximum	Total Deformation Maximum	Solid Mass
cross_member1 (mm)	65.32881087	-6.599494809	53.52337144
cross_member2 (mm)	16.99170647	-10.79779127	53.52337102
cross_member3 (mm)	11.65407274	40.74421868	33.15028024
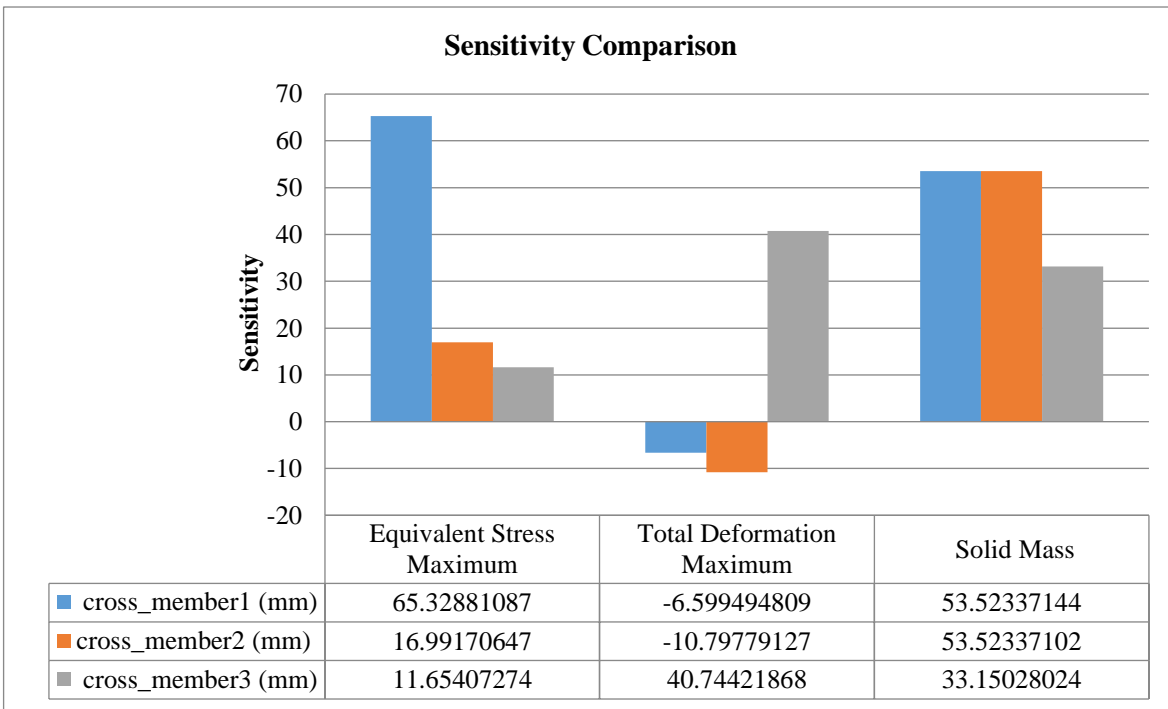
Figure 4.194: Sensitivity plot for sparse grid initialization using P100/6061 Al MMC

As illustrated in figure 4.194, the sensitivity map is constructed for all three output parameters: equivalent-stress, deformation, and solid mass. Cross-member 3 has the highest sensitivity % for total deformation. Indicating that equivalent-stress has the most effect on cross-member 1 while has the least effect on cross-member 3. Cross-member 1 and cross-member 2 have the same sensitivity of 53.523 percent for solid mass.

4.4.6 Sub-Chapter Summary

The chassis design is optimized using P100/6061 Al MMC material. The application of optimization techniques aided to determine a critical range of dimensions for which the stresses, deformation, and solid mass are maximum or minimum i.e., by interpolating 3D Response-Surface plots. The sensitivity plots are also generated for each optimization case i.e., central composite design, optimal space-filling design, sparse grid initialization, Latin hypercube sampling, and Box Behnken design. The 2D linearized graphs enabled to determine the effect of each variable on output parameters. The maximum solid mass obtained from optimization is 72.029 kg, and the minimum solid mass obtained from the analysis is 64.685 kg which is one of the key specific objectives of the study. The optimization results have shown that cross-member 3 has a maximum effect on chassis deformation compared to other variables.

The next sub-chapter involves investigating the application of different optimization techniques using Graphite Al GA 7-230 MMC material in line with sections 1.4 and 1.5.

4.5 Response-Surface Optimization using Graphite Al GA 7-230 MMC with Square section Chassis

The current Sub-chapter demonstrates the use of various optimization techniques, such as central composite design, optimal space-filling design, sparse grid initialization, Latin hypercube sampling, and Box-Behnken design, on heavy motor vehicles chassis made of Graphite Al GA 7-230 MMC material. Using 3D Response-Surface plots and sensitivity plots, the effect of various design variables on equivalent-stress, deformation, and mass is evaluated.

4.5.1 Central Composite Design Scheme using Graphite Al GA 7-230 MMC

Using Finite Element Analysis, the software analyzed the output parameters at these design points. As illustrated in column E and column F of Table 4.29, these output parameters are equivalent-stress and total deformation.

Table 4.29: DOE Table for CCD scheme using Graphite Al GA 7-230 MMC

A	B	C	D	E	F	G
Name	P5 - cross-member 1 (mm)	P6 - cross-member 2 (mm)	P7 - cross-member 3 (mm)	P3 - Equivalent-stress Max (MPa)	P4 - Total Deformation Maximum (mm)	P8 - Solid Mass (kg)
1.00	65.00	65.00	65.00	3277.61	78.33	66.99
2.00	58.50	65.00	65.00	3261.58	78.43	65.51
3.00	71.50	65.00	65.00	3514.87	78.26	68.47
4.00	65.00	58.50	65.00	3270.74	78.40	65.51
5.00	65.00	71.50	65.00	3522.25	78.23	68.47
6.00	65.00	65.00	58.50	3256.64	77.55	65.51
7.00	65.00	65.00	71.50	3217.43	76.83	68.47
8.00	59.72	59.72	59.72	3344.10	77.11	63.39
9.00	70.28	59.72	59.72	3429.54	77.06	65.79
10.00	59.72	70.28	59.72	3435.59	77.01	65.79
11.00	70.28	70.28	59.72	3312.01	76.92	68.19
12.00	59.72	59.72	70.28	3461.23	77.15	65.79
13.00	70.28	59.72	70.28	3228.51	77.05	68.19
14.00	59.72	70.28	70.28	3291.50	77.04	68.19
15.00	70.28	70.28	70.28	3458.88	76.94	70.59

Figure 4.213 illustrates the fluctuation of total deformation vs. design points. Design point number two (2) shows the most deformation, whereas design point number seven shows the

least deformation (7). The following are the dimensions that correspond to design point number two (2):

- 58.5 mm for cross-member 1, 65 mm for cross-member 2, and 65 mm for cross-member 3.

The magnitude of maximum deformation obtained from the analysis is 78.432 mm and the magnitude of minimum deformation obtained from the analysis is 76.829 mm. The maximum solid mass obtained through optimization is 70.589 kg at design point number 15, while the minimum solid mass obtained through analysis is 63.391 kg at design point number 8. For all cross members, the dimensions corresponding to design point number 15 are 70.285 mm. The Response-Surface plot helps in determining the range of optimization variable values for which the equivalent-stress is maximum or minimum. Figure 4.195 illustrates the Response-Surface plot of equivalent-stress vs cross-member 1 and cross-member 2 dimensions.
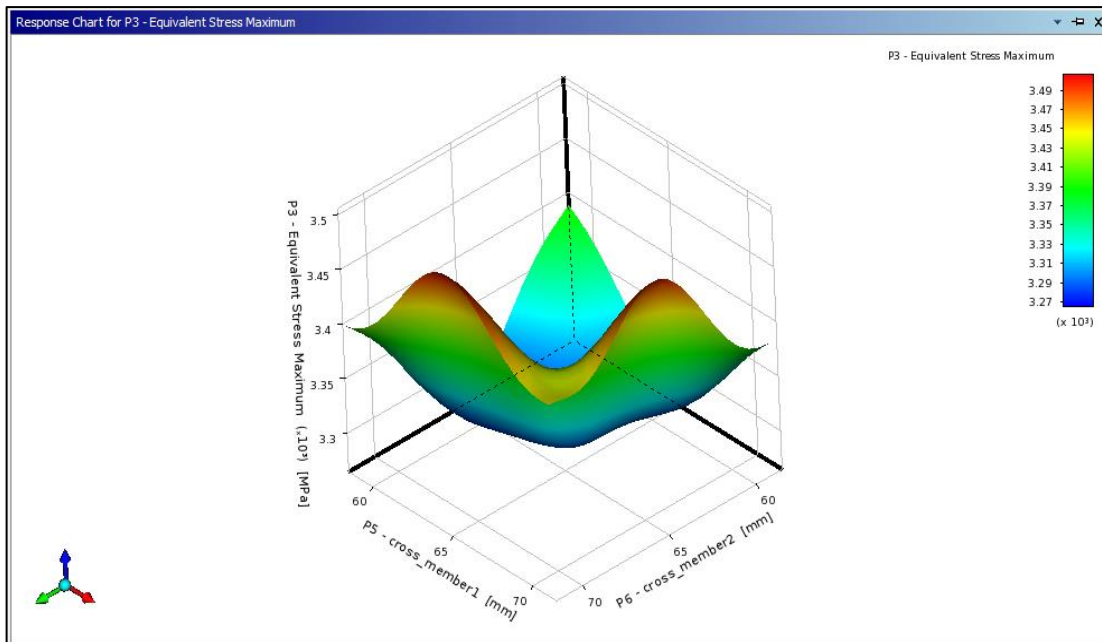
Figure 4.195: Response-Surface plot of equivalent-stress vs cross-member 1 and cross-member 2 for CCD scheme using Graphite Al GA 7-230 MMC

In the red-coloured region, two peaks of equivalent-stress can be seen. The equivalent-stress is highest for cross-member 1 dimensions varying from 62mm to 67mm and cross-member 2 dimensions varying from 69mm to 71mm, according to the first peak that formed along the cross-member 1 dimension. The equivalent-stress is higher for cross-member 1 dimensions varying from 69mm to 71mm and cross-member 2 dimensions varying from 61mm to 67mm, according to the second peak that formed along the cross-member 2 dimensions. Other dimensions of cross-member 1 and cross-member 2 have the lowest equivalent-stress, as seen in the dark blue coloured region.
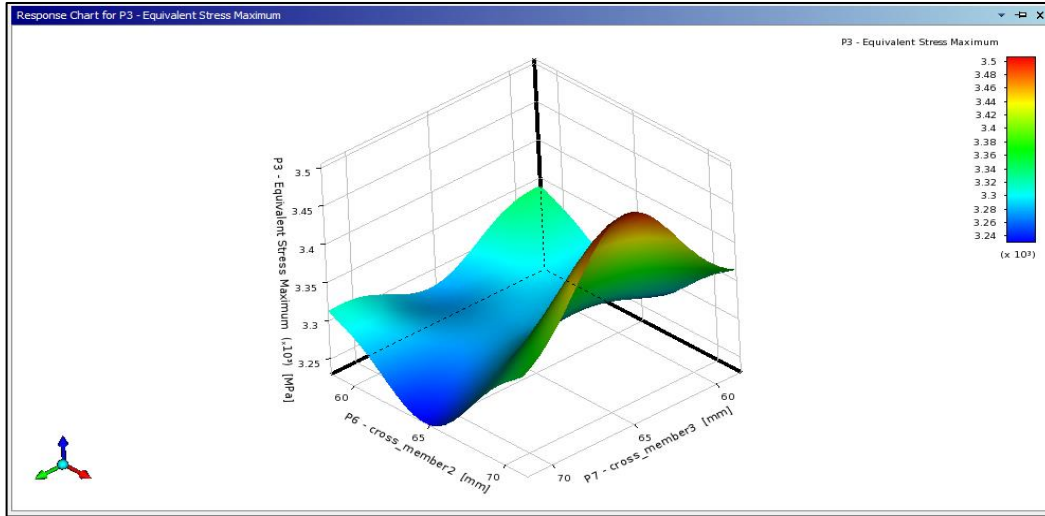
Figure 4.196: Response-Surface plot of equivalent-stress vs cross-member 2 and cross-member 3 for CCD scheme using Graphite Al GA 7-230 MMC

Figure 4.196 shows a Response-Surface plot of equivalent-stress versus cross-member 2 and cross-member 3 dimensions. As demonstrated in the red-coloured region, there is a single peak of equivalent-stress. The interpolation approach is used to find the dimensions corresponding to maximal equivalent-stress. Cross-member 3 dimensions varying from 61mm to 67mm and cross-member 2 dimensions varying from 69mm to 71mm have the higher equivalent-stress. For other values of cross-member 2 and cross-member 3 which are represented by a dark blue coloured region, the equivalent-stress is the lowest.
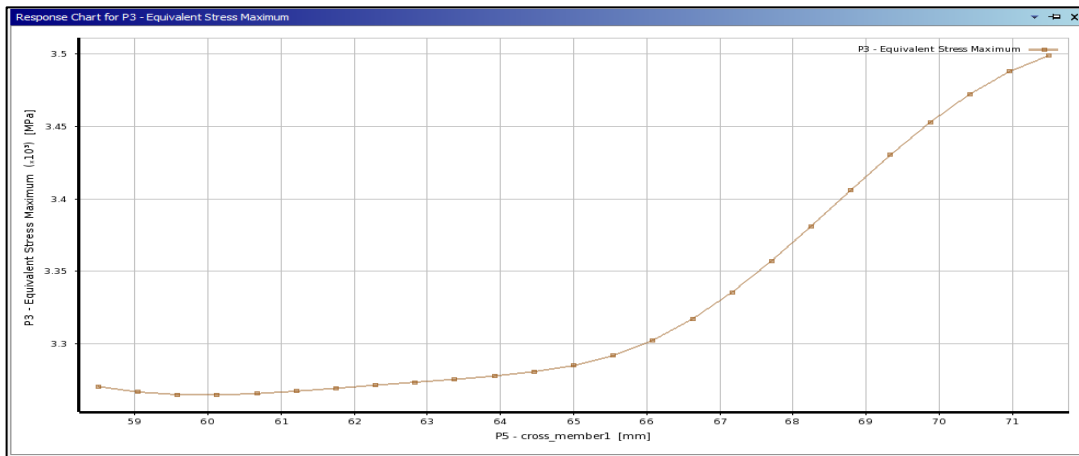
Figure 4.197: Equivalent-stress vs cross-member 1 for CCD scheme using Graphite Al GA 7-230

Figure 4.197 illustrates the variation of equivalent-stress with respect to cross-member 1 dimensions. The graph illustrates a progressive increase in equivalent-stress until cross-member 1 dimension of 65mm. At a cross-member dimension of 71mm, the equivalent-stress increases exponentially to a maximum value of 3.570 x 10^3 MPa.
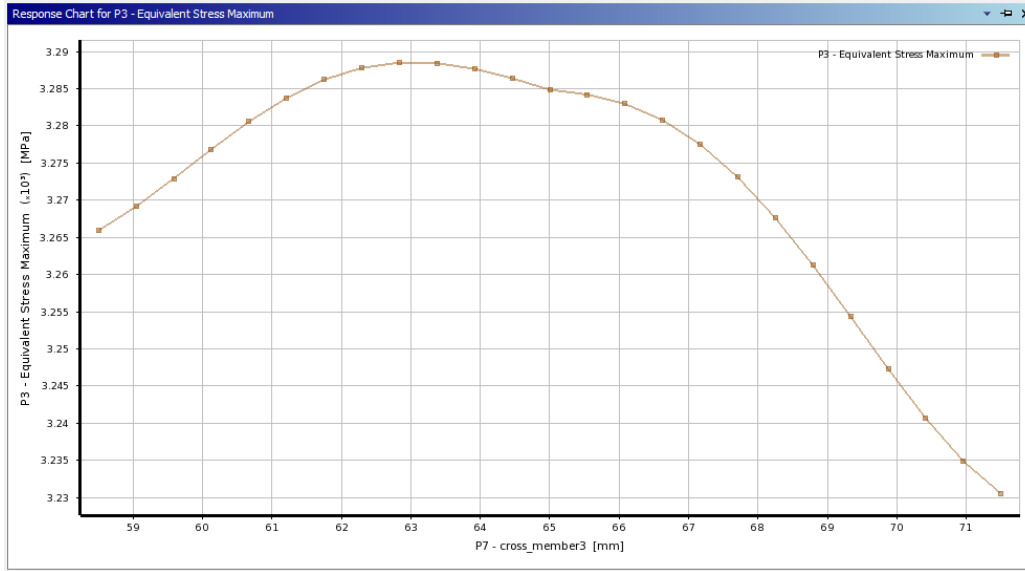
Figure 4.198: Equivalent-stress vs cross-member 3 for CCD scheme using Graphite Al GA 7-230

Figure 4.198 illustrates the variation of equivalent-stress with respect to cross-member 3 dimensions. Up to 63mm cross-member 3 dimensions, the graph indicates a progressive increase in equivalent-stress, which then reduces linearly as cross-member 3 dimensions increase. With a cross-member 3 dimension of 71.5mm, the least equivalent-stress is recorded.
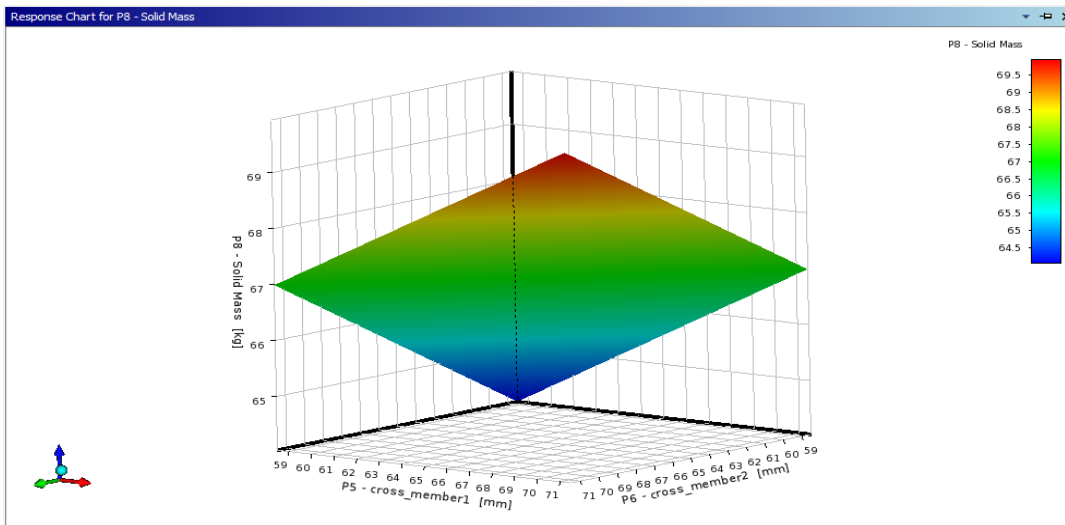
Figure 4.199: 3D Response-Surface plot of solid mass for CCD using Graphite Al GA 7-230 MMC

The Response-Surface plot of figure 4.199 illustrates the fluctuation of mass with regard to cross-member 1 and cross-member 2 dimensions. The red-coloured region represents the largest mass, while the blue-coloured region represents the least mass. Cross-member 1 dimensions varying from 68mm to 71mm and cross-member 2 dimensions varying from 68mm to 71mm have the highest mass. Cross-member 1 and cross-member 3 dimensions varying from 58.5mm to 61mm have the lowest mass.
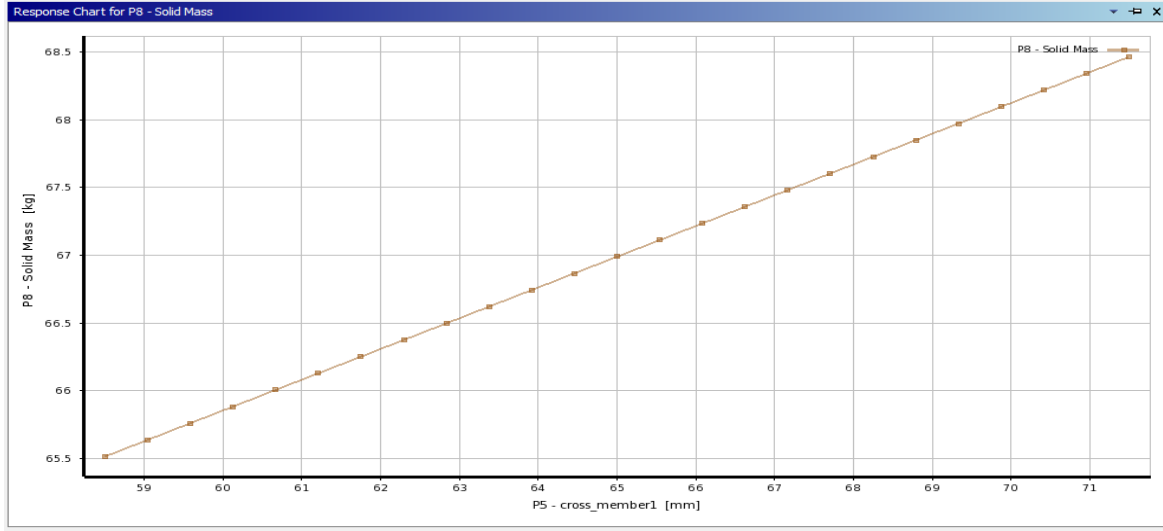
Figure 4.200: Solid mass vs cross-member 1 for CCD scheme using Graphite Al GA 7-230 MMC

Figures 4.200 and 4.201 depict the variation in chassis mass as a function of cross-member 1 and cross-member 3 dimensions. With increasing cross-member 1 and cross-member 3 dimensions, the solid mass appears to increase linearly. The cross-member 1 dimension of 58.5mm has the smallest mass of the chassis. The 58.5mm cross-member 3 and cross-member 1 dimensions have the lowest chassis mass.
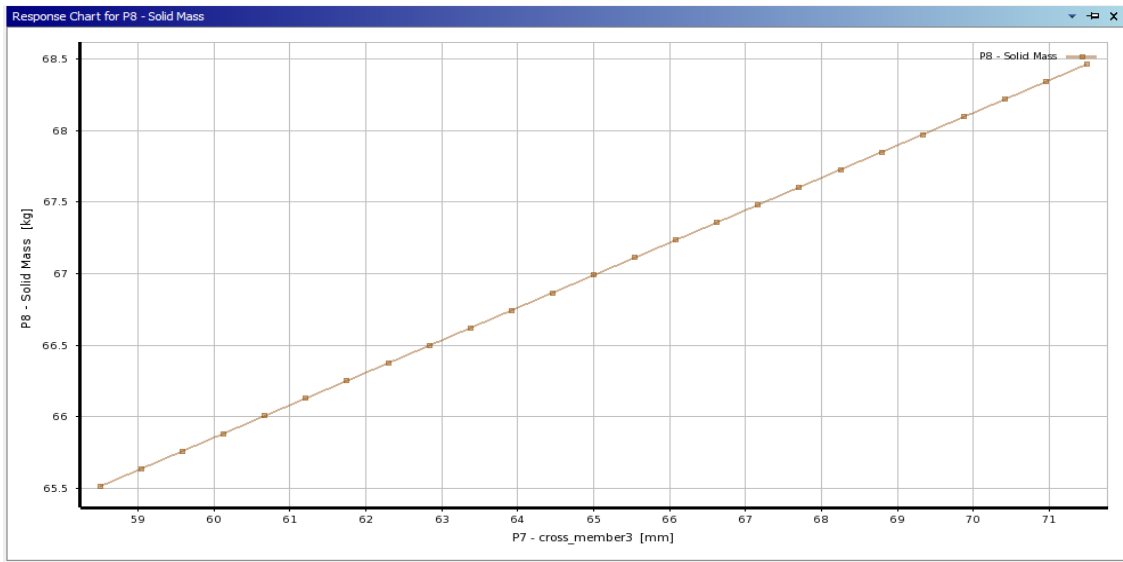
Figure 4.201: Solid mass vs cross-member 3 for CCD scheme using Graphite Al GA 7-230 MMC
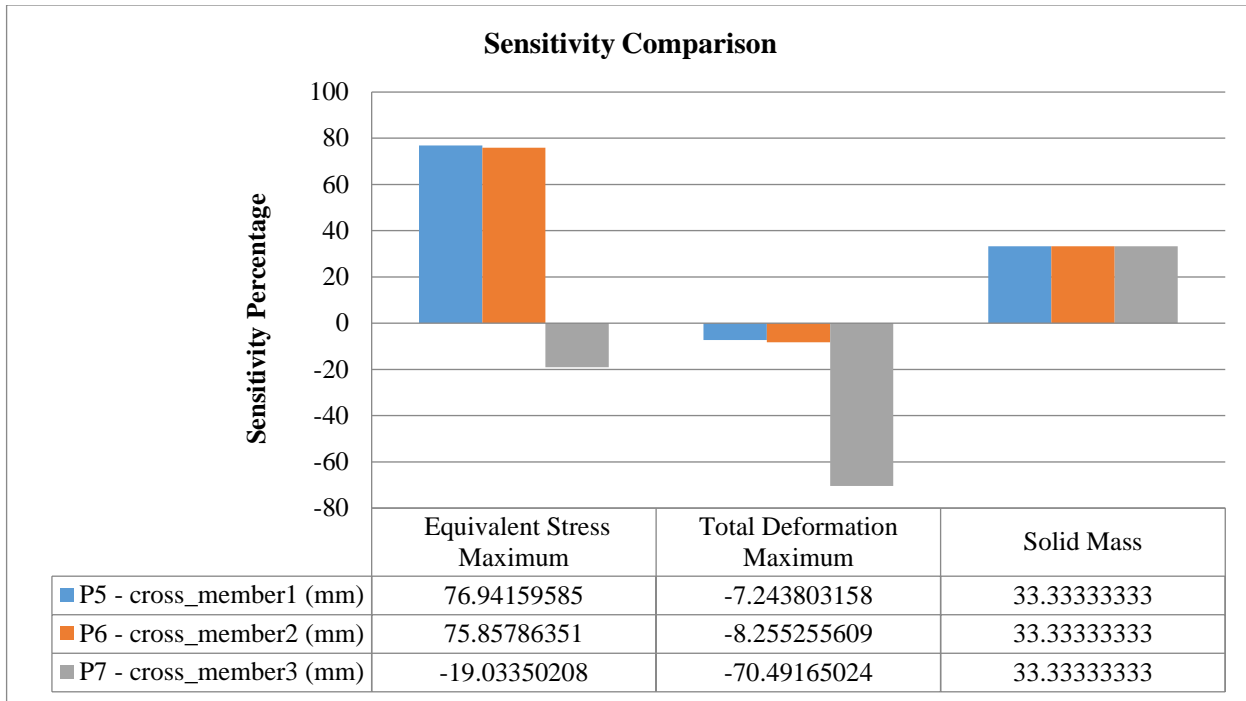
Figure 4.202: Sensitivity plot for CCD scheme using Graphite Al GA 7-230 MMC

For equivalent-stress, cross-member 1 has the highest sensitivity percentage (76.94%) and cross-member 3 has the lowest sensitivity percentage (19.034%) as shown in figure 4.202. Cross-member 3 shows the maximum sensitivity percentage for deformation, while cross-member 1 shows the minimum sensitivity percentage. This means that total deformation causes the greatest influence on cross-member 3. For solid mass, all three variables have the same sensitivity percentage, indicating that all three optimization variables have the same effect on chassis mass.

4.5.2 Optimal Space Filling Design using Graphite Al GA 7-230 MMC

The design points are generated using optimal space-filling (OSF) design as shown in table 4.30. Different combinations of cross-member 1, cross-member 2, and cross-member 3 dimensions are generated based on the optimal space-filling design scheme. The equivalent-stress, deformation, and solid mass are generated for each design point. The maximum and minimum values of these output parameters are shown in Table 4.31.

Table 4.30: DOE table for OSF using Graphite Al GA 7-230 MMC

A Name	B P5 - cross-member 1 (mm)	C P6 - cross-member 2 (mm)	D P7 - cross-member 3 (mm)	E P3 - Equivalent-stress Max (MPa)	F P4 - Total Deformation Maximum (mm)	G P8 - Solid Mass (kg)
1.00	69.33	68.47	60.67	3489.33	778.08	67.78
2.00	63.27	69.33	59.80	3235.04	770.04	66.40
3.00	59.80	66.73	68.47	3351.49	776.62	66.99
4.00	68.47	59.80	67.60	3493.44	778.58	67.19
5.00	58.93	60.67	65.87	3501.74	782.44	64.83
6.00	71.07	63.27	63.27	3347.15	786.61	67.58
7.00	66.73	62.40	58.93	3246.61	772.32	65.42
8.00	70.20	65.87	69.33	3319.29	773.51	69.35
9.00	65.87	64.13	64.13	3283.42	785.17	66.79
10.00	65.00	67.60	71.07	3464.31	769.15	68.96
11.00	61.53	71.07	65.00	3474.07	782.66	67.58
12.00	60.67	65.00	61.53	3502.20	792.34	65.22
13.00	64.13	58.93	62.40	3308.88	790.11	64.83
14.00	67.60	70.20	66.73	3471.70	778.69	69.15
15.00	62.40	61.53	70.20	3233.55	772.35	66.79

Table 4.31: Maximum and minimum values for OSF using Graphite Al GA 7-230 MMC

1	A Name	B Calculated Min	C Calculated Max
2	P3 - Equivalent-stress Max (MPa)	3233	3506.7
3	P4 - Total Deformation Maximum (mm)	768.86	793.28
4	P8 - Solid Mass (kg)	62.564	71.416

The maximum equivalent-stress obtained through optimization is 3506.7 MPa, while the minimum equivalent-stress obtained through optimization is 3233 MPa. The maximum and minimum values of deformation and solid mass output vary less. The solid mass with structural steel is 214.64 kg, while the solid mass with Graphite Al 7-230 is 62.564 kg.

Figure 4.203: Response-Surface plot of equivalent-stress vs cross-member 1 and cross-member 2 for OSF using Graphite Al GA 7-230 MMC

Figure 4.203 illustrates a Response-Surface plot of equivalent-stress with two peaks depicted in red. The maximum equivalent-stress is obtained for cross-member 2 with a length varying from 59mm to 61mm and cross-member 1 with a length varying from 59mm to 61mm. The equivalent-stress is found to be lowest in regions represented by dark blue color.

Figure 4.204: Response-Surface plot of equivalent-stress vs cross-member 2 and cross-member 3 for OSF using Graphite Al GA 7-230 MMC

Figure 4.204 shows a Response-Surface plot of equivalent-stress versus cross-member 2 and cross-member 3 dimensions. The graph illustrates maximum equivalent-stress in the red-coloured zone,

with cross-member 2-dimensions varying from 66mm to 71mm and cross-member 3-dimensions varying from 64mm to 71mm. For the region indicated in dark blue, the equivalent-stress is at its lowest.
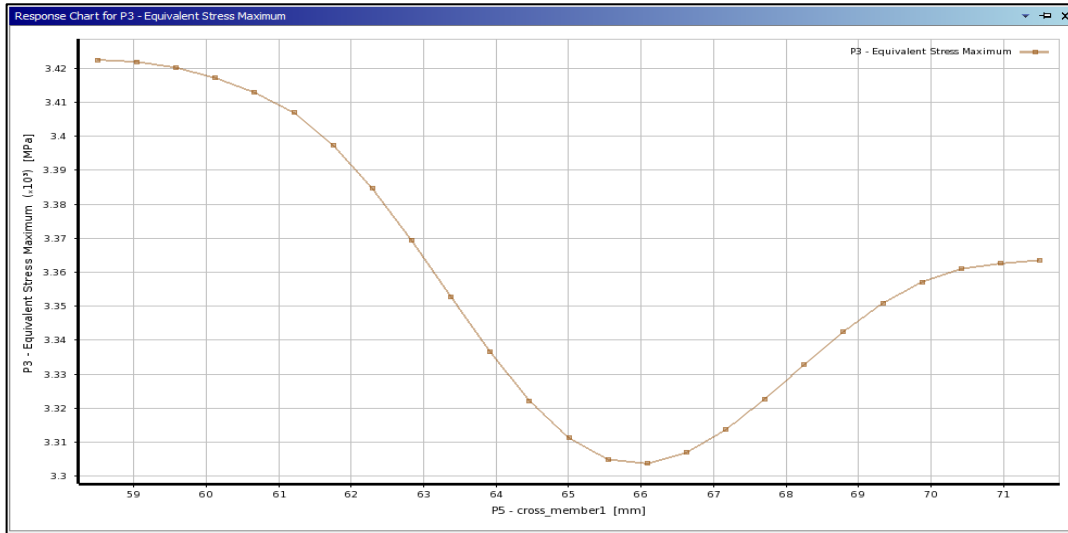
Figure 4.205: Equivalent-stress vs cross-member 1 for OSF using Graphite Al GA 7-230 MMC

Figure 4.205 illustrates the variations of equivalent-stress versus cross member 1 dimensions. The equivalent-stress declines at first, reaching a low at cross-member 1 dimension value of 66mm, and then climbs linearly to a maximum at cross-member 1 dimension value of 71mm.
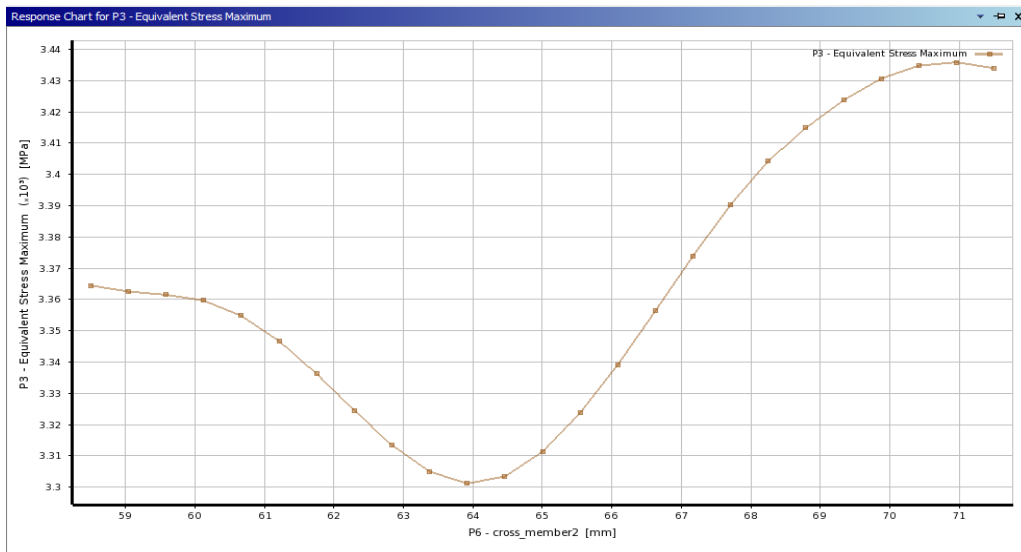
Figure 4.206: Equivalent-stress vs cross-member 2 for OSF using Graphite Al GA 7-230 MMC

Figure 4.206 represents the variation of equivalent-stress vs cross member 2 dimensions. The equivalent-stress initially decreases up to cross member 2 dimensions of 64mm, then steadily increases to a cross member 2-dimension maximum value of 71mm, and then decreases.
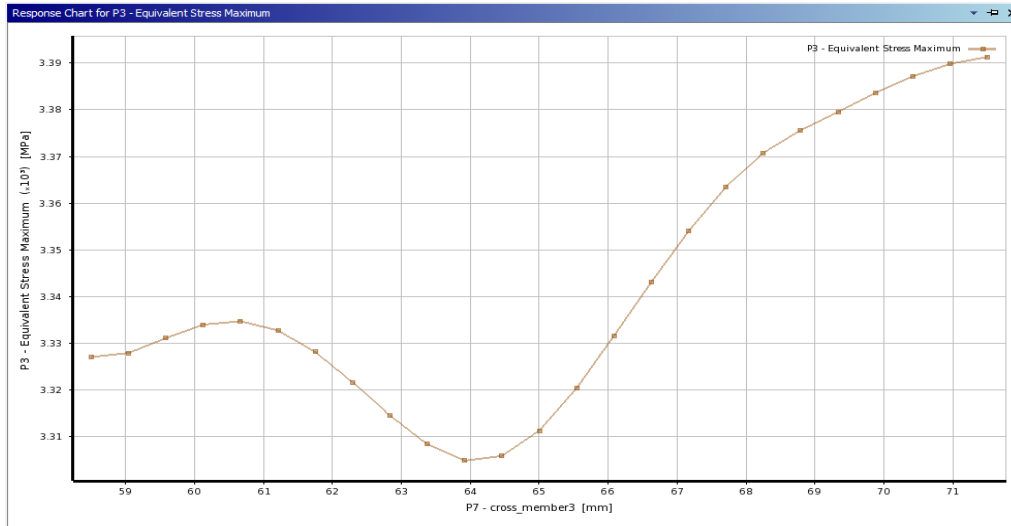
Figure 4.207: Equivalent-stress vs cross-member 3 for OSF using Graphite Al GA 7-230 MMC

Figure 4.207 illustrates the fluctuation of equivalent-stress vs cross-member 3 dimensions. The equivalent-stress rises and then falls until it reaches its lowest point at cross-member 3 dimension value of 64mm. The equivalent-stress rises linearly until it reaches its maximum, at cross-member 3 dimension value of 71mm.
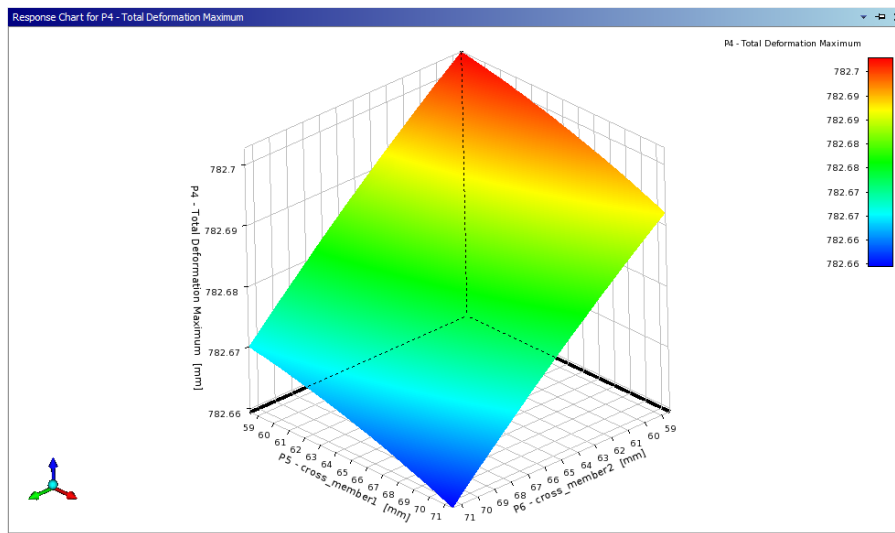
Figure 4.208: Response-Surface plot of total deformation vs cross-member 1 and cross-member 2 for OSF using Graphite Al GA 7-230 MMC

Figure 4.208 illustrates the Response-Surface plot of deformation cross-members 1 and 2 dimensions. Maximum deformation is shown for cross-member 2 dimensions varying from 59mm to 62mm and cross-member 1 dimensions varying from 59mm to 67mm. In the other dimensions, the deformation has a minimum value, which is represented by the blue zone.
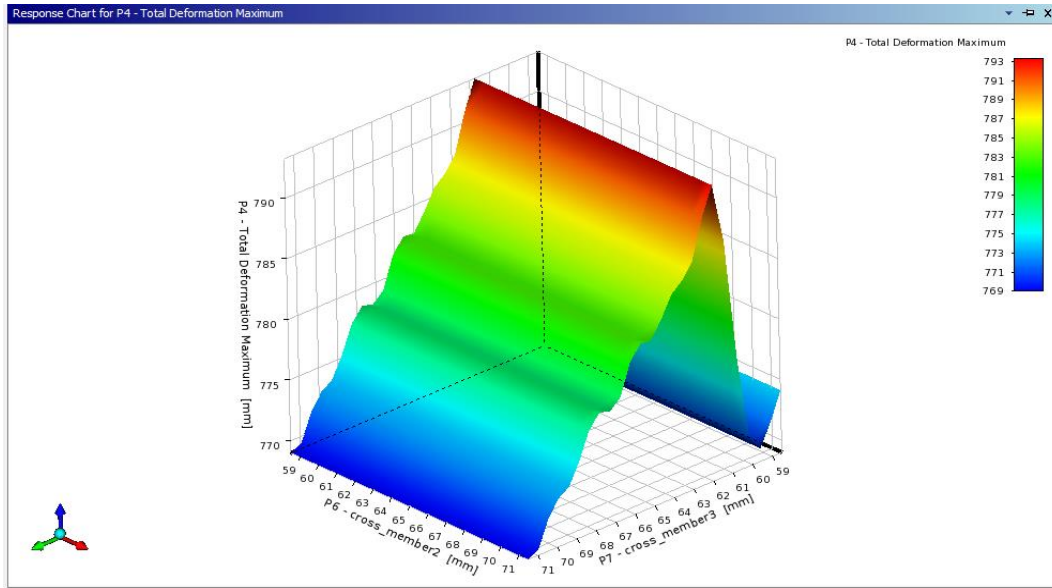
Figure 4.209: Response-Surface plot of total deformation vs cross-member 2 and cross-member 3 for OSF using Graphite Al GA 7-230 MMC

Figure 4.209 illustrates the fluctuation of deformation vs. cross-member 2 and cross-member 3 dimensions. Cross-member 3 dimensions varying from 61mm to 63mm and cross-member 2 dimensions varying from 59mm to 71mm show the most distortion.

Figure 4.210: Response-Surface plot of mass vs cross-member 1 and cross-member 2 for OSF using Graphite Al GA 7-230 MMC

Figure 4.210 illustrates the variation in mass as a function of cross-member 1 and cross-member 2 dimensions. Maximum solid mass for cross-member 1 dimensions varying from 69mm to 71mm and

cross-member 2 dimensions varying from 69mm to 71mm is shown in the graph. Cross-member 1 and cross-member 2 dimensions varying from 59mm to 62mm have the lowest mass.

Sensitivity Comparison

	Equivalent Stress Maximum	Total Deformation Maximum	Solid Mass
■ P5 - cross_member1 (mm)	-43.28592546	-0.044074706	33.33333333
■ P6 - cross_member2 (mm)	48.21222387	-0.133870035	33.33333333
■ P7 - cross_member3 (mm)	31.5323379	-89.58988601	33.33333333
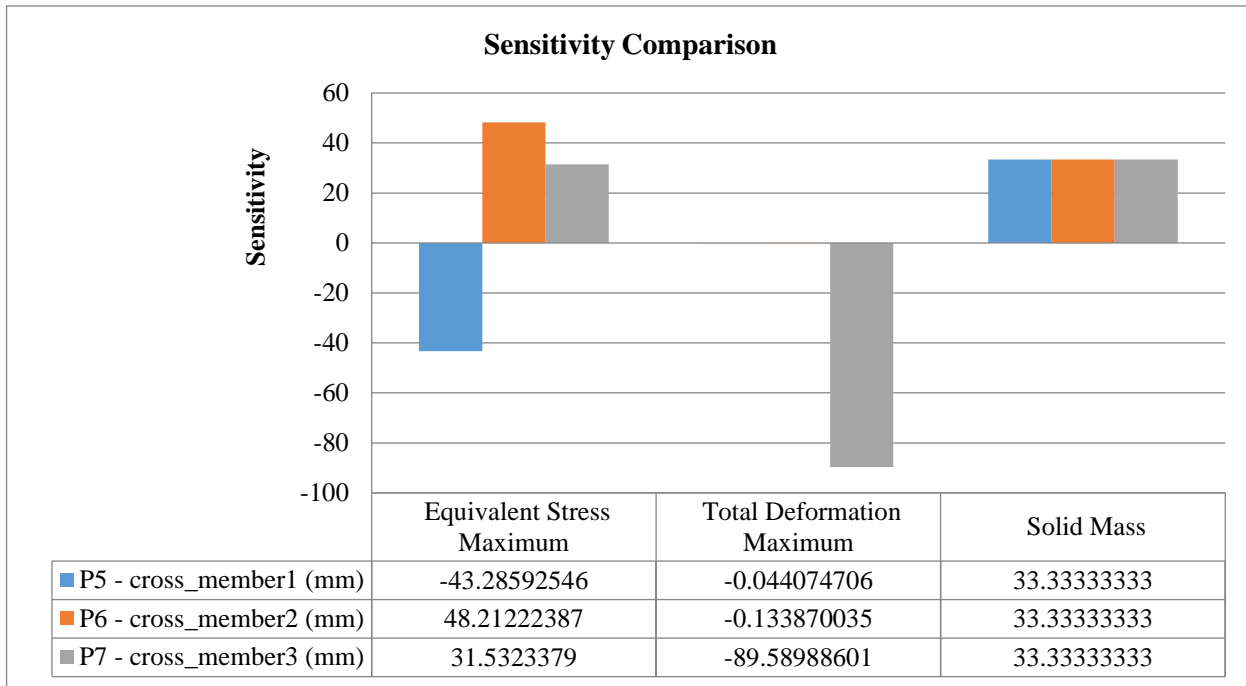
Figure 4.211: Sensitivity plot for OSF using Graphite Al GA 7-230 MMC

All three output parameters, equivalent-stress, deformation, and solid mass are generated in the sensitivity plot shown in figure 4.211. Cross-member 1 dimension has the highest sensitivity percentage for equivalent-stress, indicating that equivalent-stress has the greatest effect on cross-member 2 and the least effect on cross-member 3. Cross-member 3 has the highest sensitivity percentage for total deformation. All three optimization variables have the same effect on the mass of the chassis for solid mass.

4.5.3 Box Behnken Scheme using Graphite Al GA 7-230 MMC

The design points are generated using the Box Behnken (B-B) design. Different combinations of the cross-member 1, cross-member 2, and cross-member 3 dimensions are generated based on the Box Behnken scheme. The equivalent-stress, deformation, and solid mass are generated for each design point as shown in table 4.32. The maximum and minimum values of these output parameters are shown in table 4.33.

Table 4.32: DOE table for B-B Scheme using Graphite Al GA 7-230 MMC

A	B	C	D	E	F	G
Name	P5 - cross-member 1 (mm)	P6 - cross-member 2 (mm)	P7 - cross-member 3 (mm)	P3 - Equivalent-stress Max (MPa)	P4 - Total Deformation Maximum (mm)	P8 - Solid Mass (kg)
1.00	65.00	65.00	65.00	3277.61	783.34	66.99
2.00	58.50	58.50	65.00	3274.81	784.95	64.04
3.00	71.50	58.50	65.00	3519.97	783.12	66.99
4.00	58.50	71.50	65.00	3521.08	783.18	66.99
5.00	71.50	71.50	65.00	3505.58	781.53	69.94
6.00	58.50	65.00	58.50	3499.14	773.67	64.04
7.00	71.50	65.00	58.50	3454.27	780.46	66.99
8.00	58.50	65.00	71.50	3220.41	769.24	66.99
9.00	71.50	65.00	71.50	3224.27	767.57	69.94
10.00	65.00	58.50	58.50	3483.75	775.64	64.04
11.00	65.00	71.50	58.50	3236.77	773.35	66.99
12.00	65.00	58.50	71.50	3288.51	768.74	66.99
13.00	65.00	71.50	71.50	3417.05	767.14	69.94

Table 4.33: Maximum and minimum values for B-B Scheme using Graphite Al GA 7-230 MMC

1	A	B	C
	Name	Calculated Min	Calculated Max
2	P3 - Equivalent-stress Max (MPa)	3207.3	3531.8
3	P4 - Total Deformation Maximum (mm)	766.85	784.97
4	P8 - Solid Mass (kg)	62.564	71.416

The highest equivalent-stress obtained via optimization is 3531.8 MPa, whereas the minimum equivalent-stress obtained is 3207.3 MPa. Between maximum and minimum values, deformation and solid mass output show minimal variance. The mass of a chassis made of structural steel is 214.64 kg (Sub-section 4.3.2.2), while a chassis made of Graphite Al GA 7-230 is 62.564 kg.

Figure 4.212: Response-Surface plot of equivalent-stress vs cross-member 1 and cross-member 2 for B-B Scheme using Graphite Al GA 7-230 MMC

The red-coloured region on the Response-Surface plot of equivalent-stress displays two peaks as shown in figure 4.212. Higher equivalent-stress is observed for Cross-member 2 dimensions varying from 58.5mm to 60mm and while cross-member 1 dimensions vary from 59mm to 61mm. For places indicated in dark blue color, the equivalent-stress is found to be the lowest.
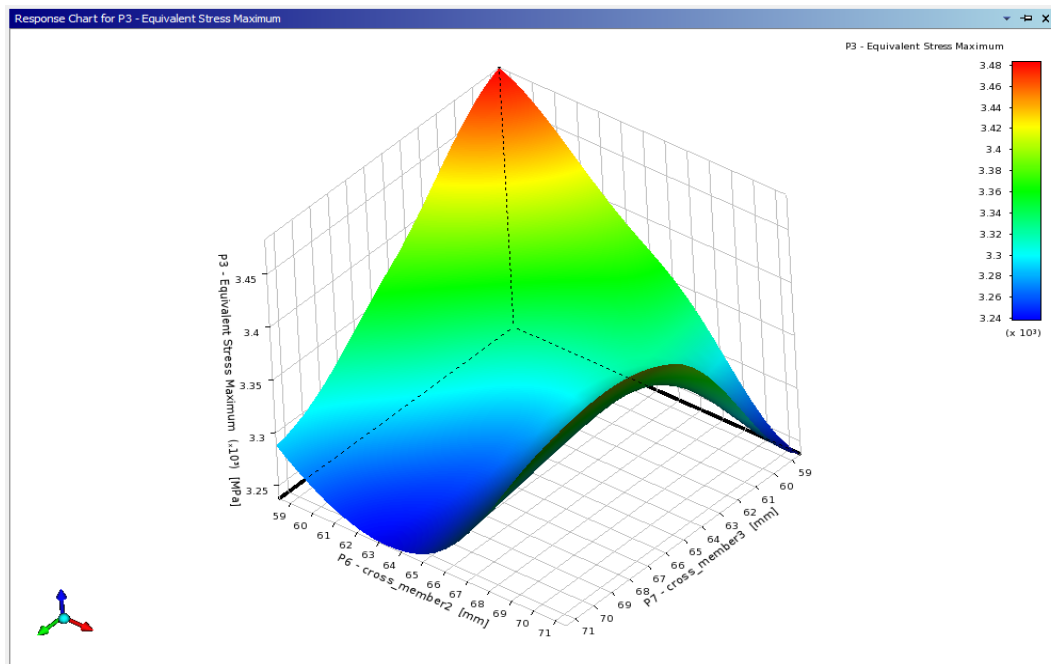
Figure 4.213: Response-Surface plot of equivalent-stress vs cross-member 2 and 3 for B-B Scheme using Graphite Al GA 7-230 MMC

Figure 4.213 shows a Response-Surface plot of equivalent-stress versus cross-member 2 and cross-member 3. The graph illustrates maximum equivalent-stress in the red-coloured region, with cross-member 2-dimensions varying from 59mm to 61mm and cross-member 3-dimensions varying from 59mm to 62mm. For the region depicted in dark blue, the equivalent-stress is at its lowest.
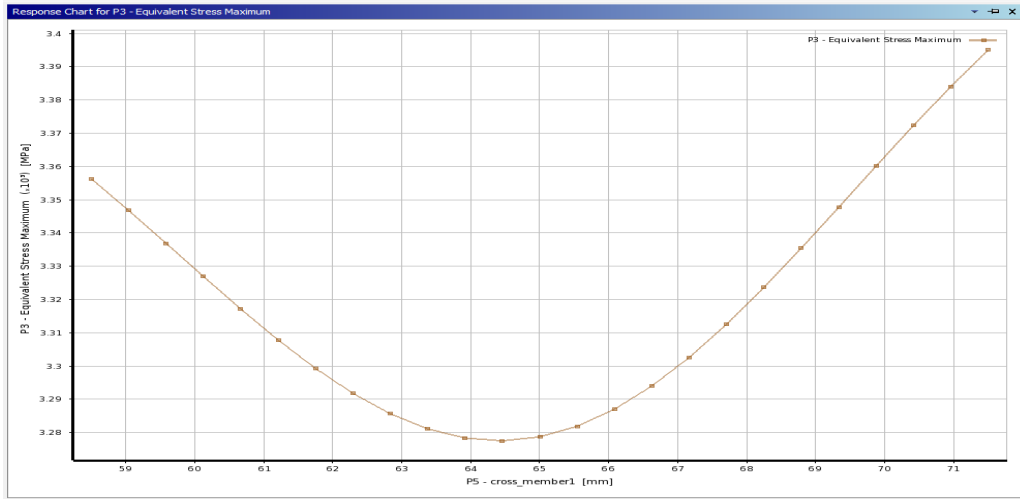
Figure 4.214: Equivalent-stress vs cross-member 1 for B-B Scheme using Graphite Al GA 7-230

Figure 4.214 illustrates the fluctuation of equivalent-stress versus cross member 1 dimensions. The equivalent-stress declines at first, reaching a minimum at cross-member 1 dimensions value of 64.5 mm and then climbs linearly to reach a maximum at cross-member 1 dimensions value of 71.5mm.
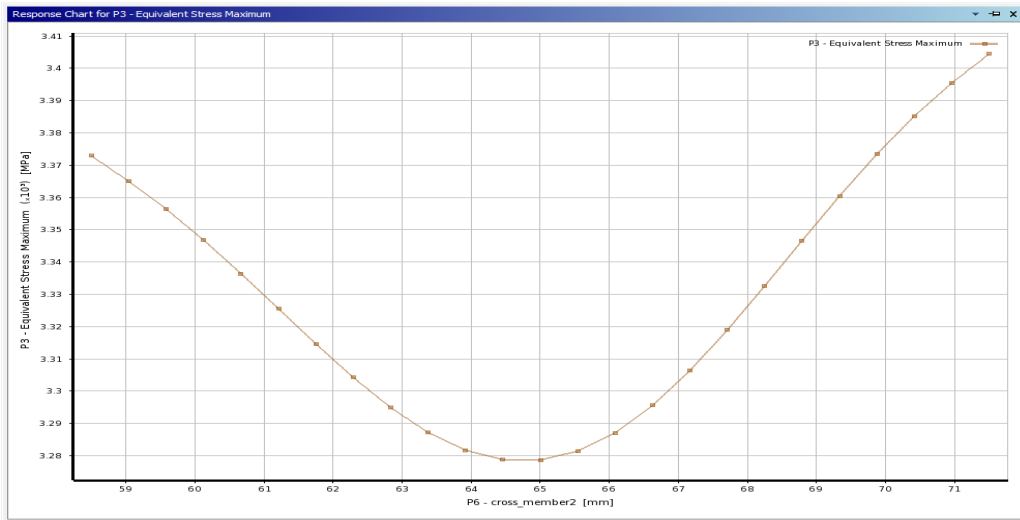
Figure 4.215: Equivalent-stress vs cross-member 2 for B-B Scheme using Graphite Al GA 7-230

Figure 4.215 illustrates the variations of equivalent-stress versus cross member 2 dimensions. The equivalent-stress drops up to cross member 2 dimension value of 65mm before increasing parabolically to a maximum, at cross member 2 dimensions value of 71.5mm.
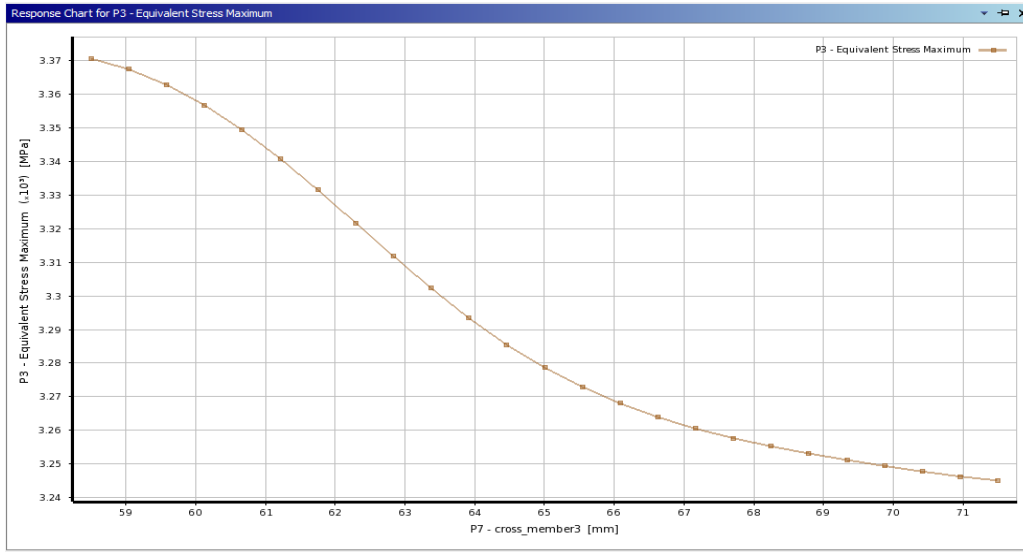
Figure 4.216: Equivalent-stress vs cross-member 3 for B-B Scheme using Graphite Al GA 7-230

Figure 4.216 illustrates the variation of equivalent-stress versus cross-member 3 dimensions. The high equivalent-stress initially reduces slowly until it reaches a minimum at, cross-member 3 dimensions value of 71.5mm.
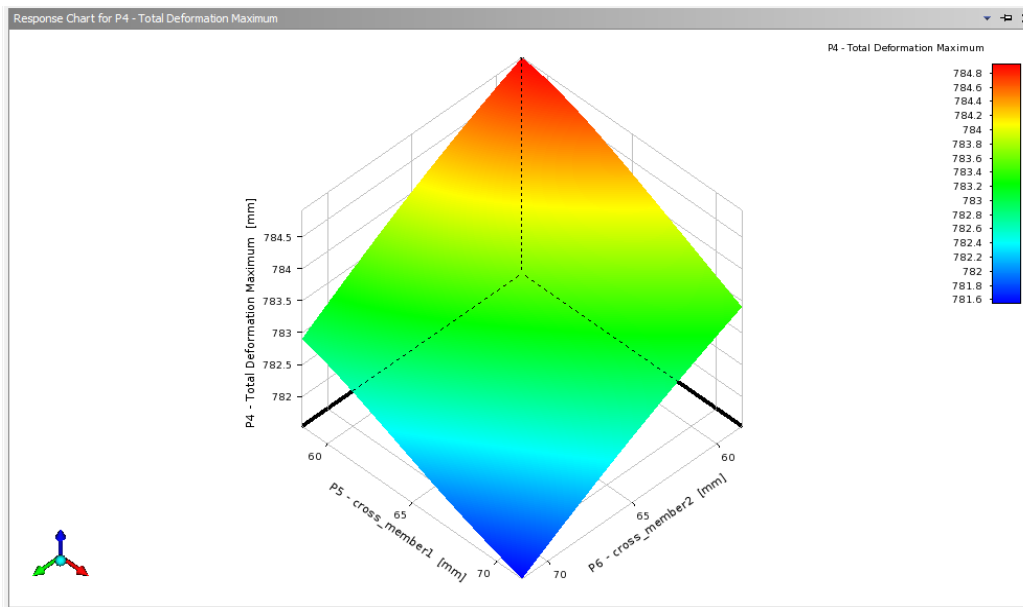
Figure 4.217: Response-Surface plot of total deformation vs cross-member 1 and cross-member 2 for B-B Scheme using Graphite Al GA 7-230 MMC

Figure 4.217 illustrates the Response-Surface plot of deformation cross-member 1 and cross-member 2 dimensions. Maximum deformation is shown for cross-member 2 dimensions varying from 59mm to 64mm and cross-member 1 dimensions varying from 59mm to 66mm. In the other dimensions, the deformation has a low value, which is represented by the blue zone.
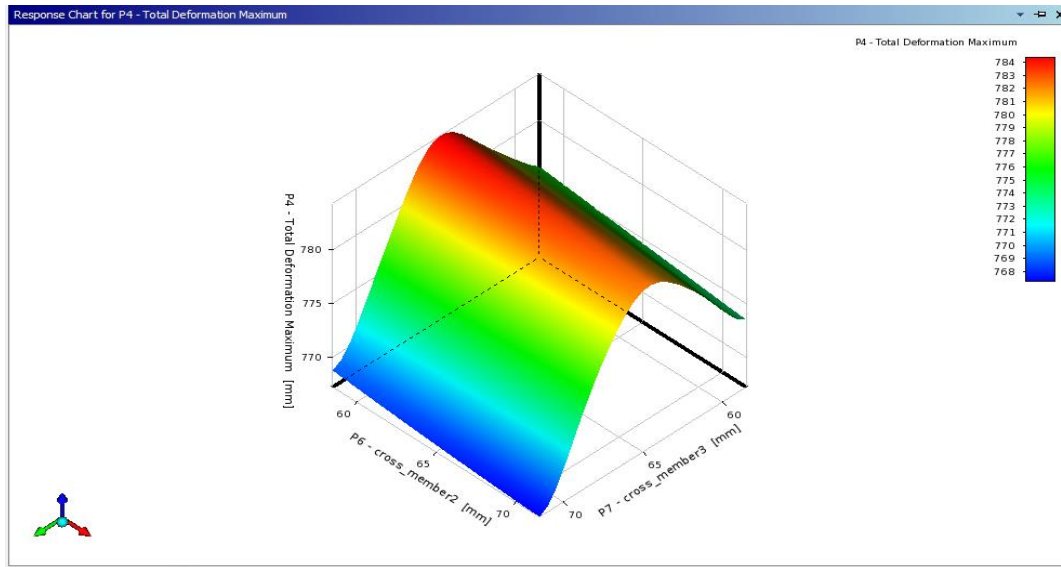
Figure 4.218: Response-Surface plot of total deformation vs cross-member 2 and cross-member 3 for B-B Scheme using Graphite Al GA 7-230 MMC

Figure 4.218 illustrates the variation of deformation vs. cross-member 2 and cross-member 3 dimensions. Deformation is higher (784.95 mm) for cross-member 3 dimensions varying from 62mm to 66mm and for cross-member 2 dimensions varying from 59mm to 71mm.
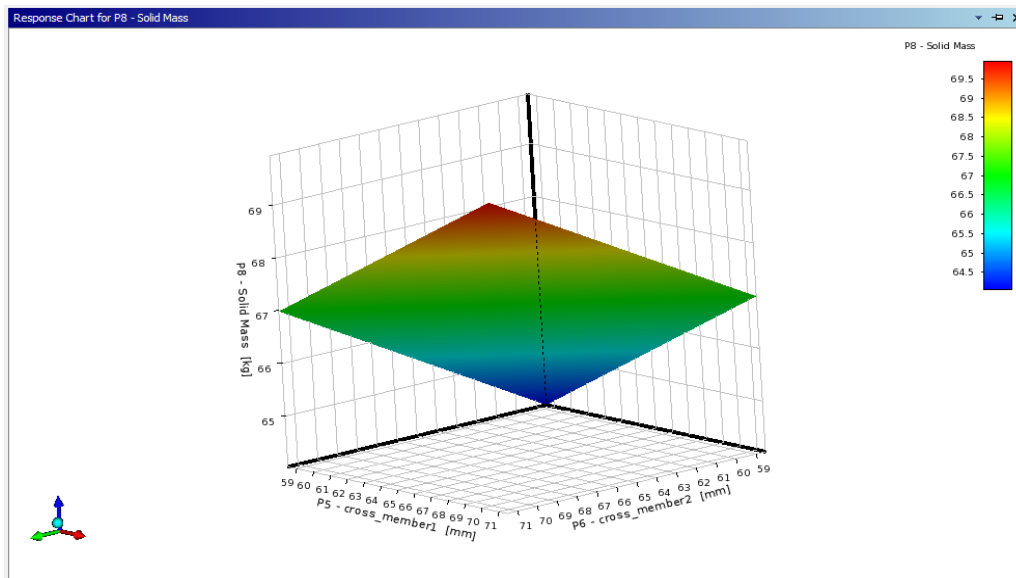
Figure 4.219: Response-Surface plot of mass vs cross-member 1 and cross-member 2 for B-B Scheme using Graphite Al GA 7-230 MMC

Figure 4.219 illustrates the variation in mass as a function of cross-member 1 and cross-member 2 dimensions. Maximum solid mass for cross-member 1 dimensions varying from 67mm to 71mm and cross-member 2 dimensions varying from 66mm to 71mm is shown in the graph. Cross-member 1 and cross-member 2 dimensions varying from 59mm to 64mm have the lowest mass of ~65 kg.

	Equivalent Stress Maximum	Total Deformation Maximum	Solid Mass
■ cross_member1 (mm)	36.20438489	-8.078516461	33.33333333
■ cross_member2 (mm)	38.51746279	-11.57309423	33.33333333
■ cross_member3 (mm)	-38.66247737	-85.34318513	33.33333333
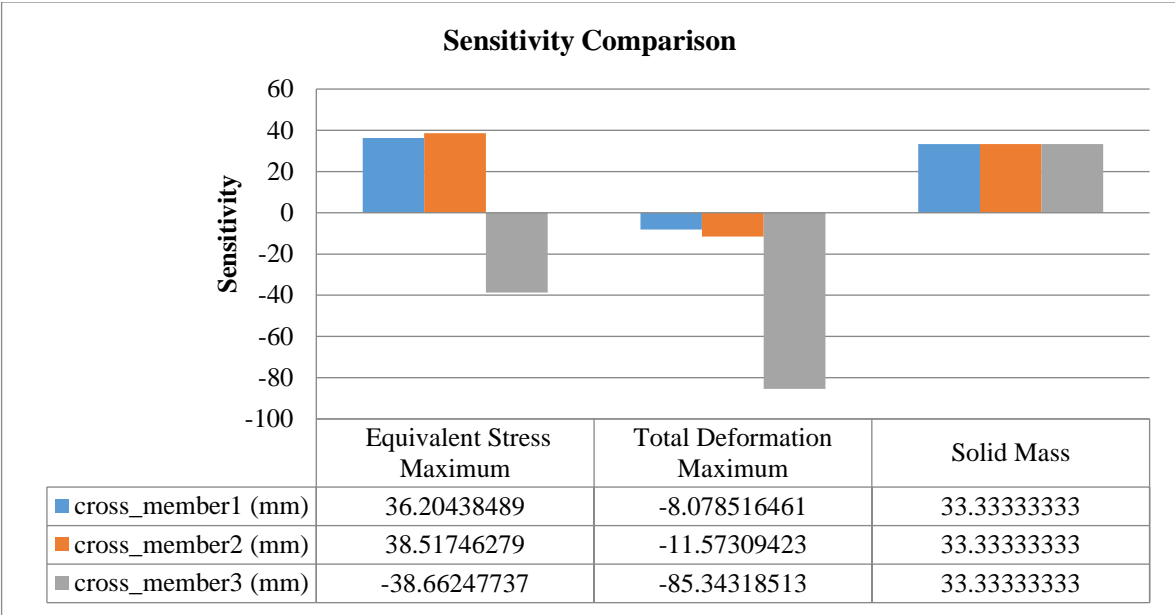
Figure 4.220: Sensitivity plot for B-B Scheme using Graphite Al GA 7-230 MMC

All three output parameters, equivalent-stress, deformation, and solid mass are generated in the sensitivity plot in figure 4.220. Cross-member 3 has the highest sensitivity percentage for equivalent-stress indicating that equivalent-stress has the most effect on cross-member 3 and has the least effect on cross-member 1. Cross-member 3 has the highest sensitivity % for total deformation. All three optimization variables have the same influence on the mass of the chassis.

4.5.4 Latin Hypercube Sampling using Graphite Al GA 7-230 MMC

The design points are generated using Latin Hypercube sampling (LHS) as shown in table 4.34. Different combinations of cross-member 1, cross-member 2, and cross-member 3 dimensions are generated based on the Latin Hypercube scheme. The equivalent-stress, deformation, and solid mass are generated for each design point. The maximum and minimum values of these output parameters are shown in table 4.35.

Table 4.34: DOE table for LHS using Graphite Al GA 7-230 MMC

A	B	C	D	E	F	G
Name	P5 - cross-member 1 (mm)	P6 - cross-member 2 (mm)	P7 - cross-member 3 (mm)	P3 - Equivalent-stress Max (MPa)	P4 - Total Deformation Maximum (mm)	P8 - Solid Mass (kg)
1.00	65.87	68.47	65.87	3459.62	78.08	68.17
2.00	68.47	65.00	66.73	3493.97	77.93	68.17
3.00	58.93	65.87	60.67	3512.16	79.55	64.83
4.00	67.60	58.93	70.20	3465.76	77.17	67.38
5.00	59.80	60.67	61.53	3391.49	79.31	64.04
6.00	71.07	59.80	59.80	3439.20	77.17	66.01
7.00	66.73	70.20	69.33	3441.64	77.31	69.55
8.00	70.20	67.60	68.47	3246.41	77.55	69.55
9.00	62.40	61.53	65.00	3267.07	78.41	65.61
10.00	61.53	66.73	71.07	3340.14	76.95	67.97
11.00	64.13	63.27	63.27	3277.09	78.75	66.01
12.00	60.67	69.33	62.40	3483.71	78.90	66.40
13.00	65.00	64.13	64.13	3486.33	78.53	66.60
14.00	69.33	71.07	58.93	3453.63	77.54	67.97
15.00	63.27	62.40	67.60	3331.45	77.91	66.60

Table 4.35: Maximum and minimum values for LHS using Graphite Al GA 7-230 MMC

1	A	B	C
	Name	Calculated Min	Calculated Max
2	P3 - Equivalent-stress Max (MPa)	3217.4	3522.2
3	P4 - Total Deformation Maximum (mm)	76.222	78.432
4	P8 - Solid Mass (kg)	62.564	71.416

The highest equivalent-stress obtained through optimization is 3522.2 MPa, while the minimum equivalent-stress obtained through optimization is 3217.4 MPa. The maximum and minimum values of deformation and solid mass output vary less. The solid mass with structural steel is 214.64 kg (sub-section 4.3.2.2), while the minimum solid mass with Graphite Al GA 7-230 MMC is 62.564 kg.
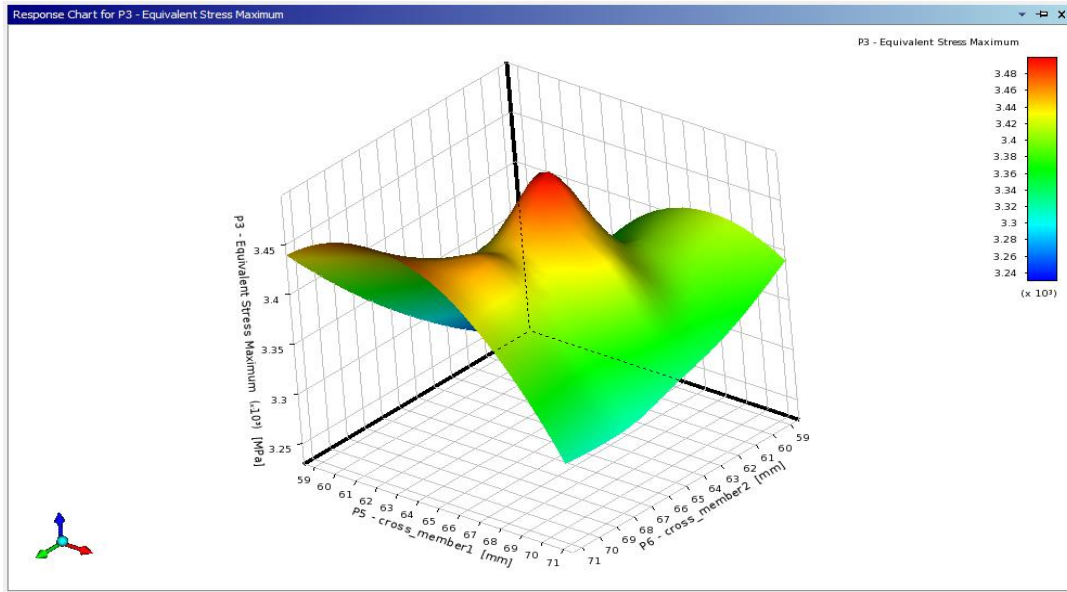
Figure 4.221: Response-Surface plot of equivalent-stress vs cross-member 1 and cross-member 2 for LHS using Graphite Al GA 7-230 MMC

Figure 4.221 illustrates a Response-Surface plot of equivalent-stress with two peaks depicted in red. The maximum equivalent-stress is obtained for cross-member 2 with a length varying from 61mm to 64mm and cross-member 1 with a length varying from 62mm to 66mm. The equivalent-stress is found to be lowest in regions represented by dark blue color.
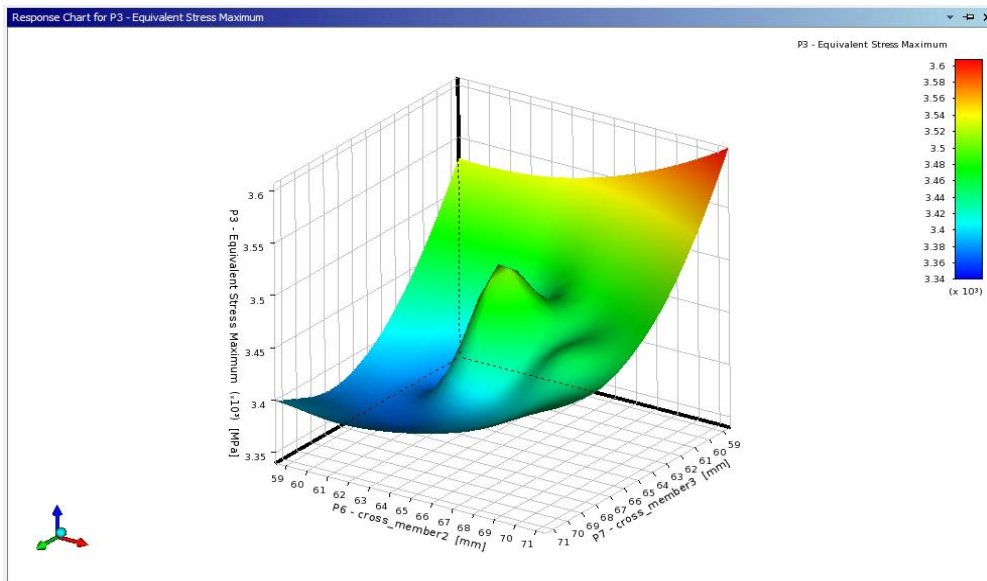
Figure 4.222: Response-Surface plot of equivalent-stress vs cross-member 2 and cross-member 3 for LHS using Graphite Al GA 7-230 MMC

Figure 4.222 illustrates the Response-Surface plot of equivalent-stress vs cross-member 2 and cross-member 3 dimensions. The plot illustrates the maximum equivalent-stress in the red region, where

the cross-member 2-dimension ranges from 66mm to 71mm and the cross-member 3-dimension ranges from 59mm to 62mm. The equivalent-stress is lowest in the region depicted in dark blue.
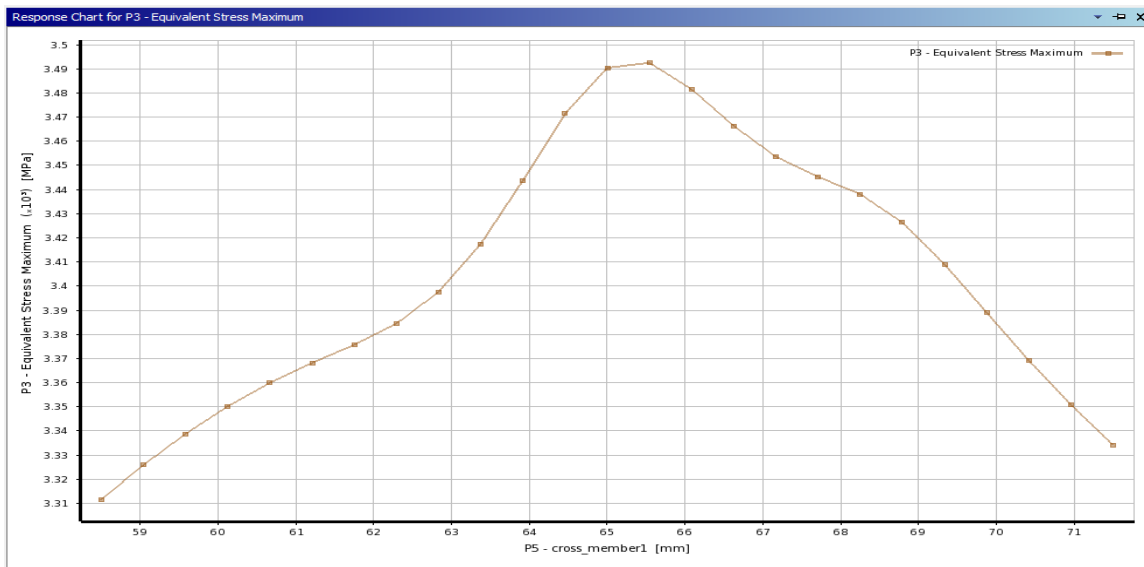
Figure 4.223: Equivalent-stress vs cross-member 1 for LHS using Graphite Al GA 7-230 MMC

Figure 4.223 illustrates the fluctuation of equivalent-stress vs cross-member 1 dimensions. The equivalent-stress grows until it reaches the 65.5mm cross-member 1 dimension, after which it drops linearly downwards.
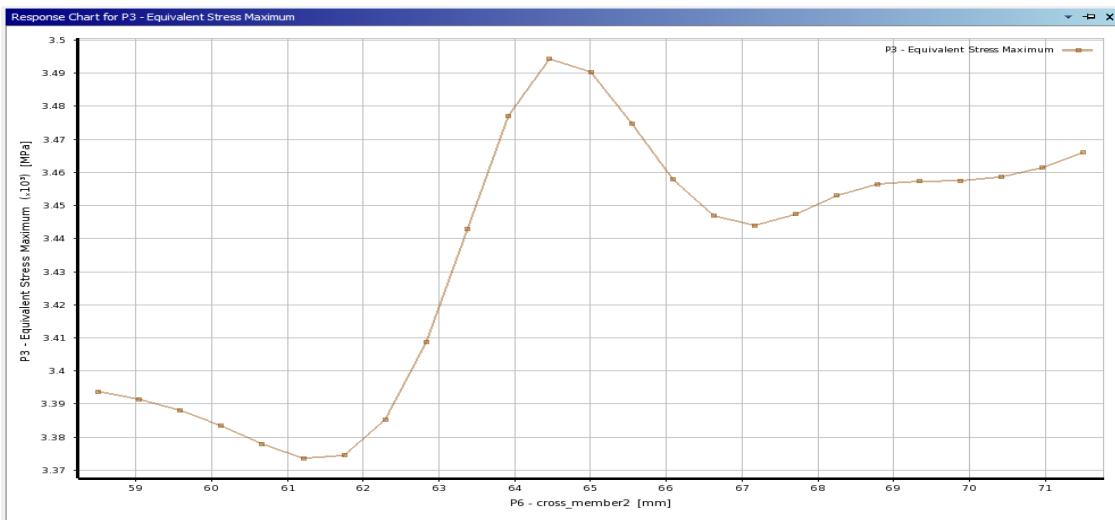
Figure 4.224: Equivalent-stress vs cross-member 2 for LHS using Graphite Al GA 7-230 MMC

Figure 4.224 illustrates the fluctuation of equivalent-stress versus cross member 2 dimensions. The equivalent-stress reduces until it reaches cross member 2 dimension value of 61.7mm, then climbs linearly to cross member 2 dimension value of 64.5mm. After that, the equivalent-stress reduces.

Figure 2.225: Equivalent-stress vs cross-member 3 for LHS using Graphite Al GA 7-230 MMC

Figure 4.225 illustrates the variation of equivalent-stress vs cross member 3 dimensions. The equivalent-stress reduces linearly until it reaches a minimum at cross member 3 dimension value of 62 mm, then increases to a high, cross member 3 dimension value of 64.5mm. After then, the equivalent-stress reduces exponentially.
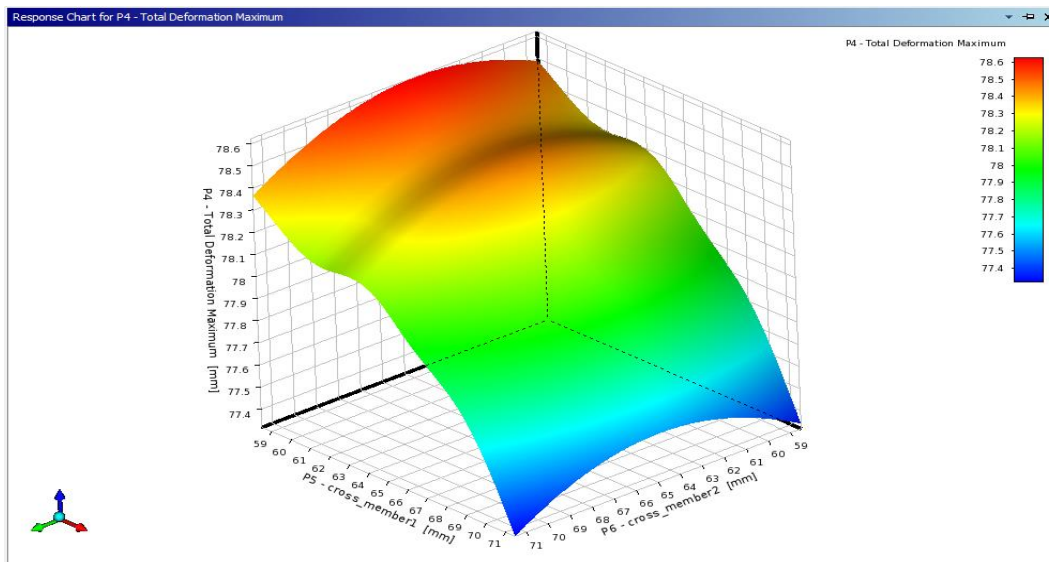
Figure 4.226: Response-Surface plot of total deformation vs cross-member 1 and cross-member 2 for LHS using Graphite Al GA 7-230 MMC

Figure 4.226 illustrates the Response-Surface plot of deformation cross-member 1 and cross-member 2 dimensions. Maximum deformation for cross-member 2 dimensions varying from 59mm to 71mm

and cross-member 1 dimensions varying from 59mm to 64mm is shown in the graph. The deformation in other dimensions indicates low values, which are represented by the blue-coloured zone.
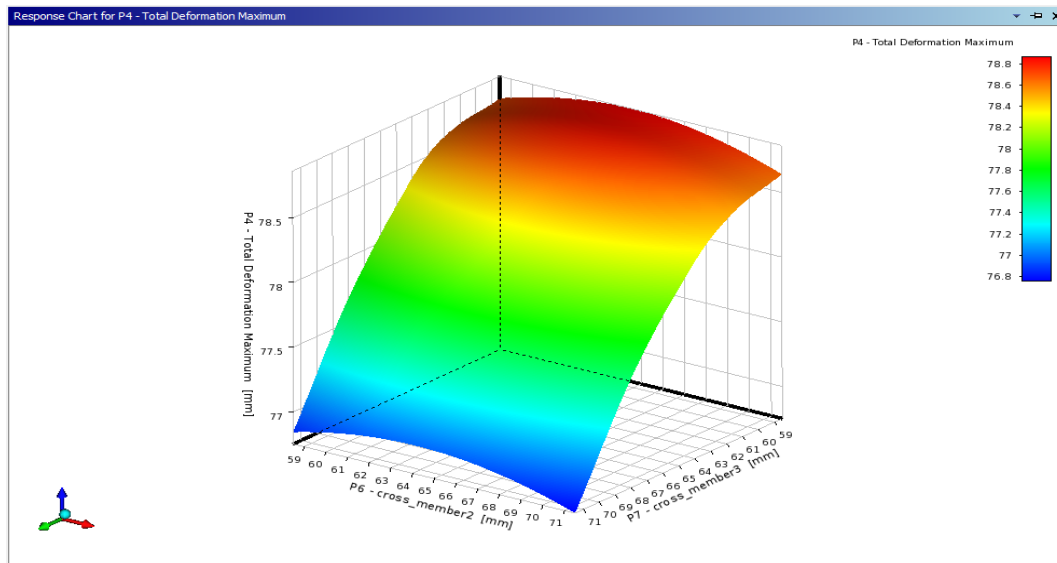
Figure 4.227: Response-Surface plot of total deformation vs cross-member 2 and cross-member 3 for LHS using Graphite Al GA 7-230 MMC

Figure 4.227 illustrates the fluctuation of deformation vs. cross-member 2 and cross-member 3 dimensions. Cross-member 3 dimensions varying from 59mm to 64mm and cross-member 2 dimensions varying from 59mm to 71mm show the most distortion.
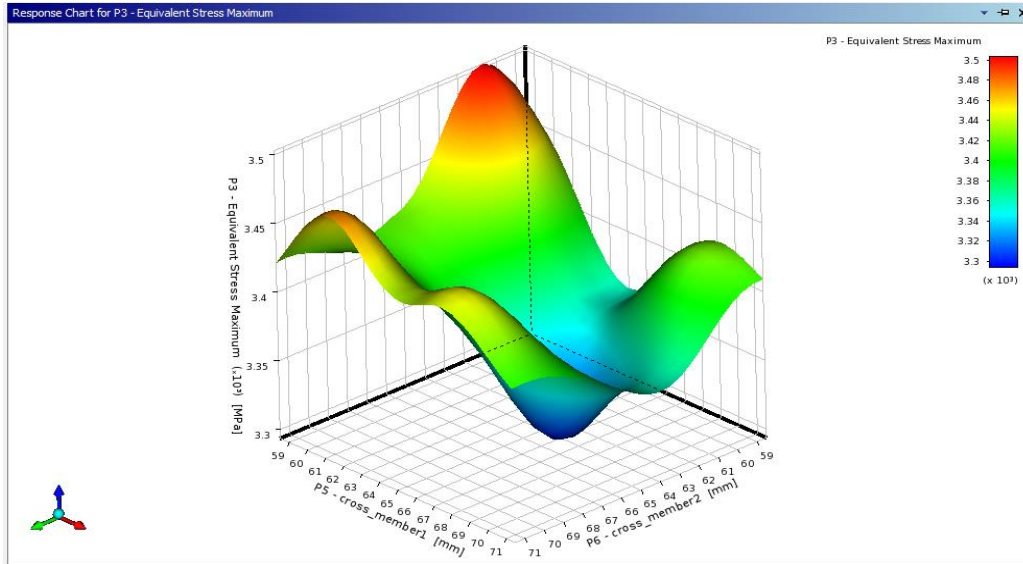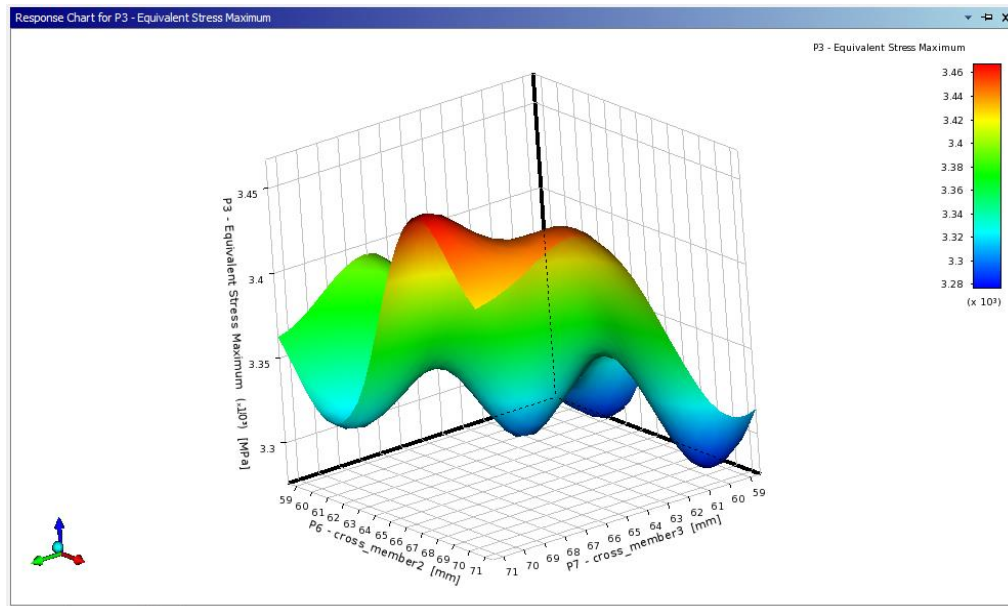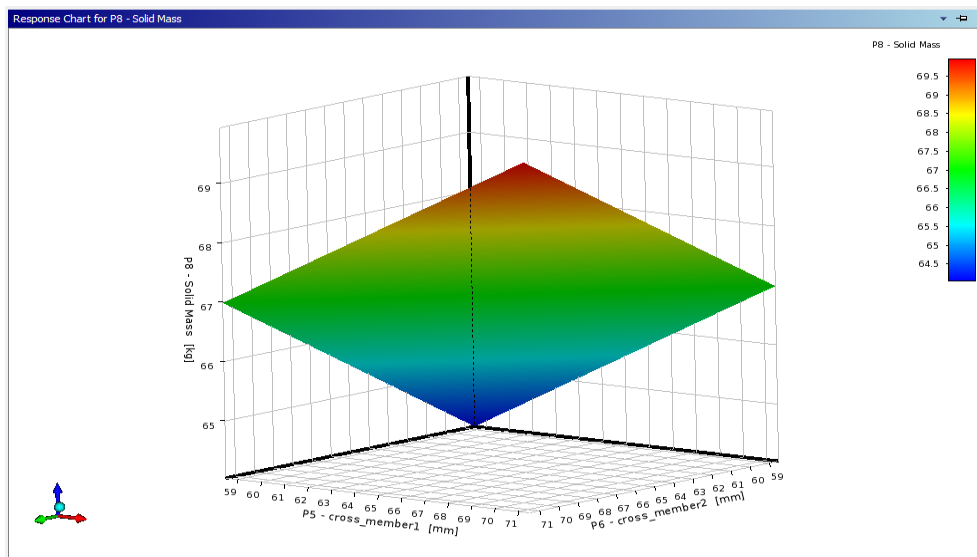

Figure 4.228: Response-Surface plot of mass vs cross-member 1 and cross-member 2 for LHS using Graphite Al GA 7-230 MMC

Figure 4.228 illustrates the variation in mass as a function of cross-member 1 and cross-member 2 dimensions. Maximum solid mass for cross-member 1 dimensions varying from 67mm to 71mm and

cross-member 2 dimensions varying from 66mm to 71mm is shown in the graph. Cross-member 1 and cross-member 2 dimensions varying from 59mm to 64mm have the lowest mass.

Sensitivity Comparison

	Equivalent Stress Maximum	Total Deformation Maximum	Solid Mass
■ P5 - cross_member1 (mm)	36.58321867	-33.23625812	33.33333333
■ P6 - cross_member2 (mm)	24.25318287	-8.299112678	33.33333333
■ P7 - cross_member3 (mm)	-32.16320222	-58.14419352	33.33333333
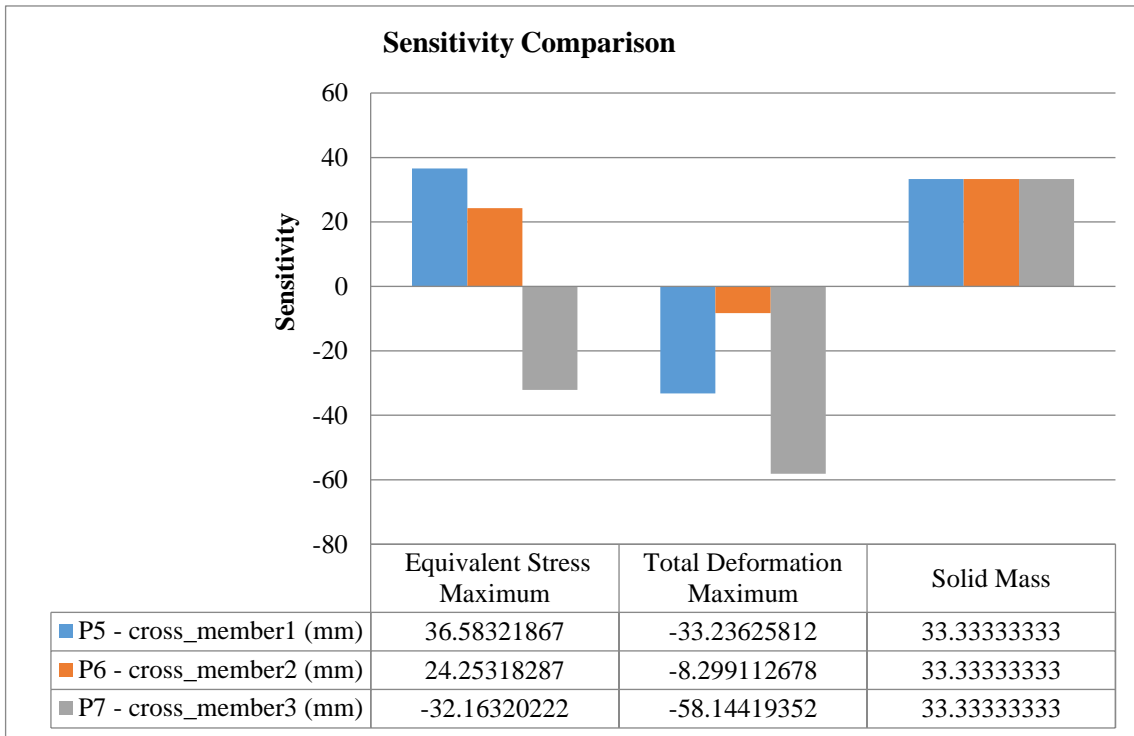
Figure 4.229: Sensitivity plot for LHS using Graphite Al GA 7-230 MMC

All three output parameters, equivalent-stress, deformation, and solid mass are created in the sensitivity plot shown in figure 4.229. Cross-member 1 dimension value has the highest sensitivity percentage for equivalent-stress indicating that equivalent-stress has the most effect on cross-member 1 and the least effect on cross-member 2. Cross-member 3 has the highest sensitivity % for total deformation. All three optimization variables have the same influence on the mass of the chassis.

4.5.5 Sparse grid initialization using Graphite Al GA 7-230 MMC

The design points are generated using sparse grid initialization (SGI) as shown in table 4.36. Different combinations of the cross-member 1, cross-member 2, and cross-member 3 dimensions are generated based on the Sparse grid initialization scheme. The equivalent-stress, deformation, and solid mass are generated for each design point as shown in table 4.36. The maximum and minimum values of these output parameters are shown in table 4.37.

Table 4.36: DOE table for SGI using Graphite Al GA 7-230 MMC

A	B	C	D	E	F	G
Name	P5 - cross-member 1 (mm)	P6 - cross-member 2 (mm)	P7 - cross-member 3 (mm)	P3 - Equivalent-stress Max (MPa)	P4 - Total Deformation Maximum (mm)	P8 - Solid Mass (kg)
1	65	65	65	3277.61	783.34	66.98
2	58.5	65	65	3261.58	784.32	65.51
3	71.5	65	65	3514.87	782.61	68.46
4	65	58.5	65	3270.73	784.02	65.51
5	65	71.5	65	3522.24	782.31	68.46
6	65	65	58.5	3256.64	775.45	65.51
7	65	65	71.5	3217.42	768.29	68.46

Table 4.37: Maximum and minimum values for SGI using Graphite Al GA 7-230 MMC

# Output Parameter Maximums						
Name	P5 - cross-member 1 (mm)	P6 - cross-member 2 (mm)	P7 - cross-member 3 (mm)	P3 - Equivalent-stress Max (MPa)	P4 - Total Deformation Maximum (mm)	P8 - Solid Mass (kg)
P3 - Equivalent-stress Max	71.5	71.38033	71.5	3723.709	783.5003	69.72
P4 - Total Deformation Max	58.5	58.5	71.5	3292.185	786.5691	65.14
P8 - Solid Mass	71.5	71.5	71.5	3723.688	783.4792	69.73
# Output Parameter Minimums						
Name	P5 - cross-member 1 (mm)	P6 - cross-member 2 (mm)	P7 - cross-member 3 (mm)	P3 - Equivalent-stress Max (MPa)	P4 - Total Deformation Maximum (mm)	P8 - Solid Mass (kg)
P3 - Equivalent-stress Max	58.5	69.54491	58.5	3186.461	781.3651	65.61
P4 - Total Deformation Max	71.5	71.5	58.5	3547.078	779.1445	68.88
P8 - Solid Mass	58.5	58.5	58.5	3243.149	782.2981	64.21

The extreme equivalent-stress obtained through optimization is 3723.7 MPa, while the minimum equivalent-stress obtained through optimization is 3186.5 MPa. The maximum and minimum values of deformation and solid mass output vary less. The solid mass with structural steel is 214.64 kg, while the solid mass with Graphite Al GA 7-230 MMC is 64.219 kg.
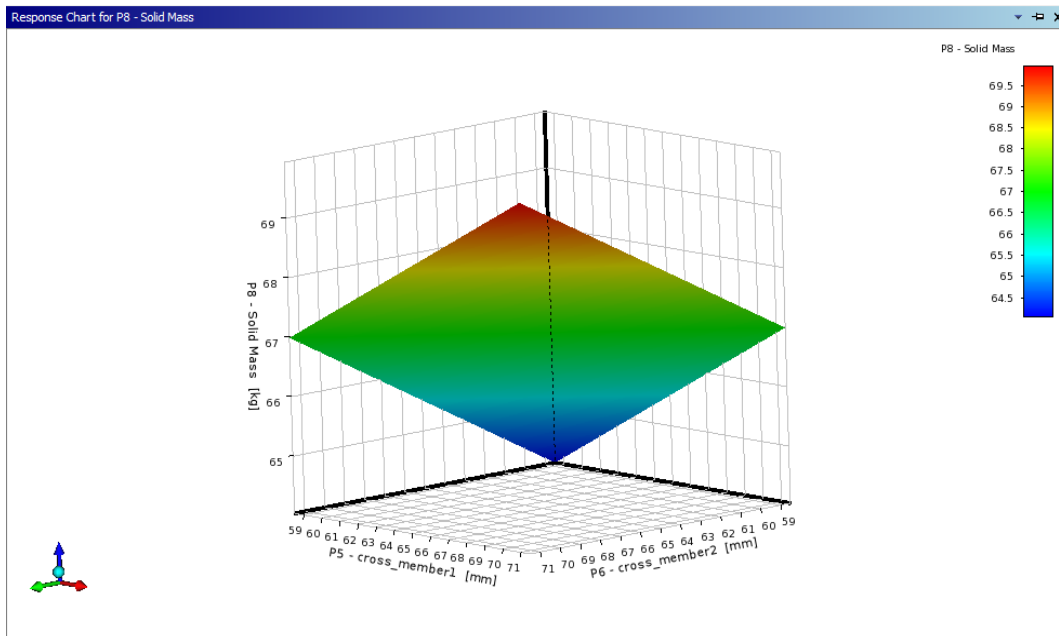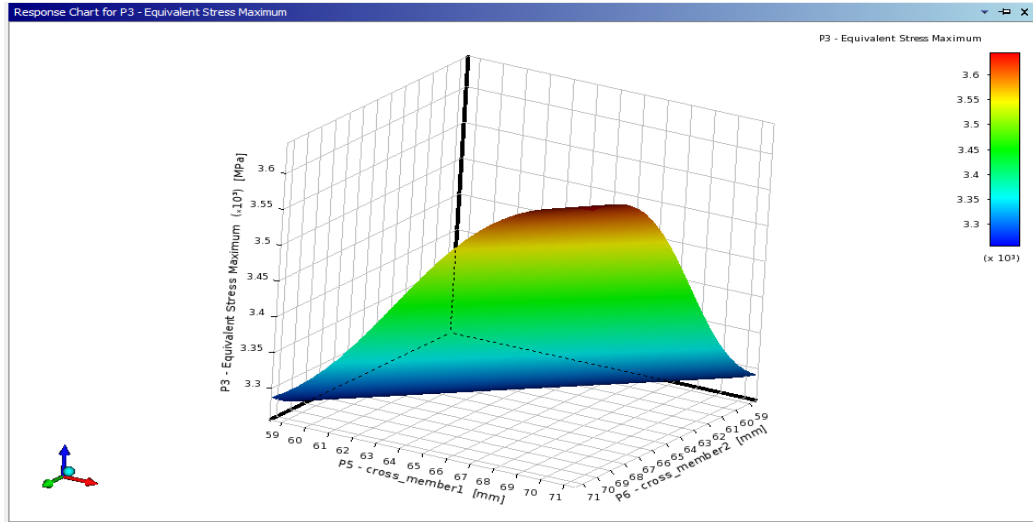

Figure 4.230: Response-Surface plot of equivalent-stress vs cross-member 1 and cross-member 2 for SGI using Graphite Al GA 7-230 MMC

Figure 4.230 displays a Response-Surface plot of equivalent-stress with two peaks in the red-coloured region. Higher equivalent-stress is observed at cross-member 2 dimension values vary from 67mm to 71mm and cross-member 1 dimension values vary from 66mm to 71mm. For places indicated in dark blue color, the equivalent-stress is found to be the lowest.

Figure 4.231: Response-Surface plot of equivalent-stress vs cross-member 2 and cross-member 3 for SGI using Graphite Al GA 7-230 MMC

Figure 4.231 shows a Response-Surface plot of equivalent-stress versus cross-member 2 and cross-member 3 dimensions. The graph illustrates maximum equivalent-stress in the red-coloured zone, with cross-member 2-dimensions varying from 68mm to 71mm and cross-member 3-dimensions varying from 67mm to 71mm. For the region depicted in dark blue, the equivalent-stress is at its lowest.

Figure 4.232: Equivalent-stress vs cross-member 1 for SGI using Graphite Al GA 7-230 MMC

Figure 4.232 illustrates the fluctuation of equivalent-stress vs cross-member 1 dimensions. The equivalent-stress remains constant up to cross-member 1 dimension of 62mm and grows rapidly up to the cross-member 1 dimension of 71.5mm.
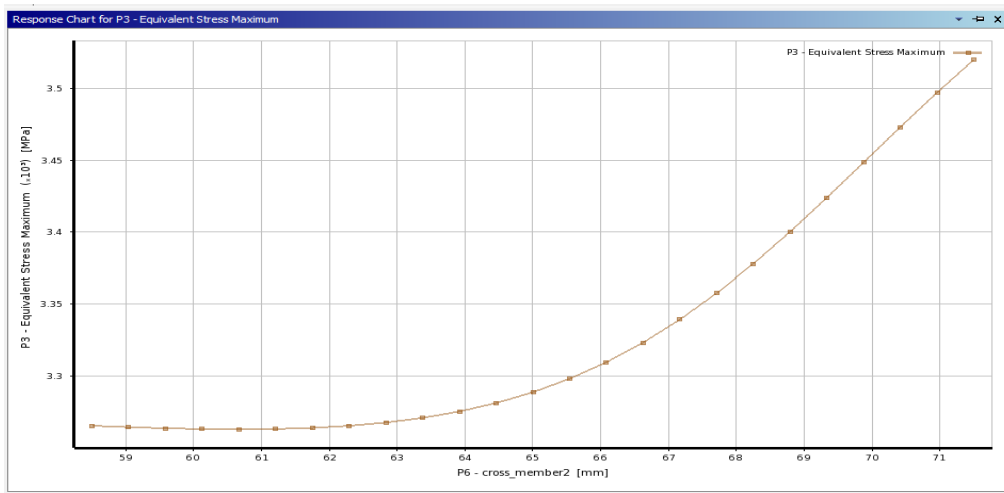
Figure 4.233: Equivalent-stress vs cross-member 2 for SGI using Graphite Al GA 7-230 MMC

Figure 4.233 illustrates the fluctuation of equivalent-stress versus cross member 2 dimensions. The equivalent-stress grows exponentially until it reaches its maximum at cross member 2 dimension value of 61.7mm.

Figure 4.234: Equivalent-stress vs cross-member 3 for SGI using Graphite Al GA 7-230 MMC

Figure 4.234 illustrates the variation of equivalent-stress vs cross member 3 dimensions. The equivalent-stress increases linearly and reaches a maximum at the cross-member-3-dimension value of 71.5mm.

Figure 4.235: Response-Surface plot of total deformation vs cross-member 1 and cross-member 2 for SGI using Graphite Al GA 7-230 MMC

Figure 4.235 illustrates the Response-Surface plot of deformation cross-members 1 and 2 dimensions. Maximum deformation is shown for cross-member 2 dimensions varying from 67mm to 71mm and

cross-member 1 dimensions varying from 67mm to 71mm. In the other dimensions, the deformation has low values, which is represented by the blue zone.

Figure 4.236: Response-Surface plot of total deformation vs cross-member 2 and 3 for SGI using Graphite Al GA 7-230 MMC

Figure 4.236 illustrates the variation of deformation vs. cross-member 2 and cross-member 3 dimensions. Cross-member 3 dimensions varying from 67mm to 71mm and cross-member 2 dimensions varying from 67mm to 71mm show the most distortion. Figure 4.237 illustrates the variation of mass vs. cross-member 1 and cross-member 2 dimensions.
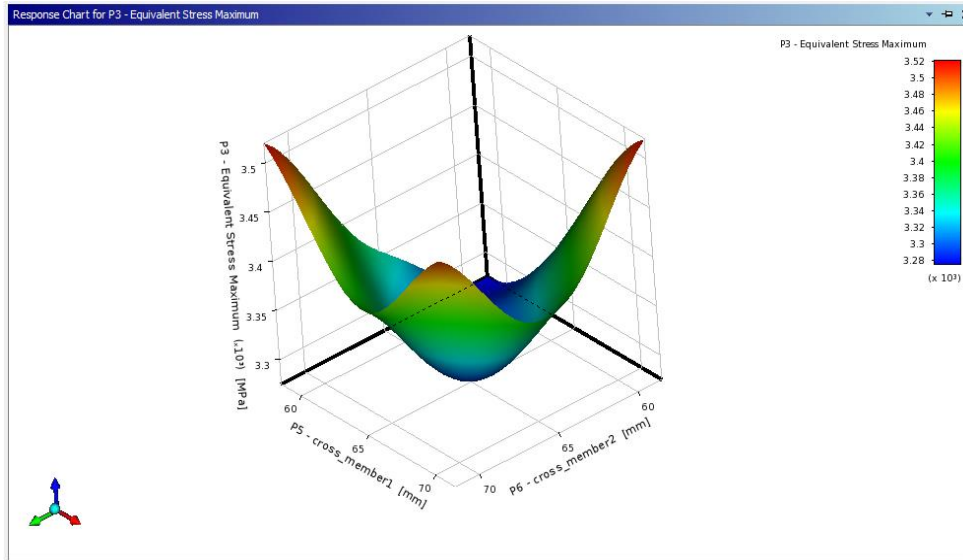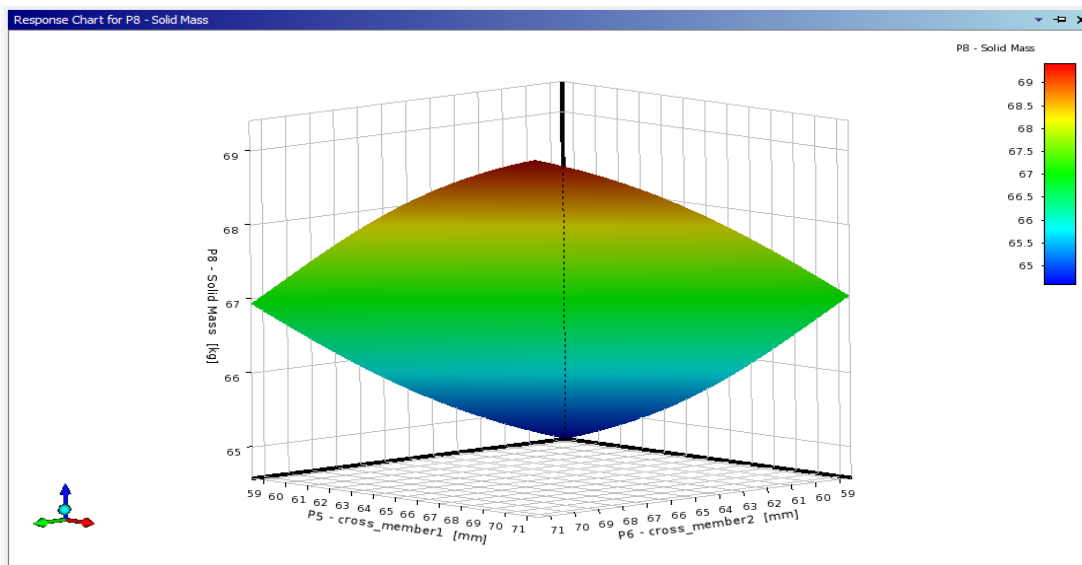

Figure 4.237: Response-Surface plot of mass vs cross-member 1 and cross-member 2 for SGI using Graphite Al GA 7-230 MMC

The maximum solid mass is shown for cross-member 1 dimensions varying from 67mm to 71mm and cross-member 2 dimensions varying from 66mm to 71mm. Cross-member 1 and cross-member 2 dimensions varying from 59mm to 64mm have the lowest mass.

The sensitivity diagram, shown in Figure 4.238, is constructed for all three output parameters: equivalent-stress, deformation, and solid mass. Cross-member 1 has the largest sensitivity % for equivalent-stress. The cross-member 3 has the highest total deformation sensitivity %.

Sensitivity Comparison

	Equivalent Stress Maximum	Total Deformation Maximum	Solid Mass
■ cross_member1 (mm)	47.43668755	-9.336696117	53.52337144
■ cross_member2 (mm)	47.66320841	-9.402009699	53.52337102
■ cross_member3 (mm)	28.93381056	22.49412108	33.15028024
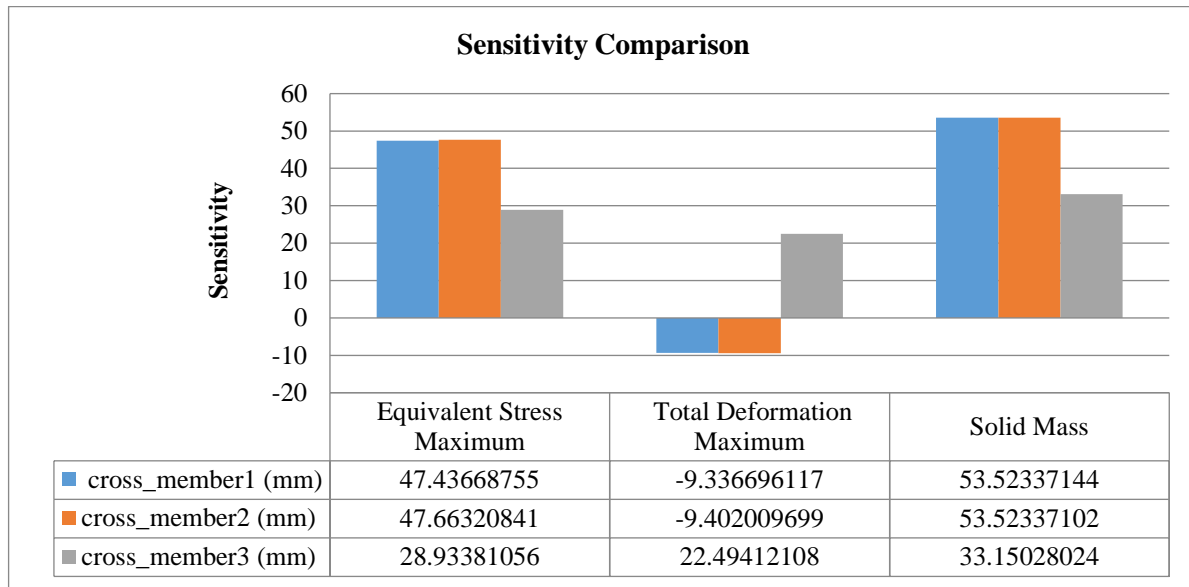
Figure 4.238: Sensitivity plot for SGI using Graphite Al GA 7-230 MMC

For solid mass, cross-member 1 and cross-member 2 have the same sensitivity percentage whereas cross-member 3 has a minimum sensitivity percentage of 33.15028024

4.5.6 Sub-Chapter Summary

Sub-Chapter has shown the application of optimization techniques in improving the design of chassis made of Graphite Al GA 7-230 material. The effect of optimization variables on equivalent-stress, deformation, and solid mass is discerned from 3D Response-Surface plots, 2D linearized plots, and sensitivity plots which is one of the key specific objectives of the study. The maximum solid mass obtained from optimization is 70.589 kg, and the minimum solid mass obtained from the analysis is 63.391 kg. The optimization results have shown that cross-member 3 causes maximum chassis deformation as compared to other variables.

The next sub-chapter investigates the application of different optimization techniques using Al 6092/SiC/17.5P MMC material in line with sections 1.4 and 1.5.

4.6 Response-Surface Optimization using Al 6092/SiC/17.5P MMC with square section chassis

The current Sub-chapter demonstrates the use of various optimization techniques, such as central composite design, optimal space-filling design, sparse grid initialization, Latin hypercube sampling, and Box-Behnken design, on heavy motor vehicles chassis made of Al 6092/SiC/17.5P MMC material. Using 3D Response-Surface plots and sensitivity plots, the effect of various design variables on equivalent-stress, deformation, and mass is evaluated.

4.6.1 Central Composite Design Scheme using Al 6092/SiC/17.5P MMC

Using Finite Element Analysis, the software analyzed the output parameters at these design points. As illustrated in columns E and F of Table 4.38, these output parameters are equivalent-stress and total deformation.

Table 4.38: DOE Table for CCD scheme using Al 6092/SiC/17.5P MMC

A	B	C	D	E	F	G
Name	P5 - cross-member 1 (mm)	P6 - cross-member 2 (mm)	P7 - cross-member 3 (mm)	P3 - Equivalent-stress Max (MPa)	P4 - Total Deformation Maximum (mm)	P8 - Solid Mass (kg)
1.00	65.00	65.00	65.00	3277.61	694.83	76.56
2.00	58.50	65.00	65.00	3261.58	695.69	74.87
3.00	71.50	65.00	65.00	3514.87	694.18	78.25
4.00	65.00	58.50	65.00	3270.74	695.43	74.87
5.00	65.00	71.50	65.00	3522.25	693.91	78.25
6.00	65.00	65.00	58.50	3256.64	687.83	74.87
7.00	65.00	65.00	71.50	3217.43	681.48	78.25
8.00	59.72	59.72	59.72	3344.10	683.96	72.45
9.00	70.28	59.72	59.72	3429.54	683.50	75.19
10.00	59.72	70.28	59.72	3435.59	683.08	75.19
11.00	70.28	70.28	59.72	3312.01	682.25	77.93
12.00	59.72	59.72	70.28	3461.23	684.31	75.19
13.00	70.28	59.72	70.28	3228.51	683.43	77.93
14.00	59.72	70.28	70.28	3291.50	683.33	77.93
15.00	70.28	70.28	70.28	3458.88	682.45	80.67

Design point number two (2) exhibits the greatest deformation, while design point number seven exhibits the least deformation (7). The dimensions for design point number two (2) are as follows:

- 58.5 mm for cross-member 1, 65 mm for cross-member 2, and 65 mm for cross-member 3. The magnitude of maximum deformation obtained from the analysis is 695.69 mm and the magnitude of lowest deformation obtained from the analysis is 681.48 mm.

The maximum solid mass achieved through optimization is 80.673 kg at design point 15, while the minimum solid mass obtained from the analysis is 72.447 kg at design point 8. For

optimization variables, the Response-Surface plot is used to determine the range of values for which equivalent-stress is largest or least. A Response-Surface plot of equivalent-stress against cross-member 1 dimension and cross-member 2 dimensions is shown in figure 4.239.

Figure 4.239: Response-Surface plot of equivalent-stress vs cross-member 1 and cross-member 2 for CCD scheme using Al 6092/SiC/17.5P MMC

In the red-coloured region, two peaks of equivalent-stress can be seen. The equivalent-stress is highest for cross-member 1 dimensions varying from 62mm to 67mm and cross-member 2 dimensions varying from 69mm to 71mm, according to the first peak that formed along the cross-member 1 dimension. The equivalent-stress is highest for cross-member 1 dimensions varying from 69mm to 71mm and cross-member 2 dimensions varying from 61mm to 67mm, according to the second peak that formed along the cross-member 2 dimension. Other dimensions of cross-member 1 and cross-member 2 have the lowest equivalent-stress, as seen in the dark blue coloured region.

Figure 4.240: Response-Surface plot of equivalent-stress vs cross-member 2 and cross-member 3 for CCD scheme using Al 6092/SiC/17.5P MMC

Figure 4.240 shows a Response-Surface plot of equivalent-stress versus cross-member 2 and cross-member 3 dimensions. As demonstrated in the red-coloured region, there is a single peak of equivalent-stress. The interpolation approach is used to find the dimensions corresponding to maximal equivalent-stress. Cross-member 3-dimension values vary from 61mm to 67mm and cross-member 2-dimension values varying from 69mm to 71mm have the highest equivalent-stress. For other values of cross-member 2 and cross-member which is represented by a dark blue coloured region, the equivalent-stress is the lowest.
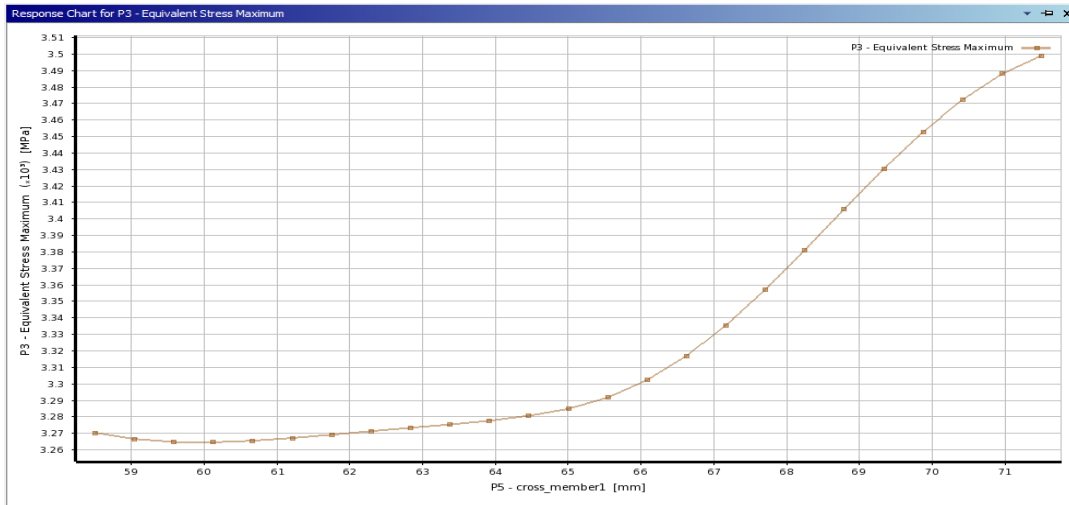
Figure 4.241: Equivalent-stress vs cross-member 1 for CCD using Al 6092/SiC/17.5P MMC

Figure 4.241 illustrates the variation of equivalent-stress with respect to cross-member 1 dimensions. The graph illustrates a progressive increase in equivalent-stress until it reaches at cross-member 1 dimension value of 65mm. At a cross-member 1 dimension of 71mm, the equivalent-stress increases exponentially and reaches the maximum value of 3.510×10^3MPa.
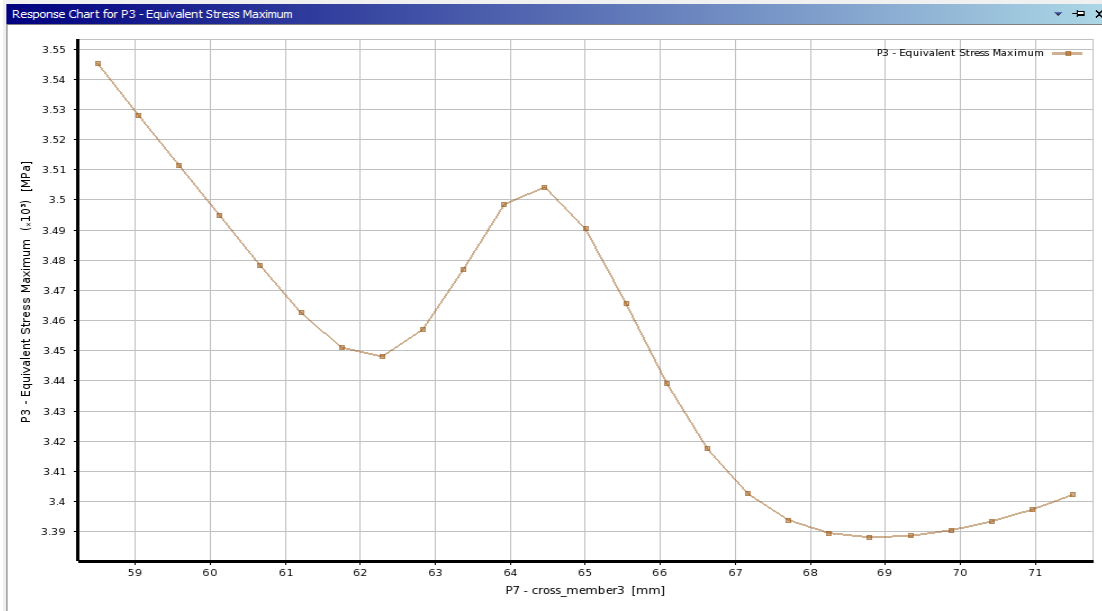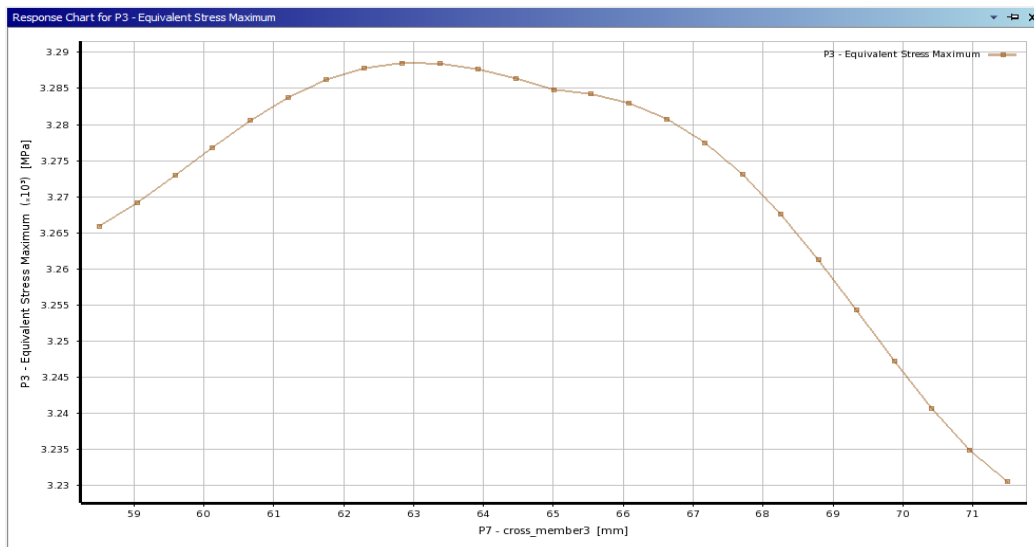

Figure 4.242: Equivalent-stress vs cross-member 3 for CCD using Al 6092/SiC/17.5P MMC

Figure 4.242 illustrates the variation of equivalent-stress with respect to cross-member 3 dimensions. Up to 63mm cross-member 3 dimensions, the graph indicates a progressive increase in equivalent-stress, which then reduces linearly as cross-member 3 dimensions increase. With a cross-member 3 dimension of 71.5mm, the least equivalent-stress is recorded.
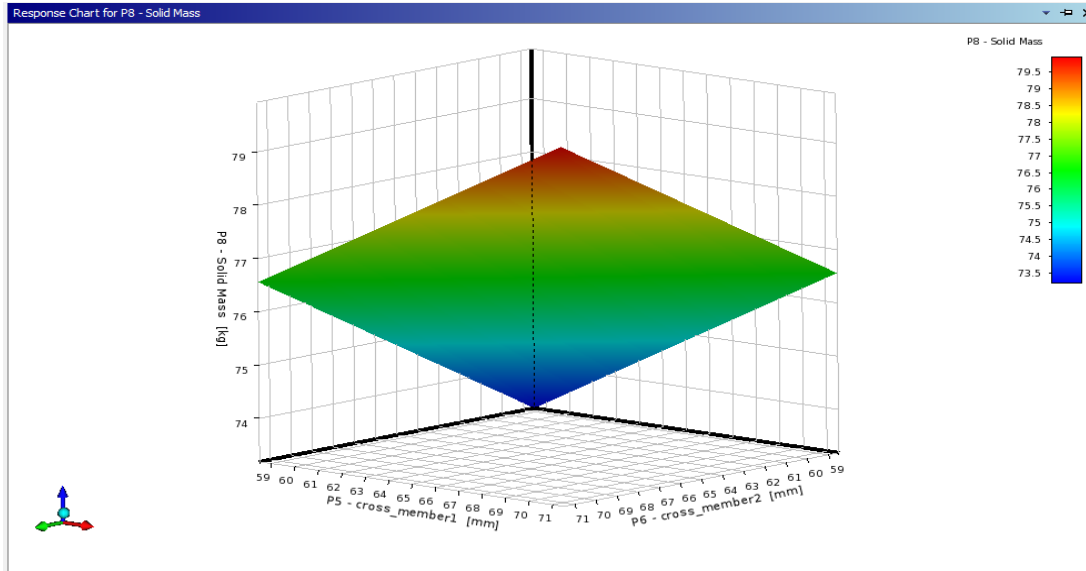
Figure 4.243: 3D Response-Surface plot of solid mass for CCD scheme using Al 6092/SiC/17.5P

The variation of mass vs. cross-member 1 and cross-member 2 dimensions is illustrated in Figure 4.243' Response-Surface plot. The red-colored region represents the largest mass, while the blue-colored region represents the least mass. Cross-member 1 dimensions varying from 68mm to 71mm and cross-member 2 dimensions varying from 68mm to 71mm have the higher mass. Cross-member 1 and cross-member 3 dimensions varying from 58.5mm to 61mm have the lowest mass.
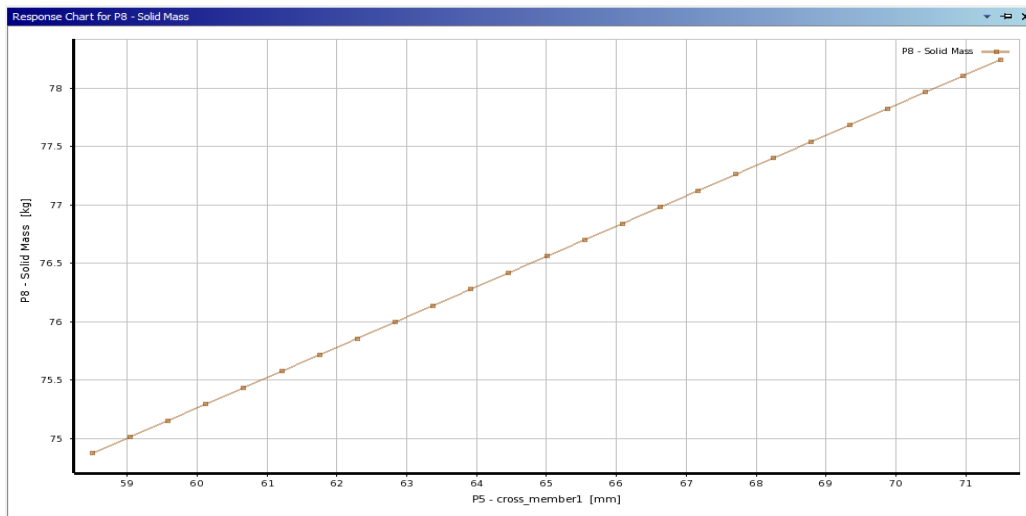
Figure 4.244: Solid mass vs cross-member 1 for CCD scheme using Al 6092/SiC/17.5P MMC

Figures 4.244 and 4.245 depict the change in chassis mass as a function of cross-member 1 and cross-member 3 dimensions. With increasing cross-member 1 and cross-member 3 dimensions, the solid mass appears to increase linearly. The cross-member 1 dimension of 58.5mm has the smallest mass of the chassis. The 58.5mm cross-member 3 and cross-member 1 dimensions have the lowest chassis mass.
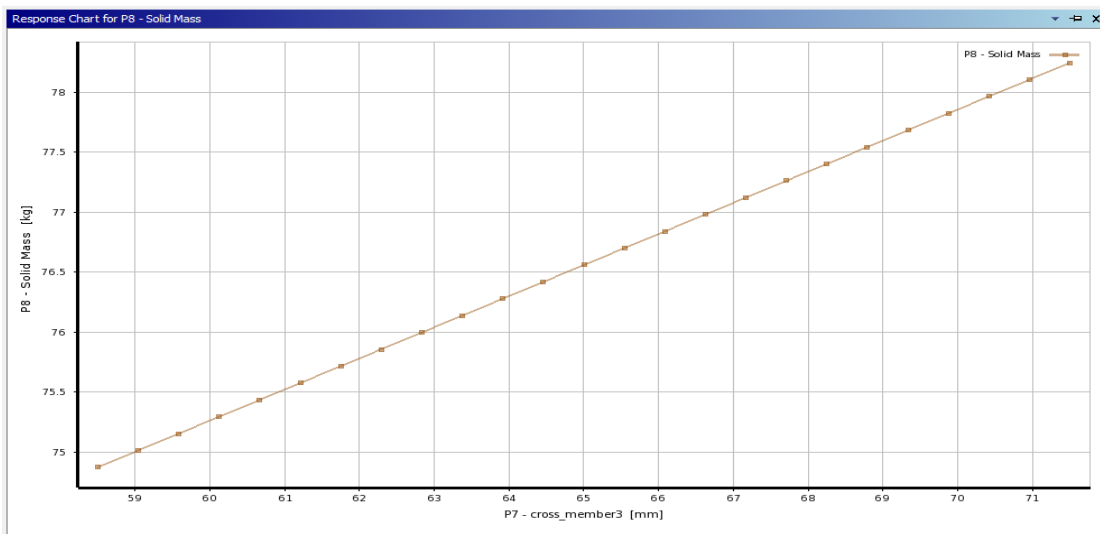
Figure 4.245: Solid mass vs cross-member 3 for CCD scheme using Al 6092/SiC/17.5P MMC
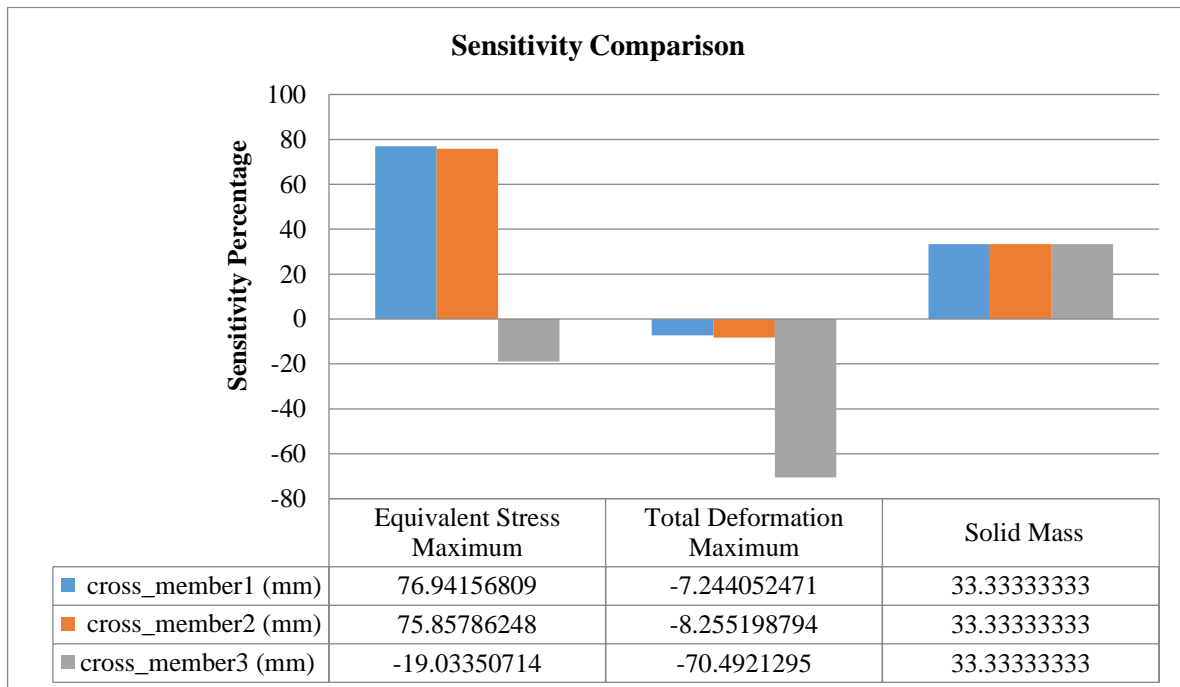
Figure 4.246: Sensitivity plot for CCD scheme using Al 6092/SiC/17.5P MMC

	Equivalent Stress Maximum	Total Deformation Maximum	Solid Mass
cross_member1 (mm)	76.94156809	-7.244052471	33.33333333
cross_member2 (mm)	75.85786248	-8.255198794	33.33333333
cross_member3 (mm)	-19.03350714	-70.4921295	33.33333333

The maximum sensitivity percentage for equivalent-stress is shown by cross-member 1 (76.94%), while the smallest sensitivity percentage is shown by cross-member 3 (19.034%) in

figure 4.246. For deformation, the maximum sensitivity percentage is shown by the cross-member 3 dimensions, and the minimum sensitivity percentage is shown by the cross-member 1 dimension. For solid mass, all three variables show the same sensitivity percentage which signifies that all the three optimization variables have the same effect on the mass of the chassis.

4.6.2 Optimal Space Filling Design using Al 6092/SiC/17.5P MMC

As indicated in table 4.39, the design points are developed utilizing the optimal space-filling design (OSF). Based on the optimal space-filling design scheme, different combinations of cross-member 1, cross-member 2, and cross-member 3 dimensions are created. For each design point, equivalent-stress, deformation, and solid mass are calculated. Table 4.40 shows the maximum and minimum values of various output parameters.

Table 4.39: DOE Table for OSF using Al 6092/SiC/17.5P MMC

A	B	C	D	E	F	G
Name	P5 - cross-member 1 (mm)	P6 - cross-member 2 (mm)	P7 - cross-member 3 (mm)	P3 - Equivalent-stress Max (MPa)	P4 - Total Deformation Maximum (mm)	P8 - Solid Mass (kg)
1.00	69.33	68.47	60.67	3489.33	690.15	77.46
2.00	63.27	69.33	59.80	3235.04	683.03	75.89
3.00	59.80	66.73	68.47	3351.49	688.86	76.56
4.00	68.47	59.80	67.60	3493.44	690.60	76.78
5.00	58.93	60.67	65.87	3501.74	694.02	74.09
6.00	71.07	63.27	63.27	3347.15	697.72	77.23
7.00	66.73	62.40	58.93	3246.61	685.05	74.76
8.00	70.20	65.87	69.33	3319.29	686.10	79.26
9.00	65.87	64.13	64.13	3283.42	696.44	76.34
10.00	65.00	67.60	71.07	3464.31	682.23	78.81
11.00	61.53	71.07	65.00	3474.07	694.22	77.23
12.00	60.67	65.00	61.53	3502.20	702.81	74.54
13.00	64.13	58.93	62.40	3308.88	700.82	74.09
14.00	67.60	70.20	66.73	3471.70	690.70	79.03
15.00	62.40	61.53	70.20	3233.55	685.08	76.34

Table 4.40: Maximum and minimum values for OSF using Al 6092/SiC/17.5P MMC

1	A	B	C
	Name	**Calculated Min**	**Calculated Max**
2	P3 - Equivalent-stress Max (MPa)	3233	3506.7
3	P4 - Total Deformation Maximum (mm)	681.98	703.64
4	P8 - Solid Mass (kg)	71.502	81.618

The highest equivalent-stress obtained through optimization is 3506.7 MPa, while the minimum equivalent-stress obtained through optimization is 3233 MPa. The maximum and minimum values of deformation and solid mass output vary less. The solid mass with structural steel is 214.64 kg (Sub-section 4.3.2.2), while the solid mass with Al 6092/SiC/17.5P MMC is 71.502 kg.

Figure 4.247: Response-Surface plot of equivalent-stress vs cross-member 1 and cross-member 2 for OSF using Al 6092/SiC/17.5P MMC

The equivalent-stress Response-Surface plot in figure 4.247 shows two peaks, which are depicted in the red region. The maximum equivalent-stress is obtained for cross-member 2 with a length varying from 59mm to 61mm and cross-member 1 with a length varying from 59mm to 61mm. The equivalent-stress is found to be lowest in regions represented by dark blue color.
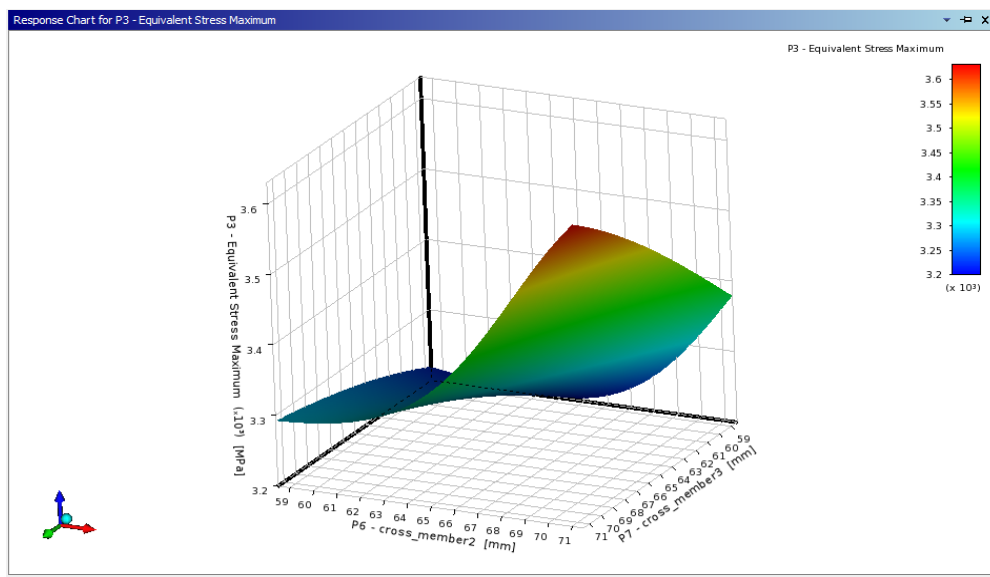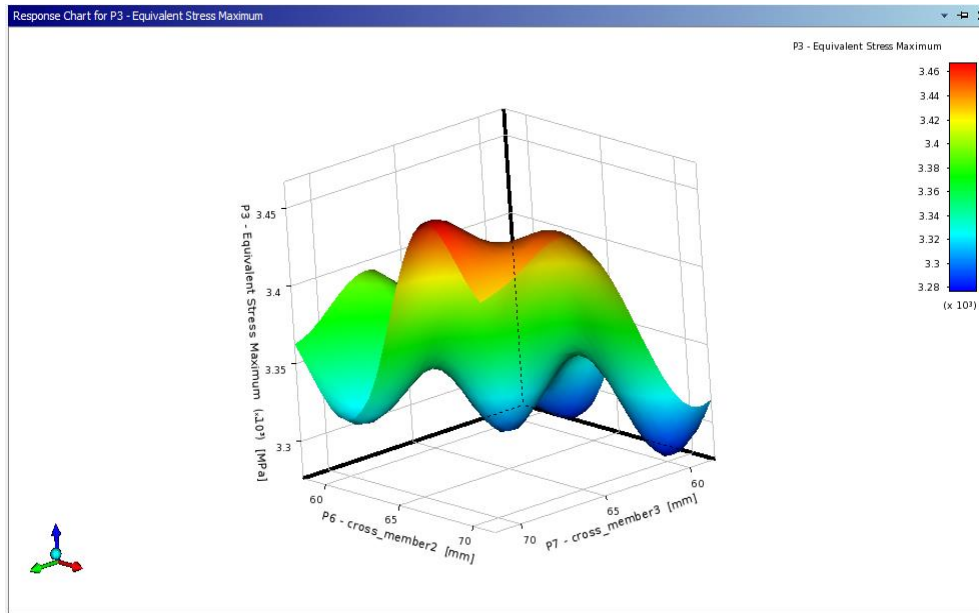
Figure 4.248: Response-Surface plot of equivalent-stress vs cross-member 2 and cross-member 3 for OSF using Al 6092/SiC/17.5P MMC

Figure 4.248 shows the equivalent-stress versus cross-member 2 and cross-member 3 dimensions Response-Surface plot. The graph illustrates maximum equivalent-stress in the red-colored zone, with cross-member 2-dimensions varying from 66mm to 71mm and cross-member 3-dimensions varying from 66mm to 71mm. For the region depicted in dark blue, the equivalent-stress is at its lowest.
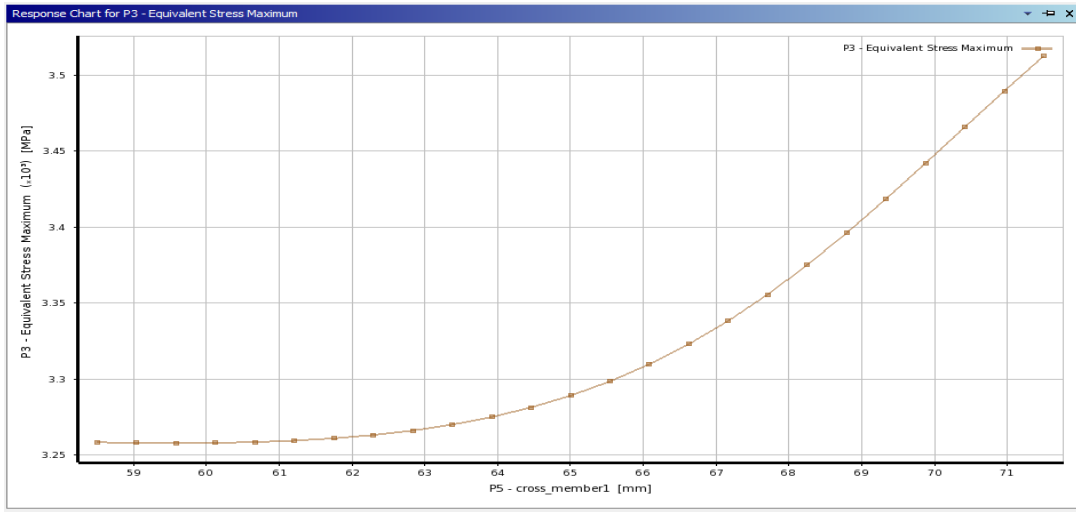

Figure 4.249: Equivalent-stress vs cross-member 1 for OSF using Al 6092/SiC/17.5P MMC

Figure 4.249 illustrates the variation of equivalent-stress vs cross member 1 dimensions. The equivalent-stress decreases initially and reaches a minimum value at the cross-member 1 dimension of 66mm before increasing linearly and reaching a maximum value (3.36 x10^3 MPa) at the cross-member 1 dimension of 71mm.

Figure 4.250: Equivalent-stress vs cross-member 2 for OSF using Al 6092/SiC/17.5P MMC

Figure 4.250 illustrates the variation of equivalent-stress vs cross member 2 dimensions. The equivalent-stress initially decreases up to cross member 2 dimension value of 64mm, then gradually increases to cross member 2 dimension value of 71mm, and then decreases.
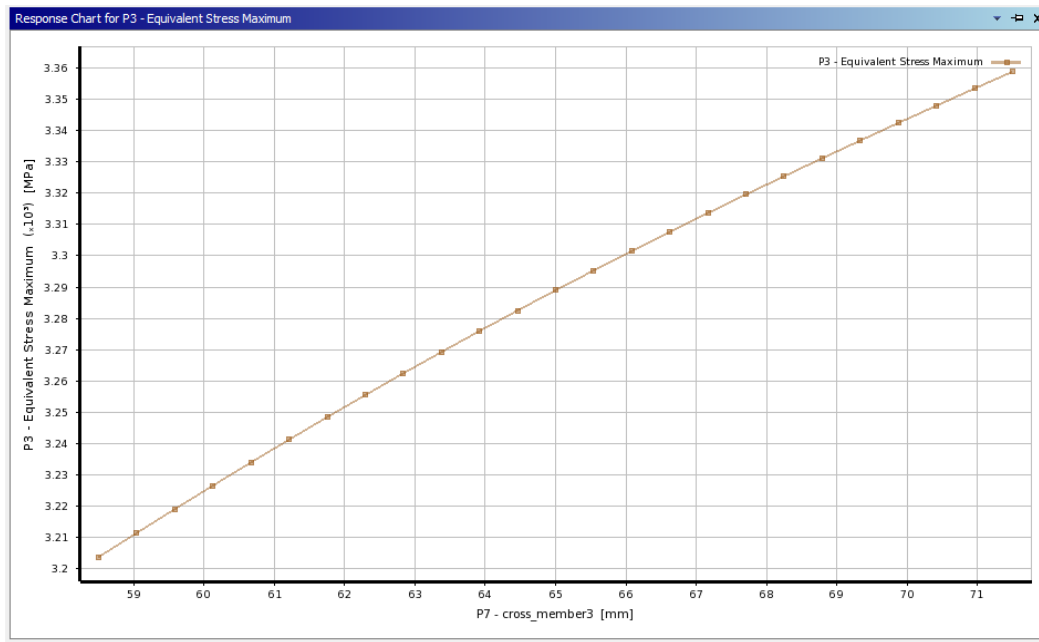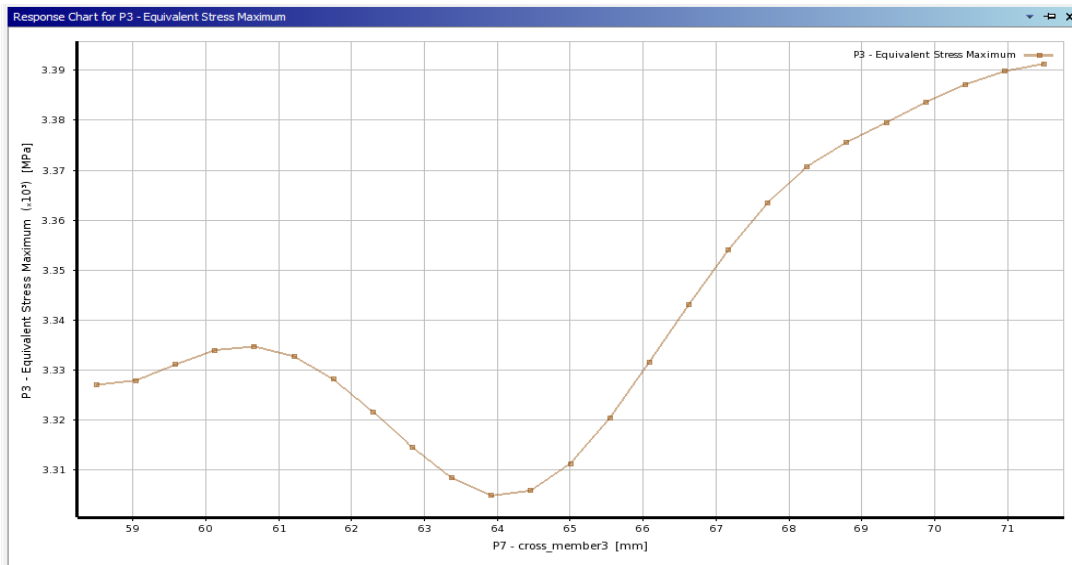

Figure 4.251: Equivalent-stress vs cross-member 3 for OSF using Al 6092/SiC/17.5P MMC

Figure 4.251 illustrates the variation of equivalent-stress vs cross-member 3 dimensions. The equivalent-stress rises and then falls to the minimum value at the cross-member 3 dimension value of 64mm. The equivalent-stress increases linearly until it reaches its maximum value at cross-member 3 dimensions of 71mm.
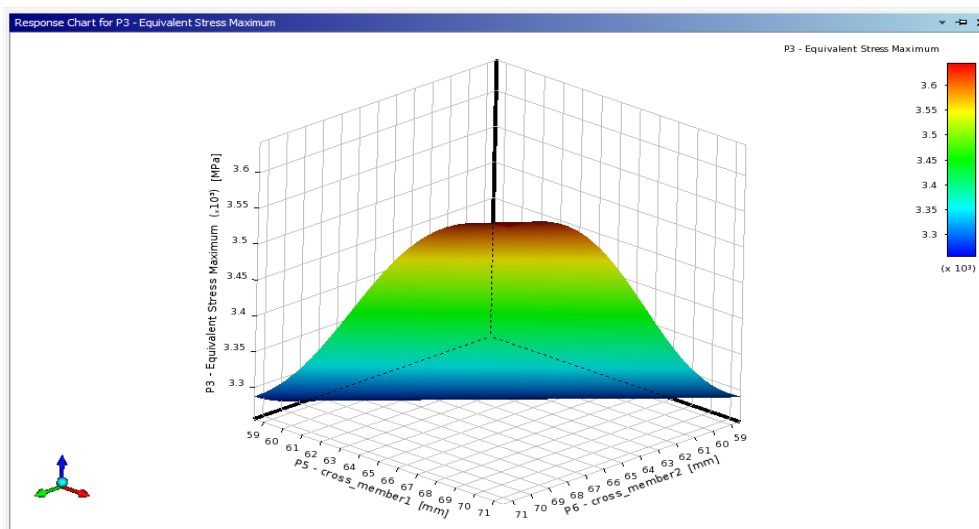

Figure 4.252: Response-Surface plot of total deformation vs cross-member 1 and cross-member 2 for OSF using Al 6092/SiC/17.5P MMC

Figure 4.252 illustrates the Response-Surface plot of deformation cross-member 1 and cross-member 2. Maximum deformation is shown for cross-member 2 dimensions varying from 59mm to 62mm and cross-member 1 dimensions varying from 59mm to 67mm. In the other dimensions, the deformation has a minimum value, which is within the blue zone.
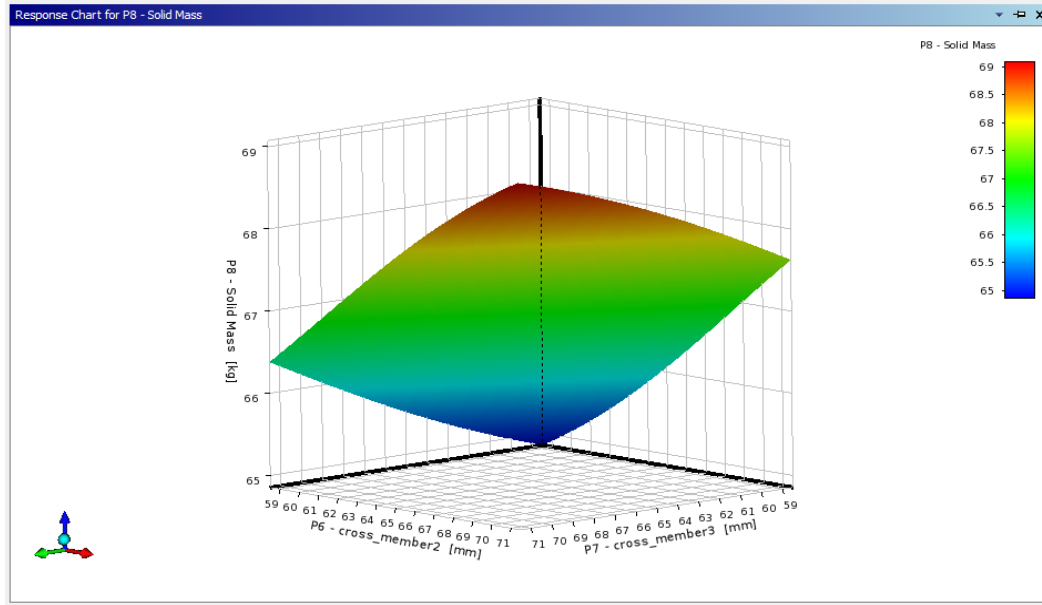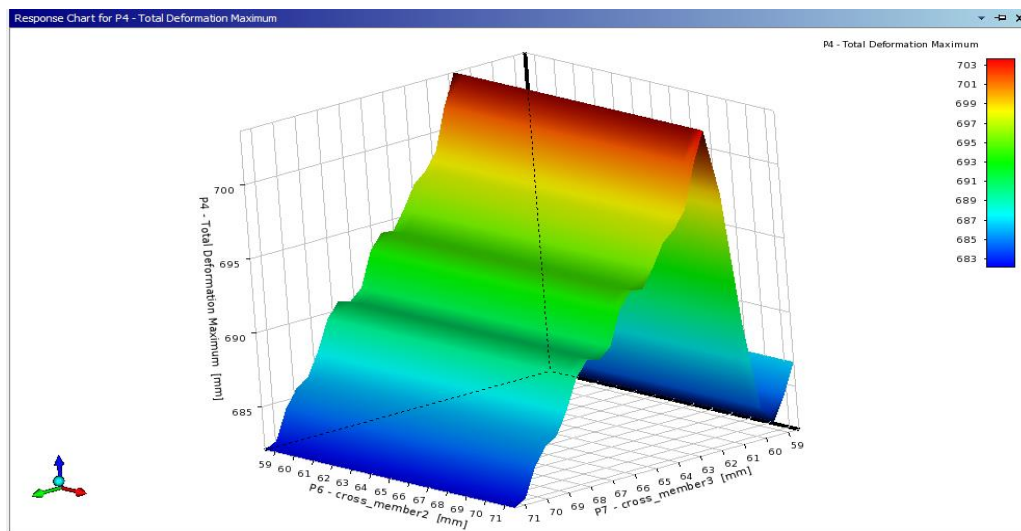

Figure 4.253: Response-Surface plot of total deformation vs cross-member 2 and 3 for OSF using Al 6092/SiC/17.5P MMC

Figure 4.253illustrates the variation of deformation vs. cross-member 2 and cross-member 3. Cross-member 3 dimensions varying from 61mm to 63mm and cross-member 2 dimensions varying from 59mm to 71mm exhibit the greatest deformation.

Figure 4.254: Response-Surface plot of mass vs cross-member 1 and cross-member 2 for OSF using Al 6092/SiC/17.5P MMC

Figure 4.254 illustrates the variation in mass as a function of cross-member 1 and cross-member 2 dimensions. Maximum solid mass for cross-member 1 dimensions varying from 69mm to 71mm and cross-member 2 dimensions varying from 69mm to 71mm is shown in the graph. Cross-member 1 and cross-member 2 dimensions varying from 59mm to 62mm have the lowest mass 76 kg.

	Equivalent Stress Maximum	Total Deformation Maximum	Solid Mass
■ cross_member1 (mm)	-43.28592622	-0.044074796	33.33333333
■ cross_member2 (mm)	48.2122154	-0.13386783	33.33333333
■ cross_member3 (mm)	31.53233122	-89.58985336	33.33333333

Figure 4.255: Sensitivity plot for OSF using Al 6092/SiC/17.5P MMC

All three output parameters, equivalent-stress, deformation, and solid mass are generated in the sensitivity plot in figure 4.255. Cross-member 1 has the highest sensitivity percentage for equivalent-stress. Cross-member 3 has the highest sensitivity % for total deformation. All three optimization variables have the same influence on the mass of the chassis.

4.6.3 Box Behnken Scheme using Al 6092/SiC/17.5P MMC

The design points are generated using Box Behnken (B-B) scheme as shown in table 4.41. Different combinations of cross-member 1, cross-member 2, and cross-member 3 dimensions are generated based on the optimal space-filling design scheme. The equivalent-stress, deformation, and solid mass are generated for each design point. The maximum and minimum values of these output parameters are shown in table 4.42.

Table 4.41: DOE Table for B-B Scheme using Al 6092/SiC/17.5P MMC

A Name	B P5 - cross-member 1 (mm)	C P6 - cross-member 2 (mm)	D P7 - cross-member 3 (mm)	E P3 - Equivalent-stress Max (MPa)	F P4 - Total Deformation Maximum (mm)	G P8 - Solid Mass (kg)
1.00	65.00	65.00	65.00	3277.61	694.83	76.56
2.00	58.50	58.50	65.00	3274.81	696.25	73.19
3.00	71.50	58.50	65.00	3519.97	694.63	76.56
4.00	58.50	71.50	65.00	3521.08	694.68	76.56
5.00	71.50	71.50	65.00	3505.58	693.21	79.93
6.00	58.50	65.00	58.50	3499.14	686.25	73.19
7.00	71.50	65.00	58.50	3454.27	692.27	76.56
8.00	58.50	65.00	71.50	3220.41	682.31	76.56
9.00	71.50	65.00	71.50	3224.27	680.84	79.93
10.00	65.00	58.50	58.50	3483.75	687.99	73.19
11.00	65.00	71.50	58.50	3236.77	685.96	76.56
12.00	65.00	58.50	71.50	3288.51	681.88	76.56
13.00	65.00	71.50	71.50	3417.05	680.45	79.93

Table 4.42: Maximum and minimum values for B-B Scheme using Al 6092/SiC/17.5P MMC

1	A Name	B Calculated Min	C Calculated Max
2	P3 - Equivalent-stress Max (MPa)	3207.3	3531.8
3	P4 - Total Deformation Maximum (mm)	680.06	696.36
4	P8 - Solid Mass (kg)	71.502	81.618

The highest equivalent-stress obtained via optimization is 3531.8 MPa, whereas the minimum equivalent-stress obtained is 3207.3 MPa. Between maximum and minimum values, deformation and solid mass output show minimal variance. The mass of a chassis made of structural steel is 214.64 kilograms, while that of a chassis made of Al/SiC MMC is 71.502 kilograms.

Figure 4.256: Response-Surface plot of equivalent-stress vs cross-member 1 and cross-member 2 for B-B Scheme using Al 6092/SiC/17.5P MMC

The equivalent-stress Response-Surface plot in figure 4.256 shows three peaks, which are depicted in the red region. The higher equivalent-stress is obtained for cross-member 2 with dimensions varying from 69mm to 71.5mm, cross-member 1 with dimensions varying from 59mm to 61mm, and another set of cross-member 2 dimensions varying from 70mm to 71mm. The equivalent-stress is found to be lowest in regions represented by dark blue color.

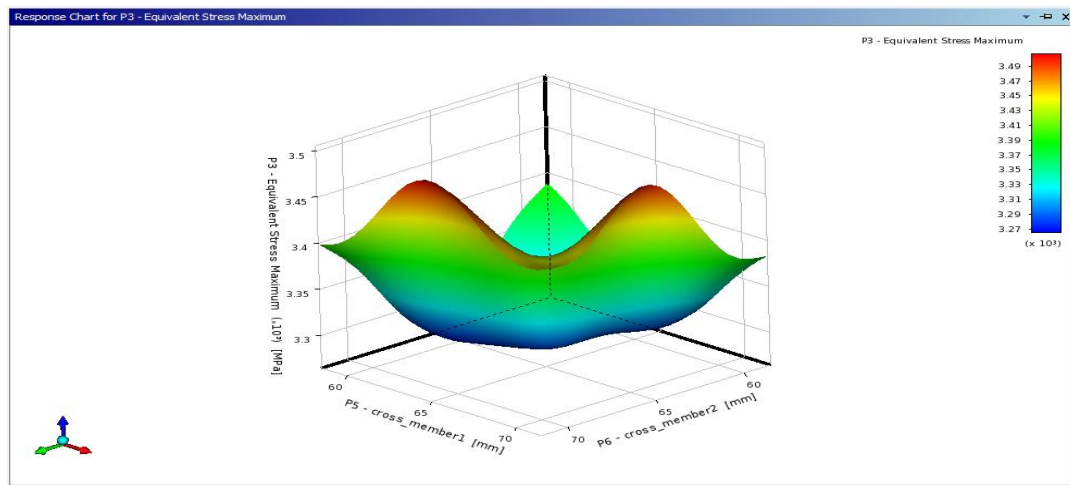

Figure 4.257: Response-Surface plot of equivalent-stress vs cross-member 2 and cross-member 3 for B-B Scheme using Al 6092/SiC/17.5P MMC

Figure 4.257 illustrates the Response-Surface plot of equivalent-stress vs cross-member 2 and cross-member 3. The plot illustrates the maximum equivalent-stress in the red region, where the cross-

member 2-dimension ranges from 59mm to 61mm and the cross-member 3-dimension ranges from 59mm to 61mm. The equivalent-stress is lowest in the region depicted in dark blue.

Figure 4.258: Equivalent-stress vs cross-member 1 for B-B Scheme using Al 6092/SiC/17.5P MMC

Figure 4.258 illustrates the fluctuation of equivalent-stress versus cross member 1 dimensions. The equivalent-stress declines at first, reaching a minimum at cross-member 1 dimension of 64.5 mm, and then climbs linearly to reach a maximum at cross-member 1 dimension value of 71.5mm.

Figure 4.259: Equivalent-stress vs cross-member 2 for B-B Scheme using Al 6092/SiC/17.5P MMC

Figure 4.259 displays the variations of equivalent-stress versus cross member 2 dimensions. The equivalent-stress drops until it reaches at cross member 2 dimension value of 65mm, then steadily climbs until it reaches its maximum at the cross member 2 dimension value of 71.5mm.

Figure 4.260: Equivalent-stress vs cross-member 3 for B-B Scheme using Al 6092/SiC/17.5P MMC

Figure 4.260 shows the variation of equivalent-stress versus cross-member 3 dimensions. The equivalent-stress is initially highest to cross-member 3 dimension of 58.5mm, then declines linearly to cross-member 3 dimension value of 71.5mm.
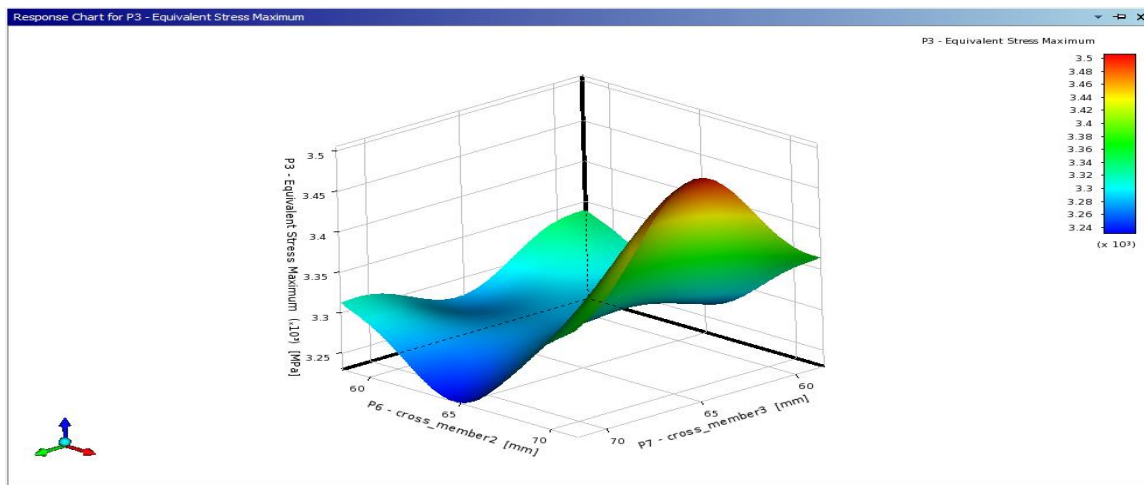

Figure 4.261: Response-Surface plot of total deformation vs cross-member 1 and cross-member 2 for B-B Scheme using Al 6092/SiC/17.5P MMC

Figure 4.261 illustrates the Response-Surface plot of deformation cross-member 1 and cross-member 2 dimensions. Maximum deformation is shown for cross-member 2 dimensions varying from 59mm

to 65mm and cross-member 1 dimensions varying from 59mm to 66mm. In the other dimensions, the deformation has a minimum value, which is represented by the blue zone.

Figure 4.262: Response-Surface plot of total deformation vs cross-member 2 and cross-member 3 for B-B Scheme using Al 6092/SiC/17.5P MMC

Figure 4.262 displays the variations of deformation vs. cross-member 2 and cross-member 3 dimensions. Cross-member 3 dimensions varying from 63mm to 66mm and cross-member 2 dimensions varying from 59mm to 71mm show higher deformation.

Figure 4.263: Response-Surface plot of mass vs cross-member 1 and cross-member 2 for B-B Scheme using Al 6092/SiC/17.5P MMC

Figure 4.263 illustrates the variation of mass vs cross-member 1 and cross-member 2 dimensions. The maximum solid mass is shown for cross-member 1 dimensions varying from 66mm to 71mm and cross-member 2 dimensions varying from 66mm to 71mm. Cross-member 1 and cross-member 2 dimensions varying from 59mm to 62mm have the lowest mass ~73 kg.

|	Equivalent Stress Maximum	Total Deformation Maximum	Solid Mass
■ cross_member1 (mm)	36.20438548	-9.572474215	33.33333333
■ cross_member2 (mm)	38.51746105	-9.014490292	33.33333333
■ cross_member3 (mm)	-38.66247993	-84.2922766	33.33333333

Figure 4.264: Sensitivity plot for B-B Scheme using Al 6092/SiC/17.5P MMC

The sensitivity chart for each of the three output parameters, equivalent-stress, deformation, and solid mass, is shown in Figure 4.264. For equivalent-stress, cross-member 3 has the largest sensitivity %. Cross-member 3 has the highest total deformation sensitivity %. For solid mass, all three optimization factors have the same influence on the chassis mass.

4.6.4 Latin Hyper Cube Sampling using Al 6092/SiC/17.5P MMC

The design points are generated using Latin hypercube sampling (LHS) as shown in table 4.43. Different combinations of the cross-member 1, cross-member 2, and cross-member 3 dimensions are generated based on Latin hypercube sampling. The equivalent-stress, deformation, and solid mass are generated for each design point. The maximum and minimum values of these output parameters are shown in table 4.44. The maximum equivalent-stress obtained from optimization is 3522.2 MPa and the minimum equivalent-stress obtained from optimization is 3217.4 MPa. The deformation and solid mass output show less variation between maximum and minimum values.

Table 4.43: DOE Table for LHS using Al 6092/SiC/17.5P MMC

A	B	C	D	E	F	G
Name	P5 - cross-member 1 (mm)	P6 - cross-member 2 (mm)	P7 - cross-member 3 (mm)	P3 - Equivalent-stress Max (MPa)	P4 - Total Deformation Maximum (mm)	P8 - Solid Mass (kg)
1.00	65.87	68.47	65.87	3459.62	692.53	77.91
2.00	68.47	65.00	66.73	3493.97	691.24	77.91
3.00	58.93	65.87	60.67	3512.16	705.60	74.09
4.00	67.60	58.93	70.20	3465.76	684.48	77.01
5.00	59.80	60.67	61.53	3391.49	703.48	73.19
6.00	71.07	59.80	59.80	3439.20	684.46	75.44
7.00	66.73	70.20	69.33	3441.64	685.70	79.48
8.00	70.20	67.60	68.47	3246.41	687.88	79.48
9.00	62.40	61.53	65.00	3267.07	695.51	74.99
10.00	61.53	66.73	71.07	3340.14	682.55	77.68
11.00	64.13	63.27	63.27	3277.09	698.54	75.44
12.00	60.67	69.33	62.40	3483.71	699.82	75.89
13.00	65.00	64.13	64.13	3486.33	696.56	76.11
14.00	69.33	71.07	58.93	3453.63	687.74	77.68
15.00	63.27	62.40	67.60	3331.45	691.03	76.11

Table 4.44: Maximum and minimum values for LHS using Al 6092/SiC/17.5P MMC

1		A	B	C
		Name	Calculated Min	Calculated Max
2		P3 - Equivalent-stress Max (MPa)	3217.4	3522.2
3		P4 - Total Deformation Maximum (mm)	676.09	695.69
4		P8 - Solid Mass (kg)	71.502	81.618

The mass of a chassis made of structural steel is 214.64 kilograms, while that of a chassis made of Al/SiC MMC is 71.502 kilograms. Figure 4.289 displays the Response-Surface plot of equivalent-stress, which reveals three peaks in the red-colored zone.
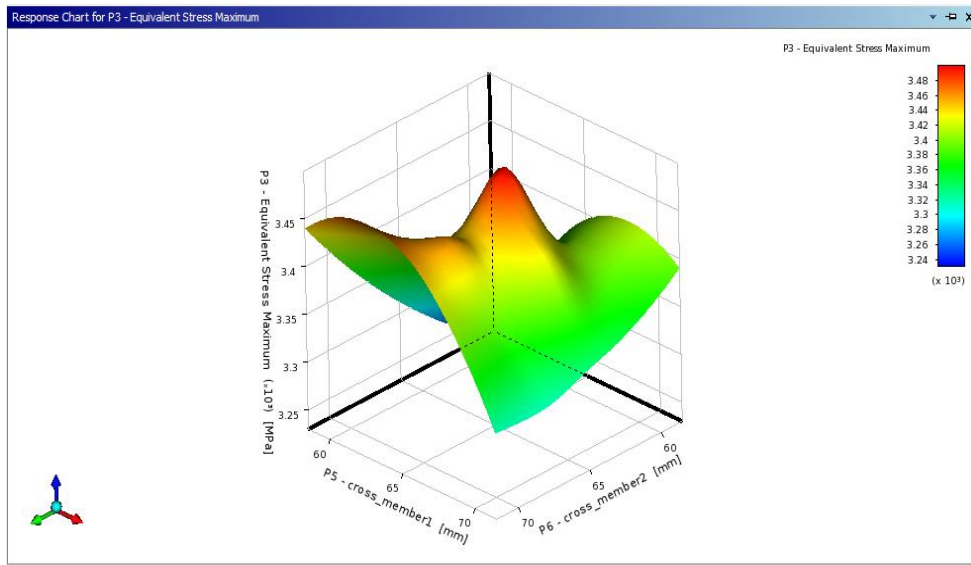
Figure 4.265: Response-Surface plot of equivalent-stress vs cross-member 1 and cross-member 2 for LHS using Al 6092/SiC/17.5P MMC

Cross-member 2 has a higher equivalent-stress at dimensions values from 61mm to 65mm, while cross-member 1 has the highest equivalent-stress at dimensions values from 62mm to 66mm as shown in figure 4.265. For regions indicated in dark blue color, the equivalent-stress is found to be the lowest.
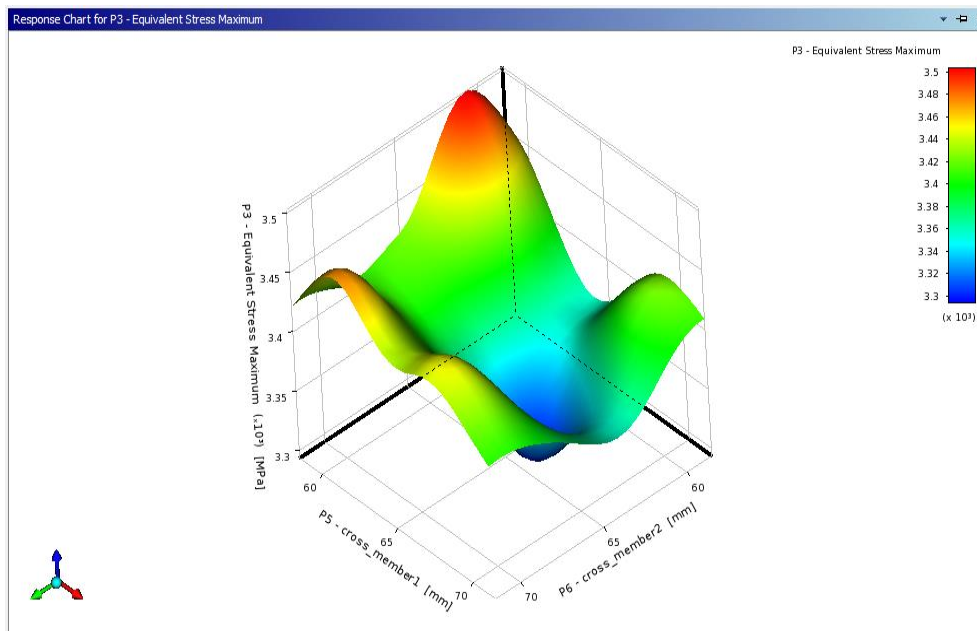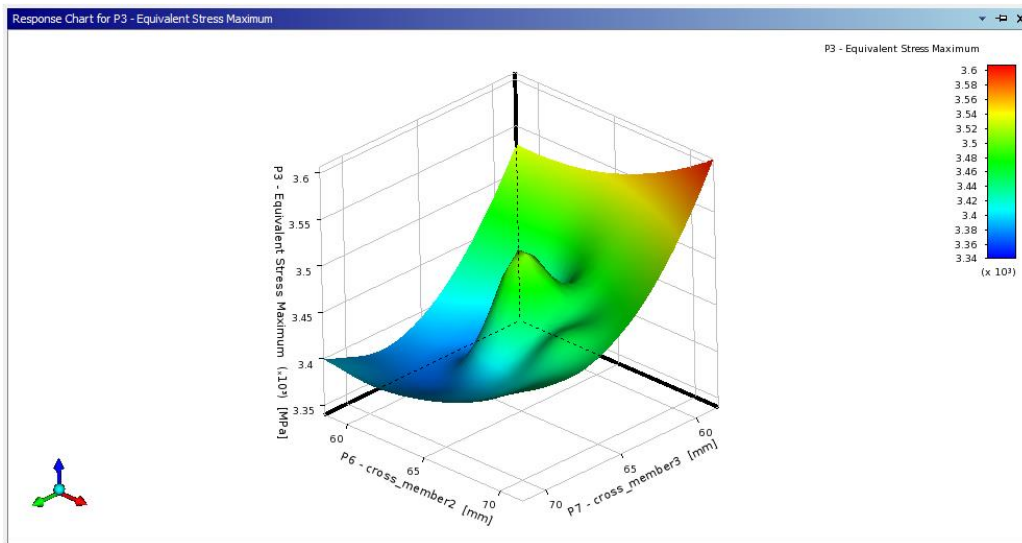

Figure 4.266: Response-Surface plot of equivalent-stress vs cross-member 2 and cross-member 3 for LHS using Al 6092/SiC/17.5P MMC

Figure 4.266 illustrates the Response-Surface plot of equivalent-stress vs cross-member 2 and cross-member 3 dimensions. The plot illustrates the maximum equivalent-stress 3.5×10^3 MPa in the red region, where the cross-member 2-dimension ranges from 65mm to 71mm and the cross-member 3-

dimension ranges from 59mm to 61mm. The equivalent-stress is lowest 3.2×10^3 MPa in the region depicted in dark blue.
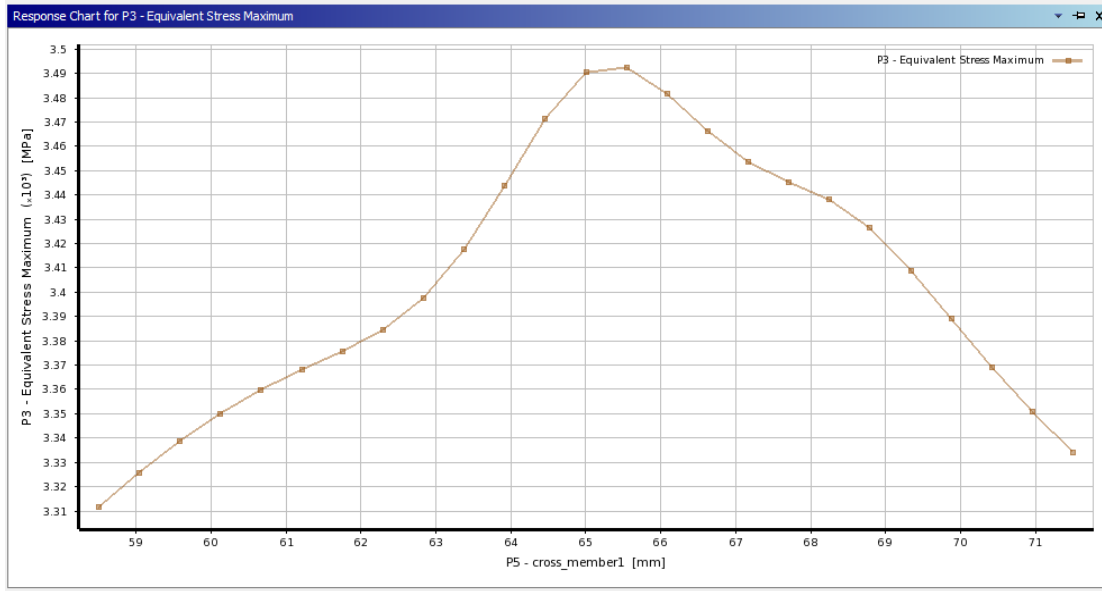
Figure 4.267: Equivalent-stress vs cross-member 1 for LHS using Al 6092/SiC/17.5P MMC

Figure 4.267 represents the variation of equivalent-stress vs cross member 1 dimensions. The equivalent-stress initially rises and reaches its peak at the cross-member 1 dimension of 65.5mm. Following that, the equivalent-stress decreases and reaches a minimum value at the cross-member 1 dimension of 71.5mm.
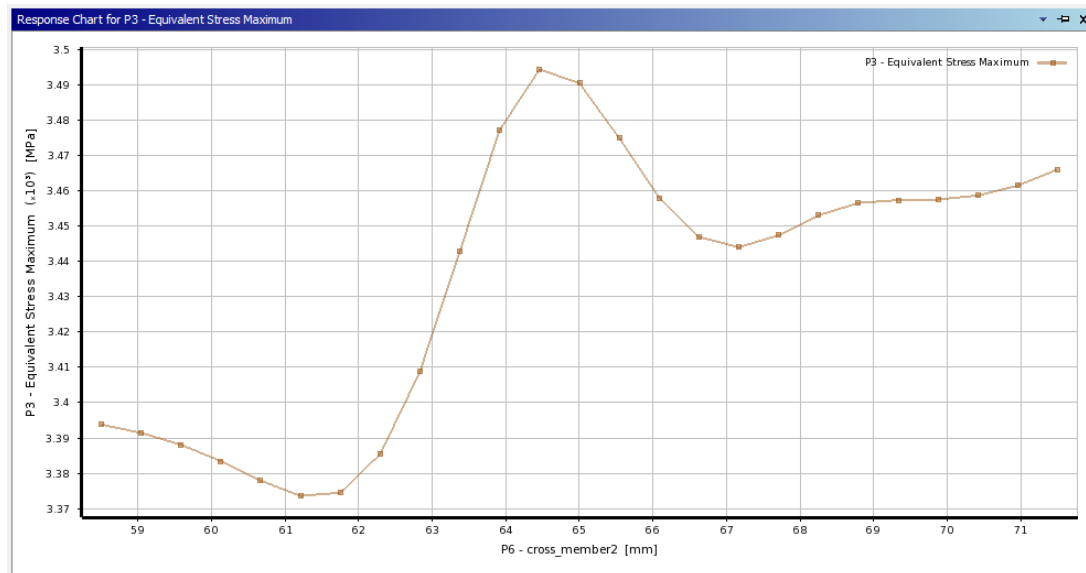
Figure 4.268: Equivalent-stress vs cross-member 2 for LHS using Al 6092/SiC/17.5P MMC

Figure 4.268 illustrates the variation of equivalent-stress vs cross-member 2 dimensions. The equivalent-stress initially decreases up to cross-member 2 dimension of 61.5mm before steadily increasing to its maximum at cross-member 2 dimension value of 64.5mm. Following that, the equivalent-stress decreases to a minimum at cross-member 2 dimension value of 67.1mm.
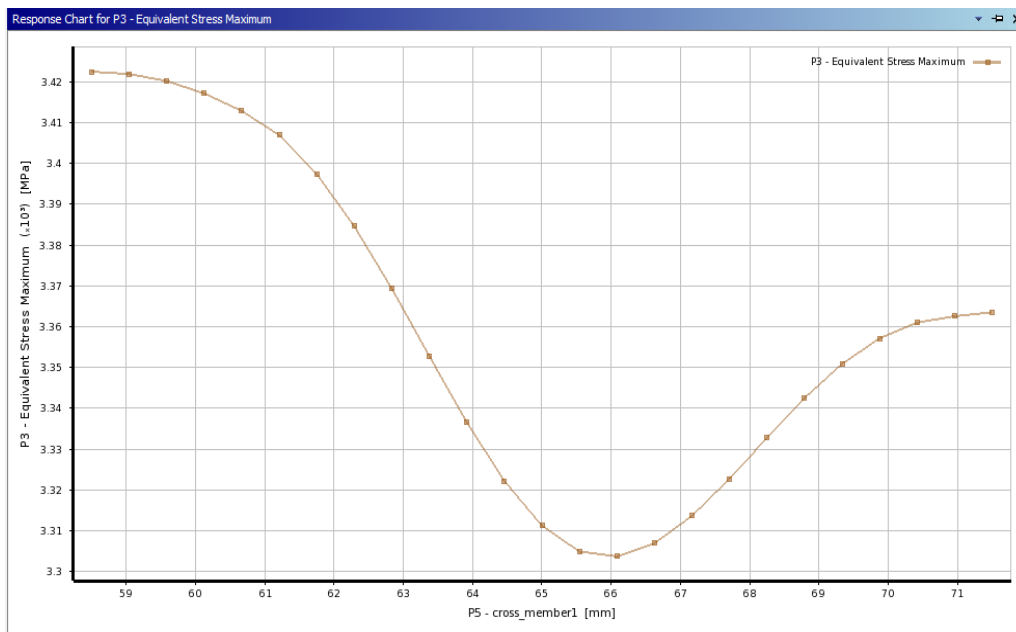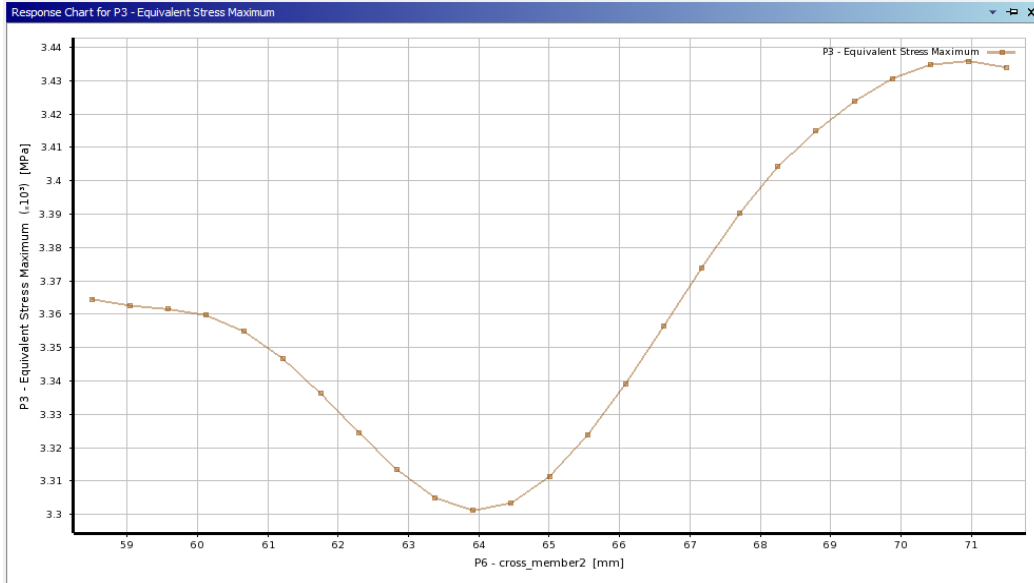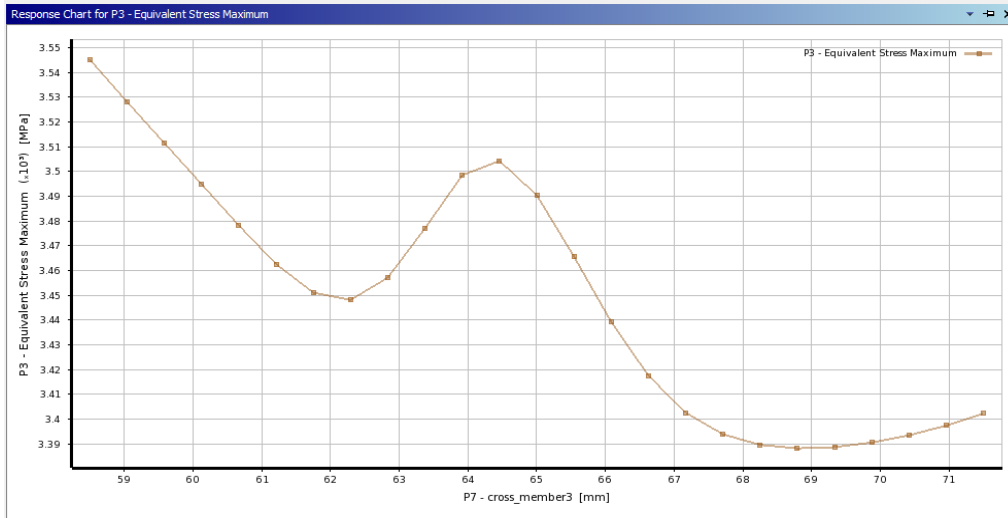

Figure 4.269: Equivalent-stress vs cross-member 3 for LHS using Al 6092/SiC/17.5P MMC

Figure 4.269 illustrates the variation of equivalent-stress vs cross-member 3 dimensions. The equivalent-stress is initially greatest at cross-member 3 dimension of 58.5mm, then decreases linearly to a minimum at cross-member 3 dimension value of 62mm. Following that, the equivalent-stress rises and reaches a peak at cross-member 3 dimension value of 64.5 mm. At the cross-member 3 dimension value of 69 mm, the equivalent-stress decreases and reaches a minimum value of 3441.6 MPa.
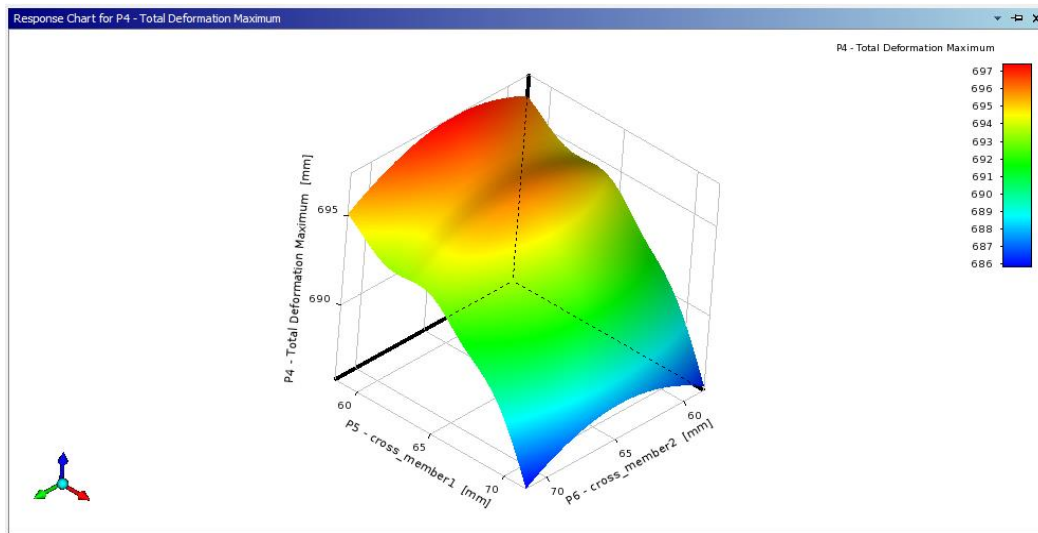
Figure 4.270: Response-Surface plot of total deformation vs cross-member 1 and 2 for LHS using Al 6092/SiC/17.5P MMC

Figure 4.270 illustrates the Response-Surface plot of deformation cross-member 1 and cross-member 2 dimensions. Maximum deformation is shown for cross-member 2 dimensions varying from 59mm to 71mm and cross-member 1 dimensions varying from 59mm to 63mm. In the other dimensions, the deformation has a minimum value, which is represented by the blue zone.
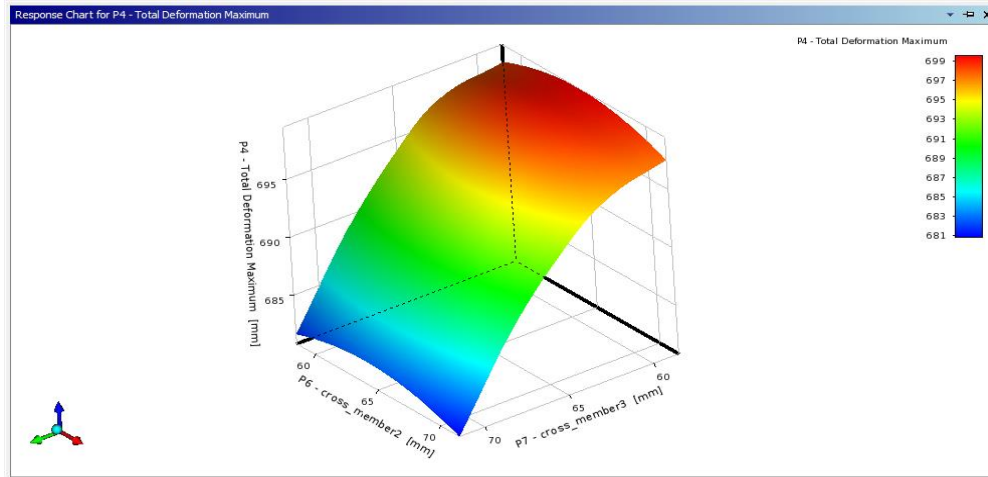
Figure 4.271: Response-Surface plot of total deformation vs cross-member 2 and cross-member 3 for LHS using Al 6092/SiC/17.5P MMC

Figure 4.271 illustrates the variation of deformation vs. cross-member 2 and cross-member 3 dimensions. Cross-member 3 dimensions varying from 59mm to 63mm and cross-member 2 dimensions varying from 59mm to 71mm exhibit the higher deformation zone.
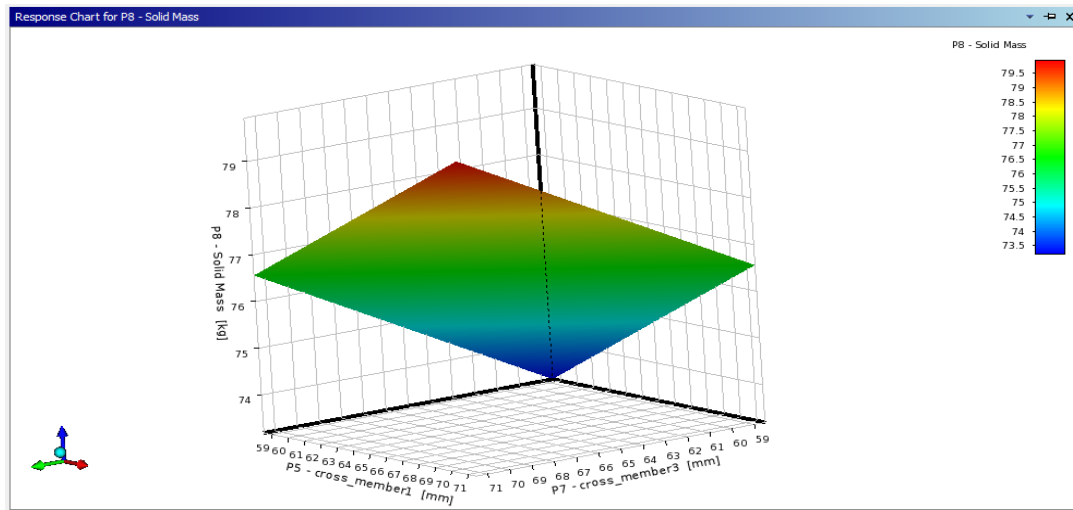
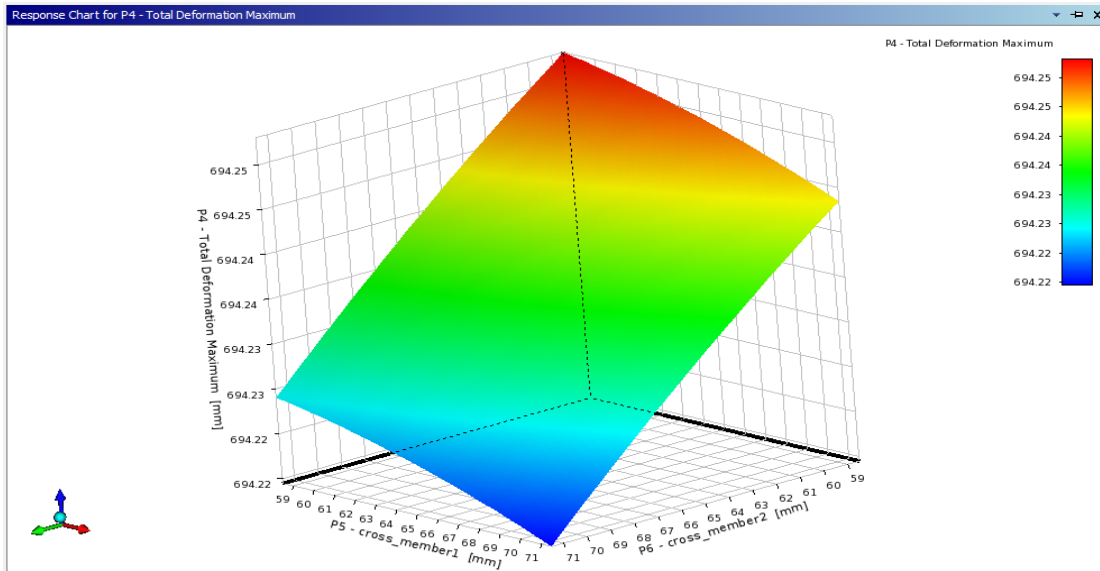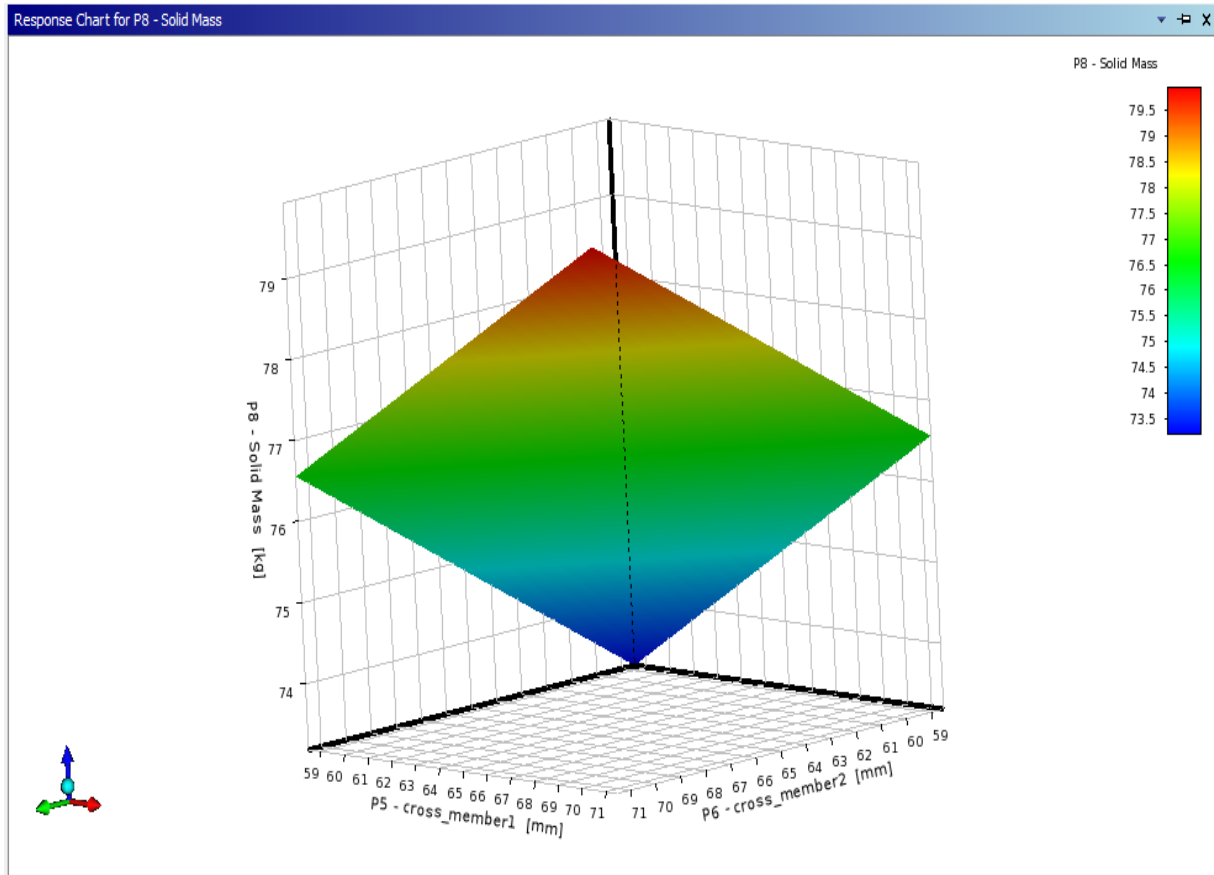Figure 4.272: Response-Surface plot of mass vs cross-member 1 and cross-member 2 for LHS using Al 6092/SiC/17.5P MMC

Figure 4.272 illustrates the variation of mass vs cross-member 1 and cross-member 3 dimensions. High solid mass is shown for cross-member 1 dimensions varying from 67mm to 71mm and cross-

member 3 dimensions varying from 67mm to 71mm. Cross-member 1 and cross-member 2 dimensions varying from 59mm to 62mm have the lowest mass 71.5 kg.
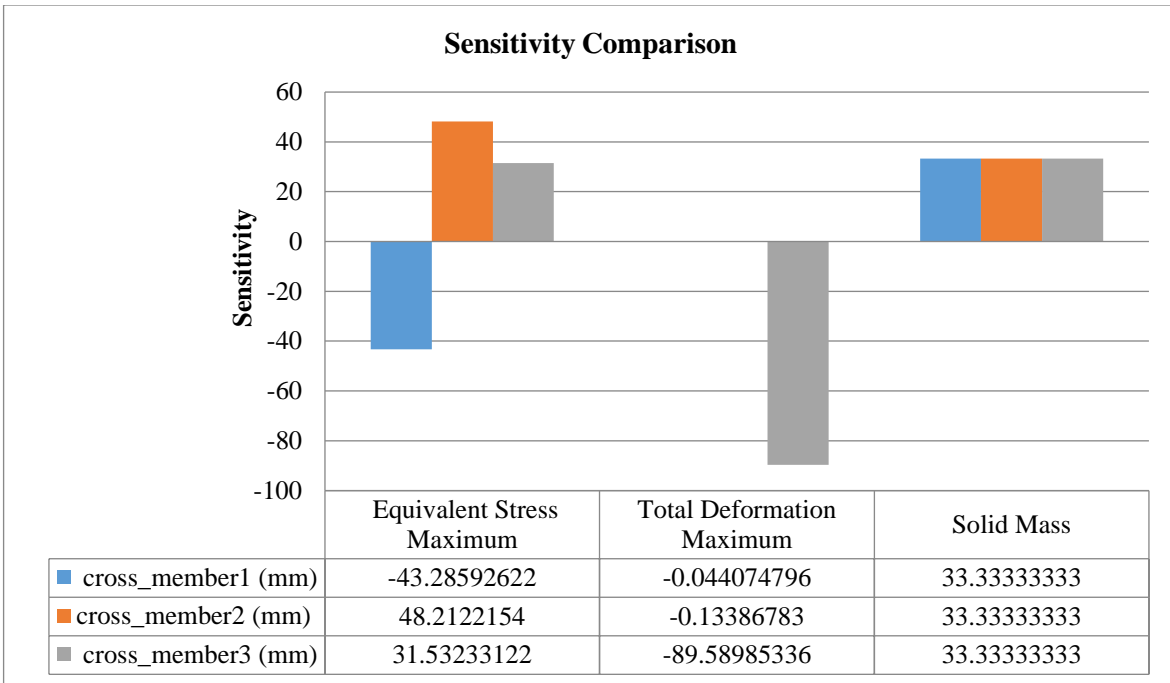

Sensitivity Comparison

	Equivalent Stress Maximum	Total Deformation Maximum	Solid Mass
cross_member1 (mm)	36.58322065	-33.23634342	33.33333333
cross_member2 (mm)	24.25318554	-8.299131979	33.33333333
cross_member3 (mm)	-32.16320727	-58.14414866	33.33333333
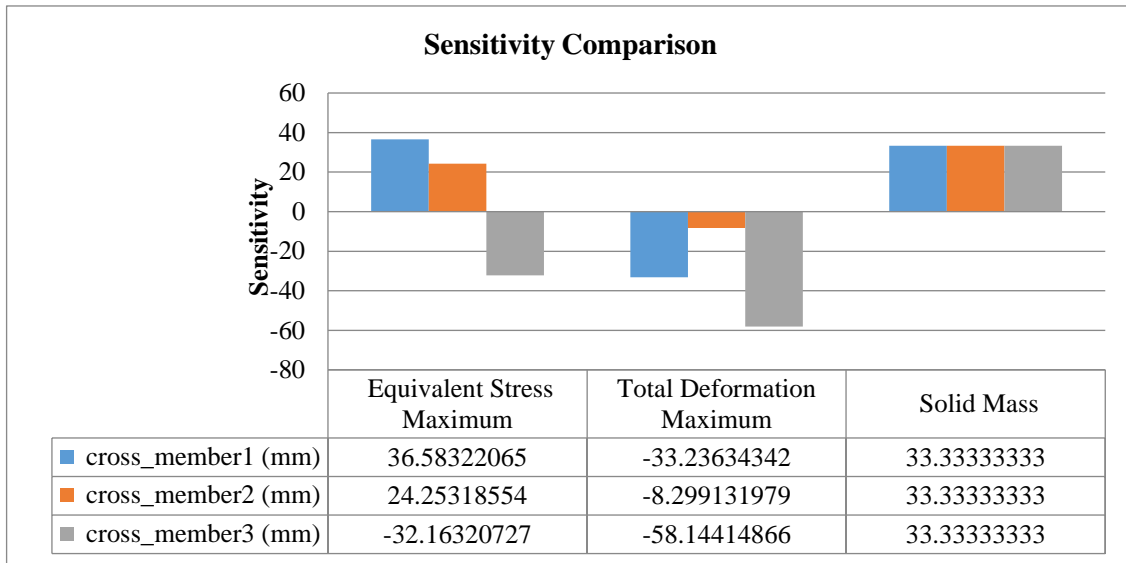
Figure 4.273: Sensitivity plot for LHS using Al 6092/SiC/17.5P MMC

Figure 4.273 illustrates the sensitivity plot, which is generated for all three output parameters, namely equivalent-stress, deformation, and solid mass. Cross-member 1 dimension has the highest sensitivity percentage for equivalent-stress. Cross-member 3 has the highest sensitivity percentage for total deformation. All three optimization variables have the same effect on the mass of the chassis for solid mass.

4.6.5 Sparse Grid Initialization using Al 6092/SiC/17.5P MMC

The design points are generated using sparse grid initialization (SGI) as shown in table 4.45. Different combinations of cross-member 1, cross-member 2, and cross-member 3 dimensions are generated based on the optimal space-filling design scheme. The equivalent-stress, deformation, and solid mass are generated for each design point. The maximum and minimum values of these output parameters are shown in table 4.46. The maximum equivalent-stress obtained from optimization is 3723.7 MPa and the minimum equivalent-stress obtained from optimization is 3186.5 MPa.

Table 4.45: DOE Table for SGI using Al 6092/SiC/17.5P MMC

A	B	C	D	E	F	G
Name	P5 - cross-member 1 (mm)	P6 - cross-member 2 (mm)	P7 - cross-member 3 (mm)	P3 - Equivalent-stress Max (MPa)	P4 - Total Deformation Maximum (mm)	P8 - Solid Mass (kg)
1	65	65	65	3277.61	783.34	66.98
2	58.5	65	65	3261.58	784.32	65.51
3	71.5	65	65	3514.87	782.61	68.46
4	65	58.5	65	3270.73	784.02	65.51
5	65	71.5	65	3522.24	782.31	68.46
6	65	65	58.5	3256.64	775.45	65.51
7	65	65	71.5	3217.42	768.29	68.46

Table 4.46: Maximum and minimum values for SGI using Al 6092/SiC/17.5P MMC

# Output Parameter Minimums						
Name	P5 - cross-member 1 (mm)	P6 - cross-member 2 (mm)	P7 - cross-member 3 (mm)	P3 - Equivalent-stress Max (MPa)	P4 - Total Deformation Maximum (mm)	P8 - Solid Mass (kg)
P3 - Equivalent-stress Max	58.5	69.544	58.5	3186.461	693.0709	74.99
P4 - Total Deformation Maximum	71.5	71.5	58.5	3547.078	691.1011	78.72
P8 - Solid Mass	58.5	58.5	58.5	3243.149	693.8984	73.39
# Output Parameter Maximums						
# Name	P5 - cross-member 1 (mm)	P6 - cross-member 2 (mm)	P7 - cross-member 3 (mm)	P3 - Equivalent-stress Max (MPa)	P4 - Total Deformation Maximum (mm)	P8 - Solid Mass (kg)
P3 - Equivalent-stress Max	71.5	71.3	71.5	3723.709	694.96	79.68
P4 - Total Deformation Maximum	58.5	58.5	71.5	3292.185	697.68	74.45
P8 - Solid Mass	71.5	71.5	71.5	3723.688	694.946	79.69

Between maximum and minimum values, deformation and solid mass output show minimal variance. The mass of a chassis made of structural steel is 214.64 kilograms, while that of a chassis made of Al 6092/SiC/17.5P MMC is 73.393 kilograms.
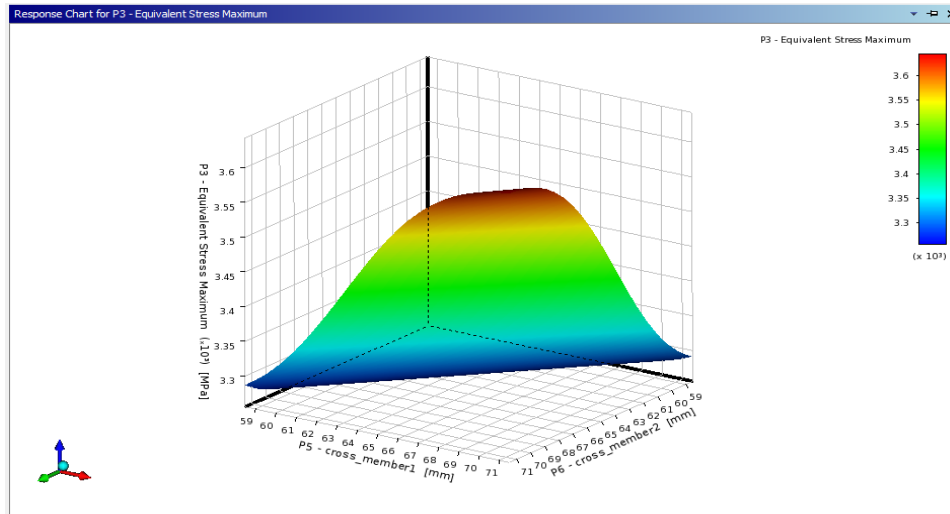
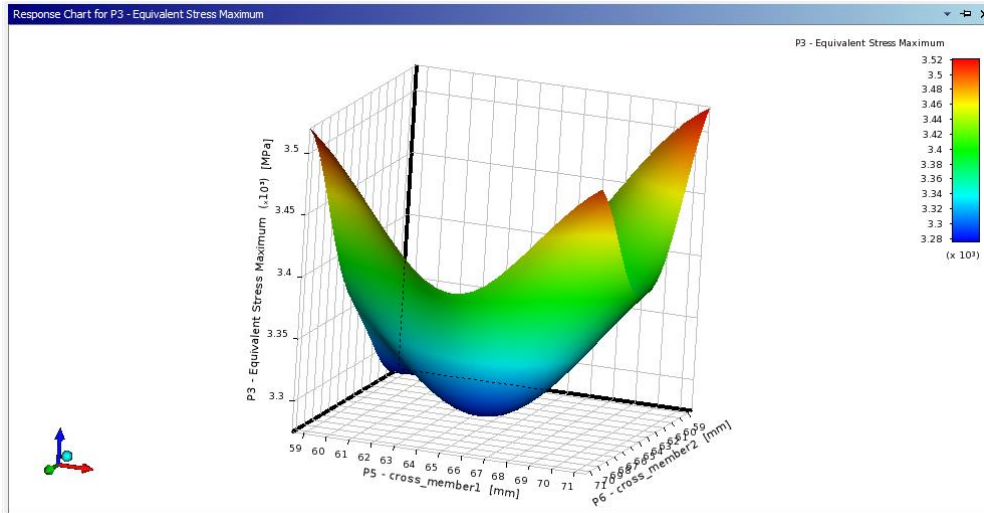
Figure 4.274: Response-Surface plot of equivalent-stress vs cross-member 1 and cross-member 2 for SGI using Al 6092/SiC/17.5P MMC

The equivalent-stress Response-Surface plot is illustrated in the red region of figure 4.274. The maximum equivalent-stress is obtained for cross-member 2 with a length varying dimensions values from 67mm to 71mm and cross-member 1 with a length varying from 67mm to 71mm. The equivalent-stress is found to be lowest in regions represented by dark blue color.
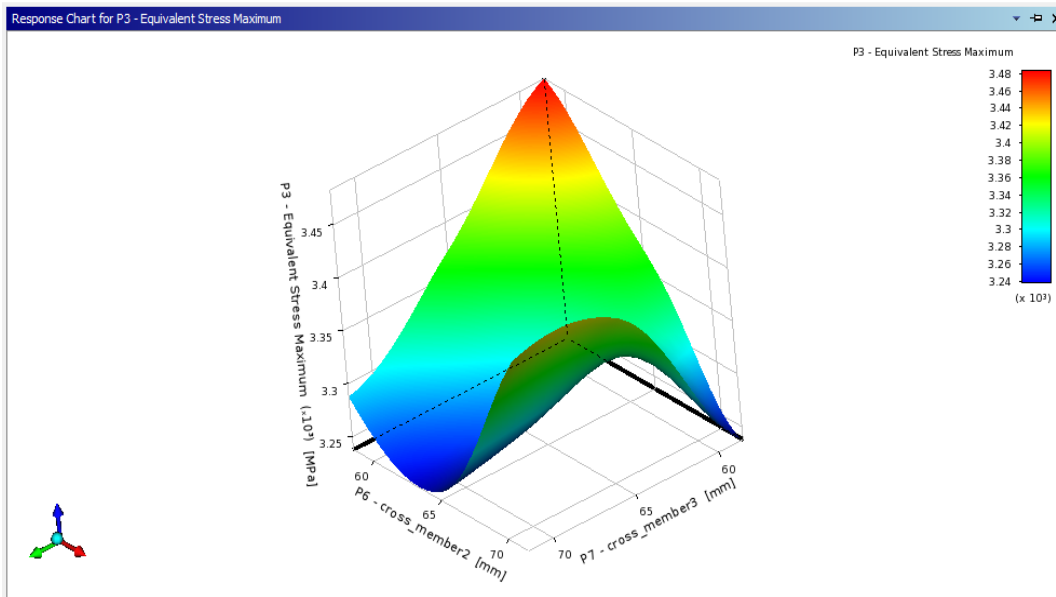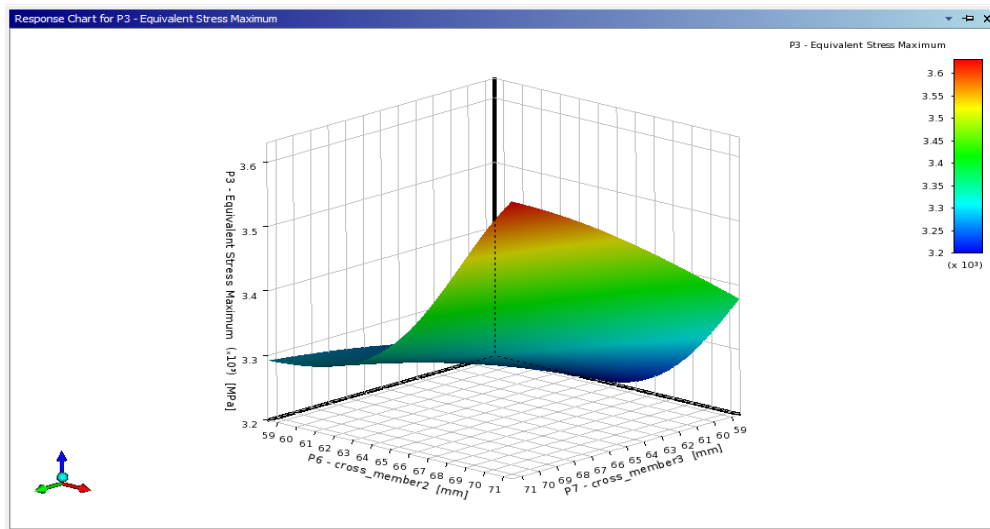

Figure 4.275: Response-Surface plot of equivalent-stress vs cross-member 2 and cross-member 3 for SGI using Al 6092/SiC/17.5P MMC

Figure 4.275 illustrates the Response-Surface plot of equivalent-stress vs cross-member 2 and cross-member 3. The plot illustrates the maximum equivalent-stress in the red region, where the cross-member 2-dimension ranges from 67mm to 71mm and the cross-member 3-dimension ranges from 61 mm to 68 mm. The equivalent-stress is lowest (~3.1 x 10^3 MPa) in the region depicted in dark blue.
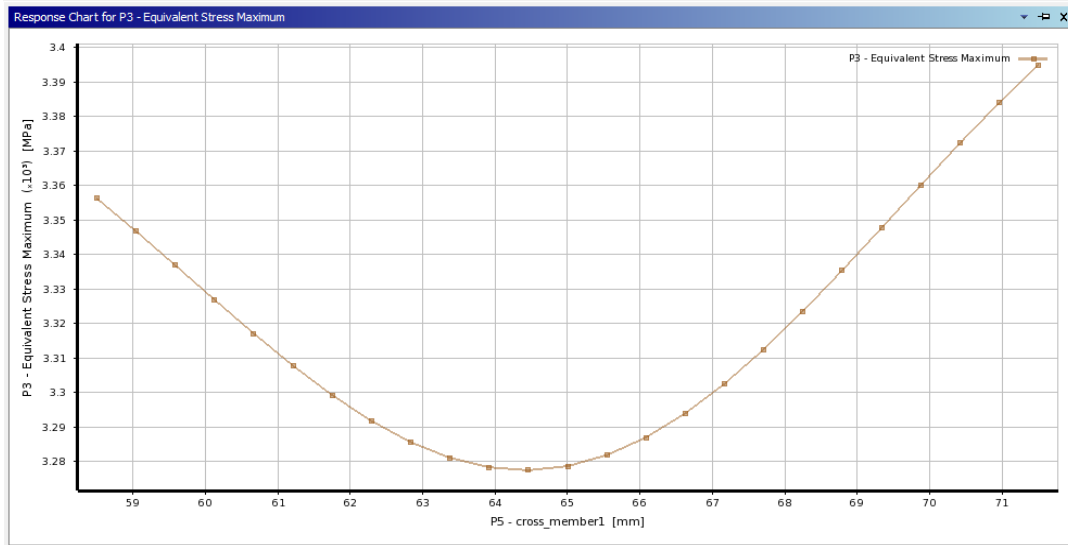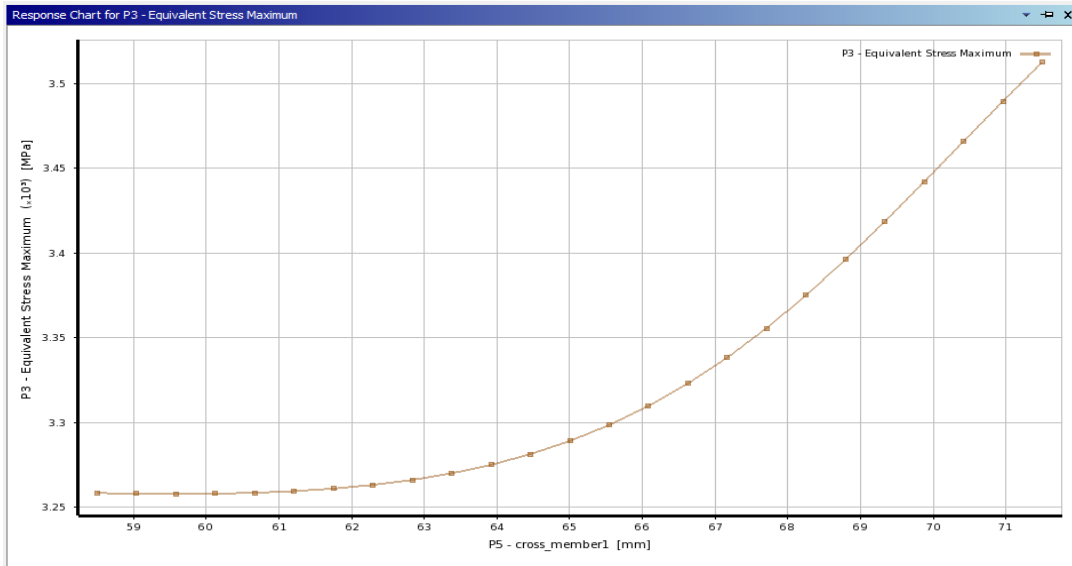

Figure 4.276: Equivalent-stress vs cross-member 1 for SGI using Al 6092/SiC/17.5P MMC

Figure 4.276 illustrates the variation of equivalent-stress vs cross member 1 dimensions. The equivalent-stress is initially constant (3.26 x10^3 MPa) up to the cross member 1 dimension value of 61.5mm and then increases exponentially to the maximum (3.54 x10^3 MPa) at the cross member 1 dimension value of 71.5mm.
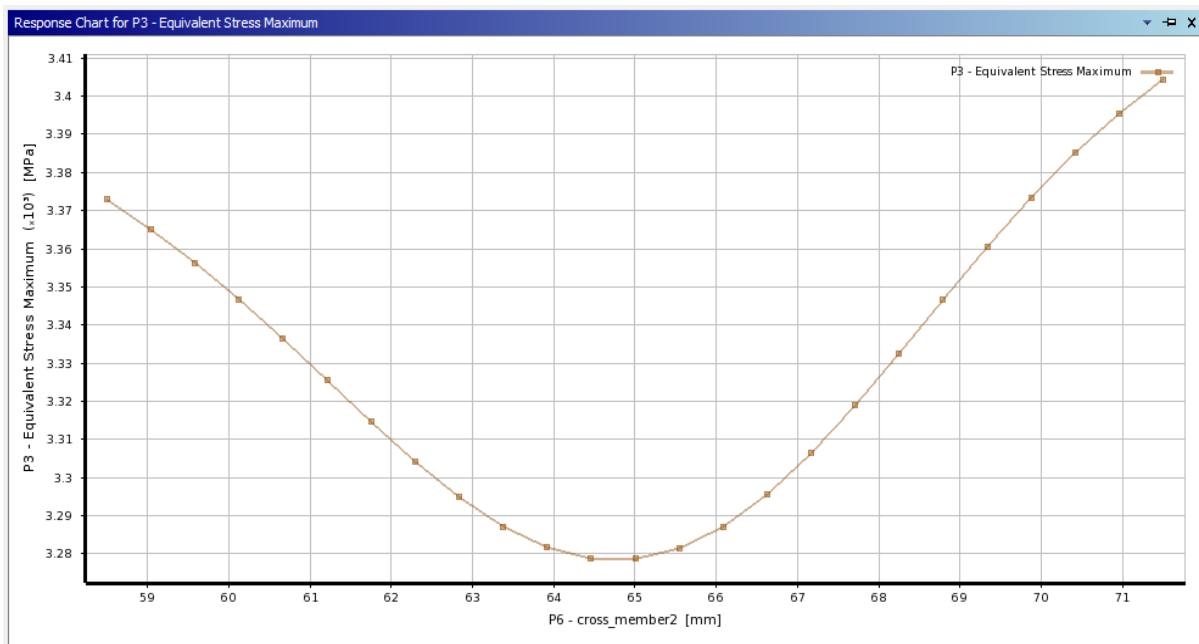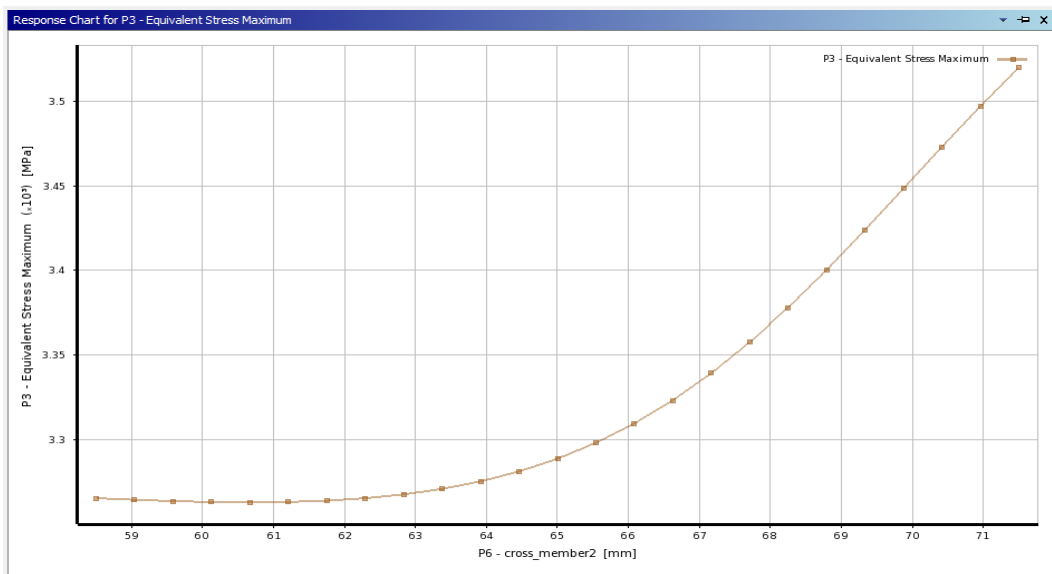

Figure 4.277: Equivalent-stress vs cross-member 2 for SGI using Al 6092/SiC/17.5P MMC

Figure 4.277 illustrates the variation of equivalent-stress vs cross member 2. The equivalent-stress is initially constant (3.2 x10^3 MPa) up to the cross member 2 dimension value of 61.5mm and then increases exponentially to the highest value (3.53 x10^3 MPa) at the cross member 2 dimension value of 71.5mm.
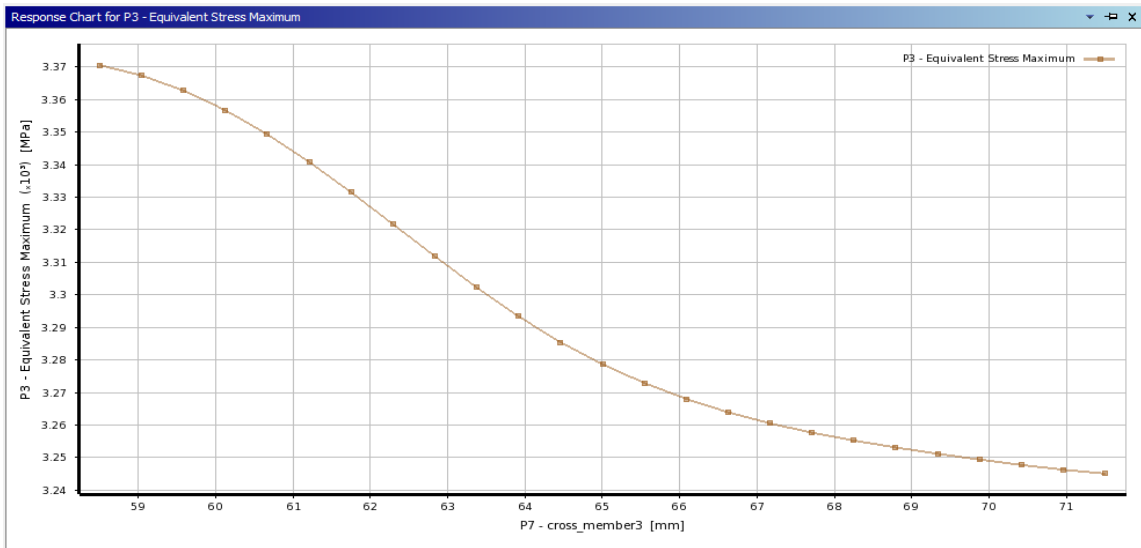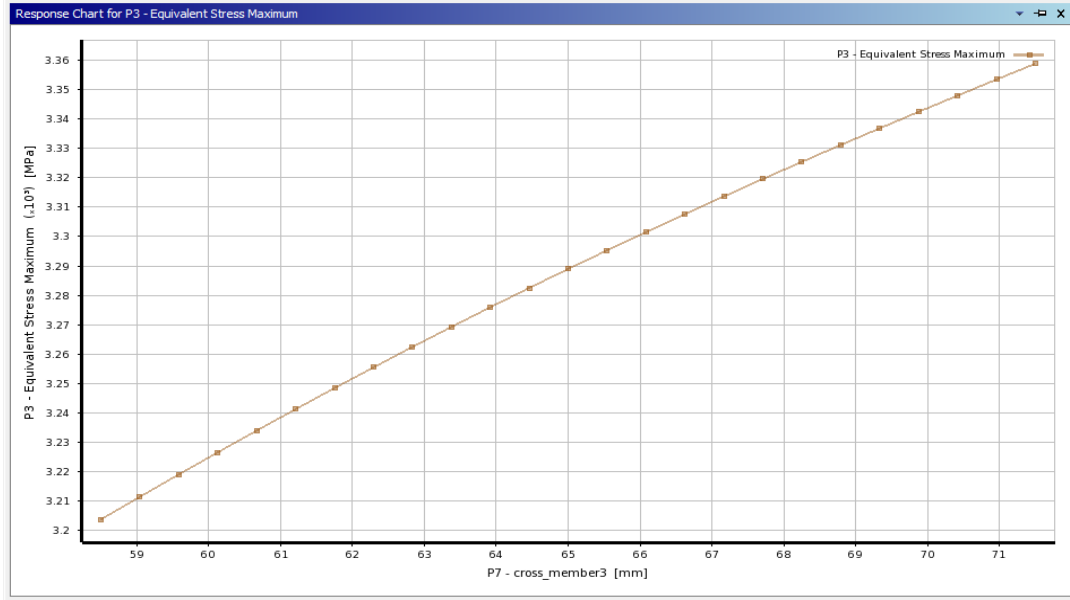

Figure 4.278: Equivalent-stress vs cross-member 3 for SGI using Al 6092/SiC/17.5P MMC

Figure 4.278 illustrates the variation of equivalent-stress vs cross-member 3 dimensions. The equivalent-stress is initially lowest at the cross-member 3 dimension value of 58.5mm, then increases linearly to its highest value at the cross-member 3 dimension value of 71.5mm.
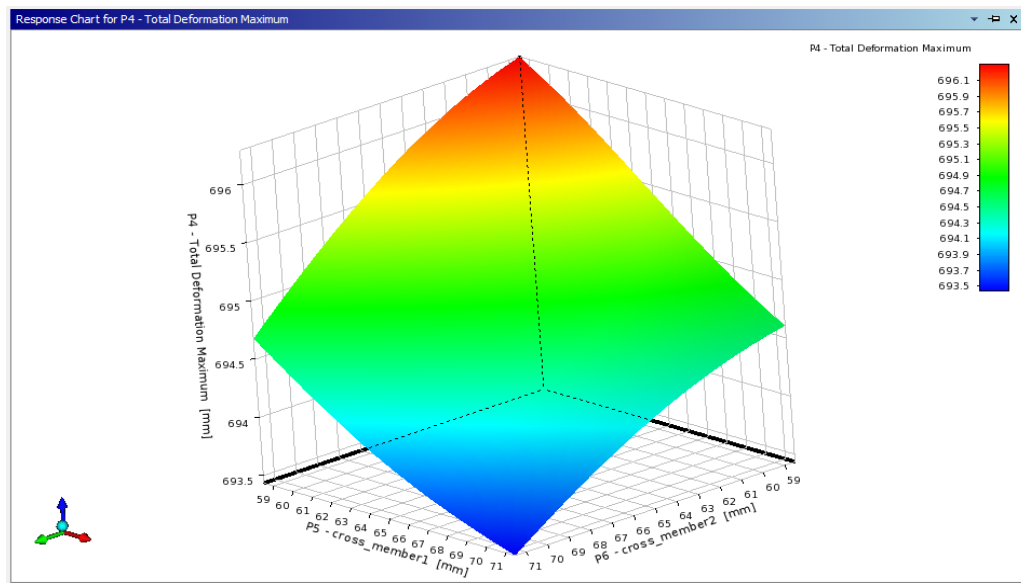
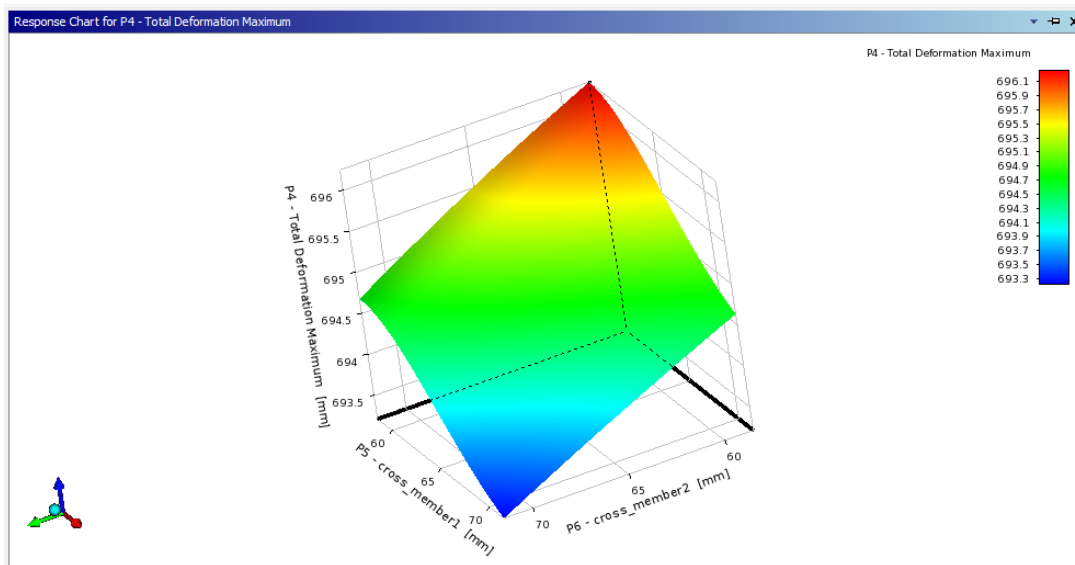
Figure 4.279: Response-Surface plot of total deformation vs cross-member 1 and cross-member 2 for SGI using Al 6092/SiC/17.5P MMC

Figure 4.279 illustrates the Response-Surface plot of deformation cross-member 1 and cross-member 2 dimensions. Maximum deformation is shown for cross-member 2 dimensions varying from 59mm to 64mm and cross-member 1 dimensions varying from 59mm to 63mm. In the other dimensions, the deformation has a minimum value, which is represented by the blue zone.
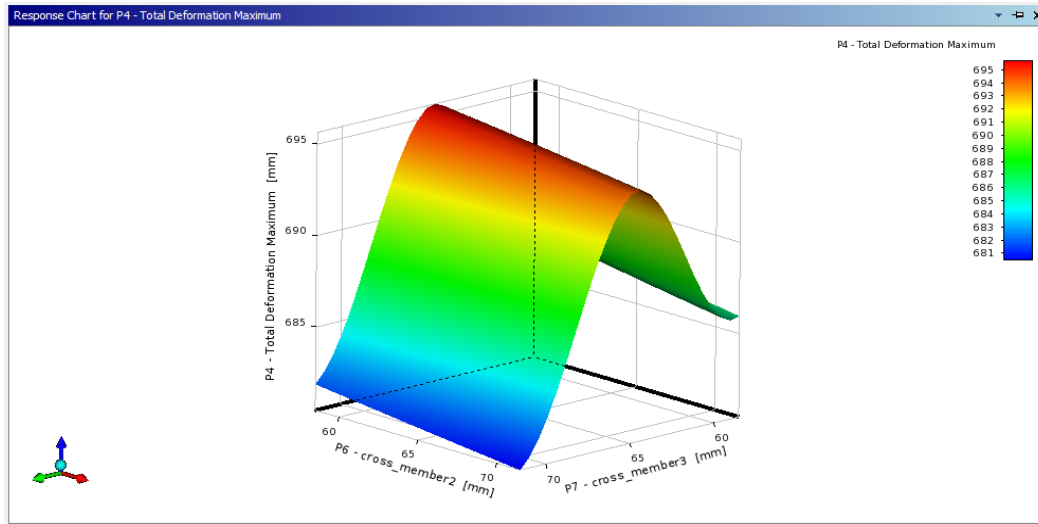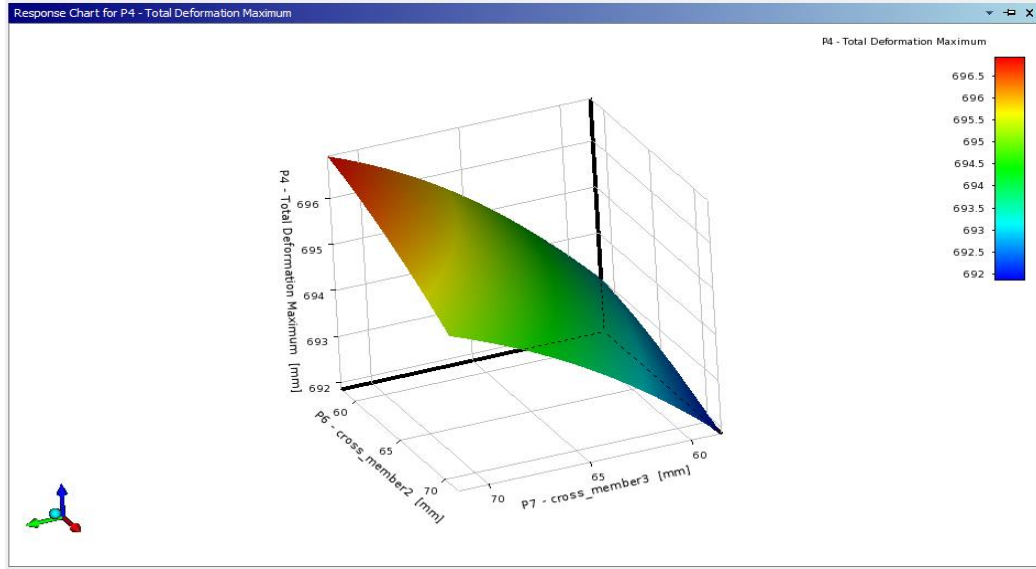

Figure 4.280: Response-Surface plot of total deformation vs cross-member 2 and cross-member 3 for SGI using Al 6092/SiC/17.5P MMC

Figure 4.280 illustrates the variation of deformation vs. cross-member 2 and cross-member 3 dimensions. The higher deformation 697 mm is observed for cross-member 3 dimensions varying from 66mm to 71mm, and for cross-member 2 dimensions varying from 59mm to 68mm.
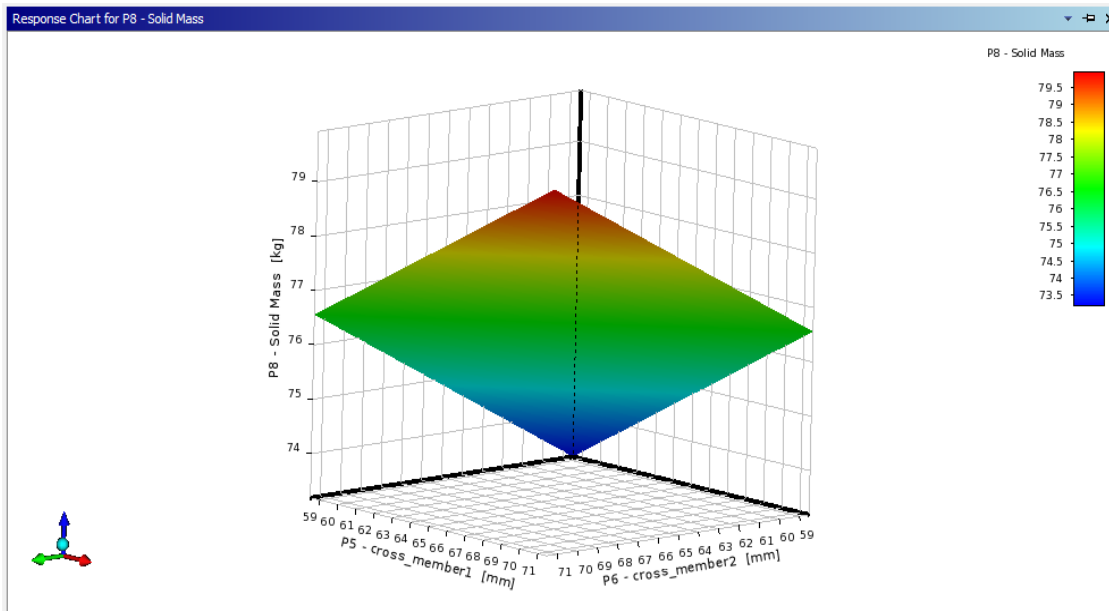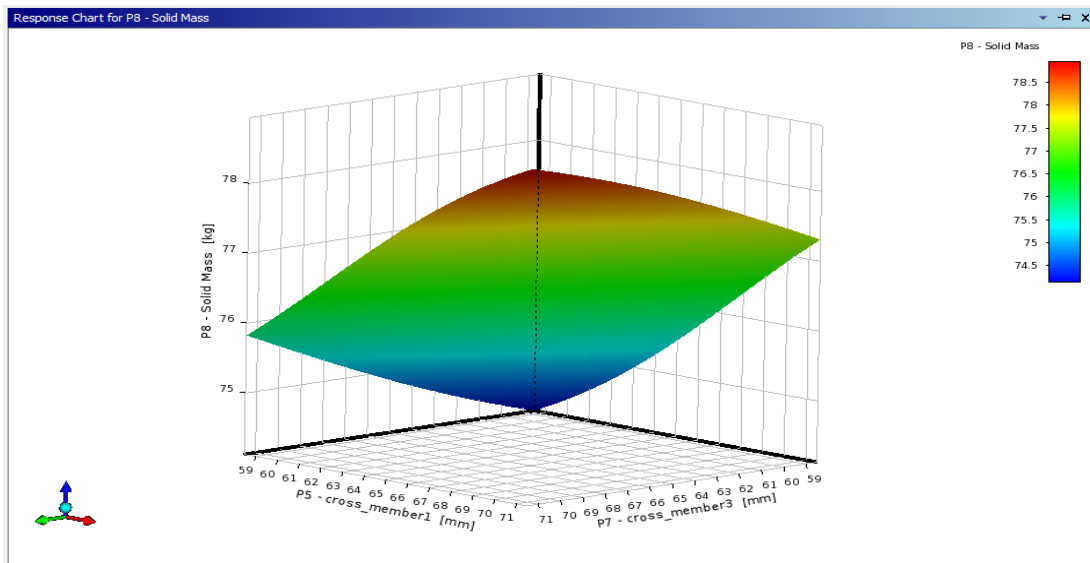

Figure 4.281: Response-Surface plot of mass vs cross-member 1 and cross-member 3 for SGI using Al 6092/SiC/17.5P MMC

Figure 4.281 illustrates the variation of mass vs cross-member 1 and cross-member 3 dimensions. The maximum solid mass is shown for cross-member 1 dimensions varying from 67mm to 71mm and cross-member 3 dimensions varying from 67mm to 71mm. Cross-member 1 and cross-member 2 dimensions varying from 59mm to 62mm have the lowest mass 73.4 kg.
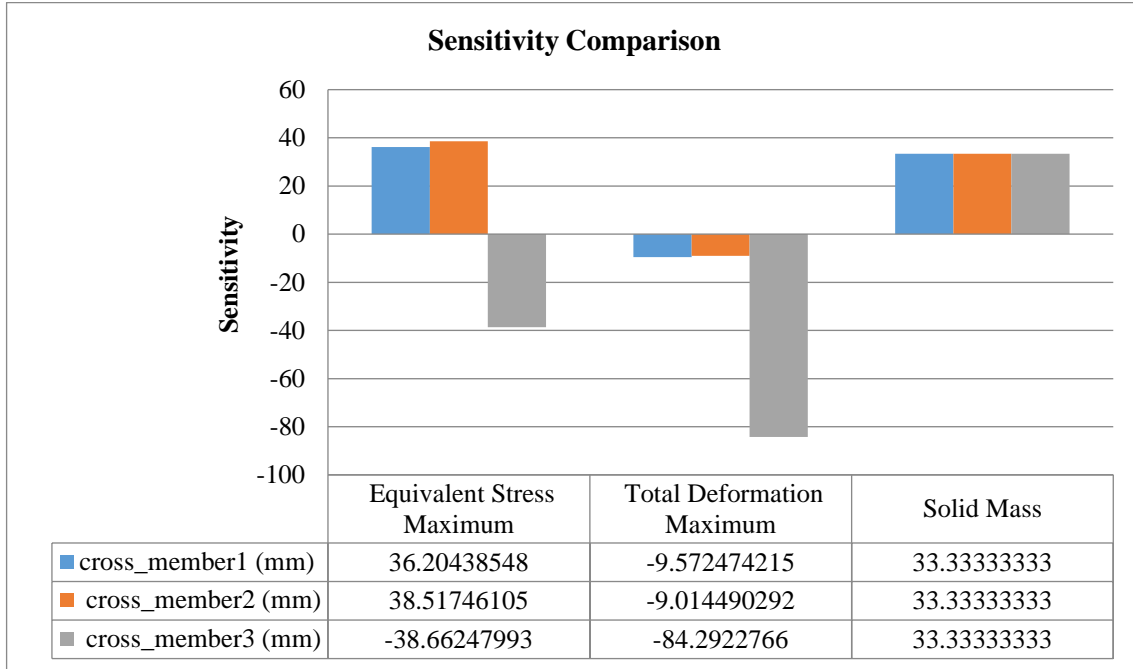
Sensitivity Comparison

	Equivalent Stress Maximum	Total Deformation Maximum	Solid Mass
cross_member1 (mm)	47.43668219	-9.336879467	53.52337144
cross_member2 (mm)	47.66321275	-9.401950916	53.52337102
cross_member3 (mm)	28.93381132	22.49481957	33.15028024
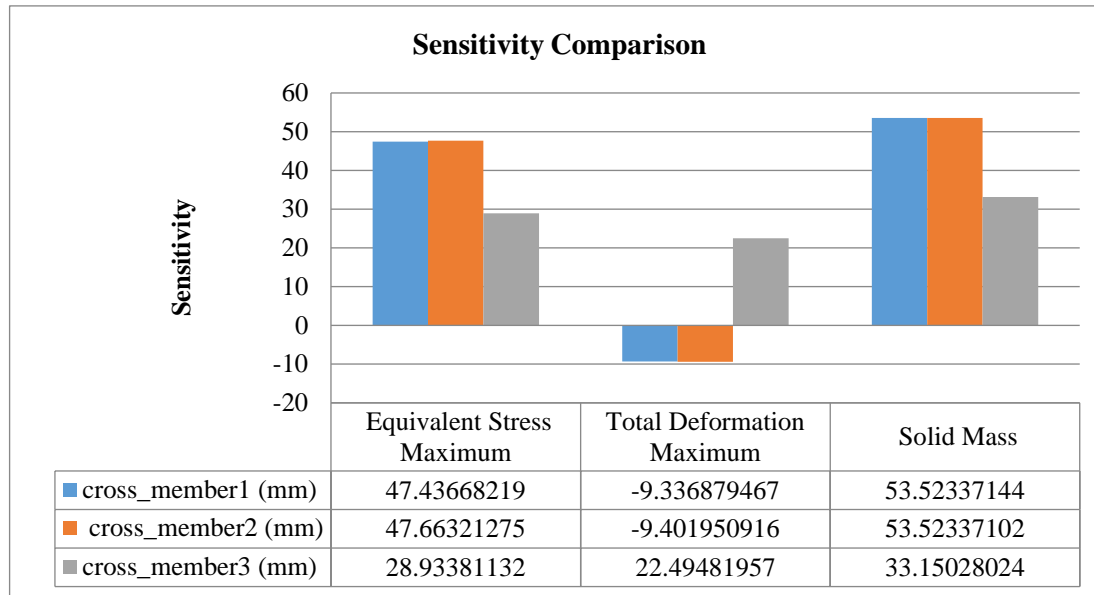
Figure 4.282: Sensitivity plot for SGI using Al 6092/SiC/17.5P MMC

Figure 4.282 illustrates the sensitivity plot, which is generated for all three output parameters, namely equivalent-stress, deformation, and solid mass. Cross-member 2 has the highest sensitivity percentage for equivalent-stress. Cross-member 3 has the highest sensitivity percentage for total deformation. Cross-members 1 and 2 have a similar sensitivity percentage of 53.523 for solid mass, whereas cross-member 3 has a minimum sensitivity percentage of 33.15.

4.6.6 Sub-Chapter Summary

Sub-Chapter has shown the application of optimization techniques in improving the design of chassis made of Al 6092/SiC material. The effect of optimization variables on equivalent-stress, deformation, and solid mass is discerned from 3D Response-Surface plots, 2D linearized plots, and sensitivity plots. The optimization results have shown that cross-member 3 has a maximum effect on chassis deformation compared to other variables. The maximum solid mass obtained from optimization is 80.673 kg, and the minimum solid mass obtained from the analysis is 72.447 kg which is one of the specific objectives.

In the next sub-chapter, the focus will be on the possibility of using the I-section and T-Section geometry profile of the chassis using finite element analysis as per specific objectives presented in section 1.4.

4.7 FEA Analysis of Chassis (St52E) using T section and I section

The current sub-chapter presents the FEA structural analysis results of the T section, and I section profile geometry on transverse members of the chassis and compare them with the square section analysis. The shear stress and deformation plots are generated for both design types and a comparative analysis is conducted based on these output parameters.

4.7.1 FEA Analysis using I section

The CAD design of the transverse I section is shown in figure 4.283. The FEA simulation is conducted on an I section design to determine stress and total deformation.
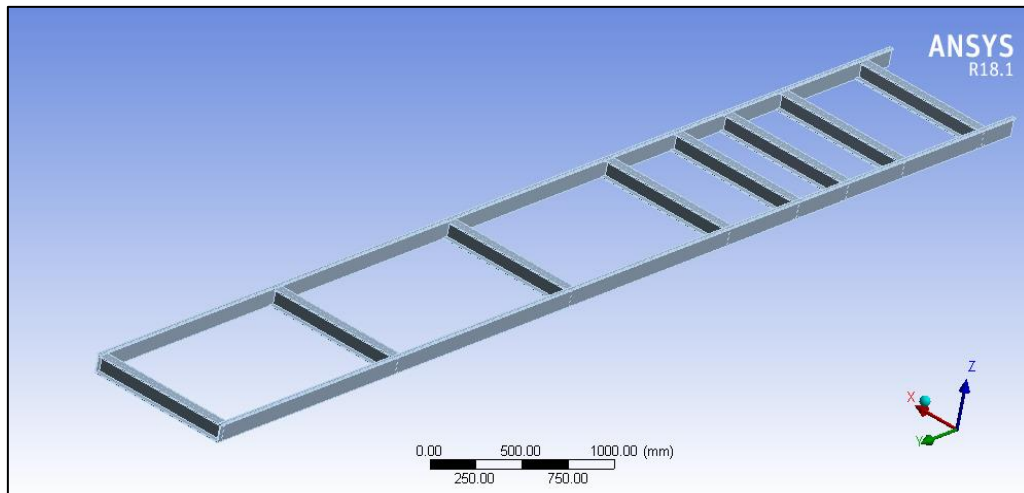
Figure 4.283: CAD design of transverse I section

The shear stress plot of the I section chassis is shown in figure 4.284. The maximum shear stress is observed at the corner regions as shown with the magnitude of 5014.1 MPa. The equivalent-stress plot is shown in figure 4.285 with the value of 32635 MPa.
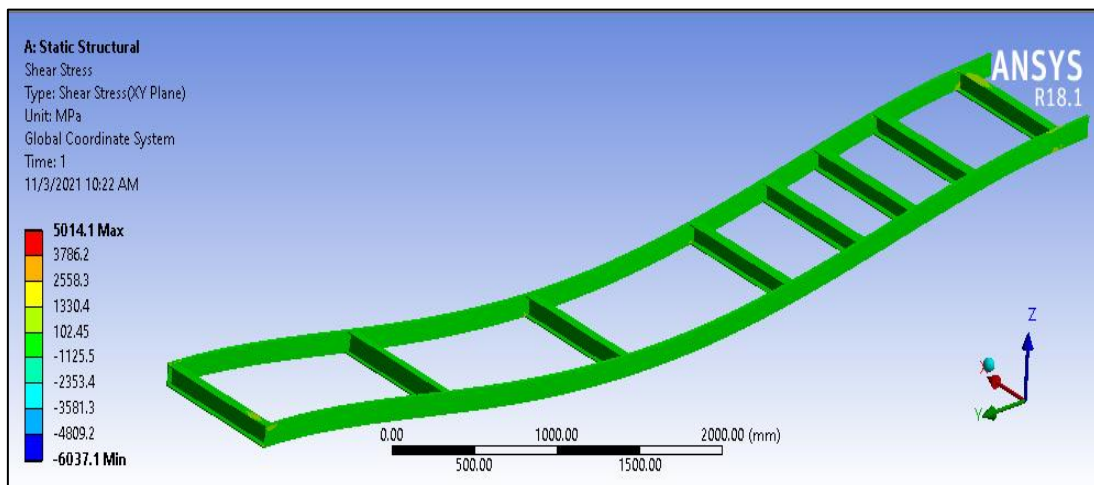
Figure 4.284: Shear stress of transverse I section
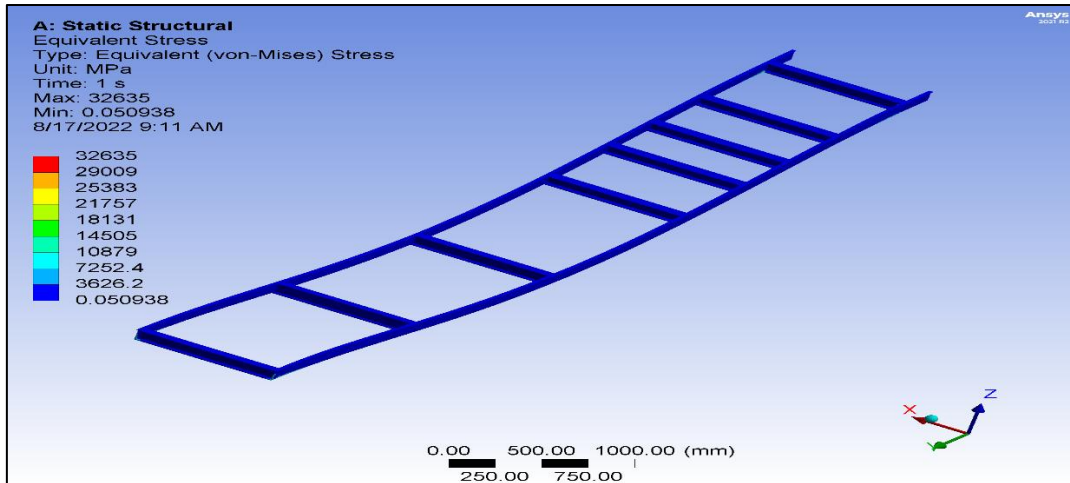
Figure 4.285: Equivalent-stress of transverse I section
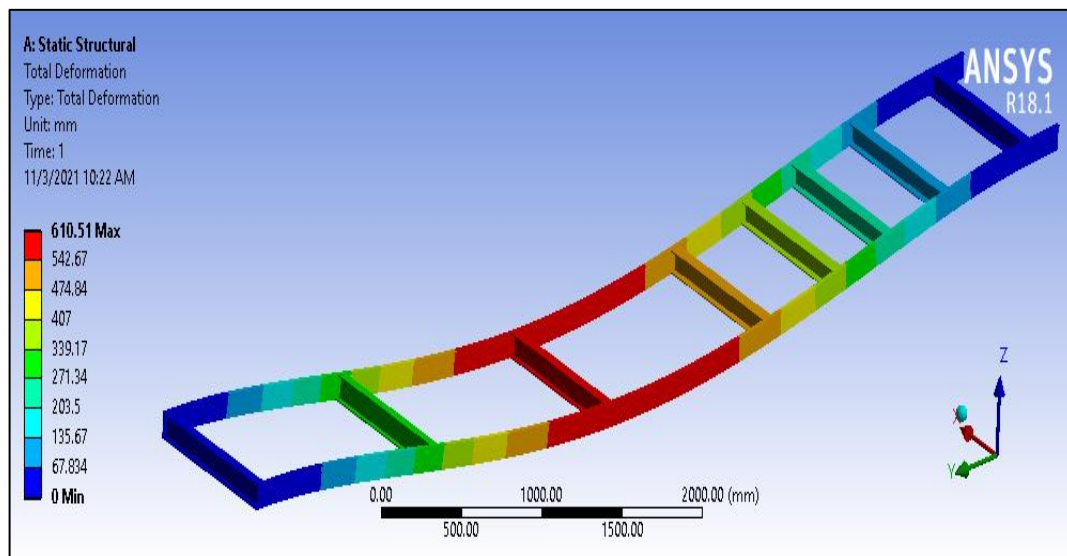
Figure 4.286: Total deformation of transverse I section

The total deformation plot obtained for the transverse I section is shown in figure 4.286. The maximum deformation is observed at the mid-section with a magnitude of 610.51 mm and the deformation reduces on moving towards the fixed support region according to the test requirement discussed in later sections.

4.7.2 FEA Analysis using the T section

The CAD design of the transverse T section is shown in figure 4.287. The FEA simulation is conducted on a T section design to determine stress and total deformation.
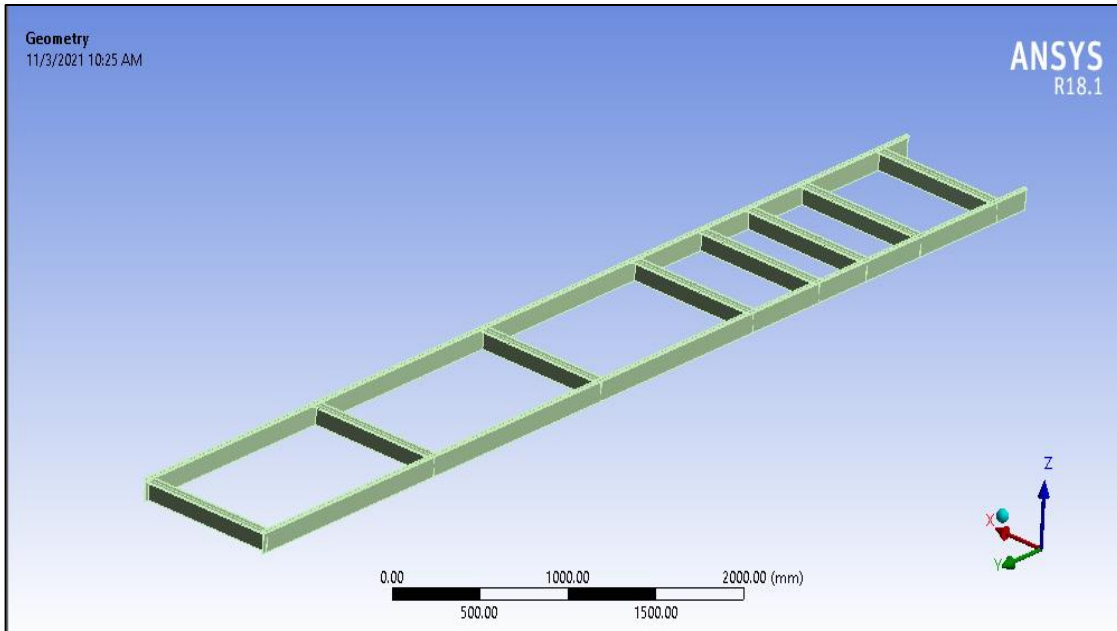
Figure 4.287: CAD design of transverse T section

The shear stress plot of the T section chassis is shown in figure 4.288. The maximum shear stress is observed at the corner regions with a magnitude of 8070.9 MPa. The equivalent-stress plot is shown in figure 4.289 with the value of 24562 MPa.
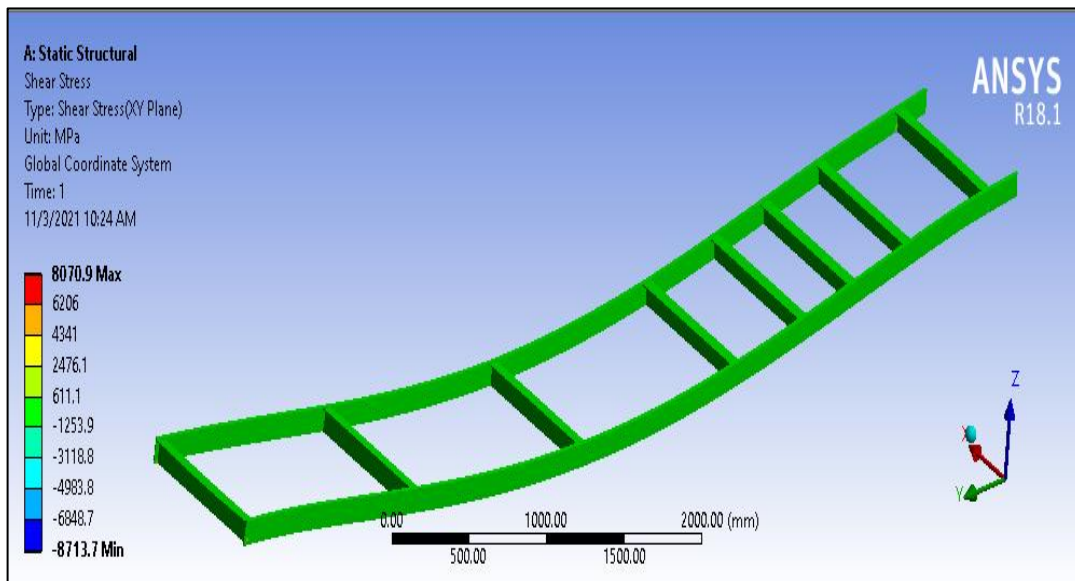
Figure 4.288: Shear stress of transverse T section
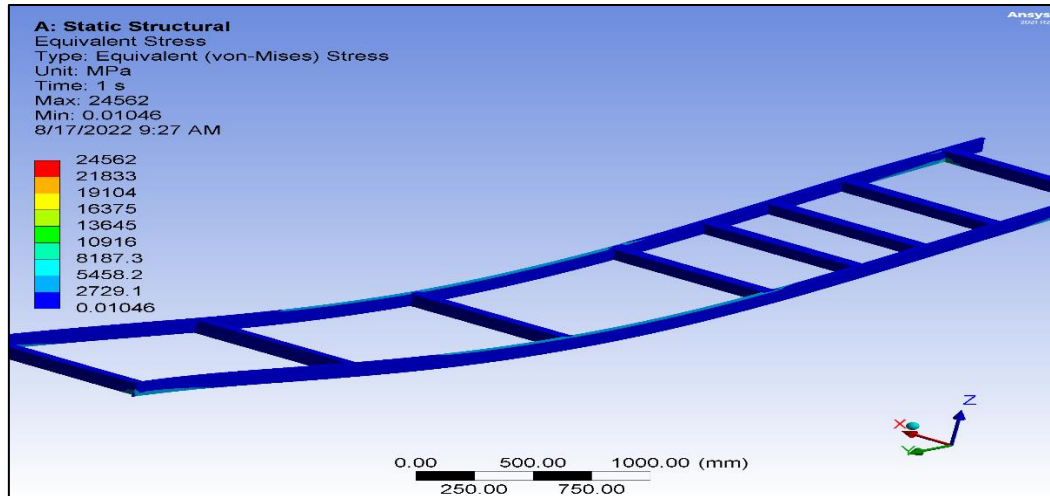
Figure 4.289: Equivalent-stress of transverse T section

The total deformation plot obtained for the transverse T section is shown in figure 4.290.
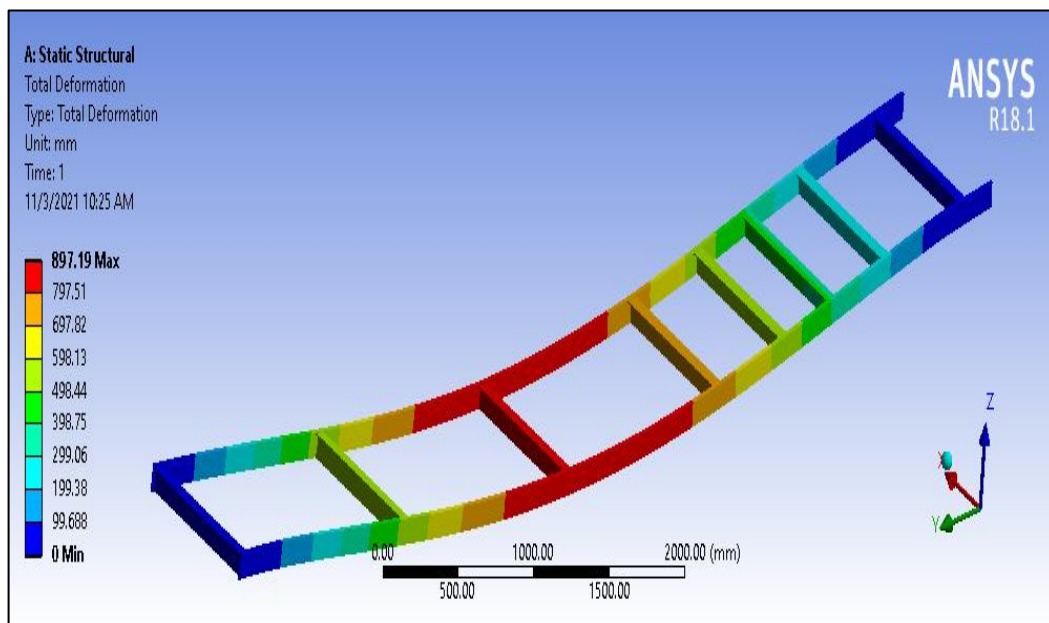
Figure 4.290: Total deformation of transverse T section

The maximum deformation is observed at the mid-section with a magnitude of 897.19 mm and the deformation reduces on moving towards the fixed support region.

4.7.3 FEA Analysis using square section

The CAD design of the transverse square section is shown in figure 4.291. The FEA simulation is conducted on a square section design to determine stress and total deformation.
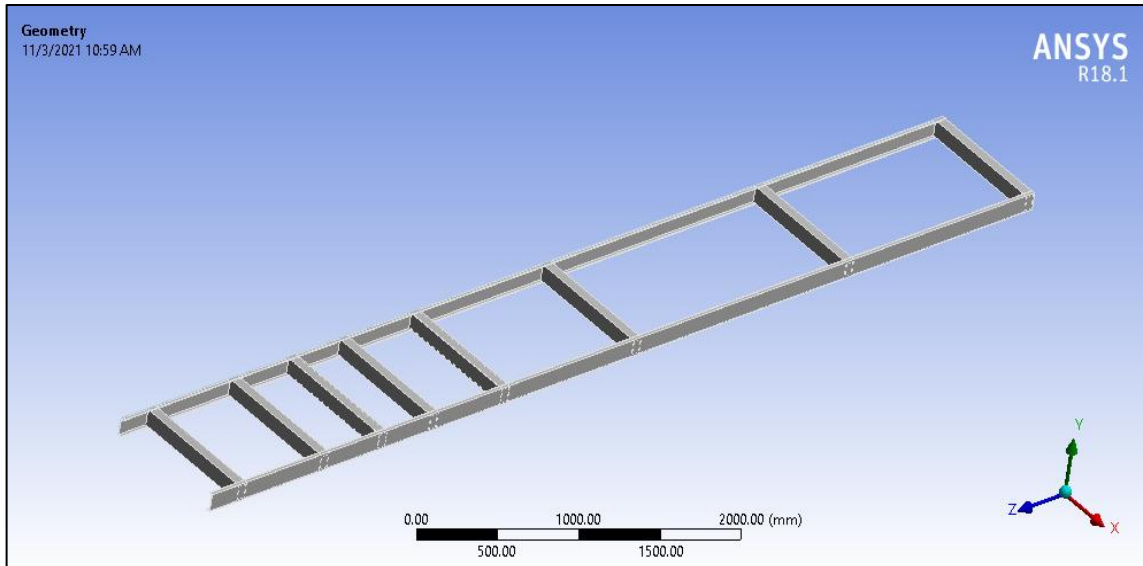
Figure 4.291: CAD design of transverse square section
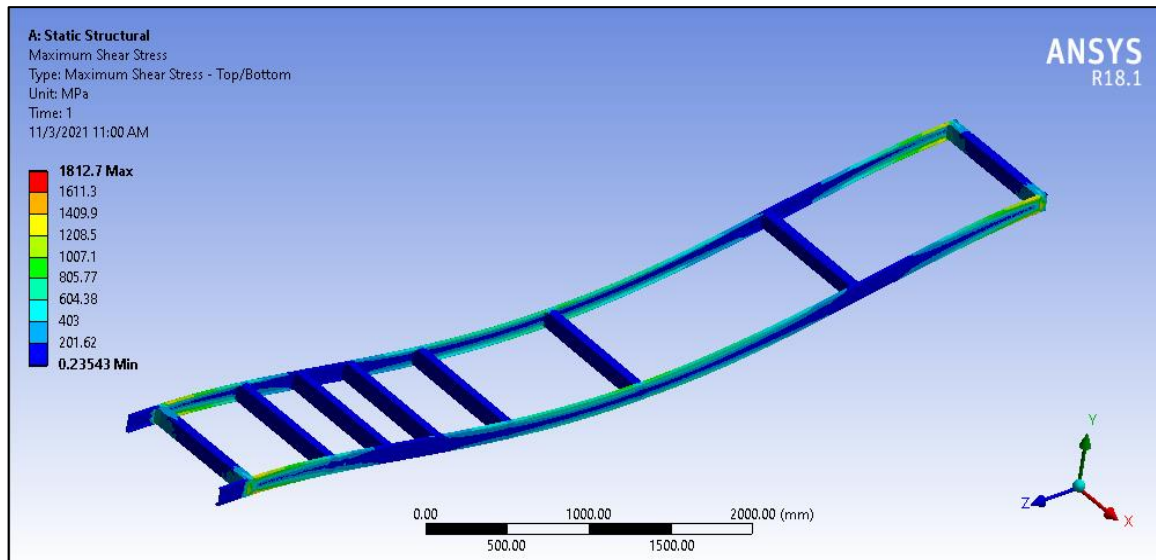
Figure 4.292: Shear stress of transverse square section

The shear stress plot of the square section chassis is shown in figure 4.292. The maximum shear stress is observed at the corner regions with a magnitude of 1812.7 MPa. Figure 4.293 displays the total deformation plot for the transverse square section.
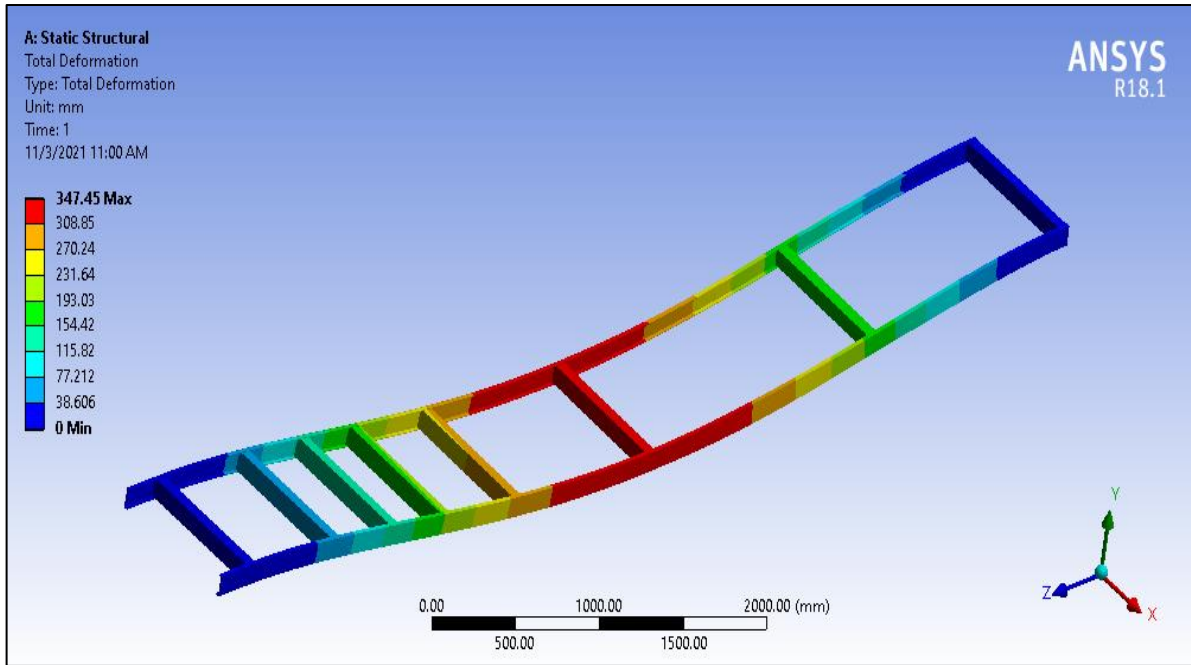
Figure 4.293: Total deformation of transverse square section

The mid-section exhibits the greatest deformation, with a magnitude of 347.45 mm, and the deformation decreases as one moves closer to the fixed support region. Table 4.47 shows a comparison of the results from different profiles.

Table 4.47: Results comparison between different profiles

Profile	Shear stress (MPa)	Deformation (mm)
I section	5014.1	610.51
T section	8070.9	897.19
Square section	1812.7	347.45

The shear stress and deformation comparison are made for different profiles as shown in figures 4.294 and 4.295.
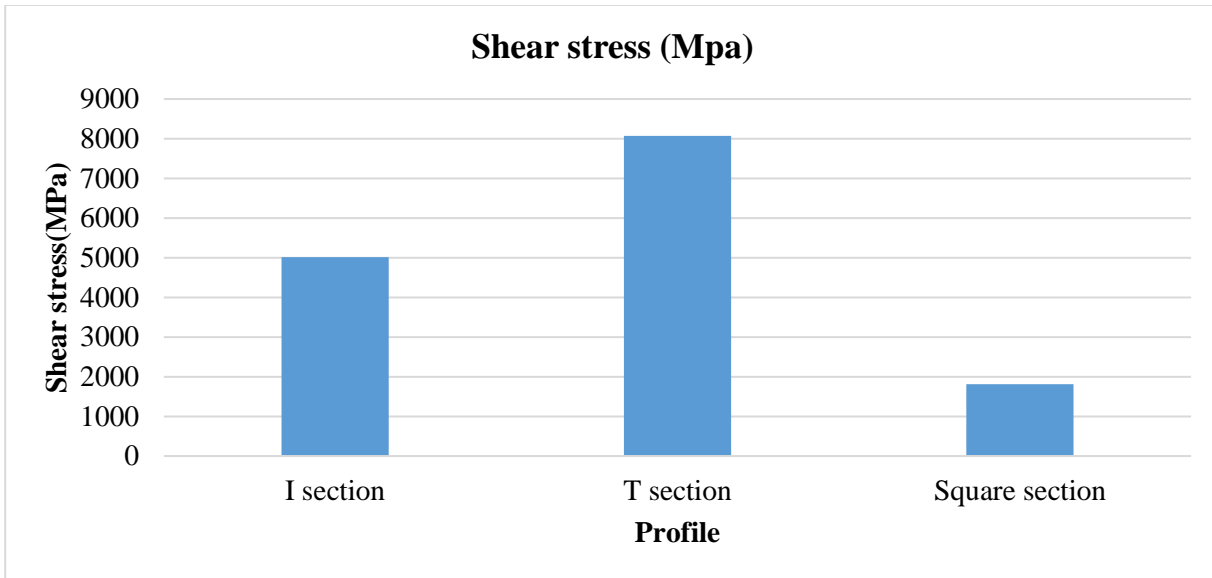
Figure 4.294: Shear stress comparison between different profiles
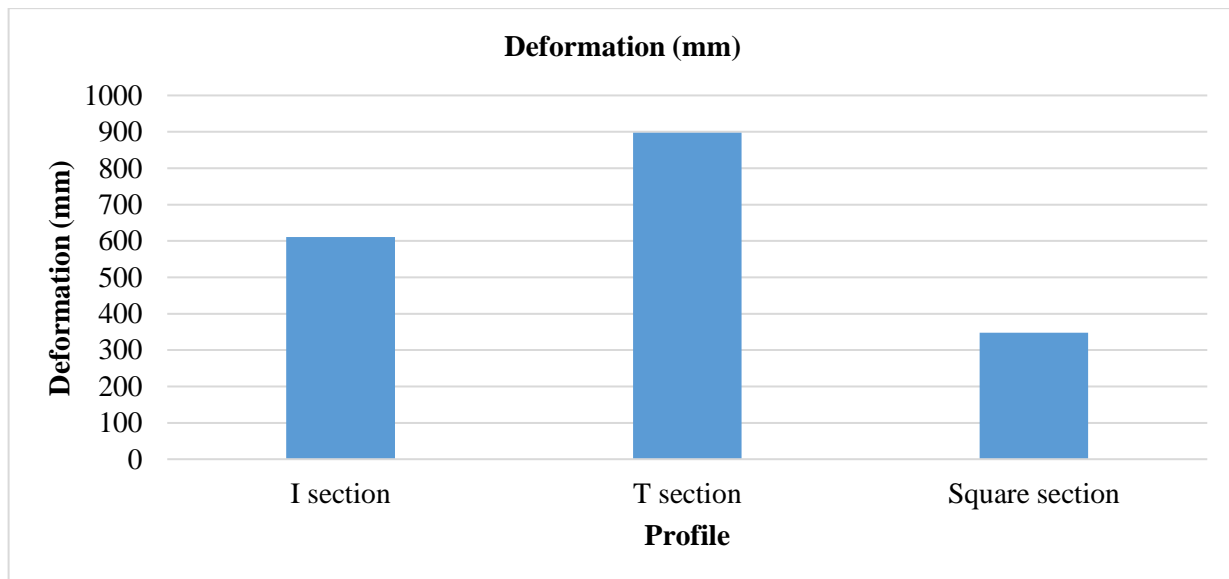
Figure 4.295: Deformation comparison between different profiles

The comparison shows minimum shear stress for the square section and maximum shear stress for the T section profile. Similarly, the deformation obtained for the T section profile is maximum, and deformation obtained for the square section is minimum. The results conclude the non-suitability of the I or T section profile for HMV chassis. This is further validated by the commercial test on these profiles (see section 4.9.1).

4.7.4 Sub-Chapter Summary

The FEA structural analysis results are obtained for the square section, I Section, and T section profile. The comparison shows minimum shear stress for the square section and maximum shear stress for the T section profile. The deformation obtained for the T section profile is maximum and the deformation obtained for the square section is minimum.

The results conclude the FEA analysis results have shown that stresses and deformation generated on chassis with I and T sections are very high compared to the square section. Due to this high magnitude of stress and deformation, the I and T-shaped lateral members are unfit for HMV chassis. This exercise fulfills some of the specific objectives (c,g, and h) of the study (see § 1.4).

In the next sub-chapter, the use of the six-sigma tool to evaluate the robust design of the chassis will be discussed.

4.8 Six Sigma Evaluation of Two Variables

The current sub-chapter presents an application of the six-sigma tool in the robust design of chassis. The sigma level and probability distribution chart data are presented.

4.8.1 Design Points Generated using DOE

For generating the design of the experiments table, the optimization variable was selected i.e., cross-member 1. The equivalent-stress, total deformation, and solid mass are evaluated as shown in Table 4.48.

Table 4.48: Design Points generated

A	B	C	D	E	F
Name	P5 - cross-member 1 (mm)	P9 - cross-member 2 (mm)	P3 - Equivalent-stress Max (MPa)	P4 - Total Deformation Maximum (mm)	P8 - Solid Mass (kg)
1	69.46366887	58.30449669	3524.30585	347.3484616	213.0182538
2	73.92733775	62.76816556	3268.206139	347.1517151	219.5107084
3	60.53633113	69.46366887	3263.290373	347.2832876	214.6413675
4	67.23183444	67.23183444	3559.508211	346.9559688	217.8875948
6	62.76816556	60.53633113	3265.487472	347.5904054	209.7720265
7	65	73.92733775	3520.280778	346.7094195	221.1338221
8	71.69550331	71.69550331	3266.228748	346.5846775	224.3800493

The goodness of fit curve is generated in figure 4.296, which shows the variation of observed values from expected values. The graph shows the little variation of observed values (i.e., red, green, and blue boxes) from expected values (straight curve).
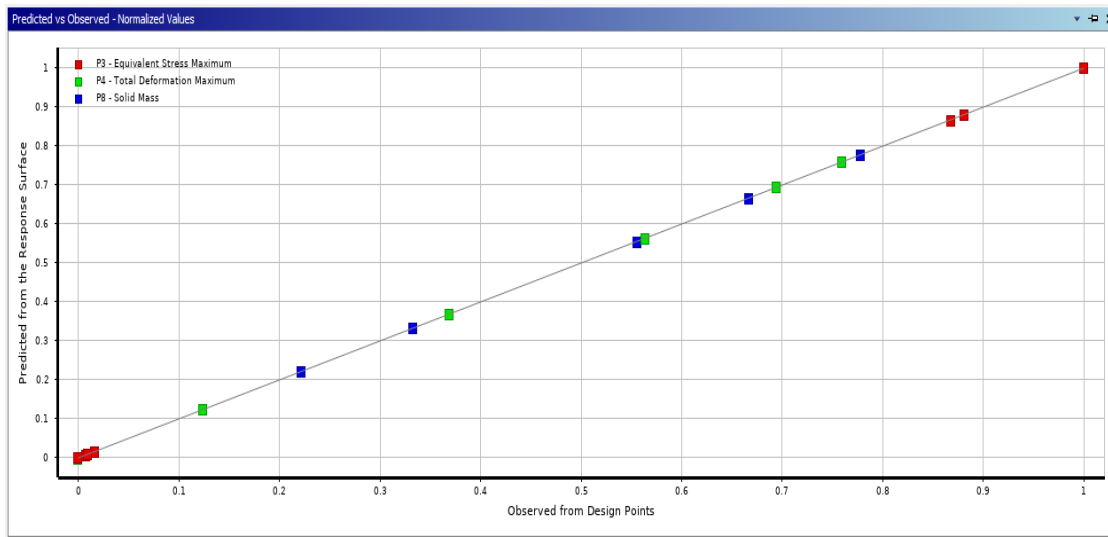
Figure 4.296: Goodness of fit curve
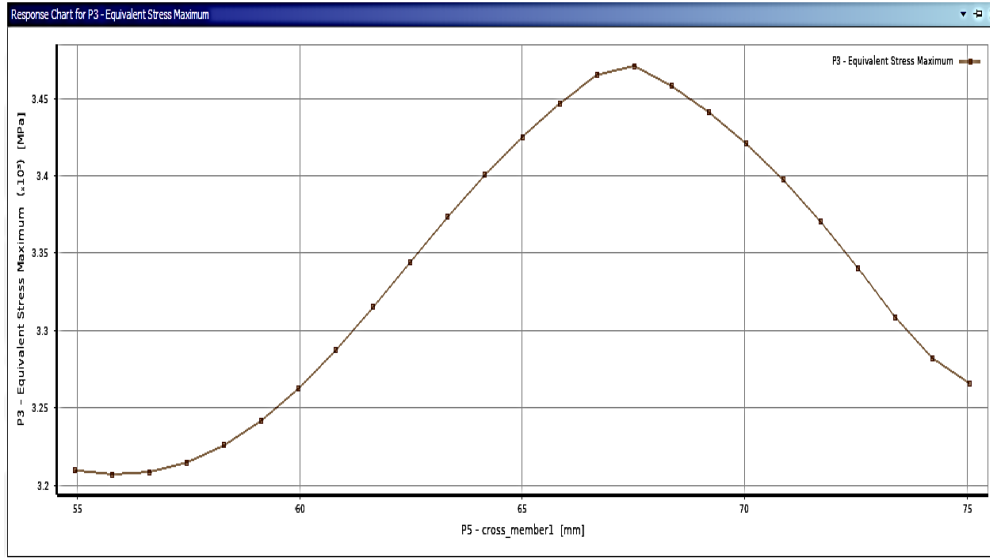
Figure 4.297: Equivalent-stress vs cross-member 1

Figure 4.297 illustrates the variation of equivalent-stress vs cross-member 1 dimensions. The curve shows growth in equivalent-stress up to the 67 mm value of cross-member 1 dimension and then decreases to a minimum at 75 mm dimension value.
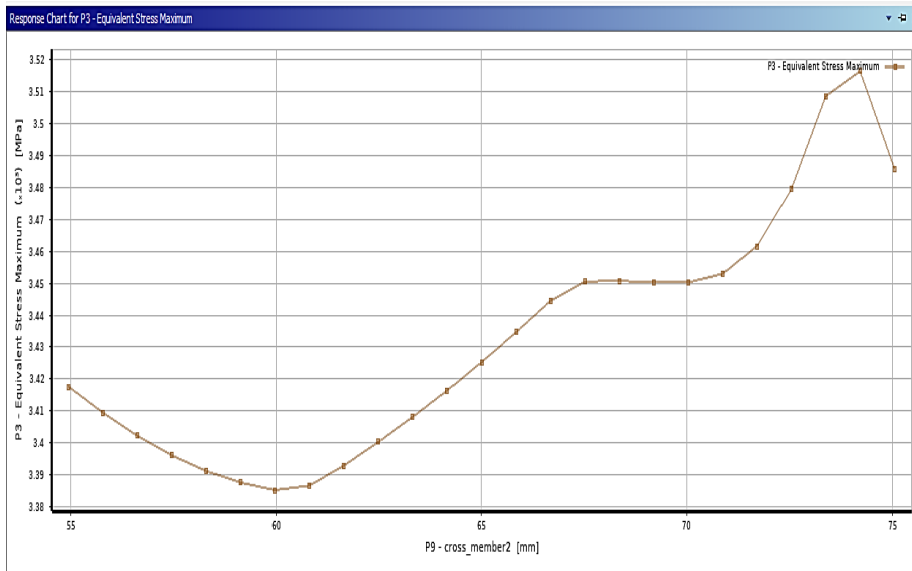
Figure 4.298: Equivalent-stress vs cross-member 2

Figure 4.298 illustrates the variation of equivalent-stress with respect to cross-member 2 dimensions. The equivalent-stress decreases as cross-member 2-dimension increases, reach a minimum at cross-member 2-dimension value of 60 mm, and then increases. Table 4.49 shows the probability density and sigma level for various design points, and figure 4.299 shows the probability density curve for cross-member 1.

Table 4.49: Probability and sigma level for cross member1

#	P5 - cross-member 1 (mm)	
P5	**Probability**	**Sigma Level**
52.67351	6.93E-05	-3.810609428
53.6866	0.000252189	-3.478420858
54.69968	0.000809289	-3.152537809
55.71276	0.002148096	-2.85555317
56.72585	0.005457793	-2.545389656
57.73893	0.01277508	-2.232981525
58.75202	0.027322248	-1.921692149
59.7651	0.053619497	-1.610728143
60.77819	0.096978052	-1.298964545
61.79127	0.16178963	-0.987129316
62.80436	0.249619881	-0.675686419
63.81744	0.357963685	-0.363907117
64.83053	0.479190255	-0.052185973
65.84361	0.602433255	0.259650356
66.8567	0.716073904	0.571217537
67.86978	0.81138902	0.883026494
68.88286	0.88390661	1.194744733
69.89595	0.933980665	1.506111088
70.90903	0.96544886	1.817750379
71.92212	0.983367303	2.128865415
72.9352	0.992687972	2.441557546
73.94829	0.997032121	2.751309202
74.96137	0.998903415	3.062744819
75.97446	0.999633289	3.376770432
76.98754	0.99984779	3.611508788
78.00063	0.999896803	3.711059108
79.01371	0.999930688	3.810609428

As per less sigma level data obtained for cross member1 in table 10.2, the chassis design is the least reliable with cross-member 1 dimensions varying from 56.72 mm to 73.94 mm. The chassis design is more reliable for cross-member 1 dimensions varying from 52.67 mm to 56.72 mm and 74.96 mm to 79.01 mm. From the probability density plot in figure 4.299, the high probability (more than .99) is obtained for cross-member 1 dimension varying from 73.94 mm to 79.01 mm.
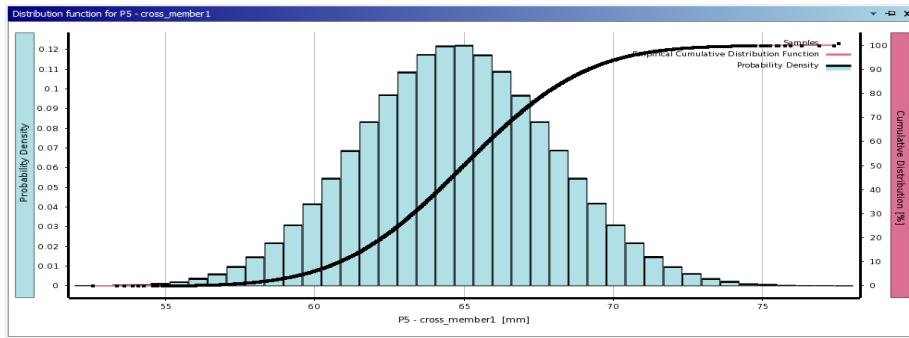
Figure 4.299: Probability density curve for cross-member 1

Table 4.50 shows the probability and sigma levels for cross member2.

Table 4.50: Probability and sigma level for cross member2

#	P9 - cross-member 2 (mm)	
P9	Probability	Sigma Level
51.31878079	6.93E-05	-3.810609428
52.36439823	0.000110005	-3.694856813
53.41001568	0.000187914	-3.556501018
54.45563312	0.000628963	-3.225409435
55.50125057	0.001745274	-2.920870561
56.54686802	0.004683917	-2.598330252
57.59248546	0.011349524	-2.27846229
58.63810291	0.025136445	-1.957634664
59.68372035	0.050983962	-1.635387136
60.7293378	0.094406016	-1.314101576
61.77495524	0.160533369	-0.992268146
62.82057269	0.25124799	-0.670567679
63.86619014	0.363583778	-0.348895777
64.91180758	0.489190504	-0.027098706
65.95742503	0.615859334	0.294623731
67.00304247	0.731135349	0.616250352
68.04865992	0.825850683	0.937894504
69.09427736	0.896085339	1.259556714
70.13989481	0.943088887	1.581244271
71.18551226	0.971473378	1.902902602
72.2311297	0.986936594	2.224321601
73.27674715	0.994567403	2.547004794
74.32236459	0.997953623	2.870922905
75.36798204	0.999274072	3.18413816
76.41359948	0.999764169	3.496353788
77.45921693	0.999888311	3.690994523
78.50483437	0.999930688	3.810609428

As per less sigma level data obtained for cross member2 in table 10.3, the chassis design is least reliable with cross-member 2 dimensions varying from 55.501 mm to 74.322 mm. The chassis design is more reliable for cross-member 2 dimension values varying from 51.318 mm to 55.501 mm and 75.36 mm to 78.504 mm. From the probability density plot in figure 4.300, the high probability (more than .99) is obtained for cross-member 2 dimensions varying from 73.27 mm to 78.504 mm.
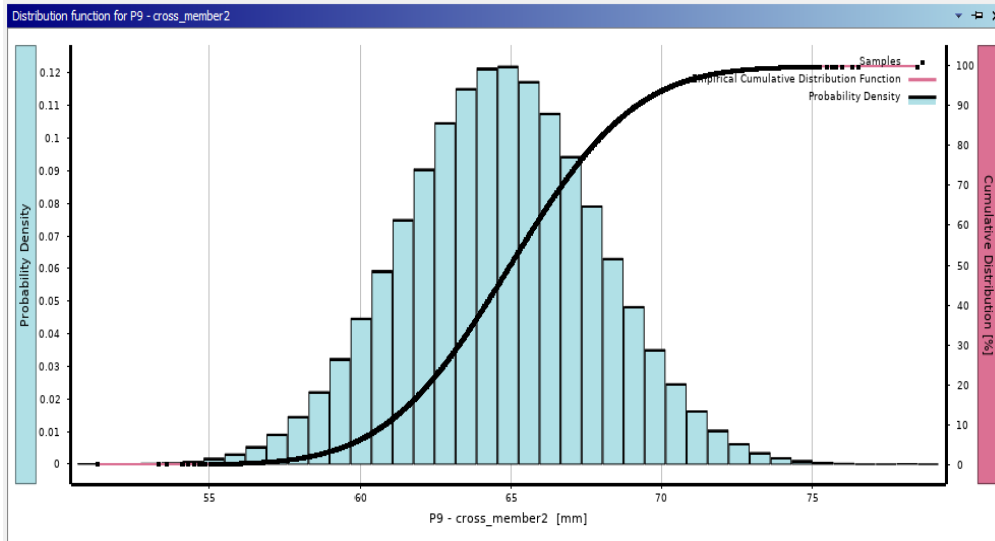
Figure 4.300: Probability density curve for cross-member 2

4.8.2 Sub-Chapter Summary

Sub-Chapter has presented an application of the six-sigma tool in the robust chassis design. The sigma level and probability distribution chart data are presented which is a key part of the research hypothesis & objectives. The reliability study is conducted on two variables of HMV chassis. The appropriate range of values for cross-member 1 and cross-member 2 is determined for which the design is most reliable and least reliable. From the probability density study, the dimension range of cross-member 1 and cross-member 2 with maximum probability is determined. From the six-sigma chart, the chassis design is the least reliable with a cross-member with one dimension varying from 56.72 mm to 73.94 mm and a cross-member with two dimensions varying from 55.501mm to 74.322 mm.

The next sub-chapter will present the commercial experimental testing of the chassis made of conventional steel to establish the failure mode and location in line with specific objectives.

4.9 Commercial Validation

4.9.1 Commercial Experimental Testing of the St52E chassis

The chassis (made of St52E) was commercially investigated experimentally under flexural loading conditions to establish the failure mode and location. The front and back ends of the chassis have two supports. A transverse load is applied to the two longitudinal members of the chassis. The following sections present the results of commercial tests performed on the steel chassis with the various cross-section profiles investigated.

4.9.1.1 Commercial Vehicle chassis test using square section

The results obtained from the commercial experimental test are shown in figure 4.301. The acceptable range of equivalent stress should be between 3220 MPa and 3527.7 MPa. The laboratory observed stress is 3480 MPa. The industry-acceptable range of deformation should be between 338 mm - 347.89 mm. The FE simulation results are close (6 % and 2% respectively) to the observed test value, refer to figure 4.1 and figure 4.3.

COMMERCIAL VEHICLE CHASSIS TEST ASSESMENT REPORT

PART NAME: - Chassis   REPORT NO: - DC01
PART NO: -   Ch971   DATE: 08.06.21
                              GR.NO:- Trial test
VENDOR: -   M/S MAPL   QTY: - 01 No.

Structure Design :-

SIDE VIEW OF CHASSIS

TOP VIEW OF CHASSIS

All dimensions are in mm

PARAMETERS	SPECIFICATIONS	OBSERVATIONS	REMARKS
Equivalent stress	3220 - 3527.7	3480	OK
Deformation	338 - 347.89	342.05	OK
Safety factor	1.07 - 1.25	1.13	OK
Solid Mass	200 - 228.82	213.08	OK

ACCEPTED

For Metalman Auto Pvt. Ltd.,
For METALMAN AUTO PVT. LTD.,
Authorised Signatory.

CHECKED BY- Abhinash Panwar   APPROVED BY: - Rohit Singh

Figure 4.301: Commercial Vehicle chassis test results using **square** section

No permanent deformation is observed. Under the flexural loading conditions, the square section chassis can sustain the loading conditions. Therefore, a square profile cross-section is suitable for application for an HMV chassis.

4.9.1.2 Commercial Vehicle chassis test using I section

Under similar flexural loading conditions, the experimental investigation of the I section chassis was carried out. Figure 4.302 presents the results.

COMMERCIAL VEHICLE CHASSIS TEST ASSESMENT REPORT

PART NAME: - Chassis
PART NO: -   Ch971

VENDOR: -   M/S MAPL

REPORT NO: - DC18
DATE: 16.12.21
GR.NO:- Trial test
QTY: - 01 No.

Structure Design :-

ALL DIMENSIONS ARE IN MM

PARAMETERS	SPECIFICATIONS	OBSERVATIONS	REMARKS
Equivalent stress	3220 - 3527.7	32642, SS-5019	NOK
Deformation	338 - 347.89	618	NOK
Safety factor	1.07 - 1.25	2.51	NOK
Solid Mass	200 - 228.82	244.5	NOK

REJECTED

For Metalman Auto Pvt. Ltd.,
For METALMAN AUTO PVT. LTD.,
Authorised Signatory.

CHECKED BY- Abhinash Panwar   APPROVED BY: - Rohit Singh

Figure 4.302: Commercial Vehicle chassis test results using **I** section

As before, the acceptable range of equivalent stress is between 3220 MPa and 3527.7 MPa, and the laboratory observation was 32642 MPa with a shear stress value of 5019 MPa. Similarly, the acceptable range of deformation is between 338 mm and 347.89 mm and the observation is 618 mm. Our simulation results obtained similar values of 5014.1 MPa and 610.51 mm respectively (refer to sub-section 4.7.1). This means permanent deformation has taken place and therefore the I section chassis profile is not suitable for a chassis profile.

4.9.1.3 Commercial Vehicle chassis test using T section chassis

Similarly, the results of the experimental testing on the T cross-section are depicted in figure 4.303.
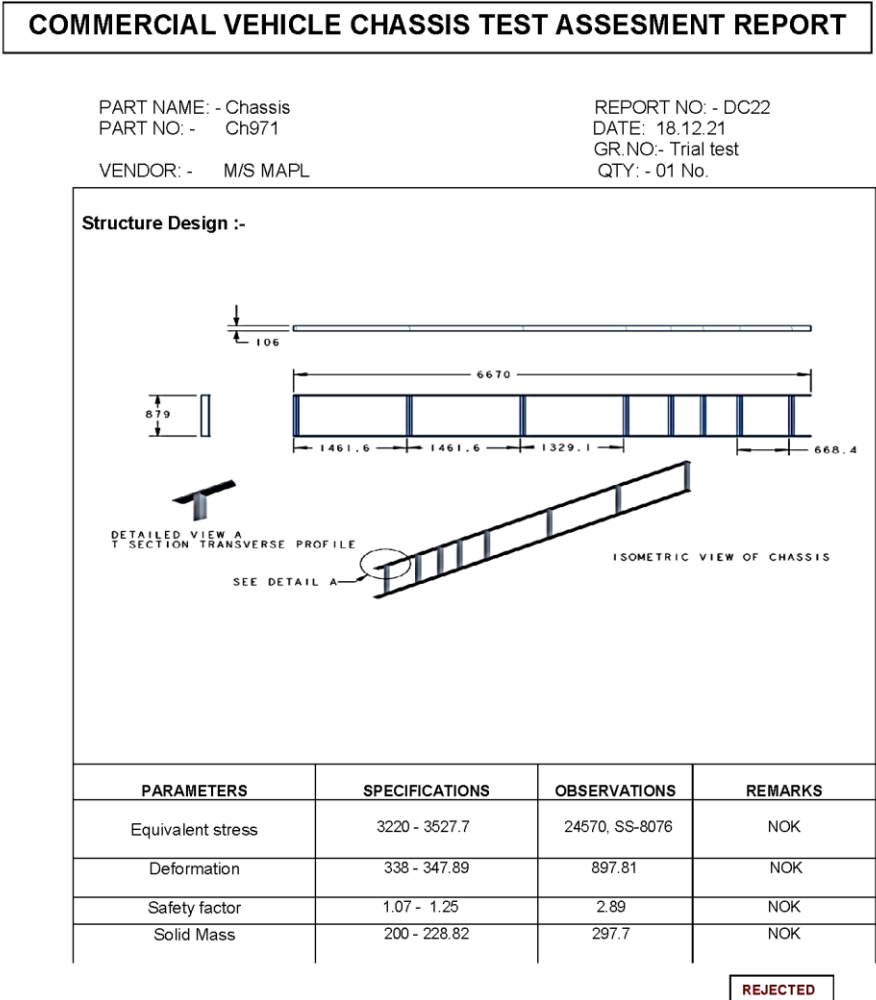
COMMERCIAL VEHICLE CHASSIS TEST ASSESMENT REPORT

PART NAME: - Chassis
PART NO: -   Ch971

VENDOR: -   M/S MAPL

REPORT NO: - DC22
DATE: 18.12.21
GR.NO:- Trial test
QTY: - 01 No.

Structure Design :-

DETAILED VIEW A
T SECTION TRANSVERSE PROFILE

SEE DETAIL A

ISOMETRIC VIEW OF CHASSIS

PARAMETERS	SPECIFICATIONS	OBSERVATIONS	REMARKS
Equivalent stress	3220 - 3527.7	24570, SS-8076	NOK
Deformation	338 - 347.89	897.81	NOK
Safety factor	1.07 - 1.25	2.89	NOK
Solid Mass	200 - 228.82	297.7	NOK

REJECTED

For Metalman Auto Pvt. Ltd.,
For METALMAN AUTO PVT. LTD.,

Authorised Signatory.

CHECKED BY- Abhinash Panwar   APPROVED BY: - Rohit Singh

Figure 4.303: Commercial Vehicle chassis test results using **T** section

According to the commercial validation, the acceptable range of equivalent stress should be between 3220 and 3527.7 MPa and observation is 24570 MPa with a shear stress value of 8076 MPa, while the acceptable range of deformation should be 338-347.89 mm and observation is 897.81 mm. Our simulation results obtained, are in close agreement with these values (refer to sub-section 4.7.2).   Under the flexural loading conditions, it was observed for the T section chassis, permanent deformation has taken place and therefore the T section chassis profile is not suitable.

4.9.2 Sub-Chapter Summary

Sub-chapter presented the manufacturing and commercial experimental investigation of the chassis conducted under flexural loading conditions. The test results obtained from experimental testing are in close agreement with FE simulation results.

The results conclude the non-suitability of the I and T section profile for HMV chassis as prohibitively high stresses and permanent deformation occurred in the chassis. which is one of the specific objectives. The percentage differences between the commercial tests and the FE simulation results further validate the accuracy of the adopted FE models.

4.10 Chapter Summary

This chapter has presented the main results of the thesis. The static structural analysis of standard steel chassis and the proposed metal matrix composites is presented. This analysis is performed using different member cross-sections (square and C). Modal analysis of the aforementioned material is also presented for the same cross sections. The best performing cross section was selected for the optimization process. The next four sub-chapters presented the response surface optimization studies of different MMCs using this cross-section. The next sub-chapter presented the FEA structural analysis of the conventional steel chassis for the square section, I Section, and T section profiles and a comparative study has been done to assess their suitability as per industry requirements discussed in the commercial validation. Sigma level and sigma level and the probability distribution are discussed as part of specific objectives.

The next chapter will present the critical outcomes of the research study and a comprehensive conclusion in line with the specific objectives and research hypothesis.

5.1 Research outcomes and Conclusions

The heavy motor vehicle (HMV) industry requires the use of lightweight and structurally efficient materials. Finite element analysis (FEA) in conjunction with modern optimization techniques is a viable approach to studying this problem. These tools combined are able to numerically and visually identify the critical aspect to be optimized in an engineering problem like chassis design.

The objective of this research is to develop a computational approach to designing an optimal chassis. A finite element model of the chassis was developed. The FE structural analysis shows higher stresses near the engine mounting region at the frontal portion of the chassis. Other critical regions of high stress and deformation were identified. The initial research question is how does one vary the geometry of an HMV chassis to be optimal. This work has methodically performed computational FE simulations of various chassis member cross-sections (square, C, T and I). It is shown that by structurally testing and modelling various chassis member profiles and evaluating these via a number of output functions (e.g., equivalent stresses), one can validate whether a particular profile will satisfy industry standards. The square cross-section was found to be the best in terms of its dynamic behavior under static loading. The T and I cross-sections were deemed not acceptable by the industry due to them exceeding industry acceptable standards.

The second research question was on the best way of performing chassis this optimization. In order to computationally optimize the modelled FE design, design points were generated via the design of experiments (DOE) using the Taguchi design. In order to determine the best method (rather than pre-choosing one method), five different methods are explored. The methods are the central composite design (CCD), optimal space fill (OSF), Behnken-Box (B-B), Sparse Grid Initialization (SGI) and the Latin Hypercube (LH) design schemes.

The optimization techniques enabled one to determine the critical range of chassis member dimensions for which stresses, deformation, and mass of chassis are maximum or minimum. The results of the different techniques were compared to find the best design points for a chassis. Furthermore, this research shows that by varying the cross-sectional profiles together with the transverse member dimensions, one is able to achieve better chassis performance.

The third research question was on the other available and practical materials for HMV chassis. In this regard, we proposed three metal matrix composites; Graphite Al GA 7-230, P100/6061 Al and Al 6092/SiC/17.5P. This step was hypothesized as an approach to reducing the weight of the chassis. In conjunction with the chassis member cross-section optimization, a few metal matrix composites (MMC) were modelled for use on the chassis. Their use significantly reduced the weight of the chassis. Although the most weight reduction is achieved using the C-type section, the stresses and deformation generated were very high when compared to the square cross-section.

Of all the MMC materials investigated, the Graphite Al GA 7-230 material shows the lowest deformation of 78.33 mm and Al 6092/SiC/17.5p shows a maximum deformation of 694.83 mm. Therefore Graphite Al GA 7-230 is recommended over other materials.

The following points are key findings in line with the objectives specified in chapter 1:

- Structural analysis results show that the maximum safety factor is observed for the P100/6061 Al MMC material and the lowest safety factor is observed for Graphite Al GA 7-230 MMC.
- The energy absorption and safety factor are evaluated for both square and C profiles. The maximum safety factor is obtained for P100/6061 Al and is minimum for Graphite Al GA 7-230 MMC.
- Vibration analysis results show that for all the materials, the mass participation factor is maximum for the translational x-direction. The high mass participation factor along the x-direction signifies that any external excitation along this direction would likely cause resonance and amplitude build-up.
- Modal analysis results are that the maximum natural frequency and deformation are observed for Graphite Al GA 7-230 MMC. The minimum natural frequency is observed for St52E material. A higher natural frequency is preferred to avoid resonance conditions.
- Equivalent-stress results show that cross-member 1 has the highest sensitivity percentage (84.019%) and cross-member 3 has the lowest sensitivity percentage (21.231%), indicating that equivalent-stress has the greatest effect on cross-member 1 and the least effect on cross-member 3. Cross-member 3 shows the maximum sensitivity percentage for deformation, while cross-member 1 shows the minimum sensitivity percentage. This means that cross-member 3 has the greatest influence on total deformation. For solid mass, all three variables have the same sensitivity percentage, indicating that all three optimization variables have the same effect on chassis mass.
- Out of all the optimization methods, the central composite design took the least time and generated maximum design points (as per the author's observation).
- Using the central composite design (CCD), the weight reduction of HMV chassis obtained using St52E material is 5.37%.
- By using P100/6061 Al MMC material, the chassis mass reduction is 68.15% over the original standard St52E chassis material.
- The weight reduction obtained using Graphite Al GA 7-230 MMC is 68.7% lower than the original St52E chassis material.
- The weight reduction obtained using Al 6092/SiC/17.5P MMC is 64.3% lower than the St52E chassis material.
- The shear stress comparison is made for different profiles i.e. Square section, I section, and T section. The comparison shows minimum shear stress for the square section and maximum shear stress for the T section profile.

- The deformation obtained for the T section profile is maximum and the deformation obtained for the square section is minimum therefore the T section profile is not suitable for chassis application.
- The results obtained from FEA analysis are validated with commercial experimental testing results with less than 10% variation.

5.2 Future Scope and further Recommendations

There is more scope for further research in chassis simulation to solve vibration, frequency response, and mode shape analysis-related problems. This chassis structure could be further dynamically analysed and improved if the industry can invest in MMC testing and development for chassis studies. Some other points to be considered for future work are:

- **Discerning Information on each optimization variable** Using RSM, the effect of each optimization variable on output parameters can be evaluated. Engineers can use the Information in prioritizing the number and type of variables rather than working on multiple variables.

- **Using user-defined optimization techniques**
  The user-defined optimization techniques can improve the design of heavy motor vehicle chassis. The user-defined optimization techniques provide flexibility in setting other conditions (objectives and constraints) based on real-world scenarios. The optimization results obtained could provide better results and good approximation to real-world problems.

- **Using other Response-Surface methods**
  The chassis can be analysed using other Response-Surface methods like cringing, non-parametric regression, and neural networks. However, selecting these methods depends upon various factors like available data, objectives, and constraints. ("Analytics - ANSYS DOE and Design Optimization Tutorial," 2022)[97].

- **Using optimization algorithms**
  Other optimization algorithms, such as screening (based on random sampling), multi-objective genetic algorithm (MOGA), Nonlinear Programming by Quadratic Lagrangian (NLPQL), Mixed-Integer Sequential Quadratic Programming (MISQP), Adaptive Single-Objective Optimization (ASO), and Multi-Objective Adaptive Optimization (MOAO), can be used to analyze the chassis (AMO). ("Analytics - ANSYS DOE and Design Optimization Tutorial" [97].

- **Manufacturing aspects of MMCs**
  MMCs can be made with two or three reinforcements, which provide better mechanical properties than single reinforced composites. There is a need to improve the damage tolerant properties, particularly fracture toughness and ductility in MMCs. Newer green composites,

and new hybrid composites with aluminum matrices could have significantly higher wear resistance, specific stiffness, and fatigue resistance. A critical aspect of MMC manufacturing is the process's parameters which can vary and can significantly influence the mechanical properties and wear behavior of these composites.

Based on these considerations, the overall recommendation is to conduct a structural analysis of the entire truck system because it is related to the actual running condition. This analysis will aid in full-body refinement and improvement. Manufacturing techniques for CFRP chassis could be investigated as future scope of the study to achieve higher quality at a lower cost.

- The chassis structure needs to be investigated for forced vibration analysis i.e., harmonic, or transient vibration as when it is in operation.
- The chassis structure can be investigated for rough and uneven road conditions.
- The chassis structure can be investigated for banking and sharp turning conditions.
- The effect of crack initiation and propagation on chassis structure requires investigation.
- The critical regions of high stress can be modified using a fillet. The reduction of the stress concentration region of the chassis requires investigation.
- The analysis can be conducted for rough driving conditions which can be analyzed under transient structural conditions.
- The structural analysis was conducted for straight lateral members. The different lateral member structure layouts can be optimized to improve the strength and fatigue life of the chassis.
- The real-time road conditions are variable due to potholes or speed breakers and therefore the chassis structure can be further analyzed under such conditions.
- Further study analysis can be conducted with rivets and joints to determine its effect on stresses and deformation.

5.3 Applying techniques to real-world problems

This thesis provides comprehensive details on using the different optimization methods. Apart from applying Response-Surface optimization techniques in chassis, other automobile components like leaf spring, helical coil suspension, wishbone arm, steering, and engine components can also be optimized. The method can also be applied in biomedical and aerospace components that demand a high strength-to-weight ratio.

REFERENCES

[1]   Reportlinker, "Global Automotive Chassis Market to Reach $74.6 Billion by 2027." https://finance.yahoo.com/news/global-automotive-chassis-market-reach-101700108.html? (Accessed Jun. 30, 2022).

[2]   Akshay Jadhav; Anvay Sonpimple, "Automotive Chassis System Market." Accessed: Nov. 15, 2018. [Online]. Available: https://www.alliedmarketresearch.com/automotive-chassis-systems-market

[3]   UNECE, "UNECE endorses stringent new vehicle emissions regulation." https://unece.org/transport/press/unece-endorses-stringent-new-vehicle-emissions-regulation (accessed Jul. 12, 2020).

[4]   J. C. Kelly, J. L. Sullivan, A. Burnham, and A. Elgowainy, "Impacts of Vehicle Weight Reduction via Material Substitution on Life-Cycle Greenhouse Gas Emissions," *Environmental Science & Technology*, vol. 49, no. 20, pp. 12535–12542, Oct. 2015, DOI: 10.1021/acs.est.5b03192.

[5]   "8 Challenges Facing the Transportation Trucking Industry (And How To Manage Them)," *1ST Incident Reporting;* https://1streporting.com/articles/challenges-of-transportation-trucking-industry/ (accessed May 19, 2021).

[6]   Daniela Paddeu; Thomas Calvert; Ben Clark; Graham Parkhurst, "New Technology and Automation in Freight Transport and Handling Systems," 2019. Accessed: Aug. 01, 2022. [Online]. Available: https://assets.publishing.service.gov.uk/government/uploads/system/uploads/attachment_data/file/781295/automation_in_freight.pdf

[7]   P. P. Sarkar, "Analysis of Failure of a Chassis Long Member Manufactured from E-46 Grade Hot-Rolled Steel Coil," *Journal of Failure Analysis and Prevention*, vol. 20, no. 3, pp. 819–832, Jun. 2020, DOI: 10.1007/s11668-020-00881-2.

[8]   J. C. England, H. Hadavinia, D. R. Marchant, and A. Aboutorabi, "Design of Automotive Metal and Composite Chassis Structures," *Recent Patents on Mechanical Engineering*, vol. 3, no. 3, pp. 211–225, Nov. 2010, DOI: 10.2174/2212797611003030211.

[9]   S. Seetharaman and M. Gupta, "Fundamentals of Metal Matrix Composites," in *Encyclopedia of Materials: Composites*, Elsevier, 2021, pp. 11–29. DOI: 10.1016/B978-0-12-819724-0.00001-X.

[10]   M. D. Birajdar and J. y Mule, "Design Modification of Ladder Chassis Frame," vol. 4, no. 10, pp. 3443–3449, 2015.

[11]   Julian. Happian-Smith, *An introduction to modern vehicle design*. Oxford: Butterworth-Heinemann, 2001. [Online]. Available: https://www.elsevier.com/books/introduction-to-modern-vehicle-design/happian-smith/978-0-08-052304-0

[12]   "Backbone chassis Explained," 2020. https://motor-car.net/innovation/car-body/item/15086-backbone-chassis (accessed Dec. 18, 2019).

[13]   "Perimeter Frame." https://www.bikes4sale.in/kb/motorcycle-frame.php (accessed Jan. 01, 2020).

[14]   P. Patole, "Perimeter Frame- All You Need To Know," 2015. https://www.bikesmedia.in/reviews/motorcycle-perimeter-frame-all-you-need-to-know.html

[15]   "Uni-body Frame." http://www.web2carz.com/autos/car-tech/2332/body-onframe-vs-unibody-construction (accessed Oct. 14, 2019).

[16] Anoop Sasidharan, "Automotive chassis-design-v2." https://www.slideshare.net/aanonline/3-automotive-chassisdesignv2 (accessed Jul. 28, 2021).

[17] E. Ghassemieh, "Materials in Automotive Application, State of the Art and Prospects," *New Trends and Developments in Automotive Industry*, 2011, DOI: 10.5772/13286.

[18] H. Saidpour, "Lightweight High-Performance Materials for Car Body Structures," in *NTI Technology Conference, CEME*, 2004, no. June. [Online]. Available: http://roar.uel.ac.uk/1332/1/NTI Presentation.pdf

[19] "Optimization process in ANSYS Workbench software." https://www.mr-cfd.com/services/design-of-experiments-doe/ (accessed Feb. 20, 2020).

[20] "Solving the Unsolvable," *ANSYS INC*. https://www.ansys.com/ (accessed Jan. 28, 2022).

[21] S. Moaveni, "Finite element analysis—theory and application with ANSYS," *Minerals Engineering*, vol. 12, no. 8. pp. 992–993, 1999. DOI: 10.1016/s0892-6875(99)90030-4.

[22] G. Chiandussi, I. Gaviglio, and A. Ibba, "Topology optimization of an automotive component without final volume constraint specification," *Advances in Engineering Software*, vol. 35, no. 10–11, pp. 609–617, 2004, DOI: 10.1016/j.advengsoft.2003.07.002.

[23] C. M. M. Reddy, "Modeling and Analysis of container chassis using FEM.," *IOSR Journal of Engineering*, vol. 4, no. 1, pp. 34–37, 2014, DOI: 10.9790/3021-04153437.

[24] Alex Haigh, "2022 Automotive Industry Trends: Doubling Down on Electric and Connected Cars," *Brand Finance Automotive Industry report*, 2022. https://brandfinance.com/insights/2022-auto-trends (accessed Aug. 01, 2022).

[25] K. H. Bhat KA, Untawale SP, "Failure Analysis And optimization of Tractor Trolley Chassis: An Approach Using Finite Element Analysis," *International Journal of Pure and Applied Research In Engineering And Technology*, vol. 2, no. 12, pp. 71–84, 2014.

[26] S. K.I. and Prof. T. S.B, "Analysis of Ladder Chassis of Eicher 20.16 Using FEM," *IOSR Journal of Applied Geology and Geophysics*, vol. 2, no. 1, pp. 06–13, 2014, DOI: 10.9790/0990-02110613.

[27] M. A. M. Nor, H. Rashid, W. M. F. W. Mahyuddin, M. A. M. Azlan, and J. Mahmud, "Stress analysis of a low loader chassis," *Procedia Engineering*, vol. 41, no. Iris, pp. 995–1001, 2012, DOI: 10.1016/j.proeng.2012.07.274.

[28] M. A. B. Marzuki, M. A. Abu Bakar, and M. F. Mohammed Azmi, "Designing Space Frame Race Car Chassis Structure Using Natural Frequencies Data From Ansys Mode Shape Analysis," *International Journal of Information Systems and Engineering*, vol. 3, no. 1, pp. 54–63, Apr. 2015, DOI: 10.24924/ijise/2015.11/v3.iss1/54.63.

[29] R. Bedri and M. O. Al-Nais, "Prestressed Modal Analysis Using Finite Element Package ANSYS," 2005, pp. 171–178. DOI: 10.1007/978-3-540-31852-1_19.

[30] Y. Ren, Y. Yu, B. Zhao, C. Fan, and H. Li, "Finite Element Analysis and Optimal Design for the Frame of SX360 Dump Trucks," *Procedia Engineering*, vol. 174, pp. 638–647, 2017, DOI: 10.1016/j.proeng.2017.01.201.

[31] H. F. Teo and R. Abd Rahman, "Statics and dynamics structural analysis of a 4.5-ton truck chassis," *Jurnal Mekanikal*, no. 24, pp. 56–67, 2007.

[32] K. G. Nalawade, A. Sabu, and B. P, "Dynamic (Vibrational) and Static Structural Analysis of Ladder Frame," *International Journal of Engineering Trends and Technology*, vol. 11, no. 2, pp. 93–98, 2014, DOI: 10.14445/22315381/ijett-v11p218.

[33] A. Sharma, P. Kumar, A. Jabbar, and M. M. Khan, "Structural Analysis of a Heavy Vehicle Chassis Made of Different Alloys by Different Cross Sections," vol. 3, no. 6, pp. 1778–1785, 2014.

[34] A. S. Abhishek Singh, Vishal Soni, "Structural Analysis of Ladder Chassis for Higher Strength," *International Journal of Emerging Technology and Advanced Engineering*, vol. 4, no. 2, pp. 254–259, 2014, [Online]. Available: www.ijetae.com

[35] S. Godse and D. A. Patel, "Static Load Analysis of Tata Ace Ex Chassis and Stress Optimisation Using Reinforcement Technique," *International Journal of Engineering Trends and Technology*, vol. 4, no. July, pp. 55–58, 2013.

[36] M. S. Bajwa, Y. Raturi, and A. Joshi, "Static Load Analysis of Tata Super Ace Chassis and Its," vol. 4, no. July, pp. 55–58, 2013.

[37] A. Gauchia, V. Diaz, M. J. L. Boada, and B. L. Boada, "Torsional stiffness and weight optimization of a real bus structure," *International Journal of Automotive Technology*, vol. 11, no. 1, pp. 41–47, 2010, DOI: 10.1007/s12239-010-0006-4.

[38] Anurag, A. Singh, A. Tripathi, A. Tiwari, N. Upadhyay, and S. Lal, "Design and analysis of chassis frame," *International Journal of Research and Engineering*, vol. 3, no. 4, pp. 31–34, 2016, [Online]. Available: https://digital.ijre.org/index.php/int_j_res_eng/article/view/147

[39] H. K. Asker, T. S. Dawood, and A. F. Said, "Stress analysis of standard truck chassis during Ramping on block using finite element method," *ARPN Journal of Engineering and Applied Sciences*, vol. 7, no. 6, pp. 641–648, 2012.

[40] Monika S, "Finite Element Analysis of Truck Chassis Frame," *International Research Journal of Engineering and Technology*, vol. 02, no. 03, pp. 1949–1956, 2015.

[41] N. Ingole and D. Bhope, "Stress Analysis Of Tractor Trailer Chassis For Self Weight Reduction," *International Journal of Engineering Science and Technology*, vol. 3, 2011.

[42] N. Tidke and D. H. Burande, "Analysis of HCV Chassis using FEA," *International Engineering Research Journal*, no. 2014, pp. 1–5, 2017.

[43] C. Karaoğlu and N. Sefa Kuralay, "Stress analysis of a truck chassis with riveted joints," *Finite Elements in Analysis and Design*, vol. 38, no. 12, pp. 1115–1130, 2002, DOI: https://DOI.org/10.1016/S0168-874X(02)00054-9.

[44] Y. K. Kutay YILMAZÇOBAN, "Truck Chassis Structural Thickness Optimization With The Help Of Finite Element Technique," *The Online Journal of Science and Technology*, vol. 1, no. 3, pp. 23–29, 2011, [Online]. Available: https://dergipark.org.tr/en/pub/tojsat/issue/22702/242337

[45] R. A. Rahman, M. N. Tamin, and O. Kurdi, "Stress Analysis of Heavy Duty Truck Chassis As a Preliminary Data for Its Fatigue Life Prediction Using Fem," *Jurnal Mekanikal*, no. 26, pp. 76–85, 2008.

[46] V. Veloso, H. S. Magalhães, G. I. Bicalho, and E. S. Palma, "Failure investigation and stress analysis of a longitudinal stringer of an automobile chassis," *Engineering Failure Analysis*, vol. 16, no. 5, pp. 1696–1702, 2009, DOI: 10.1016/j.engfailanal.2008.12.012.

[47] S. Krishna, A. Shetye, and P. Mallapur, "Design and Analysis of Chassis for SAE BAJA Vehicle Design and Analysis of Chassis for SAE BAJA Vehicle," *IOSR Journal of Engineering*, no. August, pp. 51–57, 2019.

[48] J. Denny, K. Veale, S. Adali, and F. Leverone, "Conceptual design and numerical validation of a composite monocoque solar passenger vehicle chassis," *Engineering Science and Technology, an International Journal*, vol. 21, no. 5, pp. 1067–1077, 2018, DOI: 10.1016/j.jestch.2018.07.014.

[49] K. J. Sandeep, "' Design and Simulation of Roll Cage of an All-Terrain Vehicle,'" *International Research Journal of Engineering and Technology*, vol. 07, no. 05, pp. 450–457, 2020.

[50] N. Sinha and K. Kumar, "Efficacy of Vehicle Chassis of Polymeric Composite," *Materials Today: Proceedings*, vol. 22, pp. 2638–2646, 2020, DOI: https://DOI.org/10.1016/j.matpr.2020.03.395.

[51] M. H. Mat and A. R. A. Ghani, "Design and analysis of 'eco' car chassis," *Procedia Engineering*, vol. 41, no. Iris, pp. 1756–1760, 2012, DOI: 10.1016/j.proeng.2012.07.379.

[52] S. S. Kapadne, A. S. Anap, N. K. Jagdale, A. B. Bhutada, and S. N. Khetre, "A Review on Design & Analysis of All Terrain Vehicle Chassis," *International Research Journal of Engineering and Technology (IRJET)*, vol. 06, no. 12, pp. 948–952, 2019.

[53] N. S. Kesarinath, M. Pradeep, S. Senthamilarasu, and L. Vijayaprapakar, "Fabrication of all-terrain vehicle by using continuously variable transmission system," *International Journal of Innovative Research in Advanced Engineering*, vol. 6, no. 03, pp. 8–12, 2019.

[54] K. V. R. S. N. Murthy, K. S. Manishankar, and N. K. Praveen, "Design and Analysis of BAJA Rollcage," *International Research Journal of Engineering and Technology*, vol. 7, no. 3, pp. 4563–4569, 2020.

[55] Mane and Shripad, "A Brief Study of Chassis of a BAJA ATV and its Analysis," *International Journal of Innovative Research in Science, Engineering and Technology*, vol. 7, no. 3, pp. 2924–2936, 2018, DOI: 10.15680/IJIRSET.2018.0703153.

[56] N. Sharma, "Design Report on ATV," *International Journal of Innovative Science and Research Technology*, vol. 2, no. 12, pp. 35–45, 2017, [Online]. Available: www.ijisrt.com

[57] Harshit Raj, "Design and Analysis of the Roll Cage of an ATV," *International Journal of Engineering Research and*, vol. V6, no. 09, pp. 1–5, 2017, DOI: 10.17577/ijertv6is090001.

[58] C. A. Vivas-López, D. Hernandez-Alcantara, J. C. Tudón-Martínez, and R. Morales-Menendez, "Review on global chassis control," *IFAC Proceedings Volumes (IFAC-PapersOnline)*, vol. 46, no. 2, pp. 875–880, 2013, DOI: 10.3182/20130204-3-FR-2033.00040.

[59] V. Saplinova, I. Novikov, and S. Glagolev, "Design and specifications of racing car chassis as a passive safety feature," *Transportation Research Procedia*, vol. 50, no. 2019, pp. 591–607, 2020, DOI: 10.1016/j.trpro.2020.10.071.

[60] S. Rawal, "Metal-matrix composites for space applications," *JOM: the journal of the Minerals, Metals & Materials Society* ·, vol. 53, no. 4, pp. 14–17, 2001, DOI: 10.1007/s11837-001-0139-z.

[61] N. Sinha and K. Kumar, "Optimization of volumetric composition and cross-section of carbon reinforced epoxy based polymeric composite tubes in spaceframe chassis," *Materials Today: Proceedings*, vol. 18, pp. 3812–3820, 2019, DOI: 10.1016/j.matpr.2019.07.319.

[62] F. Nturanabo, L. Masu, and J. Baptist Kirabira, "Novel Applications of Aluminium Metal Matrix Composites," in *Aluminium Alloys and Composites*, IntechOpen, 2020. DOI: 10.5772/intechopen.86225.

[63] Karl U. Kainer, *Metal matrix composites : custom-made materials for automotive and aerospace engineering*. Weinheim: Wiley-VCH Verlag GmbH, 2006.

[64] P. K. Rohatgi, C. Xiang, and N. Gupta, "4.11 Aqueous Corrosion of Metal Matrix Composites," in *Comprehensive Composite Materials II*, P. W. R. Beaumont and C. H. Zweben, Eds. Oxford: Elsevier, 2018, pp. 287–312. DOI: https://DOI.org/10.1016/B978-0-12-803581-8.09985-9.

[65] M. Avalle, G. Chiandussi, and G. Belingardi, "Design optimization by response surface methodology: application to crashworthiness design of vehicle structures," *Structural and Multidisciplinary Optimization*, vol. 24, no. 4, pp. 325–332, 2002, DOI: 10.1007/s00158-002-0243-x.

[66] A. Y. Aydar, "Utilization of Response Surface Methodology in Optimization of Extraction of Plant Materials," in *Statistical Approaches With Emphasis on Design of Experiments Applied to Chemical Processes*, V. Silva, Ed. Rijeka: IntechOpen, 2018. DOI: 10.5772/intechopen.73690.

[67] A. Y. A. E.-V. Silva, "Utilization of Response Surface Methodology in Optimization of Extraction of Plant Materials," Rijeka: IntechOpen, 2018, p. Ch. 10. DOI: 10.5772/intechopen.73690.

[68] K. M. Bower, "WHAT IS DESIGN OF EXPERIMENTS." https://asq.org/quality-resources/design-of-experiments#:~:text=Design of experiments (DOE) is,parameter or group of parameters. (accessed Jan. 10, 2020).

[69] A. K. Das and S. Dewanjee, "Chapter 3 - Optimization of Extraction Using Mathematical Models and Computation," in *Computational Phytochemistry*, S. D. Sarker and L. Nahar, Eds. Elsevier, 2018, pp. 75–106. DOI: https://DOI.org/10.1016/B978-0-12-812364-5.00003-1.

[70] M. Esteban-Bravo, A. Leszkiewicz, and J. M. Vidal-Sanz, "Exact optimal experimental designs with constraints," *Statistics and Computing*, vol. 27, no. 3, pp. 845–863, 2017, DOI: 10.1007/s11222-016-9658-x.

[71] J. Liu, J. Wang, C. Leung, and F. Gao, "A multi-parameter optimization model for the evaluation of shale gas recovery enhancement," *Energies (Basel)*, vol. 11, no. 3, 2018, DOI: 10.3390/en11030654.

[72] nist MATECH, "Response surface model example." https://www.itl.nist.gov/div898/handbook/pri/section4/pri473.htm (accessed Feb. 12, 2020).

[73] B. Ait-Amir, P. Pougnet, and A. el Hami, "6 - Meta-Model Development," in *Embedded Mechatronic Systems 2*, A. el Hami and P. Pougnet, Eds. Elsevier, 2015, pp. 151–179. DOI: https://DOI.org/10.1016/B978-1-78548-014-0.50006-2.

[74] R. Plasun, "Central Composite Designs." https://www.iue.tuwien.ac.at/phd/plasun/node32.html (accessed Jan. 10, 2020).

[75] "Overview of Space-Filling Designs," 2018. https://www.datadvance.net/product/pseven-core/generic-tool-for-design-of-experiments/ (accessed Feb. 12, 2020).

[76] G. Faber, "Uber stetige Funktionen. Mathematische Annalen," *Mathematische Annalen*, vol. 66, no. 1, pp. 81–94, Mar. 1908, DOI: 10.1007/BF01450912.

[77] H. Yserentant, "On the multi-level splitting of finite element spaces," *Numerische Mathematik*, vol. 49, no. 4, pp. 379–412, 1986, DOI: 10.1007/BF01389538.

[78] H. Yserentant, "Hierarchical bases," in *ICIAM 91*, 1992, pp. 256–276.

[79] C. Zenger, "Sparse grids," in *Notes on numerical fluid mechanics, Parallel algorithms for partial differential equations: proceedings of the Sixth GAMM-Seminar*, 1991, no. 31, p. 255.

[80] M. GRIEBEL, "A parallelizable and vectorizable multi-level algorithm on sparse grids," in *Notes on numerical fluid mechanics, Parallel algorithms for partial differential equations: proceedings of the Sixth GAMM-Seminar*, 1991, no. 31, p. 255.

[81] H.-J. Bungartz, "Dünne Gitter und deren Anwendung bei der adaptiven Lösung der dreidimensionalen Poisson-Gleichung," 1992.

[82] M. Griebel, M. Schneider, and C. Zenger, "A combination technique for the solution of sparse grid problems," *Iterative Methods in Linear Algebra*, pp. 263–281, 1992.

[83] J. Garcke, "Sparse Grids in a Nutshell," 2012, pp. 57–80. DOI: 10.1007/978-3-642-31703-3_3.

[84] "Ansys for Robust Design & Optimisation." https://wildeanalysis.co.uk/software/design-simulation/ansys/optimisation/ (accessed Mar. 10, 2020).

[85] P. N. Koch, R.-J. Yang, and L. Gu, "Design for six sigma through robust optimization," *Structural and Multidisciplinary Optimization*, vol. 26, no. 3, pp. 235–248, 2004, DOI: 10.1007/s00158-003-0337-0.

[86] YY. Perng, "Optimization in ANSYS Workbench," 2011.

[87] "ANSYS Library file." https://www.ansys.com/academic/.

[88] "Materials Used in Chassis and Body Components of the Vehicle." https://www.automotive-technology.com/articles/materials-used-in-chassis-and-body-components-of-the-vehicle (accessed Dec. 18, 2019).

[89] S. P. Rawal, "Metal-matrix composites for space applications," *JOM*, vol. 53, no. 4, pp. 14–17, 2001, DOI: 10.1007/s11837-001-0139-z.

[90] "Basic Steps of the Finite Element Method," 2019. http://davis.wpi.edu/~matt/courses/fem/fem.htm (accessed Nov. 18, 2019).

[91] A. Agarwal and L. Mthembu, "Numerical Modelling and Multi-Objective Optimization Analysis of Heavy Vehicle Chassis," *Processes*, vol. 9, no. 11, p. 2028, Nov. 2021, DOI: 10.3390/pr9112028.

[92] Amreen Taj, Saleem Sab Doddamani, and T N Vijaykumar, "Vibrational Analysis of Aluminium Graphite Metal Matrix Composite," *International Journal of Engineering Research and*, vol. V6, no. 04, Apr. 2017, DOI: 10.17577/IJERTV6IS040720.

[93] S. Madeira, O. Carvalho, V. H. Carneiro, D. Soares, F. S. Silva, and G. Miranda, "Damping capacity and dynamic modulus of hot pressed AlSi composites reinforced with different SiC particle-sized," *Composites Part B: Engineering*, vol. 90, pp. 399–405, Apr. 2016, DOI: 10.1016/j.compositesb.2016.01.008.

[94] Z. Gxowa, "Deformation behaviour of aluminum low-micron MMCs and MMNCs at warm working temperatures (0.3-0.5 Tm)," *J South Afr Inst Min Metall*, vol. 116, no. 10, pp. 963–968, 2016, DOI: 10.17159/2411-9717/2016/v116n10a11.

[95] D. D. L. Chung, "Review: Materials for vibration damping," *Journal of Materials Science*, vol. 36, no. 24, pp. 5733–5737, 2001, DOI: 10.1023/A:1012999616049.

[96] Ren Max Yi and Vipradas Aditya, "ANSYS DOE and Design Optimization Tutorial," *Design Informatics Lab, School for Engineering of Matter, Transport and Energy*, 2022.

https://designinformaticslab.github.io/productdesign_tutorial/2016/11/20/ansys.html (accessed Jan. 05, 2022).

[97] Max Yi Ren and Aditya Vipradas, "Analytics - ANSYS DOE and Design Optimization Tutorial," *Design Informatics Lab*, 2022. https://designinformaticslab.github.io/productdesign_tutorial/2016/11/20/ansys.html (accessed Jan. 15, 2022).

[98] Bruker Nano Surfaces, "Evaluating Stress, Strain, and Failure-Mode in Bending Test," *AZO materials*, 2016. https://www.azom.com/article.aspx?ArticleID=12807 (accessed Mar. 15, 2020).

[99] A. Agarwal and L. Mthembu, "Numerical Modelling and Multi-Objective Optimization Analysis of Heavy Vehicle Chassis," *Processes*, vol. 9, no. 11, p. 2028, Nov. 2021, DOI: 10.3390/pr9112028.

[100] A. Agarwal and L. Mthembu, "Weight optimization of heavy-duty truck chassis by optimal space fill design using light weight Graphite Al GA 7-230 MMC," *Materials Today: Proceedings*, no. xxxx, 2021, DOI: 10.1016/j.matpr.2021.11.053.

[101] A. Agarwal and L. Mthembu, "Modelling and FE Simulation of HVC Using Multi Objective Response Surface Optimization Techniques," *Revue des composites et des matériaux avancés*, vol. 31, no. 6, pp. 307–315, Dec. 2021, DOI: 10.18280/rcma.310601.

[102] A. Agarwal and L. Mthembu, "Design and Response Surface Optimization of Heavy Motor Vehicle Chassis Using P100/6061 Al MMC," in *Recent Advances in Materials and Modern Manufacturing*, Lecture No., D. P. I. A. Palani, P. Sathya, Ed. Singapore: Springer Singapore, 2022, pp. 1–12. DOI: 10.1007/978-981-19-0244-4_1.

[103] A. Agarwal and L. Mthembu, "FE design analysis and optimization of heavy-duty truck chassis using sparse grid initialization technique," *Materials Today: Proceedings*, 2022, DOI: https://DOI.org/10.1016/j.matpr.2022.01.471.

[104] A. Agarwal and L. Mthembu, "Structural Analysis and Optimization of Heavy Vehicle Chassis Using Aluminium P100/6061 Al and Al GA 7-230 MMC," *Processes*, vol. 10, no. 2, p. 320, Feb. 2022, DOI: 10.3390/pr10020320.

[105] A. Agarwal and L. Mthembu, "Structural analysis and weight optimization of automotive chassis by Latin hypercube sampling using metal matrix composites," *Materials Today: Proceedings*, 2022, DOI: https://DOI.org/10.1016/j.matpr.2022.02.059.

[106] A. Agarwal and L. Mthembu, "Investigation of Dynamic Factors in Different Sections of HVC by Static and Free Vibration Modal Analysis," *Annales de Chimie - Science des Matériaux*, vol. 46, no. 2, pp. 75–84, Apr. 2022, DOI: 10.18280/acsm.460203.

APPENDIX: A

MANUFACTURING AND EXPERIMENTAL TESTING INFORMATION

The current Appendix presents detailed information on the manufacturing and experimental testing of heavy motor vehicle chassis. The manufacturing process comprises 14 operations i.e., from procurement of raw material to driveline testing.

A.1 PFD Chart

The process flow diagram associated with chassis manufacturing is shown in figure A.1.

No.	Operation	Failure Mode	Control / Specification	Prevention
60	Lifting of Frame after Boxing	1. Unsafe lifting of frame	OK boxed frame	Safe lifting of frame
70	Assembly1	1. Fit Bolt Asembly 2. Nut Assembly 3. Washer Assembly 4. SWC Assembly 5. Trunion Assembly 6. Helper Bracket Assembly 7. Bump Stopper Assembly 8. L Bkt Assembly	1. No loose part 2. No wrong Part 3. No part Missing 4. Correct Orientation of Parts	1. Assembly of Child parts as per BOM/ Drawing 2. Tightening by Guns 3. Corrct Tools 4. Air Pressures 5. Operator training
80	Assembly 2	1. Front Engine Mounting Bkt Assembly LH/RH 2. Shield Panel Assembly LH/RH 3. Rear Engine Mounting Assembly LH/RH 4. Engine Mounting Cross Member Assembly LH/RH 5. Engine Support Assembly LH/RH 6. Shockup Bracket Assembly LH/RH 7. Shockup Plate Assembly LH/RH 8. Cable Shift Select Assembly LH/RH 9. Cable Guard Assembly LH/RH 10. Damper Mounting Assembly LH/RH 11. Bumper Mounting Assembly LH/RH 12. Nut Welding	1. No loose part 2. No wrong Part 3. No part Missing 4. Correct Orientation of Parts	1. Assembly of Child parts as per BOM/ Drawing 2. Tightening by Guns 3. Use of Adequate Tools 4. Air Pressures 5. Operator Training 6. Follow Sequencing
	Online Rework	1. Part Missing 2. In-complete Operation	As per specifications	1. Proper Tooling
90	Torqueing	1. Torqueing as per specification	1. No loose part & right torqueing of parts / hardware as per specification	1. Torqueing by Calibrated torque wrench
100	Lifting of Frame to Painting	1. Unsafe lifting of frame	OK assembled frame	Safe lifting of frame
110	Painting	1, Paint Viscosity 2. Paint Make	1. Asthetic appearance and paint DFT	1. No run down, 2. Paint adherance 3. Spray Gun
120	Lifting of frame after painting.	Unsafe lifting of frame	OK Painted frame	Safe lifting of frame.
130	PDI	wrong process	Product specification	1. Right labelling 2. PDI as per check sheet and Work Instruction.
140	Rework & Retorquing	wrong process	Product specification	1. Reworking 2.Retorquing
150	Labelling	Wrong lable	Production plan, production, Dispatch document	Lable writing
160	Lifting of frame after PDI for dispatch	Unsafe liftng of frame	OK Frame	Safe lifting of frame
170	Dispatch	wrong process	Loading OK Frames	As per packaging standard , work instruction / Shipment conditions

Prepared By: Rohan Verma **Approved By : Arun Patil**

Figure A.1: Process Flow Diagram for chassis manufacturing

The various operations conducted for the manufacturing of chassis are discussed :

A.2 Operational Description

➢ **OPN 0**

In this operation checking of Raw material as per the requirement given in PFD held for knowing parameter to be checked in the Inspection.

➢ **OPN 10**

This handling of Side Members will be done before reaming operation, as side members are bulky & long so should be placed properly for further operations. The selection of side members should be correct & the Handling should be perfect.

➢ **OPN 20**

This Operation is held by Reaming machine. Reaming Hole should be done for 17H7 in which machining spindle Runout & Reamer Runout should be monitored.

➢ **OPN 30**

Handling of side members & after reaming so that other child parts can be mounted easily on the chassis frame. Wrong side members should not be selected during assembly operations & also maintaining required precautions while handling Side Members due to their longevity, it's critical to handle sometimes.

➢ **OPN 40**

Loading of Side members for boxing will be occurred lifting should be proper while boxing. Also handling will be performed properly so that major issues cannot be raised.

➢ **OPN 50**

Boxing performed during this operation fitment of side members; Cross members & hardware should be done in a better way. The right side of the cross-member should be selected and located perfectly & orientation should be in the proper manner. Frame width to be maintained so that alignment is ok.

➢ **OPN 60**

Lifting of the frame after boxing should be performed in the operation. Safe lifting should be required, same boxing should be perfect.

➢ **OPN 70**

Assembly 1 will be performed in this operation & bellow child parts should be assembled while doing this-

.1 Fit Bolt Assembly

2. Nut Assembly

3. Washer Assembly

4. SWC Assembly

5. Trunnion Assembly

6. Helper Bracket Assembly

7. Bump Stopper Assembly

8. L Bkt Assembly

➢ **OPN 80**

Assembly 2 will be performed in this operation & bellow child parts should be assembled while doing this

1. Front Engine Mounting Bkt Assembly LH/RH
2. Shield Panel Assembly LH/RH
3. Rear Engine Mounting Assembly LH/RH
4. Engine Mounting Cross-member Assembly LH/RH
5. Engine Support Assembly LH/RH
6. Shock up Bracket Assembly LH/RH
7. Shock up Plate Assembly LH/RH
8. Cable Shift Select Assembly LH/RH
9. Cable Guard Assembly LH/RH
10. Damper Mounting Assembly LH/RH
11. Bumper Mounting Assembly LH/RH
12. Nut Welding

➢ **OPN 90**

In this operation, Torquing will be done as per specification in which required no loose part & right torquing of parts should be held of hardware as per specification should be performed.

➢ **OPN 100**

Now, the frame will be lifted for painting in which lifting should be safe & all assembly parts will be rechecked before lifting so that required rework can be performed.

➢ **OPN 110**

The painting will be performed in this operation so, Paint viscosity, make & appearance should be maintained throughout the frame. Paint thickness should be measured by a DFT meter. Aesthetically frame should be ok.

➢ **OPN 120**

Lifting of Frame will be held after painting of Chassis frame, Lifting will be critical as no aesthetic damage will be accepted during this movement as all child parts assembly is completed & the assembly is heavy.

➢ **OPN 130**

100% Inspection done in this operation. After completing all the operations parts were moved to the Final Inspection area for 100% Checking of the Parts as per the inspection plan, For Knowing Dimension Results on the part. If parts are found not Ok, the parts get Rejected & put in the NCP area.

A.3 Material Testing Report

The material testing report is generated for ST52E material as shown in figure A.2. The induction heat treatment process is conducted followed by hardness testing and metallographic observation. The magnetic particle inspection was conducted, and no cracks were observed.

METALMAN AUTO PVT. LTD.		Form No.	MAPL/F/PROD/51
METALMAN AUTO PVT. LTD. Material Test Report		Issue:	01
		Sheet No.	1/1

Report No.	18030018	Date	15/09/2020
Part Name.	HMV CHASSIS	Raw Material	ST52E
Part No./ Rev. No.	R140671(218384RE/B)20010302	Raw Material Used	ST52E
Material TC	Received Ok	Heat No.	B239(5567)
Heat Treatment Process	Induction Hard. & Temp. (HT30T)	Quantity	10 Nos.
Induction Hardening	K22C18	Chemical Composition	
Batch, done & date	14/09/2020	Report No. & Date	

Induction Heat Treatment Process Parameters (as per Std.)

Machine no.	2	KW	100 KW	
Location	X	Location	X	OK
Power (kW)%	18 %	Rotation	no	
Start Heating Time	After2 secs	Frequency KHZ	30 khz	
Heat Dwell Time	1.65 Sec	Polymer% (Without factor)	2%	
Scan Speed (Feed)	150 mm/min	Total Cycle Time	14 Sec	
Total Heating Time	2 sec	Quenching Bath Temp.	27 °C	
Total Quenching Time	8 secs	Tempering Temp.	160°C @ 90 min.	

Quality requirements for induction hardening for 'X' (as per std.)

Test	Specification	Observation			Remark
Hardness	52 − 59 HRC	56 - 57 HRC			OK
Case Depth @ X Loc.	1.0 mm min. @ 440 HV1 (45 HRC)	Pad 1	A = 2.30 mm		OK
			B = 2.20 mm		
		Pad 2	A = 2.40 mm		
			B = 2.10 mm		
MPI	No Crack	No Crack Found			OK

Metallographic Observation:

Test	Specification	Observation		Remark
Case Microstructure	Fine Tempered Martensite at 400X	Fine Tempered Martensite		OK
	5% ITP depth at 100X	Paid 1	Paid 2	OK
		A- 1.3, B- 1.2 mm	A-1.4, B-1.3 mm	
	50 % Martensite Depth at 100X	A -1.9, B − 1.8 mm	A-1.8, B- 1.8 mm	OK
	HAZ at 100X	A-2.5, B − 2.3 mm	A -2.5, B -2.3 mm	OK
Core Microstructure	Pearlite + Ferrite	Ferrite / Pearlite		OK
Grain	5 − 8	7		OK

Figure A.2: Material Test report for St52E

A.4 Vehicle Testing for square-section chassis

Using an example geometry, a three-point-bend test can be used to examine stress-strain performance, elastic modulus in bending (flexural modulus), and failure limits in bending [98]. The ASTM E855, ASTM D790 or ISO 178, and ASTM C1684 or C1161 standards, respectively, address the properties of flat metallic spring materials, flexural properties of plastics, and three-point bend tests for ceramics [98]. This test can determine the material's fracture toughness, as figure A.3.
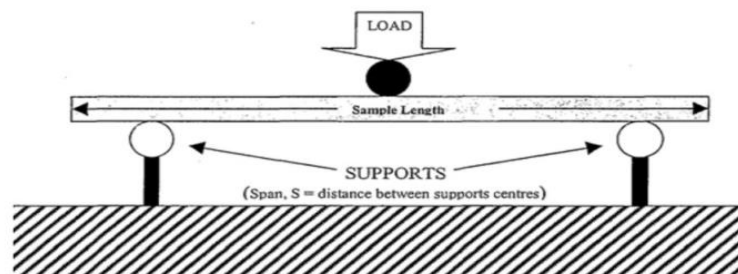

Figure A.3: Commercial Vehicle chassis test setup conditions[98]

APPENDIX B

SUMMARY OF THE ARTICLES PUBLISHED

This appendix presents a summary of the articles published based on this thesis:

1. A. Agarwal, L. Mthembu (2021). **Numerical Modelling and Multi-Objective Optimization Analysis of Heavy Vehicle Chassis**. Processes, 9(11), 2028. DOI: http://dx.doi.org/10.3390/pr9112028. See ref.[99]. **SCOPUS, SCIE (IF 3.352)**

In this paper, the chassis is optimized using Taguchi Design of Experiments (DOE). We used central composite design (CCD) and optimal space-filling (OSF) design schemes. The chassis mass reduction obtained from the CCD scheme is approximately 5.3% and from the OSF is approximately 4.35%.

2. A. Agarwal, L. Mthembu (2021). **Weight Optimization of Heavy-Duty Truck Chassis by Optimal Space Fill Design Using Light Weight Graphite Al GA 7-230 MMC**. Materials Today: Proceedings. DOI:10.1016/j.matpr.2021.11.053. See ref [100] **SCOPUS, CPCI**

This paper focused on optimizing the heavy-duty TATA 1612 truck ladder-type frame by substituting its material from conventional steel with the lightweight Graphite Al GA 7–230 MMC material without compromising the safety and strength using the OSF design scheme. Analysis shows around 70% reduction in mass of chassis.

3. A. Agarwal, L. Mthembu (2021). **Modelling And FE Simulation of HVC Using Multi-Objective Response-Surface Optimization Techniques**. Revue des Composites et des Matériaux Avancés-Journal of Composite and Advanced Materials, Vol. 31, No. 6, pp. 307-315. DOI: https://doi.org/10.18280/rcma.310601. See ref [101] **SCOPUS, ESCI**

In this paper, the design and optimization of a heavy vehicle chassis are performed using a central composite design & the OSF design scheme (s) with the Al6092/SiC/17.5p MMC. The use of discontinuously Reinforced Aluminium-Matrix Composites aided in reducing the weight of the chassis by 66.25% and 66.68% by using CCD and the OSF design, respectively, without much reduction in strength of the chassis.

4. A. Agarwal, L. Mthembu (2022). **Optimization of Heavy Motor Vehicle Chassis Using P100/6061 Al MMC**. Lecture Notes in Mechanical Engineering, Springer Singapore. DOI: https://doi.org/10.1007/978-981-19-0244-4_1. See Ref [102] **SCOPUS, CPCI**

This paper focused on reducing the weight of chassis using lightweight P100/6061 Al MMC and optimization using an OSF design scheme. The most significant findings of the results have shown that cross-member one width has maximum effect on equivalent-stress and cross-member two widths have minimum effect on equivalent-stress and 67% weight reduction is achieved.

5. A. Agarwal, L. Mthembu (2022). **FE Design Analysis and Optimization of Heavy-Duty Truck Chassis Using Sparse Grid Initialization Technique**. Materials Today: Proceedings, ISSN 2214-7853. DOI: https://doi.org/10.1016/j.matpr.2022.01.471. See Ref [103]. **SCOPUS, CPCI**

   This article shows the static structural analysis and optimization of a ladder-type truck chassis made of Al P100/6061 Al MMC utilizing a sparse grid initialization optimization technique. The actual mass of the chassis made of standard St52E is 214.64 kg, whereas the mass of the chassis composed of MMC is 67.922 kg, showing a mass reduction of nearly 68.4 percent.

6. A. Agarwal, L. Mthembu (2022), **Structural Analysis and Optimization of Heavy Vehicle Chassis Using Aluminium P100/6061 Al and Al GA 7-230 MMC**. Processes, 10, 320. DOI: https://doi.org/10.3390/pr10020320. See Ref [104] **SCOPUS, SCIE (IF 3.352)**

   The Box–Behnken design approach is used in this paper to create and optimize chassis using P100/6061 Al and Al GA 7-230 MMC, respectively. The use of these materials helped to reduce the weight of the chassis by 68% and 70%, respectively.

7. A. Agarwal, L. Mthembu (2022). **Structural Analysis and Weight Optimization of Automotive Chassis by Latin Hypercube Sampling Using Metal Matrix Composites.** Materials Today: Proceedings, ISSN 2214-7853. DOI: https://doi.org/10.1016/j.matpr.2022.02.059. See Ref [105] **SCOPUS, CPCI**

   The Latin hypercube approach is used in this study to design and optimize a ladder-type frame for a heavy-duty truck made of Al GA 7-230 and Al6092/SiC/17.5p MMC materials. Using these materials, the chassis mass is reduced to 62.564 kg and 71.502 kg, respectively.

8. A. Agarwal, L. Mthembu (2022). **Investigation of dynamic factors in different Sections of HVC by Static and Free Vibration Modal Analysis**; Annales de Chimie - Science des Matériaux, Vol. 46, No. 2, pp. 75-84. DOI: https://doi.org/10.18280/acsm.460203. See Ref [106] **SCOPUS, ESCI**

   This paper focuses on a static structural and vibrational modal analysis of the chassis considering both conventional Structural steel and P100/6061 Al Metal Metrix Composite. The mass participation factor, natural frequency, and mode shapes are evaluated for the square and C section, respectively, using the finite element technique. It was observed that the use of the C section causes a 1.69% increase in deformation for all the natural frequencies as compared to the square section in both cases; hence it is not desirable for the design.

9. A. Agarwal, L. Mthembu (2022). **FE Structural Analysis and Experimental Investigation of HMV Chassis**. Emerging Trends in Mechanical and Industrial Engineering. Lecture Notes in Mechanical Engineering, Springer Singapore DOI: 10.1007/978-981-19-6945-4_70 <u>SCOPUS, CPCI</u>.

This work focused on the FEA structural analysis of the chassis with the primary goal of selecting the appropriate section profile on transverse elements of the chassis from the c, T, I, and square sections profile geometry. The experimental examination was carried out under flexural loading and the results were found to be quite close to the modeling results. As a result of the persistent deformation in the chassis, the results conclude that the I and T sections are unsuitable for the HMV chassis.

APPENDIX C

EXTERNAL FEEDBACK REPORT(S) FROM THE INDUSTRY

REPORT 1:

From: Ankit Parekh, P.E.   29 July 2022
Technical Manager, Motovac Group

Re: Feedback on the engineering Study titled: DESIGN OPTIMIZATION OF HEAVY MOTOR VEHICLE CHASSIS (Agarwal Abhishek-University of South Africa)

- **Overview of findings-**

This work comes up with innovative cost-reduction techniques to reduce the cost of replacing conventional ferrous materials with metal matrix composites. The experimental testing validates detailed FE structure analysis findings on traditional steel chassis to check the consideration of using square sections instead of C, I, or T section. The static, vibrational analysis and optimization of a TATA 1612 chassis using the metal matrix composite (MMC) materials resulted in excellent deformation & weight reduction results using Graphite Al GA 7-230, P100/6061 Al despite the prohibitive stresses obtained. These findings will benefit any R & D team to prefer which of the MMCs can be used per their requirement, especially where increasing fuel prices are serious concerns, along with other technical requirements. However, the potential for Al MMCs in this area is barely tapped and represents an excellent opportunity for substantial growth. Aluminum metal matrix composites are suitable replacements, not only for steel but also for aluminum alloys in various automotive systems and components.

- **Knowledge base: Requirement of weight-saving R & D-**

There are many ways to achieve light weight without compromising the strength and safety requirements. Ideally, it is common practice to completely replace the existing structural material with the material of higher yield strength, with a possible reduction in section dimensions. The other way of achieving weight savings is to selectively replace conventional steel in specific areas with lighter materials, as suggested in this work. Further studies involving aluminum-intensive designs also showed the potential for minimal net-vehicle costs with substantial mass reductions.
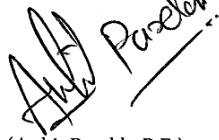
By applying the various mass reduction techniques, the mass can be reduced independent of vehicle size, functionality, class, or model. Aluminum alloys and composites are also competing to replace many various traditional steel components in vehicles, such as valve covers, torque converter and transmission housings, crankcase, control arms, cradles, suspension links, door frames, steering wheels, dashboards, sheet panels and beams are also being replaced by alloy aluminium alloys and composites. Since the chassis is the heaviest part of a vehicle, the strength and toughness of the chassis can affect vehicle performance and is essential to occupant survivability in severe crashes. Therefore, more complex, and sophisticated industrial manufacturing demands a broader selection of materials that provide high stiffness-to-weight, hardness and wear resistance, and lower CTE than conventional ones. Applications of aluminum and composite materials with aluminum base design produce high-performance vehicles with safety improvements and energy efficiency that are resistant to corrosion and with

reduced masses. I am confident that apart from the core body frame structure, weight-saving technology features in other areas can add up to substantial secondary weight reductions elsewhere.

▪ **Conclusion-**

From the preceding review, it is evident that the future of MMCs in various industrial and commercial applications is very bright. The main challenges and barriers that have been identified in the present industry include lack of property modeling, lack of design data, and high costs of primary and secondary processes. Several other challenges must be overcome to intensify the engineering usage of MMCs. Design, research, product development efforts, and business development skills are required to overcome these challenges. This research study will accelerate and help potentially in further development of R&D opportunities to redefine new roles and the possibility of MMCs in larger automotive applications. The design of composite materials with specific properties can, moreover, be accomplished using finite element modelling techniques. It is possible to predict the properties of a particular material of specified composition using these techniques. In the same way, using these techniques makes it possible to design materials to offer selected properties. The report has well covered the scope of choosing the MMCs over steel using a few Taguchi-based optimization methods.

This review is entirely based on the academic work's technical and industrial aspects provided. To the best of my knowledge and belief, no conflict of interest exists with any financial interest, membership, employment, consultancies, patent-licensing arrangements, or non-financial interest in the subject matter or materials discussed here.

MOTOVAC (PTY) LTD
P.O. Box 2486 Plot 4803
Old Lobatse Road, GABORONE
Tel: 3974163   Fax: 3906341
VAT No: C00737501113

(Ankit Parekh, P.E.)
Technical Manager (Mechanical Engineering)
Motovac Group
South Africa. Botswana. Namibia

REPORT 2:

Industry feedback on: DESIGN OPTIMIZATION OF HEAVY MOTOR VEHICLE CHASSIS (Abhishek Agarwal-University of South Africa)

This research study shows the critical aspects of the HMV chassis design, safety, selection of appropriate sections and new materials. These aspects are essential for design engineers and must be considered in all production processes, especially during assumptions and constructions of chassis or frames.

The design process of chassis and frames, especially in special heavy vehicles, is a fundamental stage in the total production process involving solutions from conception to evaluation, including safety, comfort, aesthetics, ergonomics, manufacture, and cost to find the optimal solution within certain constraints.

The vehicle's dynamic properties and static or geometric parameters depend on the chassis. Also, vibration phenomena in heavy vehicles are an essential issue. When a chassis is modified, structural calculations must be conducted to ensure the predicted stress in the chassis isn't too high, as considered in the study.

In everyday use, a chassis will bend and twist in regular operation, so if there's a sudden change from a low-stressed area to a high-stress zone, unusual performance occurs, resulting in a stiff section meeting a sloppy section. Therefore, one of the fundamental and most important stages is the proper development of the chassis and frame of the vehicle significantly. Truck chassis are regularly modified for change of purpose, and the critical aspects of doing this are well sorted out from prior practical performance and millions of miles of real-life experiences.

Another critical issue of vehicle design is selecting the suitable material according to required experimental and/or analytical data and properties. Nowadays, a wide range of alloys in available with different properties, heat treatments and manufacturing opportunities.
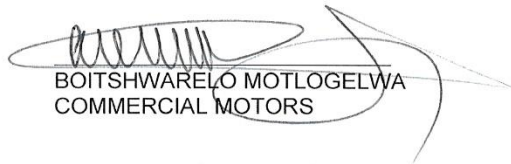
Thus, these new materials as aluminum alloys, and metal matrix composite materials, are more often used even as vehicle bodywork (body panel). Depending on the application, the design engineer has to consider the material and mechanical properties due to the forces expected during the vehicle's operation. A sufficiently strong force will produce a definite amount of

deformation. Thus, the design engineers must understand and compare many parameters of the materials.

In the industry, we want everything to be perfect because of our liability to build a better vehicle, and I know that perfection comes with experience. These issues are significant for vehicle designers and engineers and must be considered in all production processes, especially during assumptions and constructions of chassis or frames. Advanced materials are essential for boosting the fuel economy of modern automobiles while maintaining safety and performance. Because it takes less energy to accelerate a lighter object than a heavier one, lightweight materials offer great potential for increasing vehicle efficiency.

I am confident that this work will provide the fundamental background to choose the optimal design criteria as well as material information for further R& D to implement in the industry.

Best of Luck.

BOITSHWARELO MOTLOGELWA
COMMERCIAL MOTORS

COMMERCIAL MOTORS (PTY) LTD
Plot 5664
Kubu Road
Broadhurst Industrial
P. O. BOX 2276, Gaborone
Botswana
Tel: (267) 3908694
Fax: (267) 3908704

TATA